ANNUAL REPORT
OF THE
INSTITUTE OF PHYSICS
ACADEMIA SINICA

1971

Published by

The Institute of Physics, Academia Sinica
Nankang, Taipei, Taiwan, Republic of China
August 1972

中央研究院物理研究所集刊

編輯委員會

編輯委員

吴大猷（主席）

王唯農（主編）

林爾康

楊毓東

汪羣從

蔣炯

助理編輯

簡來成

總務

余良才

Editorial
Board

T. Y. Wu
W. N. Wang
E. K. Lin
Y. T. Yang
C. T. Wang
C. Chiang

本集刊每年在八月出版一次

非賣品

中央研究院
物理研究所集刊
第二卷

發行人：吳大猷

編輯者：中央研究院物理研究所集刊編輯委員會

出版者：中央研究院物理研究所　臺北市南港區

印刷者：崇文企業有限公司

中華民國六十一年八月出版

中央研究院物理研究所集刊

第二卷

中央研究院物理研究所印行

CONTENTS 目錄

The Clock Paradox in the Relativity……*T. Y. Wu* (吳大猷) and *Y. C. Lee* 1

Investigation of Excited States of ^{4}He through Deuteron-induced Three-particle Reactions on ^{6}Li ……………… *E. L. Haase*, *R. Hagelberg*, and *W. N. Wang* (王唯農) 19

Investigation of T=0 Excited States of ^{4}He Via the ^{4}He (d, d′, t) ^{1}H and ^{4}He (d, d′, d) ^{2}H Reactions ……………… *E. K. Lin* (林爾康), *R. Hagelberg*, and *E. L. Haase* 27

A Study of the Level Structure in ^{57}Fe from the (d, p) Reaction on ^{56}Fe……………… *H. M. Sen*, *A. R. Majumder* and *E. C. Lin* (林爾康) 43

Circle Theorem for Ice-Rule Ferroelectric Method ……………… *K. S. Chang*, *S. Y. Wang* (王守益) and *F. Y. Wu* 65

Investigation of ^{26}Mg (d, p) ^{27}Mg Reaction below 3 MeV ……………… *E. K. Lin* (林爾康), *W. N. Wang* (王唯農), *J. G. Yu* (余建國), and *W. C. Tung* 69

Kinematically Complete Investigation of T=0 Excited State of ^{4}He by Inelastic Scattering of α-particle on ^{4}He ……………… *E. L. Haase*, *W. N. Wang* (王唯農), and *M. A. Fawzi* 71

Boltzmann Equation with Fluctuations ……………… *P. S. Lee*, and *T. Y. Wu* (吳大猷) 73

Differential Cross Sections for Elastic Scattering of Low-Energy Protons from ^{24}Mg and ^{26}Mg ……………… *W. N. Wang* (王唯農), *E. K. Lin* (林爾康), and *C. L. Tung* (董歧龍) 83

Investigation of the ^{27}Al (p, γ) ^{28}Si Reaction in the Proton Energy Range 925—2760 KeV…………*T. H. Hsu* (許東鴻), *E. K. Lin* (林爾康), *C. C. Hsu*, *Y. C. Lin*, *P. K. Tseng*, *C. W. Wang* (王建萬), and *W. S. Hsu* 91

A Sensitive Discharge Switch Function as a Pulse Generator or a Self-tone Modulator……… *B. Chen*, *S. C. Yeh*, and *W. N. Wang* (王唯農) 107

Damped Radio Frequency Sized Effect of Indium Antimonide at Room Temperature……… *Y. T. Yang* (楊毓東) , *H. T. Ho*, *C. C. Pei*, *S. C. Yang*, and *B. H. Yue* ……………………………………………… 113
Excitation Spectra of Magnesium Donors in Silicon… *L. T. Ho* (何侗民) 127
On the Young's Interference Pattern ………………… *C. Chiang* (蔣炯) 139
Properties and Responses of Frog Skin Membranes…*C. Chiang* (蔣炯) 143
A Theory of the Muller-Lyer Illusion …………… *C. Chiang* (蔣炯) 155
Electronic Conduction in Ultra Thin Semi-metal Films ……………………………… *N. T. Liang* (梁乃崇) and *S. Y. Wang* (王守益) 163
大氣及颱風運動模型 I. 邊界條件 ………………………… 大氣物理組同仁 177
颱風中心之運動…………………………………………………… 大氣物理組同仁 199
地轉風假設下區域性大氣運動之探討 ……………………………………………………………………… *K. S. Wang* and *C. T. Wang* (汪羣從) 217
On the Energy Generation and Transformation over the East China Sea durning Winter ……………………………… *L. C. Chien* (簡來成) 229
Diffraction of a Plane Pulse by a Rectangular Opening ………………………………………………………………………… *H. C. Wang* (王懷柱) 243
船舶縱向下水之探討 ……………………*Y. Z. Lee*, *Y. T. Dai* (戴堯天) *C. Y. Liu*, *Y. N. Chen* and *C. T. Wang* (汪羣從) 259

中央研究院物理研究所集刊

第二卷

中央研究院物理研究所印行

CONTENTS 目錄

The Clock Paradox in the Relativity......T. Y. Wu (吳大猷) and Y. C. Lee 1
Investigation of Excited States of ^{4}He through Deuteron-induced Three-particle Reactions on ^{6}Li.......... E. L. Haase, R. Hagelberg, and W. N. Wang (王唯農) 19
Investigation of T=0 Excited States of ^{4}He Via the ^{4}He (d, d', t) ^{1}H and ^{4}He (d, d', d) ^{2}H Reactions.............E. K. Lin (林爾康), R. Hagelberg, and E. L. Haase 27
A Study of the Level Structure in ^{57}Fe from the (d, p) Reaction on ^{56}Fe..........H. M. Sen, A. R. Majumder and E. C. Lin (林爾康) 43
Circle Theorem for Ice-Rule Ferroelectric Method...............K. S. Chang, S. Y. Wang (王守益) and F. Y. Wu 65
Investigation of ^{26}Mg (d, p) ^{27}Mg Reaction below 3 MeV...............E. K. Lin (林爾康), W. N. Wang (王唯農), J. G. Yu (余建國), and W. C. Tung 69
Kinematically Complete Investigation of T=0 Excited State of ^{4}He by Inelastic Scattering of α-particle on ^{4}He..........E. L. Haase, W. N. Wang (王唯農), and M. A. Fawzi 71
Boltzmann Equation with Fluctuations............................P. S. Lee, and T. Y. Wu (吳大猷) 73
Differential Cross Sections for Elastic Scattering of Low-Energy Protons from ^{24}Mg and ^{26}Mg............................W. N. Wang (王唯農), E. K. Lin (林爾康), and C. L. Tung (董岐龍) 83
Investigation of the ^{27}Al (p, γ) ^{28}Si Reaction in the Proton Energy Range 925—2760 KeV..........T. H. Hsu (許東鴻), E. K. Lin (林爾康), C. C. Hsu, Y. C. Lin, P. K. Tseng, C. W. Wang (王建萬), and W. S. Hsu 91
A Sensitive Discharge Switch Function as a Pulse Generator or a Self-tone Modulator...........B. Chen, S. C. Yeh, and W. N. Wang (王唯農) 107
Damped Radio Frequency Sized Effect of Indium Antimonide at Room Temperature...........................Y. T. Yang (楊毓東), H. T. Ho, C. C. Pei, S. C. Yang, and B. H. Yue.......................... 113
Excitation Spectra of Magnesium Donors in Silicon.............L. T. Ho (何侗民) 127
On the Young's Interference Pattern..........................C. Chiang (蔣烱) 139
Properties and Responses of Frog Skin Membranes..............C. Chiang (蔣烱) 143
A Theory of the Muller-Lyer Illusion..........................C. Chiang (蔣烱) 155
Electronic Conduction in Ultra Thin Semi-metal Films......................N. T. Liang (梁乃崇) and S. Y. Wang (王守益) 163
大氣及颱風運動模型 I. 邊界條件 .... 大氣物理組同仁 177
颱風中心之運動 .... 大氣物理組同仁 199
地轉風假設下區域性大氣運動之探討 ....K. S. Wang and C. T. Wang (汪群從) 217
On the Energy Generation and Transformation over the East China Sea durning Winter.......................... L. C. Chien (簡來成) 229
Diffraction of a Plane Pulse by a Rectangular Opening.......................... H. C. Wang (王懷柱) 243
船舶縱向下水之探討 ....Y. Z. Lee, Y. T. Dai (戴堯天), C. Y. Liu, Y. N. Chen and C. T. Wang (汪群從) 259

Annual Report of the Institute of Physics, Academia Sinica, 1971

The Clock Paradox in the Relativity Theory *

TA-YOU WU and Y. C. LEE

Department of Physics, State University of New York, Buffalo, New York 14214

Received: 11 *May* 1971

Abstract

A system S' (rocket) starts from rest in an inertial system S, and after a series of accelerated, uniform and decelerated motions, comes back to rest at its initial position in S. An exact calculation is carried out, from the standpoint of S, of the time intervals for the arrivals at S of light signals sent back by S'. From the standpoint of S', S has made a round trip after undergoing a series of free falls in gravitational fields and coasting motions. An exact calculation is carried out for the 'proper time' intervals in S from the standpoint of S'. It is shown that there is exact agreement between S and S' in their reckonings of the total time intervals for the two frames, namely, both S and S' agree quantitatively, to them, the time interval is longer for S than for S'.

The accelerated motion of S' relative to S explicitly used in the treatment of the problem in the present work is that under time-independent field and subject to the condition of *local* Lorentz contraction and dilation; the resulting motion turns out to be that obtained earlier by Møller on entirely different considerations. The result of the present treatment is, however, more general than this particular motion seems to imply, since by an arbitrary coordinate transformation, it can be made to include an infinite number of accelerated frames including time-dependent fields, all within the framework of flat space-time. General remarks are given for the clock problem in the general theory of relativity in the sense of Einstein's curved space.

1. *The Clock Paradox*

The question concerned is the following: Imagine a pair of clocks, one of which remains at rest in an inertial frame, and the other sets out on a trip (on a rocket, say), and after a time returns to rest in the inertial frame. Will the travelling clock be slower than the one at home? Will they both agree exactly by how much one is slower than the other?

This problem is sixty years old. In a paper in 1911, Einstein (1911) gave a simple theory in which (1) he employed the Doppler effect formula of the special theory of relativity and obtained the effect of uniform acceleration of a reference frame on the Doppler shift, and (2) he introduced the equivalence principle for the acceleration of a frame and a gravitational field. Einstein concluded that a clock that has travelled, say in a circular path, will 'lose time', because the rate of the clock is slower in the accelerated motion.

---

*This paper has been published in International Journal of Theoretical Physics, Vol. 5, No. 5 (1972), pp. 307-323.

That a returned clock should have lost time compared with the one at home is so strange a conclusion that Einstein specifically wrote an article (Einstein, 1918) in 1918, in the form of a dialogue between a critic and himself, to show (1) how the trip will be viewed from the standpoints of both frames, (2) how the reciprocal symmetry (in the sense of the special theory of relativity) will be destroyed in this case by the accelerated motion of the rocket, and that both frames will agree that the returned one will be slow, and (3) that this is due to the loss of time, or the 'slowing down of the clock', of the rocket *during* the accelerated portion of the rocket's trip when it *turns back*.

For definiteness, let us pose the following situation. From the standpoint of the inertial system S, the rocket (or the travelling twin) S' goes through the following sequence of events:

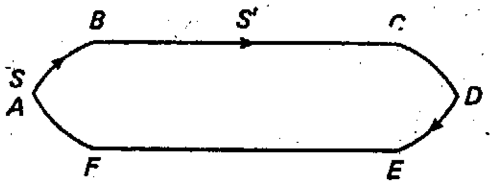

(1.1)

A–B: S' starts off, with acceleration a (in the positive x direction), reaching the velocity v at B.

B–C: S' shuts off its engine and moves with a uniform velocity v relative to S.

C–D: S' starts its engine and decelerates, reducing its velocity relative to S to zero.

D–E: S' keeps its engine and starts accelerating toward S, reaching the velocity $-v$ at E.

E–F: S' shuts off its engine and moves with constant velocity $(-v)$ toward S.

F–A: S' starts its braking engine, and moves with acceleration $-a$, coming to rest at A.

From the standpoint of the rocket S' who regards itself as at rest, S will go through the following events:

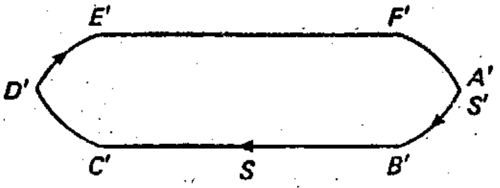

(1.2)

A'–B': S starts 'falling' in a (universal) gravitation field $-g$ (in the negative x direction), attaining a velocity $-v$ (relative to S') at B'

B'–C': The gravitational field is removed, and S keeps on moving with the (constant) velocity $-v$.

C'–D': A (universal) gravitational field g in the positive x-direction is turned on. S comes to stop (relative to S') at D'.

D'–E': The same field g continues to act, and S 'falls' from D' to E', attaining the velocity v (relative to S').

E'–F': The field g is removed and S moves with the constant velocity v.

F'–A': A gravitational field $-g$ is turned on, and S is brought to rest at A'.

During A'–B', C'–D', D'–E' and F'–A', S' itself is in the same universal gravitational field as S, but S' is held fixed by some external agency.

During the uniform relative motion parts B'–C', E'–F', S will say that the clock of S' is slow according to the time dilatation relation. If $\Delta\tau_{S'}$ is the proper time interval recorded by S' for each of these parts, and ΔT_S is the time interval recorded by synchronised clocks attached to the frame S, then

$$2\Delta T_S = \frac{2\Delta\tau_{S'}}{\sqrt{(1-\beta^2)}} \tag{1.3}$$

But with equal right, S' will say that the clock of S is slow compared with that of S', and if $\Delta\tau_S$ is the (proper) time interval recorded by S (for each of the uniform relative motion parts) and $\Delta T_{S'}$ the time interval recorded by synchronised clocks attached to the frame S', then

$$2\Delta T_{S'} = \frac{2\Delta\tau_S}{\sqrt{(1-\beta^2)}} \tag{1.4}$$

Einstein pointed out, however, that during the 'turning around' parts C'–D', D'–E' in (1.2), S is at a higher gravitational potential than S', and the clock of S is faster than that of S'. The clock in S will during C'–D'' and D'–E' 'gain' time and more than compensate the 'loss' as given by (1.4). If the time intervals during C'–D', D'–E' are very short compared with those for the uniform motion parts, the 'gain' during C'–D', D'–E' by the clock of S will be such as to bring the total time ΔT recorded by S (for the trip B'–C', C'–D', D'–E', E'–F') to be longer than that $\Delta T'$ recorded by S', in accordance with (1.3), i.e.,

$$\Delta T = \frac{\Delta T'}{\sqrt{(1-\beta^2)}} \tag{1.5}$$

The above statement of Einstein has been expressed in explicit form by Tolman (1934). Let us view the trip from the standpoint of S' as in (1.2). Let τ_{AB}, τ_{BC}, τ_{CDE}, τ_{EF} $(=\tau_{BC})$, τ_{FA} $(=\tau_{AB})$ be the proper time intervals as recorded by S, and let t_{BC}, t_{CDE}, t_{EF} $(=t_{BC})$, t_{FA} $(=t_{AB})$ be the time intervals as recorded by synchronised clocks at various points in (1.2) attached to S'.† Then, by (1.4),

$$\tau_{BC}\,(=\tau_{EF}) = \sqrt{(1-\beta^2)}\,t_{BC}\,(=\sqrt{(1-\beta^2)}\,t_{EF}) \tag{1.6}$$

---

† We shall, without causing confusion, drop the prime for B', C', etc. in the subscripts for the τ's and t's.

Let the average distance between S and S' during the turning around portion C'–D'–E' be approximately taken to be $x = vt_{BC}$. Since $v = gt_{CD}$, the Doppler effect expression gives

$$\tau_{CDE} \cong \left(1 + \frac{gx}{c^2}\right) t_{CDE} \tag{1.7}$$

$$= t_{CDE} + 2\beta^2 t_{BC} \tag{1.7a}$$

The total time for the whole trip is, for S, from (1.6) and (1.7a),

$$\begin{aligned} \tau &= \tau_{AB} + 2\tau_{BC} + \tau_{CDE} + \tau_{FA} \\ &= 2[\sqrt{(1-\beta^2)} + \beta^2]\, t_{BC} + 2\tau_{AB} + t_{CDE} \\ &\cong 2(1 + \tfrac{1}{2}\beta^2 + \cdots)\, t_{BC} + 2\tau_{AB} + t_{CDE} \end{aligned} \tag{1.8}$$

If we make the time intervals τ_{AB}, T_{CDE} very short compared with τ_{BC} and t_{BC}, then (1.8) becomes

$$\tau \cong \frac{1}{\sqrt{(1-\beta^2)}} \times \text{time for the trip recorded in } S' \tag{1.9}$$

This is in approximate agreement with (1.3). It is important to note that the $\cong$ sign in (1.9) arises not so much because of the neglect of τ_{AB} and t_{CDE} in (1.8) as because of the approximations made in obtaining (1.7).

In 1956, Dingle (1956) in a series of articles renewed the question of whether the returned twin from a rocket trip is younger than his brother who has stayed home. He believed that there should be no difference in their aging, that all earlier conclusions, including Einstein's, are erroneous. His questioning of these earlier works by many physicists has led to a great flux of discussions. Most authors (Arzelies, 1966) maintain the conclusion of Einstein. In most cases, the arguments amount to the simple statement that since the rocket S' has undergone accelerated and decelerated motions, it is not on equal footing with S which is an inertial system, and hence the reciprocal symmetry in the sense of the special theory of relativity has been removed. This part of the argument is of course correct. But then, because of attempts to simplify the problem for the non-specialist, the following argument is usually put forward: One can make the time intervals for the accelerated and decelerated parts very short compared with the time intervals for the uniform relative motion parts [see (1.1) or (1.2)] and in the limit negligible. Then, since only S is a 'preferred' (in the sense that it is an inertial) frame, one must only employ the relation (1.3). This part of the argument is unfortunately misleading. We have seen in the preceding section from the approximate treatment by Tolman that it is precisely the acceleration (or, an equivalent gravitation field) during the 'turning around' of the rocket that 'slows down its clock' (relative to the inertial frame S), and that one obtains the result (1.9) in an *approximation* only, which is *not* exactly the relation (1.3). The point that seems to have been forgotten in many 'elementary' discussions of the clock paradox is that while the 'compensations' in (1.8) and (1.9) must come from the accelerated motions, the correct result [(3.20) and (3.22) in the following] should really be independent of the strength of the accelerating and decelerating field which determine the length of time for these accelerated and decelerated parts. The undue prominence given the uniform relative motion parts (coasting of the rocket) and the consequent appearance of the Lorentz relation (1.3) are unfortunate, for they tend to divert the attention from the accelerated motion, which is essential in the clock paradox problem, to the expression (1.3) for uniform relative motion. In actual fact, the uniform relative motion parts [*B–C*, *E–F*, *B'–C'*, *E'–F'* in (1.1) and (1.2)] are non-essential, and one would have essentially the same 'paradox' if one does away with these (coasting) parts entirely. In the following section, an analysis of the clock problem with, and also without, the uniform relative motion parts in (1.1) and (1.2) will be carried out to illustrate this point.

In the literature, attempts have been made to convince one of the immediate applicability of the expression (1.3) for the time intervals for the whole trip as recorded by S and S' (assuming negligible times for the accelerated parts of the motion) by the following argument. Let there be a set of triplets instead of a pair of twins. Let C stay home (in an inertial frame); let A be moving away in a rocket with velocity v (relative to C). At a certain point in space, A meets B who is travelling toward C with velocity $-v$ (relative to C). A and B do not stop; B just sets his clock according to that of A. B finally passes by C. It is then claimed that the time recorded by C (for the interval between the passing by of A and that of B) is longer than that recorded by B, in accordance with (1.3). This argument is a special case of a general theorem in the special theory of relativity, namely, that in a Minkowski diagram, the time interval measured on a straight line AB (which is the time axis) is longer than the sum of time intervals measured along a series of straight lines AC, CD, . . . DB (each being a time axis in another Lorentz frame) which together with AB form a polygon. The implication of this argument is that we make use of the awareness of the accelerations to remove the reciprocal symmetry of the Lorentz frames, but have ignored the effects of the accelerations on the time measures of the systems. On this argument, one might as well contend with two Lorentz frames since the use of a third frame does not add to the resolution of the problem.

2. *Arbitrary Motion Relative to an Inertial Frame*

We shall study an accelerated motion that can be treated exactly in the clock problem.

Let (X,T) be the space and time coordinates in an inertial frame S and let x,t be those in a frame S' which may be accelerated under the time-independent field. Let $v(x,T)$ be the velocity of a fixed point x in S' relative to S at time T and let X be the space coordinate of the point p so that $X = X(x,T)$ and

$$v(x,T) = v(x(X,T),T) \tag{2.1}$$

The velocity of the point p in S is

$$v = \left(\frac{\partial X}{\partial T}\right)_x \tag{2.2}$$

If we assume that in S' the unit of length is the same as that in S, then the condition of local Lorentz contraction is expressed by

$$\left(\frac{\partial X}{\partial x}\right)_T = \sqrt{\left(1 - \frac{v^2}{c^2}(x, T)\right)} \tag{2.3}$$

From this, one obtains the equation

$$\left(\frac{\partial v(x, T)}{\partial x}\right)_T = \left[\frac{\partial}{\partial T}\sqrt{\left(1 - \frac{v^2}{c^2}(x, T)\right)}\right]_x \tag{2.4}$$

This is equivalent to

$$\left(\frac{\partial v(X, T)}{\partial X}\right)_T = -\frac{1}{c^2} v(X, T)\frac{\partial v}{\partial T}(X, T) \tag{2.5}$$

in which v is regarded as a function of X, T through the transformation (2.1).

To obtain the relation between the time t and the coordinates X and T, we shall introduce the conditions of local Lorentz time dilatation and relativity of motion of S and S', namely,

$$\sqrt{(g_{44})}\, d\tau = \sqrt{\left(1 - \frac{v^2}{c^2}(x, T)\right)}\, dT \tag{2.6}$$

and

$$v(X, T) = \left(\frac{\partial X}{\partial T}\right)_x = -\frac{1}{\sqrt{(g_{44})}}\left(\frac{\partial x}{\partial t}\right)_X = v(x, t) \tag{2.7}$$

where τ is the proper time in S' in the sense that if the metric in S' is $(dy = dz = 0)$

$$ds^2 = -(dx^2 + dy^2 + dz^2)/c^2 + g_{44}\, dt^2 \tag{2.8}$$

then

$$ds^2 = g_{44}\, d\tau^2 \tag{2.9}$$

so that

$$d\tau = \sqrt{(1 - \frac{v^2}{c^2})}\, dt \tag{2.10}$$

where

$$v^2 = \frac{1}{g_{44}}\left(\frac{\partial x}{\partial t}\right)_X^2 \tag{2.7'}$$

Note that the τ called the proper time above and defined by (2.9) is not the normal proper time τ_0 defined by $d\tau_0 = ds$ which will be related to τ here by $d\tau_0 = \sqrt{(g_{44})}\, d\tau$. In the present work, we make use of τ in the calculation of τ_0.

The conditions (2.3) and (2.6) are valid at a point (X,T) or (x,t). Our object is to find a class of accelerated frames S' (with respect to S) with the transformation

$$x = x(X,T), \qquad t = t(X,T) \tag{2.11}$$

and satisfying (2.3) and (2.6). The hypothesis that a transformation (2.11) exists between the (X,T) in an inertial frame and the (x,t) coordinates implies that the space is Euclidean. In this case, we can integrate the differential equations (2.5) and (2.6) since no curvature of space is involved.

Equation (2.5) can be solved by the method of separation of variables, namely, by setting

$$v = \xi(X)\,\zeta(T)$$

which leads to

$$v = \frac{\lambda c^2 T + C_1}{\lambda X + C_2}, \qquad \lambda, C_1, C_2 \text{ being constants.}$$

If the initial condition is

$$v \to aT \qquad \text{at } X = 0 \qquad \text{as } T \to 0$$

then

$$v = \frac{aT}{1 + (aX/c^2)} \tag{2.12}$$

Putting this into (2.2), one obtains the equation of motion of the point p ($x = 0$ in S'),

$$\frac{dX}{dT} = \frac{aT}{1 + (aX/c^2)} \tag{2.13}$$

To obtain the relationship between X and x, we may first integrate (2.13) to obtain

$$\left(1 + \frac{aX}{c^2}\right)^2 - \frac{a^2 T^2}{c^2} = f(x) \tag{2.14}$$

where $f(x)$ is an arbitrary function of x. On the other hand we can also integrate the Lorentz contraction equation (2.3) in which v is given by (2.12). The integration yields

$$\left(1 + \frac{aX}{c^2}\right)^2 - \frac{a^2 T^2}{c^2} = \left(\frac{ax}{c^2} + b(T)\right)^2 \tag{2.14'}$$

where $b(T)$ is an arbitrary function of T. However, by comparing the above two equations (2.14) and (2.14') we see that $b(T)$ must actually be a pure constant b, independent of T, and $f(x)$ is just $[(ax/c^2) + b]^2$. Our initial conditions then require $b = 1$, so that we have

$$\left(1 + \frac{aX}{c^2}\right)^2 = \left(1 + \frac{ax}{c^2}\right)^2 + \left(\frac{aT}{c}\right)^2 \tag{2.15}$$

n (2.7), (2.13) and (2.15) we obtain

$$\frac{(aT/c)}{1+(aX/c^2)} = v = -\frac{1}{\sqrt{(g_{44})}}\left(\frac{dx}{dt}\right)_X = \frac{aT/c}{\sqrt{(g_{44})}\,[1+(ax/c^2)]}\frac{dT}{dt}$$

From Equations (2.6), (2.7), (2.8) and the assumption that g_{44} does not depend on t, one can show that

$$g_{44} = \left(1+\frac{ax}{c^2}\right)^2 \tag{2.16}$$

The above equation in dT/dt can be integrated, and with the initial condition

$$t=0 \qquad \text{when } T=0$$

we obtain

$$\frac{2at}{c} = \ln\left(1+\frac{aX}{c^2}+\frac{aT}{c}\right) - \ln\left(1+\frac{aX}{c^2}-\frac{aT}{c}\right) \tag{2.17}$$

Using (2.15) in (2.17), we obtain

$$+\frac{1}{c\,[1+(ax/c^2)]}\left(\frac{dx}{dt}\right)_X = -\frac{aT/c}{\sqrt{\{[1+(ax/c^2)]^2+(aT/c)^2\}}} = -\tanh\frac{at}{c} \tag{2.18}$$

and (2.7) becomes

$$\frac{1}{c}\left(\frac{dX}{dT}\right)_x = \frac{aT/c}{1+(aX/c^2)} = \tanh\frac{at}{c} \tag{2.18a}$$

In (2.18a), since x is held fixed, t is also the proper time τ in S'.

Equations (2.15) and (2.17) now transform the metric

$$ds^2 = -dX^2/c^2 + dT^2 \tag{2.19}$$

into

$$ds^2 = -dx^2/c^2 + \left(1+\frac{ax}{c^2}\right)^2 dt^2 \tag{2.20}$$

In (2.20), for a given constant a, x is restricted to the region $x > -(c^2/a)$. It is seen from (2.13) and (2.15) that the limiting value $x = -(c^2/a)$ corresponds to $v = c$ beyond which v should not pass.

For convenience, we write three consequences of equations (2.15) and (2.17) namely,

$$\frac{aT}{c} = \left(1+\frac{aX}{c^2}\right)\tanh\left(\frac{at}{c}\right) \tag{2.21}$$

$$\frac{aT}{c} = \left(1+\frac{ax}{c^2}\right)\sinh\left(\frac{at}{c}\right) \tag{2.22}$$

$$1+\frac{aX}{c^2} = \left(1+\frac{ax}{c^2}\right)\cosh\frac{at}{c} \tag{2.23}$$

Equation (2.15) describes the motion of a fixed point p in S' from the standpoint of S. It is the so-called hyperbolic motion.

Equation (2.23) describes the motion of a fixed point p in S from the standpoint of S'.

If S' is accelerated along the $-X$ direction, we have only to replace a in all the equations (2.12)–(2.23) by $-a$, and obtain

$$\left(1-\frac{a(x-x_0)}{c^2}\right)^2=\left(1-\frac{a(X-X_0)}{c^2}\right)^2-\frac{a^2}{c^2}(T-T_0)^2 \tag{2.24}$$

$$\frac{a(T-T_0)}{c}=\left(1-\frac{a(X-X_0)}{c^2}\right)\tanh\frac{a(t-t_0)}{c} \tag{2.25}$$

$$\frac{a(T-T_0)}{c}=\left(1+\frac{a(X-X_0)}{c^2}\right)\sinh\frac{a(t-t_0)}{c} \tag{2.26}$$

$$1-\frac{a(X-X_0)}{c^2}=\left(1-\frac{a(x-x_0)}{c^2}\right)\cosh\frac{a(t-t_0)}{c} \tag{2.27}$$

where x_0, X_0, T_0, t_0 are constants to be determined by the appropriate initial conditions. In this case, equations (2.7) and (2.13) become

$$v=\left(\frac{dX}{dT}\right)_x=-\frac{a(T-T_0)}{1-(a/c^2)(X-X_0)} \tag{2.28}$$

$$v=-\frac{1}{1-[a(x-x_0)/c^2]}\left(\frac{dx}{dt}\right)_X=\left(\frac{dX}{dT}\right)_x=-\overset{c}{\underset{\wedge}{}}\tanh a(t-t_0)/c \tag{2.28a}$$

At this point, it is of considerable interest to note that the transformation (2.15) and (2.17) are precisely that derived by Møller (1943) on completely different considerations. Møller starts from a static metric assumed to be

$$ds^2=-(dx^2+dy^2+dz^2)/c^2+g_{44}\,dt^2 \tag{2.8}$$

where $g_{44}=g_{44}(x)$. g_{44} is determined by the Einstein equations $R_{\mu\nu}=0$, which lead to $g_{44}=[1+(gx/c^2)]^2$, g being a constant. The curvature tensor $R^{\lambda}_{\mu\nu\sigma}$ for this metric vanishes, showing the space to be Euclidean. With the help of the equations of the geodesic, the transformation (2.15) and (2.17) is found. We have arrived at (2.15) and (2.17) on the basis of the local Lorentz transformation properties (2.3), (2.6), (2.7) with the assumption that in (2.7), g_{44} is a function of x but not of t.

3. *Resolution of the Clock Paradox*

We shall now study the clock problem as stated in (1.1) and (1.2) of Section 1, by treating the accelerated parts of the trip A–B, C–D–E, F–A, and A'–B', C'–D'–E', F'–A' by means of the accelerated motion described by equations (2.9)–(2.24) and (2.25)–(2.28) of the preceding section.

(A) *From the Standpoint of S*

Referring to the figure in (1.1), let the origins of the coordinate systems $S(X)$ and $S'(x)$ be coincident at $T = t = 0$.

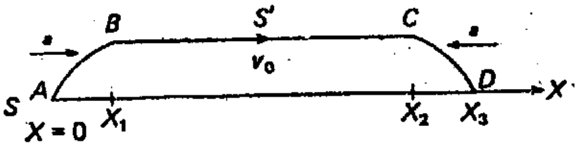

(3.1)

The rocket $S'(x = 0)$ moves according to (2.9), (2.7), (2.18)–(2.18a), (2.21)–(2.23). Part A–B: For the motion of the point $x = 0$ (fixed in S'), the t in (2.18a), (2.22), (2.23) becomes the proper time τ_0 in S' (i.e., the time registered by one and the same clock at $x = 0$ fixed in S'). When $x = 0$ reaches the velocity v_0 (relative to S frame) we have†

$$\tanh a\Delta\tau_1 = v_0 \tag{3.2}$$

$$aT_1 = \sinh(a\tau_{01}) = \frac{v_0}{\sqrt{(1 - v_0^2)}} \tag{3.3}$$

$$1 + aX_1 = \cosh(a\tau_{01}) = \frac{1}{\sqrt{(1 - v_0^2)}} \tag{3.4}$$

where T_1 is time, measured by the synchronised clocks attached to S, X_1 is the distance traversed by S' $(x = 0)$ when it has reached the velocity v_0 (i.e., the part A–B). In the following, the subscript 1, 2, 3, . . . refer to the parts A–B, B–C, C–D, etc. respectively of the trip. The same subscripts 1, 2, 3, . . . are also used for the A'–B', B'–C', C'–D', etc. in the following section from the standpoint of S'.

To obtain the time interval ΔT_1 recorded by one clock fixed at $X = 0$ in S, let S' send light signals back to S. Let τ be the proper time in S'. Then‡

$$\Delta T_1 = \int_0^{\Delta\tau_1} \sqrt{\left(\frac{1 + v}{1 - v}\right)}\, d\tau \tag{3.5}$$

where by (3.2) $a\Delta\tau_1 = \tanh^{-1} v_0$. Thus

$$\Delta T_1 = \frac{1}{a}\left[\frac{v_0}{\sqrt{(1 - v_0^2)}} + \frac{1}{\sqrt{(1 - v_0^2)}} - 1\right]$$

---

† In the following, we simplify writing by choosing the unit of time such that $c = 1$. All time, velocity, acceleration T, t, v, v_0, a are to be replaced by cT, ct, v/c, v_0/c, a/c^2, to convert to c.g.s. units

‡ ΔT_1 only represents the time interval for the clock at $X = 0$ to intercept all the light signals sent to it by the clock attached to $x = 0$ within $\Delta\tau_1$. It does *not* really represent the time of travel of the rocket $(x = 0)$ from A to B as recorded by the clock at $X = 0$. The sum in (3.10) is, however, the total time interval for the whole trip of S', as recorded by one and the same clock at $X = 0$ in S.

From the symmetry of the situation, it is clear that for the part *C–D*,

$$\Delta T_3 = \Delta T_1 \tag{3.6}$$

and for the parts *D–E*, *F–A*,

$$\Delta T_4 = \int_0^{\Delta\tau_1} \sqrt{\left(\frac{1-v}{1+v}\right)}\, d\tau \tag{3.7}$$

$$= \frac{1}{a}\left[\frac{v_0}{\sqrt{(1-v_0^2)}} - \frac{1}{\sqrt{(1-v_0^2)}} + 1\right]$$

$$\Delta T_6 = \Delta T_4 \tag{3.8}$$

For the parts *B–C*, *E–F*, if $\Delta\tau_2 = \Delta\tau_5$ is the proper time intervals in S', the sum of the intervals for the arrivals of the signals sent back by S' during these intervals is

$$\Delta T_2 + \Delta T_5 = \Delta\tau_2 \sqrt{\left(\frac{1+v_0}{1-v_0}\right)} + \Delta\tau_5 \sqrt{\left(\frac{1-v_0}{1+v_0}\right)}$$

$$= \frac{2\Delta\tau_2}{\sqrt{(1-v_0^2)}} \tag{3.9}$$

Thus the total interval recorded by one single clock in S (at rest at $X=0$) from all signals sent back by S' during its round trip is

$$\sum_{j=1}^{6} \Delta T_j = \frac{4}{a}\frac{v_0}{\sqrt{(1-v_0^2)}} + \frac{2\Delta\tau_2}{\sqrt{(1-v_0^2)}} \tag{3.10}$$

The proper time (recorded by one clock) in S' for the whole round trip is

$$\Delta\tau_0 = 4\Delta\tau_{01} + 2\Delta\tau_2 = \frac{4}{a}\tanh^{-1} v_0 + 2\Delta\tau_2 \tag{3.11}$$

(B) *From the Standpoint of S′*

The fixed point $X = 0$ in S moves in the negative x direction.

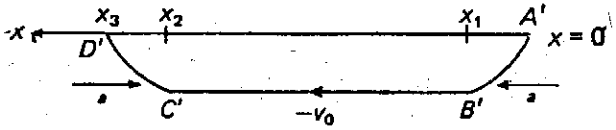

(3.12)

Part *A′–B′*. Let $\Delta\mathcal{T}_1$ be the proper time interval (registered by a clock at $X = 0$ in S) for $X = 0$ to reach the velocity $-v_0$ (relative to S'). From (2.18a),

$$a\Delta\mathcal{T}_1 = \tanh\frac{a\tau_1}{c} = v_0 \tag{3.13}$$

and the distance traversed by $X=0$ during this interval is given by (2.23) (with $X=0$) and (2.18) with $\tanh at_1 = v_0$, i.e.,

$$1 + ax_1 = \frac{1}{\cosh at_1} = \sqrt{(1-v_0^2)} \tag{3.14}$$

Parts B'–C' and E'–F'. Since the time interval for B'–C' or E'–F' in S' is $\Delta\tau_2$ in (3.8), S' would have deduced from the special theory of relativity that the combined intervals would have added to the proper time intervals of S the value $2\Delta\mathcal{T}_2$ which can be calculated as follows. Let $d\mathcal{T}$ be an element of proper time in S. For the combined B'–C' and E'–F', light signals sent by S back to S' will reach S' in interval

$$\left[\Delta\mathcal{T}_2\sqrt{\left(\frac{1+v_0}{1-v_0}\right)} + \Delta\mathcal{T}_5\sqrt{\left(\frac{1-v_0}{1+v_0}\right)}\right] = \frac{2\Delta\mathcal{T}_2}{\sqrt{(1-v_0^2)}}$$

This is now the time interval recorded by the clock in S', and is hence the proper time interval $2\Delta\tau_2$, i.e.,

$$2\Delta\mathcal{T}_2 = \sqrt{(1-v_0^2)}\,2\Delta\tau_2 \tag{3.15}$$

Part C'–D'. During C'–D' and D'–E', S' would describe S as being acted on by a gravitational field a in the positive x-direction, the motion being described by equations (2.24)–(2.27). Equation (2.24) is

$$[1 - a(x - x_0)]^2 = [1 - a(X - X_0)]^2 - a^2(T - T_0)^2 \tag{2.24}$$

The constants x_0, X_0, T_0 are determined as follows. From the standpoint of S_1 [see (3.1), (3.2) and (3.8)], at C,

$$aT = \frac{v_0}{\sqrt{(1-v_0^2)}} + \frac{a\Delta\tau_2}{\sqrt{(1-v_0^2)}}, \qquad v = v_0 \tag{3.16}$$

and (2.28) leads to

$$-\frac{a\left[\dfrac{1}{a\sqrt{(1-v_0^2)}}(v_0 + a\Delta\tau_2) - T_0\right]}{1 + aX_0} = v_0$$

At D,

$$T = \frac{2v_0}{\sqrt{(1-v_0^2)}} + \frac{a\Delta\tau_2}{\sqrt{(1-v_0^2)}},$$

$v = 0$ and

$$X = 2X_1 + \frac{v_0\Delta\tau_2}{\sqrt{(1-v_0^2)}},$$

[see (3.4)]. These lead to

$$\begin{aligned} X_0 &= 2X_1 + \frac{v_0\Delta\tau_2}{\sqrt{(1-v_0^2)}}, \\ aT_0 &= \frac{2v_0}{\sqrt{(1-v_0^2)}} + \frac{a\Delta\tau_2}{\sqrt{(1-v_0^2)}}, \\ x_0 &= 0 \end{aligned} \tag{3.17}$$

From (2.28a),

$$\tanh a(t-t_0)=-v$$

the condition $v=v_0$ when $t=\Delta\tau_1+\Delta\tau_2$ leads to

$$t_0=2\Delta\tau_1+\Delta\tau_2 \tag{3.18}$$

Thus, equation (2.25) corresponding to the case (2.24) is now

$$a\left(T-\frac{2v_0}{\sqrt{(1-v_0^2)}}-\frac{\Delta\tau_2}{\sqrt{(1-v_0^2)}}\right)=\left[1-a\left(X-2X_1-\frac{v_0\Delta\tau_2}{\sqrt{(1-v_0^2)}}\right)\right] \times\tanh(t-2\Delta\tau_1-\Delta\tau_2) \tag{3.19}$$

At D', $v=\tanh(t-2\Delta\tau-\Delta\tau_2)=0$ and the point $X=0$ of S has the time $T=\Delta\mathcal{T}_{A'-B'-C'-D'}$

$$\Delta\mathcal{T}_{A'-B'-C'-D'}=\frac{2v_0}{\sqrt{(1-v_0^2)}}+\frac{\Delta\tau_2}{\sqrt{(1-v_0^2)}} \tag{3.20}$$

From the symmetry of the situation, it is clear that the time in S for the trip A'–B'–C'–D'–E'–F'–A' as seen (or, calculated) from the standpoint of S' is twice the $\Delta T_{A'-D'}$ in (3.20), i.e.,

Total time $\Delta\mathcal{T}$ in S

$$=2\left(\frac{2v_0}{a\sqrt{(1-v_0^2)}}+\frac{\Delta\tau_2}{\sqrt{(1-v_0^2)}}\right) \tag{3.21}$$

which can be written

$$=2(\Delta\mathcal{T}_{A-B}+\Delta\mathcal{T}_{B-C}+\Delta\mathcal{T}_{C-D})$$

or,

$$a\Delta\mathcal{T}=2\left[v_0+a\sqrt{(1-v_0^2)}\,\Delta\tau_2+\frac{2v_0}{\sqrt{(1-v_0^2)}}+\frac{a\Delta\tau_2}{\sqrt{(1-v_0^2)}} -(v_0+a\sqrt{(1-v_0^2)}\,\Delta\tau_2)\right] \tag{3.22}$$

the proper time in S'

$$=4/a\tanh^{-1}v_0+2\Delta\tau_2 \tag{3.23}$$

Equation (3.21) shows complete agreement with the value given in (3.10) obtained from the standpoint of S. Equation (3.22) shows that the 'loss of time' during B'–C' and E'–F' by S in the view of S' [i.e., $2\sqrt{(1-v_0^2)}\,\Delta\tau_2$ in (3.15) compared with $2\Delta\tau_2/\sqrt{(1-v_0^2)}$ in (3.9)] is more than made up by the 'gain in time' by the S clock during C'–D', D'–E' when S is at a higher equivalent gravitational potential than S' [see (3.12)], and the clock of S is 'faster' on account of the factor $g_{44}=(1-gx)^2$ in

$$ds^2=dx^2+(1-gx)^2\,dt^2$$

(with $x=0$ at A' and $ax=2[\sqrt{(1-v_0^2)}-1]-v_0\Delta\tau_2$ at D'). The smaller 'loss of time' of the clock of S during A'–B' (when S is at a lower gravitational potential, $ds^2=-dx^2+(1+gx)^2\,dt^2$) is also more than made up by the 'gain' during C'–D'. The total result is to bring the two reckonings of the proper time intervals, by S and S', of the round trip into *exact* agreement with each other.†

It is seen from the foregoing results that all the calculations are *exact*, and no approximations involving the assumption of making the accelerated parts A–B, C–D–E, F–A (or A'–B', C'–D'–E', F'–A') very short compared with the uniform relative motion part B–C, E–F (or B'–C', E'–F') have been made. In fact, as emphasised by Einstein as early as in the 1918 paper and brought out approximately by Tolman (1934) and exactly in (3.22) above that is precisely the accelerated parts that resolve the 'paradox'. Had one literally 'neglected' the accelerated parts, (3.10) and (3.22) would have become

$$\text{Total time in } S \text{ (as reckoned by } S) = \frac{2\Delta\tau_2}{\sqrt{(1-v_0^2)}}$$

$$\text{Total time in } S \text{ (as reckoned by } S') = 2\sqrt{(1-v_0^2)}\,\Delta\tau_2$$

On the other hand, had one done away entirely with the uniform relative motion (coasting of rocket) parts B–C, E–F (B'–C', E'–F'), the results (3.10) and (3.22) would have become:

	Standpoint of S	Standpoint of S'
Total proper time in S'	$\frac{4}{a}\tanh^{-1} v_0$	$\frac{4}{a}\tanh^{-1} v_0$
Total proper time in S	$\frac{4}{a}\frac{v_0}{\sqrt{(1-v_0^2)}}$	$\frac{2}{a}\left[v_0 + \frac{2v_0}{\sqrt{(1-v_0^2)}} - v_0\right]$

---

† The results (3.10), (3.11), (3.22), (3.23) above are a little more complete than those of Møller (1943) in that here S' starts out from rest and comes back at rest to S. There are differences in details between this and Møller's work. For example, we calculate the time intervals ΔT_1, ΔT_3, ΔT_4, ΔT_6 in (3.5)–(3.8) as recorded by one clock in S, and not Møller's times T', T'' which are not the proper times of one clock. Also, as remarked in Section 2 above, the starting points in the two works are different. In an application of Møller's work, Fock (1959) has obtained an erroneous conclusion.

Fock (1959) states that the time intervals recorded by the clocks A, B in S, S' are given by

$$\tau_A - \tau_B = \frac{v^2}{c^2}\left(\tfrac{1}{2}T - \tfrac{2}{3}t\right)$$

where $t = 2v/g$ is the time for the turning around part (C–D–E in (1.8) in the present article), and T = uniformly moving part (B–C) + (E–F) + t. Thus $\tau_A - \tau_B$ can be $\gtreqless 0$, in disagreement with the results of everyone else. This strange result arises from the error of the + sign in (62.09), which should have read $U = U_0 - g(x_1 - x)$. When this correction is made, one would have

$$\tau_A - \tau_B = \frac{v^2}{c^2}\frac{T}{4}$$

which is in agreement with the approximate result of (1.8) of Tolman and others.

Here is, of course, exact agreement between the reckonings of the total proper time intervals from the standpoints of both frames.

In the calculations above, we had employed the accelerated motion represented by equations (2.15) and (2.17) [or, (2.24) and (2.25)] which correspond to motion under a time-independent field. The result, however, is in fact quite general since from $S'(x,t)$, one can carry out any arbitrary coordinate transformation to a frame S'',

$$x'' = x''(x,t), \qquad t'' = t''(x,t)$$

which will lead in general to

$$ds^2 = \sum g_{ij}\, dx_i''\, dx_j''$$

where the g_{ij} are functions of x'' and t'' and hence no longer static. The space is, however, Euclidean. The motions of S'' relative to S can be quite arbitrary and very complicated, but the description can be reduced to that of S' by the transformation above so that in a sense the treatment of the clock problem by means of S' has covered a whole (infinite number) class of accelerated motions relative to S. This class of accelerated motions has not brought in any curved space properties in the sense of Einstein's general theory of relativity.

The present work has thus treated and resolved the clock problem without having really made recourse to Einstein's theory of gravitation involving curved space. This is worth noting in view of the usual statement in the literature that an exact treatment of the clock problem (i.e., to all orders of v_0/c) calls for the general theory of relativity.

4. *General Remarks on the 'Clock Paradox' Problem*

We are now in a position to summarise what we believe is relevant in the clock problem in the relativity theory.

(1) Invariance of proper time under coordinate transformations. In the theory of relativity (special and general),

$$\begin{aligned} ds^2 &= g_{\mu\nu}\, d\chi_\mu\, d\chi_\nu \\ &= \text{invariant} \end{aligned} \tag{4.1}$$

in each group of coordinate transformations (the group in flat space-time which includes the Lorentz group, and the general group in curved space-time). Thus for a given world line C between two world points P_1 and P_2, the proper time interval

$$\Delta\tau = \int_{P_1}^{P_2} ds \text{ along } C = \text{invariant} \tag{4.2}$$

i.e., has the same value in all frames satisfying (4.1)

(2) Proper time intervals between two world-points along different world lines.

Consider a given field $g_{\mu\nu} = g_{\mu\nu}\,(x_1,x_2,x_3,x_4)$. The motion of a particle from one world point P_1 to another P_2 is uniquely given by the geodesic C

$$\delta \int_1^2 ds = 0$$

Other paths C_1, C_2 joining P_1 and P_2 will not correspond to the 'free' motion in the field $g_{\mu\nu}$, but will correspond to motions under agencies other than the field representative by $g_{\mu\nu}$, and

$$\int_{1\,C_1}^{2} ds \neq \int_{1\,C}^{2} ds \tag{4.3}$$

which follows from the definition of the geodesic.

(3) For a given field $g_{\mu\nu}$, between two arbitrarily given points P_1 and P_2, there is one and only one geodesic.

From a point P_1, there are ∞^3 geodesics issuing in all directions. Of these, one, say C, goes through P_2. Suppose another, say C_1, makes an angle θ with C at P_1. Since a geodesic is a line generated by an infinitesimal vector in a continuous series of infinitesimal parallel displacements, and since the angle between two vectors is invariant under parallel displacements, it follows that in general two geodesics from a given point P_1 cannot intersect at another arbitrarily chosen point P_2. (In the case of a spherical surface, geodesics from a point P intersect at the antipode of P only.)

(4) The clock paradox. Let S and S' be two (material) frames whose coordinates transform according to (4.1). Let us follow Einstein's argument in Section 1, namely, from the standpoint of S' (the rocket), S undergoes a series of free falls in certain universal gravitation fields during $A'B'$, $C'D'$, $D'E'$, $F'A'$ and coasting $B'C'$, $E'E'$ in (1.2). Suppose these fields are represented by a field $g_{\mu\nu}$. From the standpoint S', the frame S passes from the initial point P_1 to P_2 (in 4-space) along the geodesic of $g_{\mu\nu}$, but S' itself passes from P_1 to P_2 along a pure-time trajectory since S' has been held fixed (at rest) by means of some *external* agency. Thus the world line of S' is not a geodesic of $g_{\mu\nu}$. In general, the proper time intervals along the two world lines between P_1 and P_2 are different, according to (4.3).

The above result is general, holding for curved space as well as for flat space. It is possible to make an explicit and exact calculation of the proper time intervals in the flat space case, using the spirit of the general theory of relativity (acceleration represented by a $g_{\mu\nu}$ field). This has been done by Møller (1943), and in the present work (Sections 2 and 3).

(5) Let $S(X,Y,Z,T)$ be a strictly inertial frame, i.e., frame in flat space-time, and $S'(x,y,z,t)$ be a frame in a curved space-time (i.e., in a gravitational field in Einstein's theory). Then there is no coordinate transformation which transforms $ds^2 = -(dX^2 + dY^2 + dZ^2) + dT^2$ into $ds^2 = \sum g_{\mu\nu}\,dx_\mu dx_\nu$ with the curvature tensor $R^{\lambda}_{\mu\nu\sigma} \neq 0$. In this case there is no invariant ds^2 and there is no exact (only approximate) connection between the space-time

description in S and that in S'. One can no longer compare $d\tau_0$ in S and the $d\tau_0$ in S', and the 'clock paradox' does not have any clear and exact meaning.

References

Arzelies, H. (1966). *Relativistic Kinematics*. Pergamon Press. Contains an extensive bibliography on the clock problem.

Dingle, H. (1956). *Nature, London*, **177**, 782.

Dingle, H. (1957a). *Nature, London*, **179**, 1242.

Dingle, H. (1957b). *Nature, London*, **180**, 499, 1275.

Darwin, C. G. (1957). *Nature, London*, **180**, 976.

Einstein, A. (1911). *Annalen der Physik*, **35**, 898. Translated and contained in Einstein *et al., The Principle of Relativity*. Dover Publ. Inc., New York.

Einstein, A. (1918). *Naturwissenschaften*, **6**, 697. An exposition of the relativity theory, and of the clock paradox, in the form of a dialogue.

Fock, V. (1959). *The Theory of Space, Time and Gravitation*, Section 62, p. 214, eq. (62.16). Pergamon Press.

McCrea, W. H. (1956). *Nature, London*, **177**, 783.

McMillan, E. M. (1957). *Science, New York*, **126**, 381.

Møller, C. (1943). *Danske Vid. Sel. Mat-Fys. Med. XX*, No. 19.

Tolman, R. T. (1934). *Relativity, Thermodynamics and Cosmology*. Oxford University Press.

Annual Report of the Institute of Physics, Academia Sinica, 1971

INVESTIGATION OF EXCITED STATES OF ^{4}He THROUGH DEUTERON-INDUCED THREE-PARTICLE REACTIONS ON ^{6}Li

E. L. HAASE, R. HAGELBERG and W. N. WANG †
Institut für Experimentelle Kernphysik der Universität und des Kernforschungszentrums Karlsruhe

Received 17 December 1971
(Revised 17 February 1972)

Abstract: Excited states of ^{4}He are investigated through final-state interactions in the three-particle reactions ^{6}Li(d, α′t)^{1}H, ^{6}Li(d, α′^{3}He)n and ^{6}Li(d, α′d)^{2}H with 52 MeV deuterons. In measuring the differential cross sections, the detector of the first outgoing particle was kept at a fixed position and the second detector scanned over a range of coplanar angles favouring ^{4}He final-state interactions. The data are interpreted in terms of four isospin $T = 0$ excited states of ^{4}He at 21.9, 25.5, 28.5 and 31.8 MeV with widths of 1.8, 2.9, 5.3 and 5.6 MeV, respectively. Only the 21.9 and the 25.5 MeV levels are particularly evident. Angular correlation data indicate $J^\pi = 0^+$ or 1^+ for the level at 25.5 MeV. No evidence is found for a narrow state at 23.9 MeV reported by Franz and Fick.

E | NUCLEAR REACTIONS ^{6}Li(d, α′t), ^{6}Li(d, α′^{3}He), ^{6}Li(d, α′d), $E = 52$ MeV; measured $\sigma(E_1, E_2, \theta_1, \theta_2)$. ^{4}He deduced resonance parameters. 99 % enriched ^{6}Li target.

1. Introduction

The present work deals with the kinematically complete investigation of the reactions ^{6}Li(d, α′t)^{1}H, ^{6}Li(d, α′ ^{3}He)n and ^{6}Li(d, α′d)^{2}H, employing 52 MeV deuterons. This is the third in a series of papers describing a systematic investigation of $T = 0$ excited states of ^{4}He arising in final-state interaction (f.s.i.) in reactions with the three entrance channels ^{4}He+α, ^{4}He+d and now ^{6}Li+d.

Here we want to restrict ourselves to those aspects that are particular to the reactions with the last entrance channel. A discussion of three-particle kinematics and a comparison with several theoretical predictions is given by Haase *et al.* 1). A survey of previous work, the reaction mechanism and a summary of the results of all three investigations, have already been published 2).

The experimental procedure and the method of analysis are very similar to those of the two previous investigations. Two solid-state telescopes with particle identification are employed. The three decay channels are measured simultaneously. The data acquisition was carried out by an on-line computer, collecting event by event. Details are given elsewhere 3).

---

*This paper has been published in Nuclear Physics, A188,(1972) 89-96.

† On leave from the Institute of Physics, Academia Sinica, and Tsing Hua University, Taiwan, China.

2. Theoretical interpretation

The reaction mechanism for a two-particle transfer reaction is not as simple and not as well understood as that for inelastic scattering employed in ref. [1]). Taking the reaction mechanism to be sequential, we give a derivation of the matrix element for a three-particle reaction initiated by a transfer reaction. This is not intended as a rigorous derivation, but rather to justify our method of analysis.

The differential cross section for a reaction with three particles in a definite channel c is

$$\frac{d^3\sigma^c}{d\Omega_1\, d\Omega_2\, dE_1} = \frac{2\pi}{\hbar v_p}\rho_c |M_c|^2, \tag{1}$$

where v_p is the velocity of the projectile, ρ_c is the phase-space distribution, and M_c is the transition matrix element

$$M_c = \langle \phi_f^{(-)} | V | \phi_i \rangle, \tag{2}$$

$\phi_f^{(-)}$ being the wave function of the final state, given asymptotically by a plane wave and an incoming spherical wave in order to allow for the f.s.i. between the d+d, t+p, and ^{3}He+n systems.

The wave function of the initial state is

$$\phi_i = \phi_{Li}\phi_d\psi_i, \tag{3}$$

where ϕ_{Li} and ϕ_d are the internal wave functions of the target and the projectile, and the wave function of their relative motion is a plane wave

$$\psi_i = \exp(i\boldsymbol{k}_1 \cdot \boldsymbol{R}_1), \tag{4}$$

$\boldsymbol{R}_1$ being the vector between target and projectile, and $\boldsymbol{k}_1$ their momentum in the c.m. system. To simplify the following expressions, the internal wave functions of the incoming and outgoing particles will no longer be written explicitly.

As a representative case consider the ^{6}Li(d, α'd)^{2}H reaction. We restrict ourselves to a single $l = 0$ resonance in the ^{4}He* intermediate system, but the treatment can be extended. Coulomb and threshold effects are not considered. The wave function $\phi_f^{(-)}$ consists asymptotically of the plane waves of the α+(d+d) system and the incoming spherical waves ψ_B for the d+d, ^{3}He+n, and ^{3}H+^{1}H channels [4])

$$\phi_f^{(-)} = \exp(i\boldsymbol{k}_2 \cdot \boldsymbol{R}_2)[\exp(i\boldsymbol{q} \cdot \boldsymbol{r}) + \psi_B]. \tag{5}$$

Here $\boldsymbol{R}_2$ is the vector between the α-particle and the intermediate system, $h\boldsymbol{k}_2$ the momentum of the latter in the mass-8 c.m. system, and $\boldsymbol{r}$ is the vector between the two deuterons and $\boldsymbol{q}$ is the momentum of each deuteron in c.m. system of the recoiling intermediate (r.c.m.) system.

Then in Born approximation the matrix element is given by

$$M_c = M_1 + M_2 = \langle \exp(-i\boldsymbol{k}_2 \cdot \boldsymbol{R}_2)[\exp(-i\boldsymbol{q} \cdot \boldsymbol{r}) + \psi_B] | V | \exp(i\boldsymbol{k}_1 \cdot \boldsymbol{R}_1) \rangle \tag{6}$$

Following Watson we assume M_1 to be independent of the internal coordinates of the d+d system; M_2 can be decomposed into a product of a Breit-Wigner term and a Hankel function [5]). Noble shows that the energy dependence of the Hankel function over the width of the resonance does not lead to a significant energy dependence of the matrix element when a sufficiently localized interaction operator V is used. The energy dependence of the interior region and of the exterior one have been taken to be identical. Thus the matrix element M_c is proportional to the sum of an energy-independent term $M_1 = (C)^{\frac{1}{2}}$ and a pole term $M_2 = (\Gamma B)^{\frac{1}{2}}/(E_x - E_0 - \frac{1}{2}i\Gamma)$. For a number of N of resonances this yields a cross section identical to the one used in refs. [1,2]) and the method of analysis employed here is the same as that used in these papers. Thus we have fitted the spectra for a set of angles θ_2^l in the lab system (l = lab) for each of the reactions with the expression

$$\frac{d^3\sigma_{\text{exp}}^l}{d\Omega_1^l\, d\Omega_2^l\, dE_1^l} = F\left\{\left[C(\theta_2^l) + \sum_{n=1}^{N} \frac{\Gamma_n B_n(\theta_2^l) + (E_x - E_n)A_n(\theta_2^l)}{(E_x - E_n)^2 + \frac{1}{4}\Gamma_n^2}\right] \rho^l(E_1^l)\right\} \tag{7}$$

Here F denotes the operation of folding the "theoretical" curve with the experimental resolution, taken to have a Gaussian form.

3. Results and analysis

The raw data were reduced to two-dimensional spectra, the number of events being recorded as a function of both the energy of the α-particle E_α^l and that of one of the decay products E_2^l of the intermediate system. The spectra shown below are then obtained by summing events across each kinematical curve and projecting them onto the E_α^l axis.

3.1. THE ^{6}Li(d, α't)^{1}H REACTION

Fig. 1 shows a representative set of spectra for the ^{6}Li(d, α't) reaction plotted as a function of ^{4}He excitation energy E_x. The third level of ^{4}He at E_x = 21.9 MeV (Γ = 1.8 MeV) is strongly excited within its kinematically allowed cone between $\theta_t^l = 84°$ and 112°. The solid line is a least-squares fit with eq. (7), varying the E_n and Γ_n in common for the entire set. As already observed in ref. [1]), best fits were obtained for most spectra with the non-resonant background coefficients C and hence with the interference terms A_n equal to zero. Therefore the non-resonant term was taken to be zero for all fitted spectra. The shifting peak indicated by arrows arises from the ^{4}He$-^1$H f.s.i. in the ^{5}Li ground state. This region was excluded in the fits. Although they are not prominent, resonances at 25.5, 27.7, and 31.7 MeV were required in order to obtain an acceptable fit. These resonance parameters closely correspond to values needed to fit the other reactions investigated [1,2]). The known states at 20.2 and 21.1 MeV were also allowed for in these fits. The smallest value of χ^2 was obtained with zero intensity for these states, except for a weak contribution of the 21.1 MeV level for the spectrum for $\theta_t^l = 91°$. As this level ($J^\pi = 0^-$) should have an isotropic dis-

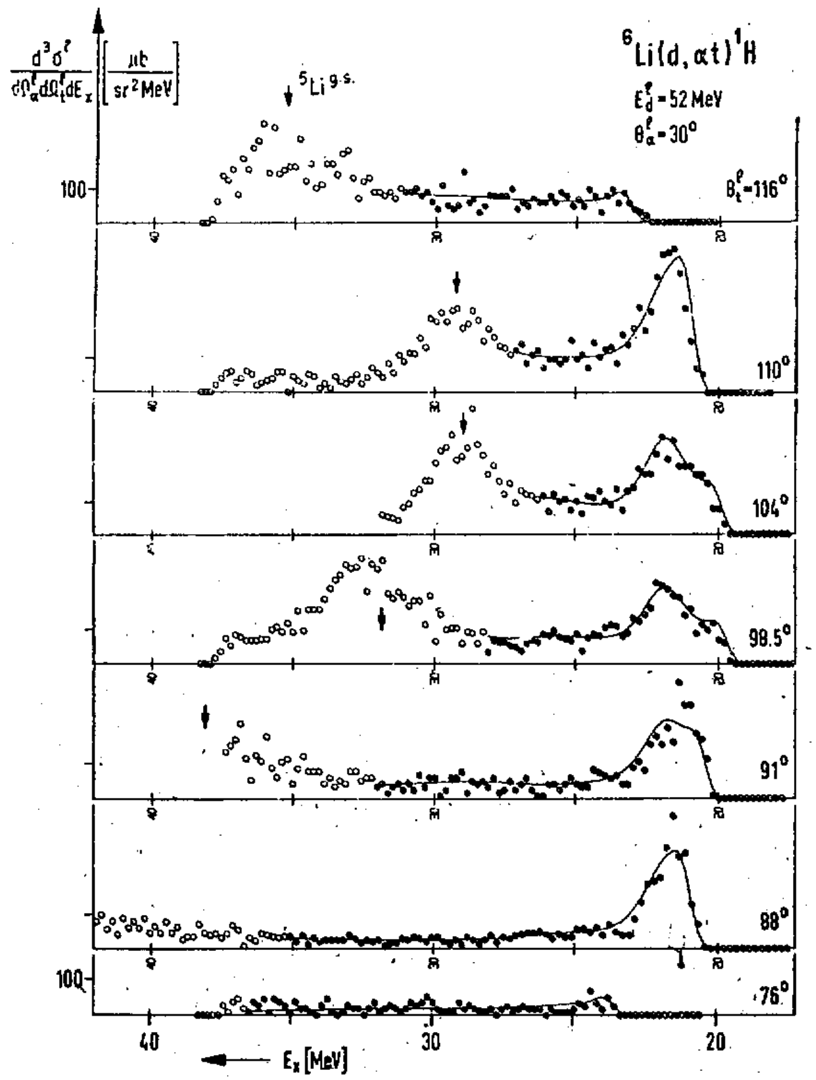

Fig. 1. Representative set of spectra for the ^{6}Li(d, α′t)^{1}H reaction as a function of ^{4}He excitation energy. Solid lines are least-squares fits with eq. (7). The 21.9 MeV resonance is strongly excited. Its recoil axis is at 98.7°.

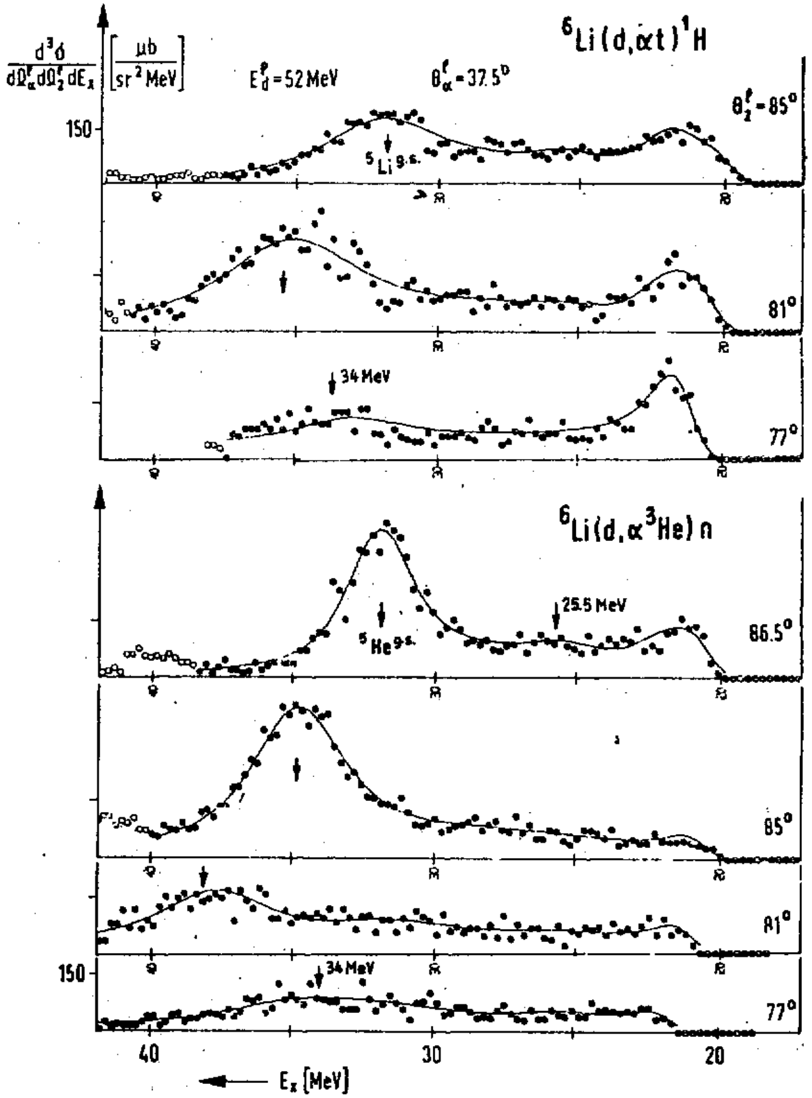

Fig. 2. Comparison between data for the ^{6}Li(d, α′t)^{1}H and ^{6}Li (d,α′ ^{3}He)n reactions. Note the bump at E_x = 34 MeV for both $\theta_2{}^l$ = 77° spectra.

tribution in the c.m. system, it should show up in all spectra within its decay cone. Thus the fits shown in fig. 1 do not include any contribution from this resonance. The top part of fig. 2 shows three spectra for $\theta^l_{\alpha'} = 37.5°$. Here the excitation of the 21.9 MeV level is not as pronounced as in the first figure. As is evident, good fits are obtained with levels at 21.9, 25.5, 28.5 and 31.7 MeV, with the average resonance parameters obtained from the other reactions. A summary of resonance parameters is given in table 2 of ref. [2]). Here the ^{5}Li ground state was also included in the fit to check its position as compared with the calculated value.

The spectra near the recoil axis for the 21.1 MeV level for the reaction ^{6}Li(d, α't) show the shoulder caused by the phase-space distribution. However this is not evident in the corresponding spectra of the reaction ^{4}He(d, α't). This is interpreted as being due to the level at 21.1 MeV which is strongly excited in the latter reaction [2]). Coulomb and threshold effects are expected to be identical as in both cases one has the decay of the same intermediate system.

The same reaction has been investigated in a previous study [6]). Owing to the lower incident energy, the different f.s.i. peaks were even less separated, and only a peak at 21.9 MeV could be clearly identified.

3.2. THE ^{6}Li(d, α'^{3}He)n REACTION

The bottom part of fig. 2 shows a set of four spectra for the reaction ^{6}Li(d, α'^{3}He) measured simultaneously. On the basis of charge independence the spectra are expected to be identical, except for effects associated with the higher threshold and the lack of ^{3}He-n Coulomb interaction. This is indeed observed. The peaks arising from the ^{5}He ground state are narrower than those from ^{5}Li, on account of the smaller width of the former. Good fits are obtained with the average resonance parameters. In fig. 2 both spectra for 77° show a bump at $E_x = 34$ MeV. If this were due to a mass-5 resonance, the peak in the lower spectrum would be displaced to the left. Hence the most likely explanation is that it is caused by ^{4}He f.s.i. More measurements at several favourable pairs of angles, preferably at higher incident energies, are needed to elucidate this point.

3.3. THE ^{6}Li(d, α'd)^{2}H REACTION

In fig. 3, part of the spectra of the ^{6}Li(d, α'd) reaction for $\theta^l_{\alpha'} = 30°$ are shown. As the threshold for this decay channel is 23.85 MeV, the first three excited states do not show up. The level at 25.5 MeV observed previously [1]) is most evident in this reaction. A large fraction of the cross section around 25.5 MeV is due to this level, the phase space bump being only of minor importance. [See figs. 7 and 8a in ref. [1]).] The level at 28.5 MeV is not particularly pronounced but it is definitely needed in order to obtain an acceptable fit. The peak around $E_x = 40$ MeV indicated by arrows is due to f.s.i. of the 4.57 MeV level of ^{6}Li. For smaller θ^l_d the quasi-free scattering begins to obscure the spectra [3, 7]). The exchange between the two deuterons does not arise as long as one is dealing with a sequential reaction.

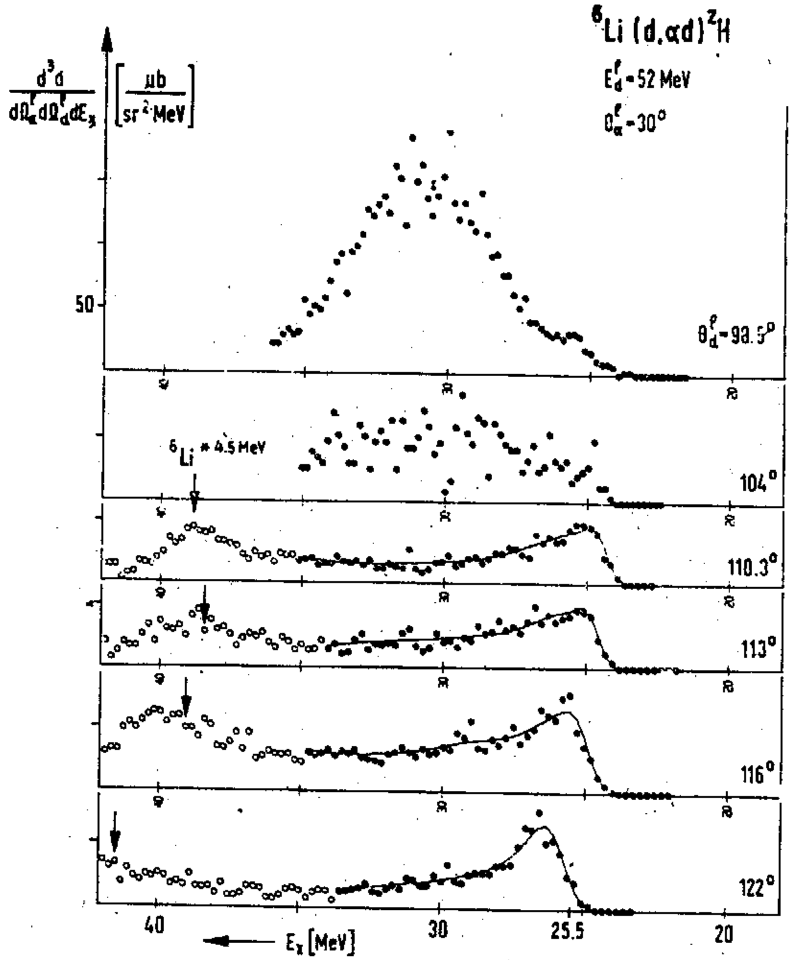

Fig. 3. Set of spectra for the ^{6}Li(d, α′d)^{2}H reaction. Solid lines are least-squares fits with eq. (7). The 25.5 MeV resonance is evident. For smaller values of $\theta_d{}^l$, the quasi-free scattering of deuterons on the α-cluster in ^{6}Li is dominant.

Franz and Fick [8]) report a weakly excited narrow 2^+ state 55 keV above the d+d threshold. It is stated to have an $l = 0$, $S = 2$ configuration, with a {2 2} partition.

The present reaction, where the incoming deuteron would capture a deuteron in ^{6}Li, should be quite suitable for forming such an intermediate system. The decay cone for such a state would extend only from $\theta_d^l = 92.3°$ to 100.7° For the spectrum at 98.5°, a large fraction of the decay deuterons should enter the solid angle subtended by the second telescope, and the state would show up as a narrow line with the experimental resolution of 2.8 channels just above the threshold. For comparison, the spectrum at 104° is entirely outside the decay cone. This permits us to give an upper limit of 25 nb/sr^2 for the excitation of such a state. The 25.5 MeV level in comparison has a cross section of about 5 μb/sr^2. A decay of such a state through the ^{3}H+p or ^{3}He+n channels, where detection would be much more difficult and the width might be larger [9]), is unlikely, as a transition from the {2 2} to the {3 1} partition is inhibited. A number of other investigations have also failed to confirm this level [see Paetz *et al.* [10]), and work cited therein].

The angular distribution was evaluated for the 25.5 MeV level. The resulting recoil c.m. system angular correlation is shown in fig. 4 and compared with the corresponding distribution from the ^{4}He(α, α't) reaction. The 0^+ or 1^+ assignment based on the isotropy is strengthened by the present reaction. No points are shown from the spectra for $\theta_d^l < 110.3°$ because of possible interference with the quasi-elastic peak. If the absence of interference is assumed, the isotropic trend continues to smaller angles, as such a c.m. distribution corresponds to a lab distribution with a minimum at the recoil axis at $\theta_d^l = 95°$.

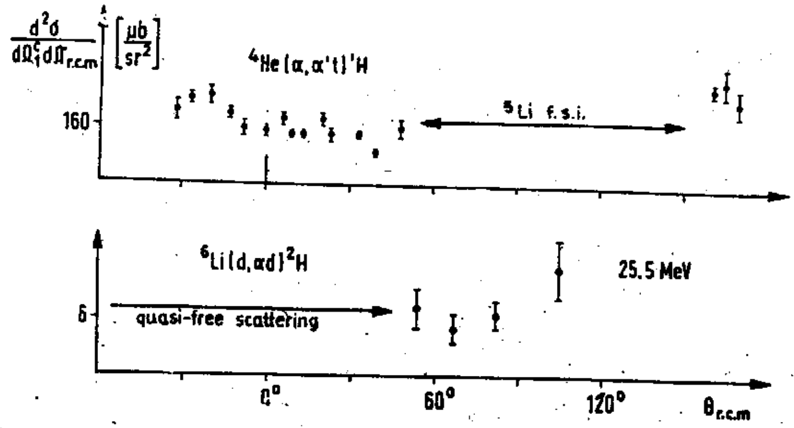

Fig. 4. Angular correlation for the 25.5 MeV level. The data for the ^{4}He(α, α't)^{1}H reaction are taken from ref. [1]).

Some phases derived from measurements of the ^{2}H($\vec{d}$, d) reaction at Basel and recently at Zürich [11]) show a rapid change near the 25.5 MeV level. It will be informative to compare our results with the results of a phase-shift analysis in terms of resonances.

4. Conclusion

Measurements reported in the present work are particularly suitable for investigating the 21.9 and 25.5 MeV levels of ^{4}He. The data are well fitted with eq. (7), the χ^2 ranging between 1.05 and 1.40 per degree of freedom. The resonance parameters found are $E_x = 21.9 \pm 0.1$ MeV with $\Gamma = 1.8 \pm 0.1$ MeV for the ^{3}H+^{1}H channel, in good agreement with previous work. For the 25.5 MeV level the parameters are $E_x = 25.5 \pm 0.5$, 24.8 ± 0.9 and 25.8 ± 0.2 MeV with $\Gamma = 3.5 \pm 1.7$, 5.6 ± 2.1 and 3.7 ± 0.8 MeV for the ^{3}H+^{1}H, ^{3}He+n and ^{2}H+d channels, respectively, in agreement with the weighted average values of $E_x = 25.5$ and $\Gamma = 3.0$ MeV. (See table 2 in ref. [2]) for a summary of results.) The errors given are standard deviations derived from the error matrix. The model dependence is not taken into account.

The authors believe that there is now adequate evidence from three particle reactions for the existence of the 25.5 MeV level. Without postulating its existence, no acceptable fits of the many spectra investigated could have been obtained. It will be informative to check whether this level is also observed in compound reactions.

Owing to f.s.i. in the mass-5 ground states, little was learned about the higher resonances. Here only measurements at substantially higher incident energy, and possibly out of the reaction plane, would appear to lead to further progress. This is also true for the peak observed at $E_x = 34$ MeV.

The evaluation of the angular correlation of the 25.5 MeV level has provided data in an angular range not previously measured. The isotropy confirms the previous 0^+ or 1^+ assignment.

No branching ratios are given, as a direct two-particle transfer reaction involving two spin-1 particles is likely to lead to angular correlations that are more complex than those for inelastic scattering for all but isotropic distributions. Thus one cannot extrapolate the differential cross section with confidence to regions not measured. Other pertinent points are discussed in refs. [1,2]).

The authors wish to express their gratitude to Professors A. Citron, W. Heinz and H. Schopper for their encouragement and support. We would like to thank Dr. M. A. Fawzi and Mr. W. Siebert for assistance with the experiment, and Dr. D. P. Saylor for helpful discussions concerning the theory.

References

1) E. L. Haase, W. N. Wang and M. A. Fawzi, Nucl. Phys. **A172** (1971) 81
2) E. K. Lin, R. Hagelberg and E. L. Haase, Nucl. Phys. **A179** (1972) 65
3) R. Hagelberg, Ph.D. thesis, Universität Karlsruhe, 1971, and external report 3/70/15, Kernforschungszentrum Karlsruhe, 1970
4) A. Messiah, Mécanique quantique (Dunod, Paris, 1964) ch. XIX, sect. 19
5) J. V. Noble, Phys. Rev. **C1** (1970) 1742
6) J. C. Legg, W. D. Simpson and S. T. Emerson, Nucl. Phys. **A119** (1968) 209
7) R. Hagelberg, E. L. Haase and Y. Sakamoto, to be published
8) H. W. Franz and D. Fick, Nucl. Phys. **A122** (1968) 591
9) F. Seiler, Basel, to be published
10) H. Paetz gen. Schieck, T. R. Donoghue, R. M. Prior and S. E. Darden, Nucl. Phys. **A169** (1971) 71
11) W. Grüebler, private communication

INVESTIGATION OF $T=0$ EXCITED STATES OF ^{4}He VIA THE ^{4}He(d, d′ t)^{1}H AND ^{4}He(d, d′ d)^{2}H REACTIONS *

E. K. LIN [†], R. HAGELBERG and E. L. HAASE

Institut für Experimentelle Kernphysik der Universität und des Kernforschungszentrums Karlsruhe, Germany

Received 24 August 1971
(Revised 25 October 1971)

Abstract: The three-particle reactions ^{4}He(d, d′t)^{1}H and ^{4}He(d, d′d)^{2}H were investigated at an incident energy of 52 MeV. The energy spectra of tritons and deuterons were measured simultaneously with inelastically scattered deuterons with two detectors, one at a fixed angle of 31° lab and the other at varied angles ranging from 20° to 38° lab. The data are interpreted in terms of six resonances arising in final-state interaction through $T=0$ excited states of ^{4}He. Only the lower three resonances are prominent in the data.

The extracted resonance parameters (energies and widths) are consistent with those obtained from measurements of similar reactions in two other different entrance channels. A summary of results from the present measurement and the two others is presented and compared with results from the phase-shift analysis. Singles spectra from the ^{4}He(d, d′)^{4}He* reaction were also obtained and used in addition to the coincidence data in the analysis. The validity of the sequential reaction mechanism is examined.

E | NUCLEAR REACTIONS ^{4}He(d, d′t), ^{4}He(d, d′d), $E=52$ MeV; measured $\sigma(E_1, \theta_1)$, $\sigma(E_1, E_2, \theta_1, \theta_2)$. ^{4}He deduced levels, resonance parameters, angular correlations, partial widths. Natural gas target.

1. Introduction

In recent years, considerable effort has been devoted to the spectroscopic investigation of the ^{4}He nucleus. Experimentally, the structure of the first several excited states of ^{4}He has been extensively investigated by means of inelastic scattering $^{1-5}$) and of two-body nuclear reactions ^{11}). See also ref. ^{7}) and work cited there. Many theoretical calculations $^{6-10}$) have been made to predict the general features of the energy spectrum. As a result, a consistent picture of the first three $T=0$ excited states of ^{4}He at 20.2, 21.4 and 22.2 MeV has been obtained. The present knowledge of the excited states of ^{4}He has been summarized by Meyerhof and Tombrello ^{11}) and reviewed more recently by Werntz and Meyerhof ^{7}).

An alternate possibility for the experimental investigation of the excited states of ^{4}He is to study the three-particle reactions with intermediate ^{4}He resonances appearing in the exit channel through final-state interaction (f.s.i.) between two of the outgoing particles. Experimental work for such a study has been recently reported by Haase *et al.* ^{12}) on the ^{4}He(α, α' t)^{1}H and ^{4}He(α, α' d)^{2}H reactions, Assimakopoulos

---

*This paper has been published in Nuclear Physics, A179 (1972) 65–79.

[†] On leave from the Institute of Physics, Tsing Hua University and Academia Sinica, Taiwan, China.

et al. [13]) on the $^2H(^3He, p\,t)^1H$ reaction and Lin *et al.* [14]) on the $^7Li(p, \alpha' p)^3H$ reaction. From kinematically complete measurements at a bombarding energy of 24 MeV, Assimakopoulos *et al.* [13]) have deduced the energies (E) and widths (Γ) of two resonances, corresponding to the first and unresolved higher excited states of ^4He at $E_1 = 20.01 \pm 0.02$ MeV, $\Gamma_1 = 0.12 \pm 0.02$ MeV and $E_2 = 21.36 \pm 0.10$ MeV, $\Gamma_2 = 2.0 \pm 0.2$ MeV, respectively, Lin *et al.* [14]) have observed two resonances in the coincidence spectra measured at $E_p = 9.1$ MeV and interpreted it as due to the strong $p + {}^3H$ f.s.i. through the first and second excited states of ^4He at 20.1 and 21.2 MeV Furthermore, a series of coincidence measurements have been performed in this laboratory. In previous work Haase *et al.* [15]), the reactions $^4He(\alpha, \alpha' t)^1H$, $^4He(\alpha, \alpha' {}^3He)n$ and $^4He(\alpha, \alpha' d)^2H$ at $E_\alpha = 104$ MeV were investigated over a wide range of angles; five resonances corresponding to $T = 0$ states of ^4He up to 32 MeV excitation were reported and the resonance energies and widths were extracted from a detailed analysis of the coincidence spectra.

The present work is a continuation of the experimental investigation on the ^4He nucleus using the following three-particle reactions induced by deuterons of 52 MeV:

$$d + {}^4He \rightarrow d' + {}^4He^* \quad \begin{array}{l} \rightarrow t + {}^1H \\ \rightarrow d + {}^2H. \end{array} \qquad (1)$$

An investigation of similar reactions [16]) is also completed namely, the $^6Li(d, \alpha' t)^1H$, $^6Li(d, \alpha' {}^3He)n$ and $^6Li(d, \alpha' d)^2H$ reactions, in which ^4He resonances also appear through f.s.i. between a pair of the outgoing particles. All these reactions selectively excite only $T = 0$ states of ^4He. The combined data from measurements of these reactions should be useful for a comparative study of $T = 0$ excited states of ^4He as well as the reaction mechanism responsible.

In summary, the purpose of this paper is: (i) to provide data from the present investigation on reactions (1), (ii) to summarize the results on the spectroscopic information of ^4He from measurements of reactions with three different entrance channels, $\alpha + {}^4He$, $d + {}^4He$ and $d + {}^6Li$; and to compare with results of the phase-shift analysis by Werntz and Meyerhof [7]) and (iii) to examine the validity of the sequential reaction mechanism.

2. Experimental procedure

The experiment was carried out using 52 MeV deuterons from the Karlsruhe isochronous cyclotron. The reactions $^4He(d, d' t)^1H$ and $^4He(d, d' d)^2H$ were performed simultaneously employing a ^4He gas target at 1 atm NTP. The inelastically scattered deuterons were detected in coincidence with tritons and deuterons from the decay of $^4He^*$ The experimental method is the same as that used in a previous measurement [15]) except that the time-of-flight (TOF) particle identification [17]) was adopted for the inelastically scattered deuterons. This method employs a discriminator window set on the particle identifier signal generated by summing the TOF signal and an adjustable fraction of the energy signal. An ORTEC time pick-off was used to obtain the timing signal. The detector was a 3 mm ion-implanted silicon solid-state device; it was placed at a distance of 125 cm from the target. The effective target thickness was defined by a 10 mm collimator near the gas target and the solid angle was defined by a 10 mm slit on a 18 mm diam. collimator in front of the detector.

To detect the tritons and deuterons a solid-state telescope, consisting of a 110 μm thick ΔE detector and 1 mm thick E detector, was used in conjunction with an ORTEC particle identifier with a discriminator set on tritons and deuterons. This telescope with a collimator of 17 mm diam. was located at a distance 292 mm from the center of the target.

The coincidence resolving time was set to 30 ns. Coincident events were taken in the reaction plane at pairs of angles chosen from a calculation of kinematics [18]. The detector for the inelastic deuterons was kept at a fixed lab angle of 31° and the other varied over several angles ranging from 20° to 38° lab. The correction for random coincidences is small, as for the previous measurement [15]. Measurement of singles spectra from the ^{4}He(d, d′)^{4}He* reaction were also made simultaneously during the run and the data obtained were used in addition to the coincidence data in the analysis.

3. Results and analysis

Fig. 1 shows a set of coincidence spectra from the ^{4}He(d, d′ t)^{1}H reaction. The energy resolution was about 300 keV. The spectrum for $\theta_2^1 = 37°$ corresponds to the recoil axis of ^{4}He* for 20.2 MeV excitation. From fig. 1 it is readily observed that all the spectra are characterized by a single prominent bump peaking at about 21.2 MeV of excitation and little structure above. At large angles the 20.2 MeV 0^+ state shows up as a shoulder at the upper end. Another feature can be seen from fig. 1; there appears a sharp drop near ≈ 21 MeV excitation. Measurements of the ^{6}Li(d, α′ t)^{1}H reaction [16] near the recoil axis do not show such a drop in the energy spectra; there the 21.1 MeV resonance is not excited and a pronounced peak occurs at 21.9 MeV. For the reactions compared, the decay mode is the same and the Coulomb effect as well as threshold effects would have the same influence. A discussion of this point is given elsewhere [16].

The measured coincidence spectra for the ^{4}He(d, d′ d)^{2}H reaction are presented in fig. 2. They exhibit rather little structure. Here the intensities are much lower than in the t + ^{1}H exit channel.

An understanding of the energy spectra for the reactions investigated generally requires a convenient parameterization of data. We assume the process to be sequential. A long lived intermediate system is formed in a direct reaction, and then decays independent of its mode of formation like a compound nucleus. The inelastic particle and the intermediate system move in opposite directions in their c. m. system,

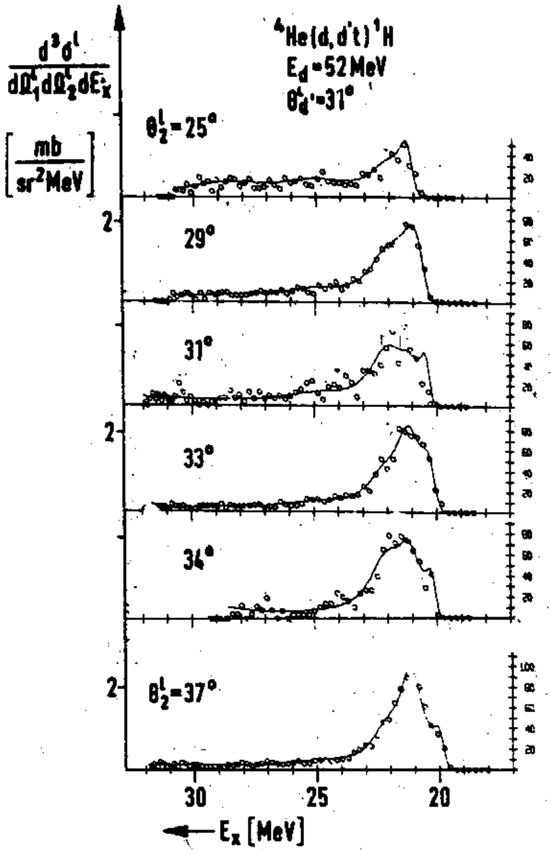

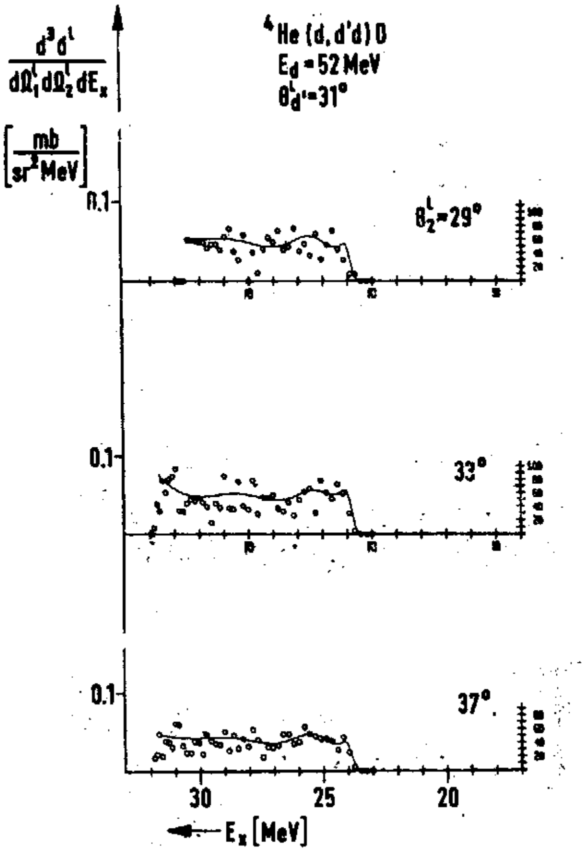

Fig. 1. Coincidence spectra from ^{4}He(d, d't)^{1}H reaction. They are plotted as a function of excitation energy in ^{4}He. The solid line is obtained from the fitting as discussed in the text.

Fig. 2. Coincidence spectra from ^{4}He(d, d'd)^{2}H reaction. They are plotted as a function of excitation energy in ^{4}He. The solid line is obtained from the fitting as discussed in the text.

and thus their interaction is neglected. For the broader resonances the applicability of this simple model may cease to be valid and higher order graphs might have to be taken into account. Following the approach of Goldberger and Watson [19]) and the formalism of Humblet and Rosenfeld [20]), the differential cross section for a given lab. angle $\theta_2^{\text{lab.}}$ in the three-particle reaction can be expressed [15]) as

$$\frac{d^3\sigma_{\text{exp}}^{\text{lab.}}}{d\Omega_1^{\text{lab.}}\, d\Omega_2^{\text{lab.}}\, dE_1^{\text{lab.}}} = F\left\{\left[C(\theta_2^{\text{lab.}}) + \sum_n \frac{\Gamma_n B_n(\theta_2^{\text{lab.}}) + (E_x - E_n)A_n(\theta_2^{\text{lab.}})}{(E_x - E_n)^2 + \frac{1}{4}\Gamma_n^2}\right] \rho^{\text{lab.}}(E_1^{\text{lab.}})\right\}, \quad (2)$$

where C is a constant non-resonant term, the B coefficients give the intensity of Breit-Wigner single-level resonances and the A coefficients give the intensity of interference between the resonances and the non-resonant background. Coulomb and threshold effects, interference between levels and coupling between decay channels are not taken into consideration and are neglected in the derivation of eq. (2). F symbolizes the operation of folding the expression in the curly brackets with the experimental resolution.

For the detailed explanation of above equation, see ref. [15]). Using this equation energy spectra for each reaction are fitted simultaneouly with an automatic fitting programme employing an IBM 360-65 computer. Resonance positions and widths are varied together as parameters and coefficients A, B, C are adjusted individually for each spectrum until a minimum of χ^2 is reached. Generally there are about 100 data points for each spectrum included in the fitting. The resulting coefficients vary smoothly with angle as demonstrated by the angular correlations.

In analysing data from singles spectra in the ^{4}He(d, d′) reaction, the following general form [21]) of the matrix element is used:

$$|M_c^{\text{seq}}|^2 = U^2 \sum_{l=0}^{\max} \left[C_l(E) + \sum_n \frac{\frac{1}{2}\Gamma_{ln} B_{ln}(E) + (E-E_{ln}) A_{ln}(E)}{(E-E_{ln})^2 + \frac{1}{4}\Gamma_{ln}^2} \right] \tag{3}$$

This expression is related to eq. (2) by integrating over the solid angle $\Omega_{\text{r.c.m.}}$ in the recoil c.m. system. Multiplying eq. (3) with the appropriate phase-space factor ρ and summing over three decay channels (t + ^{1}H, ^{3}He + n and d + ^{2}H), one obtains the differential cross section $\mathrm{d}^2\sigma/\mathrm{d}\Omega_1^{\text{lab.}}\mathrm{d}E_1^{\text{lab.}}$. We assume on the basis of the coincidence spectra that the intensities for the t + ^{1}H and ^{3}He + n channels are equal and the intensity for the d + ^{2}H channel is one-third of the former. A deviation from this assumption might have a slight effect above the d′ + d threshold.

3.1. THE ^{4}He(d, d′ t)^{1}H AND ^{4}He(d, d′ d)^{2}H REACTIONS

The reactions studied excite only $T = 0$ states of ^{4}He, inasmuch as isospin conservation holds. The second excited state of ^{4}He, a 0^-, $T = 0$ state at 21.4 MeV proposed by Barrett *et al.* [22]), is forbidden in the α-^{4}He inelastic scattering investigated previously [15]); it is allowed in the present reactions. We included this state in the energy parameterization. An attempt to fit energy spectra with only a single Breit-Wigner resonance gave a very poor result. Two fits including more resonances with different extreme assumptions were carried out and they gave equally acceptable fits for the ^{4}He(d, d′ t)^{1}H reaction:

(i) resonances at 22.0 and 21.1 MeV plus a weak one at 20.2 MeV interfere with a significant non-resonant background;

(ii) the non-resonant background is assumed to be zero and further resonances at 25.1, 28.6 and 31.4 MeV were included. Though these latter are not evident in the rather unstructured data for higher excitation energies, the parameters are consistent with those observed in other reactions.

The latter fits are shown in fig. 1. It is felt that the latter assumption is more reasonable; for other reactions [15,16]) the non-resonant term was negligibly small and in the present analysis the non-resonant term would certainly not be isotropic either. Incidentally the spectrum for $\theta_2^{\text{lab.}} = 25°$ is beyond the edge of the decay cone for the 21.1 MeV resonance.

The only interfering reaction would be caused by $T = \frac{1}{2}$ resonances of ^{3}He between 7.5 and 16 MeV excitation, shifting in ^{4}He excitation energy with changing $\theta_2^{\text{lab.}}$ However, no evidence was found for such resonances. Quasifree scattering can be excluded on the basis of its large negative Q-value.

The first three $T=0$ excited states at 20.2, 21.1 and 22.0 MeV are below $d+{}^2H$ threshold. They are not excited in the ${}^4He(d, d'd){}^2H$ reaction. The measured spectra from this reaction can be adequatly fitted with the same other three higher resonances as for the $t+{}^1H$ decay channel. Fig. 2 shows the data for three of the simultaneously fitted spectra from this reaction. The results are listed for comparison in table 1 and further dicussed in sect. 4.

Having achieved satisfactory fits and extracted ${}^4He$ resonance positions and widths, one may become more ambitious and try to get information on the spin and parity of these states. We have performed an angular correlation analysis for the ${}^4He(d, d't){}^1H$ reaction and the results are shown in fig. 3. An angular correlation analysis for the ${}^4He(d, d'd){}^2H$ reaction was not made, since statistics of data from this reaction at some angles are meager.

The first excited state of ${}^4He$ at 20.2 MeV is well known to be 0^+. It is just above threshold (19.82 MeV) of the ${}^4He(d, d't){}^1H$ reaction and was found to be very weakly excited here. Its intensity is much lower than in the ${}^4He(\alpha, \alpha' t){}^1H$ reaction [15] in

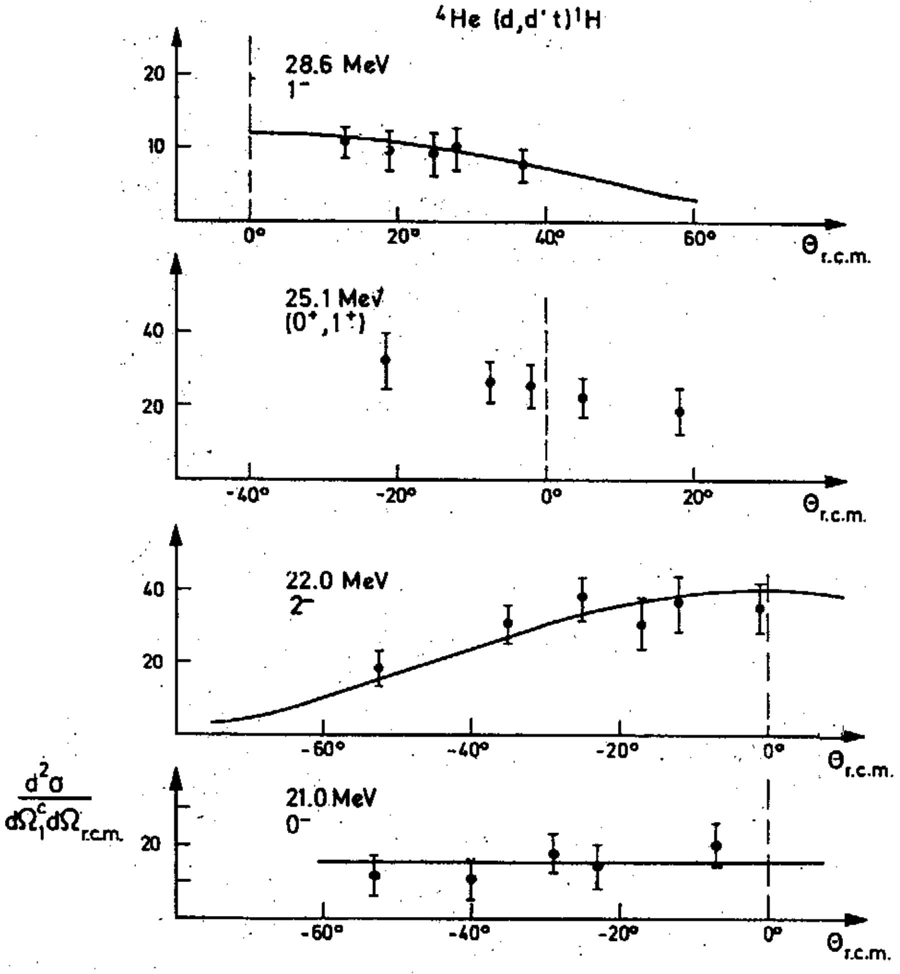

Fig. 3. Angular correlations in the r.c.m. system for the ${}^4He(d, d't){}^1H$ reaction measured at $\theta_1^{lab.}=31°$. Twenty units correspond to about 90 μb/sr². The quoted errors are derived from counting statistics and normalization error.

which the measured angular correlation for this state shows an isotropic distribution. Fig. 3 gives the angular correlations in the recoil c.m. system (r.c.m.) for the excited states at 21.1, 22.0, 25.1 and 28.6 MeV for the ^{4}He(d, d' t)^{1}H reaction. It is seen that the second excited state at 21.1 MeV has an isotropic angular distribution as expected for a 0^- state. The 22.0 MeV 2^- resonance is a non-natural parity state; it shows up as a prominent peak in the other ^{4}He f.s.i. spectra [15,16]. The measured angular correlation can be fairly well fitted with a $\cos^2\theta$ distribution [15,23]) for a 2^- state, as observed in the ^{4}He(α, α' t)^{1}H reaction. A new excited state at 25.5 MeV was reported in the previous work [15]). Evidence for this state is also seen in the reactions studied here. As can be seen from fig. 3, it has a more or less isotropic distribution. This is consistent with a previous 0^+ or 1^+ assignment [15]) for this state. Previous work [11,15]) indicates the 28.5 MeV state to be 1^-, $S=1$. The measured angular correlation for this state was compared with a $\cos^2\theta$ distribution [15]) from the impulse-approximation theory for a 1^- state with channel spin $S=1$ and a consistent fit within the errors is observed in fig. 3. The experimental data of the higher excited state at 31.4 MeV are uncertain, as the spectra extend only to ≈ 31 MeV excitation. The angular correlation for this state is incomplete. It was suggested in a resonance interpretation of the ^{3}H(p, n)^{3}He reaction [7]) that a 2^+, $T=0$ state might exist in ^{4}He near 31 MeV excitation energy. The present data are insufficient to give an positive identification for this state, though such a resonance is needed to fit the data.

3.2. THE ^{4}He(d, d')^{4}He* REACTION

A typical distribution of the ^{4}He(d, d')^{4}He* reaction is presented in fig. 4. This spectrum was measured at angle $\theta^{\text{lab.}} = 37.9°$. Also shown in fig. 4 for comparison is a coincidence spectrum at the same angle $\theta_1^{\text{lab.}} = \theta_2^{\text{lab.}} = 37.9°$. Here the square of the

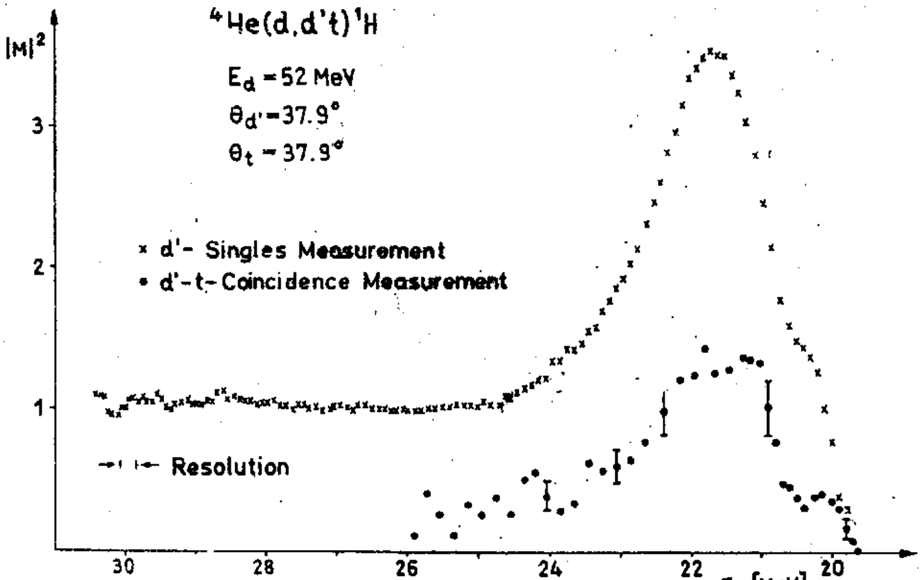

Fig. 4. Comparison of the ^{4}He(d, d') singles and the ^{4}He(d, d' t)^{1}H coincidence spectra. Note that as ordinate the matrix element $|M|^2$ is plotted (see text).

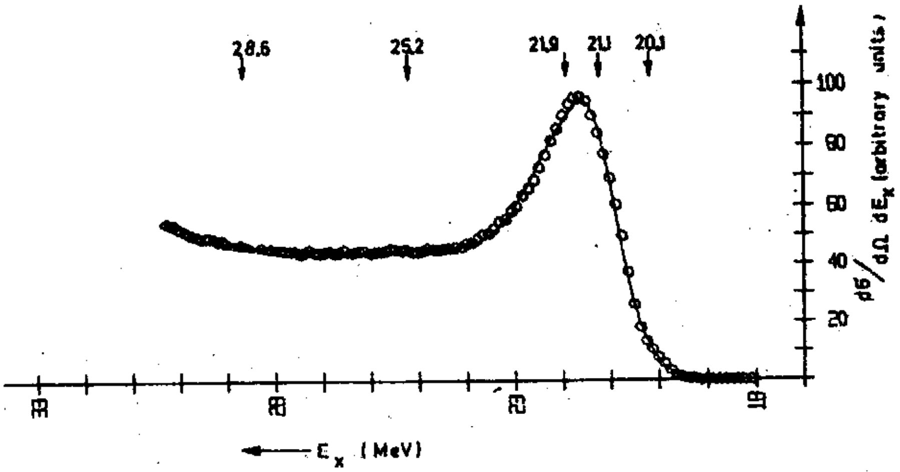

Fig. 5. A representative fit of a singles spectrum for the ^{4}He(d, d′) reaction from the computer output The experimental data are those at $\theta_l = 31°$. The solid curve is obtained from the fitting as discussed in the text.

matrix element is shown in arbitrary units to eliminate the distortions due to different shape of the phase-space distribution for singles and coincidence spectra (obtained, not quite exact, by dividing the spectra by the phase-space distributions folded with the experimental resolution). For this pair of angles the 20.2 MeV state is more pronounced, as is also the sharp drop near $E_x = 21$ MeV. On the high-energy side one sees a continous distribution with a broad maximum. The elastic peak is far off to the right.

Having the information obtained from the coincidence spectra, in particular, the values for the relative intensity of the different decay channels and evidence for freedom from interfering reactions, one can proceed to analyse the singles spectra with confidence. The fitting of singles spectra provides a way to avoid the troublesome interference between resonances. We obtained a satisfactory fit with an inclusion of six resonances as shown in fig. 5. In table 1 we list the representative results from the fit of two singles spectra at $\theta^{\text{lab.}} = 31°$ and 38°. Also included in table 1 is the average relative intensity for six resonances fitted at these two angles. The second resonance appears at energy $E_2 = 21.1$ MeV with width $\Gamma_2 = 0.80$ MeV. The third resonance ($E_3 = 22.0$ MeV, $\Gamma_3 = 1.80$ MeV) occurs at the expected energy for the 2^- state. These values are comparable to the early values ($E_2 = 20.7$ MeV, $\Gamma_2 = 1.4$ MeV; $E_3 = 21.9$ MeV, $\Gamma_3 = 1.6$ MeV) from ^{4}He(d, d′) singles spectra [21]. The positions of three resonances at 20.2, 22.0 and 28.6 MeV also agree fairly well with those from a previous ^{4}He(α, α′) singles measurement [21].

3.3. SUMMARY OF THE RESULTS ON RESONANCE PARAMETERS

It should be pointed out that of all the reactions leading to exited states of ^{4}He investigated at this laboratory, the ^{4}He(d, d′ t)^{1}H reaction and the corresponding singles spectra are the only ones to give information on the second excited (0^-) state of ^{4}He. It is felt that the resonance parameters so obtained are more precise than those derived from the phase-shift analysis, though Coulomb and threshold effects have been neglected. It is expected that taking them into account will lower the resonance position. The results for the 21.9 MeV resonance are in agreement with results from the other reactions. As far as the higher resonances are concerned, the data presented in this paper are not conclusive when considered by themselves. However they are entirely consistent with the results of the other reactions investigated.

Resonance positions and widths obtained in fitting data from coincidence and singles measurements are summarized in table 1. As can be seen by comparison, they are in good agreement. For the 20.2, 22.0 and 28.6 MeV resonances our results on J^π are consistent with those of Meyerhof and Tombrello [11]). If our interpretation of the 22.0 and 28.6 MeV states is correct, the shape of angular correlations is not affected if they interfere with each other, although both have $S=1$. The 22.2, 25.1 and perhaps 31.4 MeV resonances appear to be isotropic in the measured angular correlation. If, as the 20.2 MeV resonance is known to be, all are $S=0$, then interference occurs only between non-adjacent resonances, as different channel spins do not interfere. For the coincidence analysis the neglect of interference between the adjacent resonances, the 0^- and the 2^- levels at 21.1 and 22.0 MeV respectively, might be severe. However, in a singles spectrum there can be no interference, as the interference between resonances of different J^π terms drop out upon integration over the solid angle $\Omega_{\mathrm{r.c.m.}}$.

TABLE 1

Resonance positions and widths (MeV) obtained in fitting data from coincidence and singles measurements

Coincidence measurement		Singles measurement from ^{4}He(d, d′)^{4}He*		
^{4}He(d, d′t)^{1}H	^{4}He(d, d′d)^{2}H	$\theta^{\mathrm{lab.}}=31°$	$\theta^{\mathrm{lab.}}=38°$	relative intensity (average over two angles)
20.2 ±0.1 (Γ=0.20±0.08)	–	20.1 ±0.1 (0.20±0.08)	20.2 ±0.4 (0.20±0.08)	0.012
21.1 ±0.1 (Γ=0.8 ±0.1)	–	21.2 ±0.1 (0.8 ±0.1)	21.1 ±0.1 (0.6 ±0.1)	0.54
22.0 ±0.1 (Γ=1.8 ±0.1)	–	21.9 ±0.1 (1.7 ±0.1)	22.0 ±0.1 (2.0 ±0.1)	1.14
25.1 ±0.2 (Γ=2.9 ±0.3)	25.2±0.1 (2.2±0.3)	25.2 ±0.1 (3.3 ±0.5)	25.1 ±0.1 (2.9 ±0.5)	0.01
28.6 ±0.2 (Γ=3.8 ±0.4)	28.7±0.2 (4.6±0.5)	28.6 ±0.1 (4.1 ±0.2)	28.6 ±0.1 (3.1 ±0.2)	0.032
31.4 ±0.3 (Γ=2.8 ±0.6)	31.9±0.3 (4.9±1.1)	31.5 ±0.2 (2.8 ±0.1)	31.8 ±0.2 (5.6 ±0.7)	0.18

A dash means that the level is below threshold. The errors given here are derived from error matrix, to indicate the sensitivity of statistics. The actual errors are more than these values as described in the text.

To estimate the uncertainly in the deduced values of position (E) and width (Γ) for each resonance, we calculated the error matrix in the simultaneous fits of the energy spectra. The values derived from the fits with χ^2 deviating by unity turn out to be quite small, ranging between a few tens of keV up to one MeV, when many spectra are fitted simultaneously. With inclusion of the primary energy calibration error and systematic error arising in the fitting process, the actual errors were estimated to be, on the average, about 10% of the width in position and about 20% of width in width, as reflected by the fluctuation of values listed in table 1.

4. Comparison with measurements of α-particles on ⁴He and deuterons on ⁶Li reactions

In what follows we compare the present results with measurements of the following reactions [15, 16]:

$$^4\mathrm{He}(\alpha,\alpha'\,\mathrm{t})^1\mathrm{H},\quad ^4\mathrm{He}(\alpha,\alpha'\,^3\mathrm{He})\mathrm{n},\quad ^4\mathrm{He}(\alpha,\alpha'\,\mathrm{d})^2\mathrm{H}, \tag{4}$$

$$^6\mathrm{Li}(\mathrm{d},\alpha'\,\mathrm{t})^1\mathrm{H},\quad ^6\mathrm{Li}(\mathrm{d},\alpha'\,^3\mathrm{He})\mathrm{n},\quad ^6\mathrm{Li}(\mathrm{d},\alpha'\,\mathrm{d})^2\mathrm{H}. \tag{5}$$

All reactions listed above lead to $T=0$ ^{4}He resonances appearing in the exit channel through f.s.i. between a pair of the outgoing particles.

As regards the positions and widths of resonances extracted from the reactions investigated in this paper, they agree resonably well with the values found from reactions (4) and (5). A comparison of results from these various reactions is presented in table 2. The first column of table 2 gives the average positions of resonances appearing in the three different entrance channels. The consistancy obtained in this analysis confirms the resonance parameters determined. No dependence of the resonance parameters on either $\theta_1^{\mathrm{lab.}}$ or $\theta_2^{\mathrm{lab.}}$ was observed.

As far as the measured energy spectra are concerned, the resonances appearing in the $\alpha+{}^4$He and d$+{}^4$He entrance channels with the same t$+{}^1$H decay channels are about equally intense, while the resonances observed in the two d$+{}^2$H decay channels are much weaker in the lab. system. The 0^- resonance at 21.1 MeV is forbidden in the t$+{}^1$H and ^{3}He$+$n channels of reactions (4). It was observed in the ^{4}He(d, d′ t)^{1}H reaction, but not in the t$+{}^1$H and ^{3}He$+$n channels of reaction (5). The 2^- resonance at 21.9 MeV shows up in the α-^{4}He and d-^{4}He reactions with an angular correlation of a 2^- distribution. It appears even more pronounced in both t$+{}^1$H and ^{3}He$+$n channels of reactions (5).

Data from reactions of all three entrance channels indicate that a new $I=0$ excited state of ^{4}He exists at ≈25.5 MeV. In particular, it shows up clearly in the spectra from ^{6}Li(d, α′ d)^{2}H reaction. The observed resonance for this state in each case is rather broad, having a width of ≈3 MeV. The investigation of the ^{4}He(α, α′)^{4}He* reaction by Gross *et al.* [5]) also reveals a peak at ≈26 MeV excitation. It would be a candidate for a second 0^+ state at this excitation as predicted recently by Hutzelmeyer [24]). As one goes up to higher excitation at 28.5 and 31.7 MeV, the resonance widths in all three entrance channels become much larger

TABLE 2

Comparison of resonance positions and widths obtained in fitting data from 8 reactions

$T=0$	^{4}He+α			^{4}He+d		^{6}Li+α		
	a)	b)	c)	d)	e)	f)	g)	h)
20.2 0^+	20.20 ± 0.08 ($\Gamma=0.20\pm0.08$)	–	–	20.2 ± 0.1 (0.20 ± 0.08)	–	not observed		–
21.1 0^-	forbidden		–	21.1 ± 0.1 (0.8 ± 0.1)	–	not observed		–
21.9 2^-	21.9 ± 0.1 ($\Gamma=1.8\pm0.1$)	21.9 ± 0.1 (1.9 ± 0.1)	–	22.0 ± 0.1 (1.8 ± 0.1)	–	21.9 ± 0.1 (1.8 ± 0.1)	consistent with other values	–
25.5 ($0^+, 1^+$)	25.5 ± 0.1 ($\Gamma=2.9\pm0.1$)	25.6 ± 0.1 (3.1 ± 0.2)	at most weak	25.1 ± 0.2 (2.9 ± 0.3)	25.2 ± 0.1 (2.2 ± 0.3)	25.5 ± 0.5 (3.5 ± 1.7)	24.8 ± 0.9 (5.6 ± 2.1)	25.8 ± 0.2 (3.7 ± 0.8)
28.5 1^-	28.3 ± 0.1 ($\Gamma=5.3\pm0.1$)	28.3 ± 0.1 (5.3 ± 0.2)	28.7 ± 0.1 (5.0 ± 0.15)	28.6 ± 0.2 (3.8 ± 0.4)	28.7 ± 0.2 (4.6 ± 0.5)		27.7 ± 0.3 (3.1 ± 1.1)	consistent
31.7	31.7 ± 0.1 ($\Gamma=5.6\pm0.2$)	31.7 ± 0.2 (5.5 ± 0.2)	31.9 ± 0.1 (5.9 ± 0.2)	31.4 ± 0.3 (2.8 ± 0.6)	31.9 ± 0.3 (4.9 ± 1.1)		consistent	
number of spectra fitted	14+8	13	14	6	3	13	4	4

A dash means that the level is below threshold. Errors are derived from error matrix, to indicate sensitivity on statistics only. The actual errors are more than these values as discussed in the text. Consistent means that good fits were obtained with the average values for the corresponding resonance, but these values were permitted to vary.

a) ^{4}He(α, α' t)^{1}H. b) ^{4}He(α, α' ^{3}He)n. c) ^{4}He(α, α' d)^{2}H. d) ^{4}He(d, d′ t)^{1}H.
e) ^{4}He(d, d′ d)^{2}H. f) ^{6}Li(d, α' t)^{1}H. g) ^{6}Li(d, α' ^{3}He)n. h) ^{6}Li(d, α' d)^{2}H.

TABLE 3

Differential cross sections in mb/sr for the α-^{4}He and d-^{4}He reactions

Levels (MeV)	^{4}He+α			^{4}He+d	
	a)	b)	c)	d)	e)
20.2	1.3	–	–	<0.05	–
21.1	–	–	–	2.0	–
21.9	3.4	1.8	–	1.5	–
25.5	14	13	<3	2.2	0.34
28.5	17	13	17	0.45	0.43
31.7	36	32	36	1.13	1.03

Above values are dependant on the magnetic substate populations assumed in the text.

a) ^{4}He(α, α't)^{1}H.

b) ^{4}He(α, α' ^{3}He)n.

c) ^{4}He(α, α'd)^{2}H.

d) ^{4}He(d, d' t)^{1}H.

e) ^{4}He(d, d' d)^{2}H.

The angular correlations obtained from ^{4}He(α, α' t)^{1}H and ^{4}He(α, α' ^{3}He)n reactions [15] are more complete than those from the ^{4}He(d, d' t)^{1}H reaction. Nevertheless, the measured angular correlations in the present investigation are consistent with the measurements of the former two reactions. This enables us to make assignments of spin and parity of five ^{4}He resonances excluding the higher one at 31.7 MeV which appears at the end of the measured spectra with ambiguity in the fitting process.

If the sequential decay implies that the decay of the intermediate system is independent of formation, then the branching ratios for the decay of the various three-particle reactions leading to the same intermediate system ought to be the same. In order to see whether the branching ratios for the three decay channels (t+^{1}H, d+^{2}H and ^{3}He+n) from α-particles on ^{4}He and deuterons on ^{4}He and deuterons on ^{6}Li reactions agree with each other, respectively, we estimated the differential cross sections $d\sigma/d\Omega_1^c$, by assuming an isotropic distribution for the 20.2, 21.1, 25.5 and 31.7 MeV states and a $\cos^2\theta_{\text{r.c.m.}}+\sin^2\theta_{\text{r.c.m.}}\sin^2\phi_{\text{r.c.m.}}$ dependence [15] for the 21.9 and 28.5 MeV states. The results are listed in table 3. It is seen that the branching ratios for the α+^{4}He and d+^{4}He reactions discussed here are fairly compatible with each other, although some quantitative difficulties may arise from the above assumption made for the evaluation of the integrated cross sections. Unfortunately the existing ^{6}Li data do not permit a similar comparison. It would be interesting to see how these branching ratios can be related to those that could be derived from an analysis of elastic scattering data [7].

5. Discussion and conclusion

We have interpreted the observed ^{4}He resonances arising in f.s.i. between t-^{1}H and d-^{2}H pairs via sequential decay. The method of analysis used here is the same as the one used in the investigations of the α-particle on ^{4}He and deuterons on ^{6}Li reactions [15, 16]). Significant results of these three investigations may be summarized as follows:

(i) Within the experimental errors the three entrance and three exit channels give consistent resonance parameters for positions and widths. These parameters are a property of the intermediate system only, independent of the angles of measurement.

(ii) Within the experimental errors some angular correlations in the r.c.m. system extracted from the ^{4}He(α, α′ t)^{1}H and ^{4}He(α, α′ ^{3}He)n reactions exhibit the property of invariance to a rotation by 180° around the normal to the reaction plane.

(iii) Above features indicate a sequential process to be the reaction mechanism for all three different entrance channels. The evaluation of the branching ratios for the decay of the intermediate system into the different channels consistutes a check on this point. As is discussed in sect. 4, the branching ratios calculated from two of the three different channels do show a consistent picture.

Additional indication for the reaction mechanism comes from the angular correlation. The angular correlations in the r.c.m. system are determined by the population of the magnetic substates of the levels. Except for simple cases such as isotropy, they depend on the reaction mechanism. The symmetry of the angular correlations about the recoil axis ($\theta_{\mathrm{r.c.m.}} = 0$) is predicted by the zero-range PWBA as well as by the theory described in ref. [15]). It is gratifying to observe that these simple models account for the experimental data. Measurements on heavier nuclei will lead to better understanding of the range of applicability of these models.

It is interesting to compare the deduced resonance positions and widths with values previously obtained for $T=0$ excited states of ^{4}He from a thorough phase-shift analysis [7, 11]). Fig. 6 shows the comparison for the level scheme of ^{4}He. In a recent phase shift analysis [27]) the energies are given as 21.1 MeV for the 0^- and 22.1 MeV for the 2^- level. The agreement is seen to be very good. Four levels of $T=0$ states are confirmed here. The singles measurement of the ^{4}He(d, d′)^{4}He*-reaction investigated reenforces this conclusion. As regards the level widths, our values (except for the first excited state) are significantly smaller than those given in ref. [11]). This effect has been previously noted [25]). However one should point out that in particular the widths are dependent on which formalism is used to parametrize the data. A comparison with theoretical predictions is made in ref. [15]).

It is clear that the reactions of the kind investigated here are well suited for the study of $T=0$ excited states of ^{4}He and to deduce more reliable and precise level energies and widths. An analysis of the data leads to more insight into highly excited states of ^{4}He.

Finally, we note that the mass-5 ground state appears at several large angles quite pronounced in the energy spectra from both α-particles on ^{4}He and deuterons on ^{6}Li reactions and obscures the data seriously. It will be interesting to continue the investigation of these reactions in a plane perpendicular to the reaction plane where one may get rid of the troublesome interference from mass-5 resonances.

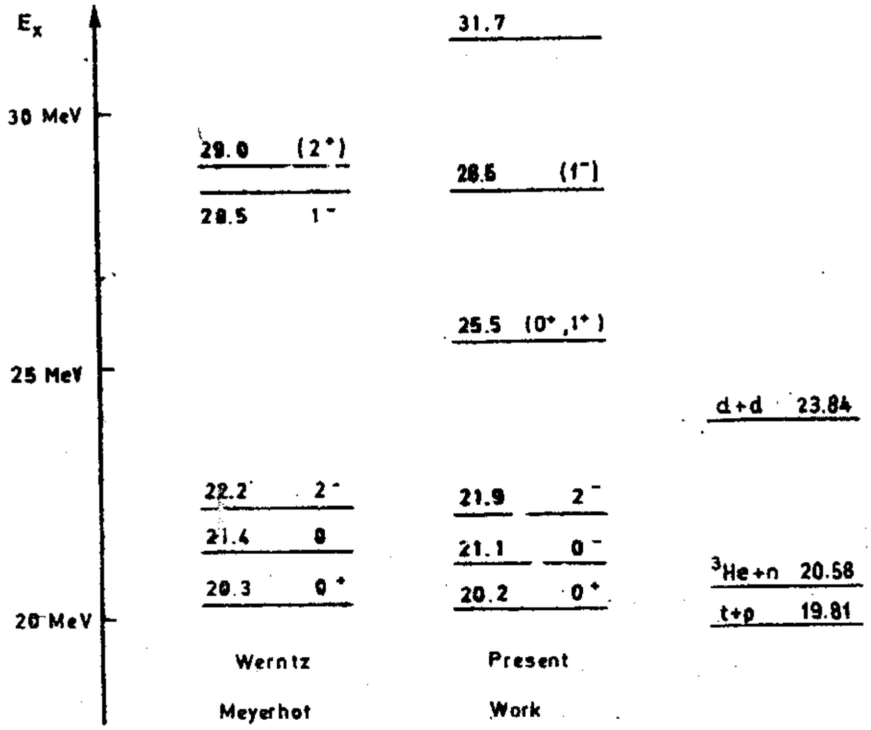

Fig. 6. Energy level diagram for $T=0$ states in ^{4}He. The resonance positions shown are weighted averag values obtained from the eight reactions investigated.

It is interesting to compare the phase-shift analysis method with the one used in the present investigation. The experimental difficulties of carrying out a coincidence measurement are compensated by the yield of spectra covering a large range of excitation energies starting at the threshold. The added recoil energy makes the simultaneous measurement of the various decay channels readily possible. The present method offers higher selectivity in many cases. It is applicable even when for lack of a stable target the phase-shift analysis cannot be carried out. However, particularly at low incident energies, one does have to concern oneself with possible interference from other FSI and the quasielastic scattering.

The energy spectra often show more structure [see ref. [26]) for instance] and are so easier to interpret. This is attributed to the fact that in the formation of the intermediate system Coulomb and centrifugal forces and, more important, the non-resonant terms play less of a role. In favourable cases, as in a polarisation experiment, only selected magnetic substates are populated.

The authors are indebted to Prof. H. Schopper, Prof. W. Heinz and Prof. A. Citron for their encouragement and support. We would like to thank Prof. W. N. Wang and Dr. M. A. Fawzi for the help in the experimental part of this work. One of authors (E.K.L.) also wishes to thank the research groups in this institute for giving him kind hospitality while he stayed in the pleasant atmosphere in the Kernforschungszentrum Karlsruhe.

References

1) R. Frosch, R. E. Rand, M. R. Yearian, H. L. Crannell and L. R. Suelzle, Phys. Lett. **19** (1965) 155
2) J. Cerny, C. Detraz and P. Pehl, Phys. Rev. Lett. **15** (1965) 300
3) P. D. Parker, P. F. Donovan, J. V. Kane and J. F. Mollenauer, Phys. Rev. Lett. **14** (1965) 15
4) L. E. Williams, Phys. Rev. **144** (1966) 815
5) E. E. Gross, E. V. Hungerford, III, J. J. Malanify, H. G. Pugh and J. W. Watson, Phys. Rev. **178** (1969) 1584
6) P. Kramer and M. Moshinsky, Phys. Lett. **23** (1966) 574
7) C. Werntz and W. E. Meyerhof, Nucl. Phys. **A121** (1968) 34
8) I. Sh. Vashakidze and V. I. Mamasaklisov, Sov. J. Nucl. Phys. **6** (1968) 532
9) T. T. S. Kuo and J. B. McGrovy, Nucl. Phys. **A134** (1969) 633
10) P. P. Szydlik, Phys. Rev. **C1** (1970) 146
11) W. E. Meyerhof and T. A. Tombrello, Nucl. Phys. **A109** (1968) 1
12) E. L. Haase *et al.*, Proc. Int. Conf. clustering phenomena in nuclei, Bochum (1969) p. 223
13) P. A. Assimakopoulos, E. Beardsworth, D. P. Boyd and P. F. Donovan, Nucl. Phys. **A144** (1970) 272
14) W. K. Lin, F. Scheibling and R. W. Kavanagh, Phys. Rev. **C1** (1970) 816
15) E. L. Haase *et al.*, Technical report KFK 1055, Kernforschungszentrum Karlsruhe (1970);
E. L. Haase, W. N. Wang and M. A. Fawzi, Nucl. Phys. **A172** (1971) 81
16) E. L. Haase, R. Hagelberg and W. N. Wang, to be published;
R. Hagelberg, KFK External report 3/70-15, Kernforschungszentrum Karlsruhe (1970)
17) H. Brückmann, E. L. Haase, W. Kluge and L. Schänzler, Nucl. Instr. Meth. **67** (1969) 29
18) G. G. Ohlsen, Nucl. Instr. Meth. **37** (1965) 240
19) M. L. Goldberger and K. M. Watson, Collision theory (Wiley; New York, 1964) p. 540
20) J. Humblet and L. Rosenfeld, Nucl. Phys. **26** (1961) 529
21) E. L. Haase *et al.*, Proc. Symp. on few-body problems, light nuclei and nuclear interactions, Brela 1967, p. 451
22) B. R. Barrett, J. D. Walecka and W. E. Meyerhof, Phys. Lett. **22** (1966) 450
23) D. P. Saylor and E. L. Haase, to be published
24) H. Hutzelmeyer, private communication
25) V. V. Komarov and H. A. Salman, Phys. Lett. **31B** (1970) 52
26) M. D. Goldberg, Prog. in fast-neutron physics, eds. G. C. Phillips, J. B. Arisu and J. R. Risser (University of Chicago Press, Chicago, 1963) p. 3
27) I. Ya. Barit and V. A. Sergeev, Yad. Fiz. **13** (1971) 1242

A STUDY OF THE LEVEL STRUCTURE IN ^{57}Fe FROM THE (d, p) REACTION ON ^{56}Fe*

H. M. SEN GUPTA and A. R. MAJUMDER
Department of Physics, University of Dacca, Dacca, Pakistan
and
E. K. LIN
Tsing Hua University and Academia Sinica, Taiwan, China
and
Institut für Experimentelle Kernphysik des Kernforschungszentrum, Karlsruhe, Germany

Received 19 August 1969
(Revised 22 September 1970)

Abstract: The reaction ^{56}Fe(d, p)^{57}Fe is investigated at 12 MeV using the Aldermaston multi-channel magnetic spectrograph. The angular distributions of protons leading to various states in ^{57}Fe upto an excitation of 6.7 MeV are measured over an angular range 5°–175°. The data are analysed with the distorted wave Born approximation calculations; a satisfactory agreement is found in most cases upto about 100°. Spin, parity and the spectroscopic factors for various states are obtained and the positions of the single-quasiparticle energies determined. The results are compared with those for the isotonic nuclei ^{55}Cr and ^{59}Ni and with the pairing theory.

E | NUCLEAR REACTIONS ^{56}Fe(d, p), $E = 12$ MeV; measured $\sigma(E_{p'}, \theta)$. ^{57}Fe deduced levels, J, π, S. Enriched target.

1. Introduction

A great deal of effort has in recent years been expended in studying the (d, p) reactions in different target nuclei; in conjunction with the distorted wave Born approximation (DWBA) theory of nuclear reactions, these measurements have been utilized to extract information regarding the single-particle neutron states [1]. While a comparison of the shape of the measured angular distributions with the predictions of the DWBA gives the orbital angular momentum of the transferred neutrons, thus providing considerable information on the parities and angular momenta of the nuclear states involved, the absolute yield of the proton groups gives the spectroscopic factors. These quantities can be directly calculated by using the pairing theory [2,3]) and it has, for example, been shown that for even-mass target nuclei the sum of the spectroscopic factors $\sum_i S_i$ for all levels (with the same parity and angular momentum) belonging to a particular shell-model state j is equal to the occupation number U_j^2 of the pairing theory [3]).

The 1f-2p shell-model region continues to be one of particular interest in the perio-

---

*This paper has been published in Nuclear Physics, A160 (1971) 529–546.

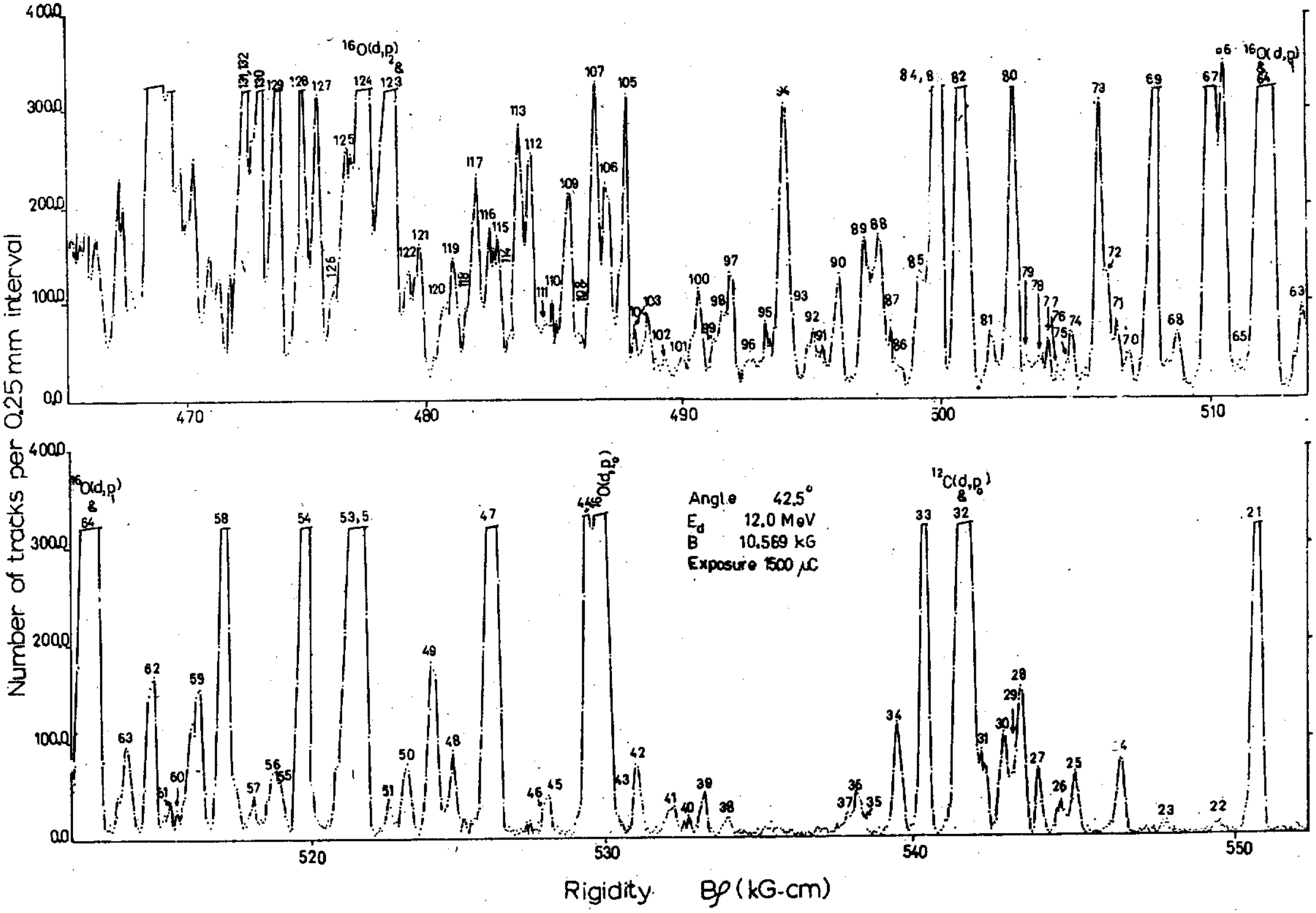

Fig. 1. Energy spectrum of protons at a lab angle of 42.5° arising from the (d, p) reaction in ^{56}Fe (clear part of the spectrum is not shown).

dic table of elements. It has usually been considered to be a region amenable to the conventional spherical shell-model studies on one hand [4]) and a strong coupling deformed Nilsson model on the other [5])

To extract the full advantage of such a comparison, an accurate measurement of level positions and their sequence with a high-resolution spectrograph is indispensible. The present work on the (d, p) reaction on ^{56}Fe at 12 MeV was undertaken with this in view. Other works on this reaction include those of Bochin *et al.* [6]) at 6.6 MeV and Cohen *et al.* [7]) at 15 MeV, where some of the well-established levels are either not observed or are unresolved; a recent study by Gridnev *et al.* [8]) was connected only with the transitions to the 2p levels. A preliminary account of the present work with the Butler plane wave analysis has been given elsewhere as a short communication [9]). Some of the measurements have since then been repeated and extended to include higher excitation [≈ 6.7 MeV, as against ≈ 3.2 MeV of our previous work [9])] and the results have now been analysed in terms of the DWBA.

The present paper gives a comprehensive account of the spectroscopic information thus obtained on the levels in ^{57}Fe with a comparison with the isotonic nuclei ^{59}Ni and ^{55}Cr.

2. Experimental procedure

The reaction ^{56}Fe(d, p)^{57}Fe has been studied using the Aldermaston Tandem Van de Graaff accelerator and the multi-channel magnetic spectrograph. A detailed account of the experimental techniques has been given by Middleton and Hinds [10]).

The target was self-supporting and isotopically enriched to 99 % of ^{56}Fe with a nominal thickness of 100 μg · cm^{-2}. It was bombarded with a deuteron beam of energy 12 MeV and the emitted particles were magnetically analysed and detected simultaneously at 24 angles between 5° and 175° in an Ilford K2 nuclear emulsion of thickness 50 μm. All the particles except protons were stopped in a polythene absorber, 0.25 mm thick, so that only the protons were recorded. The plates were scanned in Dacca and the energy spectra were obtained at each angle; a typical spectrum is shown in **fig. 1**.

Angular distributions were measured for all levels observed upto an excitation energy of ≈ 6.7 MeV including the unresolved ground and 0.014 MeV states. The absolute cross-section scale was obtained from our previous measurement of the yield of the elastic deuteron groups from ^{56}Fe [Majumder and Sen Gupta [11])].

3. Distorted wave Born approximation analysis

The angular distribution data were analysed in terms of the zero-range DWBA theory of direct reaction rather than the Butler plane wave theory used in the previous work [9]). The calculations were carried out on the IBM 7090 computer of the University of Pittsburgh[†] using the programme JULIE developed by Bassel *et al.* [12]).

[†] The calculations were carried out by Professor B. L. Cohen.

The optical-model potential was of the form

$$U(r) = -V(1+e^{x})^{-1}+4iW\left(\frac{d}{dx'}\right)(1+e^{x'})^{-1}+V_C(r),$$

with

$$x = (r-r_{0s}A^{\frac{1}{3}})/a_s, \qquad x' = (r-r_{0I}A^{\frac{1}{3}})/a_I$$

and $V_C(r)$ is the Coulomb potential due to a uniformly charged sphere of radius $R_C = r_C A^{\frac{1}{3}}$. A spin-orbit term given by

$$\left(\frac{\hbar}{m_{\pi}c}\right)^{2} V_{s.o.}\, L\cdot\sigma\, r^{-1}\left(\frac{d}{dr}\right)(1+e^{x})^{-1}$$

was added to the above potential for the proton.

The deuteron and proton optical-model parameters 11,13,14) are listed in table 1. The bound state potential was taken as the Woods-Saxon type with geometrical parameters r_{0s} = 1.25 fm and a_s = 0.65 fm and the depth of the real potential is adjusted while keeping the shape fixed until the binding energy is matched.

TABLE 1

Parameter values of the optical model used in DWBA calculations

Particle	V (MeV)	W (MeV)	r_{0s} (fm)	a_s (fm)	r_{0I} (fm)	a_I (fm)	r_C (fm)	$V_{s.o.}$ (MeV)	Ref.
deuteron	90.0	21.0	1.15	0.81	1.34	0.68	1.15		11,13)
proton	47.9	11.5	1.25	0.65	1.25	0.47	1.15	8.76	14)
neutron	adjusted a)		1.25	0.65					

a) See text for details.

The calculations were carried out for orbital angular momentum transfer l between 0 and 4 using Q = −1, 1, 3 and 5. Fig. 2 illustrates the proton angular distributions predicted by the DWBA theory for Q = 3 MeV. The characteristics of the forward peaks for each l-value is given in table 2 and is found to be about the same for (d, p) angular distributions from ^{57}Fe and ^{58}Fe [refs. 15,16)].

Some of the measured angular distributions together with the DWBA analysis are displayed in figs. 3-8. Good agreement is found in most cases upto about 100° and it is possible thereby to assign the orbital angular momentum transferred for the levels

TABLE 2

Position of the forward peak predicted by the DWBA calculations

l	0	1	2	3	4
Angle	54° a)	13°	25°	30°	40°

a) Second peak.

as shown in table 3. Some of the tentative assignments of the previous Butler plane wave analysis [9]) have now been corrected.

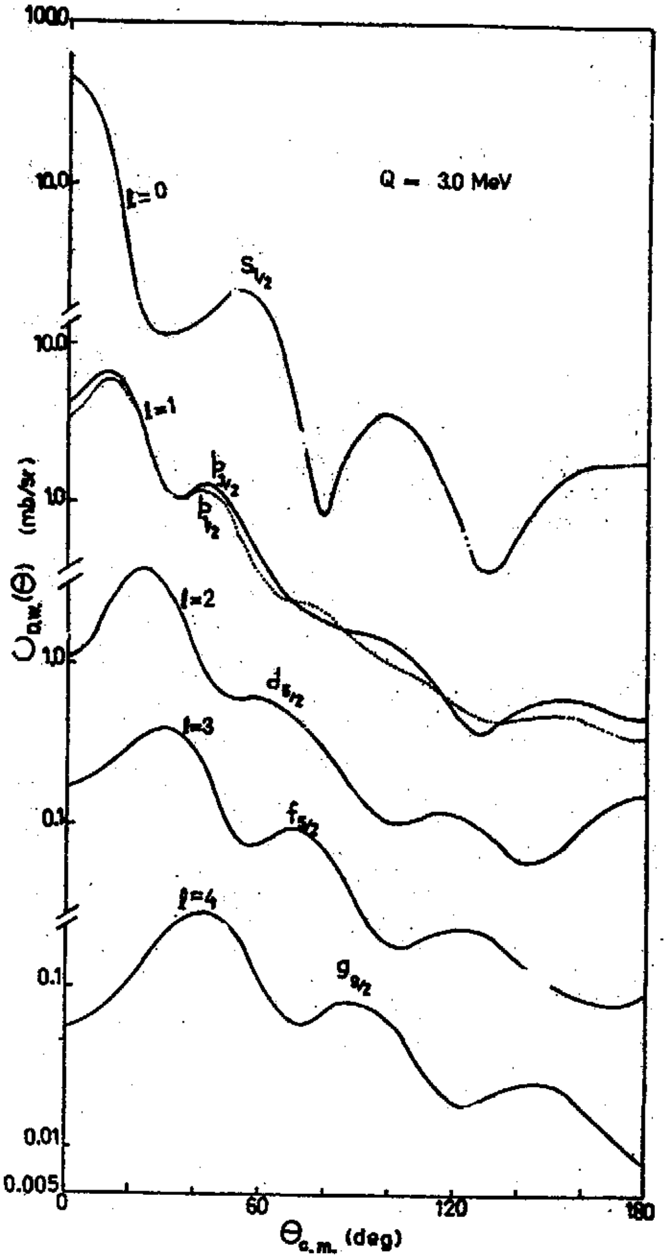

Fig. 2. Angular distributions obtained from the DWBA calculations for l = 0, 1, 2, 3 and 4 with Q = 3.0 MeV.

The DWBA cross sections for such a transfer reaction can be factored into the above mentioned kinematic part governing the shape of the angular distribution (fig. 2) for different l-values and a structure part which determines the properties of the nuclear states. The latter information is obtained from the relation

$$\sigma_{\exp}(\theta) = \frac{3}{2}\,\frac{2J+1}{2J_1+1}\, S\sigma_{DW}(\theta).$$

Here J and $J_i(=0)$ are respectively the spins of the final and initial nuclear states; $\sigma_{exp}(\theta)$ and $\sigma_{DW}(\theta)$ are the measured and the DWBA cross sections respectively and S is the spectroscopic factor. The factor $\frac{3}{2}$ is introduced to take into account the finite range of the nuclear force in the deuteron. The spectroscopic transition strength $(2J+1)S$ and hence the spectroscopic factor S are obtained. In obtaining these quantities for different levels, the Q-dependence of DWBA cross sections was taken into consideration.

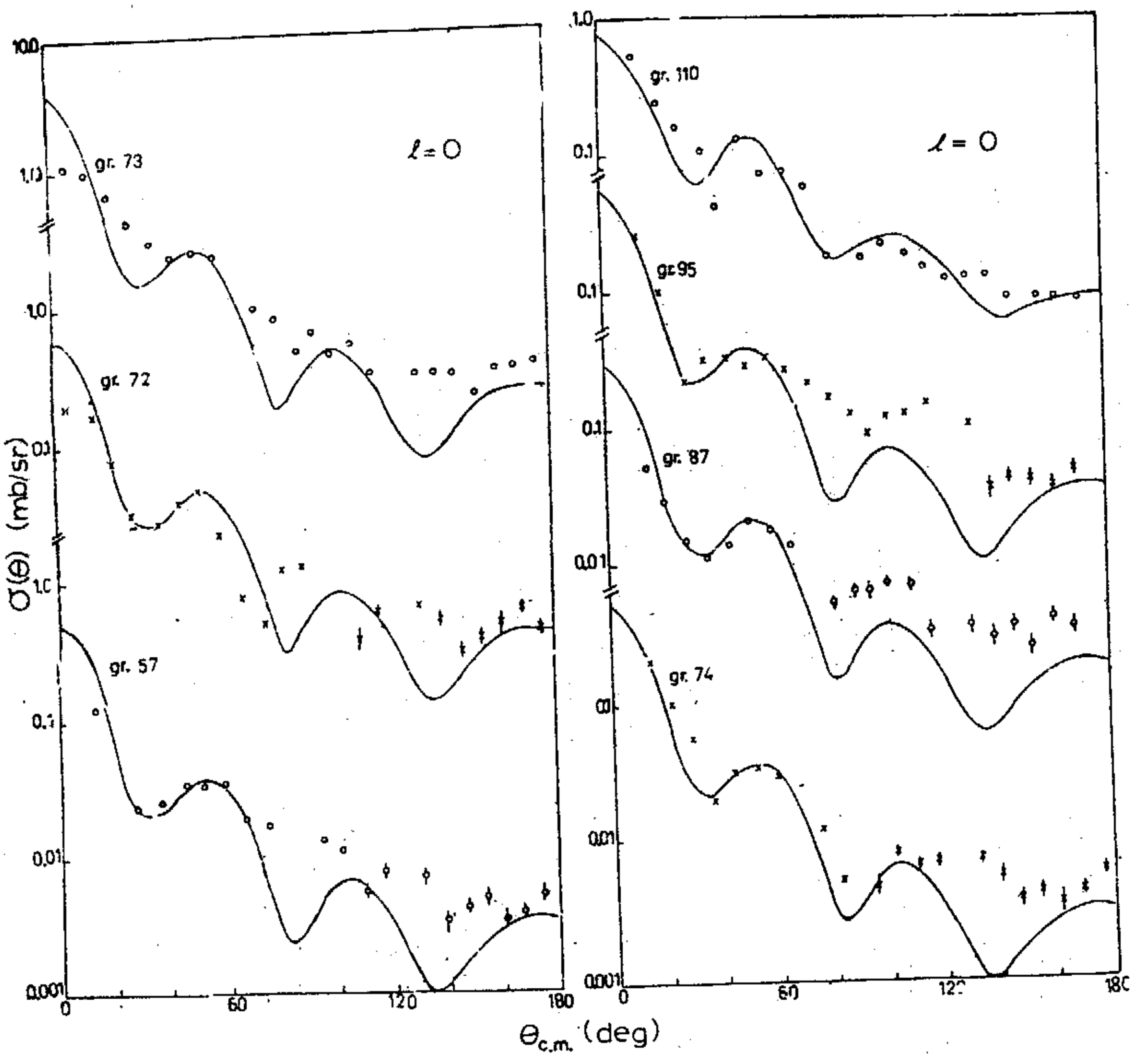

Fig. 3. Experimental angular distributions fitted to $l = 0$ curves; the DWBA curves in this and in figs. 4–8 were calculated with the optical-model parameters shown in table 1.

4. Results and discussion

In this section we discuss the results of the comparison of the experimental angular distributions with the DWBA predictions for the states showing predominantly stripping character; only a casual mention will be made for the distributions showing no stripping pattern.

4.1. STRIPPING LEVELS

Table 3 lists the observed energy levels, orbital angular momenta, peak cross sections, suggested J-values and spectroscopic factor for each level. The observed energy levels are compared with those of the isotonic nuclei ^{55}Cr [ref. [17])] and ^{59}Ni [ref. [18])] as shown in fig. 9; only those belonging to the 2p and 1f states are given in the figure by way of example. Also listed in the table for a comparison is the transition strength $(2J+1)S$ deduced by Cohen *et al.* [7]) in their experimental studies of (d, p) reactions

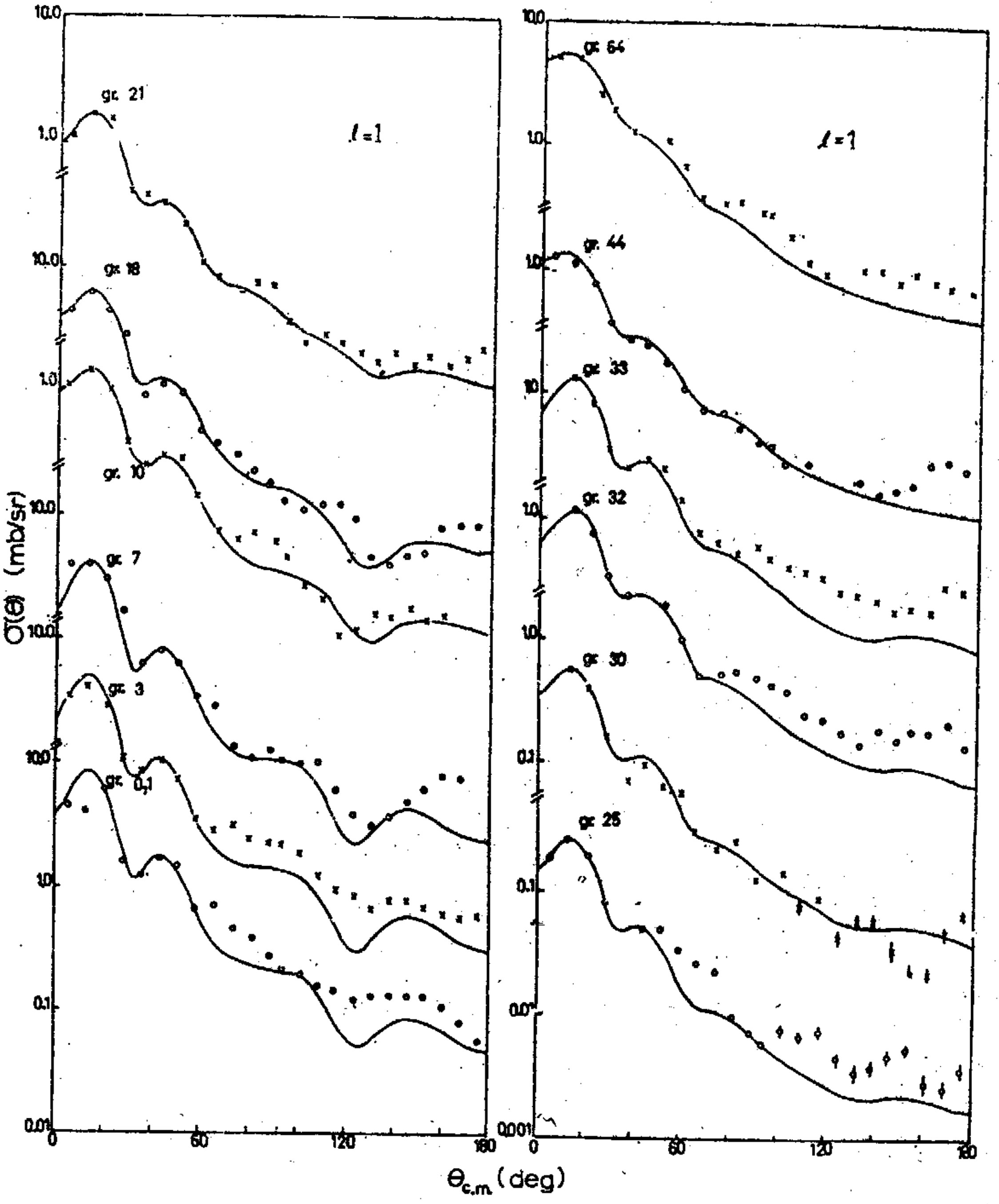

Fig. 4. Experimental angular distribution data fitted to $l = 1$ curves (the $p_{\frac{3}{2}}$ and $p_{\frac{1}{2}}$ states are listed in table 3).

on medium mass nuclei. While the principal effort in their work was with the nickel isotopes, they also measured the proton spectra from the ^{56}Fe(d, p) reaction using a natural iron target with insufficient energy resolution and statistics. Also the optical-model parameters they used are not considered appropriate. Nevertheless, a comparison between the $(2J+1)S$ values, obtained from a more detailed analysis of the present work, indicated a fair agreement with those of theirs. The only discrepancy in the assignment of the *l*-value is for the unresolved groups 52 and 53 and the group 64, the present assignment being 1+3 and 1 respectively (figs. 8 and 4) against $l = 0$ by Cohen *et al.* 7). These groups are quite intense and any uncertainty in shape or magnitude of cross section from background elimination etc. will be very small. It may be mentioned that a few contradictions in the assignment of *l*-values have also been ob-

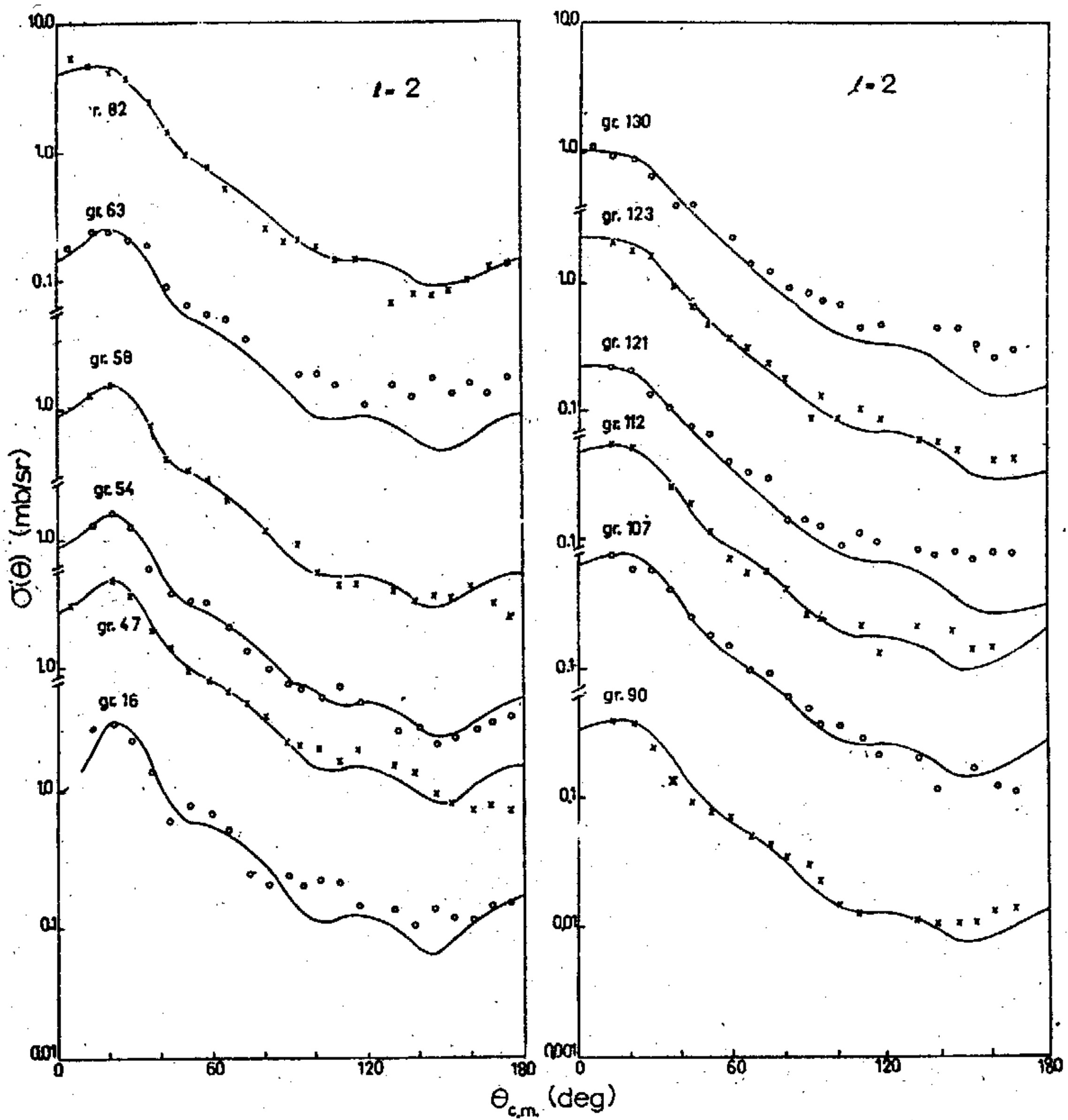

Fig. 5. Experimental angular distributions fitted to $l = 2$ curves.

served by Fulmer *et al.* [19]) when they repeated their earlier measurements [7]) on ^{58,60}Ni(d, p) reactions with better energy resolution and more complete angular distributions, in which case they preferred new assignments to their previous ones.

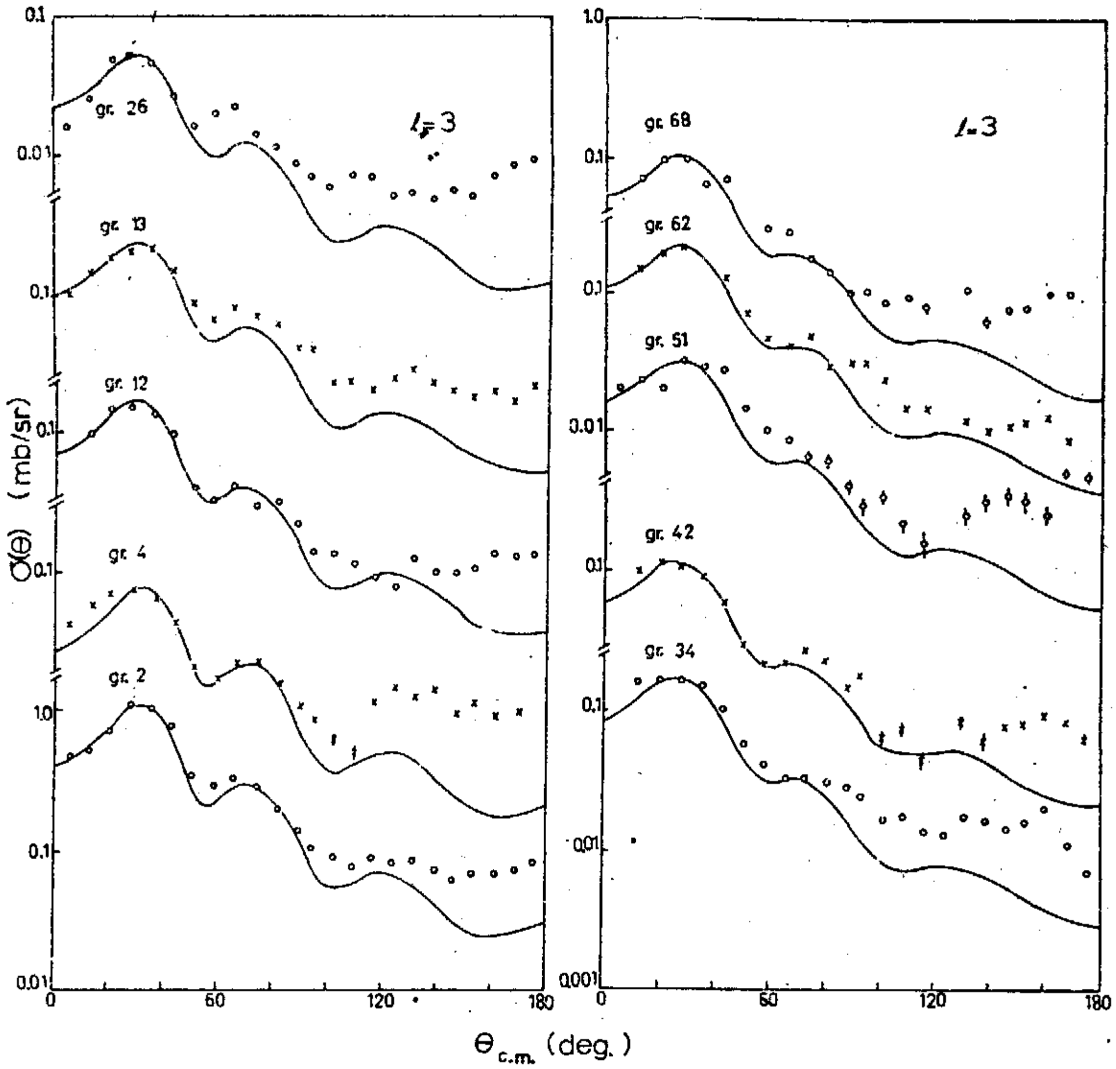

Fig. 6. Experimental angular distribution data fitted to $l = 3$ curves.

The contradiction in l-value between the present work and ref. [7]) for the two above mentioned levels may perhaps be similarly resolved. A detailed comparison is not however possible, as they could not observe all the levels in ^{57}Fe.

Table 3 also includes the $(2J+1)S$ values obtained by Gridnev *et al.* [8]) who investigated only the $l = 1$ levels with (d, p) reactions in medium-mass nuclei including ^{56}Fe at $E_d = 6.6$ MeV. There is a reasonable agreement with ours except for group 9. It is possible that the transition strength 0.48 quoted by them is distributed over the groups 9, 10 and 11, which improves agreement with the present value and with Cohen *et al.* [7]).

From simple shell-model considerations, the low-lying 2p-1f$_{\frac{5}{2}}$ states and also 2d$_{\frac{5}{2}}$,

$1g_{9/2}$ and $3s_{1/2}$ states are expected to be excited in the present ^{56}Fe(d, p) reactions. The measured spectroscopic strength sums for these states are shown in table 4; also included are the results from (d, p) reactions in ^{54}Cr, ^{56}Fe and ^{58}Ni [refs. [8,17–19]] and from the predictions of the pairing theory. The parameters of the theory were taken from refs. [2,20]. The experimental sum strength was found to be 11.4 for 2p and $1f_{5/2}$ states in fair agreement with the value 10 expected from the pairing theory. They also agree reasonably well with the results of Gridnev *et al.* [8]) for p-states in ^{57}Fe and for the isotonic nuclei ^{55}Cr and ^{59}Ni.

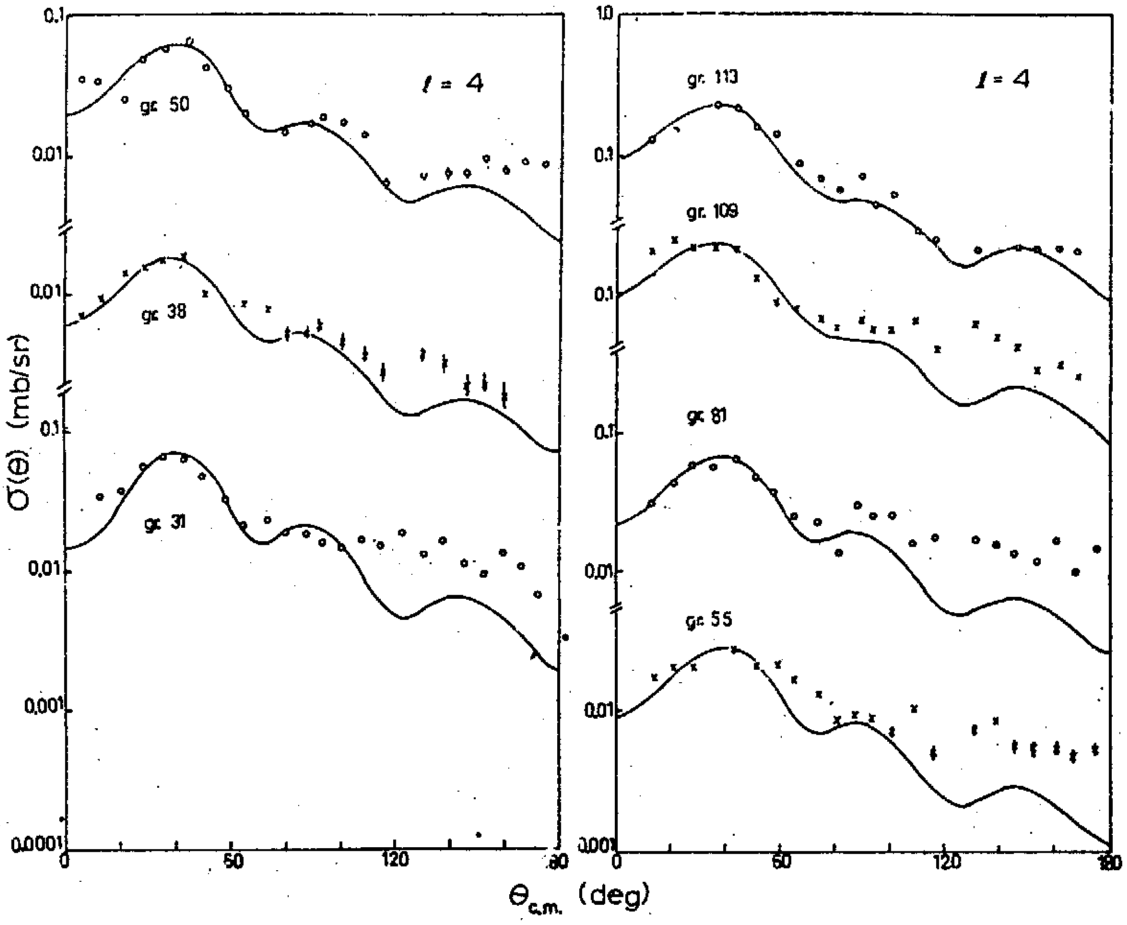

Fig. 7. Experimental angular distribution data fitted to $l = 4$ curves.

The sum rule analysis of S and the determination of the unperturbed single-particle energies E_j depends on the assignment of a shell-model state J. The experimental values of E_j were determined as the centre of gravity of the spectroscopic factors from the relation [19])

$$E_j = \sum_l S_l(j)E_j / \sum_l S_l(j),$$

where the summation is carried over all the levels belonging to the same shell-model state j. In the iron region, there is an ambiguity in assignment of an $l = 1$ state as $p_{3/2}$ or $p_{1/2}$. Lee and Schiffer [21]) have shown that the spin assignments of the levels in the

2p shell can be made on the basis of the empirically established *J*-dependence in the angular distributions. In the present experiment, however, the characteristic Lee-Schiffer back-angle behaviour in angular distributions of $l = 1$ levels is not clearly observed. In ^{57}Fe the few low-lying levels are known to have unambiguous spin and parity assignments [22]; we accepted these assignments for the present analysis, while all other $l = 1$ levels were considered to be $\frac{1}{2}$. A further difficulty was with the yield of the unresolved ground and 0.014 MeV states. In the (d, p) experiments it is difficult to obtain separate angular distributions for these states. Bjerregaard *et al.* [23]) have estimated the ratio of the intensity for these two states to be approximately 1 : 3. The above assumptions give the best agreement with the predictions of the pairing theory on the spectroscopic factors for all the levels belonging to the shell-model state *j*, $\sum S$, which is the emptiness U_j^2 of shell *j* [ref. [3])].

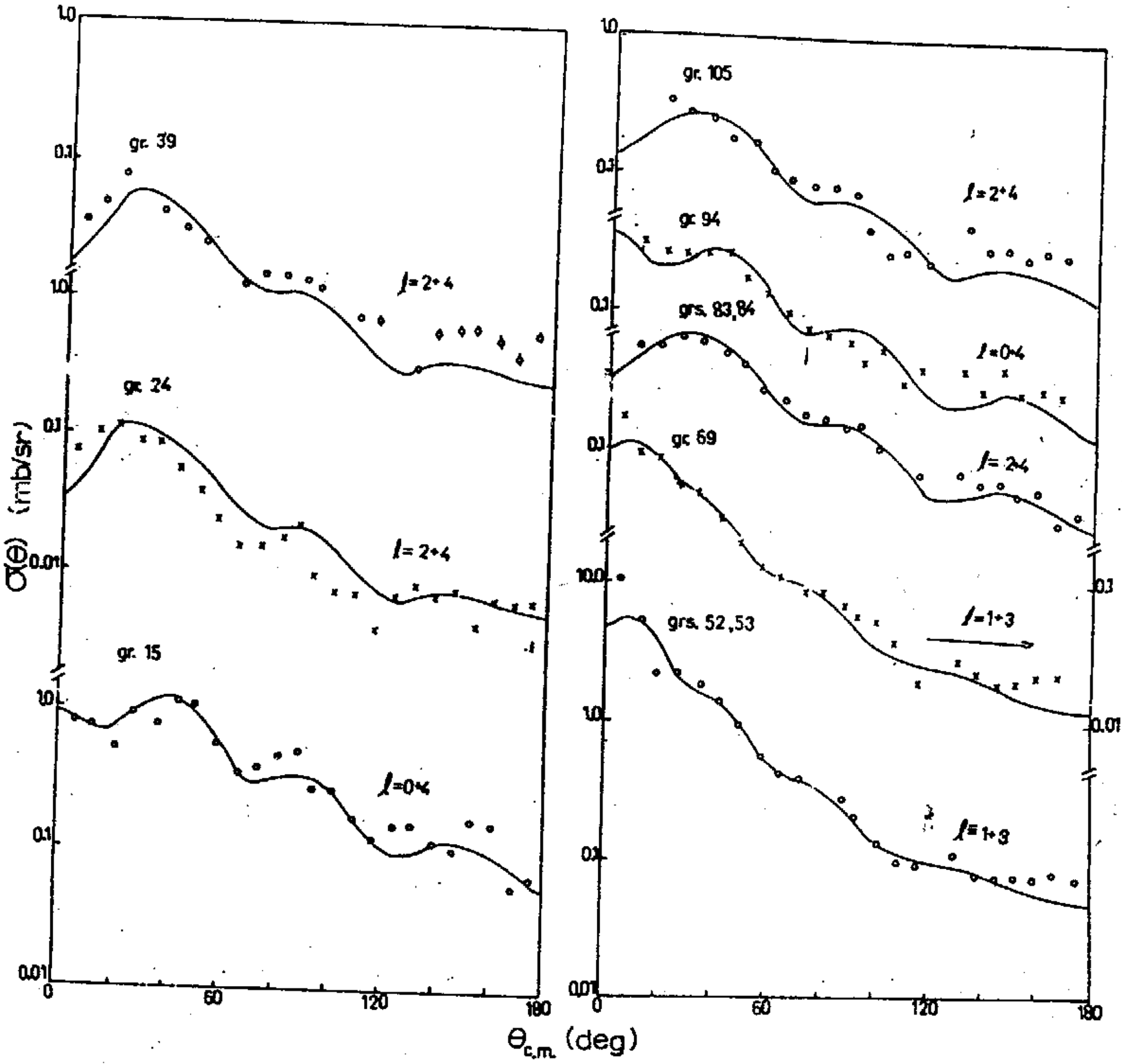

Fig. 8. Experimental angular distributions fitted to a mixture of *l*-values.

Table 5 summarizes the results for $\sum S$ and E_j and shows a comparison with pairing theory and also with those for the isotonic nuclei from (d, p) reactions [8,17–19,24])

TABLE 3

Results of the ^{56}Fe(d, p)^{57}Fe reaction

Group	Excitation (MeV)	$\sigma_{max}(\theta)$ (mb/sr)	l	$(2J+1)S$			J^π	S
				a)	b)	c)	a)	a)
0	0	5.976	1	0.304	2.20	1.73	$\frac{1}{2}^-$	0.152
1	0.014		1	0.914			$\frac{3}{2}^-$	0.229
2	0.136	1.080	3	2.450			$\frac{5}{2}^-$	0.408
3	0.366	3.884	1	0.755	0.990	0.88	$\frac{3}{2}^-$	0.189
4	0.703	0.074	3	0.172			$\frac{5}{2}^-$	0.029
5	1.002		n.s.					
6	1.196		n.s.					
7	1.264	3.984	1	0.525	0.680	0.84	$\frac{3}{2}^-$	0.131
8	1.356	0.141	3	0.301			$\frac{5}{2}^-$	0.050
9	1.630	0.896	1	0.090	0.082	0.48	$\frac{3}{2}^-$	0.023
10	1.725	1.494	1	0.154	0.195		$\frac{3}{2}^-$	0.039
11	1.975	0.131	1	0.016			$\frac{1}{2}^-$	0.008
12	2.117	0.158	3	0.290	0.672		$\frac{5}{2}^-$	0.048
13	2.207	0.220	3	0.405	0.371		$\frac{5}{2}^-$	0.068
14	2.335	0.174	1	0.016			$\frac{1}{2}^-$	0.008
15	2.454	1.162	0	0.014			$\frac{1}{2}^+$	0.007
			+4	2.700			$\frac{9}{2}^+$	0.270
16	2.506	3.818	2	0.658			$\frac{5}{2}^+$	0.110
17	2.565	1.577	1	0.212			$\frac{1}{2}^-$	0.106
18	2.687	6.225	1	0.667	0.600	0.80	$\frac{3}{2}^-$	0.167
19	2.763		n.s.					
20	2.818		n.s.					
21	2.910	1.660	1	0.188	0.092	0.36	$\frac{1}{2}^-$	0.094
22	2.985		n.s.					
23	3.062	0.043	0	0.004			$\frac{1}{2}^+$	0.002
24	3.104	0.116	2	0.018			$\frac{5}{2}^+$	0.003
			+4	0.177			$\frac{9}{2}^+$	0.018
25	3.177	0.234	1	0.025			$\frac{1}{2}^-$	0.013
26	3.223	0.054	3	0.077			$\frac{5}{2}^-$	0.013
27	3.247	0.231	0	0.018			$\frac{1}{2}^+$	0.009
28	3.284		n.s.					
29	3.302		n.s.					
30	3.318	0.589	1	0.056			$\frac{1}{2}^-$	0.028
31	3.345	0.067	4	0.141			$\frac{9}{2}^+$	0.014
32	3.372	1.148	1	0.115	0.21	0.25	$\frac{1}{2}^-$	0.058
33	3.425	1.296	1	0.129			$\frac{1}{2}^-$	0.064
34	3.473	0.165	3	0.197			$\frac{5}{2}^-$	0.033
35	3.544	0.021	4	0.041			$\frac{9}{2}^+$	0.004
36	3.560	0.028	4	0.054			$\frac{9}{2}^+$	0.005
37	3.579	0.022	4	0.043			$\frac{9}{2}^+$	0.004
38	3.767	0.018	4	0.035			$\frac{9}{2}^+$	0.004
39	3.791	0.077	2	0.010			$\frac{5}{2}^+$	0.002
			+4	0.010			$\frac{9}{2}^+$	0.001
40	3.834	0.047	3	0.068			$\frac{5}{2}^-$	0.011
41	3.861		n.s.					
42	3.890	0.110	3	0.132			$\frac{5}{2}^-$	0.022
43	3.937	0.048	3	0.053			$\frac{5}{2}^-$	0.009
44	3.974	1.324	1	0.124	0.101		$\frac{1}{2}^-$	0.062

^{56}Fe(d, p)^{57}Fe

TABLE 3 (continued)

Group	Excitation (MeV)	$\sigma_{\max}(\theta)$ (mb/sr)	l	$(2J+1)S$ a)	$(2J+1)S$ b)	$(2J+1)S$ c)	J^π a)	S a)
45	4.039	0.047	3	0.054			$\frac{5}{2}^-$	0.009
46	4.091		n.s.					
47	4.141	4.858	2	0.678	0.918		$\frac{5}{2}^+$	0.113
48	4.201	0.300	1	0.030			$\frac{1}{2}^-$	0.015
49	4.239	0.610	2	0.070			$\frac{5}{2}^+$	0.012
50	4.310	0.072	4	0.112			$\frac{9}{2}^+$	0.011
51	4.345	0.032	3	0.033			$\frac{5}{2}^-$	0.005
52	4.382	10.385	1 +	0.440			$\frac{1}{2}^-$	0.220
53	4.448		3	0.825	0,132 [d]		$\frac{5}{2}^-$	0.138
54	4.492	1.378	2	0.200	0.211		$\frac{5}{2}^+$	0.033
55	4.525	0.028	4	0.050			$\frac{9}{2}^+$	0.005
56	4.547	0.050	0	0.006			$\frac{1}{2}^+$	0.003
57	4.571	0.132	0	0.012			$\frac{1}{2}^+$	0.006
58	4.594	1.561	2	0.200	0.402		$\frac{5}{2}^+$	0.033
59	4.655	0.190	3	0.176			$\frac{5}{2}^-$	0.029
60	4.695		n.s.					
61	4.717		n.s.					
62	4.744	0.218	3	0.220			$\frac{5}{2}^-$	0.034
63	4.785	0.249	2	0.032			$\frac{5}{2}^+$	0.005
64	4.824	5.286	1	0.486	0.220 [d]		$\frac{1}{2}^-$	0.243
65	4.899		n.s.					
66	4.914	1.082	2	0.131	0.662		$\frac{5}{2}^+$	0.022
67	4.978	1.943	2	0.229			$\frac{5}{2}^+$	0.033
68	5.001	0.095	3	0.085			$\frac{5}{2}^-$	0.014
69	5.049	1.823	1 + 3	0.063 0.284			$\frac{1}{2}^-$ $\frac{5}{2}^-$	0.032 0.047
70	5.080		n.s.					
71	5.099		n.s.					
72	5.117	0.196	0	0.012			$\frac{1}{2}^+$	0.006
73	5.139	1.146	0	0.066			$\frac{1}{2}^+$	0.033
74	5.172	0.207	0	0.008			$\frac{1}{2}^+$	0.004
75	5.195		n.s.					
76	5.219		n.s.					
77	5.234		n.s.					
78	5.250	0.097	0	0.006			$\frac{1}{2}^+$	0.003
79	5.271	0.048	0	0.006			$\frac{1}{2}^+$	0.003
80	5.289	1.122	2	0.121	0.312		$\frac{5}{2}^+$	0.020
81	5.334	0.062	4	0.113			$\frac{9}{2}^+$	0.011
82	5.360	4.724	2	0.458	1.270		$\frac{5}{2}^+$	0.076
83	5.419	0.644	2 +	0.034			$\frac{5}{2}^+$	0.006
84	5.444		4	0.773			$\frac{9}{2}^+$	0.077
85	5.465	0.426	2	0.045			$\frac{5}{2}^+$	0.008
86	5.502	0.054	0	0.003			$\frac{1}{2}^+$	0.002
87	5.520	0.053	0	0.005			$\frac{1}{2}^+$	0.003
88	5.545		n.s.					
89	5.563	0.586	2	0.056			$\frac{5}{2}^+$	0.009
90	5.609	0.396	2	0.056			$\frac{5}{2}^+$	0.009
91	5.647		n.s.					
92	5.661		n.s.					

TABLE 3 (continued)

Group	Excitation (MeV)	$\sigma_{\max}(\theta)$ (mb/sr)	l	$(2J+1)S$			J^π	S
				a)	b)	c)	a)	a)
93	5.688		n.s.					
94	5.708	0.322	0	0.004			$\frac{1}{2}^+$	0.002
			+4	0.453			$\frac{9}{2}^+$	0.045
95	5.743	0.272	0	0.010			$\frac{1}{2}^+$	0.005
96	5.772		n.s.					
97	5.802	0.142	2	0.017			$\frac{5}{2}^+$	0.003
98	5.825	0.245	2	0.026			$\frac{5}{2}^+$	0.004
99	5.844	0.072	0	0.010			$\frac{1}{2}^+$	0.005
100	5.864	0.283	2	0.032			$\frac{5}{2}^+$	0.005
101	5.900		n.s.					
102	5.918		n.s.					
103	5.936		n.s.					
104	5.956	0.130	2	0.014			$\frac{5}{2}^+$	0.002
105	5.983	0.360	2	0.016			$\frac{5}{2}^+$	0.003
			+4	0.333			$\frac{9}{2}^+$	0.033
106	6.025	0.642	2	0.067			$\frac{5}{2}^+$	0.011
107	6.044	0.771	2	0.087			$\frac{5}{2}^+$	0.014
108	6.083		n.s.					
109	6.103	0.264	4	0.267			$\frac{9}{2}^+$	0.027
110	6.130	0.547	0	0.034			$\frac{1}{2}^+$	0.017
111	6.148		n.s.					
112	6.171	0.528	2	0.060			$\frac{5}{2}^+$	0.010
113	6.194	0.234	4	0.267			$\frac{9}{2}^+$	0.027
114	6.212	0.059	0	0.004			$\frac{1}{2}^+$	0.002
115	6.230	0.361	2	0.032			$\frac{5}{2}^+$	0.005
116	6.252	0.078	4	0.067			$\frac{9}{2}^+$	0.007
117	6.270	0.263	4	0.300			$\frac{9}{2}^+$	0.030
118	6.305		n.s.					
119	6.323		n.s.					
120	6.340		n.s.					
121	6.370	0.225	2	0.020			$\frac{5}{2}^+$	0.003
122	6.408	0.113	2	0.012			$\frac{5}{2}^+$	0.002
123	6.427	2.047	2	0.200			$\frac{5}{2}^+$	0.033
124	6.496		n.s.					
125	6.512	0.529	2	0.047			$\frac{5}{2}^+$	0.008
126	6.542	0.234	0	0.010			$\frac{1}{2}^+$	0.005
127	6.571	0.460	2	0.047			$\frac{5}{2}^+$	0.008
128	6.589	0.892	2	0.067			$\frac{5}{2}^+$	0.011
129	6.640	0.891	2	0.067			$\frac{5}{2}^+$	0.011
130	6.672	1.129	2	0.093			$\frac{5}{2}^+$	0.016
131	6.703	1.030	2	0.093			$\frac{5}{2}^+$	0.016
132	6.725							

---

[a]) Present work. [b]) Cohen *et al.* [7]). [c]) Gridnev *et al.* [8]); they have studied only $l = 1$ transitions. [d]) These are $l = 0$ transitions according to Cohen *et al.* [8]).

A few weak groups were observed between group 37 and group 38 which are hardly above background and a few between groups 123 and 124 which are not well resolved; these are not included in the table, or in the analysis.

TABLE 4

Sum of the transition strength $(2J+1)S$

Single-particle state in 28–50 shell	^{56}Fe		Pairing theory	^{54}Cr		^{58}Ni	
	a)	b)		b)	c)	d)	e)
2p	5.62	5.4	4.8	5.1	4.53	6.6	4.88
$1f_{5/2}$	5.81		5.3		5.06	5.2	6.3
$1g_{9/2}$	> 6.08		9.8		> 6.7	10.6	11.6
$2d_{5/2}$	> 4.03		6.0		> 2.94	4.5	
$3s_{1/2}$	> 0.21		2.0		> 0.69	> 0.96	

a) Present work. b) Ref. 8). c) Ref. 17). d) Ref. 18). e) Ref. 19).

A summary of the separation between $2p_{1/2}$–$2p_{3/2}$ states in this mass region has been made by Rosalky *et al.* 24) and the present value (1.95 MeV) is in good agreement with these (≈ 1.70 MeV). The present value of the ratio $\sum S_{1/2}/\sum S_{3/2}$ (≈ 1.6) is also in fair agreement with the sum rule prediction of 2.0 MeV.

The $\sum S$ values for the $1f_{5/2}$ states are in excellent agreement with those in ^{54}Cr and ^{58}Ni as well as with the prediction of the pairing theory. The energies E_j also agree very well with those in ^{54}Cr, but are about 1 MeV higher than those in ^{58}Ni and those predicted from pairing theory (tables 4 and 5).

TABLE 5

Results for ΣS and E_j and comparison with those for isotonic nuclei and pairing theory

s.p. state in 28–50 shell	$\Sigma S = U_j^2$					
	^{56}Fe	Pairing theory	^{54}Cr		^{58}Ni	
	a)		b)	c)	d)	e)
$2p_{3/2}$	0.78	0.71	0.56		0.76	0.67
$2p_{1/2}$	1.26	0.97	0.66		1.18–1.30	1.1
$1f_{5/2}$	0.97	0.91		0.84	0.88	1.05
$1g_{9/2}$	> 0.61	0.98		0.67		1.16
$2d_{5/2}$	> 0.67	1.0		0.49		
$3s_{1/2}$	> 0.11	1.0		0.35		0.53

s.p. state in 28–50 shell	E_j (MeV)					
	^{56}Fe	Pairing theory	^{54}Cr		^{58}Ni	
	a)		b)	c)	d)	e)
$2p_{3/2}$	1.02	0	0.14		0.11–1.3	0.3
$2p_{1/2}$	2.97	2.63	1.80		2.4 –3.4	2.2
$1f_{5/2}$	2.06	0.93		2.01	1.0	0.6
$1g_{9/2}$	> 4.03	3.09		> 2.09		3.5
$2d_{5/2}$	> 4.77	> 4		> 3.43		6.0
$3s_{1/2}$		> 4		> 3.74		7.3

a) Present work. b) Ref. 24). c) Ref. 17). d) Ref. 18). e) Ref. 19).

The small values of $\sum S$ for the states $3s_{\frac{1}{2}}$, $2d_{\frac{5}{2}}$ and $1g_{\frac{9}{2}}$, in particular for the former, (all $l = 2$ and 4 transitions are assumed to correspond to the $2d_{\frac{5}{2}}$ and $1g_{\frac{9}{2}}$ states) suggest that these states are partially excited within the range of present excitation and as such our data analyses for these states are incomplete. Their appearance at low excitation indicates a considerable fragmentation and energy spread of the single-particle state arising from the residual interaction.

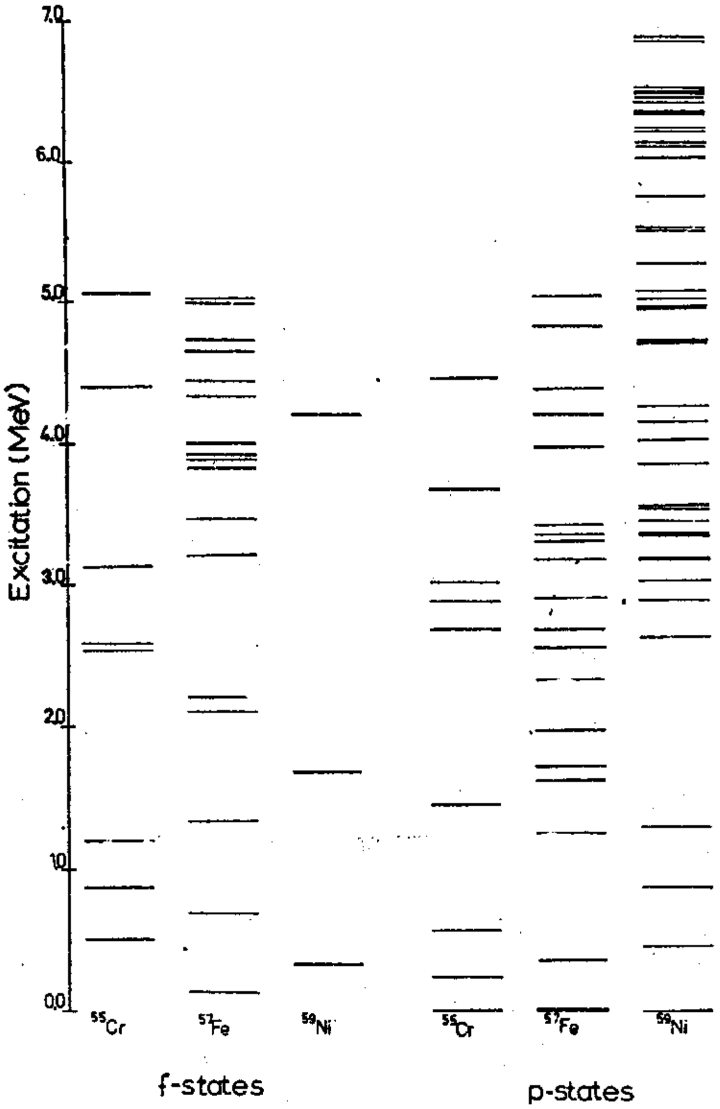

Fig. 9. Energy level scheme for the isotonic nuclei ^{55}Cr [ref. [17]], ^{57}Fe (this work) and ^{59}Ni [ref. [18]] as obtained from (d, p) reactions (only the 2p-$1f_{\frac{5}{2}}$ states are shown).

It is interesting to note that while many $l = 3$ transitions are observed in the (d, p) reactions in ^{54}Cr [ref. [17]] and ^{56}Fe (present work) (fig. 9) only three $l = 3$ levels in ^{58}Ni(d, p) reactions [18,19] were observed which carry the expected spectroscopic strength. The situation is all the more interesting for the $g_{\frac{9}{2}}$ state. While the shell-model strength found by Cosman *et al.* [18]) is completely carried by one level in ^{59}Ni without fragmentation, against four levels observed by Fulmer *et al.* [19]), in the present experiment many $l = 4$ transitions have been found, even then the strength is not exhausted; in ^{55}Cr one level was observed upto an excitation of 6.6 MeV carrying $S = 0.67$.

TABLE 6

ΣS and E_j values for 2p states in Fe isotopes

Nucleus	ΣS		$\Sigma S_{\frac{1}{2}}/\Sigma S_{\frac{3}{2}}$	E_j (MeV)		Ref.
	$2p_{\frac{3}{2}}$	$2p_{\frac{1}{2}}$		$2p_{\frac{3}{2}}$	$2p_{\frac{1}{2}}$	
^{54}Fe	1.49	1.5	1.0	1.52	≈ 3.5	[a])
^{56}Fe	0.78	1.26	1.6	1.02	2.97	[b])
^{58}Fe	0.65	1.03	1.6	0.22	1.02	[c])

[a]) Ref. [25]). [b]) Present work. [c]) Ref. [16]).

Table 6 shows the values of $\sum S$ and E_j for the p-states in the iron isotopes. Data for ^{54}Fe and ^{58}Fe are taken from refs. [25,16]). As can be seen from a comparison of E_j, the $p_{\frac{3}{2}}$ and $p_{\frac{1}{2}}$ states are decreasing with the increasing number of neutrons from a 28 closed shell as expected from the pairing theory. It is remarkable that the $p_{\frac{1}{2}}$ state moves down rapidly when two neutrons are added to the ^{56}Fe. In general. the observed energy variation of the $p_{\frac{1}{2}}$ state in the Fe isotopes is consistent with the tendency found in the Ni isotopes [19]). As regards the spectroscopic factors, the data $\sum S$ indicate that relative degree of filling of the $2p_{\frac{3}{2}}$ and $2p_{\frac{1}{2}}$ orbits become considerably large as the filling shell contains more neutrons.

Fig. 10 illustrates the intensity distribution amongst the levels belonging to a given shell-model state. The spread of these levels has a simple interpretation in terms of the giant resonance theory of Lane *et al.* [26]), namely, that they are approximately equal to the imaginary part of the optical potential [7,19]). The cross indicates the position of the centre of gravity E_j of these levels (fig. 10) listed in table 5. It appears that the proton holes in the $1f_{\frac{7}{2}}$ shell have no significant effect on the shift of the location of the 2p and $1f_{\frac{5}{2}}$ states in ^{55}Cr and ^{57}Fe even though the energy spectra are markedly different in these cases (fig. 9), which is a direct consequence of the difference in the proton number [27]).

4.2. NON-STRIPPING LEVELS

A few weak levels designated "n.s." (table 3) have been observed which do not exhibit any characteristic stripping angular distribution. Some of the distributions are displayed in fig. 11. These levels cannot be described by a configuration neutron coupled to the ground state of ^{56}Fe and are to be associated with a different reaction mechanism.

The states around 1 MeV (1.002 MeV and 1.196 MeV), for example, may be ac-

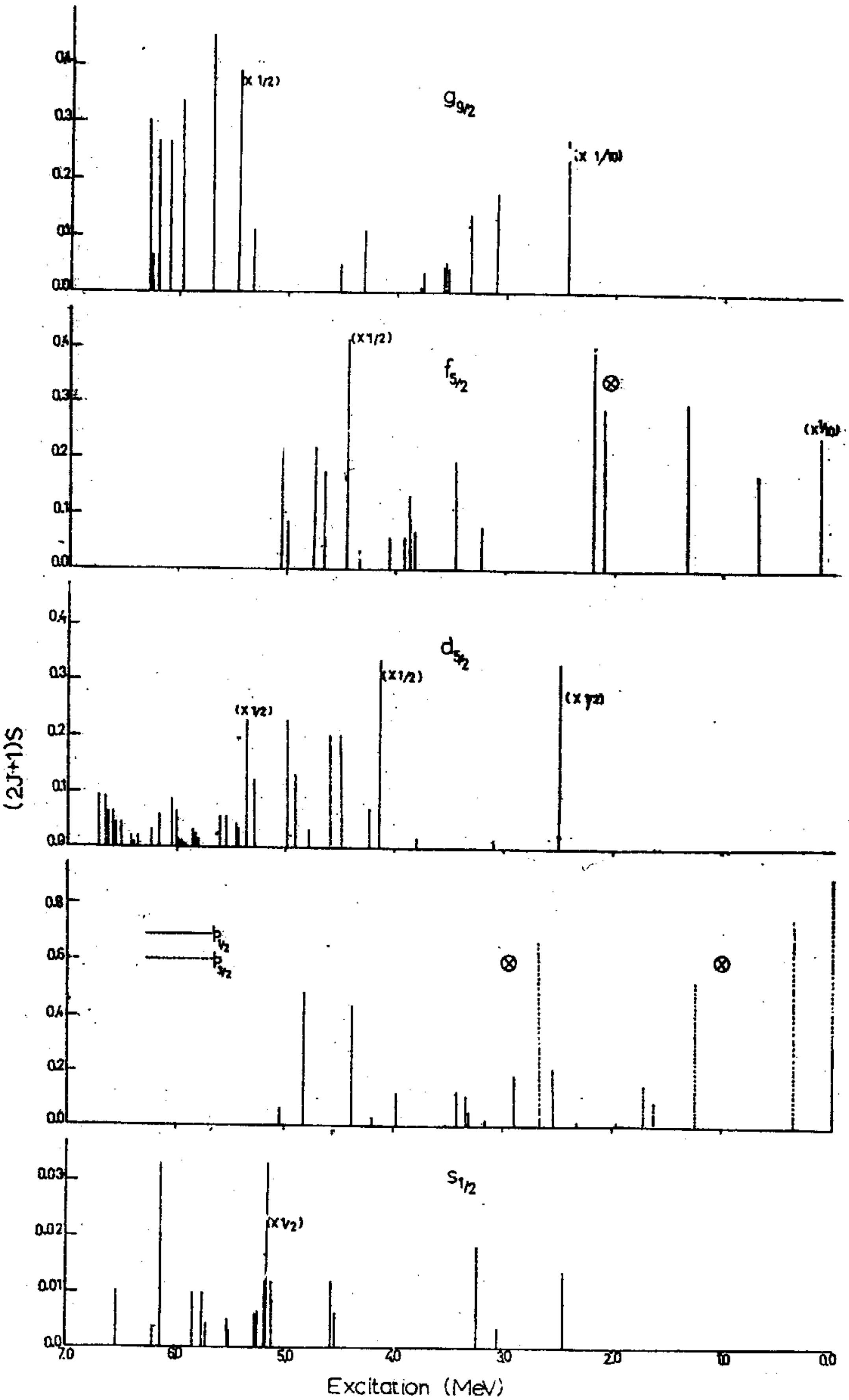

Fig. 10. Distribution of spectroscopic strength amongst the components of shell-model state *j*.

counted for by a weak coupling of the captured neutron from the (d, p) reaction to the quadrupole vibrational phonon[†].

It is also apparent that some of the angular distributions (figs. 3–8) displaying single-particle characteristics may have some small contributions from non-stripping processes. A detailed discussion must follow a full Hauser-Feshbach calculation.

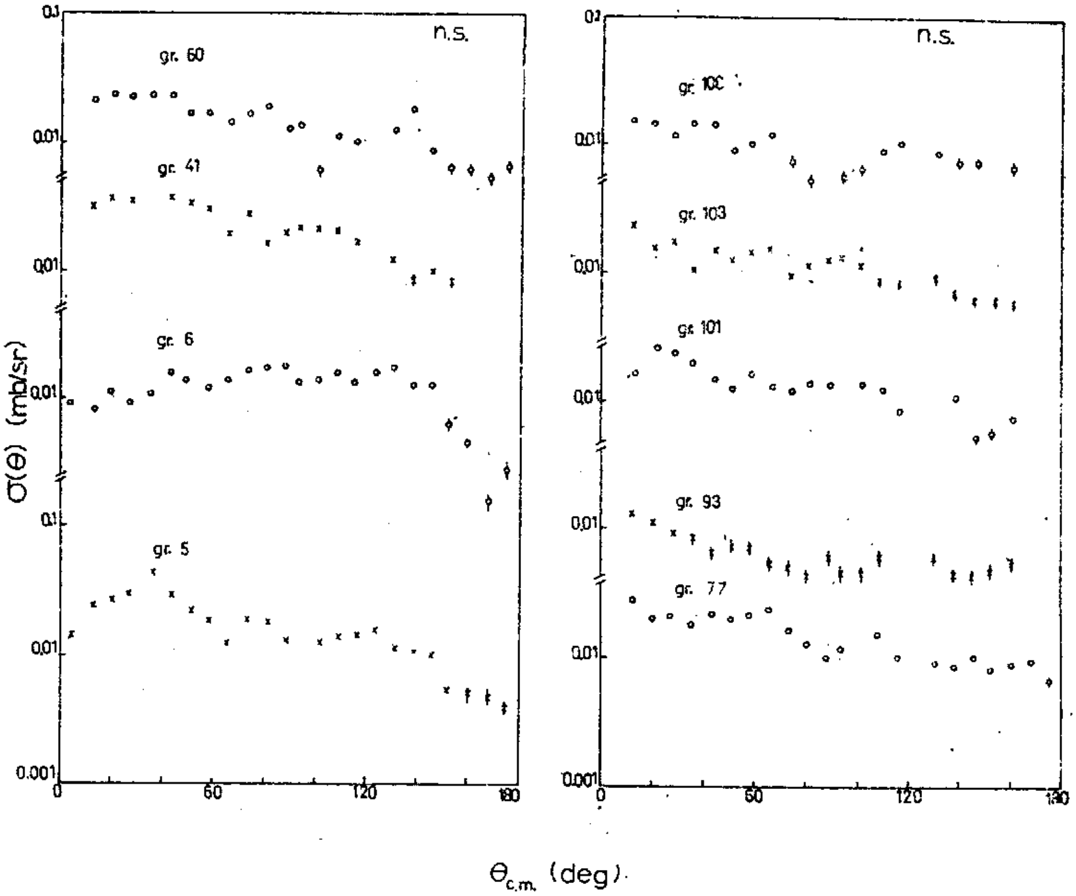

Fig. 11. Experimental angular distributions for some of the observed non-stripping levels.

5. Conclusions

The spectroscopic factor S for the shell-model states excited in the ^{56}Fe(d, p)^{57}Fe reaction and the position of the centre of gravity of these states as deduced from the present DWBA analysis agree reasonably well with those of the isotonic nuclei ^{54}Cr and ^{58}Ni. A comparison with the occupation number U_j^2 of the pairing theory shows good agreement. The obtained values of E_j give a $2p_{\frac{1}{2}}$–$2p_{\frac{3}{2}}$ spacing of 1.95 MeV; this agrees well with the values found from a study of (d, p) reaction [8]) in this mass region (≈ 1.7 MeV).

It is interesting to note the energy gaps between $2p_{\frac{1}{2}}$ and $1f_{\frac{5}{2}}$, and between $1f_{\frac{5}{2}}$ and $1g_{\frac{9}{2}}$ states. Table 5 shows a gap of ≈ 1 MeV between the former two states and of

---

[†] The lowest 2^+ state in ^{56}Fe is at 0.84 MeV.

$\gtrsim$ 2 MeV between the latter two, being smaller than the values 1.6 MeV and 2.9 MeV respectively found in ^{58}Ni [ref. [19])].

The measured spectroscopic factor for the $3s_{\frac{1}{2}}$ state reveals that the state in ^{56}Fe is just about to start filling, in contrast to the larger value of $\sum S$ in ^{54}Cr and ^{58}Ni [refs. [17,19])] observed within the present excitation. The appearance of $2d_{\frac{5}{2}}$ and $3s_{\frac{1}{2}}$ components is indicative of a considerable fragmentation and spread of the spectroscopic strength; many more components of these lie at higher excitation than investigated in the present experiment. The $1g_{\frac{9}{2}}$ state is similarly seen to be widely spread over several levels in a range of $\gtrsim$ 3 MeV.

It is clear that the present study of the ^{56}Fe(d, p) reaction upto 6.7 MeV excitation permits us to obtain useful precise spectroscopic information on the 2p–$1f_{\frac{5}{2}}$ states. To get complete spectroscopic information on the higher states ($1g_{\frac{9}{2}}$, $2d_{\frac{5}{2}}$ and $3s_{\frac{1}{2}}$ states) would require an investigation of the energy spectra at still higher excitation. This is a difficult task and the result will cease to have any good degree of accuracy, since the level density is now increasing quite rapidly.

Finally, about the quality of the DWBA fit. The agreement is satisfactory in most cases upto about 100°. The discrepancy at large angles may be due to the inadequacy of the DWBA theory in that region or an uncertainty in background subtraction for weak levels and a finite compound nuclear cross section. Their effect on S (which is obtained from a normalization to the small angle cross section) and hence on E_j is however negligible in comparison to the usual uncertainty in absolute DWBA cross section.

The authors would like to thank Professor M. Innas Ali for his interest in the work and Dr. S. Hinds for kindly exposing the plates at Aldermaston for us. They are indebted to Professor B. L. Cohen for performing the DWBA calculations at the University of Pittsburgh and to Professor F. B. Malik and Mr. M. S. Chowdhury for helpful discussions. One of the authors (E.K.L.) also wishes to thank Professor Schopper for kind hospitality during stay at the Kernforschungszentrum Karlsruhe.

References

1) M. H. Macfarlane and J. B. French, Rev. Mod. Phys. **32** (1960) 567
2) L. S. Kisslinger and R. A. Sorensen, Mat. Fys. Medd. Dan. Vid. Selsk. **32** (1960) No. 9; Rev. Mod. Phys. **35** (1963) 853
3) S. Yoshida, Phys. Rev. **123** (1961) 2122; Nucl. Phys. **38** (1962) 380
4) S. Cohen, R. D. Lawson, M. H. Macfarlane, S. P. Pandya and M. Soga, Phys. Rev. **160** (1967) 903; J. B. McGroy, Phys. Rev. **160** (1967) 915
5) W. Scholz and E. B. Malik, Phys. Rev. **147** (1966) 836; F. B. Malik and W. Scholz, Phys. Rev. **150** (1966) 919
6) V. P. Bochin, K. I. Zherebtsova, V. S. Zolotarev, V. A. Komarov, L. V. Krasnov, V. F. Litvi Yu. A. Nemilov, B. G. Novatsky and Sh. Piskorzh, Nucl. Phys. **51** (1964) 161
7) B. L. Cohen, R. H. Fulmer and A. L. McCarthy, Phys. Rev. **126** (1962) 698
8) K. A. Gridnev, K. I. Zherebtsova, V. A. Komarov, L. V. Krasnov, V. F. Litvin and Yu. A. Nemilov, Sov. J. Nucl. Phys. **8** (1969) 639

9) H. M. Sen Gupta, A. H. M. A. Hannan, A. H. Khan and A. Hossain, Nuovo Cim. **49** (1967) 207
10) R. Middleton and S. Hinds, Nucl. Phys. **34** (1962) 404
11) A. R. Majumder and H. M. Sen Gupta, Nucl. Phys. **A118** (1968) 151
12) R. H. Bassel, R. M. Drisko and G. R. Satchler, Oak Ridge National Laboratory Report, ORNL-3240, 1962
13) C. M. Perey and F. G. Perey, Phys. Rev. **132** (1963) 755
14) F. G. Perey, Phys. Rev. **131** (1963) 745
15) R. A. Sorensen, E. K. Lin and B. L. Cohen, Phys. Rev. **142** (1966) 729
16) E. D. Klema, L. L. Lee, Jr. and J. P. Schiffer, Phys. Rev. **161** (1967) 1134
17) B. Bock, H. H. Duhm, S. Martin, R. Rüdel and R. Stock, Nucl. Phys. **72** (1965) 273
18) E. R. Cosman, C. H. Paris, A. Sperduto and H. A. Enge, Phys. Rev. **142** (1966) 673
19) R. H. Fulmer, A. L. McCarthy, B. L. Cohen and R. Middleton, Phys. Rev. **133** (1964) B955
20) B. L. Cohen, Phys. Rev. **130** (1963) 227
21) L. L. Lee, Jr. and J. P. Schiffer, Phys. Rev. **136** (1964) B405; Phys. Rev. Lett. **12** (1964) 108
22) Nuclear Data, ed. by K. Way (Academic Press, New York, 1970)
23) J. H. Bjerregaard, P. F. Dahl, O. Hansen and G. Sidenius, Nucl. Phys. **51** (1964) 641
24) D. M. Rosalky, D. J. Baugh, J. Nurzyński and B. A. Robson, Nucl. Phys. **A142** (1970) 469
25) D. S. Gemmell, L. L. Lee, Jr., A. Marinov and J. P. Schiffer, Phys. Rev. **144** (1966) 923;
A. Sperduto and J. Rapaport, MIT Laboratory for Nucl. Sci. Progress Report (NYO-2668), 1961 (unpublished) p. 137
26) A. M. Lane, R. G. Thomas and E. P. Wigner, Phys. Rev. **98** (1955) 693
27) R. K. Jolly, Phys. Rev. **136** (1964) B683

Annual Report of the Institute of Physics, Academia Sinica, 1971

Circle Theorem for the Ice-Rule Ferroelectric Models*

Kun Shu Chang and Shou-Yih Wang
National Tsing Hua University, Hsinchu, Taiwan, Republic of China

and

F. Y. Wu
Department of Physics, Northeastern University, Boston, Massachusetts 02115

(Received 20 July 1971)

We show that the circle theorem on the distribution of zeros of the partition function breaks down for the ferroelectric potassium dihydrogen phosphate (KDP) model if the field lies outside the first quadrant. We also use a recent result by Suzuki and Fisher to establish the circle theorem for the antiferroelectric F model with a staggered electric field. Numerical results on the distribution of zeros for a 4×4 lattice are given.

INTRODUCTION

A central problem in the theory of phase transitions has been the investigation of the distribution of zeros of the partition function.[1] For the Ising ferromagnet in a magnetic field, Lee and Yang[1] showed that all zeros of the partition function lie on the unit circle, a result known as the "circle theorem." This circle theorem has recently been extended to a number of other models.[2] One particular model which has been discussed is the ice-rule ferroelectric model of hydrogen-bonded crystals.[3] For the ferroelectric potassium dihydrogen phosphate (KDP) model Suzuki and Fisher[2] (SF) showed that all zeroes of the partition function with an electric field in the *first quadrant* lie on the unit circle

---

*This paper has been published in Physical Review, 4A (1971) 2324-2327.

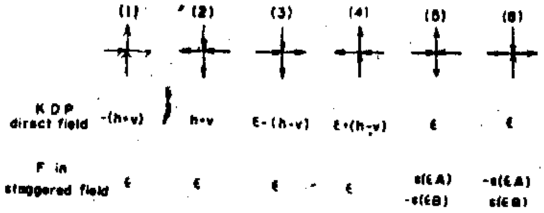

FIG. 1. Vertex configurations and energies of the KDP model in a direct electric field (h, v) and the F model in a staggered field. The staggered field varies sign from site to site (see text).

at temperatures below the transition temperature T_0. This result has been confirmed by numerical calculations carried out by Katsura, Abe, and Ohkouchi[4] (KAO) for finite lattices. KAO have also computed the zeros of the antiferroelectric F model in a direct field, and found that, in general, they do not lie on the unit circle. Two questions now arise: (i) Does the circle theorem hold for the ferroelectric KDP model with field outside the first quadrant? (ii) Is there a circle theorem for the F model in a staggered field? The second question is of importance because in an antiferroelectric model it is the staggered field which plays the role of a direct field in a ferroelectric model. We address ourselves to these two questions in the present paper.

CIRCLE THEOREM

To answer the first question we have carried out numerical studies on the partition function of a 4×4 KDP lattice with an electric field in the *second quadrant*. Our result shows that the circle theorem does not hold in this case. In fact, it is easy to see the breakdown of the circle theorem by considering just a 1×1 lattice. We remind the readers of the definition of the model as that given in Fig. 1.[3] Let us consider an electric field (h, v) in the second quadrant with $h = -v$. For a periodic 1×1 lattice only the four vertices (1)–(4) are allowed, the partition function then takes the form

$$Z = 2 + y(z + z^{-1}) , \tag{1}$$

where $y = e^{-\beta\epsilon}$, $z = e^{-2\beta v}$. It is now easy to see that the zeros of Z, $z = -y^{-1} \pm (y^{-2} - 1)^{1/2}$, do not lie on the unit circle. Thus we conclude by this counter example that in general the circle theorem does not hold for the KDP model if the field lies outside the first quadrant. Numerical results which confirm this conclusion for a 4×4 KDP lattice will be given presently.

The second question can be answered affirmatively as follows. The F model with a staggered field is defined with the energy parameters as shown in Fig. 1. Notice that the vertices (5)–(6) have energies $+s$ or $-s$ depending on which sublattice, A or B, the vertex belongs. However, this model with position-dependent energies can be transformed into one with uniform energies. The trick is to reverse, in the enumeration of states, the arrow directions along every other zigzag path in the

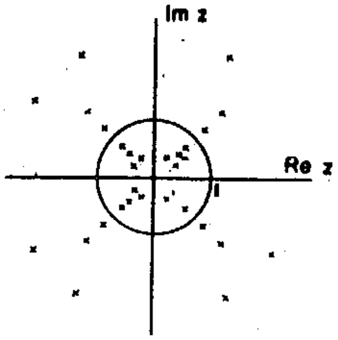

FIG. 3. Distribution of zeros for the 4×4 KDP lattice with $h = -v$ at $\epsilon/kT = 0.5$ $(T > T_0)$.

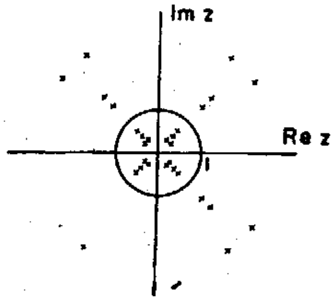

FIG. 2. Distribution of zeros for the 4×4 KDP lattice with $h = -v$ at $\epsilon/kT = 0.7$ $(T < T_0)$.

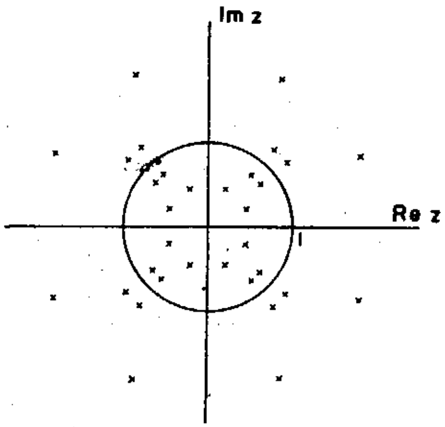

FIG. 4. Distribution of zeros for the 4×4 KDP lattice with $h = -v$ at $\epsilon/kT = 0.1$ $(T > T_0)$.

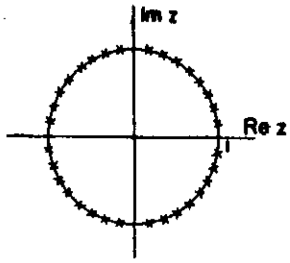

FIG. 5. Distribution of zeros for the 4×4 F lattice with a staggered field at $\epsilon/kT = 0.7$ ($T < T_0$).

northeast-southwest direction.[5] One then has an equivalent model with the following energy assignments:

$$e_1 = s, \quad e_2 = -s, \quad e_3 = e_4 = \infty, \\ e_5 = e_6 = e_7 = e_8 = \epsilon \; . \tag{2}$$

where e_i is the energy of the ith vertex, and, in addition to the vertex configurations (1)–(6) of Fig. 1, two new vertices [numbered (7) and (8)] with four arrows in or out are included. This model is however precisely a special case of the situation considered by SF with a direct field $h = v = \frac{1}{2}s$ in the first quadrant.[6] The result of SF now establishes the following *circle theorem for the F model*.

The zeros of the F model in a staggered field lie on the unit circle for $T < T_0$, where $T_0 = \epsilon/(k \ln 2)$ is the transition temperature.

NUMERICAL RESULTS

For a 4×4 lattice, the zeros of the partition function in an external direct or staggered field can be obtained by the solution of a quartic equation. With $y = e^{-\beta\epsilon}$, $z = e^{-2\beta v}$, or $z = e^{-\beta s}$, we find by explicit enumerations the following expressions for the partition function: for KDP with $h = -v$,

$$Z_{\text{KDP}} = v^{16}(z^{16} + z^{-16}) + 8y^{12}(z^{12} + z^{-12}) + (4v^{16} + 48v^{14} + 124v^{12} + 16y^{10} + 12v^{8})(z^{8} + z^{-8}) \\ + (248y^{12} + 496y^{10} + 48y^{8} + 8y^{4})(z^{4} + z^{-4}) + (6y^{16} + 96y^{14} + 432y^{12} + 496y^{10} + 288y^{8} + 32y^{6} + 2); \tag{3}$$

F with a staggered field,

$$Z_F = (z^{16} + z^{-16}) + 16y^{4}(z^{12} + z^{-12}) + (140y^{8} + 32y^{6})(z^{8} + z^{-8}) \\ + (256y^{12} + 384y^{10} + 144y^{8})(z^{4} + z^{-4}) + (256y^{16} + 640y^{12} + 384y^{10} + 152y^{8}). \tag{4}$$

Introducing the variable

$$u = z^{4} + z^{-4} \tag{5}$$

we find

$$Z_{\text{KDP}} = y^{16}u^{4} + 8y^{12}u^{3} + (48y^{14} + 124y^{12} + 16y^{10} + 12y^{8})u^{2} \\ + (224y^{12} + 496y^{10} + 48y^{8} + 8y^{4})u + (184y^{12} + 496y^{10} + 288y^{8} + 32y^{6} + 2), \tag{6}$$

$$Z_F = u^{4} + 16y^{4}u^{3} + (140y^{8} + 32y^{6} - 4)u^{2} + (256y^{12} + 384y^{10} + 144y^{8} - 48y^{4})u \\ + (256y^{16} + 640y^{12} + 384y^{10} - 128y^{8} - 64y^{6} + 2). \tag{7}$$

These are quartic polynomials in u, and the zeros of Z can now be found by the solution of a quartic equation. The corresponding values of z can then be obtained by solving (5). Notice that since (5) involves only z^4, we have always at least four z's locating on a circle. This is due to the periodic boundary condition imposed on the model which has the consequence of conserving the number of down arrows from row to row.[3] In Figs. 2–7 we present results on numerical calculations of the zeros of

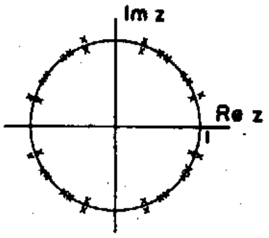

FIG. 6. Distribution of zeros for the 4×4 F lattice with a staggered field at $\epsilon/kT = 0.5$ ($T > T_0$).

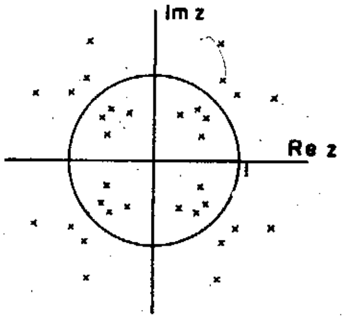

FIG. 7. Distribution of zeros for the 4×4 F lattice with a staggered field at $\epsilon/kT = 0.1$ ($T > T_0$).

Z_{KDP} and Z_F for a 4×4 lattice at three different temperatures, $\epsilon/kT = 0.7$, 0.5, and 0.1. The transition temperature is located at $\epsilon/kT_0 = \ln 2 = 0.693$. Figure 6 confirms that the zeros of the F model in a staggered field lie on the unit circle for $T < T_0$. It is also to be noted that our variable z is related to the conventional fugacity variable $\bar{z} = e^{-\beta\bar{v}}$, where $\bar{v} = \sqrt{2}v$ is the magnitude of the applied field, by the relation $z = \bar{z}^{\sqrt{2}}$. Evidently $|z| = 1$ implies $|\bar{z}| = 1$.

ACKNOWLEDGMENT

One of us (F.Y.W.) wishes to thank Professor Shien-Siu Shu for the hospitality extended to him during his stay at the National Tsing Hua University.

---

[*] Work supported in part by the National Science Council of the Republic of China, and in part (F.Y.W.) by the National Science Foundation under Grant No. GP-25306.

[1] T. D. Lee and C. N. Yang, Phys. Rev. 87, 410 (1952).

[2] M. Suzuki and M. E. Fisher, J. Math. Phys. 12, 235 (1971), and references cited therein.

[3] For an extensive review on the theory of ferroelectric models see E. H. Lieb and F. Y. Wu, in *Phase Transitions and Critical Phenomena*, edited by C. Domb and M. S. Green, (Academic, London, to be published).

[4] S. Katsura, Y. Abe, and K. Ohkouchi, J. Phys. Soc. Japan 29, 845 (1970).

[5] For further details see Fig. 2 and discussions preceding Eq. (10) in C. Fan and F. Y. Wu, Phys. Rev. B 2, 723 (1970).

[6] See Eq. (2.54) of Ref. 2.

Investigation of the ^{26}Mg(d, p)^{27}Mg Reaction below 3 MeV (*)(**)

E. K. Lin, W. N. Wang and J. G. Yu

Tsing Hua University and Academia Sinica - Taiwan

W. C. Tung

Institute of Nuclear Energy Research, Atomic Energy Council - Taiwan

(ricevuto il 4 Maggio 1971; manoscritto revisionato ricevuto il 13 Luglio 1971)

Summary. — A study was made of the reaction ^{26}Mg(d, p)^{27}Mg in the deuteron energy range from 2.0 to 3.0 MeV. Angular distributions in the range of $(30 \div 140)^\circ$ at $E_d = 2.1$, 2.3, 2.5, 2.7, 2.8 and 3.0 MeV were measured. Excitation functions ranging from 2.0 to 3.0 MeV were obtained for the reactions leading to the ground and first excited states of ^{27}Mg. The direct stripping effect was found to give a considerable contribution to the P_0-transition, and its significance appears to increase gradually at bombarding energies from 2.1 to 3.0 MeV. The distorted-wave Born approximation (DWBA) was used to calculate the spectroscopic factor for the ground state. The measured angular distributions of higher proton transitions indicate that compound nucleus formation becomes more important relative to the stripping process.

(*) **This paper has been published** in Nuovo Cimento, 8A (1972) 801-811, **also in Annual Report of the Institute** of Physics, Academia Sinica, (1970) 61-72.

(**) Work performed at the Physics Research Center in Hsinchu and supported by the Academia Sinica and Tsing Hua University.

Annual Report of the Institute of Physics. Academia Sinica, 1971

KINEMATICALLY COMPLETE INVESTIGATION OF $T=0$ EXCITED STATES OF ^{4}He BY INELASTIC SCATTERING OF α-PARTICLES ON ^{4}He *

E. L. HAASE, W. N. WANG † and M. A. FAWZI

Institut für Experimentelle Kernphysik der Universität und des Kernforschungszentrums Karlsruhe,

Received 11 March 1971
(Revised 17 May 1971)

Abstract: Using 104 MeV α-particles coincidence measurements were carried out for the following reactions: $^{4}\mathrm{He}(\alpha, \alpha' t)^{1}\mathrm{H}$, $^{4}\mathrm{He}(\alpha, \alpha' {}^{3}\mathrm{He})\mathrm{n}$ and $^{4}\mathrm{He}(\alpha, \alpha' d)^{2}\mathrm{H}$. In measuring the correlations, the detector of the inlastic α-particle was kept at a fixed position and the second detector scanned over a range of coplanar angles favouring ^{4}He final-state interactions.

The data can be fitted consistently with five $T = 0$ excited states of ^{4}He, at 20.2 MeV, 21.9 MeV, 25.5 MeV, 28.5 MeV and 31.8 MeV with widths (Γ) of 0.2 MeV, 1.8 MeV, 2.9 MeV, 5.3 MeV and 5.6 MeV, respectively. The validity of the sequential reaction mechanism is examined. The internal consistency of the level parameters for the three decay channels as well as the symmetry of the extracted angular correlations about 0 and 90° in the recoil c.m. system agree very well with the model of sequential decay. The angular correlations agree well with the predictions of a simple theory using the impulse approximation.

E | NUCLEAR REACTIONS $^{4}\mathrm{He}(\alpha, \alpha' t)$, $^{4}\mathrm{He}(\alpha, \alpha' {}^{3}\mathrm{He})$, $^{4}\mathrm{He}(\alpha, \alpha' d)$, $E = 104$ MeV; measured $\sigma(E_1, E_2, \theta_1, \theta_2)$. ^{4}He deduced resonance parameters. Natural gas target.

*This paper has been published in Nuclear Physics, A172 (1971) 81-98

† On leave from the Institute of Physics, Academia Sinica, and Tsing Hua University, Taiwan, China.

Annual Report of Institute of Physics, Academia Sinica, 1971

Boltzmann Equation with Fluctuations

Paul S. Lee and Ta-You Wu (吳大猷)

Statistical Physics Laboratory
State University of New York at Buffalo

Abstract

From the Liouville equation, by the method of multiple-time-scales, a generalized Boltzmann equation with fluctuations is obtained on the statistical considerations of the randomness of the many-particle correlations in the macroscopic picture. These fluctuations lead to an H theorem in which the H function decreases, with fluctuations, with time toward equilibrium. These fluctuations furnish a source for a random force term introduced by Fox and Uhlenbeck in the Boltzmann equation.

Introduction

The following properties of the Boltzmann equation are well known:

(1) As a consequence of the Stosszahlansatz in the formulation of the collision integral, the Boltzmann equation is not invariant upon the reversal of time, and the time arrow is expressed by the H theorem

$$\frac{dH}{dt} \leq 0 \qquad \text{(I. 1)}$$

(2) The monotonic decrease of the H function shows that the Boltzmann equation describes a monotonic approach to equilibrium without fluctuations.

On the other hand, in the attempts by Boltzmann(3),(4) to reinterpret the H theorem in views of the criticisms of Loschmidt and Zermelo, the Probability basis of the H theorem was emphasized, namely, when the state of the gas is not that of equilibrium, the collision integral is to represent the overwhelmingly large probability that the collision leads to a decrease in the value of the H function. From the collision integral and the definition of the H function, it follows that this probability of decrease of H remains the same if the velocities of the two colliding particles are reversed.* According to this reformulation of the meaning of the H theorem, the H function can rise above the minimum (or, equilibrium) value given by $\frac{dH}{dt}=0$, only to decrease to the minimum value again with a large probability. While the physical and probability considerations are all satisfactory, there does seem to be a lack of an explicit mathematical expression of these fluctuations, especially from the point of view of the usual Boltzmann equation.

---

* But this does not mean that H decreases both in the forward and the backward directions of time.

Very recently, Fox and Uhlenbeck(5) have studied the question of fluctuations. On statistical theoretical but more or less ad hoc ground, they introduce a random "force" term in the usual (linearized) Boltzmann equation. On the assumption of general statistical properties concerning this term, they have been able to justify and to extend the earlier theory of Landau and Lifshitz(7) in which terms representing fluctuations are added in a heuristic manner to the hydrodynamical equations.

Since 1946, the theory of the formulation of a kinetic equation (a generalized Boltzmann equation) on the basis of the Liouville equation has been developed by many authors. (2),(3),(9) The so-called B-B-G-K-Y hierarchy of equations have been treated by two methods, namely, the "functional" method of Bogoliubov which is similar to and an extension of the Chapman-Enskog method of solving the Boltzmann equation, and the "multiple-time-scale" method suggested by Krylov and Bogoliubov (10) for nonlinear mechanics and applied by Frieman(6) and Sandri(11) to the kinetic theory problem. It has been found in both methods that under certain assumptions about the initial conditions (on the many-particle correlations), one obtains a kinetic equation which reduces to the usual Boltzmann equation upon making some approximations. This generalized Boltzmann equation also contains no fluctuations, but leads to a monotonic approach to thermodynamic equilibrium.

The purpose of the present work is to obtain a kinetic equation with fluctuations from the B-B-G-K-Y hierarchy of equations of the Liouville equation, with the method of "multiple-time-scale", on consideration of the lack of definite knowledge about the initial microscopic state of the gas.

Kinetic Equation with Fluctuations

We start with the Liouville equation

$$\frac{\partial D}{\partial t}=\{H,D\} \qquad \text{(II-1)}$$

where H is the Hamiltonian of the system (N partices, without external fields), D the density (probability) in Γ space,

$$H=\sum_{i=1}^{N}\frac{1}{2m}p_i^2+\sum_{1=i<j}^{N}\phi(|r_i-r_j|)$$

$$\int\cdots\int D(q_1,\ q_N,\ p_1,\ p_N,t)\ dX_1\cdots dX_N=1, \qquad \text{(II-2a)}$$

$$dX_i=dq_i\ dp_i,$$

and the curly brackets denote the Poisson brackets. Let F_s be defined by

$$F_s(X_1,\cdots X_s,t)\equiv V^s\int\cdots\int DdX_{s+1}\cdots dX_N \qquad \text{(II-2b)}$$

so that F_s has the dimension $(\text{momentum})^{-3s}$. V is the volume of the system.

$$\frac{N}{V}\int F_1(q,p,t)\ dp=n(q,t) \qquad \text{(II-2c)}$$

is the number density of particles at q and t. From the Liouville equation, one obtains the B-B-G-K-Y hierarchy of equations(12)

$$\frac{\partial F_1}{\partial t}+K_1F_1^{(1)}=n_0\ L_1\ (1;2)\ F_2\ (1,2) \qquad \text{(II-3)}$$

$$\frac{\partial F_2}{\partial t} + \mathbf{H}_2\ F_2 = n_0\ L_2\ (1,2;3)\ F_3\ (1,2,3), \tag{II-4}$$

where

$$n_0 = \frac{N}{V},\quad K_1 = \frac{1}{m}\ p_1 \cdot \nabla_1, \tag{II-5a}$$

1 is the particle index,

$$L_1\ (1;j) = \iint dq_j\ dp_j\ \nabla_1\ \varnothing_{1j} \frac{\partial}{\partial p_1}$$

$$L_2(1,2;j) = L_1(1;j) + L_1(2;j), \tag{II-5b}$$

$$\mathbf{H}_2 = \sum_{i=1}^{2} \frac{1}{m}\ p_i \cdot \nabla_i - \sum_{\substack{i=1 \\ j \neq i}}^{2}\ \nabla_i\ \varnothing_i \cdot \frac{\partial}{\partial p_i},\ \text{etc}$$

The formal solution of (II-4) is

$$\begin{aligned} F_2\ (1,2;t) &= e^{-\mathbf{H}_2 t}\ F_2\ (1,2;0) \\ &\quad + n_0 e^{-\mathbf{H}_2 t} \int_0^t d\lambda e^{\mathbf{H}_2 \lambda}\ L_2(1,2;j) F_3(1,2,j;\lambda), \end{aligned} \tag{II-6}$$

and (II-3) becomes

$$\begin{aligned} &\frac{\partial F_1}{\partial t} + K_1 F_1 \\ &= n_0\ L_1(1;j)\ \{e^{-\mathbf{H}_2 t}\ F_2(1,2;0) + n_0\ e^{-\mathbf{H}_2 t} \int_0^t d\lambda e^{\mathbf{H}_2 \lambda}\ L_2(1,2;j) F_3(1,2;\lambda)\} \end{aligned} \tag{II-7}$$

F_3 (1, 2, 3; t) is given by the next equation in the hierarchy (II-3, 4) in terms of F_4 (1, 2, 3, 4; t), etc. If these functions are known from their initial conditions, then the "kinetic equation" (II-7) in principle completely determines F_1 $(q,\ ;t)$ without any random fluctuations.

Now in the spirit of statistical theories, we do not possess, nor are we interested in, a knowledge of the microscopic state of a system (a gas of N particles). We can only specify a macroscopic state, in terms of macroscopic properties. But any given macroscopic state corresponds to a large number of microscopic states. For example, a knowledge of the macroscopic quantities n, u, E

Particle density: $n(r,t) = n_0 \int F_1\ d\ ,$ (II-8a)

Mean Flow velocity: $u(r,t) = n_0 \int \frac{p}{m} F_1\ dp,$ (II-8b)

Mean energy density: $E(r,t) = n_0 \int \frac{p^2}{2m}\ F_1\ dp,$ (II-8c)

leaves the function F_1 $(q,p;t)$ still unspecified. In this sense, we shall regard the initial values of the F_s as random functions.

We shall express the kinetic equation (II-7) in a form which is closer to the usual Boltzmann equation. Let τ_1, τ_1, τ_2 be the characteristic times defined by the time of a collision, the time between two successive collisions and the time, say, for sound to traverse a macroscopic distance, namely,

$$\tau_0 = \frac{r_0}{u},\ \tau_1 = \frac{\lambda}{u},\ \tau_2 = \frac{L}{u_3} \tag{II-9}$$

where r_0, λ, L are respectively the range of intermolecular interaction, the mean free path and a macroscopic length, and u is the mean thermal speed of the molecules, and u_s is the speed of sound in the system. For ordinary temperatures and densities,

$$\tau_0:\tau_1:\tau_2 \cong 10^{-12}:10^{-8}:10^{-4} \qquad \text{(II-10)}$$

In a gas, the state evolves in time in a complicated way. Let the time t be replaced by the three independent time variables

$$t = t\ (\tau_0, \tau_1, \tau_2) \qquad \text{(II-11a)}$$

with

$$\frac{\partial \tau_n}{\partial t} = \in^n, \quad n = 0, 1, 2, \qquad \text{(II-11b)}$$

where $\in$ is a parameter$\ll 1$ ($\in \cong 10^{-4}$ in equation (II-10)).

These three time scales are independent since their origins are completely arbitrary. In fact even when a gas has come to thermal equilibrium, processes involving collisions persist, These collisions lead to fluctuations (in n, u and E in (II-8)) in the time-scale τ_1.

We shall expand all functions F_1, F_2, F_3, ... in powers of $\in$

$$F_1 = \sum_n \in^n F_1^{(n)}\ (\tau_0, \tau_1, \ldots)$$
$$F_s = \sum_n \in^n F_s^{(n)}\ (\tau_0,\ \tau_1, \ldots),\quad s = 2, 3, \ldots N \qquad \text{(II-12)}$$

From (II-11), we have

$$\frac{d}{dt} = \frac{\partial}{\partial \tau_0} + \in \frac{\partial}{\partial \tau_1} + \in^2 \frac{\partial}{\partial \tau_2} + \ldots \qquad \text{(II-13)}$$

Equations (II-3), (II-4) become, on dropping the subscript 1 from F_1,(12)

$$\frac{\partial F^{(0)}}{\partial \tau_0} + K_1\ F^{(0)} = 0, \qquad \text{(II-14)}$$

$$\frac{\partial F^{(0)}}{\partial \tau_1} + \frac{\partial F^{(1)}}{\partial \tau_0} + K_1 F^{(1)} = n_0 L_1(1;j) F_2^{(0)}(1,j), \qquad \text{(II-15)}$$

$$\frac{\partial F_2^{(0)}}{e \tau_0} + \mathbf{H}_2 F_2^{(0)} = 0, \qquad \text{(II-16)}$$

$$\frac{\partial F_2^{(0)}}{\partial \tau_1} + \frac{\partial F_2^{(1)}}{\partial \tau_0} + \mathbf{H}_2 F_2^{(1)} = n_0 L_2(1,2;j) F_3^{(0)}(1,2,j), \qquad \text{(II-17)}$$

$$\frac{\partial F_s^{(0)}}{\partial \tau_0} + \mathbf{H}_s\ F_s^{(0)} = 0, \qquad \text{(II-18)}$$

where $\mathbf{H}_s$ is obtained from $\mathbf{H}_2$ in (II-5) by extending the sumnation to $i = s$.

Let us make the Ansatz

$$F_2^{(0)}(1,\ 2;\ \tau_0,\ \tau_1, \ldots) = F^{(0)}\ (1;\ \tau_0,\ \tau_1 \ldots)\ F^{(0)}\ (2;\ \tau_0,\ \tau_1, \ldots) + G^{(0)}\ (1,\ 2;\ \tau_0,\ \tau_1, \ldots). \qquad \text{(II-19)}$$

The solution of (II-14) is

$$F^{(0)}\ (1;\ \tau_0,\ \tau_1, \ldots)\ e^{-K_1 \tau_0} F^{(0)}\ (1;\ \tau_0 = 0,\ \tau_1, \ldots) \equiv Z^{(1)}_{-\tau_0}\ F^{(0)}\ (1;\ 0,\ \tau_1, \ldots), \qquad \text{(II-20)}$$

or

$$F^{(0)}\ (1;\ 0,\ \tau_1, \ldots) = Z^{(1)}_{\tau_0}\ F^{(0)}\ (1;\ \tau_0,\ \tau_2, \ldots). \qquad \text{(II-20a)}$$

The solution of (II-16) is

$$F_2^{(0)}(1,\ 2;\ \tau_0,\ \tau_1,\ldots)=e^{-\mathbf{H}_2\tau_0}F_2^{(0)}(1,\ 2;\ 0,\ \tau_1,\ldots) \qquad \text{(II-21)}$$

$$=\overset{(2)}{Z}_{-\tau_0}(1,2)\Big[\overset{0}{\prod_{i=1}^{2}}\overset{(1)}{Z}_{\tau_0}(i)\ F^{(0)}(i;\ \tau_0,\tau_1,\ldots)+G^{(0)}(1,\ 2;\ 0\ \tau_1,\ldots)\Big]$$

It is important to note here that the two-particle correlation function $G^{(0)}(1,\ 2;\ \tau_0,\tau_1,\ldots)$ at $\tau_0=0$ must not be set equal to zero, but $G^{(0)}(1,\ 2;\ 0,\ \tau_1,\ldots)$ must be left as an unknown random function in the $\tau_1,\ \tau_2,\ldots$ time scales.

If we put (II-21) into (II-15) and set

$$\frac{\partial F^{(0)}}{\partial\tau_1}=n_0\ L_1(1,2)\ \overset{(2)}{Z}_{-\infty}\Big[\prod_{i=1}^{2}\overset{(1)}{Z}_{\infty}F^{(0)}(i)+G^{(0)}(1,\ 2;\ 0,\ \tau_1,\ldots) \qquad \text{(II-22)}$$

where

$$\overset{(1)}{Z}_{\infty}(1)=\lim_{\tau_0\to\infty}e^{\pm K_1\tau_0}$$

$$\overset{(2)}{Z}_{\pm\infty}(1,2)=\lim_{\tau_0\to\infty}e^{\pm\mathbf{H}_2\tau_0}, \qquad \text{(II-22a)}$$

then equation (II-15) will approach, as $\tau_0\to\infty$ (*i. e.*,$\gg\tau_0$),

$$\frac{\partial F^{(1)}}{\partial\tau_0}+K_1\ F^{(1)}\to 0, \qquad \text{(II-23)}$$

and $F^{(1)}$ does not increase secularly in the τ_0 scale. On combining (II-14) and (II-22), and using (II-11) we obtain

$$\left(\frac{\partial}{\partial t}+K_1\right)F^{(0)}(1) \qquad \text{(II-24)}$$

$$=n_0\ L_1\overset{(2)}{Z}_{-\infty}\prod_{i=1}^{2}\overset{(1)}{Z}_{\infty}(i)\ F^{(0)}(i)+n_0\ L_1(1;2)G^{(0)}(1,\ 2;\ \tau_1,\ldots)$$

where

$$G^{(0)}(1,\ 2;\ \tau_1,\ldots)=\overset{(2)}{Z}_{-\infty}G^{(0)}(1,\ 2;\ 0,\ \tau_1,\ldots) \qquad \text{(II-25)}$$

$G^{(0)}(1,\ 2;\ \tau_1,\ldots)$ is ths the value of the two-particle correlation function traced back, in accordance with the equations of motion of the two particles governed by the Hamiltonian H_2 in (II-2). If we impose the condition that

$$G^{(0)}(1,\ 2;\ \tau_1,\ldots)=0, \qquad \text{(II-26)}$$

equation (II-24) is then the generalized Boltzmann equation obtained by Bogoliubov,$^{(1)}$$^{,(12)}$

$$\left(\frac{\partial}{\partial t}+K_1\right)F^{(0)}=n_0\ L_1(1;2)\overset{(2)}{Z}_{-\infty}\prod_{i=1}^{2}\overset{(1)}{Z}_{\infty}\ F^{(0)}(i), \qquad \text{(II-27)}$$

which reduces to the usual Boltzmann equation if the inhomogeneity of $F^{(0)}$ within a region of the size of the range r_0 of intermolecular interaction is neglected. In this case, there is no fluctuation.

The initial condition (II-26), however, is too strong a condition and must be examined more closely. We must remember that the time variables τ_0 and τ_1 are independent in the sense that, if we regard the time t as a linear sequence, at any instant t , there are imbedded in t the variables τ_0, τ_1 whose origins are independent and arbitrary. In an interval of order τ_1 there will be of the order $\frac{1}{\epsilon}$ intervals of τ_0, and $\frac{1}{\epsilon}$ independent origins of these $\frac{1}{\epsilon}$ intervals of τ_0 over each of which the time scale τ_0 spans. The condition (II-26) amounts then to setting the correlation $G^{(0)}(1, 2; 0, \tau_1, \ldots) = 0$ independently of t in the τ_1, $\tau_2, \ldots$ scales. The condition is of course mathematically permissible; but it defines a time arrow by an initial instant, or a "past", at which there are no correlations so that the system evolves in that direction of time in which the particles become correlated by virtue of their interactions. The result is the time irreversible Boltzmann equation. From the physical point of view, the assumption of (II-26), or other definite knowledge about the initial condition of the gas, is not consistent with the spirit of the theory of macroscopic description of a gas.

In view of the discussions on the statistical point of view following (II-7) above, we shall regard $G^{(0)}(1, 2; \tau_1, \ldots)$ in (II-25) as an experimentally unknown random function in the τ_1 time scale. Equation (II-24) is then a "Boltzmann equation" with a random force term, namely,

$$\left(\frac{\partial}{\partial t} + K_1\right) F^{(0)}(1)$$

$$= n_0\, L_1(1,2)\, Z^{(2)}_{-\infty} \prod_{i=1}^{2} Z^{(1)}_{\infty}\; F^{(0)}(i) + \widetilde{C}(1;t) \tag{II-28}$$

where

$$\widetilde{C}(q_1, p_1; t) \equiv n_0 \iint dq_2\, dp_2\; \nabla_1 \varnothing_{12} \cdot \frac{\partial}{\partial p_1} G^{(0)}(1, 2; t) \tag{II-29}$$

is a random function since $G^{(0)}(1, 2; t)$ is a random function.

On writing

$$F^{(0)} = f(1+\varphi) \equiv f + \widetilde{f} \tag{II-30}$$

where f is a solution of the Boltzmann equation (II-27), and for "small" fluctuations

$$|\widetilde{f}| \ll f \tag{II-31}$$

one obtains the linearized kinetic equation

$$\left(\frac{\partial}{\partial t} + K_1\right) \widetilde{f}$$

$$= n_0\, L_1\, Z^{(2)}_{-\infty} \left[Z^{(1)}_{\infty} f(1)\, Z^{(1)}_{\infty} \widetilde{f}(2) + Z^{(1)}_{\infty} f(2)\, Z^{(1)}_{\infty} \widetilde{f}(1) \right] + \widetilde{C}(1; t). \tag{II-32}$$

If we are interested in the fluctuations from the equilibrium state, i. e.,

$$f = f_{equ.}(p), \tag{II-33}$$

this linearized equation becomes

$$\left(\frac{\partial}{\partial t}+\frac{1}{m}p\cdot\nabla\right)\varphi(q,\ p;\ t)$$
$$=\iint dp_1\ d\Omega\ g\ \sigma(g,\ \theta)\ f_{equ}(p_1)\ [\varphi(q',\ p';\ t)+\varphi(q',\ p_1';\ t) \tag{II-34}$$
$$-\varphi(q,\ p;\ t)-\varphi(q,\ p_1;\ t)]+\widetilde{C}\,(q,\ p;\ t)$$

where $g=\frac{1}{m}|p_1-p|$, σ is the cross-section of the two-body collision, and $d\Omega$ is the solid angle of the scattering, and p', p_1' are the momenta of the two particles such that after collision at q they become p, p_1 respectively. Equation (II-34) without the $\widetilde{C}$ term is the usual linearized Boltzmann equation in the Chapman-Engskog solution of the Boltzmann equation. Equation (II-34) is just that recently obtained by Fox(5) who introduces a random force term in the usual linearized Boltzmann equation on statistical considerations. The approach from the Liouville equation in the present work thus has furnished a source for a fluctuation term in the Boltzmann equation.

The H-Theorem

The original statement of the H theorem (I-1) by Boltzmann on the basis of the Boltzmann equation has been criticized by Loschmidt and Zermelo. These criticisms were based on the assumption that the evolution of the H function is determined by dynamical laws. In fact, if the kinetic equation, written in the form

$$\frac{\partial F}{\partial t}=I(F) \tag{III-1}$$

is time-reversal invariant, i. e., if upon time reversal

$$\begin{gathered} t\rightarrow-\tau, \\ p\rightarrow-p, \\ F(q,\ p;\ t)\rightarrow F(q_1-q;-\tau)\equiv\sim F(q,\ p;\ \tau), \end{gathered} \tag{III-2}$$

(III-1) goes into

$$\frac{\partial \widetilde{F}}{\partial\tau}=I(\widetilde{F}), \tag{III-3}$$

then it can readily by seen that

$$\frac{dH}{dt}=0. \tag{III-4}$$

The Boltzmann equation containing the Stosszahlansatz is however not a consequence of dynamical laws and is not invariant under time reversal. That the Boltzmann equation leads to (I-1) is therefore not subject to the objections of Loschmidt and Zermelo. Boltzmann has subsequently reformulated the H theorem by giving it a probability interpretation. The collision integral is taken to give the probable decrease of H whenever H is above the asymptotic minimum given by $\frac{dH}{dt}=0$. The H function for one individual system may rise, but the average of the H function of a large number of systems is to be described by the H-theorem (I-1), This formulation of the H-theorem has been discussed by Boltzmann,(3) P. and T. Ehrenfest(4) and ter Hear(8). It remains, as noted in the Introduction above, to have an explicit theory for describing the decrease of the H function on the average but with fluctuations.

We shall first show that the fine-grained time behavior (in the τ_0 time scale) of the system as described by the Liouville equation does not yield fluctuations. Let us take equation (II-3), and write

$$F(\tau_0,\ \tau_1,\ldots)=f(\tau_1,\ldots)+\varphi(\tau_0,\ \tau_1,\ldots) \tag{III-5}$$

where f is the "slowly" varying part, i. e.,

$$f(\tau_1,\ldots)=\lim_{T\to\infty}\frac{1}{T}\int_0^T F(\tau_0,\ \tau_1,\ldots)\,d\tau_0, \tag{III-6}$$

or

$$\lim_{T\to\infty}\frac{1}{T}\int_0^T \varphi(\tau_0,\ \tau_1,\ldots)d\tau_0=0. \tag{III-6a}$$

Similarly, for the G in

$$F_2(1,\ 2)=F_1(1)F_1(2)+G(1,\ 2), \tag{III-7}$$

we write

$$G(\tau_0,\ \tau_1,\ldots)=g(\tau_1,\ldots)+\chi(\tau_0,\ \tau_1,\ldots), \tag{III-8}$$

where

$$g(\tau_1,\ldots)=\lim_{T\to\infty}\frac{1}{T}\int_0^T G(\tau_0.\ \tau_1,\ldots)d\tau_0. \tag{III-9}$$

On making expansions of F, G as in (II-12), and if we assume the initial condition

$$G^{(0)}(\tau_0=0,\ \tau_1,\ldots)=0, \tag{III-10}$$

we obtain for $f(\tau_1,\ldots)$ the generalized Boltzmann equation (II-27). If we define the coarse-grained time H function by

$$\overline{H}=\iint f\ \ln f\ dq\ dp\ , \tag{III-11}$$

then we obtain

$$\frac{dH}{dt}=\frac{dH}{d\tau_1}\leq 0, \tag{III-12}$$

which is the H theorem in the usual form from the Boltzmann equation. The fine-grained time H function is defined by F of (III-4)

$$H=\iint F\ \ln F\ dq\ dp \tag{III-13}$$

in the τ_0 time scale, In this time scale, F is given by the time-reversal invariant equation (II-3), and it follows from (III-1)—(III-4),

$$\frac{dH}{d\tau_0}=0.$$

We summarize the above result by saying that if we assume the initial condition (III-10), then the Liouville equation leads to an H function which decreases monotonically in the coarsegrained τ_1 time scale, but in the fine-grained τ_0 time scale remains constant. There are no "fluctuations".

Let us now use the kinetic equation (II-28) with the random term $\widetilde{C}\ (q,\ p;\ t)$. On putting (II-30) into (III-13) we obtain

$$\frac{dH}{dt}=\frac{d}{dt}\iint F\ln F\,dq\,dp$$

$$=\iint dq\,dp\,[(1+\ln f)\frac{\partial f}{\partial t}+(1+\ln f)\frac{\partial \tilde{f}}{\partial t}+\ln(1+\phi)\frac{\partial F}{\partial t}] \qquad \text{(III-15)}$$

The first term is the $\frac{dH}{dt}$ as given by the usual Boltzman equation and is $\left(\frac{dH}{dt}\right)_{Boltz}\leq 0$.

The other two terms contain the fluctuations $\tilde{f}$ determined by the random function $\tilde{C}(q,p;t)$ in (II-32) and may have all values $\gtreqless 0$. It is to be noted that these fluctuations in H are in the τ_1 (mean free) time scale. These fluctuations in H correspond to fluctuations in the entropy in the approach of a system to equilibrium.

The authors wish to express their appreciation of the discussions with Dr. Y. C. Lee on this work.

REFRENCES

1. Bogoliubov, N. N. J. Phys. (USSR) **10**, 256, 265 (1946); Monograph translated (1962) by E. K. Gora and published in Studies in Statistical Mechanics, ed. by J. de Boer and G. E. Uhlenbeck, New York: Interscience Publishers, (1962).
2. Boltzmann, L. (1898) Lectures on Gas Theory, English translation by S. G. Brush, Berkeley, Univ. of Calif. Press, (1964).
3. Born, M. & Green, H. S. (1946, 1947) Proceedings of the Royal Society (London) A188, 10; ibid **189**, 103; ibid **190**, 455; ibid, **191**, 168.
4. Ehrenfest, P. & T. (1911) article in Enzyklopadie in Mathematischen Wissenschaften, Vol. IV, Pt. 32 (English translation, Cornell Univ. Press, 1959).
5. Fox, R. F. Contributions to the Theory of Non-equilibrium Thermodynamics, Ph. D. dissertation (1969), Rockefeller univ., New York.
6. Frieman, E. A. J. Math. Phys. **4**, 410 (1963).
7. Landau, L. & Lifshitz, E. Fluid Mechanics, Pergamon Press, (1959).
8. ter Hear, D. Elements of Statistical Mechanics, N. Y., 1954, Appendix I.
9. Kirkwood, J. G. (1945, 1947) J. Chem. Phys, **14**, 180 (1946); ibid, **15**, 72 (1947).
10. Krylov, N. M. & Bogoliubov, N. N. "Introduction to Nonlinear Mechanics", English translation by S. Lefshetz, Princeton Univ. Press, (1947).
11. Sandri, G. Phys. Rev. Letters **11**, 178 (1963); Ann. Phys. **24**, 332, 380 (1963).
12. Wu, Ta-You Kinetic Equations of Gases and Plasmas, Addison-Wesley, (1966), Chapter 3, Sects 1-6.
13. Yvon, J. La Theorie Statistique des Fluideset d'Équation d'État, Paris, (1935).

Annual Report of the Institute of Physics, Academia Sinica, 1971

Differential Cross Sections for Elastic Scattering of Low-Energy Protons from ^{24}Mg and ^{26}Mg*

W.N. Wang (王唯農), *E.K. Lin* (林爾康) *and C.L. Tung* (董岐龍)

Academia Sinica and Tsing Hua University

Abstract

The Mg^{24,26} (p,p) Mg^{24,26} differential cross sections have been measured at $Ep=1.5$-3.0 MeV by using targets of high enrichment in Mg^{24} and Mg^{26} respectively. Excitation functions for the elastic scattering of protons have been obtained at center-of-mass scattering angles near 130° and 150° for proton energies between 1.5 and 3.0 MeV. Scattering angular distributions were measured at three energies in this range. The elastic scattering excitation functions exhibit conspicuous resonances at $Ep=1.63$ MeV for the Mg^{24} (p,p) case and at $Ep=2.03$ MeV for the Mg^{26} (p,p) case. The measured angular distributions show a characteristic of symmetry about 90° at resonance and a characteristic of Coulomb scattering at non-resonant energies. Differential cross sections for elastic scattering of protons from Mg^{26} were found to be somewhat larger than those from Mg^{24} in the energy range investigated.

1. INTRODUCTION

The elastic scattering of protons has been studied rather extensively in the last decade. A large volume of data has been accumulated at variously high energies. However, the low-energies experiment has been performed over limited energies at few scattering angles. The investigation of elastic proton scattering on even-even nuclei at low energies is well known to be a useful tool for studying nuclear energy levels at high excitation. Measurement of the angular distributions and excitation functions would serve to give a knowledge of the resonant energies and widths of compound nuclei. From phase-shift analysis of elastic scattering data, it is possible to determine definite values for the momenta and parties of the excited states form in the compound nucleus.

The Tsing Hua Van de Graaff accelerator provides a variable-energy source of protons at low energies for such scattering studies. A program was planned at this laboratory for investigation on proton resonance reactions for a series of target nuclei and bombarding energies, with the aim of studying high-lying levels in compound nuclei. The present experiment was undertaken to measure the differential cross sections for the elastically scattered protons from ^{24}Mg and ^{26}Mg at the bombarding energies below 3 MeV. This paper describes the experiment and presents the data obtained. The continuation work in deal with the analysis is

---

(*) Work performed at the Physics Research Center in Hsinchu and supported by the Academia Sinica and Tsing Hua University.

in progress.

Previous works on $^{24}Mg(p,p)^{24}$ Mg and $^{26}Mg(p,p)^{26}$ Mg reactions at low energies have been reported in refs. 1 and 2 and refs. 3 and 4 respectively. Many resonances in the energy region of $Ep=1$-4 MeV have been reported.

2. EXPERIMENTAL

The proton beam at energies between 1.5 and 3.0 MeV from the Tsing Hua Van de Graaff accelerator was used to bombard targets of ^{24}Mg and ^{26}Mg. The elastically scattered protons were analyzed with two ORTEC surface-barrier detectors. The detection system was adjusted to select and count only the desired elastically scattered protons. The accumulation of beam was performed by using a current integrator and a monitor. The monitor was employed as a check on the beam integrator system and on the uniformity of the target for the angular distribution. The total number of protons scattered elastically at a given angle was determined from the sum of two runs. A more extensive descript ion of the experimental arrangement has been given previously(5).

The targets of ^{24}Mg and ^{26}Mg were prepared by the vacuum evaporation(6) of magnesium in high enrichment (~99%) and were deposited onto a thin carbon backing (~10μg/cm²). The targets used in this experiment is of~30 Mg/cm² thick. The thickness was determined by assuming that the scattering was Rutherford near 1 MeV and was checked by comparing the data taken from the (d,p) reaction with values obtained in the previous experiment in this laboratory for studies of the Mg(d,p) reactions(7).

Data were collected at laboratory angles of 130° and 150° in steps of 15 keV from $Ep=1.5$ MeV to 3.0 MeV to obtain energy excitation functions; the proton energies range investigated corresponds to excitation energies of 3.73 MeV to 5.17 MeV and 9.71 MeV to 11.25 MeV in the compound nuclei ^{25}Al and ^{27}Al respectively. In addition, data were also taken at three different energies and angle ranges of 50° to 150° to get angular distributions.

3. RESULTS AND DISCUSSION

In Figs. 1 and 2 are shown the yield curves for protons scattered elastically from ^{24}Mg and ^{26}Mg, respectively, at the laboratory angles of 130° and 150°. The full line is drawn through the data points. For comparison, the calculated Rutherford cross section is also shown in Figs. 1 and 2 by the dash line. The experimental uncertainty in the measured absolute cross sections is of the order of 10%. The principal sources of uncertainty were the nonuniformity of the target and the beam integration.

For ^{24}Mg, the only resonance type structure appearing in the yield curves was observed at $Ep=1.5$-1.9 MeV. In this region there is a pronounced resonance at $Ep=1.63$ MeV, corresponding to ^{25}Al level with excitation energy 3.85 MeV, This characteristic is similar to the yield curve of Mooring et al ( ) measured at an angle of 164°, which shows the striking resonance at $Ep=1.63$ MeV. Valter et al(2) have assigned this level to have odd parity and $\frac{1}{2}$ unit of angular momentum. The other significant feature of the measured yield curves is that both cross sections at $\theta_{lab}=130°$ and $\theta_{lab}=150°$ tend to decrease gradually as Ep increase and a minimum appears near $Ep=3.0$ MeV. It has been shown⁽²⁾ that there is a resonance at $Ep=3.14$ MeV. In general, the observed cross sections are about 30% higher than the Rutherford scattering cross sections.

The differential cross sections as a functon of angle for the elastically scattered protons from ^{24}Mg are shown in Fig. 3. The data were recorded in 10° step from 50° to 160°. The angular distributions vary smoothly as a function of energy. The differential cross section decreases with increasing bombarding energy. The trend follows closely with the Rutherford curve at off-resonance region. Significant deviation from Rutherford scattering was observed in the angular distribution at $Ep=3.0$ MeV. All data points at angles larger than 90° are lower than the Rutherford curve.

For ^{26} Mg, the measured excitation functions as shown in Fig. 2 indicate some resonances appearing at Ep between 2.1 MeV and 2.5 MeV and a conspicuous anomaly at $Ep=2.03$ MeV in the elastic proton yield. This corresponds to a doublet with resonance energies at $Ep=2.025$ MeV and 2.050 MeV with widths $\Gamma=40$ keV and 70 keV, respectively, as observed in ref. 4. Our data gives $\Gamma=50$ keV for the 2.03 MeV resonance. The corresponding energies of excited states in the compound nucleus ^{27}Al are 10.222 MeV and 10.245 MeV. These two resonance states were found (4,8) to be $3/2^-$ and $1/2^+$ respectively. As is seen from Fig. 4, the measured angular distribution for the 2.03 MeV resonance show a characteristic of symmetry about 90°, while the measured angular distributions at other energies in the off-resonance region follow the Rutherford curve. The results of measurements are in fairly agreeement with those of the earlier works. (3,4)

It is noticeable that there is somewhat change in the manitude of the cross sections for elastic scattering of protons from ^{24}Mg and ^{26}Mg. The measured magnitudes of the differential cross sections for ^{26}Mg are somewhat larger than those for ^{24}Mg. The other noticeable change in the differential cross sections is the fluctuation as the energy of the incident proton changes. The ^{24}Mg data in the excitation functions show rather smooth curves except near $Ep=1.63$ MeV resonance. However, we have missed many very narrow resonances in this energy range. The large thickness of the target used and insufficient energy resolution made it difficult to study fine structure of narrow resonant levels in the compound nuclei ^{25}Al and ^{27}Al in the present experiment for the elastic proton scattering.

ACKNOWLEDGEMENTS

The authors would like to acknowledge the support of this work by the National Council on Science Development of China. Thanks are also due to Mr. L.P. Liang and Mr. P.S. Song for their providing assistance in this work.

REFERENCES

1. E.P. Mooring, L.J. Koester, Jr., E. Goldberg, D. Saxon and S.G. Kaufmann, Phys. Rev. 84,703 (1951).

2. A.K. Valter, V.E. Storizhko and A.I. Popov, Soviet Physics JETP 17,39 (1963).
3. J. Walinga, Physica 36,215 (1967).
4. M.C. Mertz, Ph.D thesis, Illinois Institute of Technology 1965 (unpublished)
5. E.K. Lin, W.N. Wang, T. Chiao, T.J. Lee, C.C. Hsu and Y.C. Yang, Chin. J. Phys 4,6 (1966).
6. E.K. Lin, G.C. Kiang and H.S. Tzeng, Chin. J. Phys. 6,67 (1968).
7. E.K. Lin, W.N. Wang, J.G. Yu and W.C. Tung, Nuo. Cim. 5A (1971).
8. P.M. Endt and C. Van der Leun, Nucl. Phys. A105, 111 (1967).

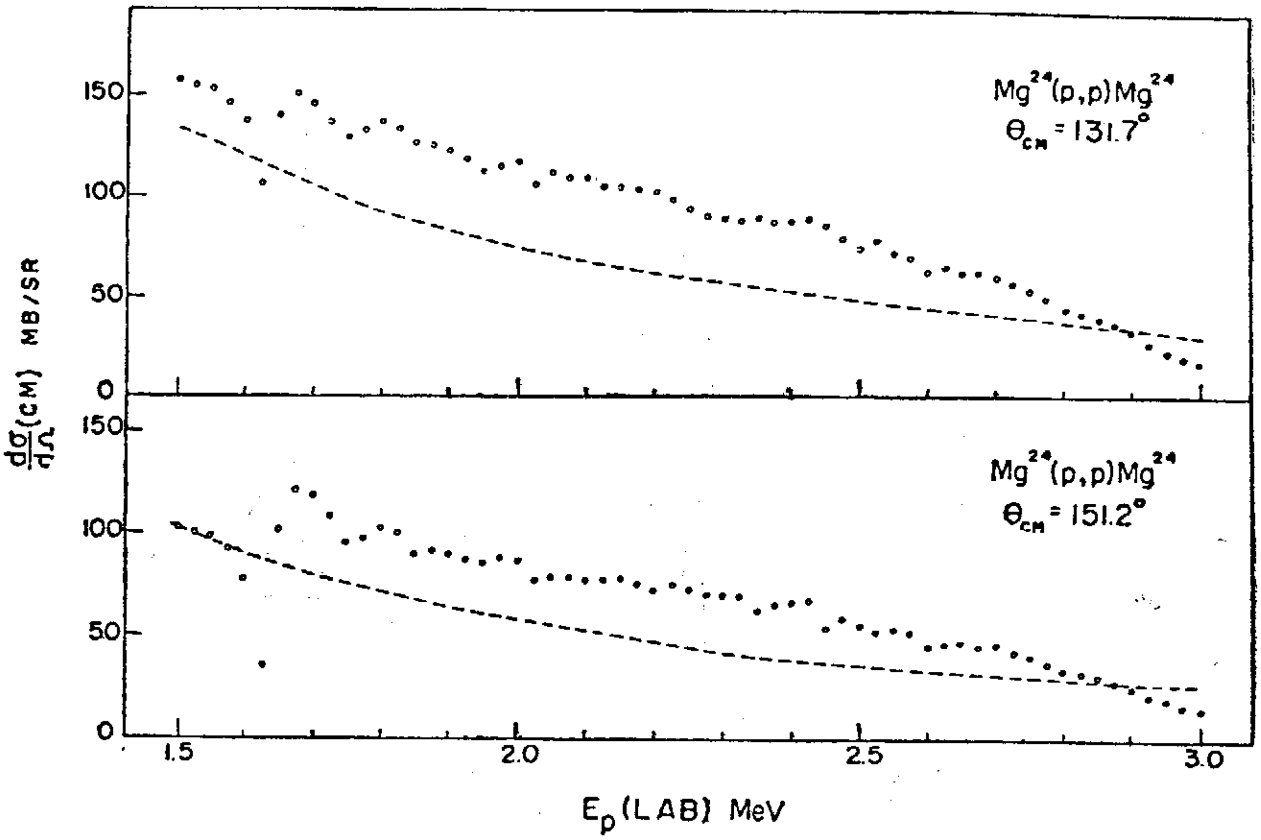

Fig.1 Differential cross section for protons scattered elastically from ^{24}Mg as a function of incident proton energy. The dash line represents the theoretical Rutherford cross section.

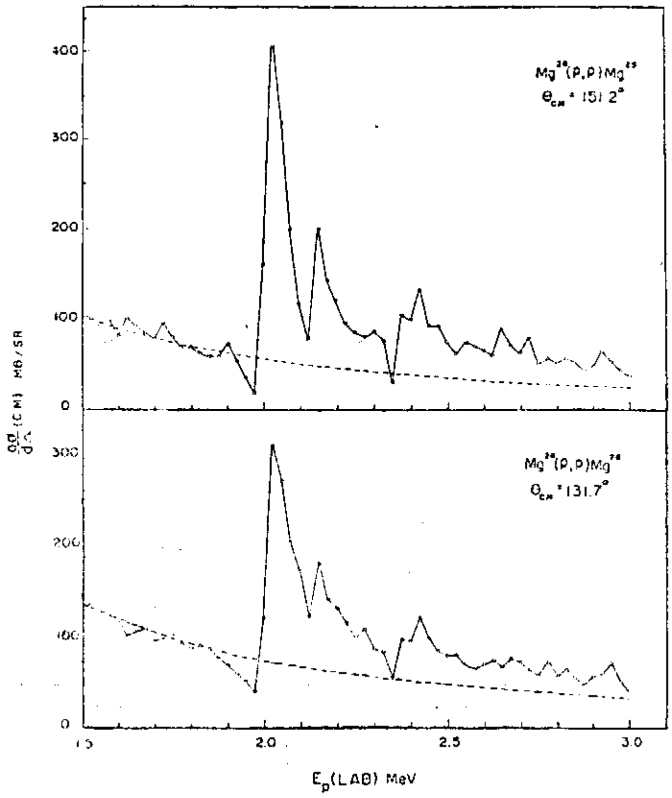

Fig.2 Differential cross section for proton scattered elastically from ^{26}Mg as a function of incident proton energy. The dash line represents the theoretical Rutherford cross section.

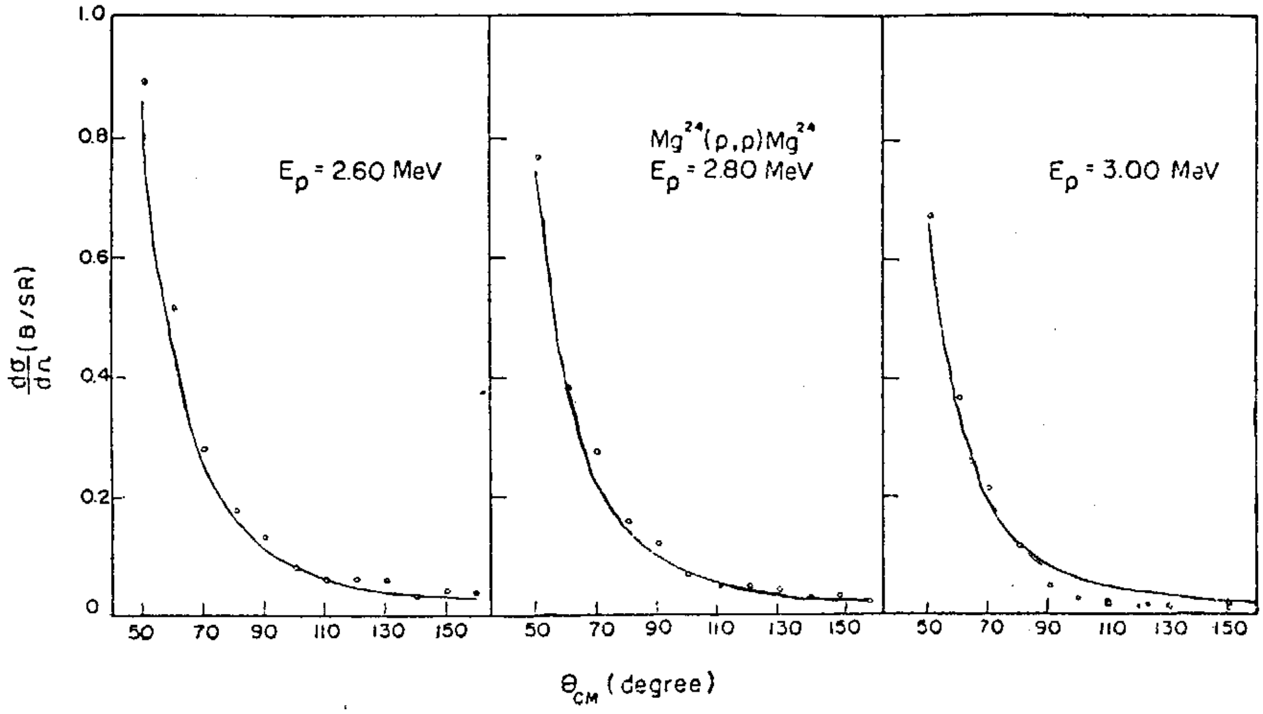

Fig.3 Angular distributions of elastically scattered proton at different energies from ^{24}Mg.

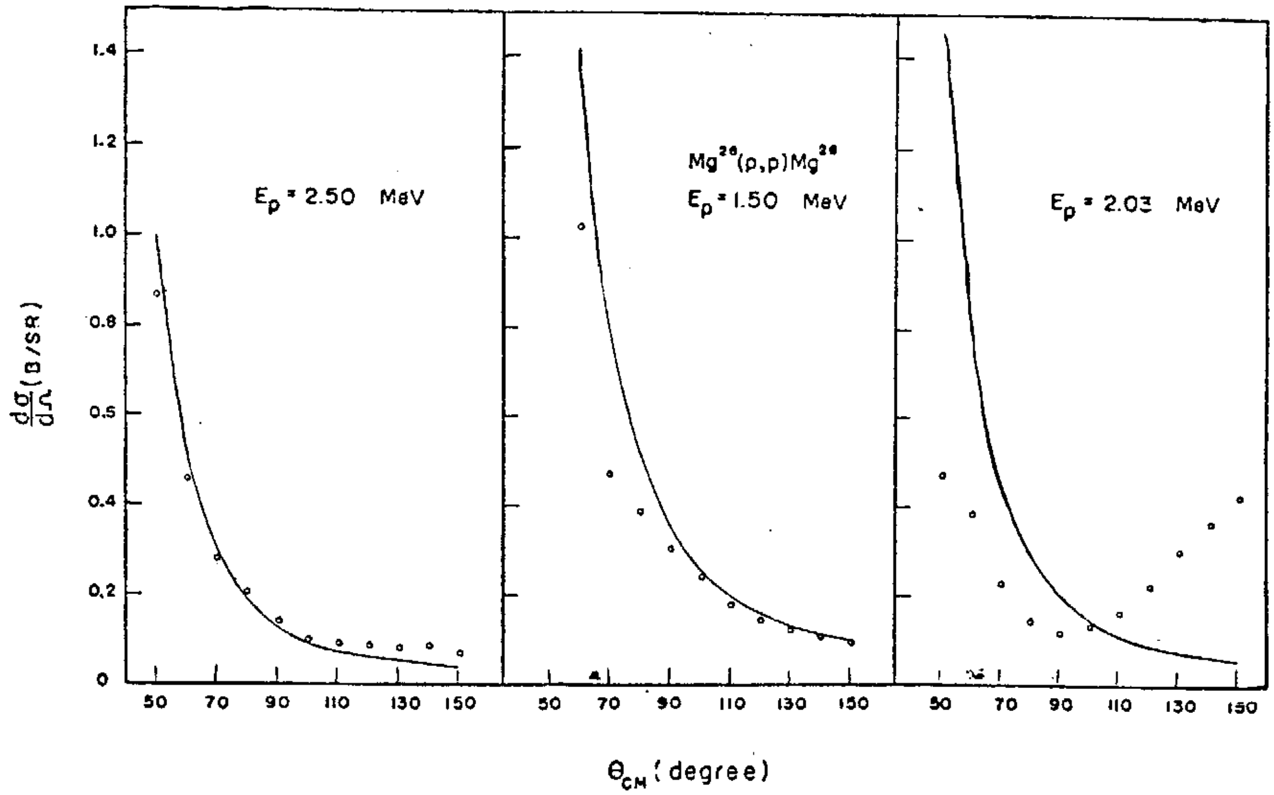

Fig.4 Angular distributions of elastically scattered protons at different energies from ^{26}Mg.

Annual Report of the Institute of Physics, Academia Sinica, 1971

Investigation of the $^{27}Al(p,\gamma)^{28}Si$ Reaction in the Proton Energy Range 925-2760KeV(*)

T.H. Hsu(**), E.K. Lin (林爾康), C.C. Hsu, Y.C. Liu, and P.K. Tseng
C.W. Wang (王建萬) and W.S. Hsu

Tsing Hua University, Academia Sinica
and Taiwan University

Abstract

The $^{27}Al(p,\gamma)^{28}Si$ reaction has been studied in the proton energy range 925-2760 KeV. Seventy-four resonances were observed. Gamma-ray spectra of two new strong resonances at 2720 and 2748 KeV, corresponding to the 14.310 and 14.237 MeV levels in ^{28}Si, were measured by a 50-cc Ge(Li) detector. Decay schemes for these two resonance levels were proposed and branching ratios of the de-excitation of gamma-rays were determined. From arguments on transition probabilities it seems to favor a spin assignment for both resonance levels to be $J^{\pi}=3^{+}$.

1. INTRODUCTION

In recent years, a considerable amount of spectroscopic information on a large number of nuclei has been obtained from the analysis of the (p,γ) reaction(1). In particular, the $^{27}Al(p,\gamma)^{28}Si$ reaction has been extensively investigated (2-6). Previously the $^{27}Al(p,\gamma)^{28}Si$ experiments have been performed, mainly with proton energies from 1.0-2.0 MeV. For $E_p=$ 0.2-1.4 MeV the results available in 1967 were summarized by Endt and Leun(7). The excitation curves obtained show many narrow resonances corresponding to compound nuclear states of ^{28}Si in the region of ~13MeV excitation. Among these resonances, de-excitation gamma-ray spectra from several strongly excited resonances, which populate a large number of ^{28}Si levels, in this proton energy range have been investigated, and the information on decay properties, spins and parities of the ^{28}Si levels has been obtained.

Recently Meyer et al(5), who have studied the $^{27}Al(p,\gamma)^{28}Si$ reaction in the energy region $E_p=$1.01-2.00 MeV, have observed a new resonance at $E_p=1683.7$ KeV. Lam et al(6) have reported an extensive investigation on a proton resonance at $E_p=1724$ KeV. The resonances at proton energies above 2.0MeV have been investigated by Gibson et al(3), who have reported six proton resonances at energies between 1262 KeV and 2319 KeV, and by Lyons et al(4) who

---

(*) Work performed at the Physics Research Center and supported by the National Science Council of the Republic of China.

(**) On leave from the Department of Physics, University of Ottawa, Canada.

have made total yield measurements in the proton energy range 327-2584 KeV in an energy step of $\Delta E_p = 2.5$ KeV. The energies of strongly excited resonances observed in the ^{27}Al (p,γ) ^{28}Si reaction have been determined to a accuracy less than 1KeV. These values of resonance energies are now considered as a standard source for calibration of proton beam energies of the accelerator.

The present work reported herein on the ^{27}Al(p,γ) ^{28}Si reaction was carried out in an exploratory nature. The present experiment consists of yield measurements for the ^{27}Al (p,γ) ^{28}Si reaction in the proton energy range 925-2760 KeV and of gamma-ray spectra measurement at 2720 KeV and 2748 KeV resonances. Since we have extended this work to higher energies ($E_p > 2.50$ MeV), more resonances have been observed, and the corresponding level energies of ^{28}Si have been accurately determined. It was hoped that our results would present useful information on the ^{27}Al$(p,\gamma)^{28}$ Si reaction, which would be needed for dealing with the investigation of the (p,γ) reactions on target nuclei other than aluminium.

2. EXPERIMENTAL DETAILS

The protons were accelerated by the 3.0 MeV Van de Graaff accelerator at Tsing Hua University. The beam current was 5-10 μA in the proton-energy range investigated. The energy resolution of the accelerator was about 1KeV. The beam energy was determined by usual nuclear magnetic resonance method. The magnetic field was controlled by a current regulator unit supplied by the Spectro-Magnetic Industries, and was calibrated with several well-known resonances between 992 KeV and 2560 KeV in the ^{27}Al (p,γ) ^{28}Si reaction(5,7). The calibrated proton energy was related to the frequency f of the NMR fluxmeter by the equation

$$E_p = k_1 f^2 + k_2 f + k_3$$

where the constants k_1, k_2 and k_3 were determined in the calibration, and it was found that the contribution of the k_2 and k_3 terms to the calibrated energy are only about 3% and 1% of the k_1 term, respectively.

The experimental arrangement is shown in fig. 1. After passing through quadrupole magnets and collimators, the beam was focused to a fine spot on the target. Targets were prepared by vacuum evaporation of Aluminium (99.99%) foil onto gold backings (of~0.4mm thick). The thickness of the prepared targets was between a few μg/cm^2 and 20 μg/cm^2. In the course of the experiment, targets were cooled by circulating water, directly against the backings. A small target chamber was specially designed and constructed (8) for the (p,γ) experiment. Four targets can be mounted on a slowly sliding target holder driven by a small motor and they can be interchanged inside target chamber as desired without breaking the vacuum. This arrangement and water cooling of the targets permitted continuously running for periods of 24 hr or longer in the gamma-ray spectra measurement without noticeable target deterioration. A liquid nitrogen cold trap was mounted near the targets to reduce contamination buildup.

The gamma-ray were detected in a 3″×3″ NaI (Tl) crystal enclosed in a lead shield of the cylindrical shape, and also detected in a 50-cc Ge (Li) detector purchased from ORTEC, Oak Ridge. These two detectors were mounted oppositively at 90° to the beam direction and were placed as close as possible to the target (at a distance 4cm from the target) in order to increase the total gamma-ray detection efficiency. In front of both detectors, lead absorbers of ~2 mm thickness were placed in order to reduce the large low-energy count rate caused by bremsstrahlung and Coulomb excitation in the gold backing.

For yield measurement the NaI (Tl) crystal was used. After amplification the gamma-ray pulses were fed to three single channel analyzers which were set to accept pulses corresponding to photon energies 1780±71 KeV, 6880±275 KeV and above 7500 KeV, respectively. The outputs from single channel anlyzers were recorded in three scalers. The electronic arrangement is shown in fig. 2.

About thousand points were obtained for the excitation curve, covering proton energy range 925-2760 KeV. Data were taken at an energy step of $\Delta E_p = 1$-2 KeV. The integrated charges per point is 20 μc or 40 μc. Measurements were repeated at least twice for each data point in a separate day with maintaining same electronic conditions.

Measurement of de-excitation gamma-ray spectra were made at two proton resonances (E_p= 2720 KeV and 2748 KeV) by using a 50-cc Ge (Li) detector. The energy resolution of the employed detector was 2.1 KeV. The obtained gamma-ray spectra were stored simultaneously in a TMC 4096-channel analyser and a Hewlett Packard 1024-channel analyser. Since the measurement was carried out in a long run (24 hr) for a accumulation of charges up to 24000 μc in order to get sufficient number of counts, we used two multichannel analysers to record data for a consistent check. The calibration of energies of the observed gamma-ray was based on standard source gamma-rays, the 6129±0.4 KeV gamma-ray from the $^{19}F(p,\alpha\gamma)$ ^{16}O reaction originating from ^{19}F impurities and on the 511 KeV energy difference between full-energy, single-escape, and double-escape peaks.

3. RESULT

3.1 Resonance energy and excitation function

The excitation function of the ^{27}Al (p,γ) ^{28}Si reaction measured in the proton-energy range 925-2760 KeV is shown in fig. 3. Fig. 3 (a) shows the yields of the gamma-rays in the 1780±71 KeV region, which corresponding to the transition between the first and ground states of ^{28}Si. The yields of 6880±275 KeV gamma-rays and gamma-rays with energies higher than 7500 KeV are shown in figs. 3(b) and 3(c), respectively. The yield curve of fig. 3(a) show many distinct and well-isolated resonances. There appears a total of seventy-four resonances belonging to the ^{27}Al (p,γ) ^{28}Si reaction. A summary of the determinations of resonance energies and widths from the present investigation is presented in Table I. As can be seen in Table I, our data regarding to the resonance energies obtained in the proton-energy range 925-2106 KeV are overall in good agreement with earlier data reported by Lyons et al(4) and Meyer et al(5). The resonance energies given in Table I are assumed to be corrected within ±1 KeV relative to the 992 KeV resonance, except some resonances which are very weak and their data are meager. At proton energies higher than 2.58 MeV, we observed several new resonances. In the proton-energy range 2583-2760 KeV, there appears several strongly excited resonances. The relative intensity of resonances can be estimated from fig. 3. The cointrbution due to gold background was found to be rather small. In the course of the experiment, background measurements were performed by bombarding gold foil several time over long periods. The results are shown by the dash line in fig. 3(b).

3.2 De-excitation of gamma-rays at 2720 KeV and 2748 KeV resonances

It is seen from the yield curves as shown in fig. 3 that several distinct resonances appear at proton energies above 2.70 MeV. we have measured gamma-ray spectra at two of these resonances, the 2720 KeV and 2748 KeV resonances, which corresponding to the excitation energies of ^{28}Si at 14.210 MeV and 14.237 MeV, respectively. There are no previous data on the decay of these two levels.

The result of one of the above two measurements is shown in fig. 4, which presents a typical gamma-ray spectrum recorded at 2720 KeV resonance. The characteristic of the spectrum is that there exhibits a prominent gamma-ray at 12.432 MeV and most of others are weaker. The observed 12.432 MeV transition indicates that the decay of resonance feeds the first excited level of ^{28}Si at 1.78MeV. Similar feature was observed in the measured gamma-ray spectrum at 2748 KeV resonance. This means that the 14.210 MeV and 14.237 MeV resonance levels decay mainly to the 1.78 MeV level.

Tables II and III show the relative strength of gamma-rays in the decay of resonant states at 14.210 MeV and 14.237 MeV, respectively. Considering the intensity of the $\gamma\rightarrow1.78$ MeV transition as 100 per cent, gamma-ray decay schemes for above two levels populated in ^{28}Si are propcsed and presented in figs. 5(a) and 5(b).

4. DISCUSSION

Most of proton resonances found previously have been observed in the present experiment. The doublets 1364-1335 KeV and 1976-1978 KeV peaks were not resolved. Several weak resonances reported(4) by the CIT group were confirmed here, except the 1435 KeV, 2067 KeV, 2084 KeV and 2144 KeV resonances. New resonance at 1684 KeV found by Meyer et al(5) appears to be weakly excited in our measured spectra. We observed a weak resonance at 2127 KeV, while the 2120 KeV and 2140 KeV resonances as reported in ref. 4 were not observed. The weak resonances at 1922 KeV, 2127 KeV, 2159 KeV and 2541 KeV have not been previously reported. The 2541 KeV resonance was resolved from the 2537 KeV resonance.

The 1381 KeV and 1388 KeV resonances and the 2488 KeV and 2493 KeV resonances are well-resolved here. Fig. 6 show the yield curves of these resonances measured with thin target at a step of proton energy $\Delta E_p=0.50$ KeV. The corresponding half widths of them are 2.0 KeV and 1.7 KeV for the 1381 KeV and 1388 KeV resonances, and 3.7 KeV and 1.6 KeV for the 2488 KeV and 2493 KeV resonances. The resonances found in this measurement at proton energies higher than 2583 KeV are new, the observed gamma-rays for these resonances are quite intense. In this energy region a broad peak was observed, which might consist of several resonances; we identified four resonances at 2583 KeV, 2593 KeV, 2612 KeV and 2641 KeV. It is interesting to see from yield curve in fig. 3 (a) the steep rise at E_p above 2.70 MeV, where there [appears several strong resonances. Since these resonances were also observed in the yields] of gamma-rays with energies higher than 6880 KeV, as shown in figs. 3(b) and 3(c), it is believed that these resonances do belong to the ^{27}Al(p, γ) ^{28}Si reaction.

The gamma-ray transitions for the 2748 KeV and 2720 KeV resonances, as shown in figs. 5 (a) and 5(b), were obtained from the analysis of the measured gamma-ray spectra. The numbers in figs. 5(a) and 5(b) are the percentage of the branching ratio.

These were determined with uncertainty, which includes the experimental errors and the uncertainty of the effeciency of the Ge(Li) detector, of about 12 per cent for strong transitions and about 50 per cent for weak transitions. The effeciency of the 50-cc Ge (Li) detector was taken from ref. 9.

Some individual discussion of the decay data follows:

4.1 The 2720 KeV resonance

The decay from the 14.210 MeV level feeds to four lower energy levels at 12.323 MeV, 12.299 MeV, 6.27 MeV and 1.78 MeV. The $\gamma \rightarrow 1.78$ MeV transition is predominant with a branching ratio of 75 per cent. The branching ratio for the $\gamma \rightarrow 6.27$ MeV transition is 14 per cent. The $\gamma \rightarrow 12.323$ MeV and $\gamma \rightarrow 12.296$ MeV transitions are quite weak, the branching ratio was estimated to be about 3 per cent and 8 per cent, respectively. No ground state transition from the resonance level was observed.

The weak gamma-ray at 7.71 MeV is due to the de-excitation of the 12.323 MeV level to the 4.62 MeV level, the branching ratio for this transition was obtained to be 70 per cent which is in agreement within the experimental error with the pervious data of Endt and Hyeligers(10). The subsequent decay from the 6.27 MeV level goes mainly to the 1.78 MeV level and partly to the 4.62 MeV level. The branching ratio was obtained to be 90 per cent for the 6.27 MeV→1.78 MeV transition and 10 per cent for the 6.27 MeV→4.62 MeV transition. These values agree very well with the earlier measurements by Endt and Heyligers(10), and Jacobs and Engelbertink(11). Also, the sum of measured intensities for these two transitions is consistent with the strength of the $\gamma \rightarrow 6.27$ MeV transition.

The 4.62 MeV level decays to the 1.78 MeV level wih 100 per cent of the intensity of the transitions from the resonance level to the 4.62 MeV level and from the 6.27 MeV level to the 4.62 MeV level. For the transition from the 1.78 MeV level to the ground state, the observed intensity is consistent with the sum of strengths of those transitions feeding to the 1.78 MeV level, where the branching ratio for the 12.299 MeV→1.78 MeV transition given in ref. 7 is taken into consideration.

4.2 The 2748 KeV resonance

At the 2748 KeV resonance seven levels at 12.323 KeV, 12.173 KeV, 11.974 KeV, 11.898 KeV, 6.27 KeV, 4.62 KeV, and 1.78 KeV were fed from the 14.237 MeV resonance level. The branching ratios for the decay of these low lying levels are given in fig. 5(b). No ground state transition directly from the resonance level was observed.

In the subsequent decay from the 12.323 MeV level 81 per cent of the total decay was found to feed the 4.62 MeV level. The obtained branching ratio for the 12.323 MeV→4.62 MeV transition is in agreement with the value reported by Endt and Heyligers(10). Teh 12.173 MeV level decays to the 6.27 MeV with 100 per cent of the intensity of the $\gamma \rightarrow 12.173$ MeV transition Although the observed gamma-rays at 5.90 MeV is rather weak, the 12.173 Mev→6.27 MeV transition presented in ref. 7 is confirmed in the present work.

About same branching ratio (~70%) was found for the transitions from the 11.974 MeV and 11.894 MeV to the 4.62 MeV levels. The obtained values agree fairly well with the previous data of Okano(12). The 6.27 MeV→4.62 MeV transition is rather weak as compared to the 6.27 MeV→1.78 MeV transition. The intensity of the transitions feeding to the 6.27 MeV level is seen to be somewhat smaller than that of transition outgoing from the 6.27 MeV level. It is apparent that some weak transitions from highly populated levels to the 6.27 MeV level are likely missed. We were not able to observe the corresponding gamma-ray lines in the measured spctra. For the 4.62 MeV→1.78 MeV and 1.78→g.s. transitions the obtained strength of gamma-ray are consistent with the decay scheme.

It is seen that the decay scheme for two resonances at $E_p = 2720$ and 2743 KeV are somewhat similar. The 14.210 and 14.237 MeV resonant levels in ^{28}Si seem to have same spin value. As discussed above, the $\gamma \rightarrow 1.78$ MeV transition was observed about three to five times stronger than the $\gamma \rightarrow 12.323$ MeV and $\gamma \rightarrow 6.27$ MeV transitions. The 1.78 MeV, 6.27 MeV and 12.323 MeV levels are known(7) to be $J^\pi = 2^+, 3^+$ and 4, respectively. From arguments on transition probabilities and taking the fact that the ground state of ^{28}Si is 0^+ into consideration, it is favorable to suggest two resonance levels to be $J^\pi = 3^+$. This assignment gives a consistency in relative transition probabilities between present data and calculations of Weisskopf(13). However, for the 14.237 MeV resonance, as the strengths of the $\gamma \rightarrow 12.323$ MeV and $\gamma \rightarrow 6.27$ MeV transitions are comparable, it may indicate that the 14.238 MeV level would be 3^+ with possible higher spin admixture. In order to give a definite spin assignment, it would reuqire a more extensive study of the ^{27}Al (p,γ) ^{28}Si reaction with angular correlation measurements.

ACKNOWLEDGMENTS

We are indebted to Prof. W.N. Wang for his support of the present work. We are also grateful to the members of the Van de Graaff accelerator laboratory at Tsing Hua University for their technical assistance.

REFERENCES

1. Isospin in Nuclear Physics, ed. by D.H. Wilkinson (North-Holland Publishing Co., Amsterdam, 1969)
2. Y.P. Antoufiev, L.M. En-Nadi, D.A.E. Darwish, O.E. Badawy, and P.V. Sorokin. Nucl. Phys. 46,1(1963)
3. E.F. Gibson, K. Battleson, and D.K. McDaniels, Phys. Rev. 172, 1004(1968)
4. P.B. Lyons, J.W. Toevs, and D.G. Sargood, Nucl. Phys. A130, 1(1969)
5. M.A. Meyer, N.S. Wolmarans, and D. Eeitmann, Nucl. Phys. A144, 261(1970)
6. S.T. Lam, A.E. Litherland, and R.E. Azuma, Can J. Phys. 49,685 (1971)
7. P.M. Endt and C. Van Der Leun, Nucl. Phys. A105, 1(1967)

8. T.H. Hsu et al, to be published
9. F.C. Young, A.S. Figuera and G. Pfenfer (University of Maryland), unpublished (1970)
10. P.M. Endt and A. Heyligers, Physica 26,230 (1960)
11. Jacobs and Engelbertink (Utrecht), unpublished (1965)
12. Kotoyuki Okano, J. Phys. Soc. Japan 15,28 (1960)
13. V.F. Weisskopf, in Nuclear Spectroscopy Part B. p860, ed. by Fay Ajzenberg-Selove (Academic Press, New York, 1960)

Table I

Summary of ^{27}Al (p,γ) ^{28}Si yield data

Ep (KeV)			Eexc (MeV)	Half Width (KeV)
Present Work	ref.(4)	ref.(5)		
935	937		12.489	2.9
992*	992		12.543	1.3
1002	1002		12.554	12
1025*	1025	1025	12.576	1.3
1089	1090	1090	12.638	4
1096	1098	1098	12.645	6
1118*	1118	1118	12.666	1.48
1171	1172	1172	12.716	3.4
1183	1183	1183	12.728	5.8
1200	1200	1199	12.745	5.6
1213	1213	1213	12.757	2.9
1262*	1262	1262	12.805	3.2
1277	1276	1278	12.819	3.2
1317*	1317	1317	12.858	1
1329	1328	1328	12.869	3.8
	1364	1364		
1364	1365	1365	12.903	1.2
1381*	1381	1381	12.919	2.0
1388*	1388	1388	12.926	1.7
	1435			
1455	1451	1457	12.991	4.2
1502	1499	1502	13.036	5.9
1518	1514	1520	13.051	4.5
1563	1568	1566	13.095	2.7
1577	1579	1578	13.108	5.2
1588*	1589	1588	13.119	3.6
1647	1647	1647	13.176	4.1

1663		1662	13.191	4.0
	1669	1663		
	1680	1680		
1682		1684	13.209	4.0
1706	1709	1706	13.232	4.3
1724*	1726	1724	13.250	4.3
1747	1746	1749	13.272	11
1800*	1797	1800	13.323	3.4
1843	1838	1842	13.365	3.6
1902	1909	1899	13.421	2.5
1911	1917	1910	13.430	4
1922			13.441	3.2
1970	1976	1969	13.487	4.2
	1978			
2035	2041		13.550	5.9
2047	2054		13.561	2.4
	2067			
2100	2084		13.612	2.9
2106	2106		13.618	3.0
	2114			
2127	2120		13.638	3.4
	2140			
2154	2144		13.664	2.5
2159			13.669	2.5
2162	2168		13.672	4.9
2172	2171		13.682	3.7
2183	2190		13.692	3.7
2205	2212		13.713	4.2
2222	2221		13.730	3.5
2238	2249		13.746	3.2
2289	2296		13.794	3.8
2306	2312		13.811	3.3
2315	2320		13.820	2.5
2334	2334		13.838	6.3
2360	2365		13.863	2.6
2374	2375		13.877	7.7
2404	2407		13.905	3.3
2415			13.916	2.1
2449	2447		13.949	7.8
2488	2481		13.987	3.7

2493	2489	13.991	1.6
2522	2522	14.019	2.4
2537	2537	14.034	4.0
2541		14.037	2.6
2554	2560	14.050	3.2
2583	2584	14.078	2.7
2593		14.088	4.0
2612		14.106	1.6
2641		14.134	5.4
2683		14.174	3.8
2720		14.210	2.2
2729		14.218	2.1
2733		14.222	2.1
2748		14.237	3.6

* Resonannces were used for the energy calibration in the present work.

Table II

Relative strength of gamma-rays in the
decay of the 14.210 Me V resonance

Ex(MeV)	14.210	12.323	12.299	6.27	4.62	1.78
12.323	10±4					
12.299	35±4					
6.27	61±6					
4.61		7±5		5±4		
1.78	315±31		(16)	45±6	13±2	
g.s.						397±40

The errors include the statistical measurement and the uncertainty of the efficiency for Ge-detector.

The number in parenthesis is taken from the previous data of Endt and Heyligers[10].

Table III

Relative strength of gamma-rays in the
decay of the 14.237 MeV resonance

Ex (MeV)	14.237	12.323	12.173	11.974	11.898	6.27	4.62	1.78
12.323	32±5							
12.173	10±2							
11.974	15±2							
11.898	10±2							
6.27	29±5		10±3					
4.61	13±2	26±4		11±2	7±3	5±3		
1.78	97±10					42±6	70±11	
g.s.								210±21

The errors include the statistical measurement and the uncertainty of the efficiency for Ge-detector.

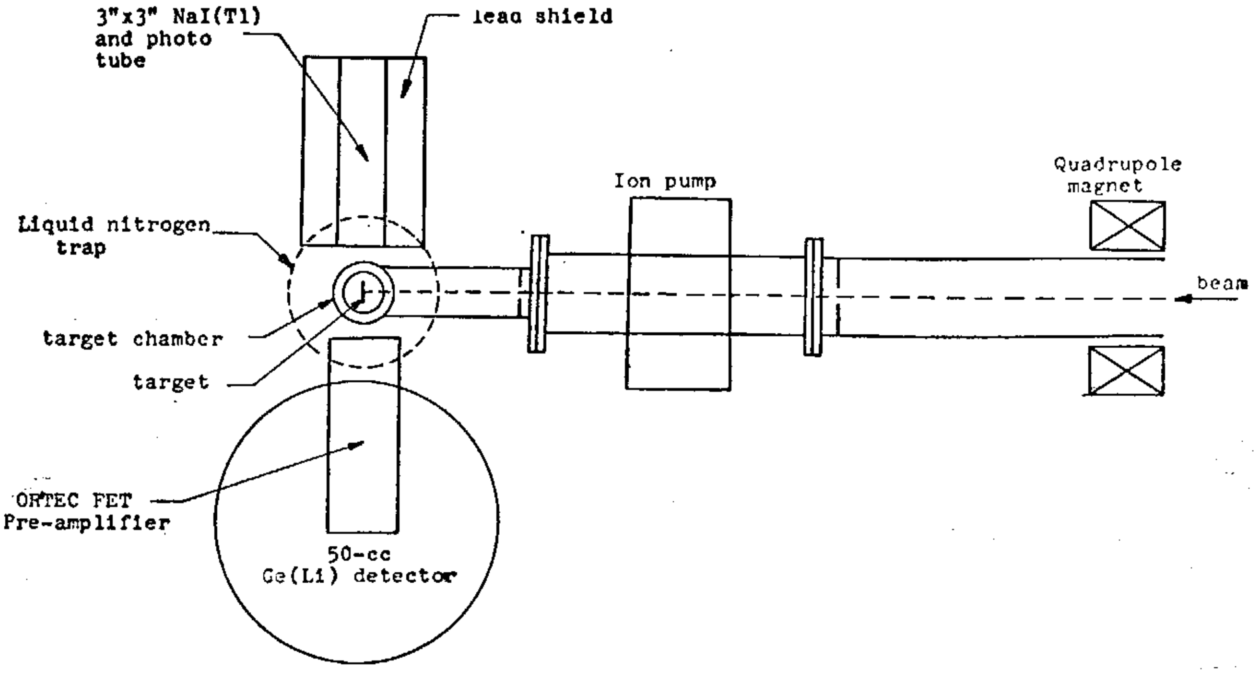
3"x3" NaI(Tl) and photo tube
lead shield
Quadrupole magnet
Ion pump
Liquid nitrogen trap
beam
target chamber
target
ORTEC FET Pre-amplifier
50-cc Ge(Li) detector

Fig. 1

Schematic view of experiment apparatus.

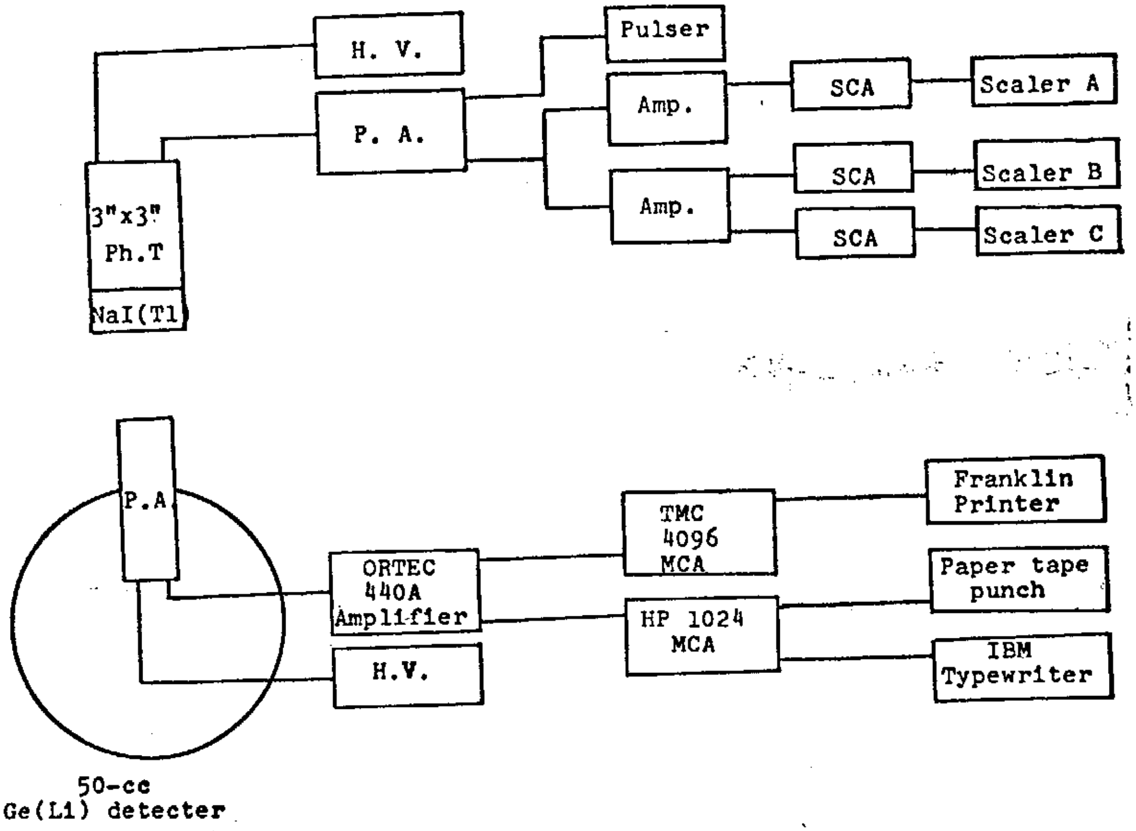
H. V.
Pulser
P. A.
Amp.
SCA
Scaler A
SCA
Scaler B
Amp.
SCA
Scaler C
3"x3" Ph.T
NaI(Tl)
P.A
Franklin Printer
TMC 4096 MCA
Paper tape punch
ORTEC 440A Amplifier
HP 1024 MCA
IBM Typewriter
H.V.
50-cc Ge(Li) detecter

Fig. 2

Block diagram of electronic circuit used in gamma-ray spectra and yield measurements

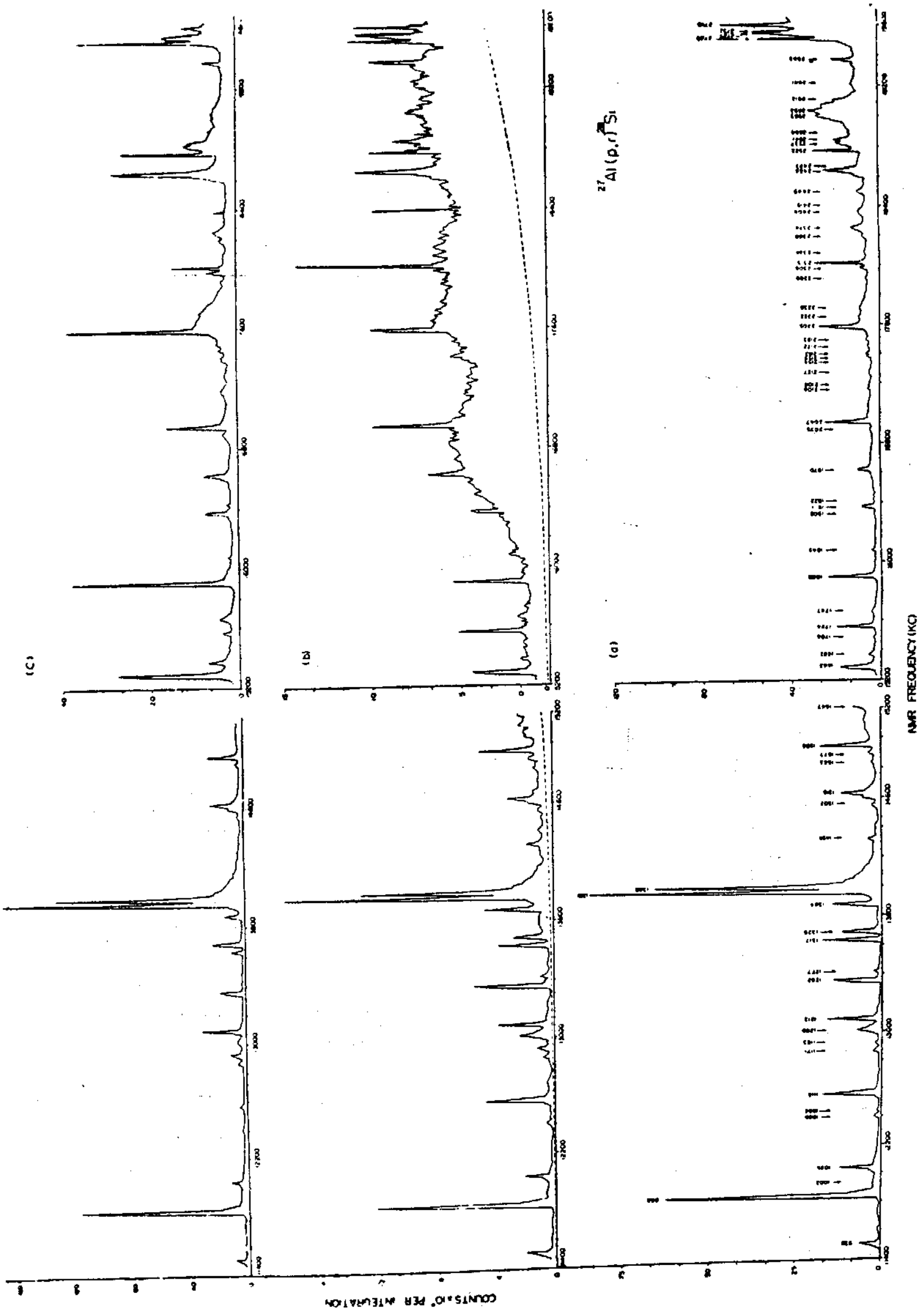

Fig. 3 .Yield curves from the ^{27}Al (p,γ) ^{28}Si reaction (a) Yield of 1780±71 KeV gamma-rays (b) Yield of 6880±275 KeV gamma-rays (c) Yield of gamma-rays with energies higher than 7500 KeV.

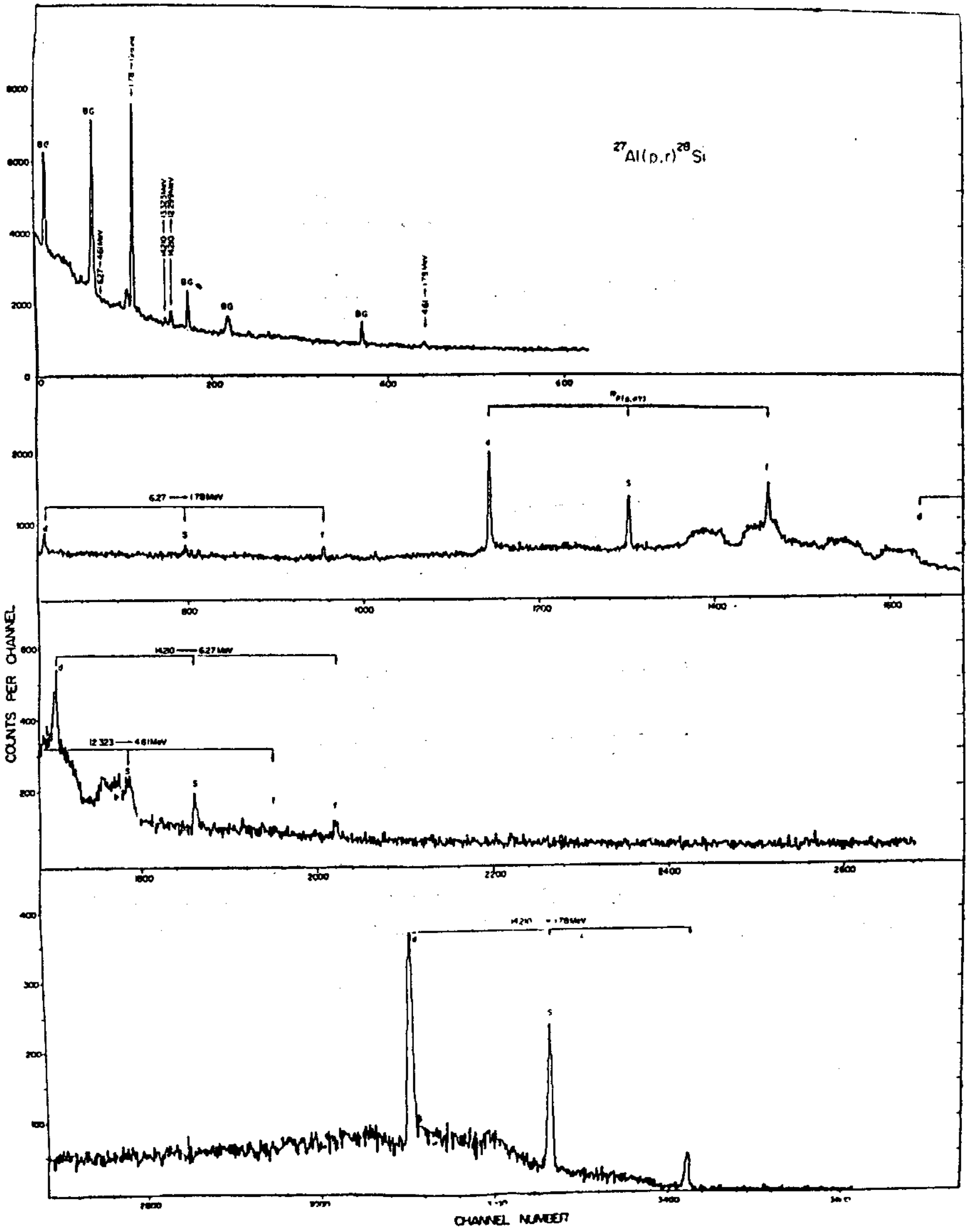

Fig. 4 A gamma-ray spectrum of the ^{27}Al (p,γ) ^{28}Si reaction at E_p=2720 KeV, B.G., background.

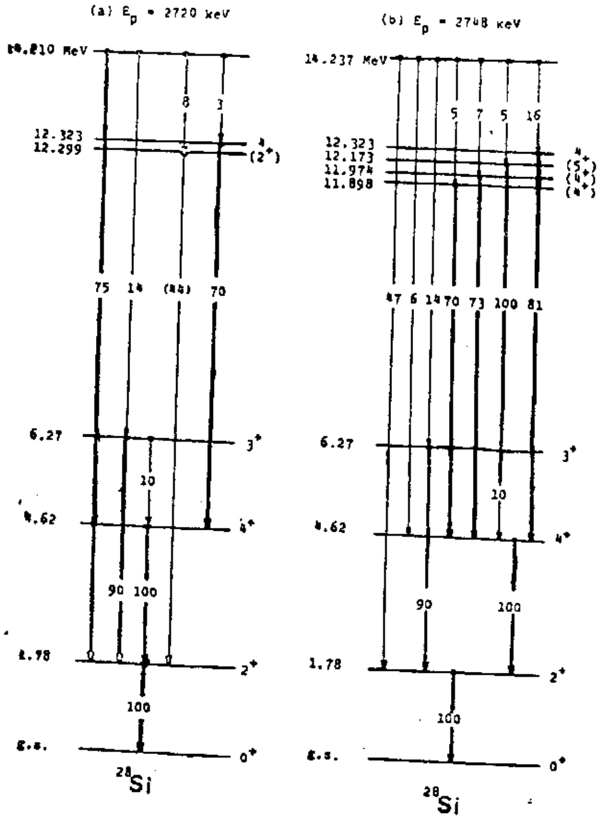
(a) E_p = 2720 keV
14.210 MeV
12.323
12.299
8
3
4
(2+)
75
14
(44)
70
6.27
3+
10
4.62
4+
90
100
1.78
2+
100
g.s.
0+
28Si
(b) E_p = 2748 keV
14.237 MeV
5
7
5
16
12.323
12.173
11.974
11.898
4
(5+)
(4+)
(4+)
47
6
14
70
73
100
81
6.27
3+
10
4.62
4+
90
100
1.78
2+
100
g.s.
0+
28Si

Fig. 5

Gamma-ray decay scheme for the levels populated in ^{28}Si at (a) the 2720 KeV resonance and (b) the 2748 KeV resonance. The number in parenthesis is taken from ref. 10.

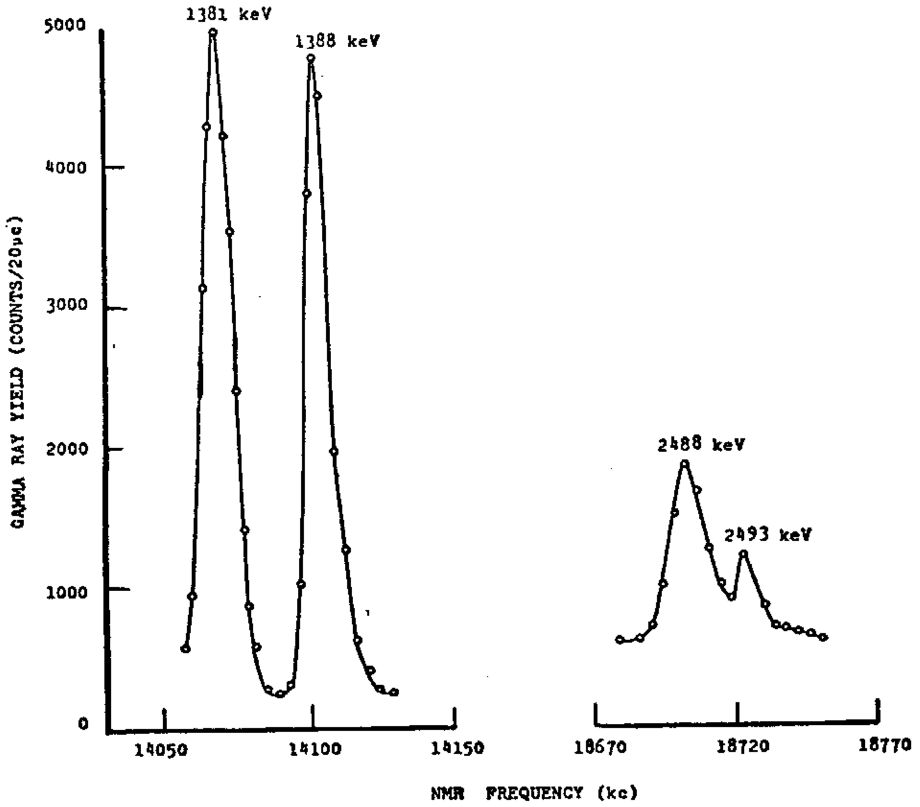

Fig. 6

Yield curves for the 1381 KeV and 1388 KeV resonances, and for the 2488 KeV and 2493 KeV resonances.

Annual Report of the Institute of Physics, Academia Sinica, 1971

A Sensitive Discharge Switch Function as a Pulse Generator or a Self-tone Modulator

Chen Bin and S. C. Yeh

Institute of Physics, National Tsing Hua University
Hsinchu, Taiwan, Republic of China

W. N. Wang (王唯農)

Institute of Physics, Academia Sinica and Tsing Hua University

Abstract

A single conventional transistor wired as a discharge switch for generating pulses or discharging the staircase waveform is described. The repetition rate of the pulse generator has been achieved from one pulse per hour to 200 kHz. And the integrating input frequencies for the staircase waveform has been tested up to 50 MHz.

Introduction

A single transistor pulse generator circuit is designed. It generates pulses with the pulse duration in seconds to minutes while the blocking duration as long as hours. The pulse rate and the duty ratio are both adjustable.

In some aspect, this one silicon transistor circuit takes place the role of the unijunction transistors. For example the voltage-variable repetition rate circuit is one of the typical usages of the ujt, and the function of this reporting circuit is very similar to that.

Circuit Description

Figure 1 shows the circuit diagram of the pulse generator, Q_1 is a silicon transistor. The base firing voltage of the transistor is approximately 0.5 volt in a workable range of temperature conditions..Around this characteristic the circuit is wired

As switch "s" is closed, capacitor C_1 is charged through R_1 and the base voltage of Q_1 begins to rise. When the base voltage reaches the firing point of the transistor, it fires. The collector current rises suddenly and the high frequency oscillation of the circuit is initiated. At the moment the transistor fires, C_1 discharges rapidly through it's low resistance path, L_1, base-emitter region and L_2 to ground. The oscillation is maintained in a short period of time until the capacitor voltage or the holding current becomes too low to sustain further oscillations. C_1 passes the oscillating frequencies to ground during circuit oscillation. The action of the collector drawing current through R_L combined with the capacitor C_L decoupling high frequencies leaves a pulse voltage appearing on the collector terminal. After the transistor cuts off C_1 begines to be charged again, and the circuit functions repeatedly.

The Oscillation

Figure 2 shows the equivalent circuit of the pulse generator. The value of $-A_I Z_2$ is estimated to be

$$-A_I Z_2 = \frac{h_{FE}}{(1+j\omega c\ r_b'{}_e)} \circ \frac{\frac{L_2}{C_2}}{R+j\left(\omega L_2-\frac{1}{\omega c_2}\right)} \qquad \text{when R is small}$$

Consider the case $(\omega L_2-\frac{1}{\omega c_2})^2 >>$ the other terms in the denominator and R is small. The real part of $-A_I Z_2$ can be written

$$R_e(-A_I Z_2) \approx \frac{h_{FE}\left(\frac{L_2}{c_2}\right)(c r_b'{}_e) - \omega^2 L_2 + \frac{1}{c_2}}{\left(\omega L_2-\frac{1}{\omega c_2}\right)^2}$$

as $\omega^2 L_2$ larger than $1/C_2$, there exists a negative resistance component in the input circuit. When the total resultant resistance in the input branch is negative, the oscillation of the circuit occurs.

The term $1/C_2$ shows the larger the value of C_2 the more negative in the resultant resistance. But C_2 is limited to a certain value by the fact that it would flat out the initial abrubt change of current; the oscillation could not be initiated if the C_2 is too large. Actually Z_2 is a high Q honeycomb type inductor, a deep oscillation of the circuit is very easy to obtain as $L_2 > L_1$.

The Staircase Waveform Discharge Switch and the Self-tone Modulator

Figure 3 shows the staircase discharge switch circuit, which needs no power supply. The pulses and the sinewave signals have been adapted as the input signal of the pumping circuit. The randum pulses are also acceptable, for there is no way for capacitor C_1 to leak before Q_1 conducting.

This circuit is born with the nature of a self-tone modulator. To working as a tone modulator we need only to adjust the value of R_1 C_1 to its suitable pulse rate and then couple the modulated signal out for transimiting. To vary the transimiting frequency vary the inductor L_1, still $L_2 > L_1$ should be obeyed.

Discussion

The blocking duration of the circuit is largely determined by the time constant R_1 C_1 while the conducting duration is determined by the value of $R_e C_1$. R_e is the effective resistance presented in the path of C_1 discharge. Thus the width of the output pulse is adjustable. Besides R_L can be minimized for getting very narrow current pulses.

For determining the length of the blocking time the linear portion of C_1 charging curve is utilized. For the one hour generating one pulse example, the blocking duration equals approximately R_1 $C_1/3$. For the long time blocking it is suggested that the charging current should be larger than a certain value, this is the initial abrubt firing condition of this circuit. The I_{CBO} of a transistor in some cases should be considered. The higher is the conducting current the fewer is the residual charge left on capacitor C_1 after each discharge. This condition allows the blocking duration longer and conducting duration shorter. To increase the conducting current, the h_{FE} value of a transistor is the larger the better. The load R_L and DC collector supply are also to be considered. Photo shows the output pulse of the circuit.

Notable Features

This circuitry has the features of long time blocking duration, short conducting duration, both can be made variable. The time interval is acurate. A continuous variable pulse rate over a few bands of R_1 C_1 can be arranged. C_1 can be large in value and small in volume for its working voltage is very low. The maximum input triggering sensitivity reaches 1.5 micrcamperes at 0.7 volt under the condition of nano amperes order of I_{CBO}.

This circuit is a power concentration device, it saves power. The collector current can be drawing from 22 μA to approximately 200 *MA* in *DC*. depend on transistor selected. If the R_L is replaced to a *DC* relay, this circuit can be used for heavy load power supply switching in programed intervals.

Test Results

The following table lists the data of several test.

Transistors used	2N834 2N3642 (I)	2N3053 HEP-75 (II)	2N3055 Audio power transistor (III)	2N3642 (IV)
R_1	1 MegΩ	5 KΩ variable	2 MegΩ variable	2 MegΩ
C_1	2000 PF	800 PF	3300 MFD	5000 MFD WV6VDC
L_1	1 μh	1 μh	455 KH, I. F. T. coil	7 μh
L_2	.25 mh	.25 mh	200 mh ferite core used	.25 mh
R_2	10 KΩ	4.7 KΩ		1 KΩ
C_2	2000 PF	100 PF	10 MFD	.05 MFD
f_0	23 MHz	23 MHz	455 kHz	11 MHz
Pulse rate	2.5 kHz	20 — 200 kHz	1 in 24 minutes	1 in an hour
Blocking time			4-24 minutes	an hour
Pulse duration	10 μsec	1 μsec	20 sec	1.7 minutes
Rise time Fall time	1 μs 3 μs	0.1 μsec	10 Msec 20 Msec	Msec order

Pulse height	1.2 V pp	20 V pp	10V pp	1.5 V pp
DC supply	7.5 V	24 V	24 V	3 V
Collector current	25 μA DC	10 MA pp measured by Tektronix 7704 Scope	20 MA DC	0.5 MA DC

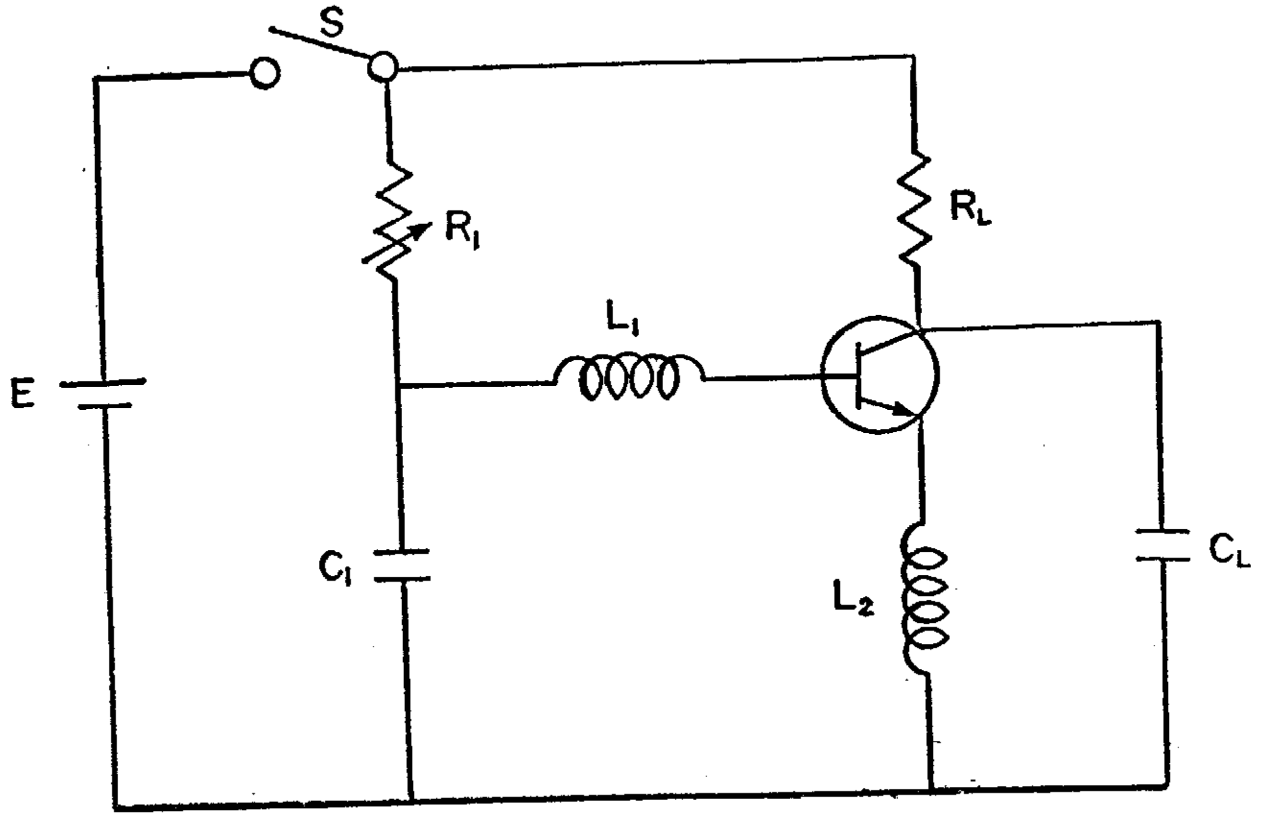
S
R₁
R_L
L₁
E
C₁
L₂
C_L

Fig. 1

The diagram of the pulse generator.

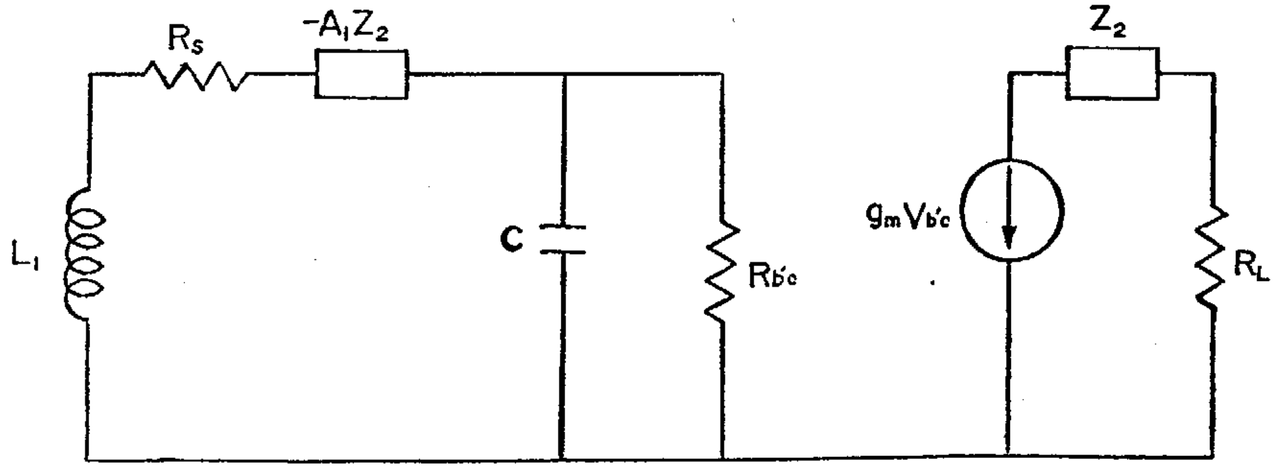
R_S
-A₁Z₂
Z₂
L₁
C
R_b'c
g_m V_b'c
R_L

Fig. 2

The equivalent circuit of the pulse generator.

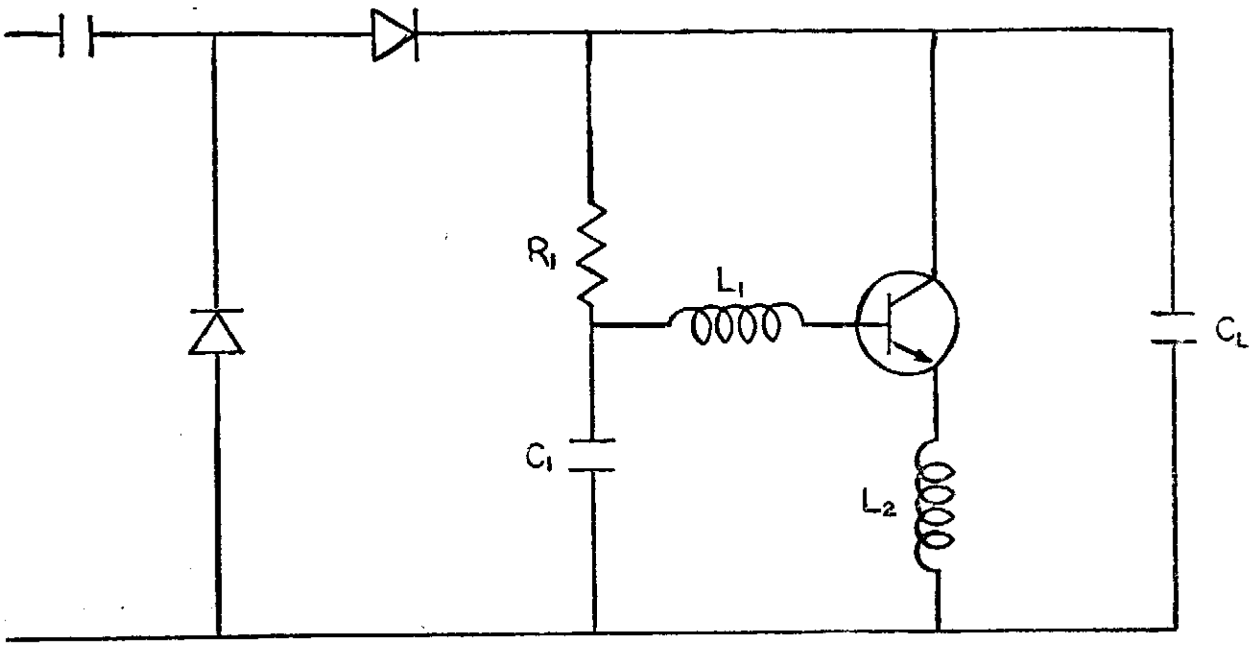

Fig. 3

The diagram of the staircase waveform discharge switch.

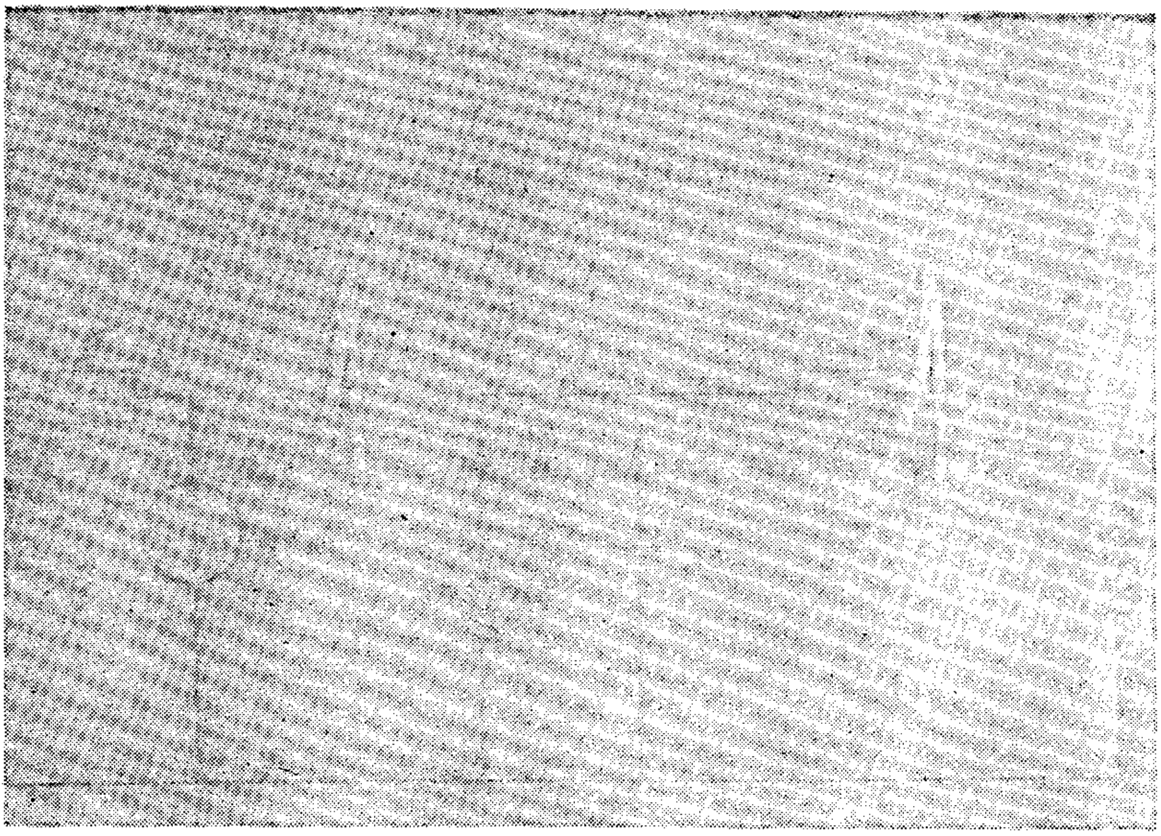

Fig. 4

The output pulse of the pulse generator

5V/cm 20μs/cm.

Annual Report of the Institute of Physics, Academia Sinica, 1971

Damped Radio Frequency Size Effect of Indium Antimonide at Room Temperature*

Yu-Tung Yang（楊毓東）， Hong-Tzer Ho, Cheng-Chih Pei, Shung-Chen Yang
and
Biao-shian Yu

Physics Department, National Tsing-Hua University
Hsin-Chu, Taiwan, Republic of China
and
Institute of Physics, Academia Sinica,
Republic of China

Abstract

Skin-depth and related parameters of In Sb have been measured by using the damped radio wave technique at room temperature. The results show that there is difference between the data obtained with a marginal oscillator-detector system and with a fixed frequency signal detector system. We found the latter is more reliable. The former can only give qualitative results.

1. Introduction

According to the electrodynamic and the electron plasma theory Fischer and Kao(1) have shown a method to study the radio frequency size effect of a conducting substance. They have used that method and a positive feed-back marginal oscillator to study the size effect of Bismuth(1). One of the purpose of the theory is for the determination of the mobility μ and the carrier concentration n of the conducting substance. The important formulae are

$$\mu = \frac{c\Delta}{\varnothing_0 H_0}, \tag{1}$$

$$n = \frac{\varnothing_0 c H_0 \Delta}{2\pi e\omega d^2}, \tag{2}$$

$$\varnothing_0 = \frac{d}{\delta(H = H^0)} = \frac{d(2\pi \omega n e c \beta)^{\frac{1}{2}}}{c(1+\beta^2 H_0{}^2)^{\frac{1}{2}}}, \tag{3}$$

$$\Delta = \frac{d}{\delta(H=0)}, \tag{4}$$

$$\beta = \frac{\mu}{c} = \frac{e\tau}{m^* c}. \tag{5}$$

where ω is a fixed frequency of the instrument, H_0 is the H-field at maximum power absorption. All the other symbols are the same as shown in the previous report(1).

For μ and n determination it is known that the shape of the experimental curves is very important. The usefulness of the method is based upon a proper curve-fitting technique. One compares the true experimental curve with the theoretical ones and finds the best fit. Once that is done, a proper Δ value is thus fixed. μ and n are calculated accordingly.

---

* Project supported by the National Science Council, Republic of China, 1971-1972.

A general positive feed-back *LC* oscillator-detector system such as a Colpitts circuit, a Franklin circuit, or a Knight circuit (2-5) can not in general provide us with a highly stable radio frequency for the test when the circuit Q is changed during the power absorption. The frequency instability becomes more serious during the slowpassage through resonance. The change of frequency will in turn cause the power absorption curve to deform, and thus the true phenomenon is blurred. Phase of the feed-back is changed when Q changes and therefore the problem becomes even more complicated.

2. Experiment and results

In order to circumvent the difficulty we decided to use the high resolution NMR instrument for the size-effect measurement. The difference between the marginal oscillator result and the fixed frequency result is shown in Fig. 2.

Our instrument consists essentially of a crystal controlled high frequency oscillator as the transmitter and a receiver which receives the power absorption signal and sends out a detected signal for record. In principle, the instrument we have is the same as that designed by Varian Associates for high resolution NMR purpose.

The experimental set-up is shown in Fig. 1. The frequency is constantly monitored at the receiver end by a Hewlett-Packard high frequency counter (model 5245L). The frequency stability of our instrument is generally within ±1 cycle at 10^7 Hz. No change of the frequency what so ever is observed during the experiment.

An InSb sample in the form of a slab is put in the receiver coil for test. The area of the slab is about 8mm×10mm. The thickness of the slab is varied by fine grinding. The samples are single crystals in 111 direction. It is 35S grade, n-type(6-8). The known mean free time τ at room temperature is about 10^{-11}sec. which makes $\omega\tau<<1$ in our case and the theory is valid.

The output signal is so strong that no lock-in amplifier is needed for amplification. The signal output is fed directly into an XY recorder.

According to the theory we also have, beside the already mentioned formulae, the thickness d and the field H_0 linear relation namely,

$$d = const.\ H_0, \qquad (6)$$

and also in case of the sample rotation,

$$\csc\theta = const.\ H_0, \qquad (7)$$

where θ is the angle between the slab face and the direction of the applied field H. Experimentally we found they could be satisfied (Fig.8 and Fig.9).

The power absorption is a function of $\varnothing$, and

$$p(\varnothing) = \frac{2\omega d}{c}\ \frac{1-2\sin\varnothing\ e^{-\varnothing}-e^{-2\varnothing}}{\varnothing(1+2\cos\varnothing\ e^{-\varnothing}+e^{-2\varnothing})} = \frac{2\omega d}{c} f(\varnothing). \qquad (8)$$

In the above formula, the function $f(\varnothing)$ depends on Δ because $\varnothing$ depends on Δ. One may select a Δ value then one can determine the form of the power absorption curve theoretically according to the eq.(8). $\varnothing_0$ at H_0 is found a constant and

$$\varnothing^0 = 2.2541 \pm 0.0001 \tag{9}$$

by computer calculation to 8 digits of the function $f(\varnothing)$.

One may fix the values of Δ in integral steps (say from 2 to 30) then draw the power absorption curve according to eq.(8) by computer calculations. The theoretical curve is compared with the experimental one and a proper fit is made. A proper Δ is thus selected and the μ and n values are determined according to the equations (1) to (5).

Alternatively, according to the equations (1) to (5) we may also have

$$\mu = \frac{c\Delta}{\varnothing_0 H_0}\left[1-\left(\frac{\varnothing_0}{\Delta}\right)^2\right]^{\frac{1}{2}} \tag{10}$$

$$n = \frac{c\Delta \varnothing_0 H_0}{2\pi e a^2 \omega}\left[1-\left(\frac{\varnothing_0}{\Delta}\right)^2\right]^{-\frac{1}{2}} \tag{11}$$

The values of μ and n of the samples are shown in Table I.

In the case of $\Delta = 4$, the result (Fig. 6) is not as good as the others and probably a better Δ value selection around 4 which is no more an integer may give better result.

The curve fitting results are shown in Fig.(3), Fig.(6), and Fig.(7). The theoretical relations as shown in eq.(6) and eq.(7) are compared with the experimental values and they show clearly the size effect nature of the InSb sample at room temperature. (Fig.(8) and Fig.(9)).

The values of μ and n found by applying the galvanomagnetic methods are 6.6×10^4 and 1.8×10^{16} respectively. They are smaller (300%) then the values shown in Table I. The experimental errors in both cases are within ±10%.

We are grateful to Prof. Y. H, Kao for his valuable advice.

References

(1) H. Fischer and Yi-Han Kao, Solid State Comm., **67**, 275-277, 1969, also Bull. Am. Phys. Soc. **12**,533,1967

(2) J. D. Idoine, Jr. and J. R. Brandenberger, Rev. Sci. Instru., **42**, 715-717, 1971.

(3) N. Sullivan, Rev. Sci. Instru., **42**,462,1971

(4) Y. T. Yang and Y. C. Chen, Rev. Sci. Instru., **37**, 1274, 1966

(5) W. D. Knight, Rev. Sci. Instru., **32**, 95, 1961

(6) T. C. Harman, R. K. Willardson and A. C. Beer, Phy. Rev. **98**,1532,1955

(7) G. L. Pearson and M. Tanenbaum, Phy. Rev., **90**,153,1953

(8) R. N. Dexter and B. Lax, Phy. Rev., **99**,635,1955

Table I

Mobility and carrier concentration in n-type InSb at room temperature according to size effect measurement by damped radio wave technique at a fixed frequency

Frequency (MHz)	d (mm)	△	H_0 (Gauss)	Mobility x 10^5 (cm^2/v-sec)	Carrier concentration (x $10^{16}/cm^3$)
21.798330	2.45	8	1590	2.143	5.67
21.798330	1.84	6	1171	2.106	5.76
21.798330	1.23	4 or about 4	755	1.940	6.22
			average	2.063	5.88

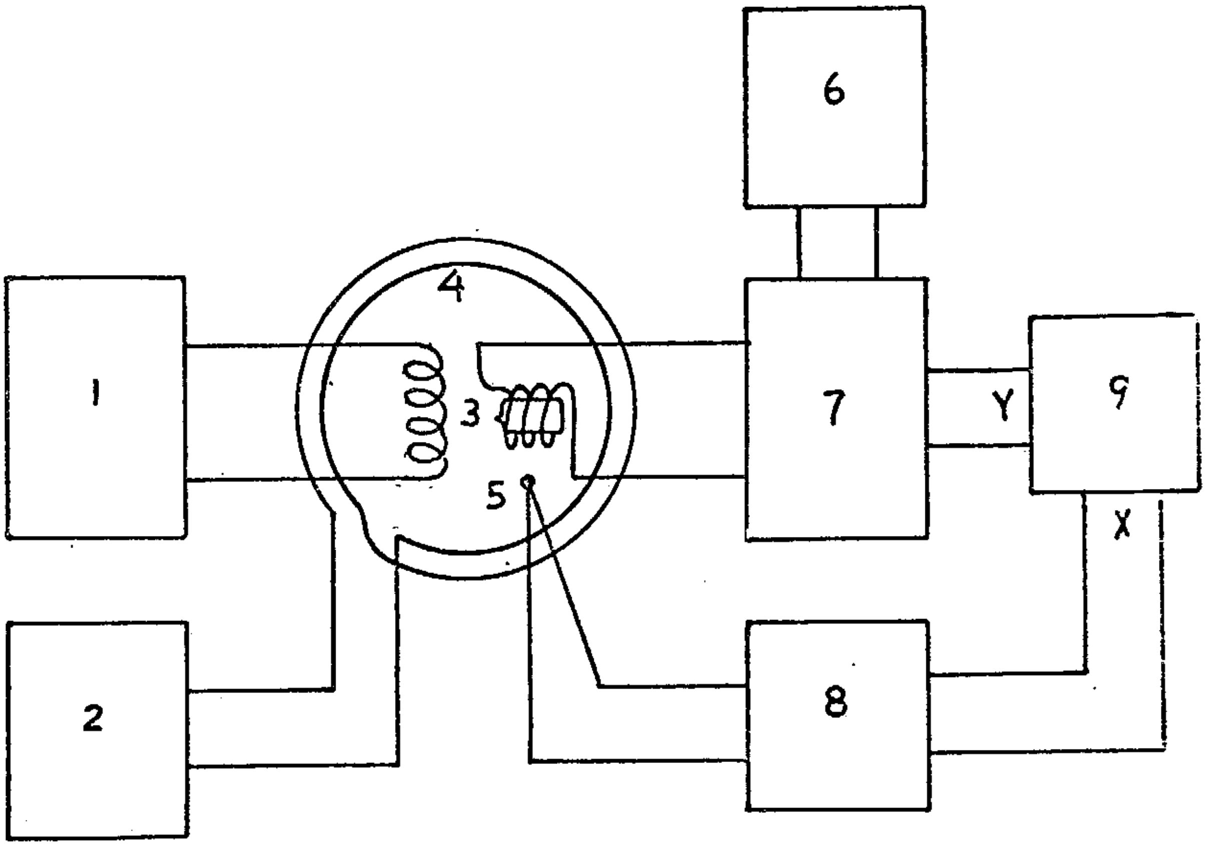

Fig. 1

Instrument set-up. 1. crystal controlled oscillator and transmitter. 2. Electromagnet power supply. 10^{-6} stability, field homogeneity is of milligauss order from high resolution NMR test. No a. c. field modulation is needed for the present experiment. 3. Transmitter-receiver cross-coil arrangement. The InSb slab is put inside the receiver coil. 4. Pole face of the magnet. 5. Gaussmeter probe. 3. Gaussmeter proper. 6. Frequency counter HP 5245L connected with the frequency check point of the receiver. 7. Receiver-detector unit. 9. X-Y recorder with millivolt range sensitivity. The frequency counter is also used as a monitor to show us the frequency stability during the experiment. The frequency meter receives no signal if the receiver-detector unit 7 is turned off alone. It means the receiver-detector unit is active if power is supplied.

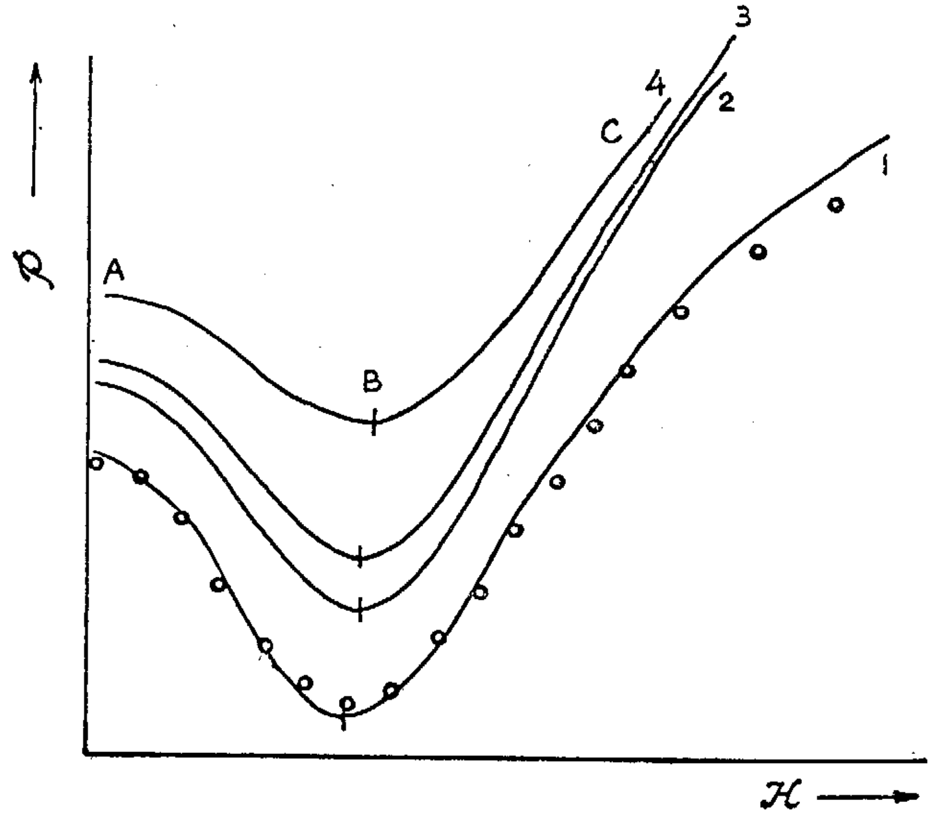

Fig. 2

Curve 1 is obtained by using the fixed-frequency technique. It is compared with a $\Delta=4$ theoretical curve (shown in circles as a result from computer calculation). The frequency is $f=21.7983$ MH$_z$. and is constant. (8 digits). Curves 2,3, and 4 are obtained by using a marginal-oscillator-detector system; Curve 2 shows $H=$a certain H_0 at $f=21.573$ MHz, and curve 4 shows a different H value at the same frequency $f=21.573$ MHz but with a small change of feed-back. Curve 3 shows the same $H=H_0$. as curve 2 except the frequency is now 21.705 MHz. All curves were obtained with the same sample of thickness d. In the case of 2,3, and 4 the frequency drops more than 10% as the curve grows from A to B to C and the shape is deformed due to phase changes in the system. The above facts show the difficulties with a marginal oscillator of positive feedback type as an instrument for the size-effect study.

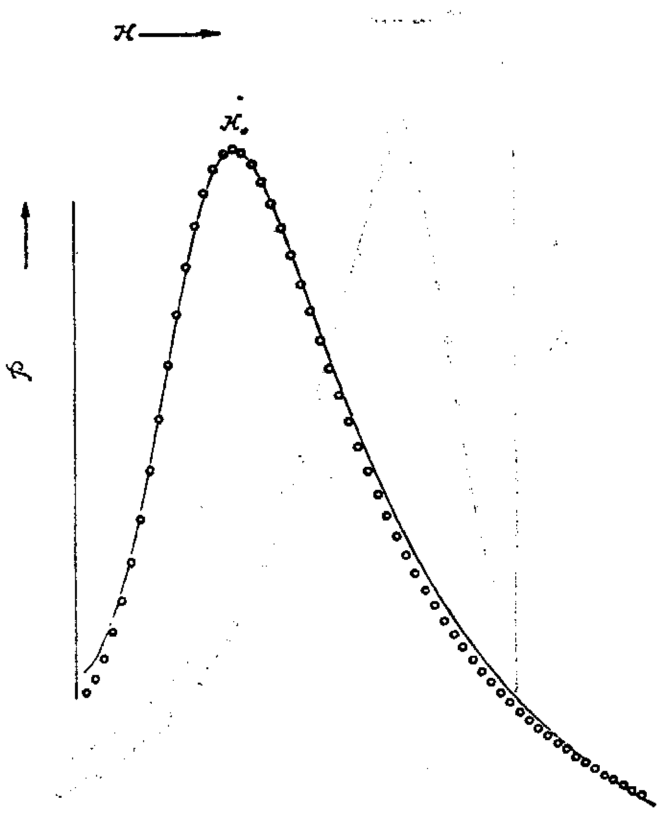

Fig. 3

Power absorption vs. H-field. o is theoretical by computer calculation. —— is the experimental result. P scale is arbitrary. H_0=1590 G, d=2.45 mm, Δ=8 is a proper fit. f=21.798330 MHz.

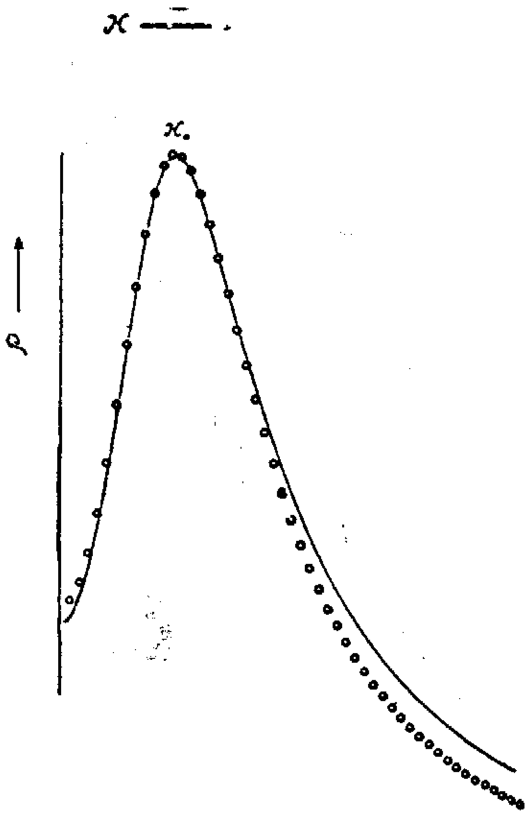

Fig. 4

Power absorption vs. H-field. o is theoretical by computer calculation. —— is the experimental result. *P* scale is arbitrary. $f=21.798330$ MHz, $H_0=1590$ G. $d=2.45$mm. $\Delta=6$ is not a proper choice, the theoretical curve falls too low at high H-field.

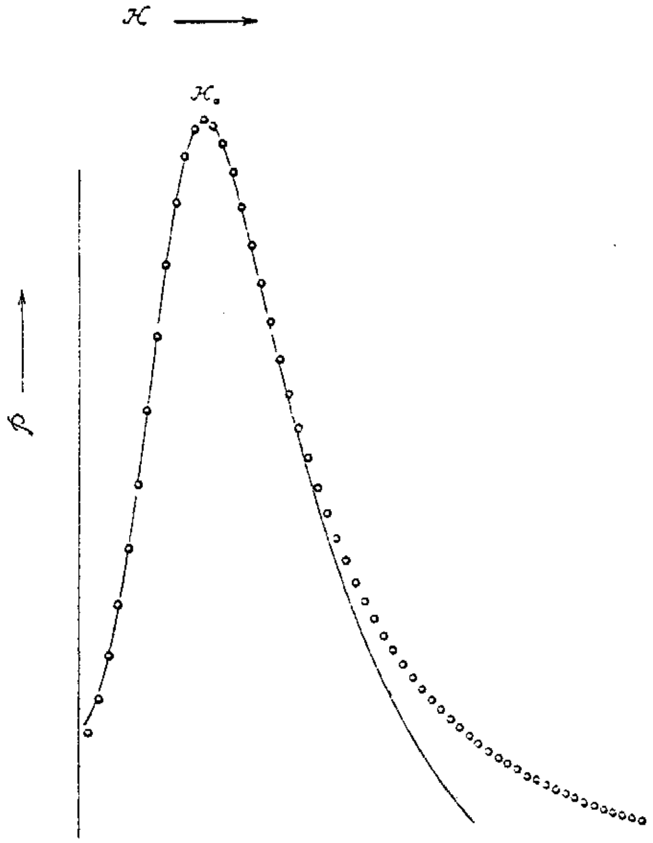

Fig. 5

Power absorption vs. H-field. o is theoretical by computer calculation. —— is the experimental result. P scale is arbitrary. f=21.798330 MHz, H_0=1590 G, d=2.45mm, Δ=10 is not a proper choice, the theoretical curve raises too high at high H-field.

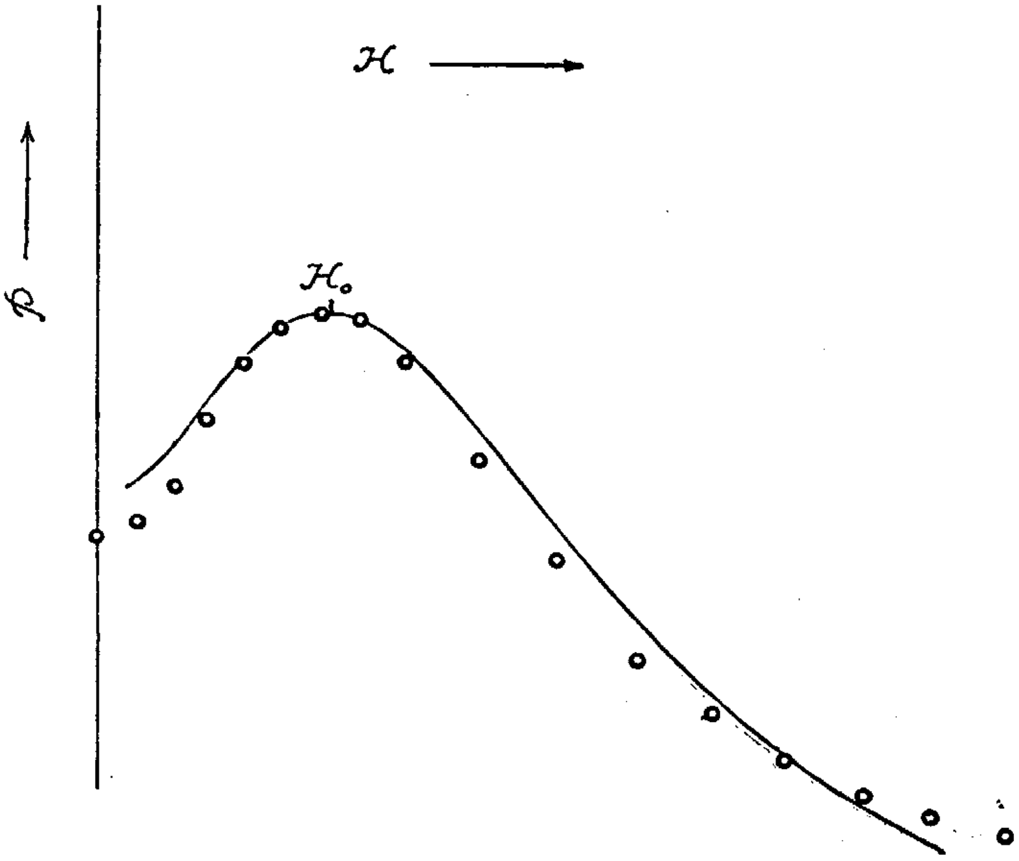

Fig. 6

Power absorption vs. H-field. o is theoretical by computer calculation. —— is the experimental result. P scale is arbitrary. $f=21.798330$ MHz, $H_0=755$ G, $d=1.23$mm, $\Delta=4$ or nearly equal to 4.

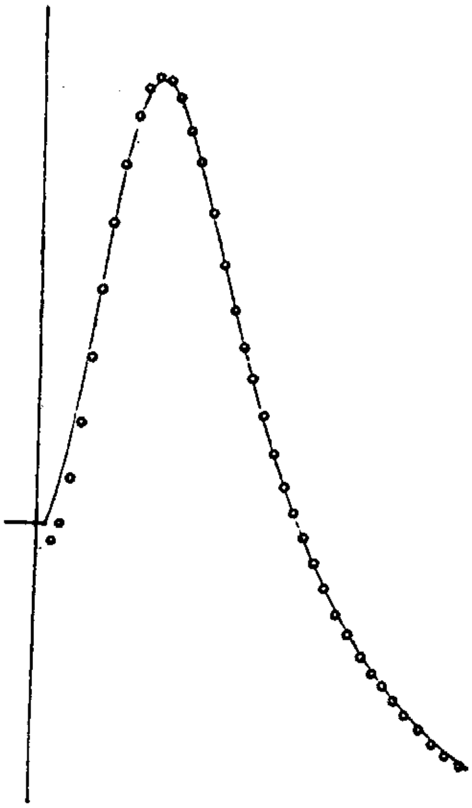

Fig. 7

Power absorption vs. H-field. o is theoretical by computer calculation. —— is the experimental result. P scale is arbitrary. $f=21.798330$ MHz, $H_0=1171$ G, $d=1.84$mm, $\Delta=6$ is a proper selection.

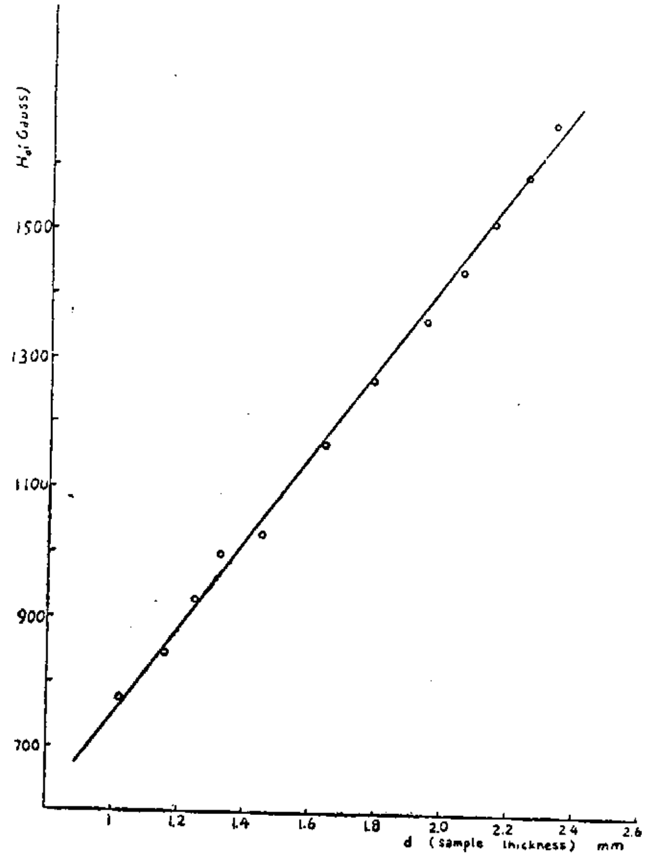

Fig. 8

H-field (H_0) vs. the sample thickness d. o is experimental and the straight line is a least square fit.

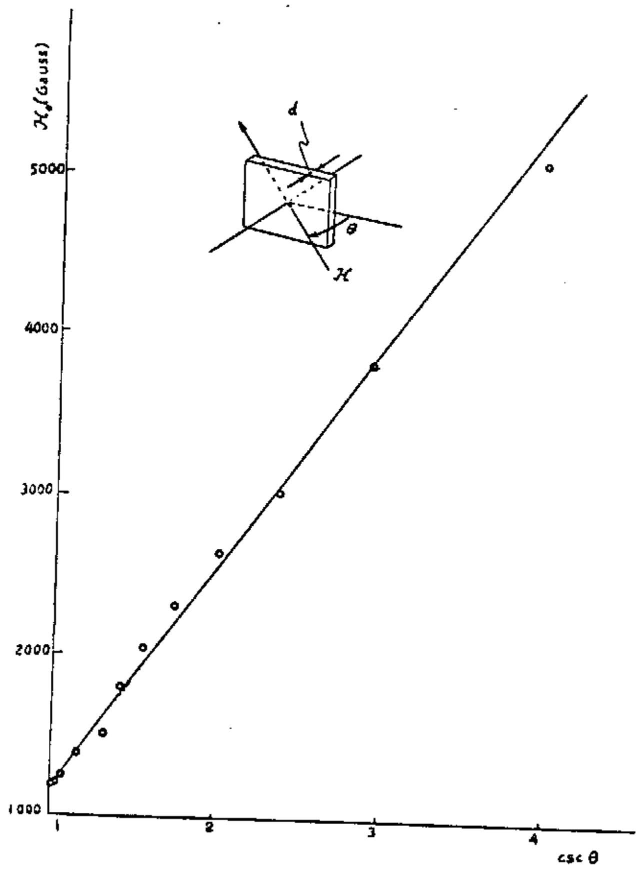

Fig. 9

H-field (H_0) vs. the achange of d due to rotation. of the sample

Annual Report of the Institute of Physics, Academia Sinica, 1971

Excitation Spectra of Magnesium Donors in Silicon

L. T. Ho (何侗民)

Institute of Physics, Academia Sinica

Abstract

The purpose of the present paper is to report and discuss the excitation spectrum of magnesium in silicon. Diffused into undoped silicon, magnesium is a heliumlike neutral donor with excitation spectrum similar to those of group-V donors in silicon. Diffused into silicon containing group-III impurities, the excitation spectrum of magnesium observed is also similar except that the spacings between corresponding excitation lines are ~4 times larger. This is consistent with a singly ionized heliumlike magnesium donor. The ionization energies of neutral and singly ionized magnesium in silicon at liquid helium temperature are (107.50±0.04) and (256.47±0.07) meV, respectively.

本文之目的乃報告並討論鎂在矽中所呈現之激發光譜。滲入純矽之鎂相當於中性氦，其激發光譜與第五類元素在矽中所呈現者類似。當矽中同時含有第三類元素時，鎂之激發光譜亦相似，唯各光譜線間之距離皆大約增長四倍，此現象可與一電離氦結構類似之鎂解釋之。在液態氦溫度時，中性鎂及電離鎂之基態之能量分別測得爲 (107.50±0.04) 及 (256.47±0.07) meV.

1. Introduction

The behavior of group-V impurities as donors and of group-III impurities as acceptors in silicon and germanium represents one of the most extensively studied and best understood aspects of semiconductor physics. The substitutional nature of these impurities, the large dielectric constant of the host, and the effective mass of the bound carrier are the significant features of the model used to explain a variety of phenomena(1-3) associated with these donors and acceptors which are solid-state analogs of the hydrogen atom. It is also now well established that the group-II elements, zinc,(4,5) mercury,(6) and beryllium(7) in germanium and beryllium in silicon ,(7) are solid-state analogs of the helium atom in that they are double acceptors; by compensation with group-V donors one can study these double acceptors in their singly ionized state which then are the analogs of singly ionized helium. The group-VI element sulfur when introduced into silicon (8-10) behaves like a heliumlike double donor; several sulfur donor centers have been discovered though the exact structures of these have not yet been established. The group-I impurity copper in germanium,(11) is another element which has been studied to some extent. The acceptor states associated with this impurity are consistent with its being substitutional.

Of the impurities which are interstitial rather than substitutional, the best-known example is that of lithium in silicon and germanium.(12,13) Transition-metal ions in silicon and germanium, both as interstitial and substitutional impurities, have been studied by Woodbury and Ludwig(14) who investigated their EPR spectra. Interstitial aluminum has been reported in electron-irradiated aluminum-doped silicon where interstitial silicon and substitutional aluminum are believed to exchange their roles;(15) it has been shown that these interstitial aluminum impurities are then donors. Recently,(16,17) the group-II element magnesium, when diffused into silicon, has been shown to behave like a double donor rather than a double acceptor. This behavior can be understood only if magnesium is interstitial rather than substitutional. Singly ionized magnesium donors can be produced by diffusing magnesium into silicon containing acceptors(17) like boron or aluminum or by electron irradiation as well as by thermally ionizing neutral magnesium.(16) The purpose of the present paper is to report and discuss the results of a detailed study of the Lyman spectra associated with both neutral and singly ionized magnesium donors in silicon.

2. Experimental Procedure

Magnesium was diffused into silicon in the following manner. Pure magnesium of 99.9948% purity was deposited by evaporation on the surfaces of the optical sample. The optical sample was sandwiched between two other specimens, all three having magnesium on the surfaces in contact, and heated at ~1200 C for ~1 hour in a helium atmosphere; the sample and the "covers" weld together and thus the magnesium does not escape into the ambient. After the heat treatment, the sample, together with the covers, was quenched in liquid nitrogen. The covers were then ground off. By following this procedure an undoped floating-zone silicon, initially p-type and of resistivity ~1700 ohm-cm, was converted to a low resistivity n-type specimen with a room temperature carrier concentration~2×10^{15} cm^{-3}. These specimens were adequate for observing the excitation spectra of neutral magnesium (Mg^0) at low temperatures. In order to study singly ionized magnesium (Mg^+) donors, low resistivity~10 ohm-cm boron-doped or aluminum-doped floating-zone silicon was used instead of pure silicon. From experience it was found that diffusion times of~10 hours were required to produce sufficient concentration of Mg^+ for the present studies. The samples were too inhomogeneous to give reliable Hall measurements. The boron concentration in most of the specimens used was~1.5×10^{15} cm^{-3} and such specimens showed only Mg^+ spectrum and no trace of Mg^0 spectrum; an upper limit of 10^{15} cm^{-3} of Mg^+ is thus estimated. It was also found that Mg^+ could be produced in specimens containing initially Mg^0 only, by subjecting them to an irradiation with high-energy electrons. In this case magnesium-doped silicon was irradiated with 1 MeV electrons from a Van de Graaff accelerator. Specimens subjected to the same heat treatment and quench failed to show the spectra if no magnesium was deposited on them initially; this check was made to satisfy ourselves that we are indeed dealing with magnesium centers, Mg^0 or Mg^+ as the case may be.

A double-pass Perkin-Elmer spectrometer, model 112G, equipped with Bausch-Lomb plane reflection gratings and appropriate filtering systems, was used for the measurements. Typical resolution is~0.5 cm^{-1}. A Reeder thermocouple with a cesium-iodide window was used as the detector. Sample temperatures~12°K are estimated in liquid-helium measurements.

3. Experimental Results and Discussion: Mg^0

The excitation spectrum for neutral magnesium donors in silicon measured with liquid helium as coolant is shown in Fig. 1. The energies of the excitation lines are given in Table I. The excitation spectrum for phosphorus donors in silicon drawn on the same energy scale as that of Fig. 1 is shown in Fig. 2 for comparison. It is evident that the lines of the two spectra are strikingly similar in spacing and relative intensities. This can also be seen from Table II where the spacings for the two spectra are compared. The labeling of the excitation lines for magnesium donor is based on this similarity. The half-width for the excitation lines of Mg^0 is approximately twice as large as that of the phosphorus lines. The factors contributing to this feature have yet to be established. The broadening of the lines could also be the reason why the a and b lines in the phosphorus spectrum are not seen in the Mg^0 spectrum.

As an interstitial impurity the donor electrons of magnesium are expected to be the two 3s valence electrons thus constituting neutral heliumlike centers. When one of these electrons is excited, the screening of the nuclear charge by the remaining electron and the other core electrons should result in hydrogenic excited states. The higher the excited state the more accurate will be this description. Comparison of energy levels of atomic hydrogen and helium shows this to be the case.(18) We expect the screening to be particularly effective for the p-like final states in the 1s→np transitions. The remarkable similarity of the spacings between the excited states of Mg^0 and those of the group-V donors is thus explained. In the same manner it is also clear why the spacings observed in the excitation spectrum of Mg^0 are strikingly close to those calculated(19) for group-V donors in the effective-mass theory.

As in the case of group-V donors, the positions of the excitation lines of Mg^0 will be determined by the location of the ground state which may lie below the effective-mass position due to the breakdown of the effective-mass theory in the vicinity of the impurity, giving the chemical splitting. The ground state is expected to be affected most seriously by this breakdown because of the large concentration of its wave function near the impurity core.(1) It is thus of interest to deduce the effective-mass ionization energy, which can perhaps be estimated by increasing the effective-mass ionization energy of group-V donors calculated by Faulkner(19) in the ratio of the first ionization energy of the helium atom to that of the ionization energy of the hydrogen atom; this turns out to be $(31.27)(24.46)/(13.6)=56.24$ meV. Here we have used the experimental values for the ionization energies of atomic helium and hydrogen, which, of course, are well known to be close to the calculated values.(20) The experimental ionization energy obtained by adding the calculated value(19) of the binding energy of the $3p\pm$ state to the experimental energy of the transition labeled $3p\pm$ in the Mg^0 spectrum is 107.50 meV; the justification for this procedure lies in the excellent agreement between the calculated and the experimental spacings of the excitation lines on the one hand and that between the spacings of the corresponding lines of phosphorus and magnesium donors on the other. Thus, it is evident that the ground state has suffered considerable chemical splitting. Presumably the sixfold degeneracy of the 1s state due to the multi-valley nature of the conduction-band minima along $\langle 100 \rangle$ is lifted in the same manner as for group-V donors, and the ground state is the totally symmetric linear combination 1s(A_1) with equal contribution of all the six $\langle 100 \rangle$ Bloch wave functions.

Recently Faulkner(19) has calculated in the effective-mass approximation the binding energies of energy levels which are not expected to be observed in the Lyman spectrum, viz., of 2s, 3s,

$3d_0$, 4s, $4d_0$, $4f_0$,..., etc. Though transitions from the ls state to these levels are not allowed in the effective-mass approximation, they may become weakly allowed due to departures from it. Kleiner and Krag(3) have ascribed several weak lines to just such transitions. We have unsuccessfully searched for the corresponding transitions in the spectrum of Mg^0 in silicon. We can not rule out that the concentration of magnesium donors in the samples used was insufficient.

As mentioned already, a significant feature of the donor levels in silicon is the chemical splitting of the sixfold degenerate ls ground state into singlet ls(A_1), doublet ls(E), and triplet ls(T_2) levels, with ls(E) and ls(T_2) close to the effective-mass position and ls(A_1) depressed considerably below it. In contrast to the case of shallower group-V donors,(33) it is not feasible to thermally populate the ls(E) and ls(T_2) for Mg^0 and observe excitation lines which originate from them. Attempts were made to observe the ls(A_1)→ls(T_2) transition which is again allowed only to the extent of the breakdown of the effective-mass theory. Such transitions have been reported for bismuth donors in silicon,(33) and selenium and tellurium donors in aluminum antimonide.(34) However, we have been unsuccessful in observing the corresponding transitions in the spectral range from 41 to 95 meV. In the course of the above measurements we found several weak excitation lines at 87.18, 87.99, and 104.90 meV which occurred in only a few of the samples examined. They appear to be due to as yet unidentified centers.

4. Experimental Results and Discussion: Mg^+

The excitation spectrum for Mg^+ donors in silicon measured with liquid helium as coolant is shown in Fig. 3. The energies of the excitation lines are given in Table III. The excitation spectrum for Mg^0 donors in silicon is also shown in the same figure for comparison; note the energy scale for Mg^0 is four times larger than that for Mg^+ and the strongest line of Mg^0 spectrum, corresponding to ls(A_1)→2p±, is brought into coincidence with the strongest line of Mg^+ spectrum. It is to be noted that the half-width for the excitation lines of Mg^+ is approximately four times as large as that of the Mg^0 lines. This might explain why the lines corresponding to the 5p±, a and b lines in the phosphorus spectrum in Fig. 2 are not observable in the Mg^+ spectrum.

While the interstitial Mg^0 is a solid-state analog of the helium atom as already mentioned, Mg^+ can be considered as the analog of singly ionized helium when one of its two 3s valence electrons is ionized. In this manner, then, the Lyman spectrum associated with Mg^+ donors is expected to be like those of group-V and Mg^0 donors in silicon except that the binding energy for each energy state is increased by a factor of 4 since now the effective nuclear charge is 2 instead of 1. This explains why in Fig. 3 the two spectra are strikingly similar in relative intensities and why the energy separations between the corresponding lines of Mg^+ are ~4 times the corresponding spacings of Mg^0. The labeling of the excitation lines for Mg^+ donors is based on this comparison.

Presented in Table IV is the comparison of energy spacings for excited states of Mg^+ and Mg^0 in silicon. The ratio of the corresponding spacings is approximately 4 as expected. It should be noted, however, that the ratio is not exactly 4 but slightly larger. This could be due to the penetration of the donor electron, the 3s valence electron, inside the inner electron shell. Thus each energy state could be more tightly bound than the corresponding state neglecting this effect. Also, the lower energy state is expected to be affected more than the higher energy state. This should also apply to Mg^0; however, since there is another 3s electron which provides shielding, the donor electron may not penetrate the inner electron shell as much, thus resulting in a smaller effect. Besides this, the orbits of Mg^+ should be smaller than those for the other donors.

As in the case of Mg^0, it is of interest to estimate the effective-mass ionization energy for Mg^+. It is reasonable to assume this to be four times the effective-mass ionization energy of group-V donors calculated by Faulkner, i. e., 125.08 meV. The experimental ionization energy obtained by adding four times the theoretical value of the binding energy of the 3p± state to the experimental energy of the transition labeled 3p± is 256.47 meV. It is thus quite clear that the ground state has suffered a very large chemical splitting.

A noteworthy feature in the Mg^+ spectrum shown in Fig. 3 is the doublet nature of the 2p± line, $2p^a\pm$ and $2p^b\pm$. At liquid nitrogen temperature this feature is obscured due to broadening. At liquid helium temperature this splitting was observed in the samples irrespective of the method used for compensation. It is tempting to ascribe this to the chemical splitting of the excited states. The irreducible representation for the 2p± state is $2T_1+2T_2$ for a T_d donor site symmetry. It could be that this state, due to chemical splitting, splits into two T_1+T_2 states, or even four states with two belonging to T_1 and the other two belonging to T_2. Since the transition from the $1s(A_1)$ ground state is allowed to an excited state belonging to T_2 and not to T_1, a doublet feature is thus expected in either case. Though the 2p± state of Mg^+ donors is still expected to be effective-mass-like, compared with the corresponding state of group-V and Mg^0 donors, its binding energy is four times larger with a smaller Bohr radius and hence a larger chemical splitting. This perhaps explains why the doublet feature of the 2p± state is not observed in the group-V and Mg^0 spectra. The $2p_0$ state lies even deeper than the 2p± state; it should have thus suffered a larger chemical splitting. It should be noted, however, that the symmetry of the $2p_0$ state is given by the combination of irreducible representations A_1+E+T_2, and the transition from the $1s(A_1)$ ground state is allowed only to an excited state belonging to T_2. Thus no splitting would be observed for the $2p_0$ line, even if the final T_2 state had a chemical shift. As for the 3p± and higher states, chemical splitting is presumably too small to be observed.

Attempts were again made to observe the $1s(A_1)\rightarrow 1s(T_2)$ transition for Mg^+, which is expected to be $\sim 256.47-125.08=131.39$ meV, if the excited 1s states are still close to the effective-mass position. No excitation lines, however, were observed in the spectral range from 107 to 135 meV. Similar attempts were also made to observe the even-parity levels like 2s, 3s, $3d_0$,..., etc., for Mg^+. An excitation line at 248.80 meV occurred only in some of the samples examined. It lies to the higher energy side of the 4p±, $5p_0$ line. Its position, however, does not agree with any of the calculated donor levels.(19) This line thus appears to be due to some as yet unidentified center. In one of the samples examined, three extra excitation lines were observed at 238.63, 239.60, and 241.26 meV, respectively. They fall near the region of 3s and $3d_0$. Again, since these lines are not reproducible in other samples, their origin is not certain.

As mentioned earlier, irradiation of magnesium-doped silicon with high energy electrons was one of the methods of compensation used for producing Mg^+ donors. Extensive studies(15) have shown that a variety of donor as well as acceptor states associated with vacancies, interstitials, and their complexes are produced in silicon as a result of irradiation with high energy electrons; with sufficient irradiation the Fermi level moves towards the middle of the energy gap. It is thus to be expected that compensation of Mg^0 could occur yielding Mg^+ donors. It is also possible(25) that the compensation occurs in the following way: A vacancy moves close to the interstitial magnesium donor, or vice versa and is annihilated yielding substitutional magnesium. The latter should be a double acceptor which in turn can compensate the magnesium donors. This is an intriguing possibility which needs further study.

The magnesium-doped silicon samples studied in the present work were irradiated with 1 MeV electrons at 10°C. Magnesium donors were only partially compensated after irradiation; thus both Mg^0 and Mg^+ spectra can be observed in the same specimen. In most of the samples compensated with group-III acceptors, the control was not sufficient to produce partial compensation and hence Mg^0 and Mg^+ excitation spectra were not observed in the same specimen. A typical example is presented in Fig. 4 which shows the appearance of the Mg^+ spectrum and a decrease in that of Mg^0 as a result of electron irradiation. It is clear that the concentration of the Mg^0 donors is decreased while the excitation spectrum for Mg^+ appears only after the sample is bombarded.

5. Concluding Discussion

In the present investigation evidence has been accumulated to support the conclusion that magnesium enters the silicon lattice interstitially and as a consequence behaves as a heliumlike double donor. The excitation spectra indicate a T_d site symmetry for the Mg^0 and Mg^+ donors. Thus, the present investigations on magnesium favor the tetrahedral rather than the hexagonal interstitial site. This is also the case for lithium donors in silicon,(12,13) the other interstitial impurity which has been extensively studied.

Another feature which emerges from these studies is how well the effective-mass theory predicts the p-states even for donors with ionization energies very much larger than the calculated(19) value of 31.27 meV, e. g., 107.50 meV for Mg^0 and 187.2 meV for one of the neutral sulfur donors.(8) The positions of the $1s(E)$ and $1s(T_2)$ have yet to be experimentally established for both Mg^0 and Mg^+ donors. As discussed already, these should be close to the effective-mass position for the 1s state. Also they should be deeper for a heliumlike donor in comparison to a hydrogenic donor.

References

(1) W. Kohn, in Solid State Physics, Vol. 5, edited by F. Seitz and D. Turnbull (*Academic, New York*, 1957), p. 257.
(2) G. W. Ludwig and H. H. Woodbury, in Ref. (1), Vol. 13, p. 223.
(3) P. Fisher and A. K. Ramdas, in Physics of the Solid State, edited by S. Balakrishna, M.

Krishnamurthi, and B. Ramachandra Rao (*Academic, New York*, 1969), p. 149.

(4) P. Fisher, R. L. Jones, A. Onton, and A. K. Ramdas, J. Phys. Soc. Japan Suppl. **21**, 224 (1966); W. J. Moore, Solid State Commun. **3**, 385 (1965).

(5) F. Barra and P. Fisher, Phys. Letters 27A, 711 (1968).

(6) R. A. Chapman and W. G. Hutchinson, Phys. Rev. **157**, 615 (1967).

(7) Beryllium in germanium is discussed in the following: H. Shenker, E. M. Swiggard, and W. J. Moore, Trans. AIME **239**, 347 (1967); W. J. Moore and R. Kaplan, Bull. Am. Phys. Soc. **11**, 206 (1965); N. D. Tyapkina, M. M. Krivopolenova, and V. S. Vavilov, Fiv. Tverd. Tela **6**, 2192 (1964). For beryllium in silicon see J. B. Robertson and R. K. Franks, Solid State Commun. **6**, 825 (1968).

(8) W. E. Krag, W. H. Kleiner, H. J. Zeiger, and S. Fischler, J. Phys. Soc. Japan Suppl. **21**, 230 (1966).

(9) G. W. Ludwig, Phys. Rev. **137**, A1520 (1965).

(10) D. L. Camphausen, H. M. James, and R. J. Sladek, Phys. Rev. **B2**, 1899 (1970).

(11) P. Fisher and H. Y. Fan, Phys. Rev. Letters **5**, 195 (1960).

(12) R. L. Aggarwal, P. Fisher, V. Mourzine, and A. K. Ramdas, Phys. Rev. **138**, A882 (1965).

(13) G. D. Watkins and F. S. Ham, Phys. Rev. **B1**, 4071 (1970).

(14) H. H. Woodbury and G. W. Ludwig, Phys. Rev. **117**, 102 (1960); G. W. Ludwig and H. H. Woodbury, Phys. Rev. Letters **5**, 98 (1960).

(15) G. D. Watkins, Radiation Damage in Semiconductors, Paris-Royaumont, 1964 (*Dunod, Paris*, 1965), p. 97.

(16) R. K. Franks and J. B. Robertson, Solid State Commun. **5**, 479 (1967).

(17) L. T. Ho and A. K. Ramdas, Phys. Letters **32A**, 23 (1970).

(18) C. E. Moore, Atomic Energy Levels, Natl. Bur. Std. (*U. S.*) Circ. No. 467 (*U. S. GPO, Washington, D. C.*, 1949), p. 5.

(19) R. A. Faulkner, Phys. Rev. **184**, 713 (1969).

(20) H. Eyring, J. Walter, and G. E. Kimball, Quantum Chemistry (*Wiley, New York*, 1944), p. **388**, Table 37.

(21) W. H. Kleiner and W. E. Krag, Phys. Rev. Letters **25**, 1490 (1970).

(22) R. L. Aggarwal and A. K. Ramdas, Phys. Rev. **140**, A1246 (1965).

(23) W. E. Krag, W. H. Kleiner, and H. J. Zeiger, Proceedings of the Tenth International Conference on the Physics of Semiconductors, Cambridge, Mass., 1970, edited by S. P. Keller, J. C. Hensel, and F. Stern (*U. S. AEC Division of Technical Information, Washington, D. C.*, 1970). p. 271.

(24) B. T. Ahlburn and A. K. Ramdas, Phys. Rev. **167**, 717 (1968).

(25) H. H. Woodbury and G. W. Ludwig, Phys. Rev. Letters **5**, 96 (1960).

Table I
Energies of excitation lines
of Mg^0 donors in silicon (in meV)

Label	Assignment	Energy
$2p_0$	$1s(A_1) \rightarrow 2p_0$	95.80±0.015
$2p\pm$	$1s(A_1) \rightarrow 2p\pm$	101.12±0.015
$3p_0$	$1s(A_1) \rightarrow 3p_0$	101.95±0.015
$4p_0$	$1s(A_1) \rightarrow 4p_0$	104.17±0.015
$3p\pm$	$1s(A_1) \rightarrow 3p\pm$	104.38±0.015
$4p\pm, 5p_0$	$1s(A_1) \rightarrow 4p\pm, 5p_0$	105.33±0.015
$5p\pm$	$1s(A_1) \rightarrow 5p\pm$	106.05±0.015
E_I		107.50±0.04

Table II
Spacings of donor excited states in silicon (in meV)

States	Theory(19)	P	Mg^0
$2p\pm - 2p_0$	5.11	5.06±0.03	5.32±0.03
$3p_0 - 2p\pm$	0.92	0.93±0.03	0.83±0.03
$4p_0 - 2p\pm$	3.07	3.09±0.03	3.05±0.03
$3p\pm - 2p\pm$	3.28	3.28±0.03	3.26±0.03
$4p\pm - 2p\pm$	4.21	4.21±0.03	4.21±0.03
$5p_0 - 2p\pm$	4.17	4.21±0.03	4.21±0.03
$5p\pm - 2p\pm$	4.97	4.94±0.03	4.93±0.03

Table III

Energies of excitation lines of Mg^+ donors in silicon (in meV)

Label	Assignment	Energy
$2p_0$	ls$(A_1) \to 2p_0$	208.63 ± 0.015
$2p^a\pm$	Is$(A_1) \to 2p^a\pm$	230.22 ± 0.015
$2p^b\pm$	ls$(A_1) \to 2p^b\pm$	230.42 ± 0.015
$3p_0$	ls$(A_1) \to 3p_0$	233.87 ± 0.015
$4p_0$	ls$(A_1) \to 4p_0$	243.00 ± 0.045
$3p\pm$	ls$(A_1) \to 3p\pm$	243.99 ± 0.015
$4p\pm, 5p_0$	ls$(A_1) \to 4p\pm, 5p_0$	247.92 ± 0.015
E_I		256.47 ± 0.07

Table IV

Comparison of energy spacings for excited states
of Mg^0 and Mg^+ donors in silicon (in meV)

States	Mg^+	Mg^0	Ratio
$3p\pm - 2p_0$	35.36±0.03	8.58±0.03	4.12±0.02
$3p\pm - 2p\pm$	(a) 13.77±0.03 (b) 13.57±0.03	3.26±0.03	4.22±0.05 4.16±0.05
$3p\pm - 3p_0$	10.12±0.03	2.43±0.03	4.17±0.06
$3p\pm - 4p_0$	0.99±0.06	0.21±0.03	4.78±0.97
$4p\pm, 5p_0 - 3p\pm$	3.93±0.03	0.95±0.03	4.14±0.16

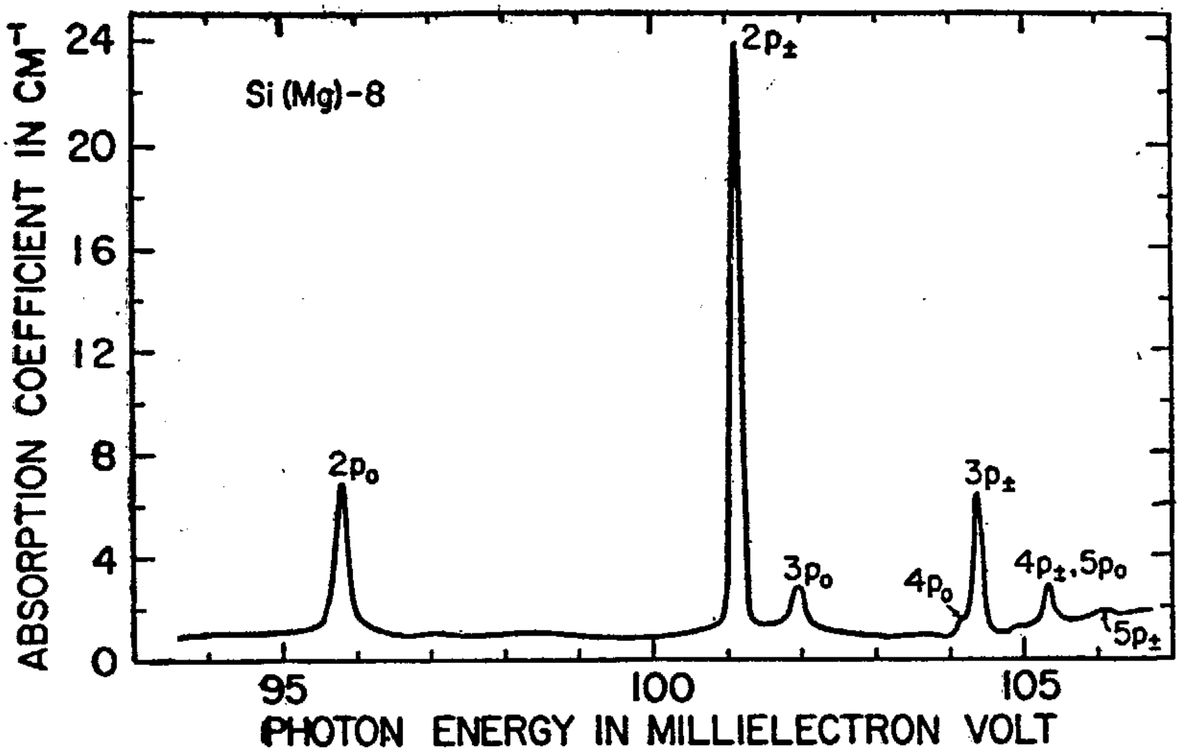

Fig. 1

Fig. 1 Excitation spectrum of Mg^0 donors in silicon. Liquid helium was used as coolant. Carrier concentration, $n(300\,K)$, estimated~1.2×10^{15} cm^{-3}.

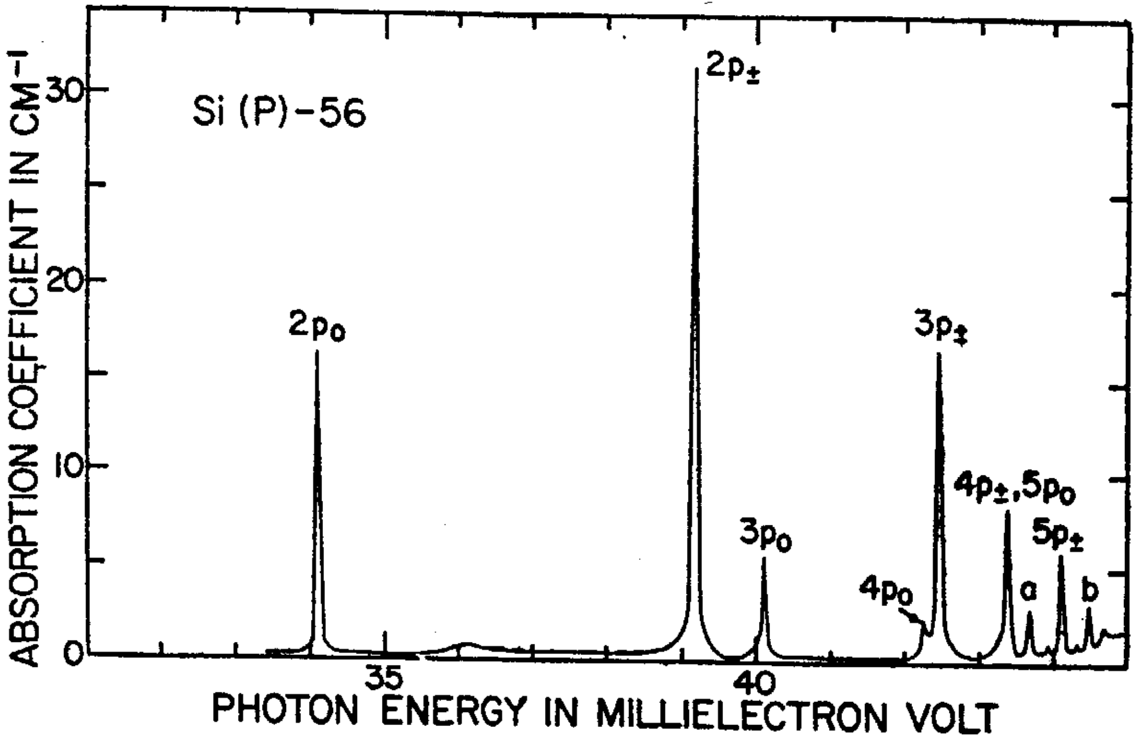

Fig. 2

Fig. 2 Excitation spectrum of phosphorus donors in silicon. Liquid helium was used as coolant. $n(300\,K)\to7.5\times10^{14}$ cm^{-3}.

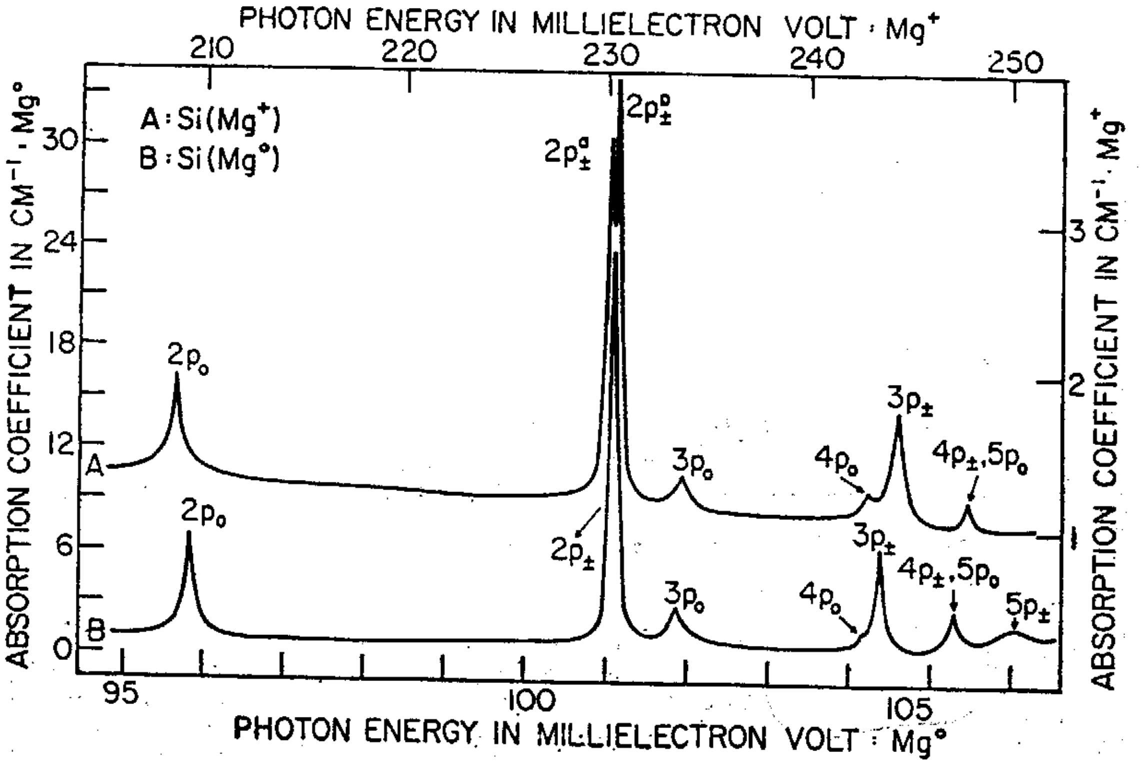

Fig. 3

Fig. 3 Excitation spectra of Mg^0 and Mg^+ donors in silicon. Liquid helium was used as coolant. Mg^+ was produced by compensation Mg^0 with boron acceptors. Note that the energy scale for Mg^0 is four times larger than that for Mg^+.

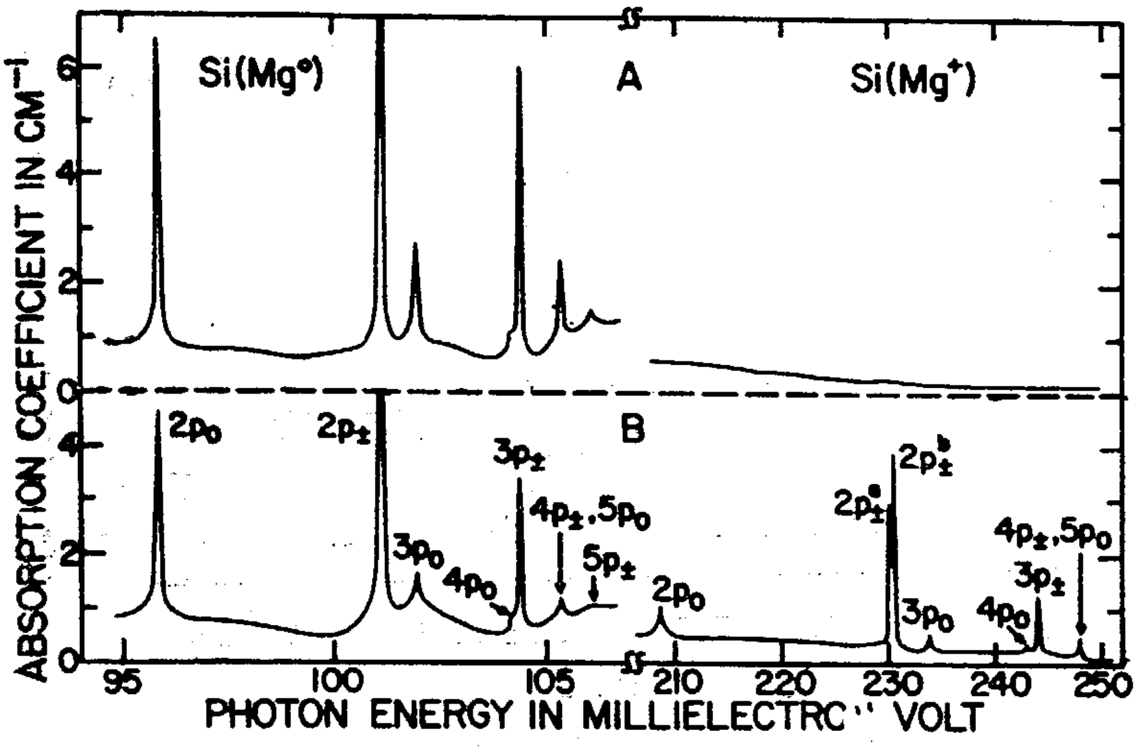

Fig. 4

Fig. 4 Effect of 1 MeV electron irradiation on a magnesium-doped silicon sample. Excitation spectra were measured using liquid helium as the coolant. A and B show the spectrum before and after the irradiation, respectively. The energy scale for Mg^0 is four times larger than that for Mg^+.

ON THE YOUNG'S INTERFERENCE PATTERN

CHUN CHIANG (蔣炯)

Institute of Physics, Academia Sinica
Nankang, Taipei, Taiwan,
The Republic of China

Young's experiment is the earliest demonstration for the existance of the light interference. Since then nearly every book on optics has the description and calculation of Young's interference pattern (see reference 1 and 2). The calculation, however, utilizes a few approximations and reader may not easily grasp their significance. The purposes of this paper are threefold: Firstly, following Oster's lead (3,4), we would like to use a graphic moire pattern to show the Young's interference phenomenon, this graph would help the reader to grasp the interference concept easily. Secondly, we would like to present an exact formula for Young's interefrence pattern, using only elementary mathematics. Thirdly, we would like to show that under what conditions this exact formula may be reduced to the approximate formula appeared usually in the text books on optics. These conditions seem not have been clearly borne out in the usual treatmant and may easily be overlooked by the reader.

The experimental arrangement of Young's interference is shown in Figure 1. Light is passed through a pinhole S so as to illuminate an aperture consisting of two narrow slits S_1 and S_2. If a white screen is placed in the region beyond the slits, a pattern of bright and dark interference bands can be observed. The white band will be observed at point P when the path difference between S_1P and S_2P is an integer number of wave length, and the wave amplitudes are constructive. In Figure 2, two series of concentric circles representing the propagating waves originated from S_1 and S_2 are shown, the spacing between two successive circles is the wave length λ. These two series of concentric circles can be repersented as follows:

$$\sqrt{x^2+(y^2-\frac{h}{2})^2}=m_1\lambda \qquad (1)$$

$$\sqrt{x^2+(y+\frac{h}{2})^2}=m_2\lambda \qquad (2)$$

where h is the distance between S_1 and S_2, m_1 and m_2 are integers $0,1,2\cdots\cdots$. Every intersection point of the circles is the location where the path difference from S_1 and S_2 is an integr number of the wave length λ. A curve correlating these intersection point is the resulting moire pattern as observed on the figure 2. This moire pattern* can be represented as (see reference 3 and 4)

$$\sqrt{x^2+(y-\frac{h}{2})^2}-\sqrt{x^2+(y+\frac{h}{2})^2}=(m_1-m_2)\lambda=n\lambda \qquad (3)$$

whare n is also an integer $0,1,2\cdots$. Eqnation (3) can be reduced to

$$\frac{y^2}{(\frac{n\lambda}{2})^2}-\frac{x^2}{(\frac{h}{2})^2-(\frac{n\lambda}{2})^2}=1 \qquad (4)$$

---

* Moire pattern is the new pattern observed when two component patterns are overlapped.

This equation represents a series of hyperbola which is the location of the constructive interference. If a screen is placed at a distance d from the slits S_1 and S_2, then the interference bands on the screen locate at the intersection points of those hyperbola with the screen. The locations of the interferance bands are

$$y = \pm \frac{n\lambda}{2}\sqrt{1+\frac{d^2}{(\frac{h}{2})^2-(\frac{n\lambda}{2})^2}} \qquad (5)$$

This is the exact formula for the Young's interference bands on a screen at a distance d from the slits. n is the difference of the wave number for the interference bands and is called the order of interference.

If $d \gg h$, and $h \gg n\lambda$, then eq.(5) reduces to the familiar equation

$$y = \pm \frac{n\lambda d}{h} \qquad (6)$$

The condition that $d \gg h$ is required for the derivation of eq. (6) is clearly stated in the optics book, however, the condition that $h \gg n\lambda$ is also reguired seems not have been clearly borne out. This condition shows that the interference bands on the screen can not be equally spaced infinitely; for a given h and λ, n must be much smaller than $\frac{h}{\lambda}$ for eq.(6) to be valid. I hope that this paper presents a conceptually simpler derivation of Young's interference formula and it gives student a clear idea and an interesting demonstration of the interference phenomenon. (To be published in Am. J. Phys. Feb. or March, 1973.)

REFERENCE

1. G. R. Fowles, *Introdoction to Modern Optics*, (Holt, Rinehart and Winston, Inc., New York, 1968), P.64
2. M. Born and E. Wolf, *Principles of Optics*, (Max Born and Emil Wolf, 1959), P.259
3. G. Oster, M. Wasserman, and C. Zwerling, *J. Opt. Soc. Am.* 54,169 (1964)
4. G. Oster, *The Science of Moire Patterns*, (Edmund Scientific Co., Barrington, New Jersey, 1964).

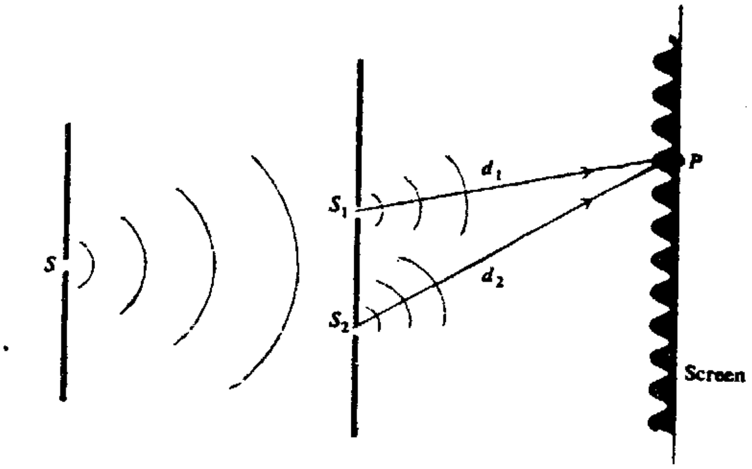

Fig. 1. Young's experiment.

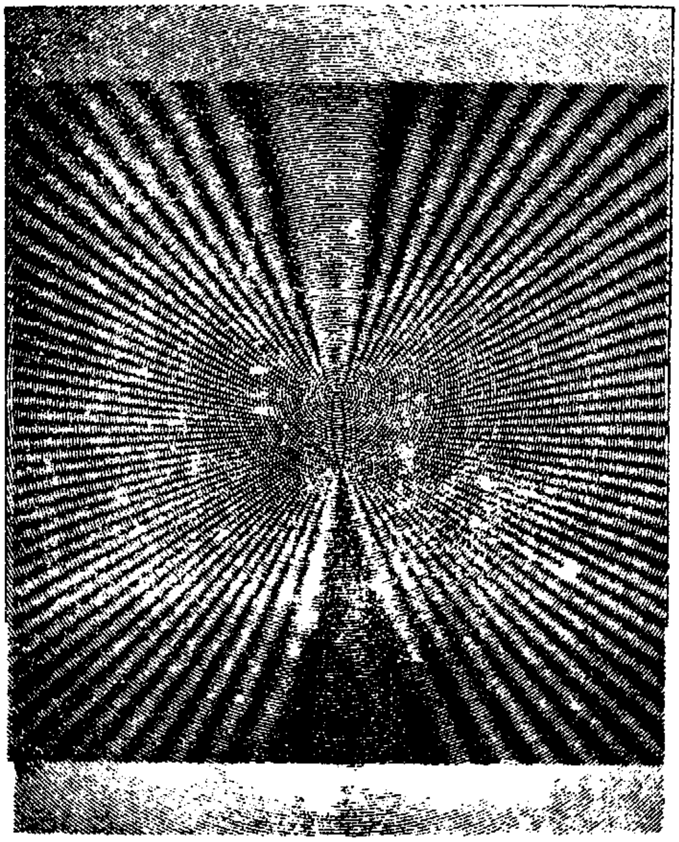

Fig. 2. Moire patterns of two series of concentric circles, showing the interference of two coherent light souces.

Annual Report of the Institute of Physics, Academia Sinica, 1971

PROPERTIES AND RESPONSES OF FROG SKIN MEMBRANES

CHUN CHIANG（蔣烱）

Institute of Physics, Academia Sinica
Nankang, Taipei, Taiwan,
The Republic of China

SUMMARY

1. The active transport species Na^+ is assumed to couple with biochemicals involved in the metabolism. The production, movement and distribution of these biochemicals are governed by known physical laws such as chemicals reactions, diffusion and migration. The transport of these biochemicals are not against the electrochemical gradient, however, the Na^+ species follows the movement of its coupled biochemicals, thus can transport against Na^+ electrochemical gradient.
2. The outside stimuli, such as the clamped voltage, the clamped current, the concentration of the bathing solution, the pressure and the temperature, are considered to perturbate the distribution of biochemicals and Na^+. The disturbance of the stimuli propagates from the boundaries inward, thus the Na^+ distribution and the membrane voltage or current show a transient phenomenon. The negative resistance of the membrane is considered to be the result of this phenomenon.

INTRODUCTION

Many data on biological membrane have been accumulated now, however, our understanding about the functions of biological membranes is fragmental. Various theories advanced seem to have dealt with only certain portions of the data and it seems that no theory has been put out to give a cohensive picture as to how the membrane operates and functions under various environmants.

The purpose of this paper is to present a unified view as to how the skin membrane functions and responds to different stimuli such as temperature, pressure, chemicals and electric field. A scheme of biochemical reaction is proposed to account for the active transport and the external stimulus is considered to perturbate this scheme of biochemical reactions. This perturbation gives rise to the oscillation or excitation behavior in membrane.

ACTIVE TRANSPORT

It has been realized that the energy has to be provided from the metabolism to transport ions against the electrochemical gradient (active transport). Many models have been proposed to explain the active transport, for example, the carrier model (1), the conformational model (2), the association induction model (3) and the cooperative model (4), However, it seems that most of the models have dealt with only a limited protion of data, and the electric properties have not been incorporated in the model. It is the attempt of this paper to propose a biochemical scheme, which would be able to explain the active transport, the voltage clamp data, the negative resistance and the temperature, preassure or chemical influences on the membranes.

In a metaboilc pathway oxygen is invoived. Ussing et al. (5) have shown that about 20 Na^+ are transported per mole of extra oxygen consumed. Also, we have observed that changing the concentration of O_2 in the solution can perturbate the frog skin membrane and change the membrane potential. Ussing and Zerahn (6) have shown that only 5% of CO_2 in air saturated in the solution can depress the open circuit potential of frog skin to zero. The influence of O_2 and CO_2 are understandalbe, because if sodium active transport involves with the metaboilsm, any chemical which upsets the equilibrium of the metabolism would affect the active transport. Besides O_2 and CO_2, ATP and many other biochemicals are involved in the metaboiism. ATP is considered to be the main energy source for the active transport. However, merely the presence of energy souce is not sufficient to transport the sodium ions against the electrochemical gradient, a physical mechanism is necessary. Recently, Wang (7) has assumed the diffusion of pyrophosphate linkage which carries sodium ions against the electrochemical potential. In this paper, an unspecified biochemical in the metabolic pathway is assumed to couple with the sodium ions which diffuse together across the membrane according to the concentration gradient of that biochemical component. The scheme is shown in Fig. 1. This whole scheme is reacting in a unit volume within the membrane, and similar unit volume extends along both Y and Z direction.

An attractive feature of this scheme is that the coupling component B continues to be produced from the metabolic pathway in the outer membrane and diffuse across the membrane to the inner membrane, where it is consumed by a similar metabolic pathway. There is no return pathway required for the coupling component B. Whereas in the carrier model, such a return pathway for the carrier is required. The only assumtions in this model are: 1) B is coupled with Na^+ rapidly with a ratio $Na:B=K$, 2) B is synthesized more at the outer membran than at the inner membrane such that a concentration gradient exists; this concentration gradient drives the Na^+ by the coupling mechanism across the membrane. The difference of rate of production of B between outer membrane and inner membrane can be arisen from the concentration difference of enzymes which catalyze the biochemical reactions or from the structure factors of the membrane. In view that biological membranes are asymetrical, this assumption seems to be justified. Mathematically, we can write following equations to describe the system

$$\frac{\partial A}{\partial t}=-k_1A+k_2B+\frac{\partial}{\partial x}\left[D_A\frac{\partial A}{\partial x}+Z_A\,AU_A\frac{\partial V}{\partial x}\right] \tag{1}$$

$$\frac{\partial B}{\partial t}=k_1A-(k_2+k_2)B+k_4C+\frac{\partial}{\partial x}\left[D_B\frac{\partial B}{\partial x}+Z_B\,BU_B\frac{\partial V}{\partial x}\right] \tag{2}$$

$$\frac{\partial c}{\partial t}=k_3B-k_4C+\frac{\partial}{\partial x}\left[D_C\frac{\partial C}{\partial x}+Z_C\,CU_C\frac{\partial V}{\partial x}\right] \tag{3}$$

where k_1, k_2, k_3 and k_4 are reaction constants which may be a function of x due to the anistoropic propesties of the membrane. D,U, and Z represent diffusion coefficient, mobility and charge respectively, and the subscripts A,B and C represent the species they refer to. There may be many chemicals involved in the reaction; for convience, we assume the system involves only species A, B and C. The above equations (1)-(3) describe the changing of concentration due to chemical reactions, the diffusion and the potential according to the scheme in Fig. (1).

Differential equations of this kind are difficult to solve. However, most of the biochemical components (except B which has been coupled with Na^+) may be neutral species, thus the potential gradient may not influence them directly. Fourthermore, we assume that for the case with no externally appled electric field, the transport of Na^+ is governed mainly by biochemical reactions, and the voltage arisen due to the accumulation of Na^+ plays littie or no offect compared with biochemical reactions; for the case with externally applied electric field, we assume that the externally applied electric field sets the boundary conditions for the Na^+ profile and pertubates the Na^+ distribution arisen from the biochemical reactions, this perturbation propagates from the boundaries inwards and changes the rates of chemical reactions. If the propagation is very fast, then the perturbation can be considered to be instantaneous; howevr, if the propagation is slow, then it takes some time for the perturbation to get through, thus a transient phenomenon is observed. With this in mind we may solve equations

$$\frac{\partial A}{\partial t}=-k_1A+k_2B+\frac{\partial}{\partial x}\left(D_A\frac{\partial A}{\partial x}\right) \tag{1'}$$

$$\frac{\partial B}{\partial t}=k_1A-(k_2+k_3)B+k_4C+\frac{\partial}{\partial x}\left(D_B\frac{\partial B}{\partial x}\right) \tag{2'}$$

$$\frac{\partial C}{\partial t}=k_3B-k_4C+\frac{\partial}{\partial x}\left(D_C\frac{\partial C}{\partial x}\right) \tag{3'}$$

instead of equations (1)-(3), and treat the experimental conditions such as clamped voltage, clamped current and concentration of the bathing solution as the boundary conditions for the sodium ion distribution or voltage profile in the membrane.

Following a similar procedure as Turing (8), the solution of equations (1)′-(3)′ can be written as follows

$$A=\sum_{s=-\infty}^{\infty}\left(a_se^{p_st}+b_se^{p_s't}+c_se^{p_s''t}\right)e^{isx} \tag{4}$$

$$B=\sum_{s=-\infty}^{\infty}\left(f_se^{p_st}+g_se^{p_s't}+h_se^{p_s''t}\right)e^{isx} \tag{5}$$

$$C=\sum_{s=-\infty}^{\infty}\left(l_se^{p_st}+m_se^{p_s't}+n_se^{p_s''t}\right)e^{isx} \tag{6}$$

where p_s, p_s' and p_s'' are roots of equation

$$(p+k_1+s^2D_a)(p+k_2+k_3+s^2D_b)(p+k_4+s^2D_c)$$
$$=k_1k_2(p+k_4+s^2D_c)+k_3k_3(p+k_1+s^2D_a) \tag{7}$$

and

$$\left.\begin{aligned}a_s(p_s+k_1+s^2D_a)&=k_2f_s\\ b_s(p_s'+k_1+s^2D_a)&=k_2g_s\\ c_s(p_s''+k_1+s^2D_a)&=k_2h_s\end{aligned}\right\} \tag{8}$$

$$\left.\begin{aligned} l_s(p_s+k_4+s^2D)&=k_3f_s \\ m_s(p_s'+k_4+s^2D_2)&=k_3g_s \\ n_s(p_s''+k_4+s^2D_2)&=k_3h_s \end{aligned}\right\} \tag{9}$$

Of the nine coefficients $a_s,b_s,c_s,f_s,g_s,h_s,l_s,m_s,n_s$ only three are independant and the rest can be determined by eqs. (8) and (9). These three independent coefficients can be determined by the boundary and initial conditions.

The voltage profile due to the ion distribution within the membrane can be calculated according to Poisson equation as follows:

$$\frac{\partial^2 V}{\partial x^2}=-4\pi\mathrm{N}a^+=-4\pi KB \tag{10}$$

combining with eq. (5), we obtain

$$\frac{\partial^2 V}{\partial x^2}=-4\pi K\sum_{s=-\infty}^{\infty}(f_se^{p_st}+g_se^{p_s't}+h_se^{p_s''t})e^{isx} \tag{11}$$

and

$$V=4\pi K\sum_{s=-\infty}^{\infty}\frac{1}{s^2}(f_se^{p_st}+g_se^{p_s't}+h_se^{p_s''t})e^{isx} \tag{12}$$

If all the coefficients f_s,g_s and h_s are of the same sign, then voltage V will decay monotonically to a stead value following a perturbation from outside stimuli, provided that p_s,p_s, and p_s'' are negative and real. However, If the coefficients are not of the same sign, V will show a peck-vally transient phenomenon. For a detailed discussion of this, see Torring (8). The value of those coefficients are determined by boundary and initial conditicns at the time the manipulations of the skin are made, such as mounting of the skin, the chemicals and concentrations in the bathing solution, the temperature, the concentration of the biochemical components within the membrane, and the timing of the perturbation. If the anions can leak through the membrane, these anions will short circuit the membrane and decreas the charge density. It is well known that $SO_4^=$ can not leak through the membrane as easily as Cl^-; thus the open-circuit voltage of a skin bathing in the chloride ringer solution is lower as observed than that in the sulfate ringer solution.

Katchalsky and Oster (9) have approched this problem by means of thermodynamics of irreversible processes; Selengny et el (10,24) have coupled the diffussion equation and Michaelian kinetic equation to treat the problem; Verhoff and Sundaresan (12) present a coupled transport theory in a steady state. The treatment present here seems to be more general and conceptually simpler in explaining the membrane transient phenomena.

ELECTRIC PERTURBATION

If a potential step is applied across the membrane, then sodium ions will migrate according to this potential step such that the potential profile at the boundaries of the membrane can be conformed to the applied voltage. This migration changes the Na^+ concentration which in turn disturb the steady state condition among various chemical components through reactions and diffusion. This disturbance propagates from the boundaries inward and, the system has to approach to a new steady state. Before the new steady state can be reached, the system may oscillate depending on the potenital steps applied and the boundary conditions at which the potential stops are applied. The current from the voltage perturbation can be written as

$$I = \int \frac{\partial Na}{\partial t} dx = k \int \frac{\partial B}{\partial t} dx$$

where one molecule of Na is assumed to couple with *k* molecule of B. Using eq. (5), we obtain

$$I = K \sum_{s=-\infty}^{\infty} \frac{1}{is} (f_s p_s e^{p_s t} + g_s p_s' e^{p_s' t} + h_s p_s'' e^{p_s'' t}) e^{isx} \tag{14}$$

the coefficients may be determined by the initial conditions and boundary conditions. However, not all the initial conditions are avaliable under the experimental situation, this is because we have no way of knowing the voltage, current or concentration of Na^+ within the membrane. Thus the conefficients can not be determined uniquely. Depending on the signs and values of the coefficients, I may decay monotonically or oscillate. Experimentally, we often observe that when the clamped voltage of the membrane is changed from one value to another, the current I does not always behave consistently. This irreproducibility of data is not due to the fault of the experimental technique, but simply due to the fact that we do not specity sufficient initial and boundary conditions. Samples with different history may have different distribution of ions and voltage profile within the membrane, thus even though the externally applied voltage may be the same, the responsing current is different. Typical current transient phenomena can be seen in Fig. (2) and in Fishman and Macey's work (11).

THE NEGATIVE RESISTANCE OF THE MEMBRANE

Many theories have been proposed to explain the negative resistences phenomenon, for example, the cooperative model (4) and the electric dipole theory (13). We would like to show that the negative resistance can be considered as a direct consequence of the oscillatory behavior of the membrane. Suppose in a voltage ramp experiment, the rate of voltage increase is m, and V=mt. Thus, the resistance is

$$R = \frac{\partial V}{\partial I} = \left(\frac{\partial V}{\partial t}\right)\left(\frac{\partial t}{\partial I}\right) = m / \left(\frac{\partial I}{\partial t}\right) \tag{15}$$

Since m is always positive, the sigh of resistane R depends on the sign of $\left(\frac{\partial I}{\partial t}\right)$. When $\left(\frac{\partial I}{\partial t}\right)$ is negative and oscillatory, negative resistane is observed. The oscillation of current is due to the spatial distribution of ions whose migration have a wave-like characteristics and this wave-like characteristics is generated by the spatial production and consumption of chemicals produced by chemical reactions and diffusion. It is obvious from this discussion that the internal responses of the biochemicals within the membrane is not instantaneous; following a perturbation at the boundary, the perturbation must propagate inward from the boundary and this propagation rate is the characteristic of the mombrane. Thus the resistance varies with voltage ramp rate m according to eq. (15) (For data, see reference 11 and 14).

CHEMICAL PERTURBATION AND CHEMICAL EXCITATION OF MEMBRANE

Following the above theory, we can interprate many chemical effects on membrane as a perturbation process. There are two ways that chemicals may perturbate the system. First, enzymes, hormones or inorganic catalysts may change the reaction rates of the biochemical reactions k_1, k_2......to k_1', k_2'......; thus, the membrane, which was in a steady state corresponding to reaction constants k_1, k_2......, is not in a steady state corresponding to the new reaction constants k_1', k_2'......after the addition of enzymes, hormones or inorganic catalyst. The system is thus gradually adjusting itself to a new steady sstate; in the process of adjusting, the system may oscillate. Second, if the concentration of the components involved in matabolic reactions is changed, other components involved in metabolic reactions have to abjust accordingly. Thus the system gradually approaches to a new steady state and oscillation may also happen in the process (for example see reference 15,16 and 17). it is commonly observed (see Fig.3) that after mounting a freshly prepared skin membrane in a chamber with ringer solutions, the voltage or current shows a sharp peck-valley phenomena; only after a period of about 10 min., the voltage reaches a relatively stable value. The peck-valley transient is due to the changing of the bathing solution from its natural environment to the ringer solution. A chemical concentration step would also cause the membrane voltage to oscillate as can be seen in Fig. 4. It is of interest to note that the concept of receptor sites can easily be incorporated into this theoretical framework. Every interface between the bathing solution and the reaction unit volume as shown in Fig. 1. can be regarded as a receptor site.

If we vary the concentration of bathing solutions continuously, $(\frac{\partial V}{\partial C})$ may be negative due to the oscillation of the voltage caused by perturbation of chemicals. This negative value of $(\frac{\partial V}{\partial C})$ would correspond to the negative resistance in current ramp experiments.

PERTURBATION AND EXCITATION BY TEMPERATURE AND PRESSURE

Temperature and pressure may also affect the membrane system in a profound way. Again, the effect of temperature and pressure can be undstood as a perturbation process. Karger and Krause (18,19) have reported that increasing or decreasing the temperature causes the open-circuit potential or short-circuit current to oscillate. Schaffeniels (20) has shown that increase of hydrostatic pressure can causes the potential to osclliate. Parise and Rivas (21) have also shown the transient conductance changes induced by preassure in artificial lipid membranes. These transient phenomena are very similar to those produced by chemicals or electrical perturbation as shown in previous figures. The main effect of temperature and pressure to the membrane is, following this theory, considered to be through the change of reaction rate constants k_1, k_2......of the biochemical reactions. It is known that k_1, k_2......are a function of temperature and pressure, thus changing of temperature or pressure would change reaction rate constants k_1, k_2......to a new set of constants k_1', k_2'......, and the system has to approach to a new steady state. During the process of approaching to the new steady state, oscillation may occure.

If we increase the temperature continuously and record the open circuit potential, $\frac{\partial V}{\partial T}$ may be negative in certain period of time due to the oscillation of the voltage. This negative value of $\frac{\partial V}{\partial T}$ would correspond to the negative resistance $\frac{\partial V}{\partial I}$ in the current or voitage ramp experiment. Similarly, it would also predict that $\frac{\partial V}{\partial P}$ would be negative under certain conditions in the pressure ramp experiment.

SATURATION EFFECT

From the scheme in Fig. (1), it is obvious that those biochemical components all exert a mutual influence on each other. Changing the concentration of one of the biochemicals would change the flux of the active transport. However, if the concentration of one of these biochomical components is higher than a critical value, then the amount of active transport will depend only on the supply of other biochemicals and no longer depend on the concentration of that particular biochemical component. This can be seen from the data of Cereijido et el on the sodium flux versus sodium concentration (22). Beyound certain sodium concentraton sodium flux no longer increases with sodim concentration. Oxygen concentration also shows a similar phenomenon (23). The other biochemical components involved in the metabolism would show a similar effect.

CONCLUSIONS

A scheme is presented to show the active transport process. The active transport species is assumed to couple with biochemicals involved in the metabolism. The movement and distribution of biochemicals are governed by known physical laws such as chemical reactions, diffusion and migration. The chemical reactions need enzymes to stimulate the speed and usually expends energy. ATP is considered to provide the energy. This energy is transmitted through the coupling biochemicals to Na^+, thus Na^+ moves against its own electrochemical gradient.

Since the membrane is relatively rigid and extends for a fixed distance, the chemical reactions can not proceed uniformly over the whole membrane. Any outside stimuli, such as voltage, current, chemicals, temperature and pressure may perturbate and modulate the spatial chemical reactions. The disturbance propagates from the receptor sites inwards. Thus the membrane voltage or current shows a transient phenomenon. This transient phenomenon is considered to be the cause of the negative resistance. (Submitted for publication)

ACKNOWLEDGMENT

The author is very grateful to Dr. T. Hoshiko for having the opportunity to be in his laboratory and for his many helpful discussions.

REFERENCES

1. R.A. Sjodin, in *Biophysics and Physiology of Excitable membranes.*, W.H. Adelman Jr. (Ed.) Van Nostrand Reinhold Company, N.Y. (1971)

2. J. Young, G. Bloudin & D. Green, *Proc. Nat. Acad. Sci.* USA, **68** (1971) 1364.
3. G.N. Ling, *Texas Reporte on Biology and Medlcine*, **22** (1964) 224.
4. J.P. Changeux, J. Thiery, Y. Tung and C. Kittel, *Proc. Natl. Acad. Sci.* USA, 57 (1967) 335.
5. H.H. Ussing, P. Kruhoffer, J. Hess Thaysen and N.A. Torn, *The Alkali Metal Ions in Biology*, Springer-Verlag, Berlin, 1960
6. H. Ussing and K. Zerahn, *Acta Phys. Scandinav.*, **23** (1951) 110.
7. J.H. Wang, *Proceed Nat. Acad. Sci.*, **67** (1970) 59.
8. A.M. Turing, *Proceed. Roy. Soc. B.*, **237** (1952) 5.
9. A. Katchalsky and G. Oster. In, *The Molecular Basie of Membrane Function*. D.C. Tosteson Editor, Pertice-Hall, Inc., Englewiod Cliffs, N.J. (1969) pp. 1-44.
10. E. Selengny, G. Broun and D. Thomas, *Physiol. Veg.*, **9** (1971) 25.
11. N.H Fishman and R.I. Macey, *Biophys. J.*, **9** (1969) 127.
12. F.H. Verhoff, and K.R Sundaresan, *Biochim. Biophys. Acta*, **255** (1972) 425.
13. B. Hamel and I. Zimmerman, *Biophys. J.*, **10** (1970) 1029.
14. O.A. Candla, *Byophys. J.*, **10** (1970) 323.
15. K. Johnston, and J. Hoshiko, *Am. J. Physioi.*, **220** (1972) 792.
16. E. Leb, T. Hoshiko and B. Lindley, *J. Gen. Physinl.*, **48** (1965) 527.
17. J. Aceves and D. Erlij, *J. Physiol.*, **212** (1971) 195.
18. W. Karger and D. Krause, *Pflugers Archiv*, **274** (1962) 340.
19. W. Karger, *Pflugers Archiv*, **274** (1962) 331.
20. E. Schaffeniels, *Cellular Aspects of Membrane Permabillty*, Pergamon Press, (1967) pg. 223.
21. M. Parisi and E. Rivas, *Biochim. Biophys. Acta*, **233** (1962) 469.
22. M. Cereijido, F.C. Herrera, W.J. Flanigan, and P.F. Curran, *J. Gen. Physiol.*, **47** (1964) 879.
23. B. McDougai and L.P. Sullivan, *Proc. Soc. Exp. Biol. and Med.*, **136** (1971) 871.
24. E. Selegny, J. Kernevez, G. Broun and D. Thomas, *Physiol. Veg.*, **9** (1971) 51.

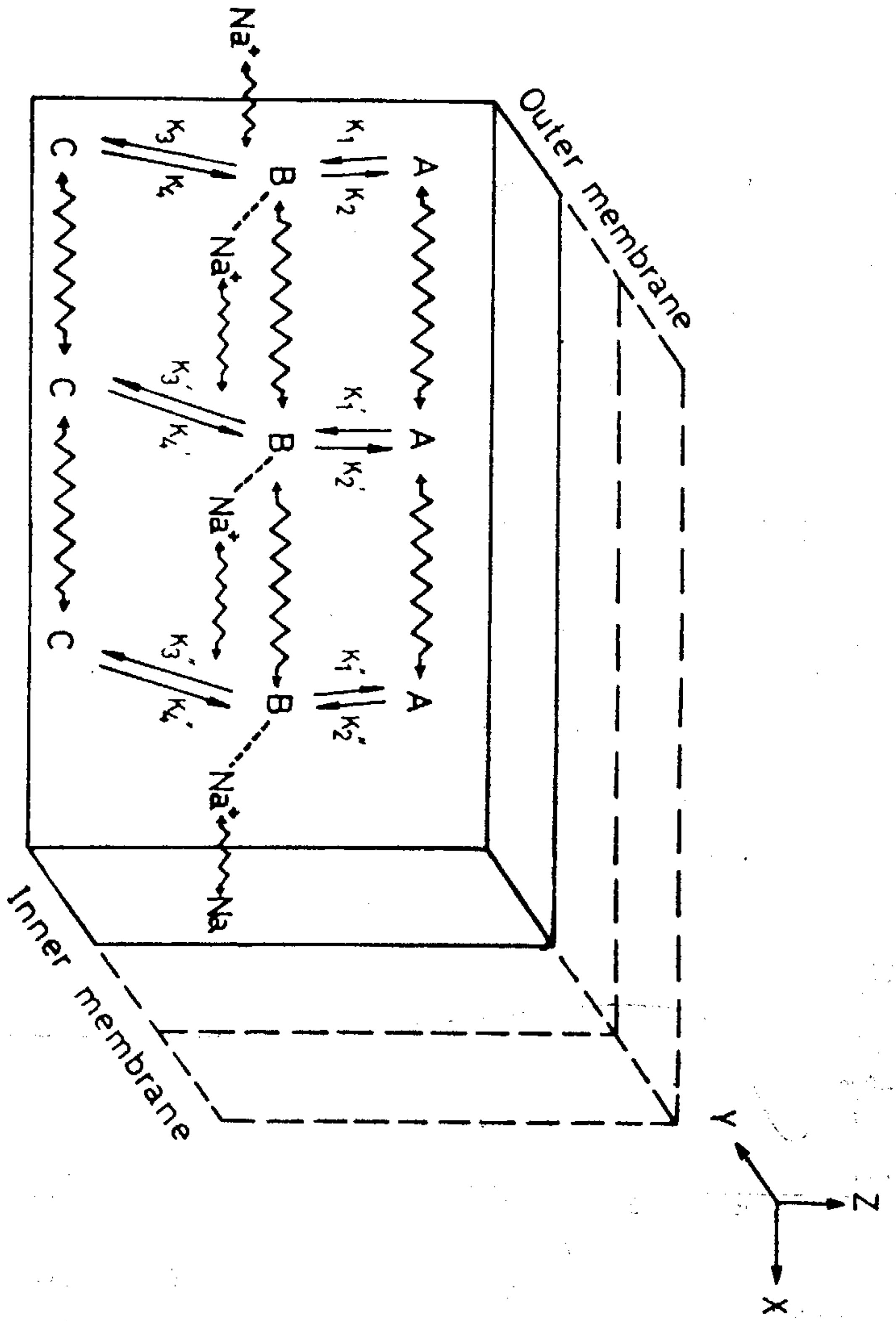
Na^+
Outer membrane
A
A
A
K_1
K_2
K_1'
K_2'
K_1''
K_2''
B
B
B
Na^+
Na^+
Na^+
Na
K_3
K_4
K_3'
K_4'
K_3''
K_4''
C
C
C
Inner membrane
Y
Z
X

Fig. 1. A biochemical scheme representing the interaction of chemical reactions and diffusion ⇄represents chemical reaction and ←~~→ represents diffusion, The scheme is enclosed in the unit reacting volume. Similar unit volume extends in the Y and Z direction.

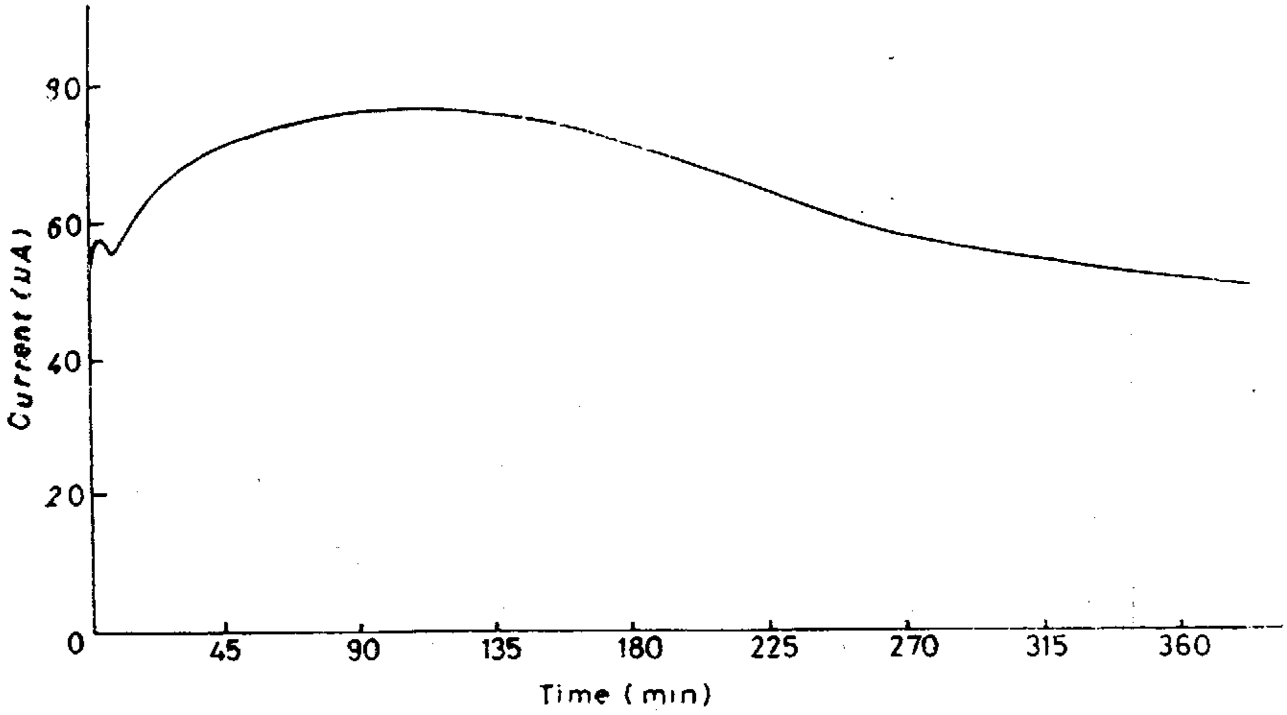

Fig. 2. Current transint of a frog skin membrane after short-circuiting the membrane (short-circuit current).

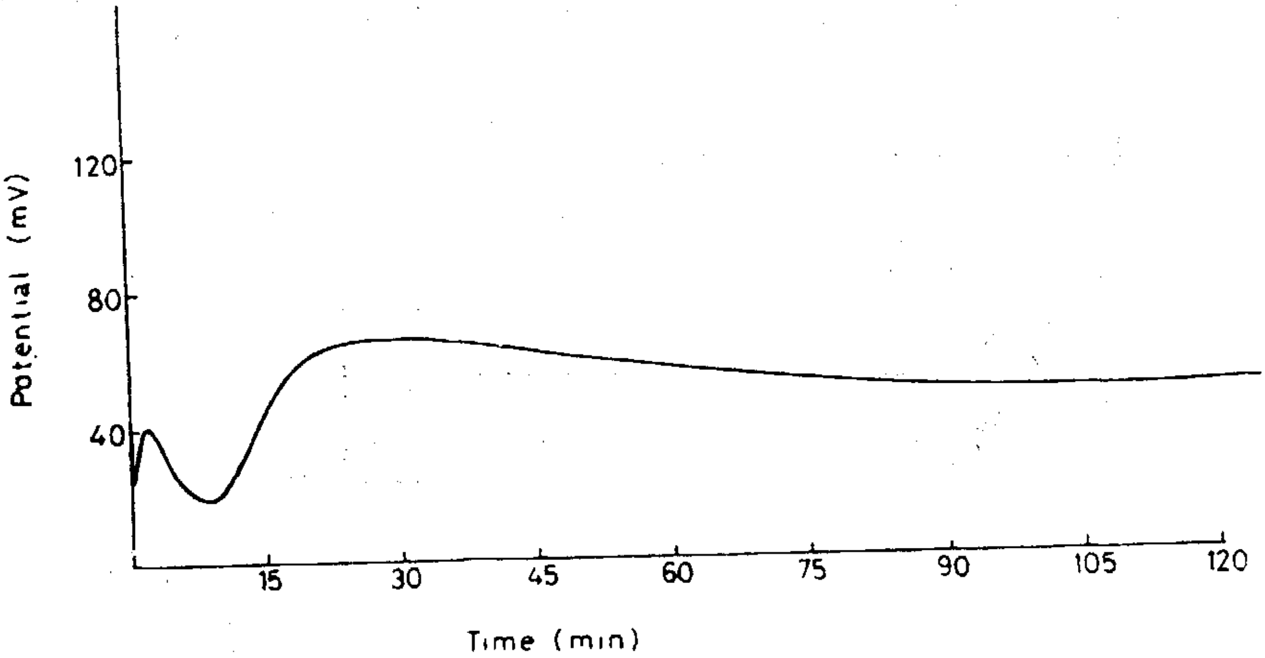

Fig. 3. Potential transient of a frog skin. The skin was immediately mounted in the chamber after desecting. The composition of bathing solution was 55 mN Na^+, 5mN K^+, 0.5mN Ca^{++} and 60.5 mN Cl^-.

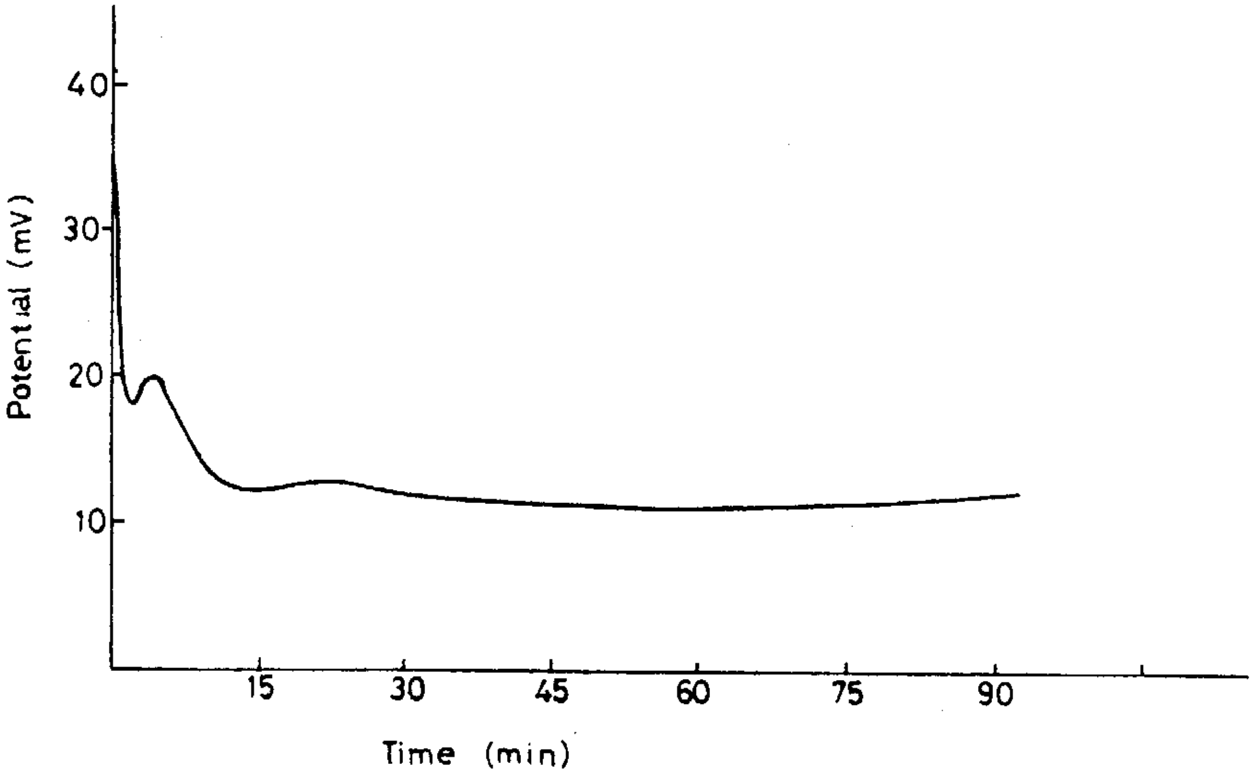

Fig. 4. KCl concentration perturbation of frog skin membrane from 5mN to 44.5mN. The composition of the bathing ringer solution was 55mN Na^+, 5mN K^+, 0.5mN Ca^{++} and 60.5 mN Cl^-.

Annual Report of the Institute of Physics, Academia Sinica, 1971

A THEORY OF THE MULLER-LYER ILLUSION

Chun Chiang (蔣烱)

Institute of Physics, Academia Sinica
Nankang, Taipei, Taiwan
The Republic of China

The concepts of the field of attention and field of vision are differentiated and defined. Perception is viewed as a series of discrete processes and the probability concept is introduced. The perceived length in the Muller-Lyer illusion is assumed to be a statistical average of all the instantaneously perceived distances between the lines forming the angles. With an assumed perception distribution function, the magnitude of the illusion can be predicted and agree with the experimental data. Alternatively, using the experimental data and this theory, the perception distribution function can be deduced. This probability distribution function is a representation of the mental activities.

The Muller-Lyer illusion has been the focus of research for many years in the hope that an understanding of this illusion will clarify some important mechanisms of perception.

The standard form of the Muller-Lyer illusion is shown in Fig. 1. The horizontal lines l_0 in Fig. 1(a) and Fig. 1(b) are of equal length. However, l_0 in Fig. 1(a) appears longer than that in Fig. 1(b).

Of the many theories proposed to explain this illusion, there is a group of theories called the confusion theory (see Woodworth and Schlosberg, 1954). The individual theories of this group differ in detail from each other; however, they all emphasize that the whole figure is responsible for the illusion. Recently, Erlebacher and Sekuler (1969) proposed that S obtains the erroneous results by incorporating, in his judgement, the distance between the ends of the lines forming the angles. Pressey (1967) proposes that "the judgement of the horizontal line is embedded in the context of judgement of varying extents, the magnitudes of which are determined by the contour forming the angles…". Piaget (1961) has used the concept of centration and decentration to explain the illusion. However, it seems that no theory has been completely satistactory. Gregory's (1966) misplaced constancy scaling theory may under certain situations explain parts of the illusion, however this does not seem to be the fundamental cause.

The purpose of this paper is to give a detailed account of another underlying mechanism as to how the angle contour may give rise to the illusion. For a review of other theories, see Over's (1968) excellent article.

When S observes a figure, his eyes do not fix on all the points of interest at the same time;

instead, his eyes fix on some point selectively. Furthermore, for every fixation, one cannot simultaneously perceive all the information within the visual field of that fixation. Only certain bits of information are perceived at one time, and other bits of information have to be perceived later. For example, while reading, one perceives each word in succession instead of all words simultaneously for every fixation (Woodworth and Schlosberg, 1954, p.505). Thus one receives the information discretely, and perception is a discrete process. It is suggested here that the field of vision and field of attention should be differentiated. The field of vision for a given orientation of the eye is defined here as the area in space which can be projected onto the retina and which is perceptable if sufficient time is allowed. The field of attention is defined as the area within the field of vision which is actually perceived at a given time. It may take several different fields of attention to map the entire area of the field of vision. Thus, even though the entire area of a given field of vision is visible at one time or another, not all the areas of field of vision are perceptable at the same time. This concept is important in understanding the perceptual mechanism of Muller-Lyer illusion. The failure of the eye-movement theory (Woodworth and Schlosberg, 1954, p. 419) is essentially due to the failure to grasp this key concept. Gibson (1950) has made the distinction of visual field and visual world; however, the concept of field of attention has not been realized and clearly distinguished from visual world or visual field. This is probably the reason for much of the controversy.

In the case of the Muller-Lyer illusion, the instantaneously perceived length within the field of attention may be l_0 at one time and $l_1, l_2 \cdots\cdots$ or l_n at other times, where $l_0, l_1 \cdots\cdots l_n$ are the distances between the lines forming the angles as shown in Fig. 1. ($l_0, l_1, l_2 \cdots\cdots$ are assumed to be parallel. Probably that is the case for most situations. However, this model can easily be extended to the case that $l_0, l_1, l_2 \cdots\cdots$ are not parallel.) The probability of perceiving $l_0, l_1 \cdots\cdots l_n$ is $P(l_0), P(l_1) \cdots\cdots P(l_n)$. Finally, the perceived length is assumed to be a statistical average of all these instantaneously perceived lengths, $l_0, l_1 \cdots\cdots l_n$. Since the whole figure is within the field of vision, the information concerning the lengths, $l_0, l_1 \cdots\cdots l_n$ keeps on flowing into the brain, and the brain simply cannot ignore this information and single out the length l_0. Consequently, the resultant perceived length is somewhere between l_0 and l_n. Mathematically, we can write the perceived length L as follows:

$$L = P(l_0)\, l_0 + P(l_1)\, l_1 + P(l_2)\, l_2 + \cdots\cdots P(l_n)\, l_n, \qquad (1)$$

where $P(l_0) + P(l_1) + \cdots\cdots P(l_n) = 1$. The value of $P(l_0)$, $P(l_1) \cdots\cdots$ depends on factors such as the subject's attention, the fixation points, the inspection period, etc. This will be discussed in more detail later.

As can be seen from Fig. la, $l_0 < l_1 < l_2 \cdots\cdots < l_n$, thus $L > l_0$. Namely, the percieved length of the horizontal line l_0 is longer than its objective length. In Fig. lb, $l_0 > l_1 > l_2 \cdots\cdots > l_n$, thus $L < l_0$. Namely, the perceived length of l_0 is shorter than its objective length.

Using the same argument, the perceived length of l_n in Fig.lb should be longer than its objective length. This was indeed reported by Mountjoy (1966).

In a previous paper (Chiang, 1968), diffraction and aberrations have been invoked as causes of the illusion. For example, due to blurring, the length of the horizontal line on the retina is actually l_0' instead of l_0; In Fig. la, l_0' is longer than l_0 due to the blurring and in Fig. lb, l_0' is shorter than l_0 due to the blurring. Thus, the perceived length L is

$$L=P(l_0')l_0'+P(l_1)l_1+P(l_2)l_2+\cdots\cdots P(l_n)l_n \tag{2}$$

and the magnitude of the illusion increases.

The above theory may also explain other forms of the Muller-Lyer illusion as shown in Fig. 2. Gergory presents the illusion in a vertical orientation, however, it seems that no experiment has demonstrated the difference between the vertical and horizontal orientation for this illusion yet.

In order to make a quantitative calculation of L, the probbaility distribution function has to be known. This distribution function may depend on the instructions, the person's experience and the fixation point of the eye. With an assumed distribution function, the illusion can be calculated and compared with experiment data. Alternatively, using the experimental data and this theory, the perception distribution function can be deduced. Thus, this theory provides a tool to investigate the perception distribution function which is a representation of the mental activities.

Case (1). If S is specifically instructed to spend equal time in fixing his eye on points along the perpendicular to l_0, then, $P(l_0)=P(l_1)=\cdots\cdots P(l_n)$, and the perceived length L can be shown, according to Eq. 1, to be equal to $l_0 \pm S_0 \cos\frac{\theta}{2}$, where S_0 is the length of the outgoing or ingoing fins, and θ is the angle between the two outgoing or ingoing fins (the positive sign applies to the outgoing fins and the negative sign applies to the ingoing fins). Note that the magnitude of the illusion $\pm S_0 \cos\frac{\theta}{2}$ is directly proportional to the length of the fins. Dewar (1967 a) has provided some data about the effect of fins' length and angle on the magnitude of illusion. Even though his experimental conditions do not correspond exactly to the requirements specified here, his data indicate that the magnitude of illusion follows a cosine function of $\frac{\theta}{2}$, as shown here, rather than an inverse relationship, as is usually believed.

Case (2). Asymmetry of the illusion: If S is specifically instructed to spend equal time in fixing his eye on points within the entire figure, then, every point within the contour line has equal probability of being perceived, thus, according to Eq.1,

$$L=\frac{\int_0^{S_0}(l_0\pm 2S\cos\frac{\theta}{2})^2\,d(S\sin\frac{\theta}{2})}{\int_0^{S_0}(l_0\pm 2S\cos\frac{\theta}{2})\,d(S\sin\frac{\theta}{2})}=(l_0\pm S_0\cos\frac{\theta}{2})+\frac{S_0^2\cos\frac{\theta}{2}}{3(l_0\pm S_0\cos\frac{\theta}{2})} \tag{3}$$

and the magnitude of illusion D is

$$D=L-l_0=S_0\cos\frac{\theta}{2}\left[1\pm\frac{S_0\cos\frac{\theta}{2}}{3(l_0\pm S_0\cos\frac{\theta}{2})}\right], \tag{4}$$

where + is for the outgoing fins case and − is for the ingoing fins case. Note that the absolute value of D is larger for outgoing fins case than that for ingoing fins case. Indeed, Binet (1895), Heymans (1889), and more recently Pollack and Chaplin (1964) have shown that the outgoing fins produce about four times as much illusion as do the ingoing fins.

The illusion D, calculated according to Eq. 4, only involves the misestimation of length due to high central brain processes. The total illusion may have an additional component arising from blurring in the optical image in the retina, as discussed elsewhere (Chiang, 1968). The effect explained by other theories (see Over's review, 1968) may also contribute to the illusion to a certain extent.

Case (3). S If is instructed to fix his eyes on the middle point of l_0, then the probability distribution function may be a normal distribution function $\frac{1}{\sqrt{2\pi}\sigma}\exp\left(-S^2\sin^2\frac{\theta}{2}/2\sigma^2\right)$ where $S\ \mathrm{Sin}\frac{\theta}{2}$ is the vertical distance from the fin to l_0, and σ is a constant. The perceived length L according to Eq.1, will then be

$$L=\frac{\int_0^{S_0}\left(l_0\pm 2S\cos\frac{\theta}{2}\right)\frac{1}{\sqrt{2\pi\sigma}}\exp\left(-S^2\sin\frac{\theta}{2}/2\sigma^2\right)d\left(S\sin\frac{\theta}{2}\right)}{\int_0^{S_0}\frac{1}{\sqrt{2\pi\sigma}}\exp\left(-S^2\sin^2\frac{\theta}{2}/2\sigma^2\right)d\left(S\sin\frac{\theta}{2}\right)} \tag{5}$$

This equation is not integrable. However, if the figure is relatively large, the value of σ is small, and the probability distribution is such that $P(l_n)\simeq 0$, then Eq. 5 may be approximated as follows:

$$L\simeq\frac{\int_0^{\infty}\left(l_0\pm 2\ S\cos\frac{\theta}{2}\right)\frac{1}{\sqrt{2\pi\sigma}}\exp\left(-S^2\sin^2\frac{\theta}{2}/2\sigma^2\right)d\left(S\sin\frac{\theta}{2}\right)}{\int_0^{\infty}\frac{1}{\sqrt{2\pi\sigma}}\exp\left(-S^2\sin^2\frac{\theta}{2}/2\sigma^2\right)d\left(S\sin\frac{\theta}{2}\right)} \tag{6}$$

$$=l_0\pm\frac{4\sigma}{\sqrt{2\pi}}\cot\frac{\theta}{2}$$

Case (4). Brightness contrast effect: The brightness contrast may affect the distribution function through varying the value of σ. By increasing the brightness contrast, the attention may be attracted away from l_0 to the contour of the fins, thus raising the value of σ in the normal distribution function. From Eq. 5, it can be shown that the magnitude of the illusion increases with σ. Thus, it would be predicted from this theory that increasing the brightness contrast will increase the magnitude of the illusion. This was indees found to be the case by Wickelgren (1965).

Case (5). Short-term transient effect: Due to the dependence of perceived length on the probability, the perceived length may be varied with time. A statistically stable averaging value of perceived length can be obtained only if a large number of instantaneous perceptions are used. It takes a relatively long time to obtain this large number of instantaneous perceptions. Thus, in the early period of perceiving, the perceived length can fluctuate at any value between l_0 and l_n, depending on the fixation point of the eye and the focus of the attention. Only after a sufficiently long period of perceiving, the perceived length reaches a stable value. Primary tests indicate that this is indeed so. The time required to reach a stable value is in the order of seconds.

Case (6). Long-term transient effect: Judd (1905), Lewis (1908) and Day (1962) have shown that the magnitude of illusion may be decreased with prolonged viewing or practice. Dewar (1967 b) suggests that this may be due to the change of attention in the horizontal shift. This kind of voluntary change of attention would change the probability distribution function by decreasing the value of σ, which, in turn, will decrease the magnitude of the illusion. In addition to this, the unit area of the field of attention may also be decreased with time. This can occur by focusing more attention to the areas of interent and ignoring the areas of less interest. With a smaller area of field of attention, less contour of the figure will be within the field; thus the magnitude of the illusion decreases. This explains the decreasing of the illusion by practice and prolonged viewing. The change of the field of attention approximates an exponential function $\exp(-t/\gamma)$ where γ is a constant the magnitude of which is estimated to be in the order of hours (from the data of Dewar 1963, and Judd 1905), and t represents time.

Case (7). If the figure is small and the whole contour of the figure is always within the field of attention, regardless of the changing of the field of attention, then prolonged viewing should not effect the magnitude of the illusion. Furthermore, if the figure is presented tachistoscopically such that one will not be able to direct his attention to horizontal line, then σ will not change with time and the magnitude of illusion should not decrease with repeated presentation. Eysenck and Slater (1958), Day (1962) and Pollack and Chaplin (1964) have indeed shown that repeated or prolonged presentations of a Muller-Lyer figure subtending a small visual angle do not result in the illusion's diminution.

Case (8). Illusion in haptic space: The above discussion is concerned with the illusion in visual space. However, the concept of field of attention should not only be applicable in visua space, but in haptic space as well. Indeed, Fisher (1966), for example, has shown that one can perceive this illusion using the somatic sense instead of the visual sense.

In summary, the concept of the field of attention and the probability distribution of perception is introduced to explain the illusion. With the assumed probability distribution function, many major experimental data can be predicted. The theory explains that the instruction, the fixation point of the eye, the size of the figure, the brightness contrast, and the period of inspection in the figure, can all have important effects on the magnitude of the illusion, and σ is a function of these factors. Alternatively, with the experimental data and this theory, the probability distribution function can be deduced. It seems that no other direct experimental method is available to map this probability distribution function. It is hoped that this paper can stimulate further experiments in this field. (To be published in Vision Research)

ACKNOWLEDGEMENT

The author is very grateful to the referee for the suggestions and the help for the preparation of this manuscript.

REFERENCES

Binet, A. (1895). *Rev. Phil.* **40**, 11-25.

Chiang, Chun (1968). *Percept. & Psychophys.* 3, 174-176.

Day, R.H. (1962). *Psychol.Monogr.* 76, No. 14, whole no. 533.

Dewar, R.E. (1967). *Percept. Motor Skills*, **24**, 708-10.

Dewar, R.E. (1967). *Canadian J: Psychol.* **21**, 520.

Dewar, R.E. (1968). *Percept. and Psychophys.* **3** (4A), 246-248.

Erlebacher, A. and Sekuler, R. (1969). *Proceedings of the 77th Annual convention of the American Psychological Association*, **4** (pt.1), 27-28.

Eysenck, H.J. and Slater, P.(1958). *Brit. J. Psychol*, **49**, 246-255.

Fisher, G.H. (1966). *Nature*, **212**, 105-6.

Gibson, J.J. (1950). *The perception of the visual world*, The Riversid Press, Cambridge, Mass. USA.

Gregory, R.L. (1966), *Eye and Brain*. London: Weidenfeld & Nicolson.

Heymans, G. (1896). *Zeitschrift für Psychologie*, **9**, 221-225.

Judd, C.H. (1905). *Psychology Monograph*, **7**, 29-55.

Lewis, E.C. (1908). *Brit.* J. *Psychol.* **2**, 294-306.

Mountjoy, P.T. (1966). *J. exp. Psychol.* **71**, 119-123.

Over, R. (1968). *Psychol. Bull.* **70**, 545-562.

Piaget, J. (1961). *Les mechanismes perceptifs*. Paris: Press Universitaires de France.

Pollack, R.H. and Chaplin, M.R. (1964). *Percept. Motor Skills*, **18**, 377-382.

Pressey, A.W. (1967). *Percept. Motor Skills*, **25**, 569-572.

Wickelgren, B. (1965). *Vision Res.* 5, 141-150

Woodworth, R.S. and Schlosberg, H. (1954). *Experimental Psychology*, Henry Holt and Company, Inc.

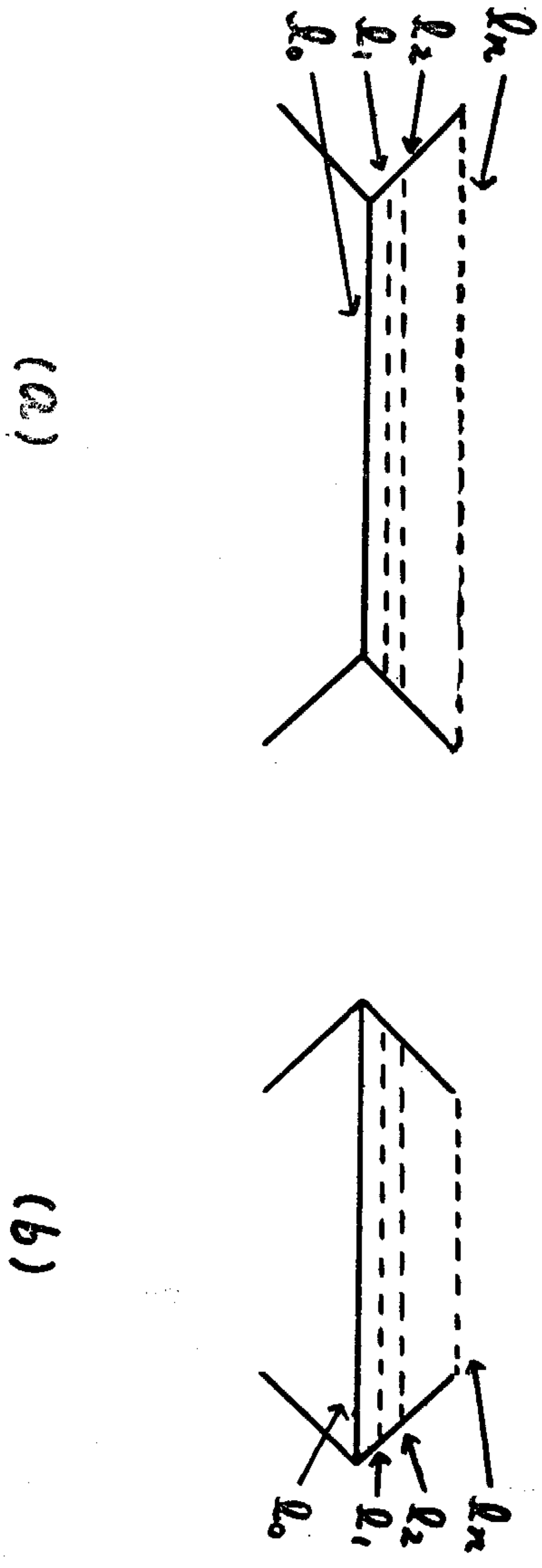
(a)
l_0
l_1
l_2
l_n
(b)
l_0
l_1
l_2
l_n

Figure 1. Muller-Lyer illusion. l_0 in (a) appears longer than l_0 in (b). $l_1, l_2 \cdots\cdots l_n$ are imaginary lines (see text).

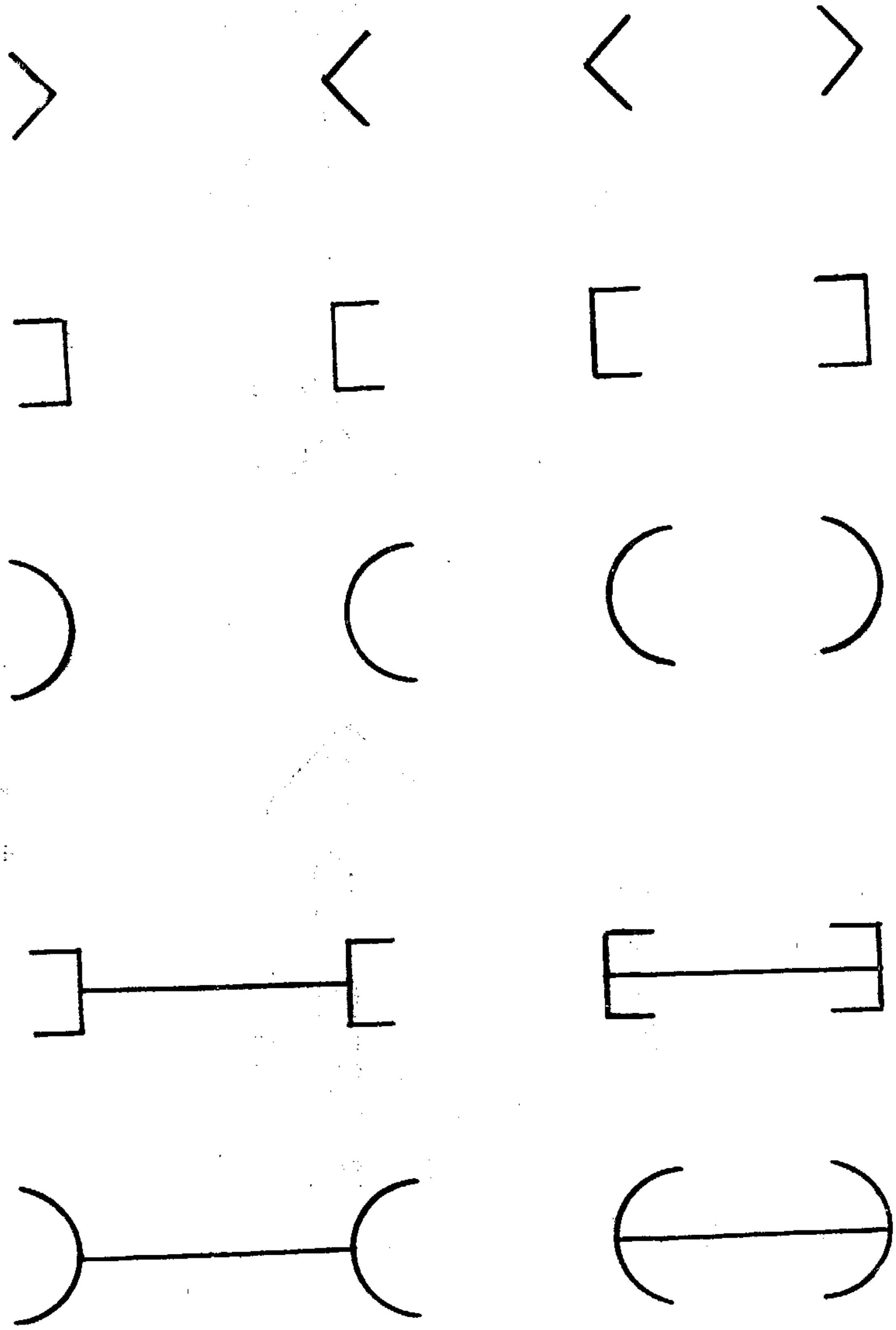

Figure 2. Variations of Muller-Lyer illusion.

Annual Report of the Institute of Physics, Academia Sinica, 1971

Electronic Conduction in Ultra Thin Semi-metal Films

N. T. Liang (梁乃崇) and Shou-yih Wang (王守益)

Institute of physics, Academia Sinica, and
National Tsing Hua University

Abstract

Ultra thin films of Bi on SiO substrate prepared at room temperature and at an approximate evaporation rate 100 Å/min have been observed to have a resistivity drop of about 5 orders of magnitude within an average thickness increase from 95 Å to 105 Å. We also note that other metallic films like Al, Sn, In exhibit much slow rates of the retistivity drop under similar evaporation conditions. The structure of these films has been observed by using an elestron microscope. It is found that the resistivity drop in Bi films follows the change in film structure from discontinuous or island film into quasi-continuous state. The origin of the sudden resistivity drop in Bi has been traced as due to the relatively lower interfacial mobility of Bi islands such that they form quasi-continuous structure without aggregating into segregated large Bi islands. The Al, Sn, In films of nominal average thickness less than 200 Å were not found to form the quasi-continuous structure on SiO substrate.

1. Introduction

An ultra thin film is usually known as the structure in which clusters of the evaporated atoms are formed on the subsrrate. These clusters are called islands or simply small particles. The physical properties have been studied(1),(2) by a number of physicists. The resistivity is found to decrease very rapidly as the nominal average thickness is increased during the evaporation. However, various metallic materials with various insulating substrates exhibit quite different decreasing slopes of resistivity versus thickness. The study of slope is important in the sense that control of the transition between high resistivity and low resistivity might be made possible and applicable as switching device.

In the following we first give a survey of theoretical results related to our problem and then describe experimental procedures. Finally we discuss our results of curves and micrographs.

2. Theoretical Accounts for Electronic Conduction in Ultra Thin Metal Films

The mechanisms of conduction of electron in an ultra thin metallic film in which islands of metallic atoms are randomly distributed are quite different from those in an parallel-sided crystalline film. In the latter type of films electrons are expressed in Bloch waves and the drift velocities are limited by phonon scattering, impurity scattering as well as the size effects. On the contrary, in an aggregated metal films with an insulating substrate one considers transmission propability through barriers. The basic mechanisms of electronic conduction may be classified simply as thermionic and tunnelling through the barriers. The thermionic emission is predominating when the separation between two particles is comparatively large. It is based on the Fermi statistics by which the distribution of electron energies allows finite fraction of electrons to have sufficient energy over the barriers. On the other hand the conduction due to tunnelling through the barriers becomes important when the gaps between metallic islands are relatively short. A brief listing of the different mechanisms of conduction of electrons in an ultra thin film which consists of both island films and quasi-continuous films is given below(3).

1. Thermionic emission. The current density J_{th} can be derived with slight modification of Richardson-Dushman formula as:

$$J_{th}=\frac{4\pi me^2 VKT}{h^3}\, e^{-\overline{\varnothing}/KT}$$

where K is Boltzmann constant, V is the applied potential, $\overline{\varnothing}$ is essentially the overall average potential of the substrate gap between two particles. We will describe $\overline{\varnothing}$ in more detail.

2. Unactivated tunnelling. There necessitates a characteristic Coulombic energy δE for an electronic charge to be injected from one island onto the nearest neighboring island. If $\delta E<KT$, the tunnelling process is essentially unactivated with tunnelling current density

$$J_{ua}=\frac{3.95\times10^{10}}{(\varDelta S)^2}\overline{\varnothing}\left[\sinh\left(\frac{eV}{KT}\right)\right]\frac{(\pi BKT)^2}{\sin\pi BKT}\cdot\left(\frac{KT}{\delta E}\right)\cdot\exp\{-1.025\varDelta S(m^*\overline{\varnothing})^{1/2}\}$$

where the quantities and units are precisely the same as reference (3). Note that the exponential factor is temperature independent.

3. Activated tunnelling. When $\delta E>KT$, the conduction mechanism for cases of large separation between islands should be mainly the activated tunnelling. The current density can be shown as

$$J_{ac}=\frac{1.24\times10^{11}}{(\varDelta S)^2}\overline{\varnothing}\sinh\left(\frac{eV}{KT}\right)\cdot\frac{\pi BKT}{\sin\pi BKT}\cdot e^{-\delta E/KT}\, e^{-1.025\varDelta S(m^*\overline{\varnothing})^{1/2}}$$

in which the symbols and units are given again in reference (3). We note that $\delta E/KT$ appears as exponential.

4. Quasi-continuous conduction. During this stage the structure of film is between the state of islands and the state which consists partly of islands and partly of connected islands. In this type of films the conduction mechanisms are tunnelling and thermionic processes for the discontinuous part and direct metallic conduction limited essentially by boundary scattering and size effects. The impedance of film will be dominated by the discontinuous part because the impedances can be considered as series connection. Since the paths of direct metallic conduction are limited by the size of the particles and connection portion between particls the paths are narrowed microscopically to the order of 100 Å. Thus the appropriate formulas would be those given in 1, 2, 3 above and those for classical and quantum mechanical size effects.

Thermionic emission and quantum mechanical tunnelling of electrons are processes in which electronic potential barrier presents the hindrance to the transmission of the electrons. Consider two metallic islands or particles each of diameter d angstroms and separated s angstroms on a sea of insulating substrate material. The transmission of an electron from one particle to the other would be accomplished via two ways: through free space or through the substrate. Since the potential barrier for free tunnellig is of the order of the work function of the metal and that for substrate tunnelling is roughly the work function of the metal less the electron affinity of the substrate, the free tunnelling current can be shown(3) to be negligible compared to that of substrate tunnelling. The average substrate barrier combined with the influence of metallic particle $\bar{\phi}$ may be described as a sum of various terms in the following:

$$\bar{\phi} = \bar{\phi}_S + \delta\bar{\phi} - \bar{\phi}_I - \bar{\phi}_F - \bar{\phi}_i$$

Where

$\bar{\phi}_s$ is the energy gap between conduction band and the Fermi level of the substrate;

$\delta\phi$ is the energy change of the conduction band edge of the substrate due to the flow of electrons between the substrate and the metallic particle when they are brought into contact;

$\bar{\phi}_I$ is the energy reduction due to image force;

$\bar{\phi}_F$ is the energy reduction due to applied field;

$\bar{\phi}_i$ is the energy reduction due to ionized impurities at the interface.

For both thermionic and quantum mechanical tunnelling processes the overall average potential barrier, $\bar{\phi}$, given above may be taken the same.

The afore-mentioned activation energy δE can be derived from the Coulomb energy difference needed in transfering an electronic charge from one neutral metallic particle to another. The origin of the force lies in the image force and the effective local electric field F'. For small F' the expression of δE can be shown as(3)

$$\delta E = \frac{e^2}{\epsilon\epsilon_0} \cdot \frac{\gamma+S}{\gamma(2\gamma+S)} - F'e(2\gamma+S).$$

For high fields,

$$\delta E = E_c - 2\left(\frac{e^3}{\epsilon\epsilon_0} F'\right)^{1/2}$$

$$E_c = e^2/(\epsilon\epsilon_0\gamma)$$

3. Experimental Procedures

The main procedures are to make ultra thin films by vacuum evaporation, to measure the resistivity changes as they are being evaporated, and to observe the structure of the films using an electron microscope. We first used a high vacuum 3×10^{-6} Torr in our vacuum evaporator system Varian VI-61 to make the substrate system. As shown in Fig. 1 this system contained a thick glass plate (Micro slide glass, made in Japan), an evaporated layer of LiF, another layer of SiO and 8 indium terminals. The layer of SiO (purity 99.9%) was abot 700—900 Å so that it can be transmitted with enough intensity of electron beams to allow an electron-microscopic study. Another use of SiO is its protection(4) against oxidation of films in addition to its function as supporting substrate. The choice of using LiF is due to its ease of detaching the film from the glass base plate when inserting in water. Now we took the substrate system out of the evaporator and connected the conducting leads from the terminals to the outside via electrical feed through. The substrate system was then placed in the evaporator again and the metallic film was now to be evaporated onto the substrate and the resistivity to be measured during the evaporation. The substrate temperature was assumed at room temperature and the rate of evaporation was kept about 100 Å/min. On each substrate system two films were simultaneously evaporated. The metallic substances Bi, Al and Sn were of 59 grade while In was 39. The thickness of each film was measured by using a microbalance(5) of which the quartz crystal was bought from NEVA Co., Japan. The accuracy of the thickness measured was estimated to within 15%. However, we must note that for an island film the thickness does not bear the usual meaning. A Keithley Electrometer of model 610B was used to measure the resistivity of films. Since the readings of the resistance were very large we used two-terminal method instead of the 4-terminal method.

Upon completion with the resistivity mersurement the film with its substrate system was taken out of the evaporator and placed in distilled water. As LiF dissolves in water the metallic film together with the substrate SiO was floating in water and detached from the glass. Then we used small cupper mesh to accomodate the film and it was ready for electron-microscopic study. The electron microscope used was Hitachi's E.M. type Hu-11c-1. Direct observation of the structure of the film and SiO substrate was made possible through transmission of electron-beam. Micrographs were obtained on Bi and Al films as well as the bare substrate SiO.

4. Results and Discussions

As shown in Fig. 2, although the resistivity drops of Bi film on SiO substrate were found to occur within 10 Å the curve Bi (1) occuring between 69Å-79 Å associated with SiO substrate thicker than 1000 Å differs from the curve Bi (2) with substrate thickness 700 Å-900 Å for which the transition takes place between 95A-105A. We also obtained curve Bi (1) when Bi was evaporated directly on the glass substrate without SiO. It has convinced us that the rougher surface condition of Si O for curve Bi (2) was the cause for the shift of transition region. However, since the observation by electron microscope will not be possible for films thicker than 1000 Å we used thinner SiO substrates (700Å-900Å).

The resistivity drops of other films are shown in Fig. 2 for Al, in Fig. 3 for Sn, in Fig. 4 for In(6). Conditions of evaporation for these films and the SiO substrate were kept the same as possible as for Bi. None of these exhibits such sharp resistivity drop as Bi. To resolve the puzzle we may recall the various mechanisms of electronic conduction given in section 2. Each resistivity drop from top to bottom of the semi-logarithm plot respectively in Fig. 2, 3 and 4 correponds to electronic conductions from thermionic emission to quantum mechanical tunnelling and finally to the size-limited quasi-continuous conduction. In case of Bi the surface mobility may be assumed not so high that quasi-continuous structure rather than larger-islands structure is formed as the evaporation proceeds. Thus we would first reach the quasi-continuous conduction. There was an evidence of this model in observing the films with electron microscope. As the intensity of electoron beam was increased we did see the motion of islands such that a number of neighboring islands of the quasi-continuous Bi film got together to become a large island with well-defined boundary of substrate material. This implies that the laternal motion and thus the agregation of islands were created by the impinging electrons of the electron microscope. On the contrary, films of Al, Sn, In could be assumed to have higher interfacial mobility such that they aggregated for a much larger thickness without forming quasi-continuous structure. The electron microscopic findings as given below apparently support this model.

The micrographs of Bi with magnification × 62,500 are shown in Fig. 5, 6, and 7. The pure SiO substrate surface, shown in Fig. 5 appears so fine and smooth that islands on it would be clearly distinguished. Fig. 6 shows the structure of segregated islands or gains with resistance $\sim 2\times10^{11}$ ohms; the two photoes were taken at different places of the same film. Figure 7 shows the quasi-continuous structure of resistance 1.6×10^{8} ohms, with the two photoes taken from two different film at identical conditions. In Fig. 8a with magnification × 62,500 we see clear islands of Al of average thickness 50 Å with resistance 2.2×10^{11} ohms whereas Fig. 8b is just Fig. 8a except the magnification reduces to ×18,750. Fig. 9(a) shows the structure of Al film of thickness 190 Å with magnification × 62,500 and resistance $\sim 2\times10^{8}$ ohms whereas Fig. 9(b) and Fig. 9(c) are taken from the same film but at different locations. The small dots (islands) in Fig. 9 are believed to be the cause of resistance difference from Fig. 8.

Acknowledgement

We are indebted to the National Science Council for financially supporting the project and and to the Chung-Cheng College of Science and Engineering and its working staff for their supprts and technical helps on the electron microscope studies.

References

(1) C.A. Neugenbauer, Phys. of Thin Films, P. 1 (1934). Academic Press, ed. by G. Hass and R.E. Thun.

(2) R.M. Hill, Contemp. Phys. Vol. 10, No. 3, pp.221-240 (1969).

(3) R.M. Hill, Proc. Roy. Soc. A, **309**, 377-395 (1969).

(4) N.T. Liang and S.Y. Wang, Proceedings of the National Science Council, No. 5, pp. 41-42 (1972).

(5) Yu-Tung Yang, Nuclear Instruments and Methods **66** (1968) 341-342.

(6) This figure is taken from the work of Chenshi Tung and Min-Hsiung Tsai, via private communication.

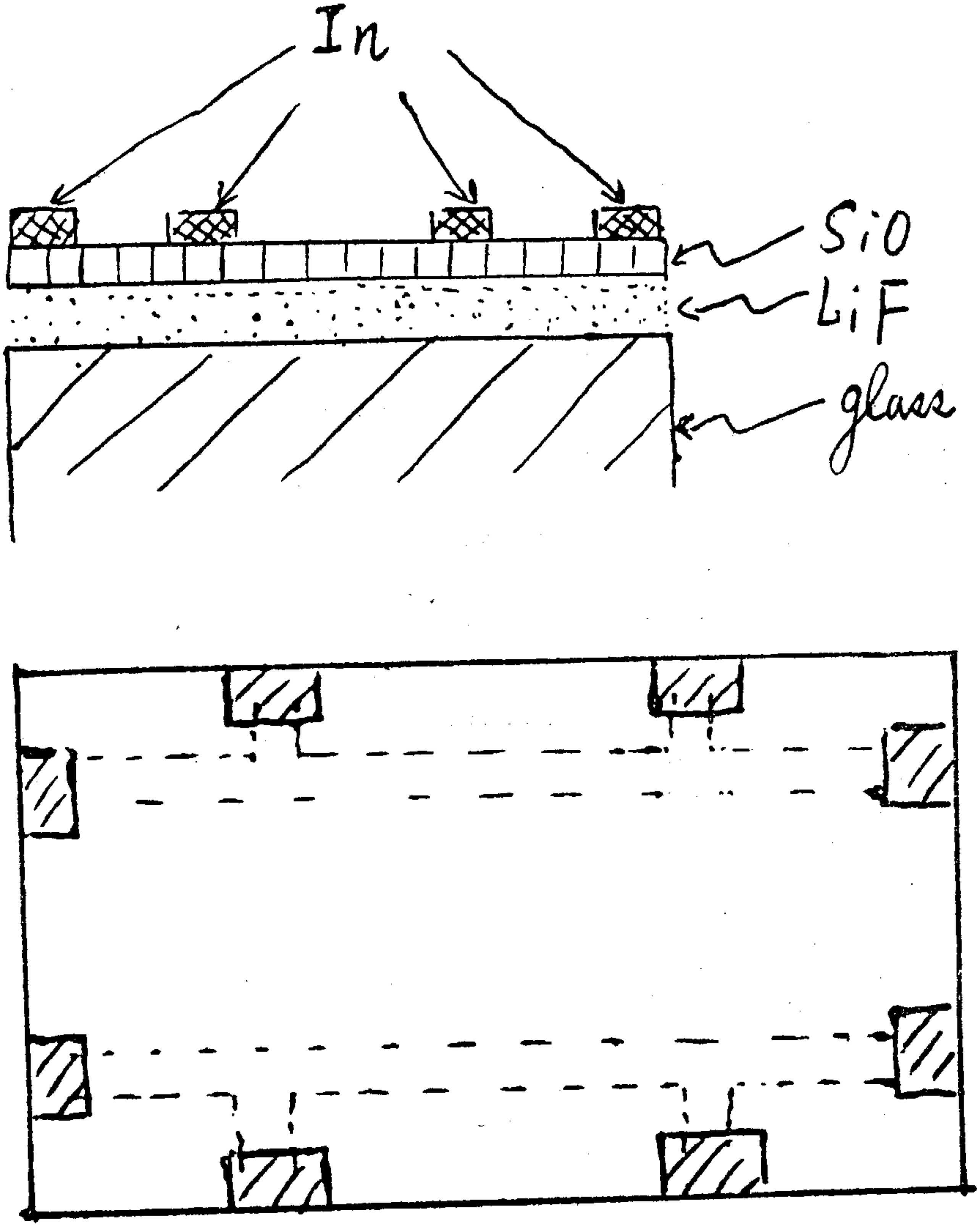
In
SiO
LiF
glass

Fig. I

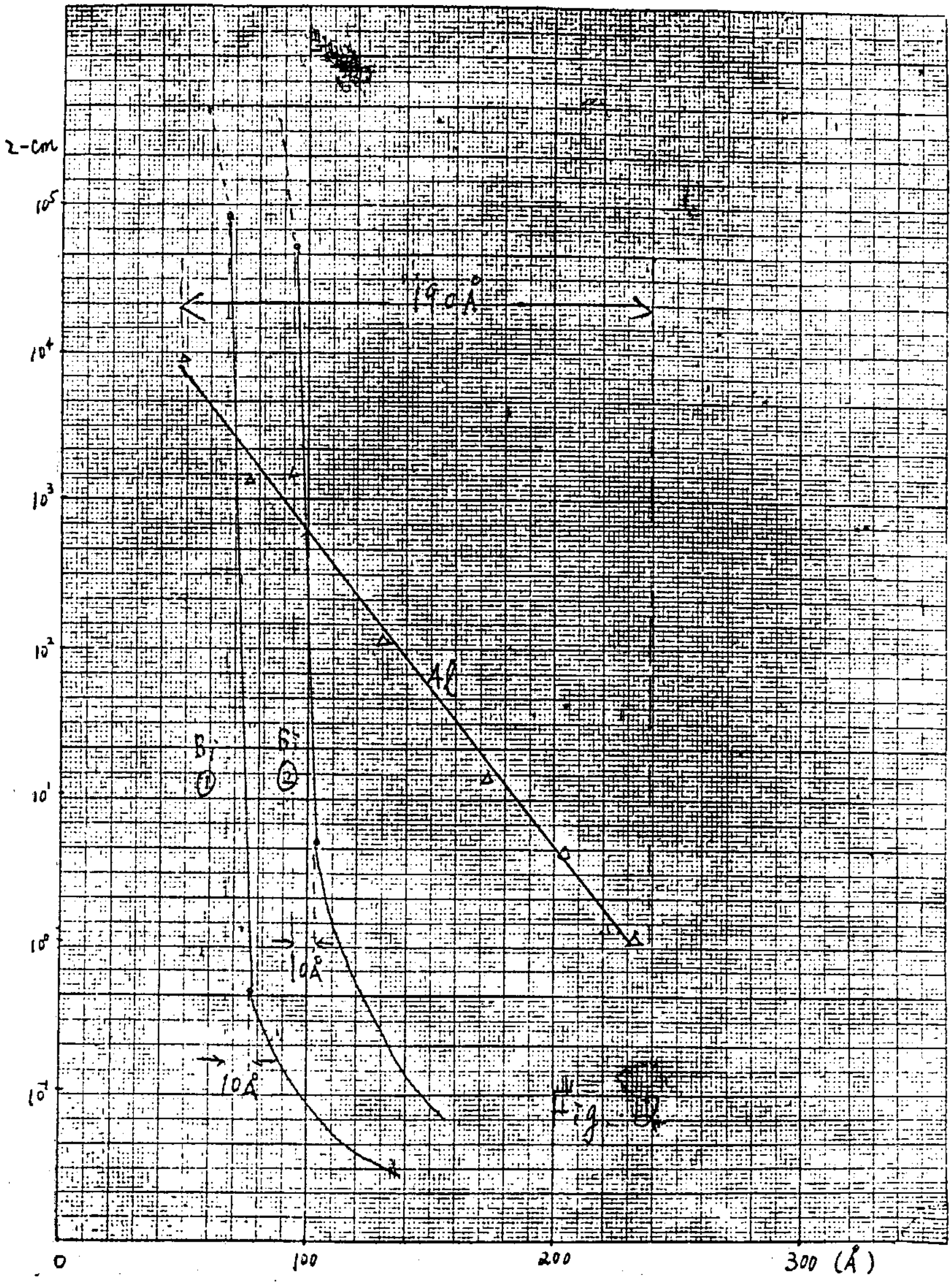
Ω-cm
10⁵
10⁴
10³
10²
10¹
10⁰
10⁻¹
190Å
Al
Bi
①
Sb
②
10Å
10Å
Fig. II
0
100
200
300 (Å)

Fig. 2

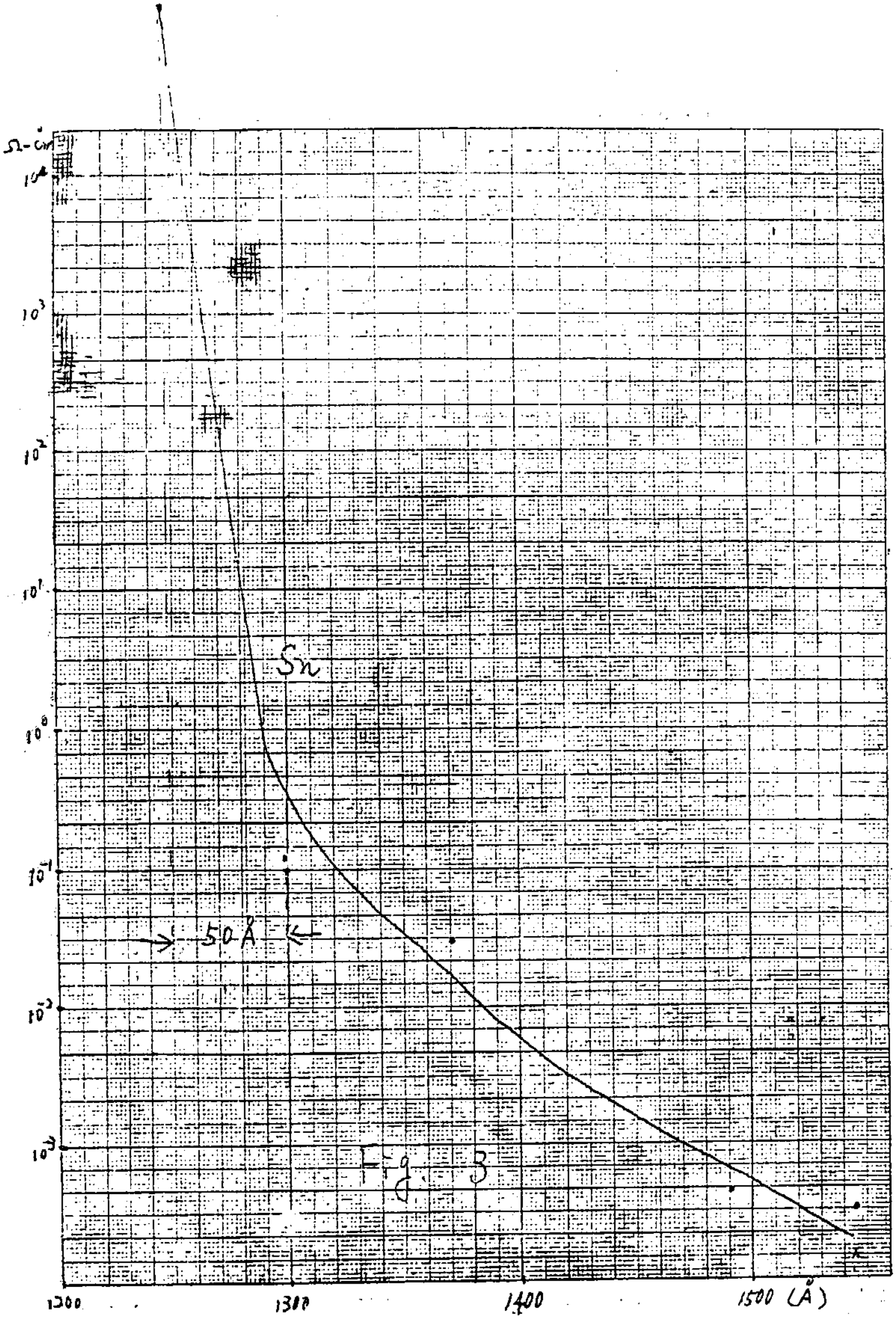
Ω-cm
10⁴
10³
10²
10¹
10⁰
10⁻¹
10⁻²
10⁻³
Sn
→ 50Å ←
Fig. 3
1200
1300
1400
1500 (Å)

Fig. 3

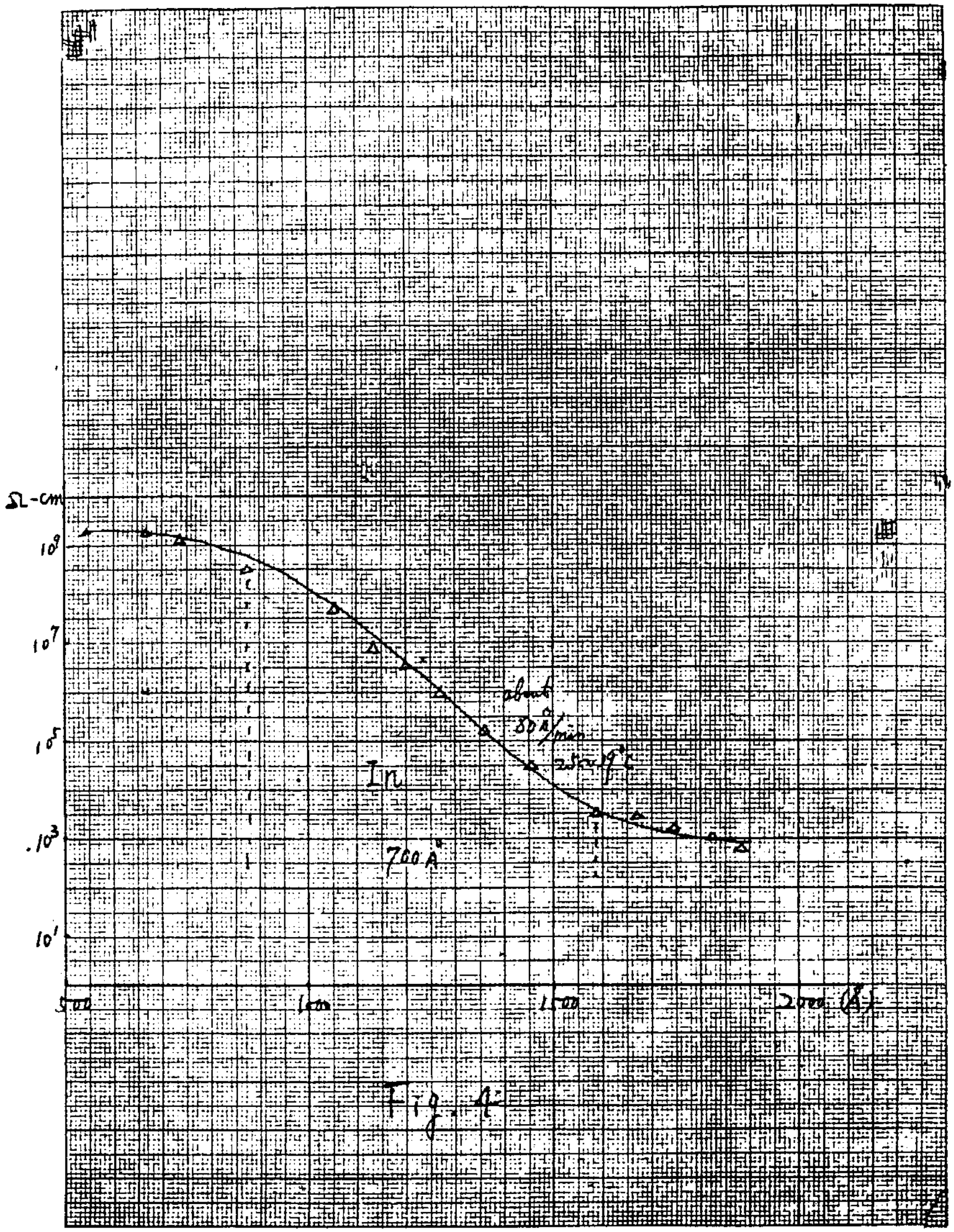
Ω-cm
10^9
10^7
10^5
10^3
10^1
500
1000
1500
2000 (Å)
about
30Å/min
25~19°C
In
700Å
Fig. 4

Fig. 4

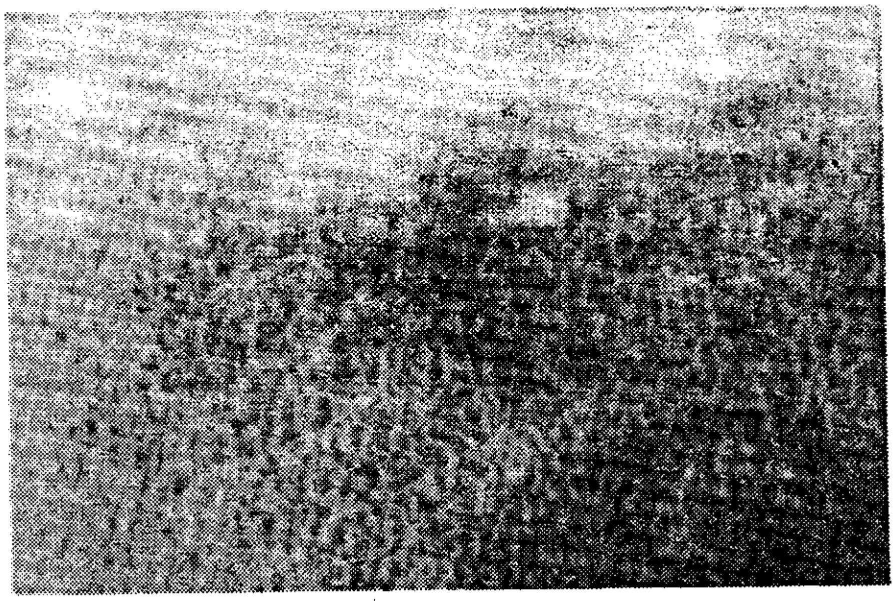

Fig. 5

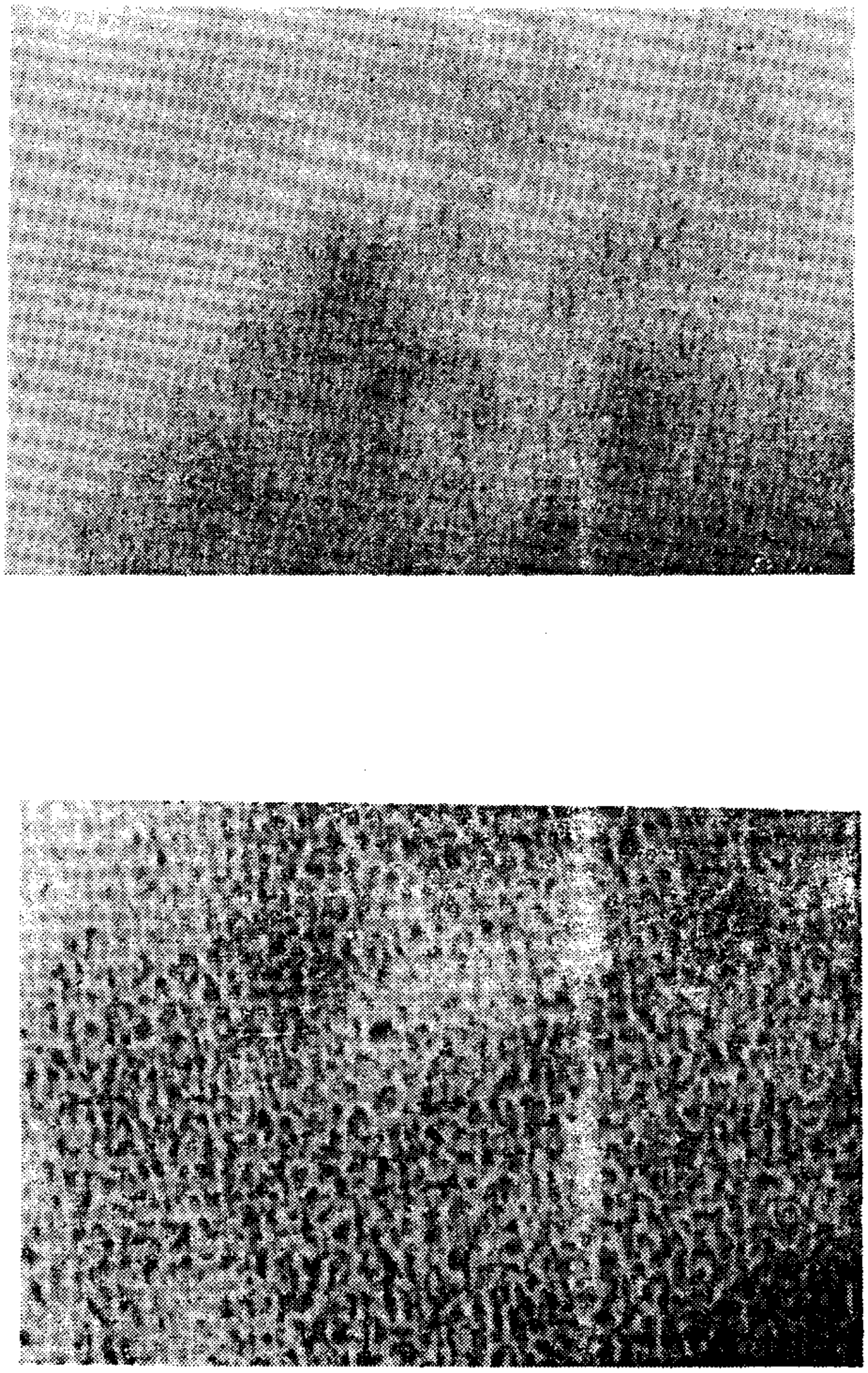

Fig. 6

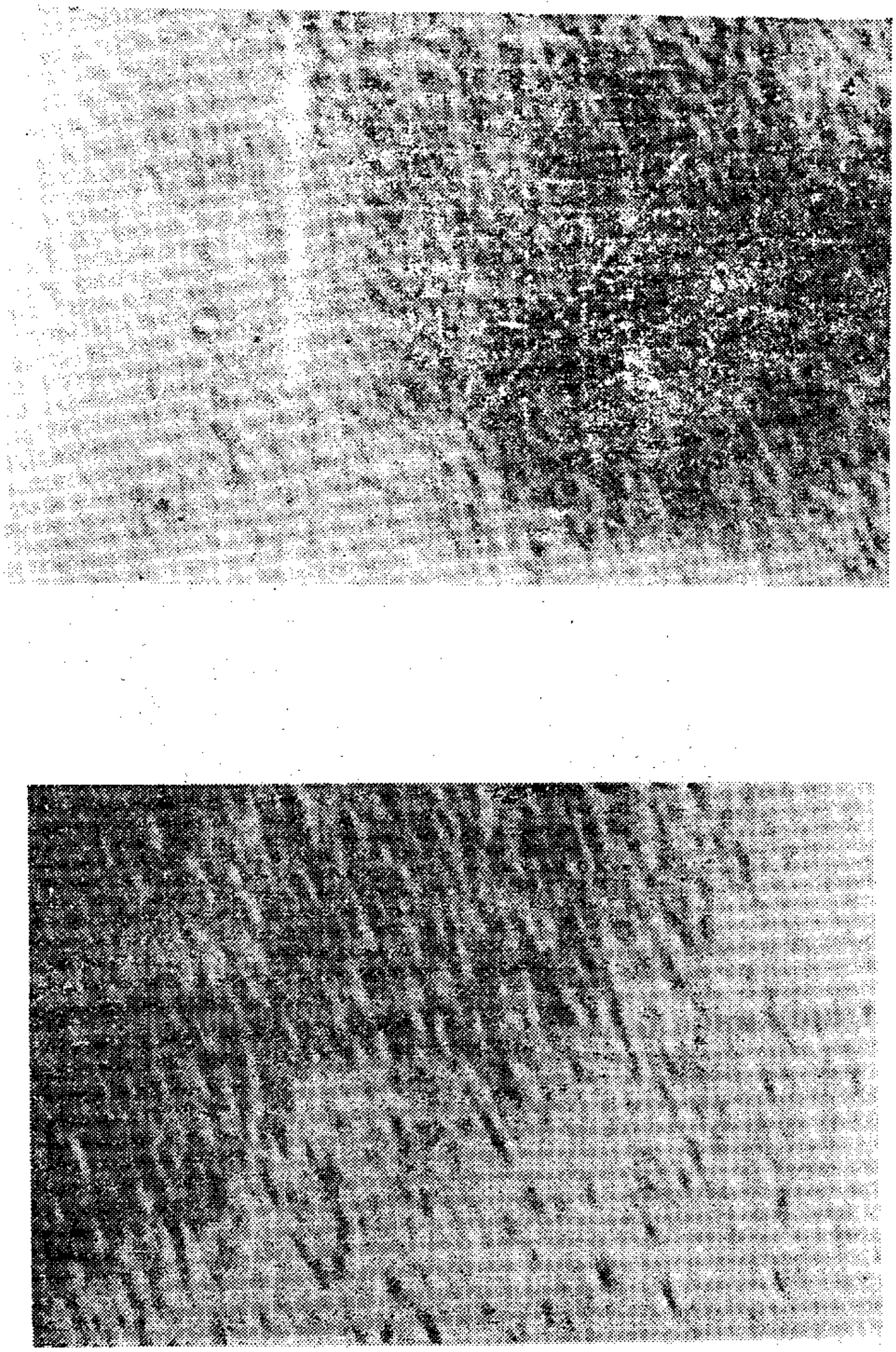

Fig. 7

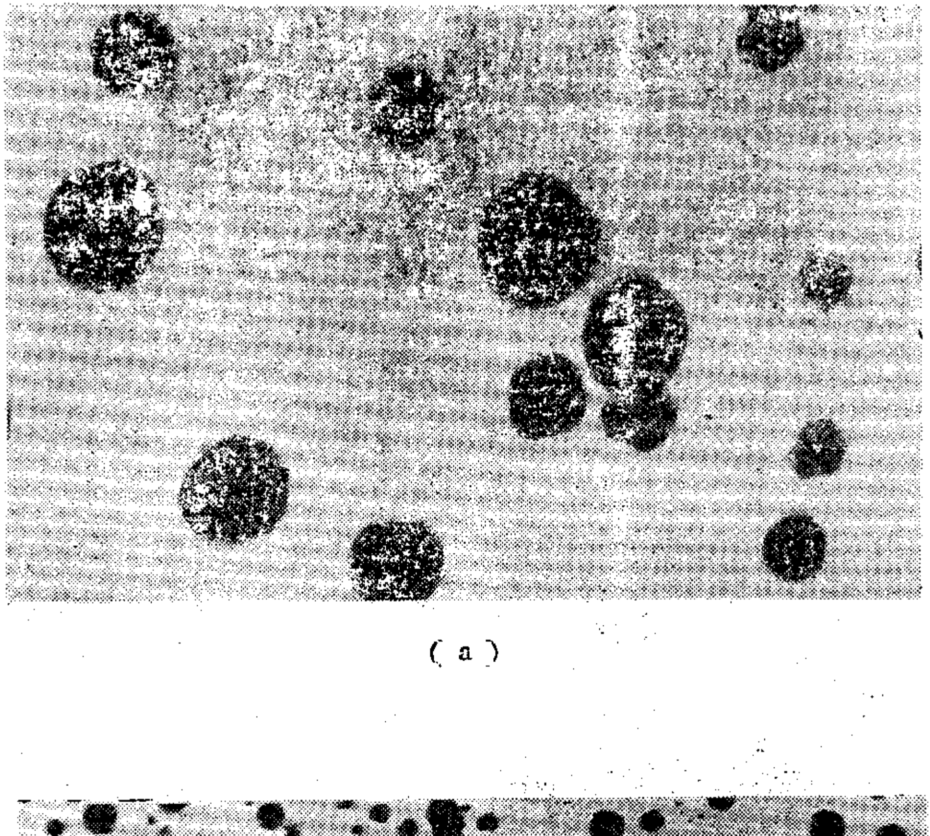

(a)

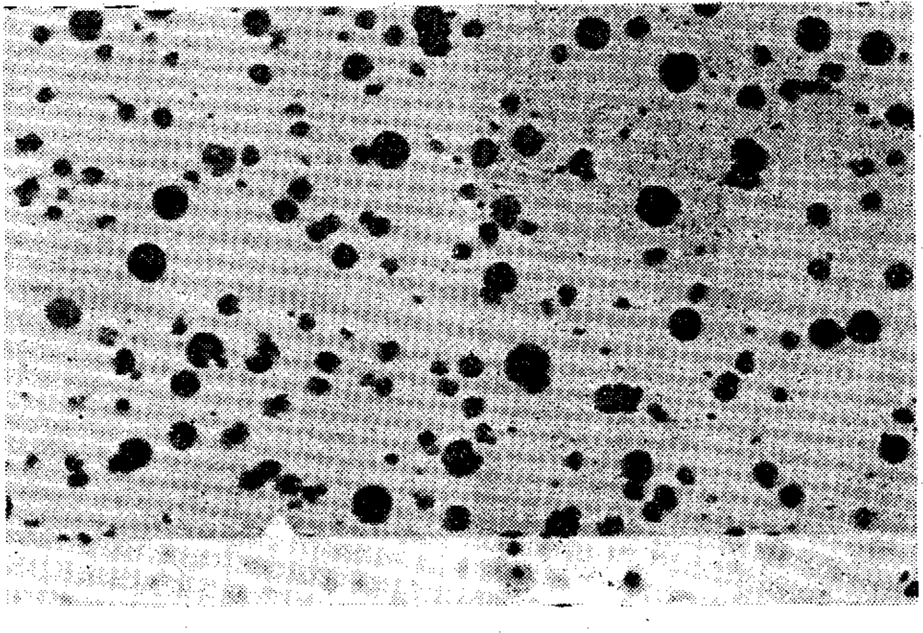

(b)

Fig. 8

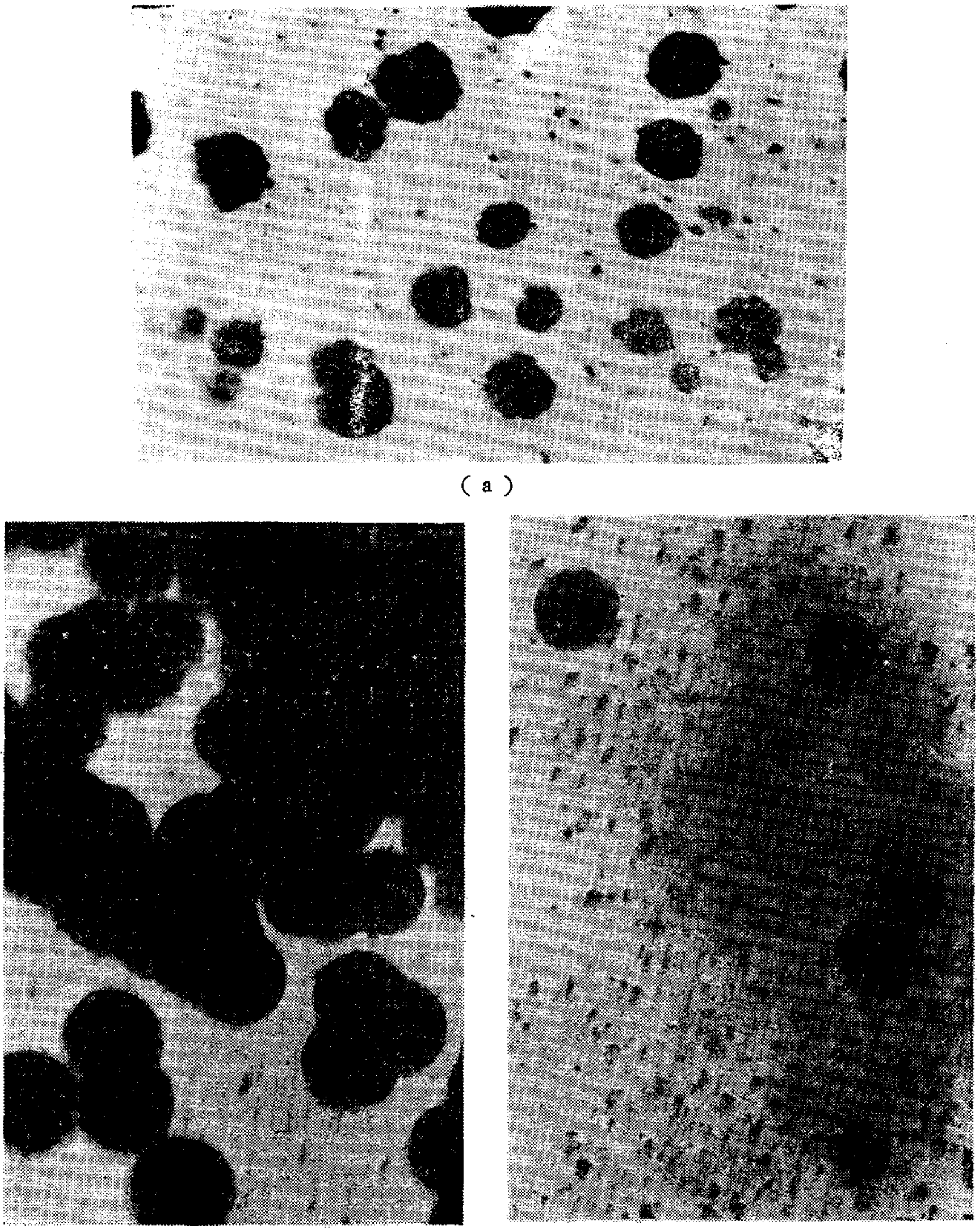

(a)

(b)

(c)

Fig. 9

大氣及颱風運動模型*

I. 邊界條件

大氣物理組同仁

1. 一般簡介

一般在研討大氣及颱風運動變化時，大多採取二種方法：第一種方法係針對某一種大氣現象，尋求有關的大氣變化因子，利用統計方法客觀地推測該種大氣現象的變化原則（Simpson, 1971; Brand, 1972；大氣物理組同仁，1972）。第二種方法係直接解控制大氣現象變化的流力、熱力等方程式，探尋大氣運動變化原則。

在第二種方法中，我們一般假設在離地面 25 公里以內的大氣爲一連續流體，基本的流力與熱力公式僅能控制大到能受地球自轉影響而又合乎 hydrostatic 情況的大氣系統。因之，在利用數值分析方法解大氣與颱風現象變化時就必需設法將小規模大氣變化現象以與控制方程式中有關變數表示出來，此方面 Smagorinsky, Manabe, Benwell, Bushby, Kasahara, Mintz 等人在彼等論着中曾提出許多建議。

國內一直鮮人在此方面進行研究，加上國內目前電子計算機的運用情況，我們將從較簡單的模型開始探討。

2. 物理數學模型

一開始我們先不考慮熱源、地面及洋面摩擦阻力等。控制大氣及颱風運動的基本方程式爲（在 x, y, p coordinates 下）：

Equation of Motion

$$\frac{dV}{dt}+k\times f\ V+g\ \nabla z=0 \qquad (1)$$

式中 V 爲水平速度向量，k 爲垂直單位向量，g 爲重力加速度，z 爲高度，t 爲時間，f 爲 Coriolis 參數。

Hydrostatic Equation

大氣層的厚度遠小於地球半徑，大氣流體運動在垂直方向可設爲

$$\frac{\partial z}{\partial p}=-\frac{1}{\rho g} \qquad (2)$$

成式中爲壓力，爲大氣質量。

Equation of Continuity

$$\nabla\cdot V+\frac{\partial\omega}{\partial p}=0 \qquad (3)$$

式中 $\omega\equiv\frac{dp}{dt}$

Equation of State

$$p=\rho RT \qquad (4)$$

式中 R 爲空氣常數，T 爲溫度

---

*本文承行政院國家科學委員會支助完成。

Fist Law of Thermodynamics

$$\frac{d\theta}{dt}=0 \tag{5}$$

式中 θ 爲 potential temperature

$$\theta\equiv T\left(\frac{p_{1000}}{p}\right)^{\frac{R}{C_P}} \tag{6}$$

式中 p_{1000} 爲 1000 mb.處之壓力，C_P 爲等壓時大氣之 specific heat。 以上六組方程式爲控制大氣運動變化的基本方程式（包含熱源等較完整方程式參見 shuman & Hovermale, 1968），原則上可解六個未知數 v, z, ω, ρ, θ, T。不過迄今在數學上仍不克解（exactly）此六組方程式，因之欲了解大氣現象之變化，祗好藉數值方法求其近似解。

3. Baroclinic Model

在 Rossby number 及 Froude number 不大的情形下，Eq. 2 代入 Eq. 1 化簡可得

$$\frac{\partial\zeta}{\partial t}+\boldsymbol{V}\cdot\nabla(\zeta+f)-(\zeta+f)\frac{\partial\omega}{\partial p}+\omega\frac{\partial\zeta}{\partial p}+\boldsymbol{k}\cdot\nabla\omega\times\frac{\partial\boldsymbol{V}}{\partial p}=0 \tag{7}$$

式中 $\zeta=\nabla\times V$，如果我們假設（Thompson, 1961）

$$\boldsymbol{V}=\boldsymbol{k}\times\frac{g}{f}\nabla z \quad \text{or } \zeta=\frac{g}{f}\nabla^2 z \tag{8}$$

代入 Eq.7 化簡可得（Haltiner, 1971）

$$\frac{\partial}{\partial t}\nabla^2 z=-J\ (z,\ \zeta+f)+\frac{\overline{f}^2}{g}\frac{\partial\omega}{\partial p}=F^1\ (z,\ \omega) \tag{9}$$

式中一代表該值在空間參平均值。此時原來運動方程式中的 high-frequency gravity-inertia waves 已被刪除，僅留下 low-frequency, quasi-geostrophic motion（Arakawa, 1971），將 Eqs. 2, 3, 4, 6, 8 代入 ζ 中化簡可得

$$\frac{\partial}{\partial t}\frac{\partial z}{\partial p}=-\frac{g}{f}J\ (z,\frac{\partial z}{\partial p})+\sigma\omega=F^2(z,\ \omega) \tag{10}$$

式中

$$\sigma=\overline{\frac{1}{\rho g\theta}\frac{\partial\theta}{\partial p}}=-\overline{\frac{\partial z}{\partial p}\frac{\partial\ \ln\theta}{\partial p}}$$

由此可見當 geostrophic wind assumption 加入時，原列六組方程式簡化爲由 Eqs. 9 及 10 解 z 及 ω 二個未知數。爲運算方便，∇^2 (Eq. 10)$-\frac{\partial}{\partial p}$(Eq. 9) 可得

$$\nabla^2\sigma\omega-\frac{\overline{f}^2}{g}\frac{\partial^2\omega}{\partial p^2}=\frac{g}{f}\nabla^2[J(z,\frac{\partial z}{\partial p})]-\frac{\partial}{\partial p}[J(z,\frac{g}{f}\nabla^2 z+f)]=F^3(z) \tag{11}$$

此爲一般常見的 ω—equation。由於式中無時間因素，ω 可直接由 z 求得。

4. Numerical Scheme

在利用 finite difference method 解 Eqs. 9, 10 及 11 時所用水平及垂直方向的 grid system 如 Figs. 1 及 2 所示。

在此 grid system 下，$F^3(z)$ 已知時，Eq. 11 可藉下敍 iteration procedure (Wang, 1970) 解 ω

$$\omega^{n+1}_{ijk}=\Big[\omega_{i+1jk}+\omega_{i-1jk}+\omega_{ij+1k}+\omega_{ij-1k}-\frac{\overline{f}^2d^2}{\sigma gm^2\Delta P^2}(\omega_{ijk+1}+\omega_{ijk-1})$$

$$-\frac{F^3_{ijk}d^2}{\sigma m^2}\Big]^n\Big/\Big[4-\frac{2\overline{f}^2d^2}{\sigma gm^2\Delta p^2}\Big]^n \qquad (12)$$

式中 n 及 $n+1$ 爲 iteration procedure 中二連續步驟，m 爲 amplification factor, d 爲 grid length. 在適宜邊界值 Eq. 12 可重複運用直至

$$\text{Max.}\,|\omega^{n+10}_{ijk}-\omega^{n}_{ijk}|\leq\epsilon$$

同理，Eq. 9 在 finite difference form 時可化爲

$$\frac{\partial z}{\partial t}^{n+1}_{ijk}=0.25\Big[\frac{\partial z}{\partial t}_{i+1jk}+\frac{\partial z}{\partial t}_{i-1jk}+\frac{\partial z}{\partial t}_{ij+1k}+\frac{\partial z}{\partial t}_{ij-1k}-F^1_{ijk}\Big]^n \qquad (14)$$

此式可重複用以求 $\frac{\partial z}{\partial t}$，直至

$$\text{Max.}\,\Big|\frac{\partial z}{\partial t}^{n+10}_{ijk}-\frac{\partial z}{\partial t}^{n}_{ijk}\Big|\leq\epsilon \qquad (15)$$

Eq. 10 可化爲

$$\partial z^{t+\Delta t}_{ijk}=\partial z^{t-\Delta t}_{ijk}+2\Delta t\cdot F^1_{ijk} \quad \text{at other time steps} \qquad (16)$$

$$\partial z^{t+\Delta t}_{ijk}=\partial z^{t}_{ijk}+\Delta t\cdot F^1_{ijk} \quad \text{at initial time step} \qquad (17)$$

$$\partial z_{ijk}\equiv z_{ijk}-z_{ijk-1} \qquad (18)$$

中爲 Δt 中 finite difference 之此 time increment,

$$\Delta t\leq\text{Min.}\frac{d}{\frac{g}{f}\Big(\Big|\frac{\partial z}{\partial x}\Big|+\Big|\frac{\partial z}{\partial y}\Big|\Big)+\Big|\omega\cdot\frac{\partial z}{\partial p}\cdot\frac{d}{d_{\Delta P}}\Big|} \qquad (19)$$

此爲 von Neumann necessary condition (Richtmyer & Morton. 1967; Hawkins, 1972) $d_{\Delta P}$ 爲 Δp 之厚度。在上敍 finite-difference system 中，除了 initial time step 用 forward difference 及 (Arakawa, 1963)

$$J(A,\ B)=\frac{1}{3}(J^1+J^2+J^3) \qquad (20)$$

如此可保持 squared vorticity 及 kinetic energy 不變，式中

$$J^1=[(A_{i+1j}-A_{i-1j})(B_{ij+1}-B_{ij-1})-(A_{ij+1}-A_{ij-1})(B_{i+1j}-B_{i-1j})]/4d^2$$

$$J^2=[A_{i+1j}(B_{i+1j+1}-B_{i+1j-1})-A_{i-1j}(B_{i-1j+1}-B_{i-1j-1})-A_{ij+1}(B_{i+1\ j+1}$$
$$-B_{i-1\ j+1})+A_{ij-1}(B_{i+1\ j-1}-B_{i-1\ j-1})]/4d^2$$

$$J^3=[A_{i+1\ j+1}(B_{ij+1}-B_{i+1j})-A_{j-1\ j-1}(B_{i-1j}-B_{ij-1})+A_{i-1\ j+1}(B_{i-1j}$$
$$-B_{ij+1})-A_{i+1\ j-1}(B_{ij-1}-B_{j+1j})]/4d^2$$

外，其餘皆用 center difference.

Numerical procedure 如圖 3 所示。

其 boundary conditions 在垂直面上爲

$$\omega=0 \quad \text{at 200mb 及 1000mb} \qquad (21)$$

在水平面上除假設 time domain 內 z at boundary 不變外，並假設

A. Free-slip boundary condiction

假設大氣在 boundary 不受摩阻力可自由流動，亦即在方向 boundary $\frac{\partial v}{\partial x}=0$，在 y 方向 boundary $\frac{\partial u}{\partial y}=0$, 可得

$$z_{boundary\ 外一層}=2z_{boundary}-z_{boundary\ 內一層} \tag{22}$$

而由 Fq. 10 可得

$$\omega_{boundary}=-\frac{g}{\sigma \bar{f}}J\left(z,\frac{\partial z}{\partial p}\right)_{boundary} \tag{23}$$

B. Fixed-boundary condition

假設 z at boundary 及 boundary 外一層在 time domain 內皆不變，$\omega_{boundary}$ 可由 Eq. 23求得。

5. Test Run

在 test run 時，我們任意以 1971 年九月廿一日 Bess 颱風時的天氣圖爲分析對象 。 Computation domain 如圖四所示。300mb, 500mb 及 700mb 的 z 值直接由天氣圖中讀出，900mb 的 z 值由下式求取

$$z_4=\frac{1}{21}\left(32\,z_{at\ 850mb}-14z_3+3z_2\right) \tag{24}$$

由於本文主要目的在探討不同 boundary conditions 在有限 domain 情形下 solutions 的變化，因之 initial data 的 smoothing 等 (Hawkins, 1972) 這兒將不考慮。

在 test run 中

$NX=20$

$NY=14$

$d=3.322\times10^5$m

$\Delta P=200$mb

$g=9.8$m/sec^2

$\sigma=-0.00355$ m/mb^2

$\epsilon=10^{-6}$

$\bar{f}=0.658\times10^{-4}$ sec^{-1}

$R/C_P=\frac{2}{7}$

boundary 取在 computation domain 內一層 (即 $i=2$, 19; $j=2$, 13)

z in meters, ω in mb/sec.

$d_{\Delta P}\cong2.15\times10^3$m.

Figure 5 爲 initial z-field, 圖中顯示颱風中心位置在 $i=12$, $j=6$ 附近，亦即東經 130° 北緯 23° 附近。在 z_4 (at 900mb) 圖中可看出 computation domain 東北方向有另一低壓，此低壓在 z-field boundary 上且變化極快，與假設 z-value 在 boundary 不變相去甚遠。此問題在進一步探討颱風運動時，將藉擴充 computation domain (say 20×20 grids) 探討之。

Figure 6 顯示在 free-slip boundary condition 下 12 小時後之 z-field。由於本文不考慮 heat source (latent heat, sensible heat etc.)，大部分 z-field 開始 filling. 此時颱風中心 ($i=11$, $i=6$) 向西移動了一個 grid size 左右，與實際颱風運動情形相似。等高線分佈情形與 $T=0.0$ 時相類似。

爲了看一下一種錯誤的 boundary condition 所能引起的後果，這兒我們令

$$\begin{cases} z_{boundary}\ \overline{\text{外一層}} = z_{boundary} \\ \omega_{boundary}\ \text{外一層} = \omega_{bonudary} \end{cases}$$

Figure 7 顯示在這種條件下 12 小時後的 z-field。此時 computation domain 東北角出現一極不合理的 pressure low，顯然由於上列條件不能同時適合方程式所致。

Figure 8-1 顯示在 fixed boundary condition 下 11.67 小時後之 z-field。其結果與 free-slip boundary condition (Fig. 6) 所得極爲類似。唯一的區別在 z_4 的東北方，fixed boundary condition 時此處仍保持 initial stage 的低壓，而 free-slip boundary condition 下，此低壓已不甚顯着。此二 boundary condition 孰優孰劣甚難定言，一般而言如 computation domain 够大，boundary 在 computation 內變化不大時，二種 boundary condition 應給予類似答案。在 computation domain 有一定範圍（且不甚大時）時，free-slip boundary condition 可能會給予較客觀的天氣變動情形（雖然不一定較準確）。

Figure 8-2 爲在 fixed boundary condition 下 23.53 小時後之 z-field。此時颱風中心 ($i=10$, $j=7$) 向西北方向又移動了一個 grid size 左右，此與實際颱風路徑相似（大氣物理組同仁，1972）。唯由於沒有 heat supply，颱風强度 decay 的異常之快。

Figures 9-1 and 9-2 顯示在下列 boundary conditions 時 12 小時及 24 小時的 z-field,

$$\begin{cases} \dfrac{\partial z}{\partial x} = 0 & \text{at } x\text{-direction boundary} \\ \dfrac{\partial z}{\partial y} = 0 & \text{at } y\text{-direction boundary} \\ \omega_{boundary} = 0 & \end{cases}$$

這種 boundary condition 用的人很多，physically 這表示在 boundary 時，大氣祇能垂直 boundary 而流動 (under geostrophic wind assumption)。因之在等高線與 boundary 交角遠離直角時，容易發生誤差。比較 Figs. 8 and 9 時可以發現接近北部 boundary 相差要必東西邊 boundarys 時爲大。

6. 結論與建議

§. 本文主旨在探討不同 boundary condition 下，solutions 可能發生的變化，Fig. 7 顯示錯誤 boundary condition 下引起的不合理結果，Figs. 6 and 8 顯示 boundary condition 正確時的結果，在有限 computation domain 時 free slip boundary condition 似乎能有限度的考慮 boundary 的變化。Fig. 9 顯示一種不違背 governing equations 但有較大缺陷的 boundary condition 下的結果。

§. 雖然本文不考慮 heat supply, 24 小時以內大氣及颱風現象之變化仍可以 baroclinic model 大致表示出來。進一步利用較大 computation domain 並考慮熱源的話，應可更精確的探討大氣及颱風現象之運動。

§. 本文所用 iteration method (Eqs. 12 and 14)，其 convergence speed 與利用 over-relaxation 方法 (with relaxation factor=0.35 for two-dimensional case, relaxation factor=0.25 for three-dimensional case) 相類似。

7. 後　　記

參加本專題研究之大氣物理組同仁包括汪羣從、彭立、簡來成、馬天驥、張能復、張月珠、梁文傑等人。本研究承中央氣象局供給資料，淸華大學計算機中心供使用 IBM 1130 電子計算機，謹致謝意。

參考文獻

Arakawa, A., Design of the UCLA General Circulation Model, Dept. Meteoro., UCLA, 1971.

Brand, S., The Tropical Cyclone Research Program at the Environmental Prediction Research Facility, Presented at the Tropical Cyclone Conference, 6-11 Feb. 1972, Tokyo.

Haltiner, G. J., Numerical Weather Prediction, John Wiley & Sons, Inc., N. Y. 1971.

Hawkins, H. F. Jr., Development of a Seven-level, Balanced, Diagnostic Model and Its Application to Three Disparate Tropical Disturbances, NOAA Tech. Memo. ERL NHRL-98,1972.

Richtmyer, R. D. & K. W. Morton, Difference Methods for Initial-Value Problems, Interscience Publishers, N. Y., 1967.

Shuman, F. G. & J. B. Hovermale, An Operational 6-layer Primitive Equation Model, J. Appl. Meteoro., 7, 525, 1968.

Simpson, R. H., The Decision Process in Hurricane Foreeasting, NOAA Tech. Memo. NWS SR-53, 1971.

Staff Members of Electronic Computation Center, 72-hr Baroclinic Forecast by the Diabatic Quasi-Geostrophic Model, J. Meteoro. Soc. Japan, 43, 246, 1965.

Thompson, P. D., Numerical Weather Analysis and Prediction, Macmillan, N. Y., 1961.

Wang, C. T., Drop-Water Impact, Annual Report of the Institute of Physics, Academia Sinica, 1970.

大氣物理組同仁，颱風中心之運動，中央研究院物理研究所集刊第二卷，1971.

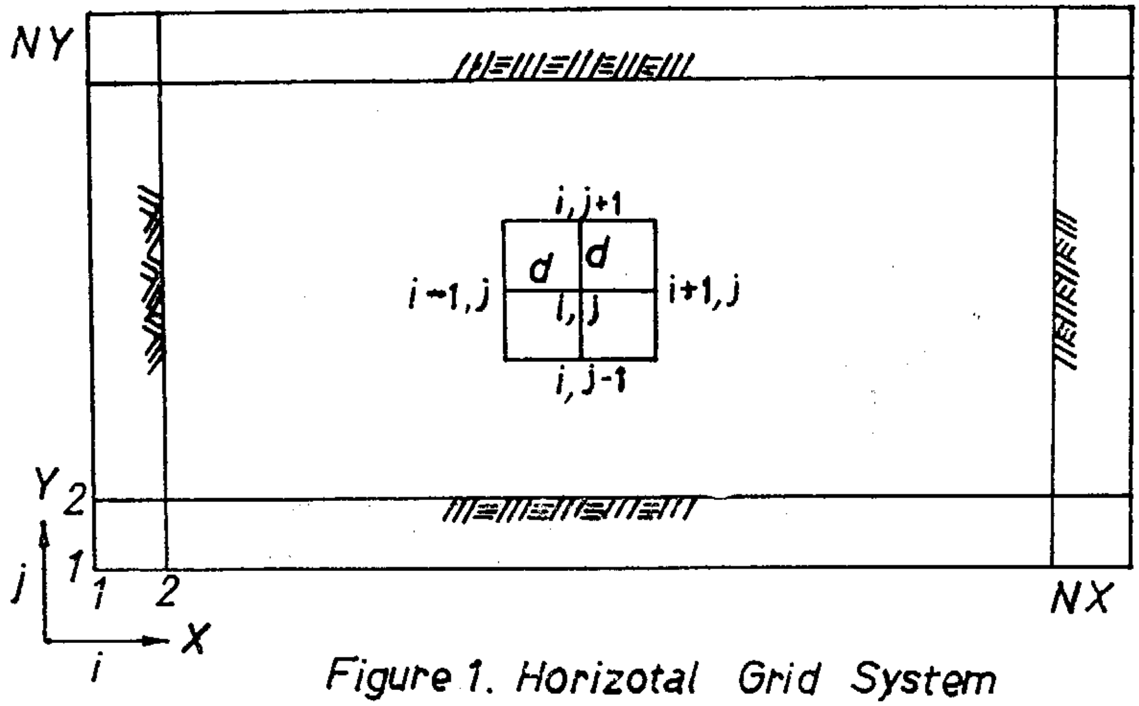
NY
i, j+1
d
d
i-1, j
i, j
i+1, j
i, j-1
Y
2
1
j
1
2
NX
X
i

Figure 1. Horizotal Grid System

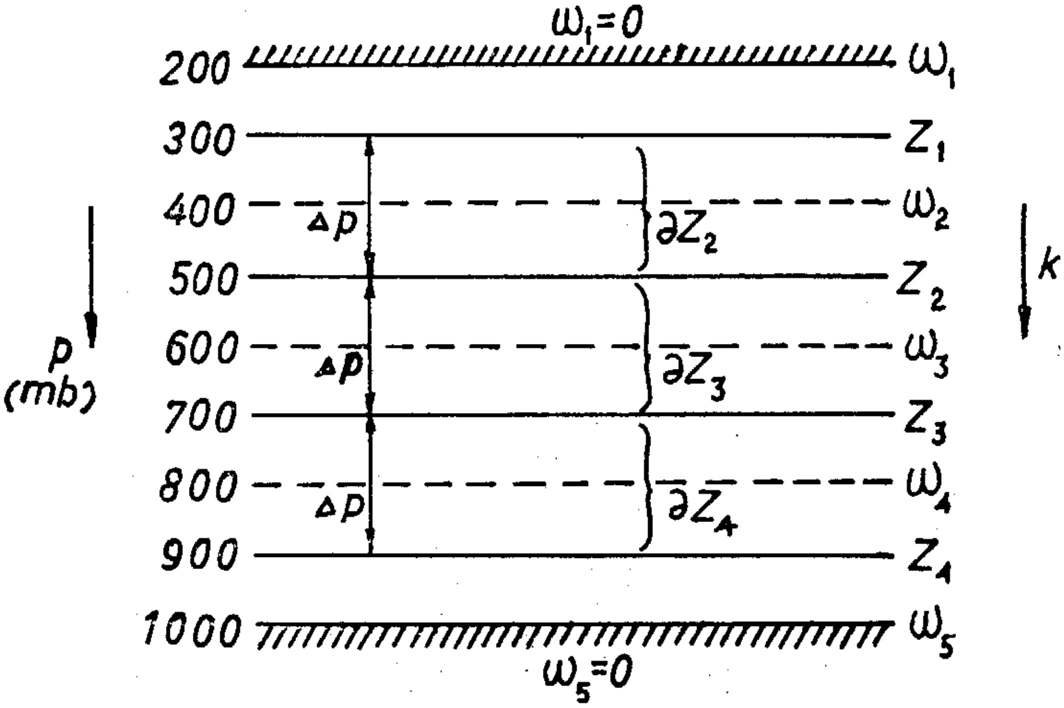
ω1=0
200
ω1
300
Z1
400
ω2
Δp
∂Z2
500
Z2
k
p
(mb)
600
ω3
Δp
∂Z3
700
Z3
800
ω4
Δp
∂Z4
900
Z4
1000
ω5
ω5=0

Figure 2. Vertical Grid System

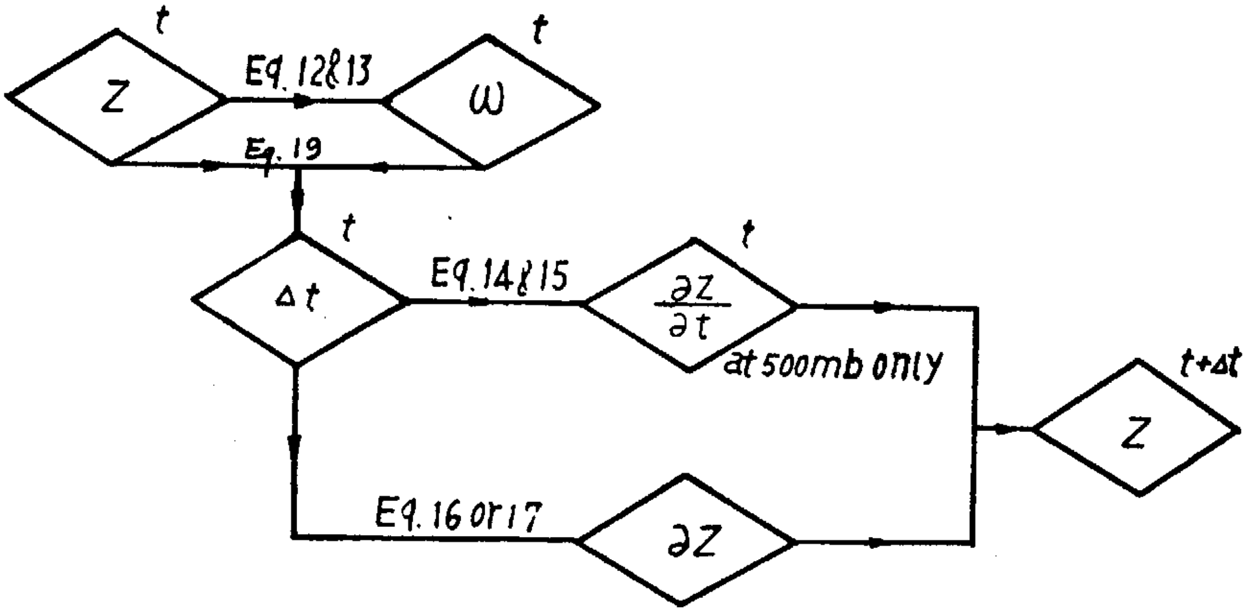
Z
t
Eq. 12&13
ω
t
Eq. 19
Δt
t
Eq. 14&15
∂Z/∂t
t
at 500mb only
Z
t+Δt
Eq. 16 or 17
∂Z

Figure 3 Numerical Procedure

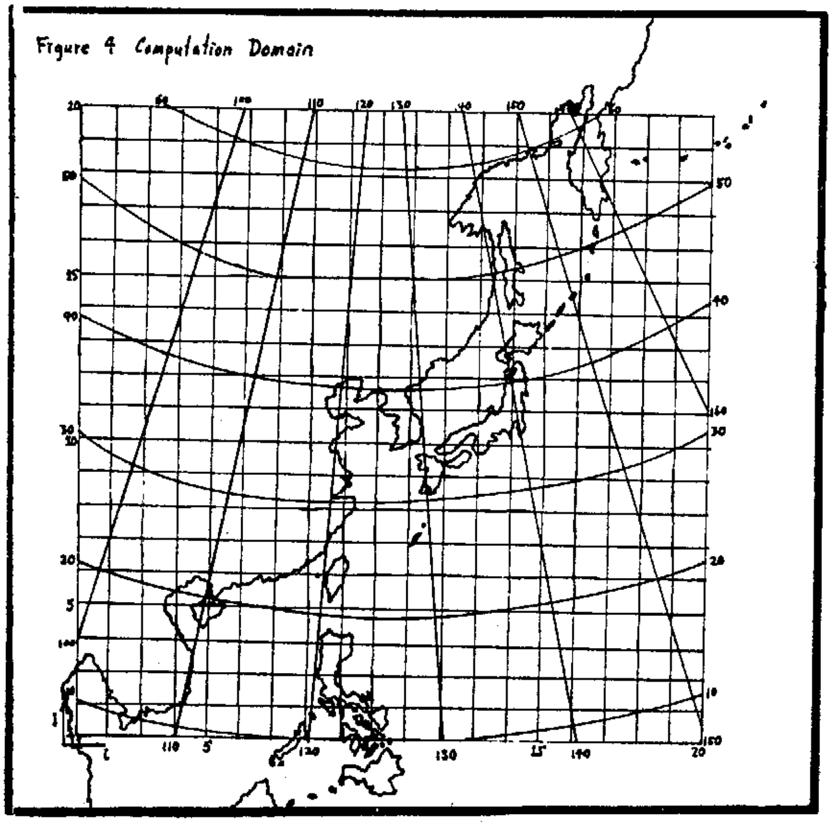
Figure 4 Computation Domain

100
110
120
130
140
150
160
50
40
30
20
10

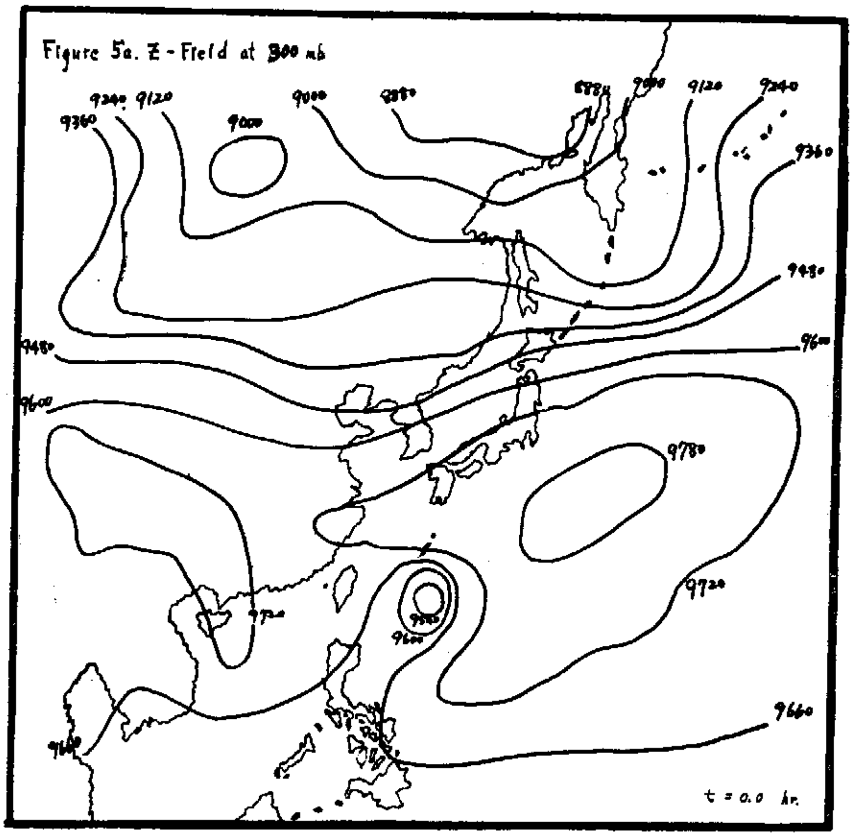

Figure 5a. Z-Field at 300 mb

9360
9240
9120
9000
9000
8880
8880
9000
9120
9240
9360
9480
9480
9600
9600
9780
9720
9720
9600
9660
9660
9600
t = 0.0 hr.

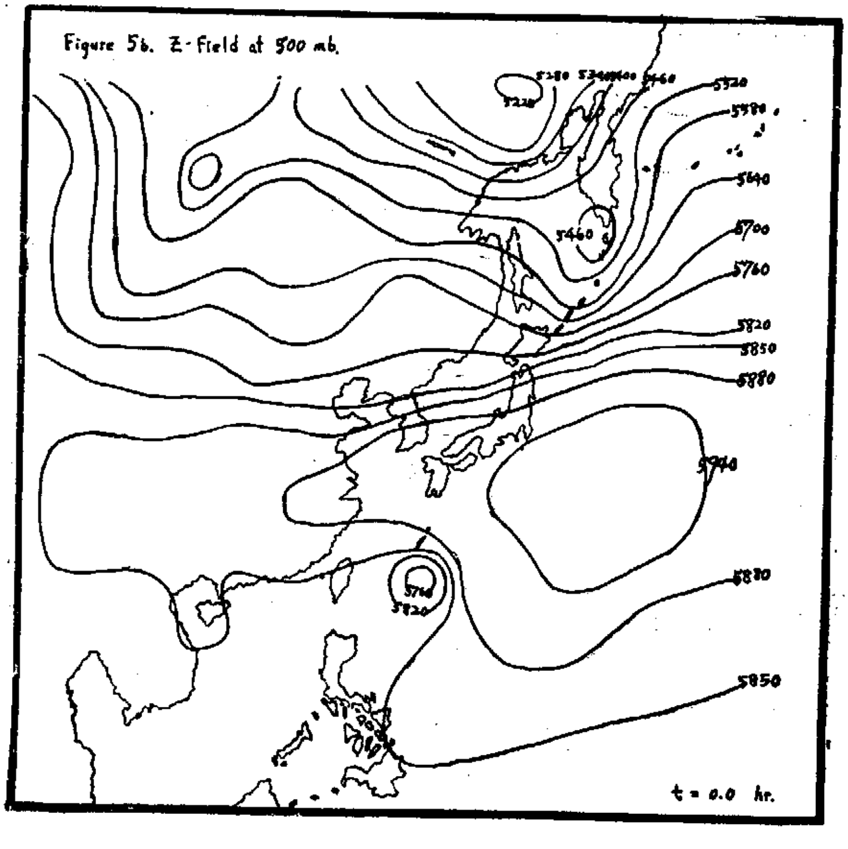

Figure 5b. Z-Field at 500 mb.

5220
5280
5340
5400
5460
5520
5580
5460
5640
5700
5760
5820
5850
5880
5940
5880
5700
5820
5850
t = 0.0 hr.

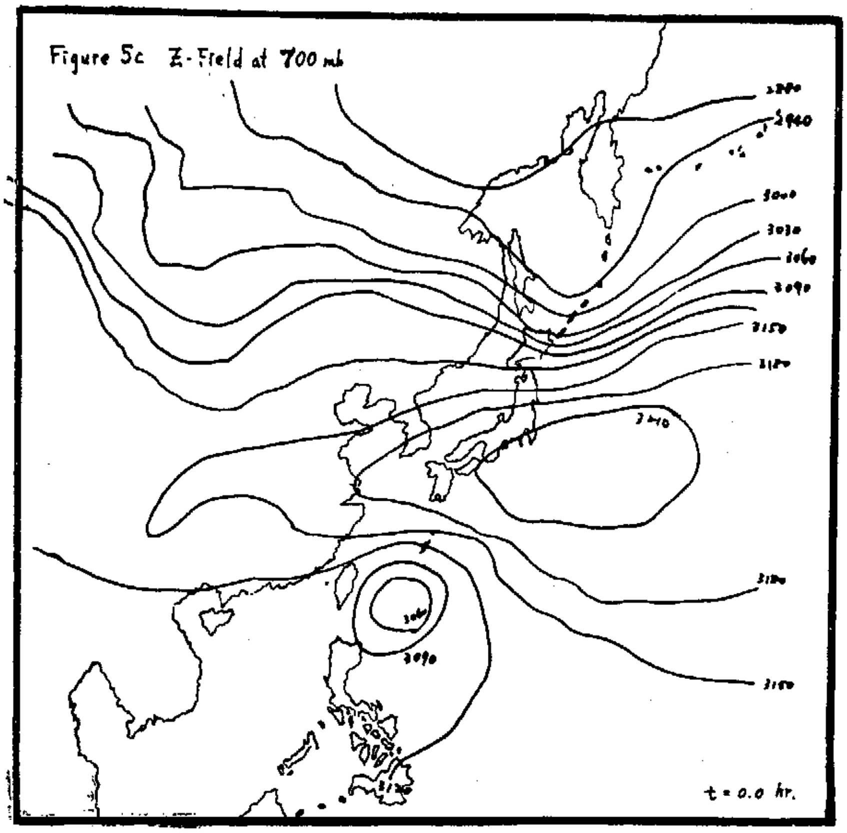

Figure 5c Z-Field at 700 mb

2880
2940
3000
3030
3060
3090
3150
3180
3210
3180
3150
3060
3090
3120
t = 0.0 hr.

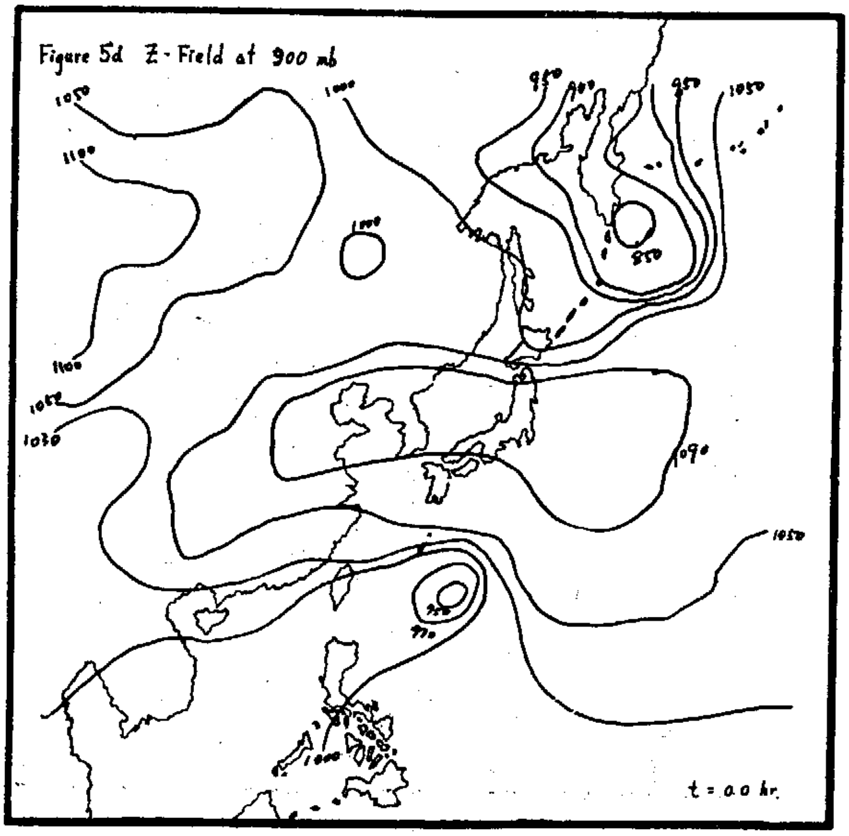

Figure 5d Z-Field at 900 mb

1050
1100
1000
950
900
950
1050
1100
850
1100
1052
1030
1090
1050
950
970
1000
t = 0.0 hr.

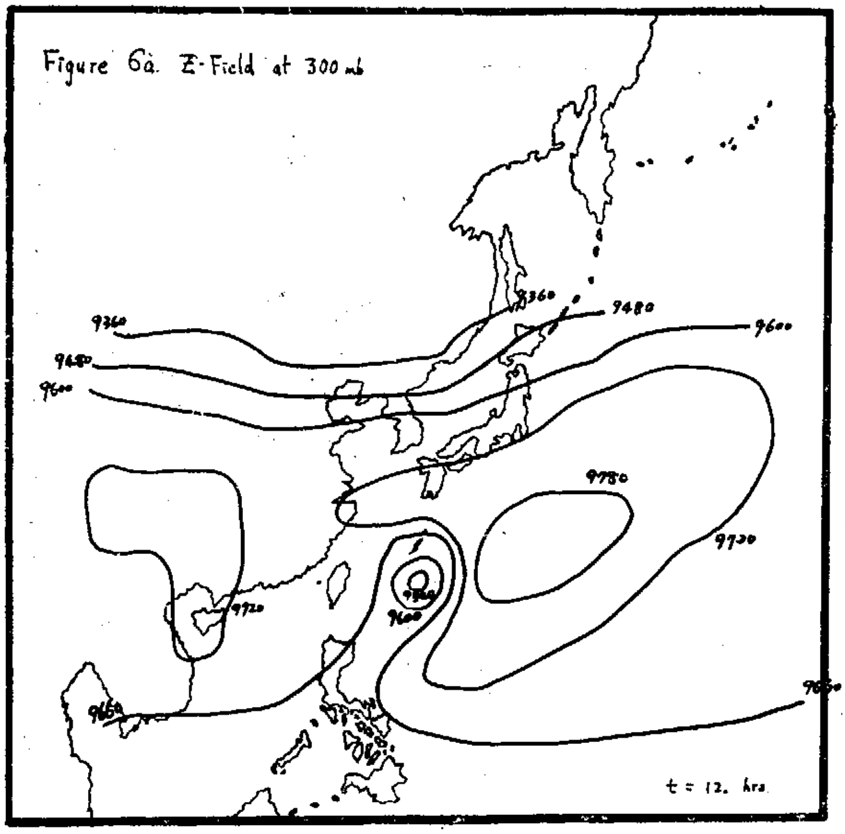

Figure 6a. Z-Field at 300 mb

9360
9480
9600
9360
9680
9600
9780
9720
9720
9600
9660
9660
t = 12. hrs.

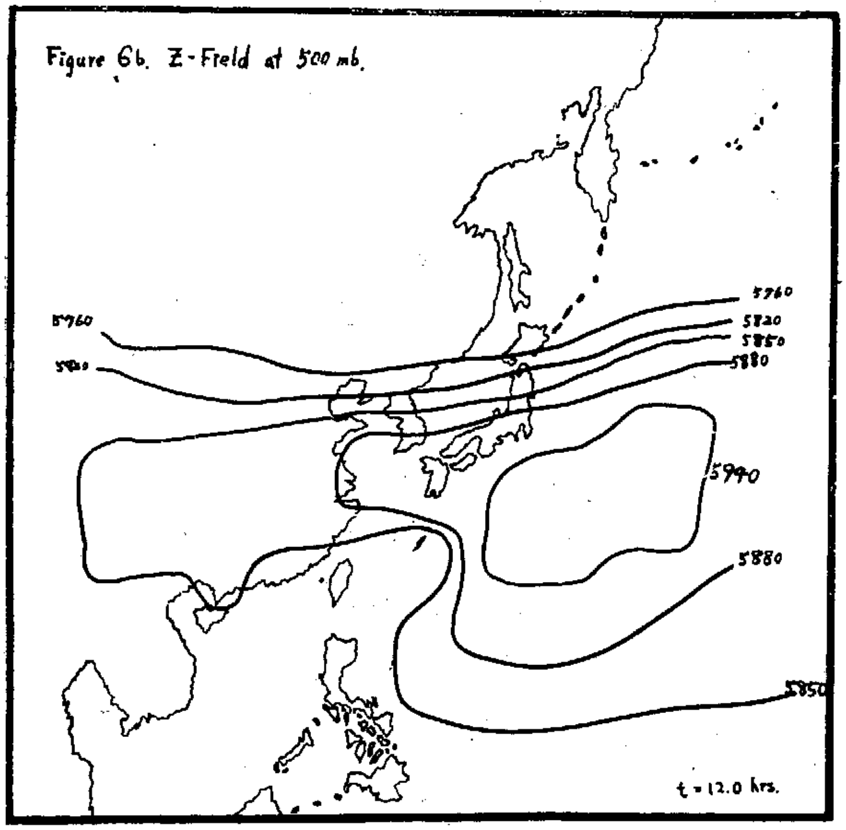

Figure 6b. Z-Field at 500 mb.

5760
5820
5850
5880
5760
5880
5940
5880
5850
t = 12.0 hrs.

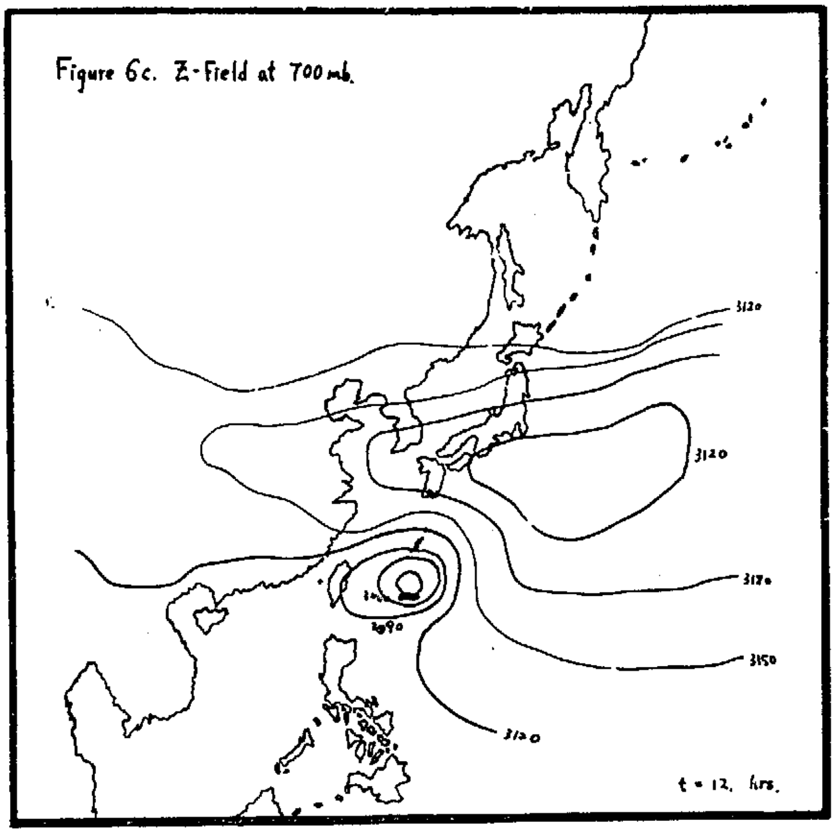

Figure 6c. Z-Field at 700 mb.

3120
3120
3170
3150
3120
3090
t = 12. hrs.

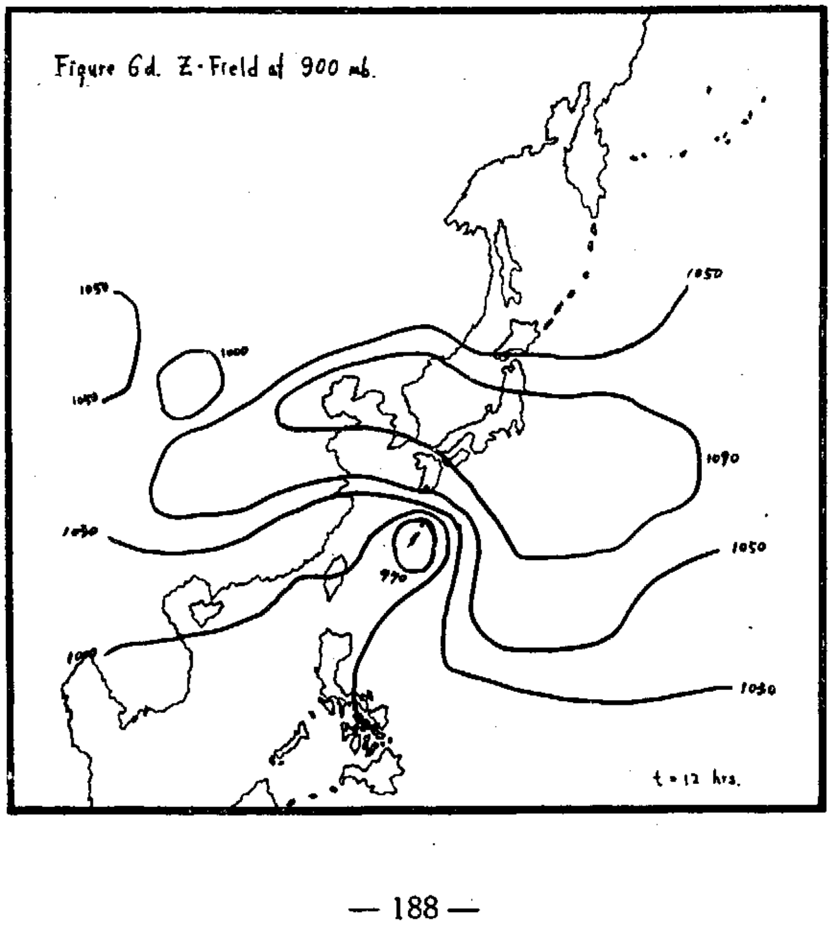

Figure 6d. Z-Field at 900 mb.

1050
1000
1050
1050
1090
1030
1050
970
1000
1030
t = 12 hrs.

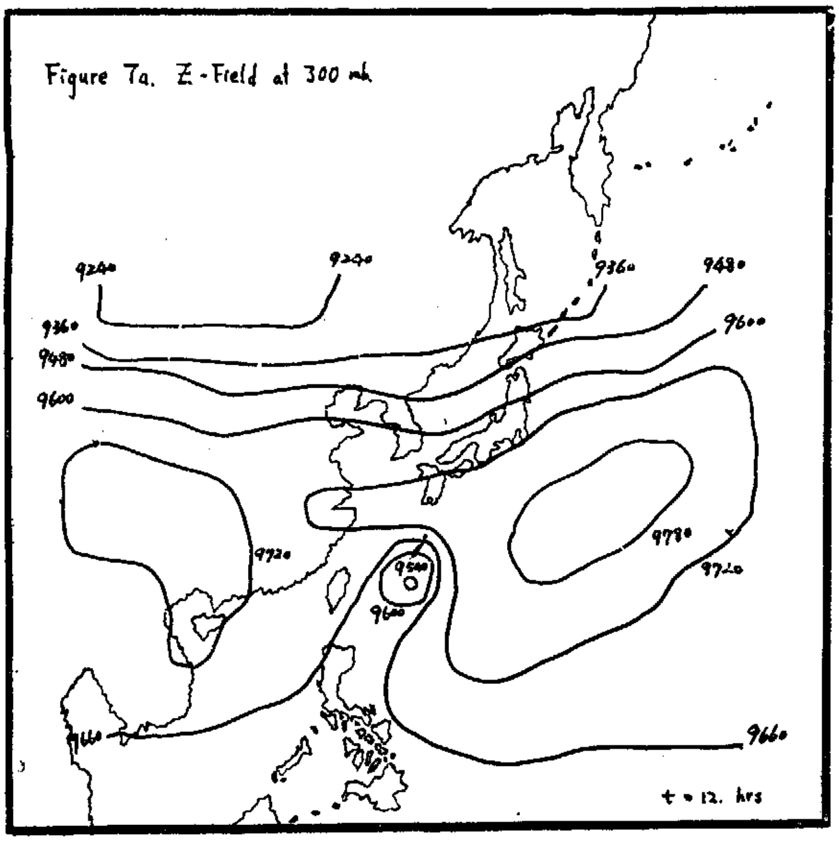

Figure 7a. Z-Field at 300 mb

9240
9240
9360
9480
9360
9480
9600
9600
9720
9500
9600
9780
9720
9660
9660
t = 12. hrs

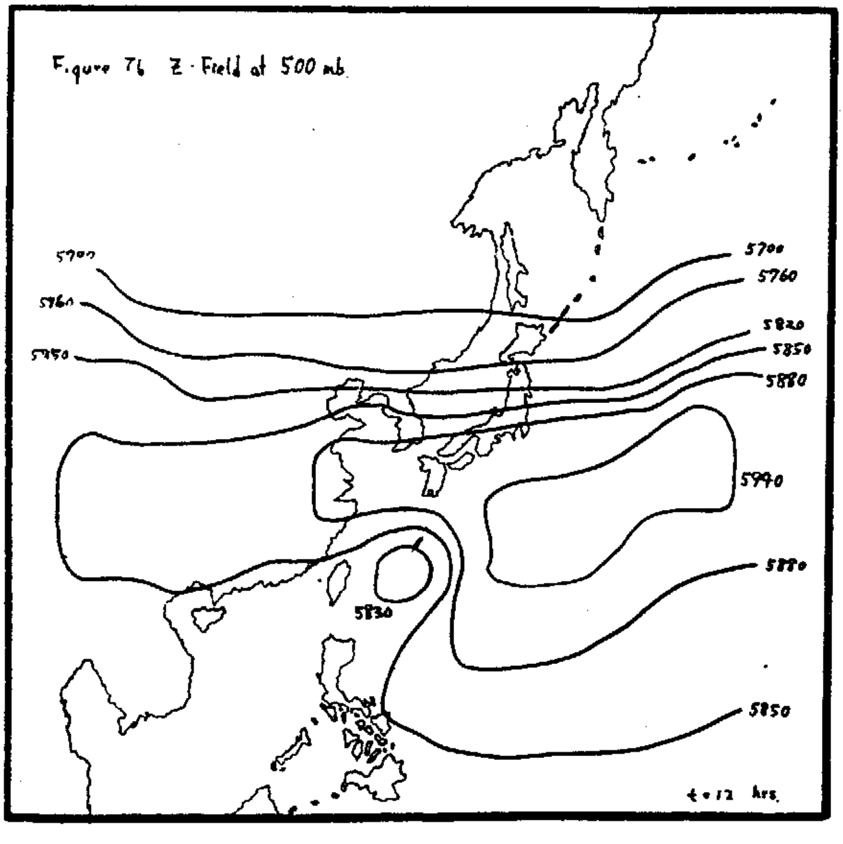

Figure 7b Z-Field at 500 mb.

5700
5760
5850
5700
5760
5820
5850
5880
5940
5880
5830
5850
t = 12 hrs.

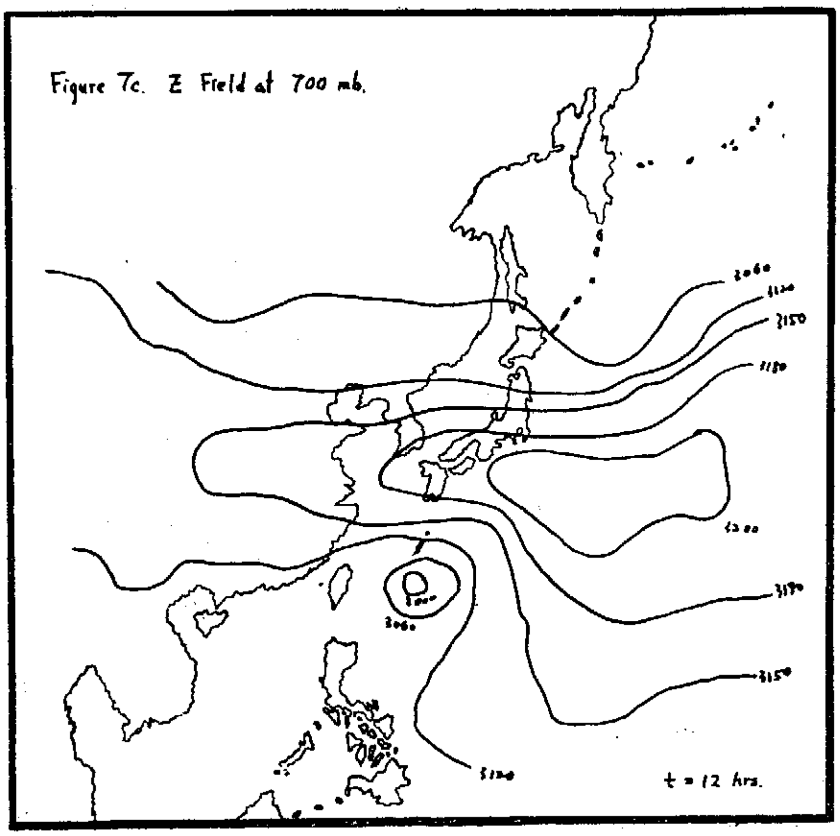

Figure 7c. Z Field at 700 mb.

3060
3120
3150
3180
3200
3000
3060
3180
3150
3120
t = 12 hrs.

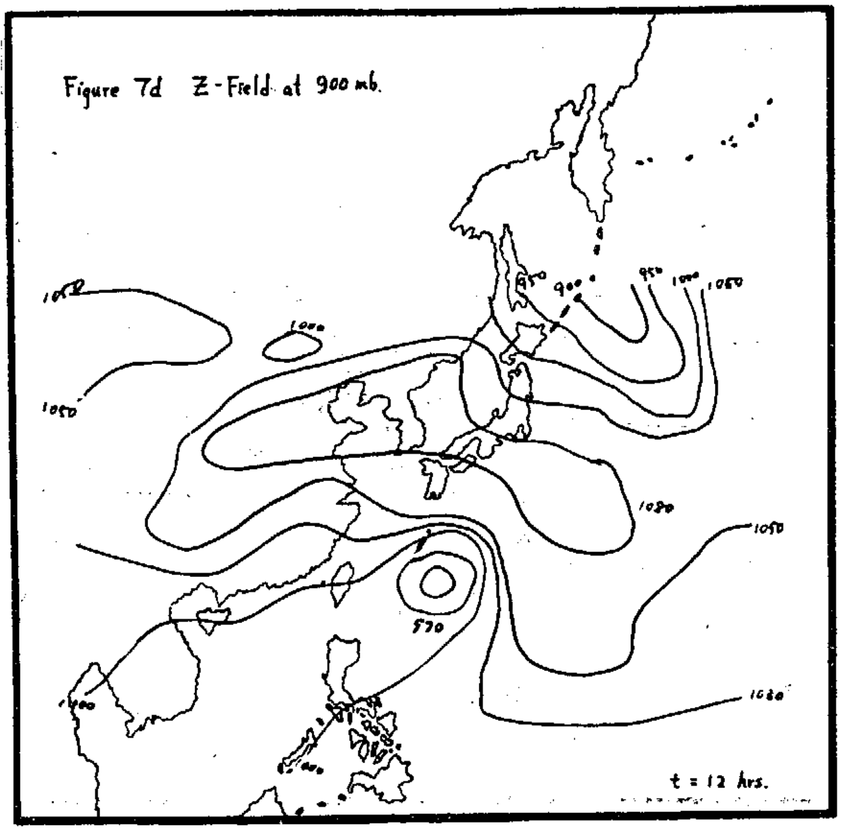

Figure 7d Z-Field at 900 mb.

1050
1000
1050
950
900
950
1000
1050
1080
1050
970
1080
1000
1000
t = 12 hrs.

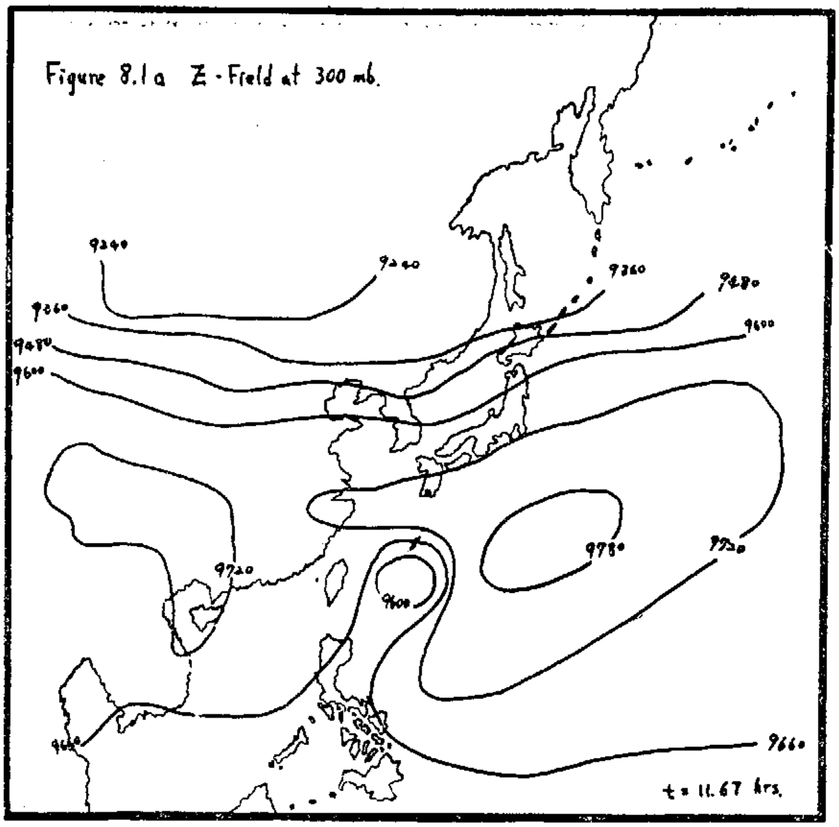

Figure 8.1a Z-Field at 300 mb.

9240
9240
9360
9360
9480
9480
9600
9600
9720
9780
9720
9600
9660
9660
t = 11.67 hrs.

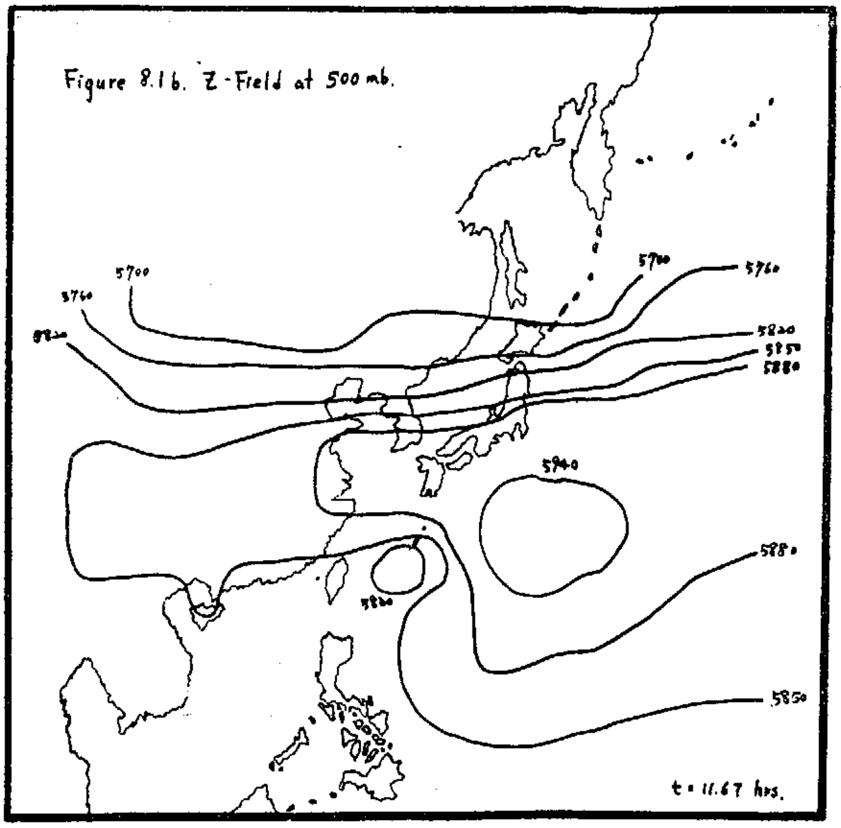

Figure 8.1b. Z-Field at 500 mb.

5700
5760
5820
5700
5760
5820
5850
5880
5940
5880
5820
5850
t = 11.67 hrs.

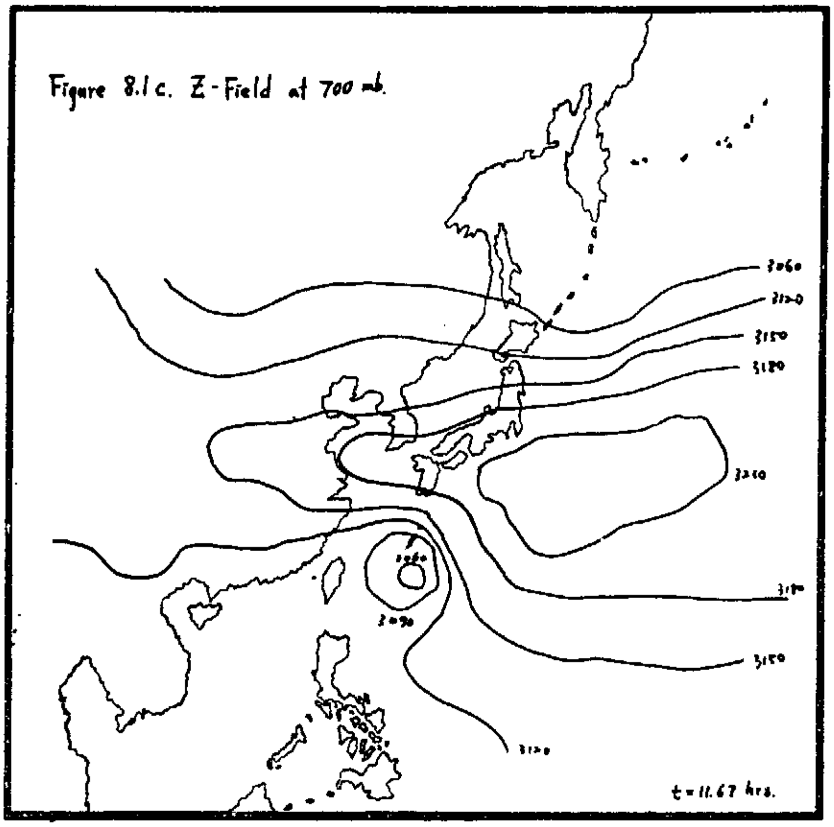

Figure 8.1c. Z-Field at 700 mb.

3060
3120
3150
3180
3210
3180
3060
3090
3150
3120
t = 11.67 hrs.

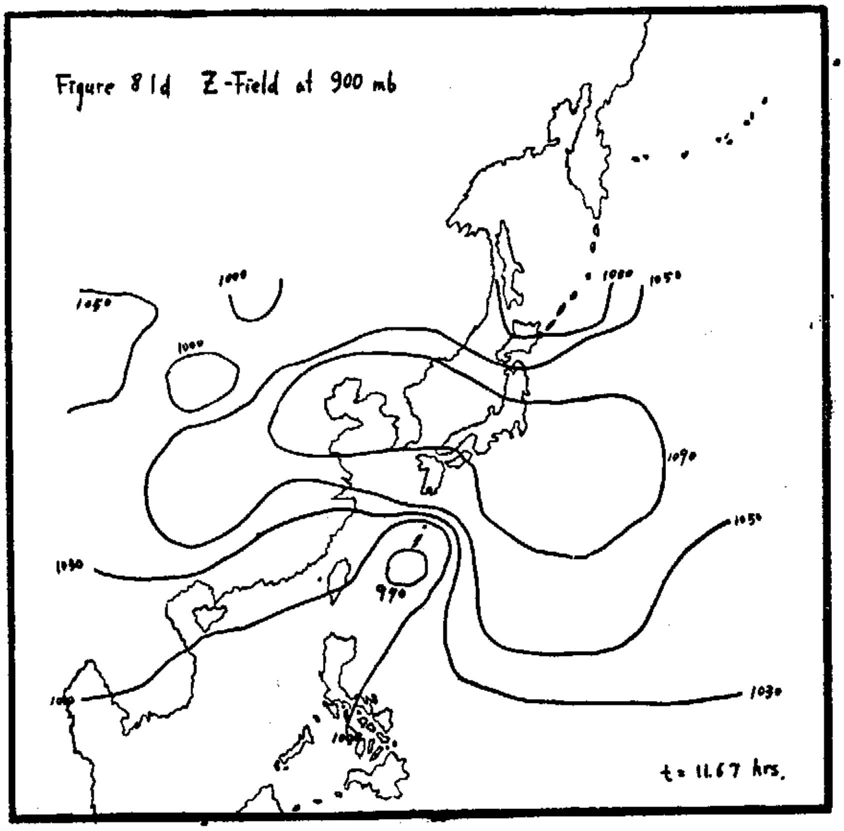

Figure 8.1d Z-Field at 900 mb

1000
1050
1000
1080
1050
1090
1050
1030
990
1030
1000
t = 11.67 hrs.

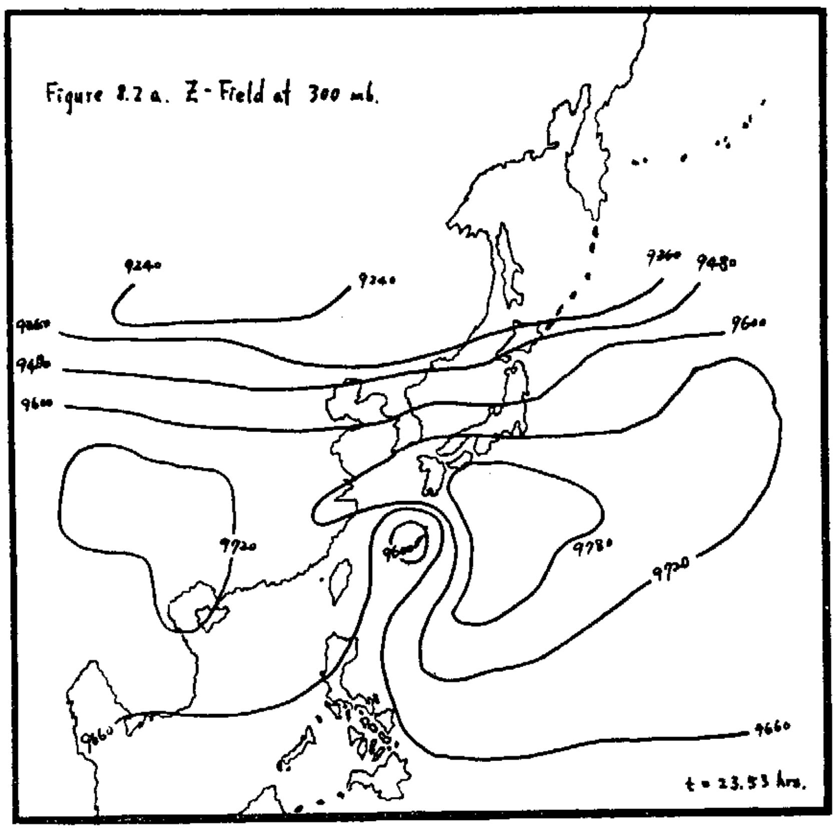

Figure 8.2 a. Z-Field at 300 mb.

9240
9240
9360
9480
9600
9360
9480
9600
9720
9600
9780
9720
9660
9660
t = 23.53 hrs.

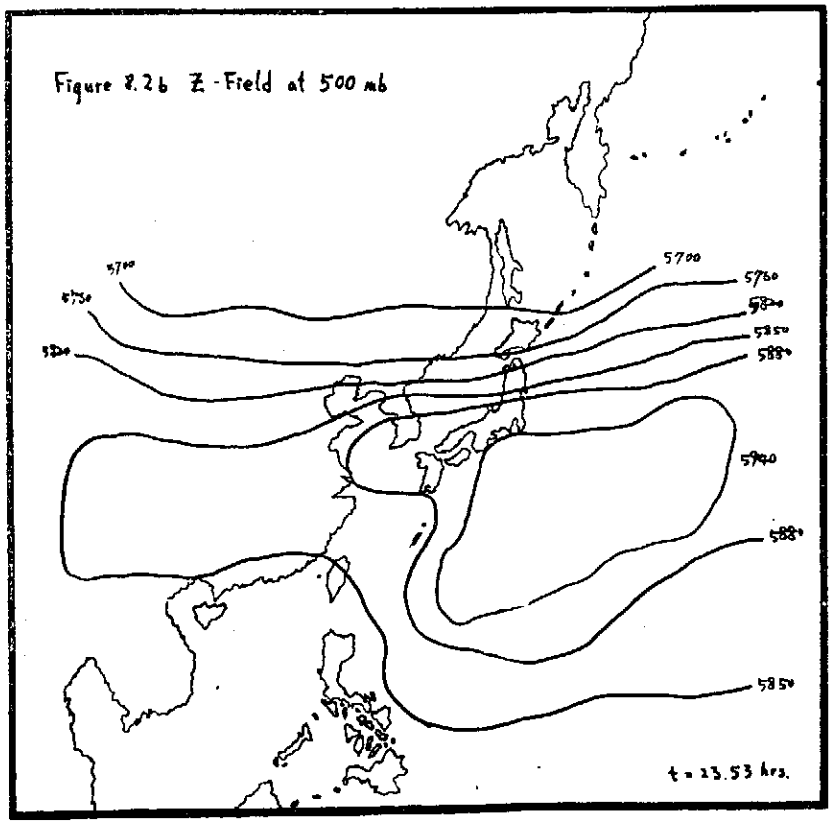

Figure 8.2 b Z-Field at 500 mb

5700
5750
5800
5700
5750
5800
5850
5880
5940
5880
5850
t = 23.53 hrs.

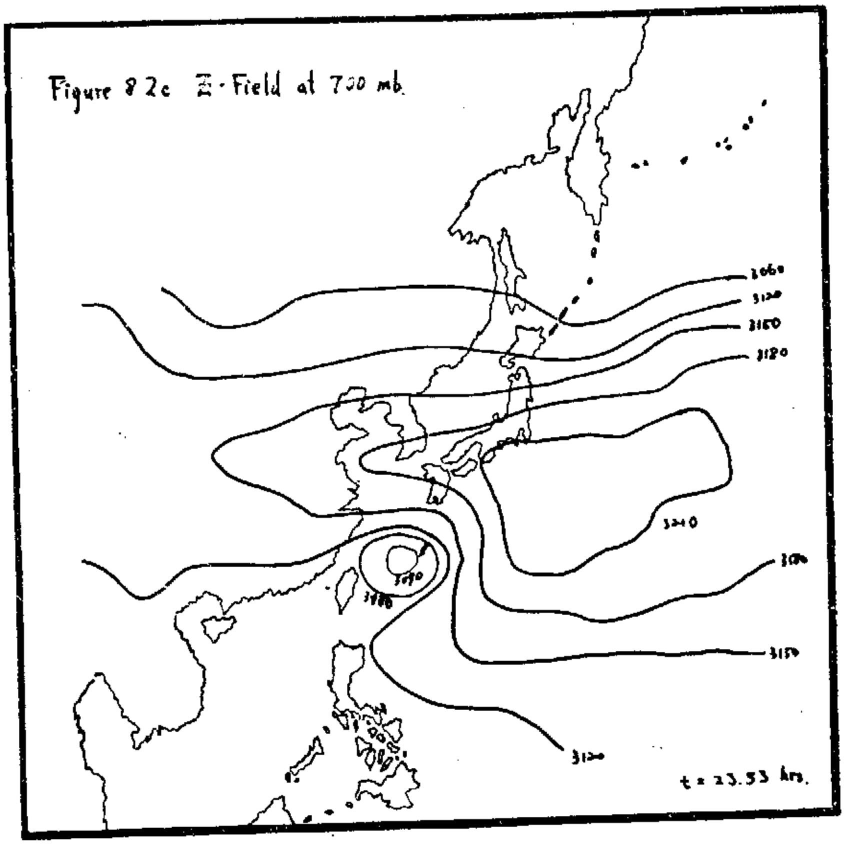

Figure 8.2c Z-Field at 700 mb.

3060
3120
3150
3180
3210
3090
3180
3180
3150
3120
t = 23.53 hrs.

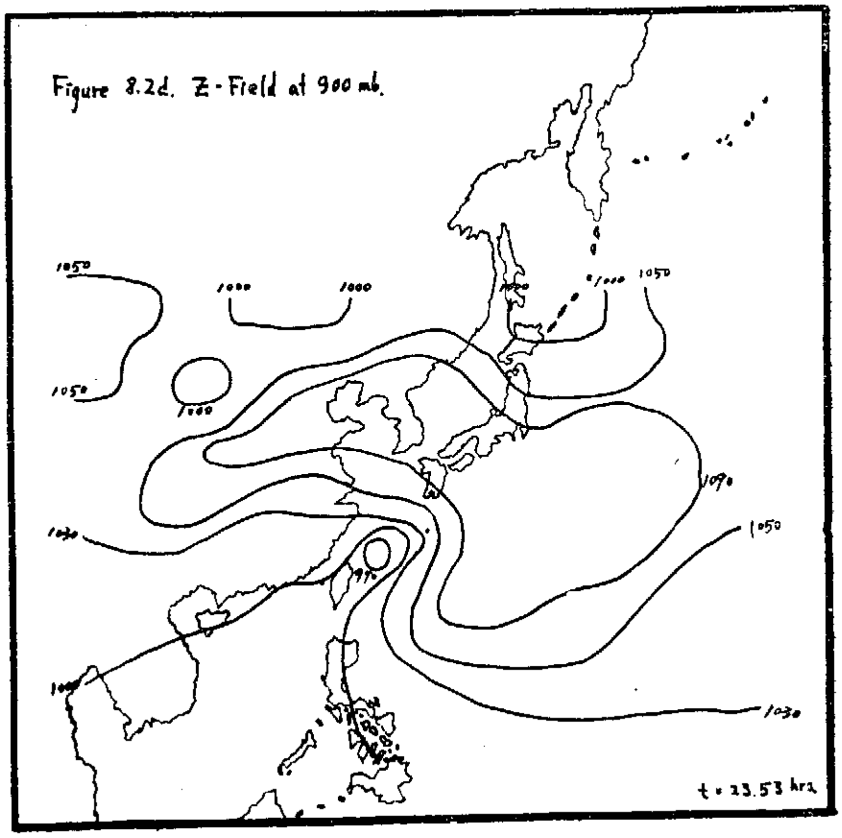

Figure 8.2d. Z-Field at 900 mb.

1050
1000
1000
1000
1000
1050
1050
1000
1090
1050
1030
970
1000
1030
t = 23.53 hrs.

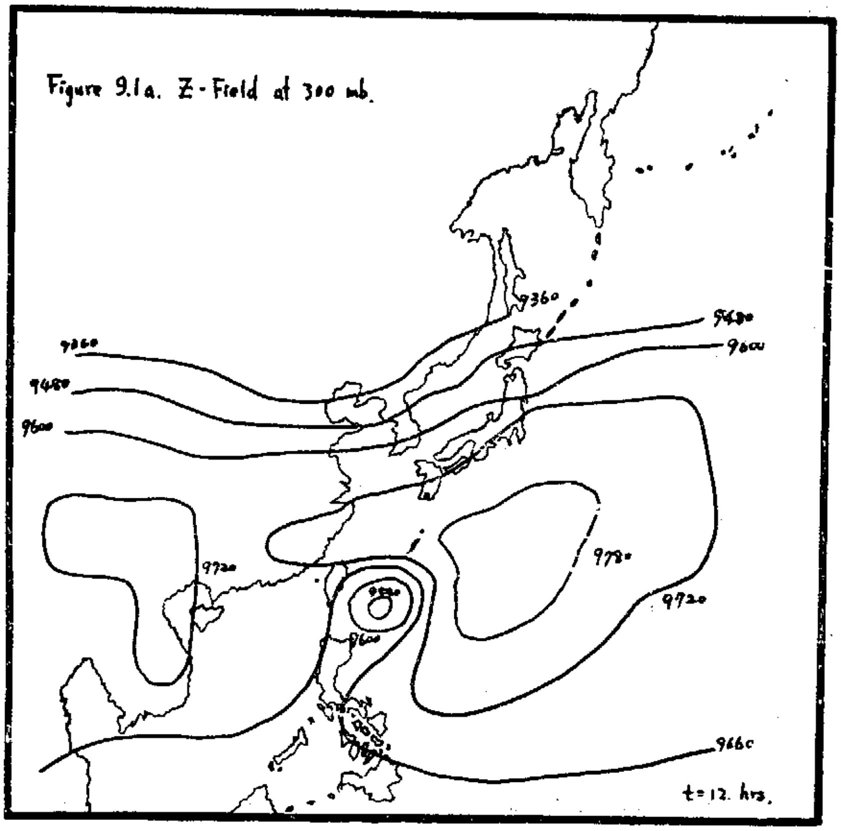

Figure 9.1a. Z-Field at 300 mb.

9360
9480
9600
9360
9480
9600
9720
9720
9720
9600
9660
t=12. hrs.

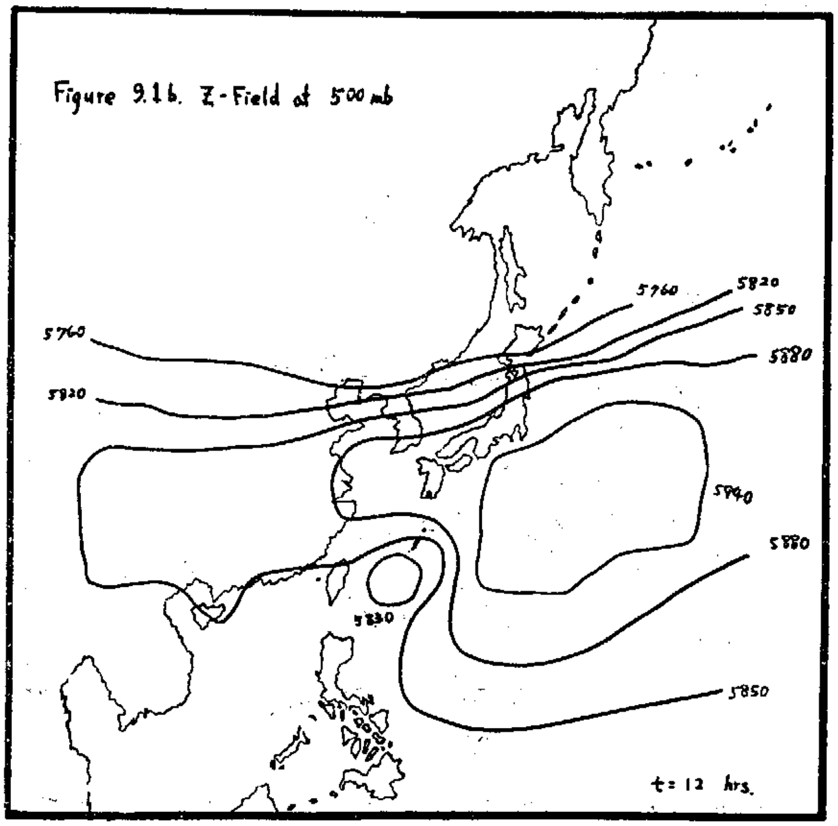

Figure 9.1b. Z-Field at 500 mb

5760
5820
5850
5880
5760
5820
5940
5880
5830
5850
t= 12 hrs.

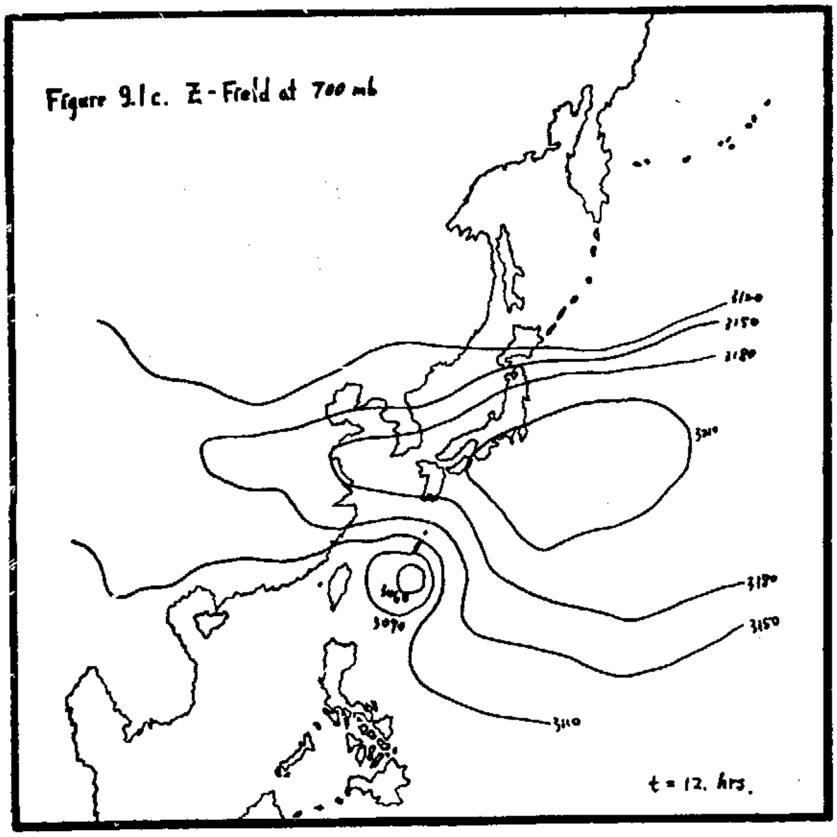

Figure 9.1c. Z-Field at 700 mb

3120
3150
3180
3210
3180
3150
3110
3090
3060
t = 12. hrs.

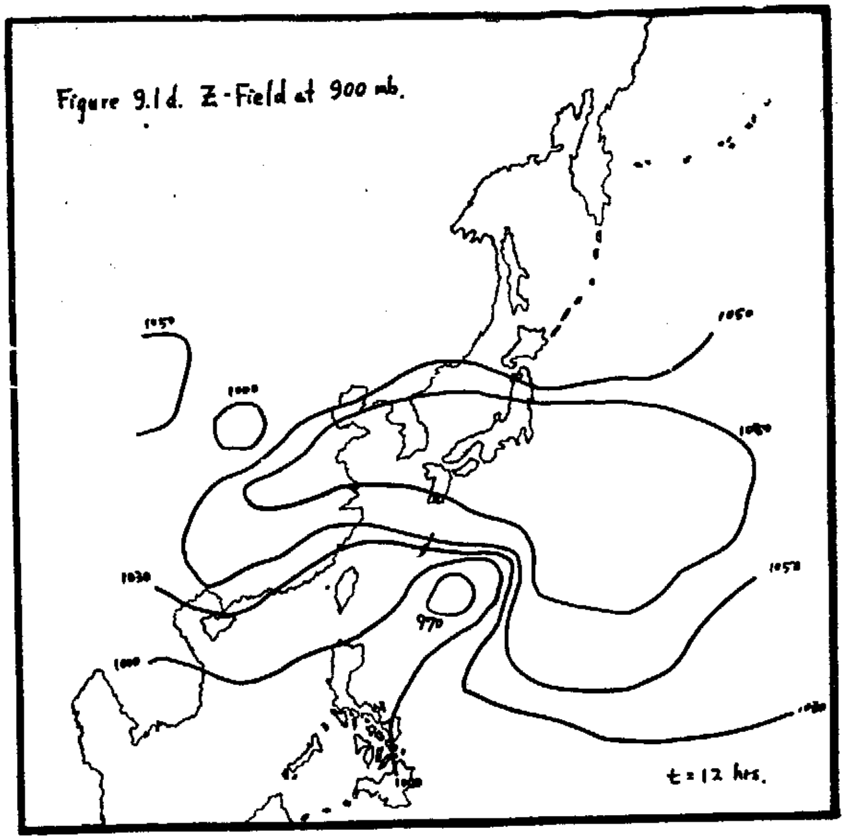

Figure 9.1d. Z-Field at 900 mb.

1050
1000
1050
1080
1030
1050
1000
970
1080
1000
t = 12 hrs.

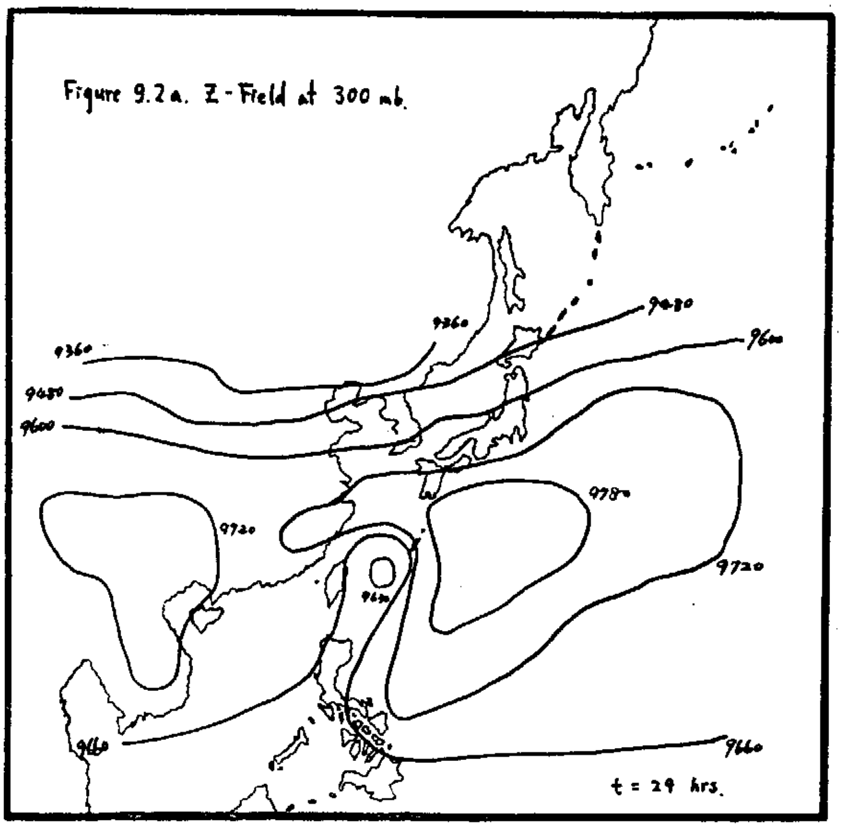

Figure 9.2a. Z-Field at 300 mb.

9360
9480
9600
9360
9480
9600
9720
9780
9720
9640
9660
9660
t = 24 hrs.

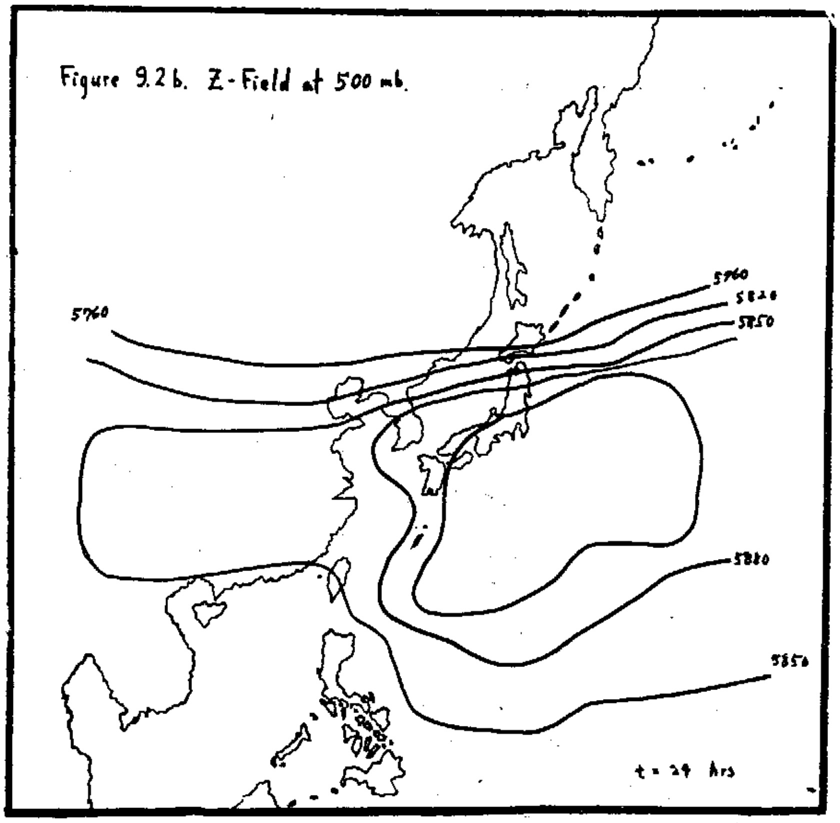

Figure 9.2b. Z-Field at 500 mb.

5760
5760
5820
5850
5880
5850
t = 24 hrs

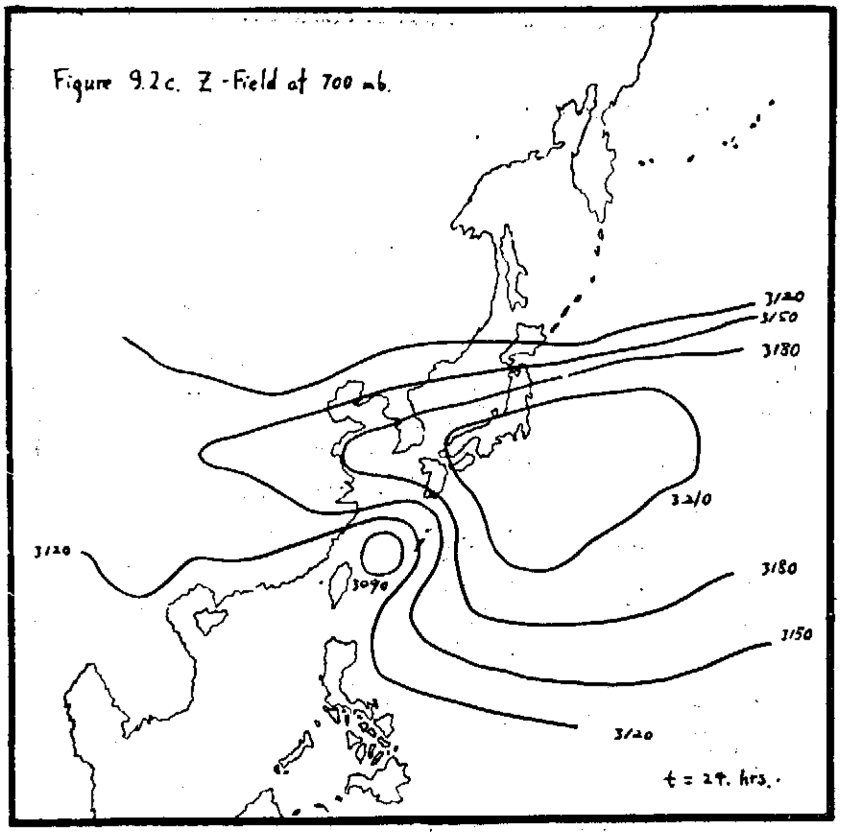

Figure 9.2c. Z-Field at 700 mb.

3120
3150
3180
3210
3120
3090
3180
3150
3120
t = 24. hrs.

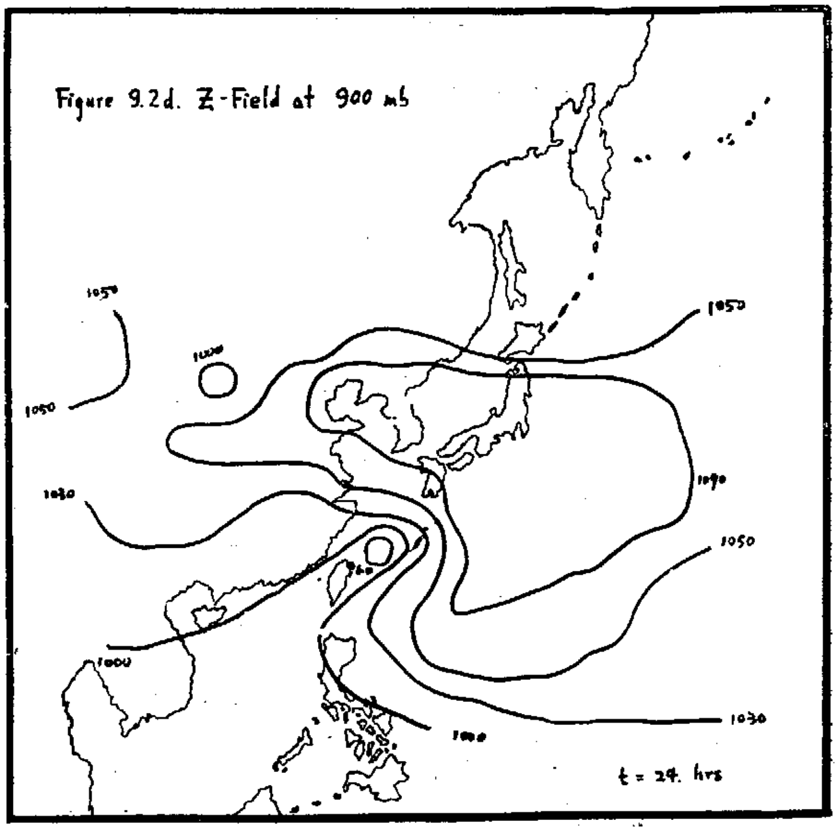

Figure 9.2d. Z-Field at 900 mb

1050
1000
1050
1050
1030
1090
960
1050
1000
1030
1000
t = 24. hrs

Annual Report of Institute of Physics, Academia Sinica, 1971

颱風中心之運動*

大氣物理組同仁

一般簡介

從以往八十七年侵臺颱風統計（大氣物理組同仁，1972）及 Gray（1970）報告中對颱風路徑、方向、速度等 persistence 之分析，可看出侵臺颱風常循相似的侵襲路徑。Hope and Neumann（1970）根據此一特性，制定出一種根據以往颱風行徑預測颱風運動之客觀預報法。其用於實際預報工作效果良好（Simpson, 1971）。本文仰在研討此種颱風客觀預報法修正引入我國之可能性。

分析方法

1. 颱風中心運動

假設已知一欲預測颱風之中心位置（x_0, y_0）、時間（t_0）、速度（v_0）及運動方向（θ_0），第一步工作是在以往颱風中尋求合於下列條件者：

1.1 其行徑通過以（x_0, y_0）爲中心，A_1 爲半徑的圓。

設任一以往颱風位置及時間爲

$$(x_j,\ y_j,\ t_j) \qquad j=1,\ 2, \ldots\ldots, nn \tag{1}$$

此條件爲

$$[(x_l-x_0)^2+(y_l-y_0)^2]^{1/2}\leq A_1\ [x_j-x_0)^2+(y_j-y_0)^2]^{1/2}\leq A_1 \text{ for any } j \tag{2}$$

1.2 其離（x_0, y_0, t_0）最近一點爲（x_l, y_l, t_l），亦即

$$(x_l-x_0)^2+(y_l-y_0)^2\leq(x_j-x_0)^2+(y_j-y_0)^2 \tag{3}$$

1.3 其運動方向與 6_0 之差不超過 A_2，亦即

$$\left|\tan^{-1}\left(\frac{y_{l+1}-y_l}{x_{l+1}-x_l}\right)-\theta_0\right|\leq A_2 \tag{4}$$

1.4 其速度與 v_0 之差不超過 A_8，亦即

$$\left|\frac{[x_{l+1}-x_l)^2+(y_{l+1}-y_l)^2]^{1/2}}{t_{l+1}-t_l}-v_0\right|\leq A_3 \tag{5}$$

1.5 其發生時間與 t_0 之差不超過 A_4，亦即

$$|t_l-t_0|\leq A_4 \tag{6}$$

若此以往颱風合於上敍條件，則進一步修正此颱風運行路徑。修正的原則乃假定在 t_0 時，擬預測颱風循其運行方向前進，漸漸地受影響以往颱風因素之影響，至 t_0+A_5 時完全循以往颱風運動方向前進。如以數學公式表示，則修正以往颱風途徑爲

$$\begin{cases} x'_k=x_0 & \text{at } t_k \text{ when} \\ y'_k=y_0 & \end{cases} \tag{7}$$

$$\begin{cases} x'_k=\dfrac{(k-l)(x_k-x_{k-1})+(A_6-k+l)(x_0-x_{0-1})}{A_6}+x'_{k-1} & \text{at } t_k \\ & \text{when } k=l+1,\ldots,l+A_6-1 \\ y'_k=\dfrac{(k-l)(y_k-y_{k-1})+(A_6-k+l)(y_0-y_{0-1})}{A_6}+y'_{k-1} & \end{cases} \tag{8}$$

---

* 本文承行政院國家科學委員會支助完成

$$\begin{cases} x'_k = x_k - x_{k-1} + x'_{k-1} \\ y'_k = y_k - y_{k-1} + y'_{k-1} \end{cases} \quad \text{at } t_k \quad \text{when } k = l + A_6, \ldots\ldots, nn-1 \tag{9}$$

假定合乎上敍條件之颱風共有N個，則預測颱風中心在任一瞬間（$t_0+\Delta t$）之運動位置（$\overline{x}'$, $\overline{y}'$)）爲

$$\begin{cases} \overline{x} = \Sigma\, x'_{t+\Delta t_t} \;/N \\ \overline{y}' = \Sigma y'_{t+\Delta t} \;/N \end{cases} \tag{10}$$

2. 颱風中心移動範圍

假定在任一時間颱風中心移動範圍由一 bivariate normal probability density function 組成，則颱風移動範圍可以一橢圓表示，該橢圓之

$$\begin{cases} \text{major axis} = k_a \times c \\ \text{minor axis} = k_b \times c \end{cases} \tag{11}$$

式中C爲

$$c = [\ln\ (1-P)^{-2}]^{0.5} \tag{12}$$

P爲有 P-probability 該颱風中心可能移入上述橢圓，k_a, k_b 爲

$$k^2 = s_x^2 + s_y^2 \pm [(s_x^2+s_y^2)^2 - 4\ s_x^2\ s_y^2\ (1-\gamma_{xy}^2)]^{1/2}/2 \tag{13}$$

之二根，而

$$\begin{cases} s_x = [\Sigma(x' - \overline{x}')^2/(N-1)]^{1/2} \\ s_y = [\Sigma(y' - \overline{y}')^2/(N-1)]^{1/2} \\ \gamma_{xx} = \Sigma(x' - \overline{x'})(y' - \overline{y'})/[\Sigma(x' - \overline{x'})^2 \Sigma(y' - \overline{y'})^2]^{1/2} \end{cases} \quad \text{at } k = l + \Delta t \tag{14}$$

此橢圓長軸與緯度夾角 Ψ 爲

$$\Psi = \tfrac{1}{2} \tan^{-1} \frac{2\ \gamma_{xy}\ s_x\ s_y}{s^2{}_x - s^2{}_y} \tag{15}$$

3. 本文主要在試驗上述方法之可行性，因之資料皆取自以往八十七侵臺颱風統計中，其主要參數變化爲

$$t_{j+1} - t_j = 6 \text{ 小時}$$

$$A_1 = 2.5° \text{ 或 } 5°$$

$$A_2 = 22.5°$$

$$A_3 = \begin{cases} 5 \text{ kt} & \text{當} \quad v_0 < 10 \text{ kt} \\ 10 \text{ kt} & 10\text{kt} \le v_0 \le 20 \text{ kt} \\ 15 \text{ kt} & v_0 > 20 \text{ kt} \end{cases} \tag{16}$$

$$A_4 = 15 \text{ 天或 } 30 \text{ 天}$$

$$A_5 = 36 \text{ 小時}$$

$$A_6 = \frac{A_5}{t_{j+1} - t_j}$$

颱　風 Gloria (1963)

1. 72小時颱風中心運動

1963 年颱風 Gloria 在九月11日掠過臺灣北部海面。三天前颱風中心約在北緯 20°，東經 131.3°，卽以這一點爲推測未來72小時颱風中心運動的起始點。首先我們假設此颱風中心運動祇受以往侵襲臺灣颱風之影響，而將以往八十七年部份九月間侵臺颱風中心每隔6小時的位置與時間記錄起來（大氣物理組同仁，1972），然後按照前節所述方法推測颱風中心運動情形。

圖 1-1 至圖 1-4 爲下列情形下

變數 ╲ 圖	1—1	1—2	1—3	1—4
A_1	5°	5°	2.5°	2.5°
A_4	15天	30天	30天	15天

颱風中心運動情形。圖中實線爲颱風實際路徑，虛線爲推測中心移動位置。由圖中可看出推測的颱風中心移動情形與實際颱風中心運動極爲接近，其差距 ϵ, 與類似颱風數目 N，爲

時　間	1—1		1—2		1—3		1—4	
	ϵ	N	ϵ	N	ϵ	N	ϵ	N
12	60.6	15	65.8	18	59.6	9	59.6	6
24	87.0	15	92.3	18	97.0	9	85.6	6
36	92.3	15	97.4	17	96.0	8	72.0	6
48	122.6	15	144.8	17	139.1	8	78.2	6
60	138.2	12	168.0	13	134.0	7	73.3	6
72	132.4	11	169.3	12	86.4	7	0.6	6

表列時間爲九月11日起始點起算之小時數，差距單位爲海哩。

本文主要目的在介紹前敍方法之可行後，而無意做預報工作。因之雖然 A_4 在不同情形下有時需要考慮八月或十月份以往颱風行徑，本文分析時却祇考慮部分九月份以往颱風行徑。同時又因本文中祇分析了幾個颱風，因之這兒也不願肯定地指明 A_1 至 A_6 應以何數值爲最佳。可以看出來的是 A_1 至 A_6 的範圍愈寬，則 N 值愈大，當然N值愈大不一定代表推測的颱風中心運動情形愈精確。欲引用此法做實際颱風預報工作時，當需進一步的分析 A_1 至 A_6 的變化。

2. 24小時颱風中心運動

上前我們敍述了從某一點颱風中心位置推測 72 小時後颱風中心位置的方法與結果。同一方法可用以推測 72 小時以上或以下颱風中心運動的情形。圖 2-1 至 2-4 爲對應於圖 1-1 至 1-4 各種情形下推測24小時颱風中心運動的情形。由於推測時間縮短，推測颱風中心移動的情形要比 72 小時颱風中心運動推測來的準。各個情形下，三天（九月八日、九日、十日）的平均 24 小時颱風中心推測差距爲

	2—1	2—2	2—3	2—4
12小時	35.0	51.2	32.3	32.3
24小時	76.5	78.4	74.7	70.9

颱風 Bess (1971)

1. 72小時颱風中心運動

1971年9月19日颱風 Bess 中心位置在北緯 20.2°，東經 139.7°，三天後侵襲臺灣。 若以9月19日爲起始點，根據本文敍述方法推測72小時內颱風中心運動情形，其結果如圖3所示。圖 3-1 至 3-4 之 A_1 與 A_4 值與圖 1-1 至 1-4 相同。推測值之差距 ϵ 與類似颱風數目 N，爲

時間	3—1		3—2		3—3		3—4	
	ϵ	N	ϵ	N	ϵ	N	ϵ	N
12小時	24.0	8	24.1	9	16.1	6	20.4	5
24小時	53.7	7	58.6	8	73.9	6	68.3	5
36小時	103.7	7	119.4	8	144.2	6	131.9	5
48小時	154.8	6	194.5	7	194.8	6	154.8	5
60小時	219.8	6	274.9	7	283.0	6	221.9	5
72小時	328.8	5	420.3	6	484.9	5	386.5	4

此颱風之推測不如颱風 Gloria 準確的一個主要原因，在推測的起始運動方向與實際運動方向相差 10° 左右。由於9月19日時颱風中心在運動路徑的轉向點上，因之當附件中所用計算機程式僅由9月19日及其前6小時颱風中心推算其起始運動方向時，誤差便發生了。

2. 24小時颱風中心運動

對應於上節情形 24 小時內颱風中心運動情形平均推測誤差爲

	4—1	4—2	4—3	4—4
12小時	29	17	18	19
24小時	34	33	40	38

由圖 4-1 至 4-4 很明顯地看出短期推測準確度要精確不少。

分析與討論

1. 72小時颱風中心運動

圖5及圖6爲颱風 Viola (1969) 及颱風 Winnie (1953) 中心在 72 小時內運動情形。加上圖 1-2 及圖 3-2 共四個颱風在 72 小時內推測行徑之平均誤差爲

時間 (hr.)	12	24	36	48	60	72
誤差 (kt.)	44	82	108	158	179	212

雖然這祇是四個任意颱風之平均誤差，由於誤差值不大，本文敍述方法顯然可以進一步研討，做爲客觀預報法中之一項參考資料。

2. 資料問題

前面分析颱風 Gloria 時運用了以往八十七年部分九月份侵臺颱風資料，現在我們將該項資料任意減半，再據以推測 72 小時內颱風中心運動情形。圖 7-1 至 7-4 中 A_1 與 A_4 對應圖 1-1 至 1-4 中之 A_1 與 A_4 値，其中心推測差距爲

時間（小時）	7—1		7—2		7—3		7—4	
	ϵ	N	ϵ	N	ϵ	N	ϵ	N
12	60.4	11	60.6	13	60.4	7	60.1	5
24	86.2	11	86.0	13	80.5	7	74.8	5
36	84.5	11	84.4	12	60.4	6	49.1	5
48	114.1	11	126.0	12	72.1	6	31.7	5
60	97.9	10	132.4	11	84.4	6	6.6	5
72	54.7	9	110.3	10	8.5	6	110.0	5

圖 7-1 至 7-3 推測差距較圖 1-1 至 1-3 爲小，圖 7-4 推測差距較圖 1-4 爲大。因之，在 A_1 至 A_6 給予固定値時，資料愈多N愈大，但推測差距却不一定減小。這個需特別指明的一點是當N增大，縮小 A_1 至 A_6 値時，推測差距大多減小。

3. 起始方向

前面已經指出颱風中心運動與起始推測點的運動方向有極大關係。圖 5 爲颱風 Viola (1969) 之運動行徑，由於 7 月 24 日颱風在轉向點上，因之一開始推測行徑就偏向北方，其推測差距也就比颱風 Winnie (1958)（圖 6）來得大。

4. 颱風中心移動範圍

圖 5 與圖 6 中除了繪出 72 小時內颱風中心之運動位置外，並在推測的颱風中心移動位置上繪出颱風中心可能移動的或然率橢圓。 0.25 及 0.50 代表有百分之廿五及百分之五十機會颱風中心會移動到該橢圓內。在預報上說，0.50 的或然率橢圓應可視爲颱風可能侵襲區。

結論與建議

1. 本文假設侵臺颱風中心之運動與以往歷年侵臺颱風中心之運動情形有關，據此而推測侵臺颱風中心在72小時內運動情形及其可能移動範圍。四個由西向東運動颱風中心 72 小時推測誤差在二百浬左右，並在颱風中心移動或然率 (0.50) 橢圓以內。
2. 欲求更精確的預報颱風動向，可在考慮以往類似颱風時，進一步考慮颱風大小、變化、運動方向，附近

脊線及槽線位置等（Jarrell & Somervell, 1970）.

後　　記

參加本專題研究大氣物理組同仁包括汪羣從、彭立、簡來成、張月珠、馬天驥、張能復、梁文傑。

參 考 文 獻

Gray, W. M., A Climatology of Tropical Cyclones and Disturbances of the Western Pacific With a Suggested Theory for Their Genesis/Maintenance, NAVWEARSCHFAC Tech. Paper No. 19-20,

Navy Weather Res. Facility, 1970. Hope, J. R. & C. J. Neumann, An Operational Technique for Relating the Movement of Existing Tropical Cyclones to Past Tracks, Monthly Weather Review, 98, 925, 1970.

Jarrell, J. D. & W. L. Somervell, Jr,. A Computer Technique for Using Typhoon Analogs as a Forecast Aid, NAVWEARSCHFAC Tech. Paper No. 6-70, Navy Weather Research Facility, 1970.

Simpson, R. H., The Decision Process in Hurricane Forecasting, NOAA Tech. Memo. NWS SR-53, 1971.

大氣物理組同仁，1884年至1970年侵臺颱風路徑統計，中研院物理所，1972。

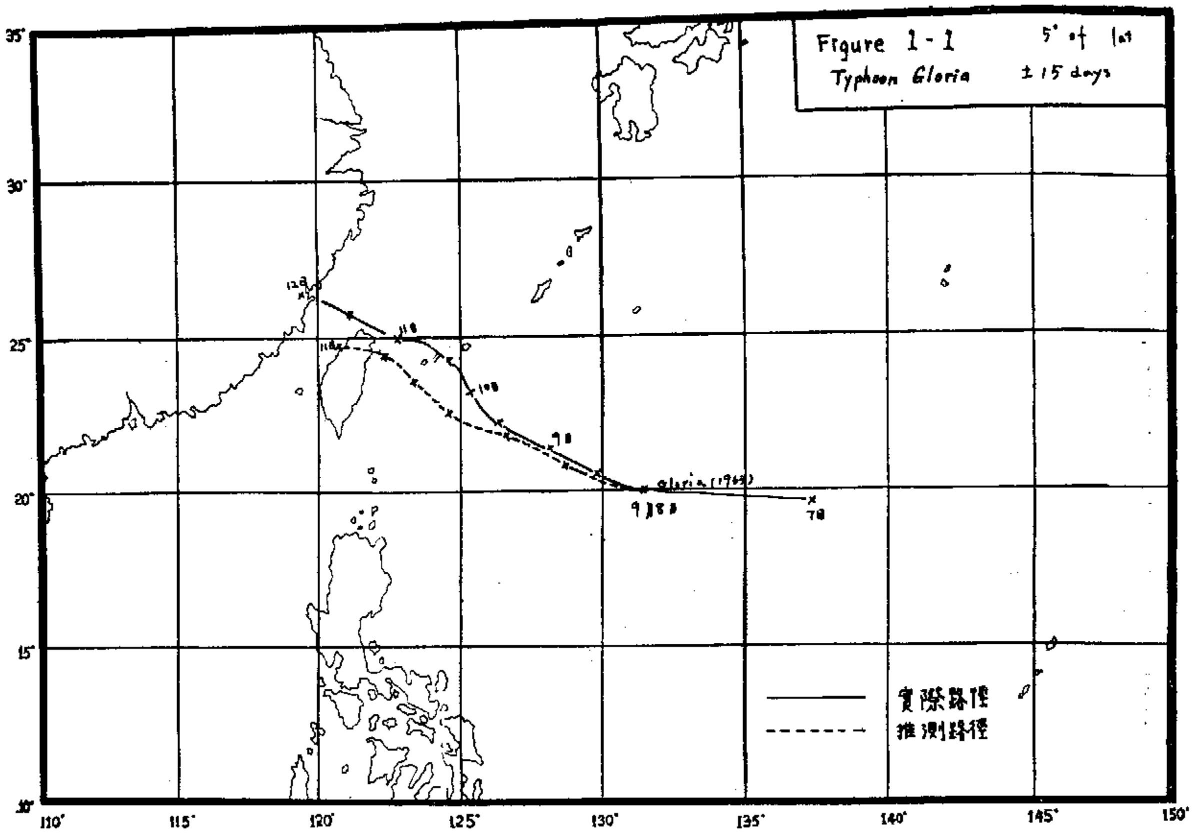
Figure 1-1
5° of lat
Typhoon Gloria
± 15 days
Gloria (1963)
12日
11日
11日
10日
9日
9月8日
7日
實際路徑
推測路徑
35°
30°
25°
20°
15°
10°
110°
115°
120°
125°
130°
135°
140°
145°
150°

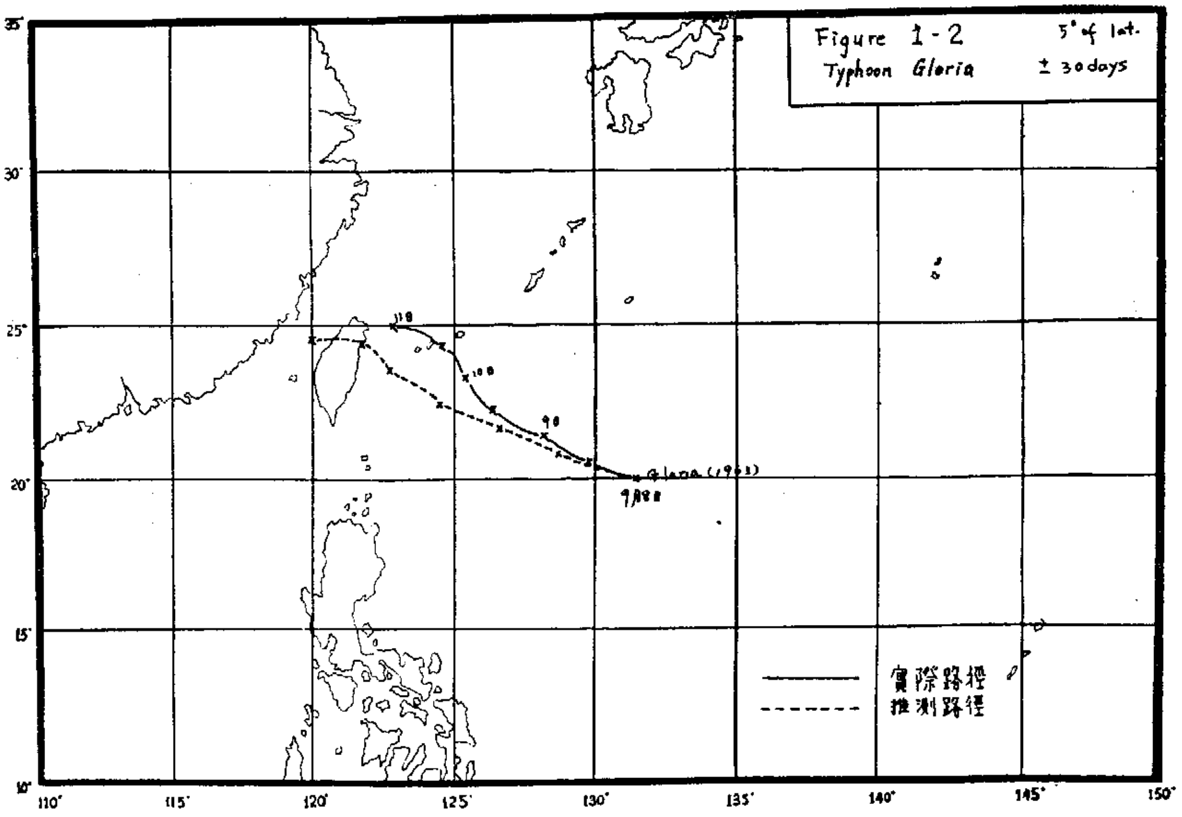
Figure 1-2
5° of lat.
Typhoon Gloria
± 30 days
Gloria (1963)
11日
10日
9日
9月8日
實際路徑
推測路徑
35°
30°
25°
20°
15°
10°
110°
115°
120°
125°
130°
135°
140°
145°
150°

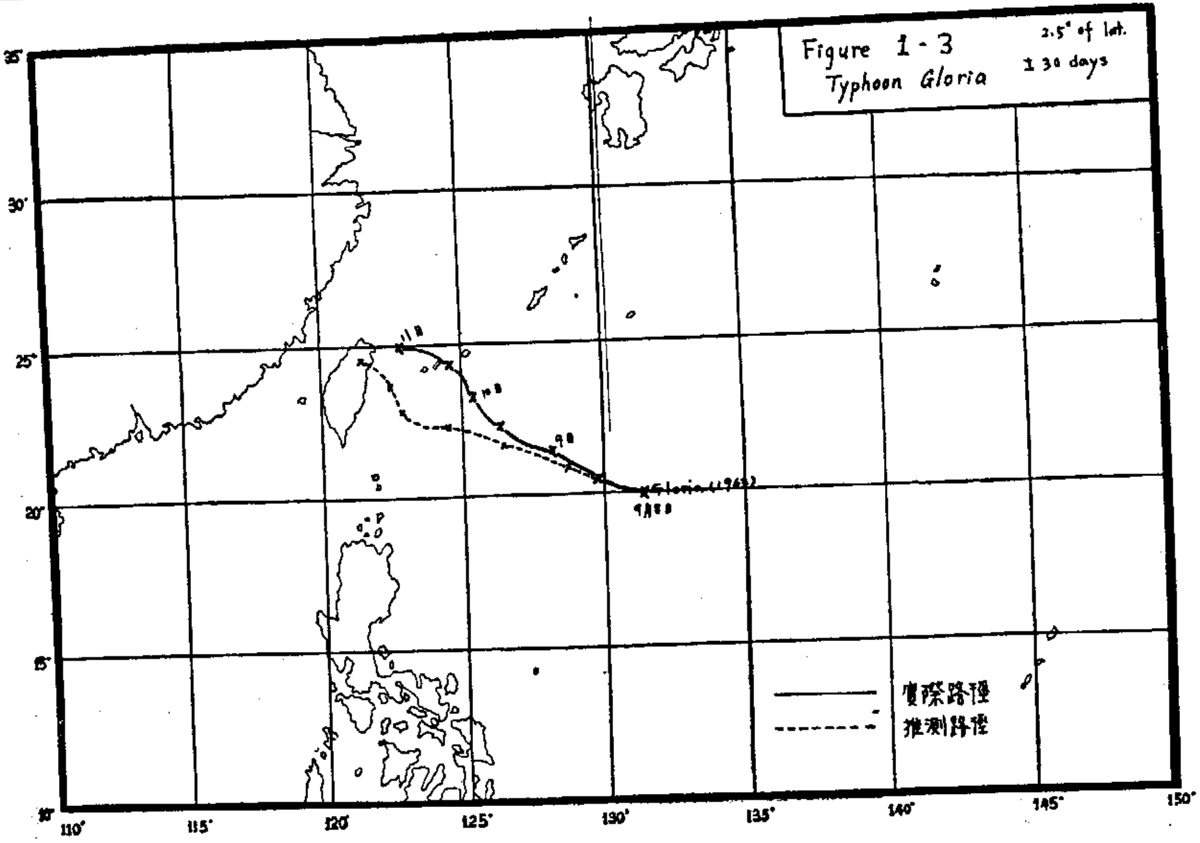
Figure 1-3
Typhoon Gloria
2.5° of lat.
± 30 days
實際路徑
推測路徑
Gloria (1963)
11日
10日
9日
9日8日
35°
30°
25°
20°
15°
10°
110°
115°
120°
125°
130°
135°
140°
145°
150°

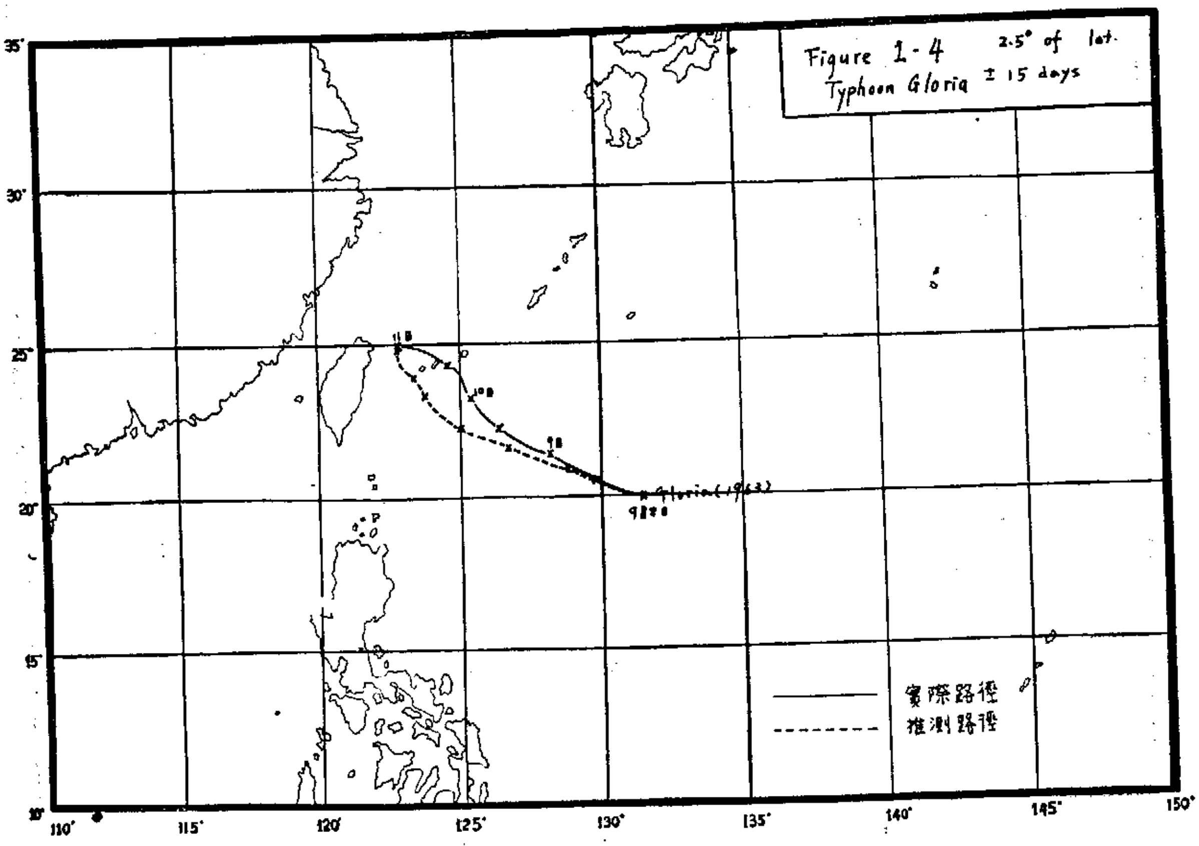
Figure 1-4
Typhoon Gloria
2.5° of lat.
± 15 days
實際路徑
推測路徑
Gloria (1963)
11日
10日
9日
9日8日
35°
30°
25°
20°
15°
10°
110°
115°
120°
125°
130°
135°
140°
145°
150°

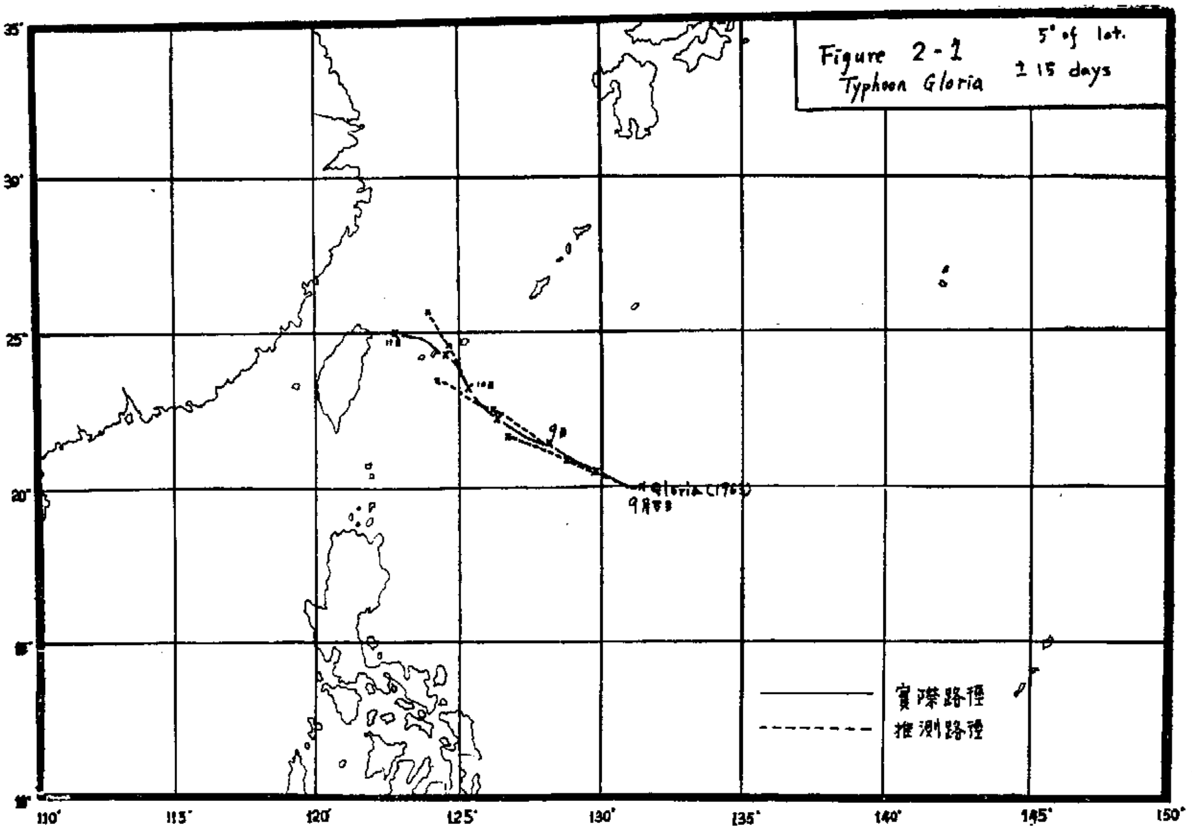
Figure 2-1
Typhoon Gloria
5° of lat.
± 15 days
11日
10日
9日
Gloria (1963)
9月8日
實際路徑
推測路徑
35°
30°
25°
20°
15°
10°
110°
115°
120°
125°
130°
135°
140°
145°
150°

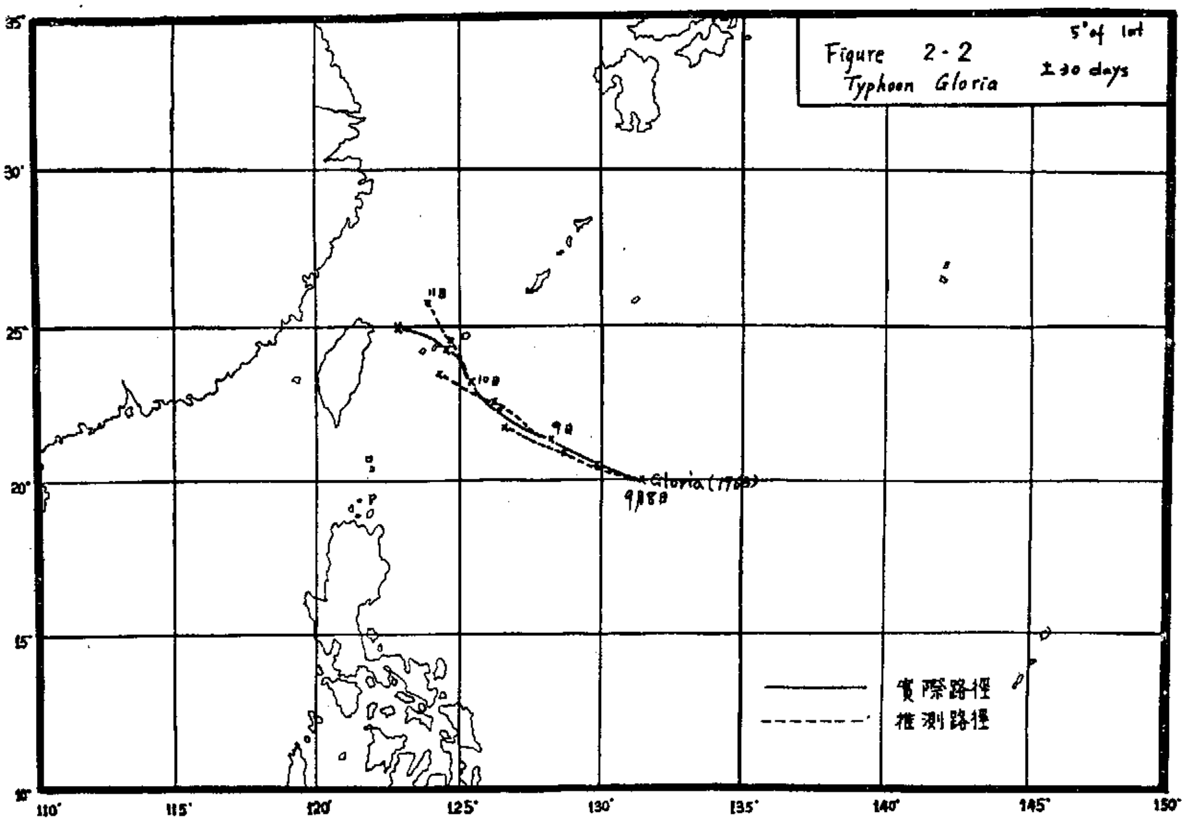
Figure 2-2
Typhoon Gloria
5° of lat
± 30 days
11日
10日
9日
Gloria (1963)
9月8日
實際路徑
推測路徑
35°
30°
25°
20°
15°
10°
110°
115°
120°
125°
130°
135°
140°
145°
150°

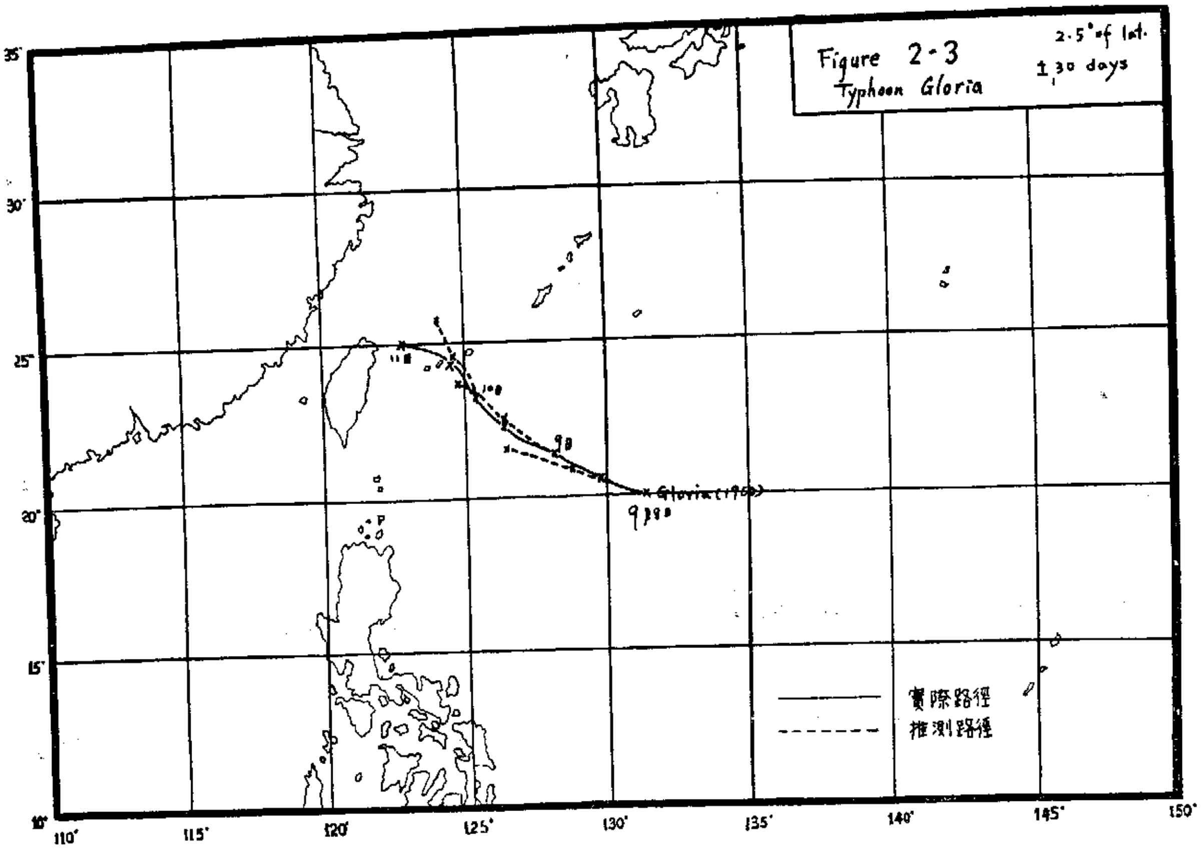
Figure 2-3
Typhoon Gloria
2.5° of lat.
± 30 days
35°
30°
25°
20°
15°
10°
110°
115°
120°
125°
130°
135°
140°
145°
150°
11日
10日
9日
Gloria (1963)
9月8日
實際路徑
推測路徑

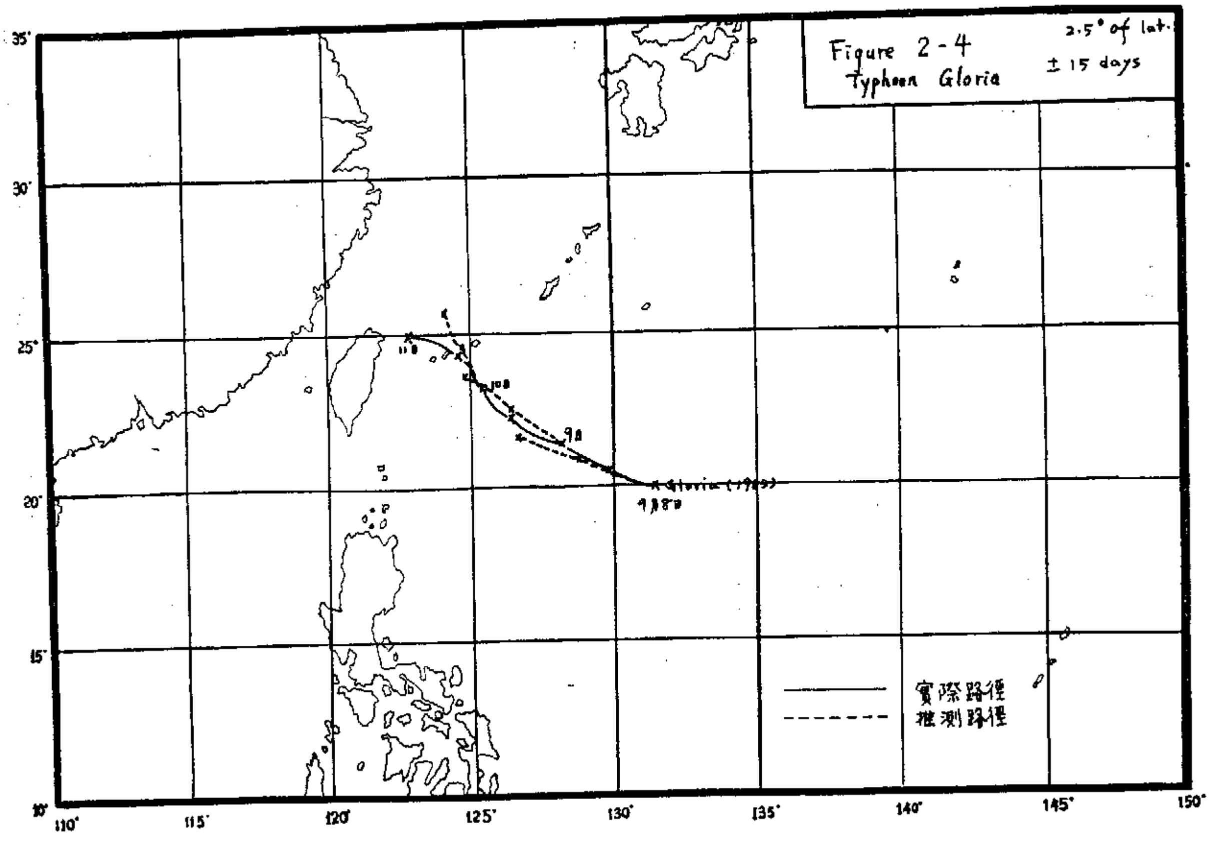
Figure 2-4
Typhoon Gloria
2.5° of lat.
± 15 days
35°
30°
25°
20°
15°
10°
110°
115°
120°
125°
130°
135°
140°
145°
150°
11日
10日
9日
Gloria (1963)
9月8日
實際路徑
推測路徑

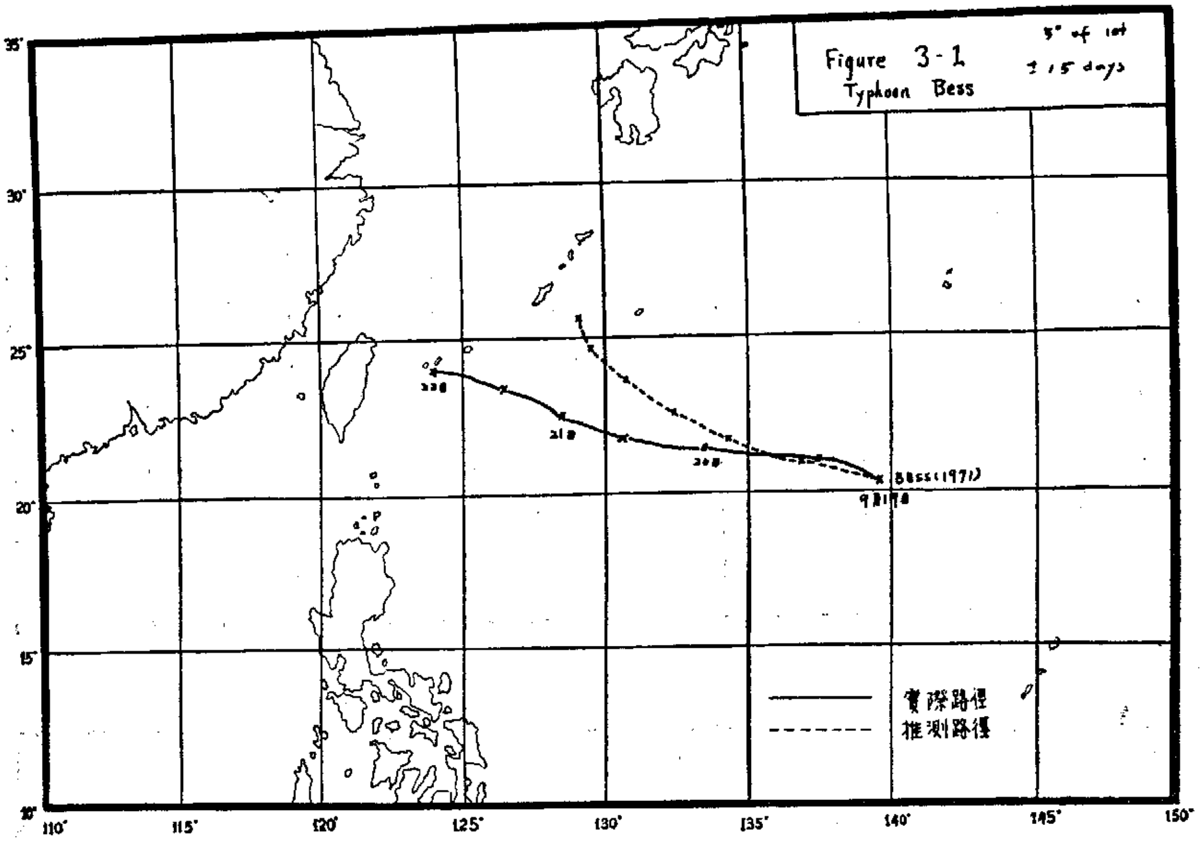
Figure 3-1
Typhoon Bess
5° of lat
± 15 days
BESS(1971)
9月19日
20日
21日
22日
實際路徑
推測路徑
35°
30°
25°
20°
15°
10°
110°
115°
120°
125°
130°
135°
140°
145°
150°

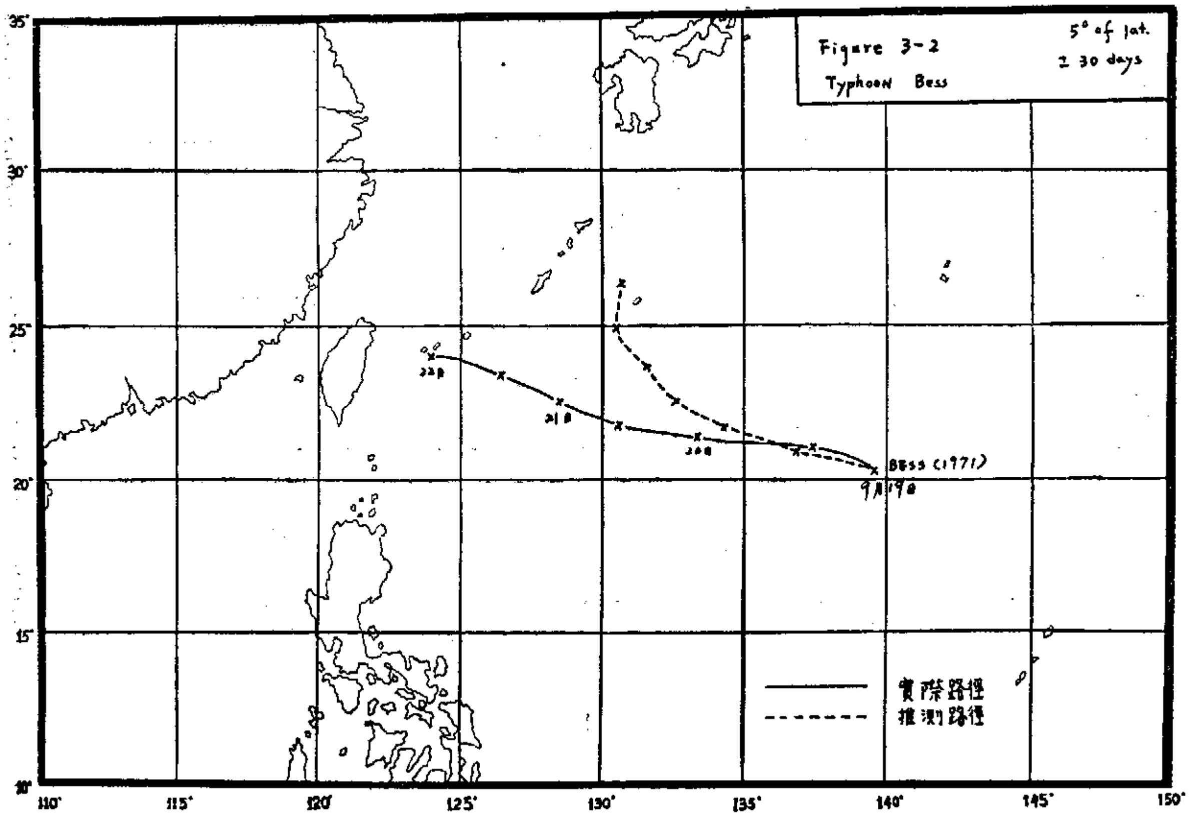
Figure 3-2
Typhoon Bess
5° of lat.
± 30 days
BESS (1971)
9月19日
20日
21日
22日
實際路徑
推測路徑
35°
30°
25°
20°
15°
10°
110°
115°
120°
125°
130°
135°
140°
145°
150°

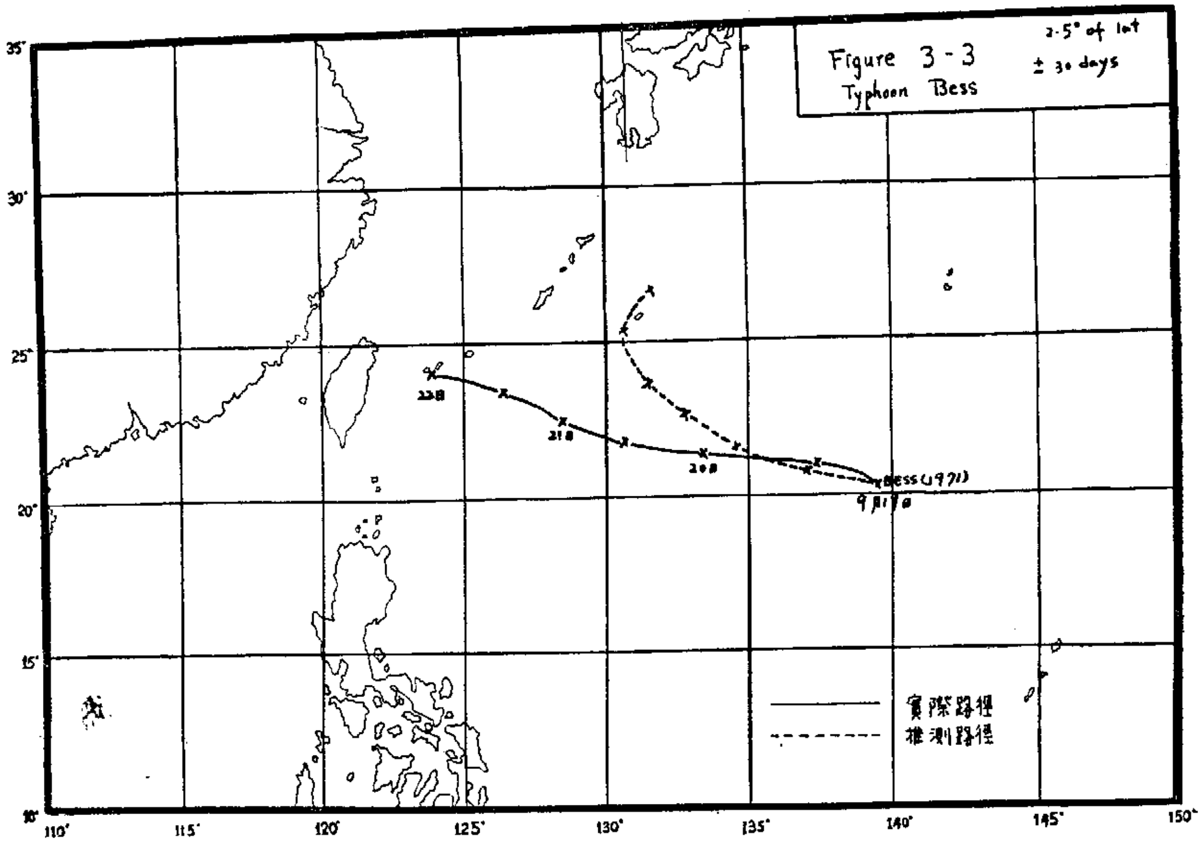
Figure 3-3
Typhoon Bess
2.5° of lat
± 30 days
35°
30°
25°
20°
15°
10°
110°
115°
120°
125°
130°
135°
140°
145°
150°
22日
21日
20日
Bess (1971)
9月19日
實際路徑
推測路徑

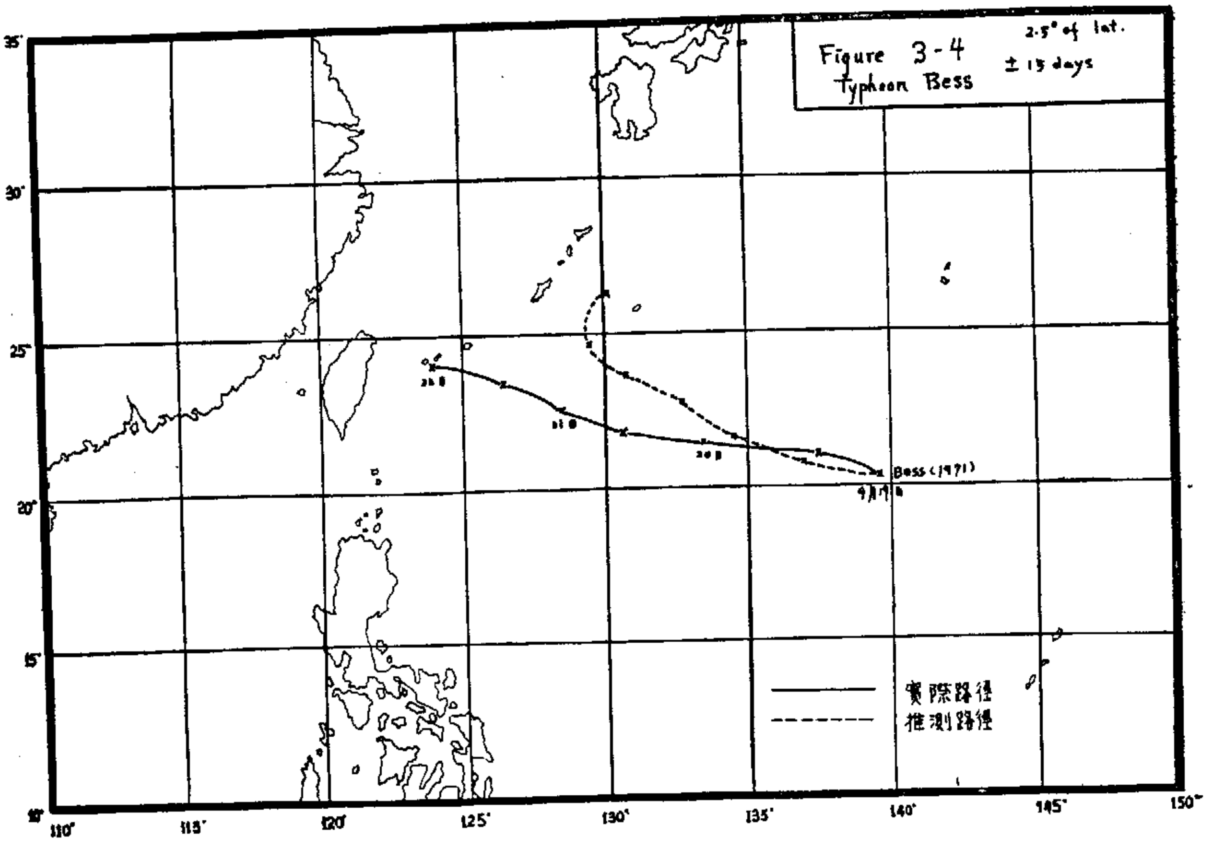
Figure 3-4
Typhoon Bess
2.5° of lat.
± 15 days
35°
30°
25°
20°
15°
10°
110°
115°
120°
125°
130°
135°
140°
145°
150°
22日
21日
20日
Bess (1971)
9月19日
實際路徑
推測路徑

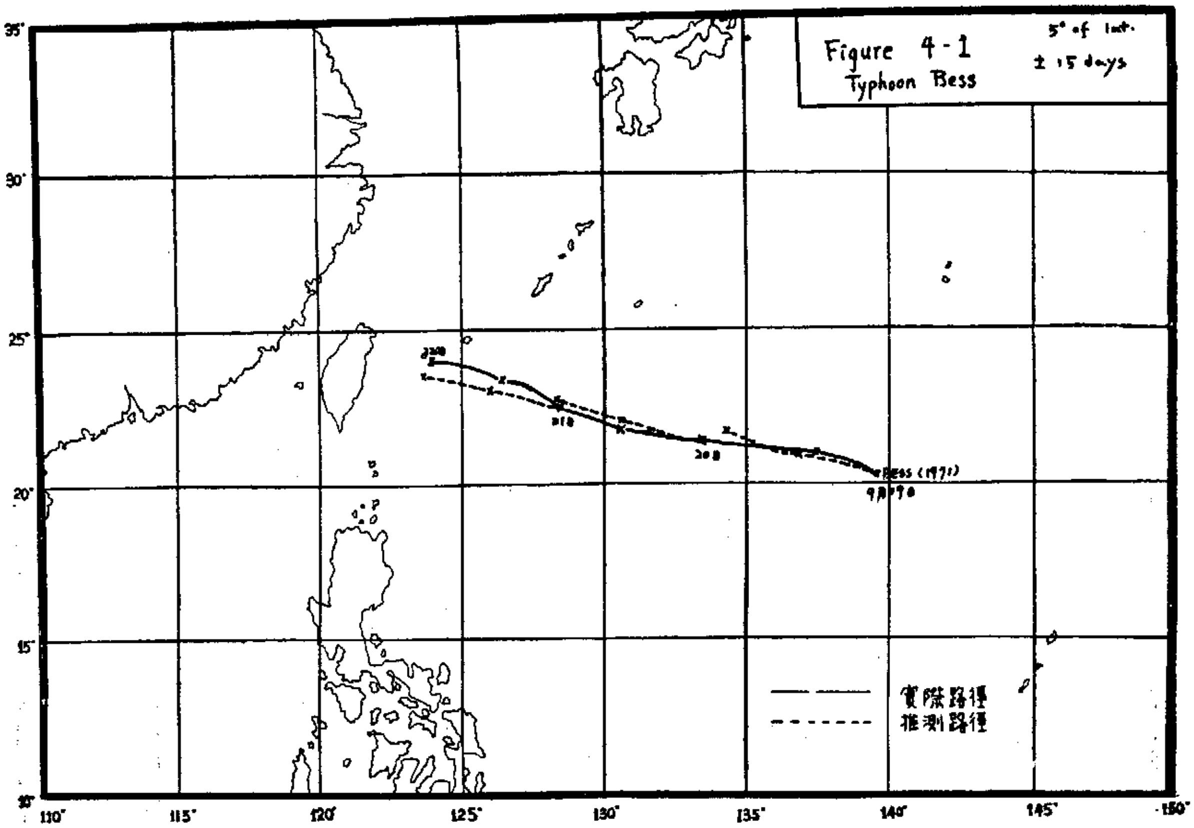
Figure 4-1
Typhoon Bess
5° of lat.
± 15 days
35°
30°
25°
20°
15°
10°
110°
115°
120°
125°
130°
135°
140°
145°
150°
22日
21日
20日
Bess (1971)
9月19日
實際路徑
推測路徑

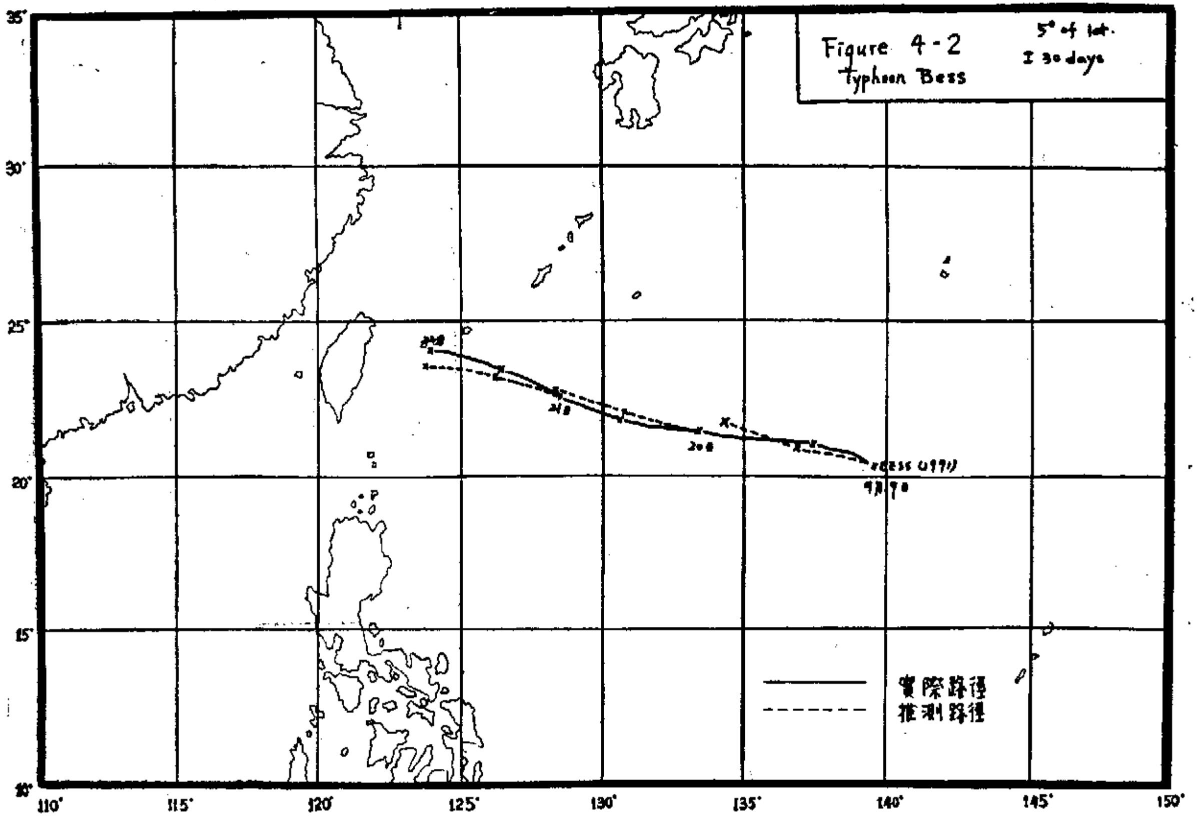
Figure 4-2
Typhoon Bess
5° of lat.
± 30 days
35°
30°
25°
20°
15°
10°
110°
115°
120°
125°
130°
135°
140°
145°
150°
22日
21日
20日
Bess (1971)
9月19日
實際路徑
推測路徑

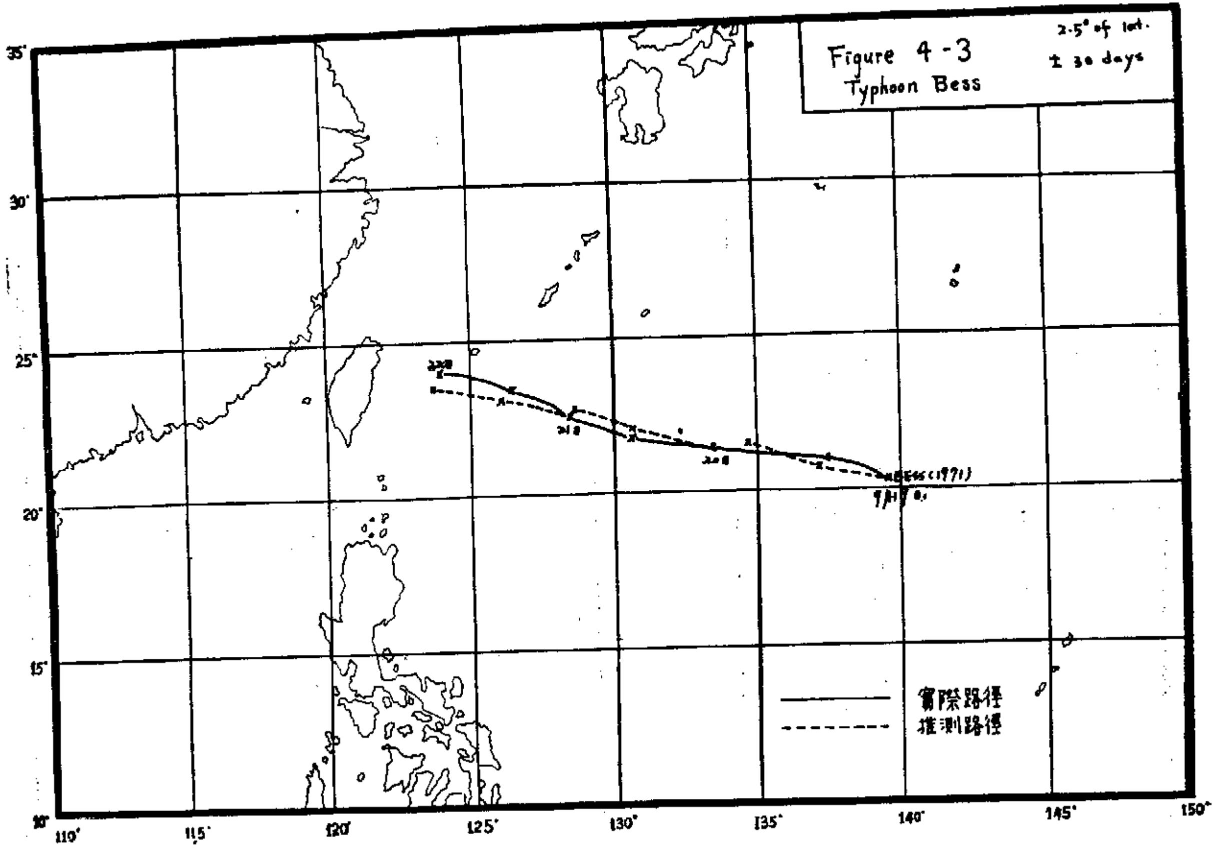
Figure 4-3
Typhoon Bess
2.5° of lat.
± 30 days
23日
21日
20日
BESS (1971)
9月17日
實際路徑
推測路徑
35°
30°
25°
20°
15°
10°
110°
115°
120°
125°
130°
135°
140°
145°
150°

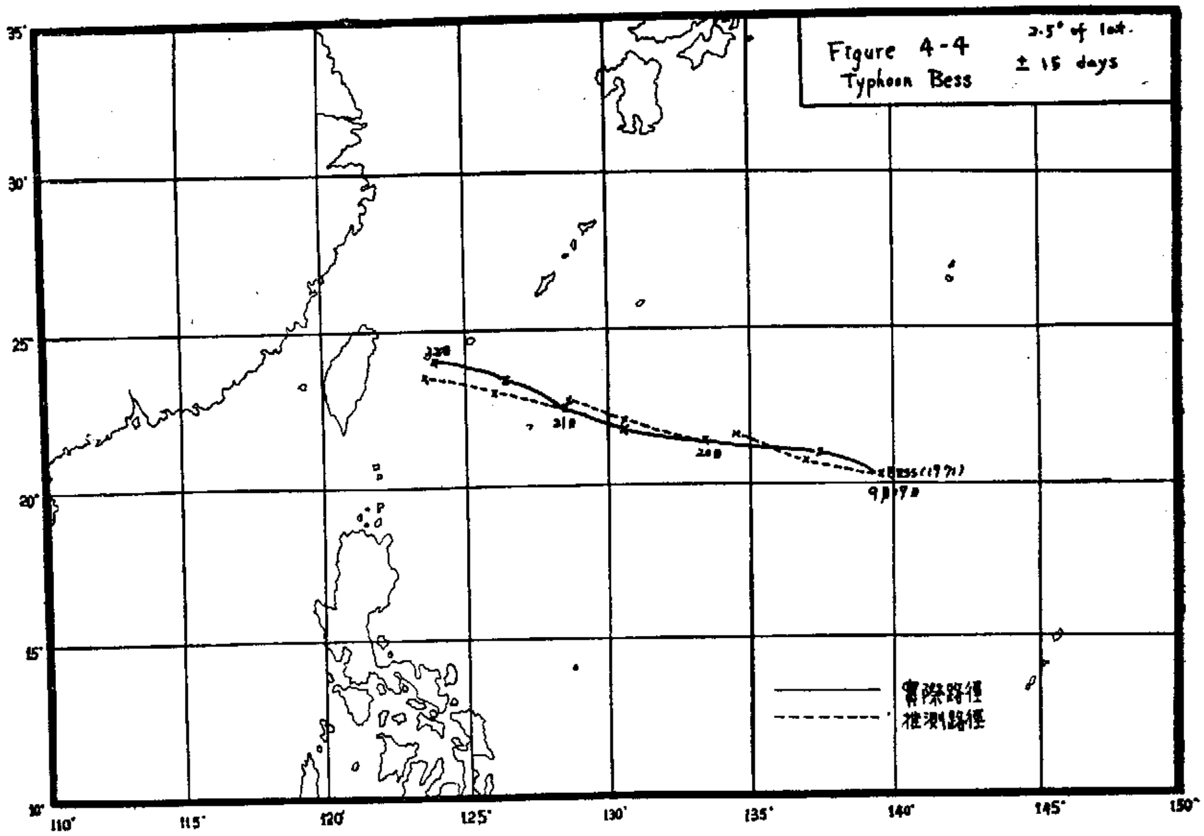
Figure 4-4
Typhoon Bess
2.5° of lat.
± 15 days
23日
21日
20日
BESS (1971)
9月17日
實際路徑
推測路徑
35°
30°
25°
20°
15°
10°
110°
115°
120°
125°
130°
135°
140°
145°
150°

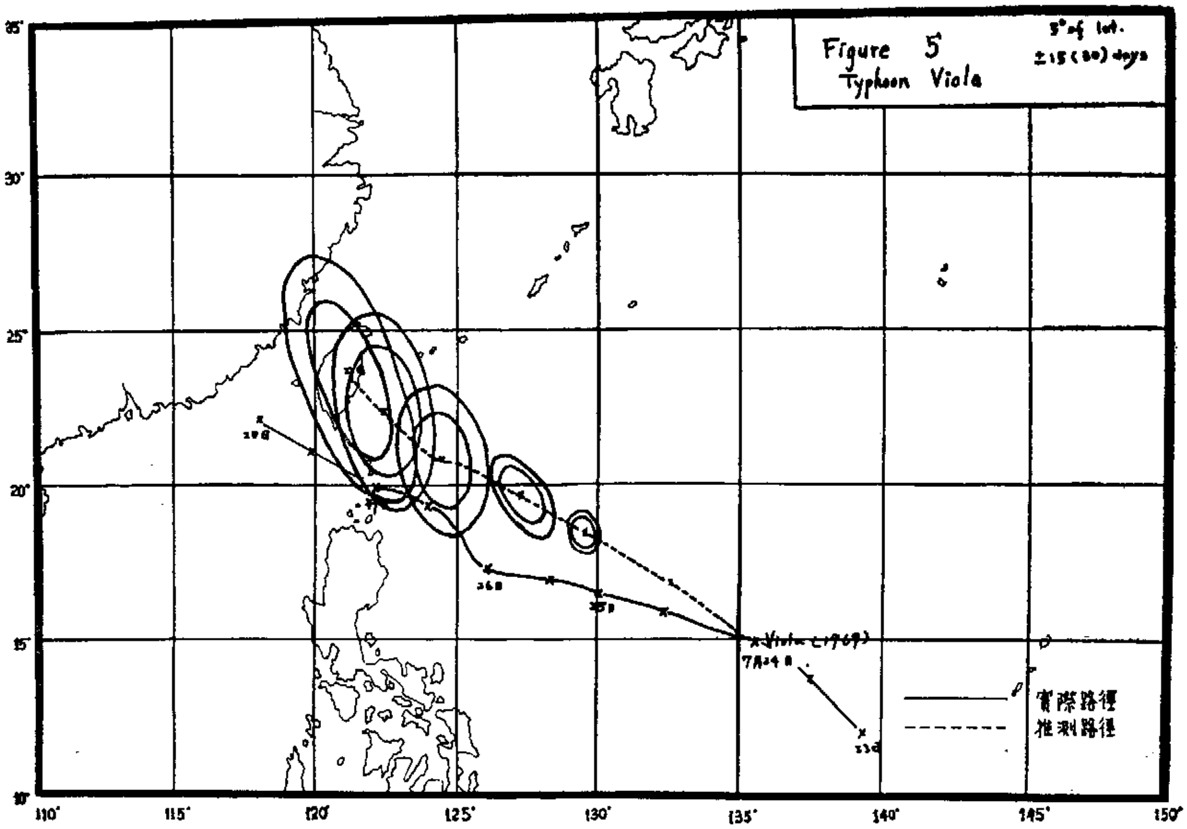

Figure 5
Typhoon Viola

5° of lat.
±15 (30) days
28日
26日
25日
Viola (1969)
7月24日
23日
實際路徑
推測路徑
35°
30°
25°
20°
15°
10°
110°
115°
120°
125°
130°
135°
140°
145°
150°

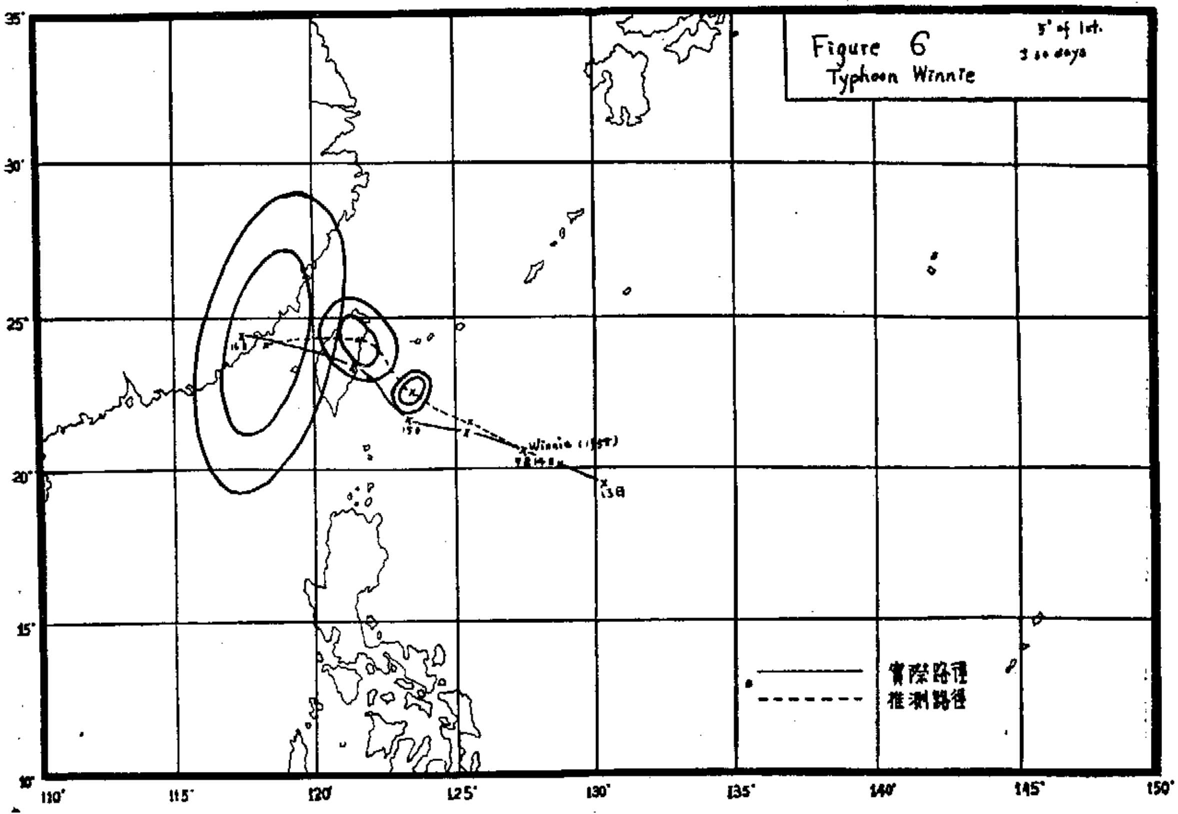

Figure 6
Typhoon Winnie

5° of lat.
± 30 days
16日
15日
Winnie (1958)
7月14日
13日
實際路徑
推測路徑
35°
30°
25°
20°
15°
10°
110°
115°
120°
125°
130°
135°
140°
145°
150°

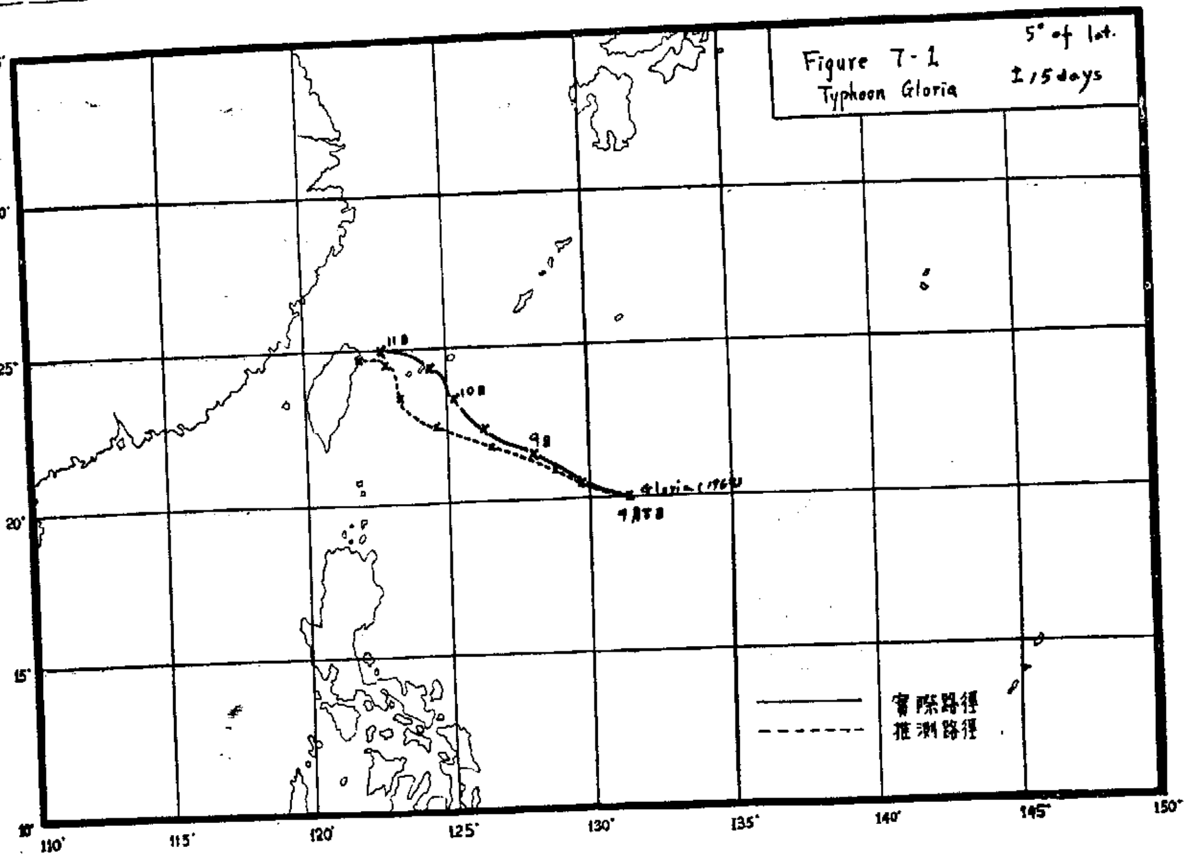
Figure 7-1
Typhoon Gloria
5° of lat.
±15 days
11日
10日
9日
Gloria (1962)
9月8日
實際路徑
推測路徑
35°
30°
25°
20°
15°
10°
110°
115°
120°
125°
130°
135°
140°
145°
150°

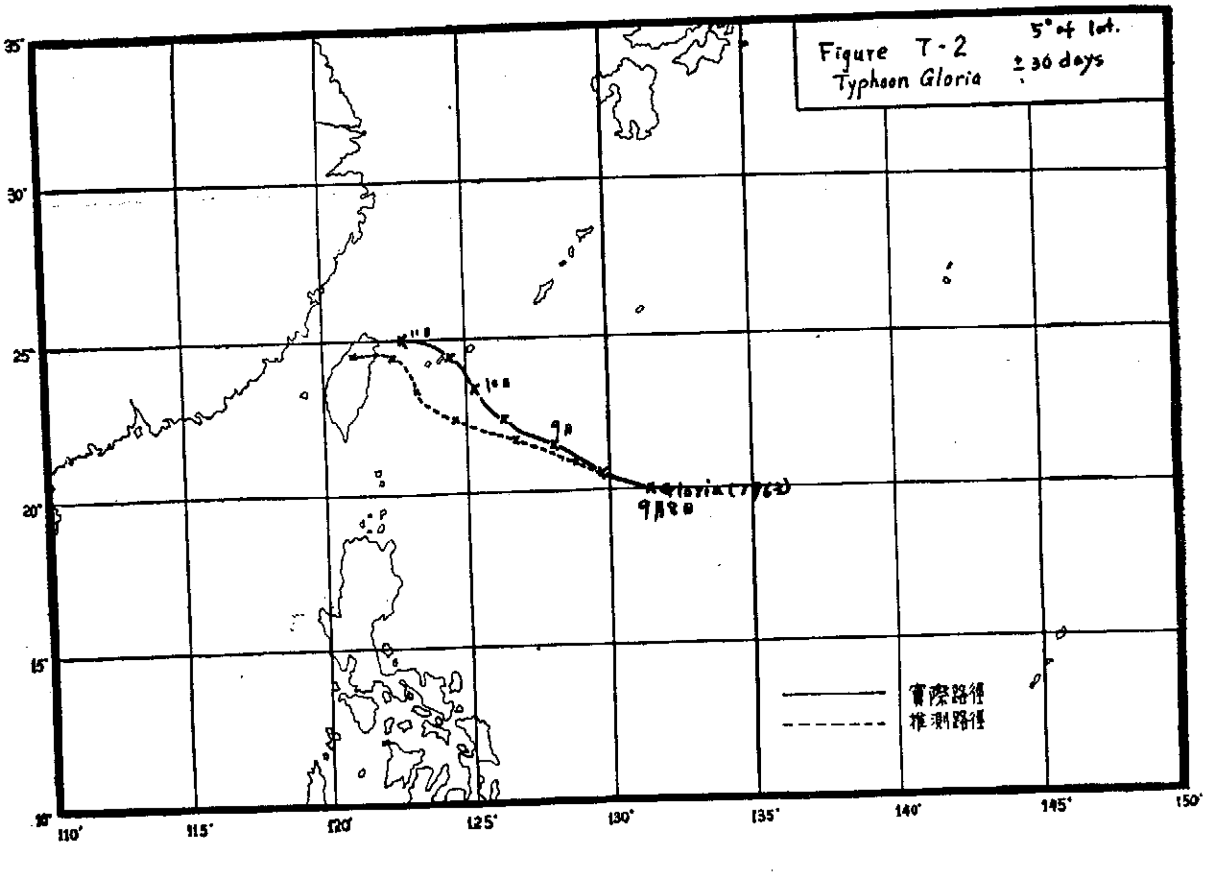
Figure 7-2
Typhoon Gloria
5° of lat.
±30 days
11日
10日
9日
Gloria (1962)
9月8日
實際路徑
推測路徑
35°
30°
25°
20°
15°
10°
110°
115°
120°
125°
130°
135°
140°
145°
150°

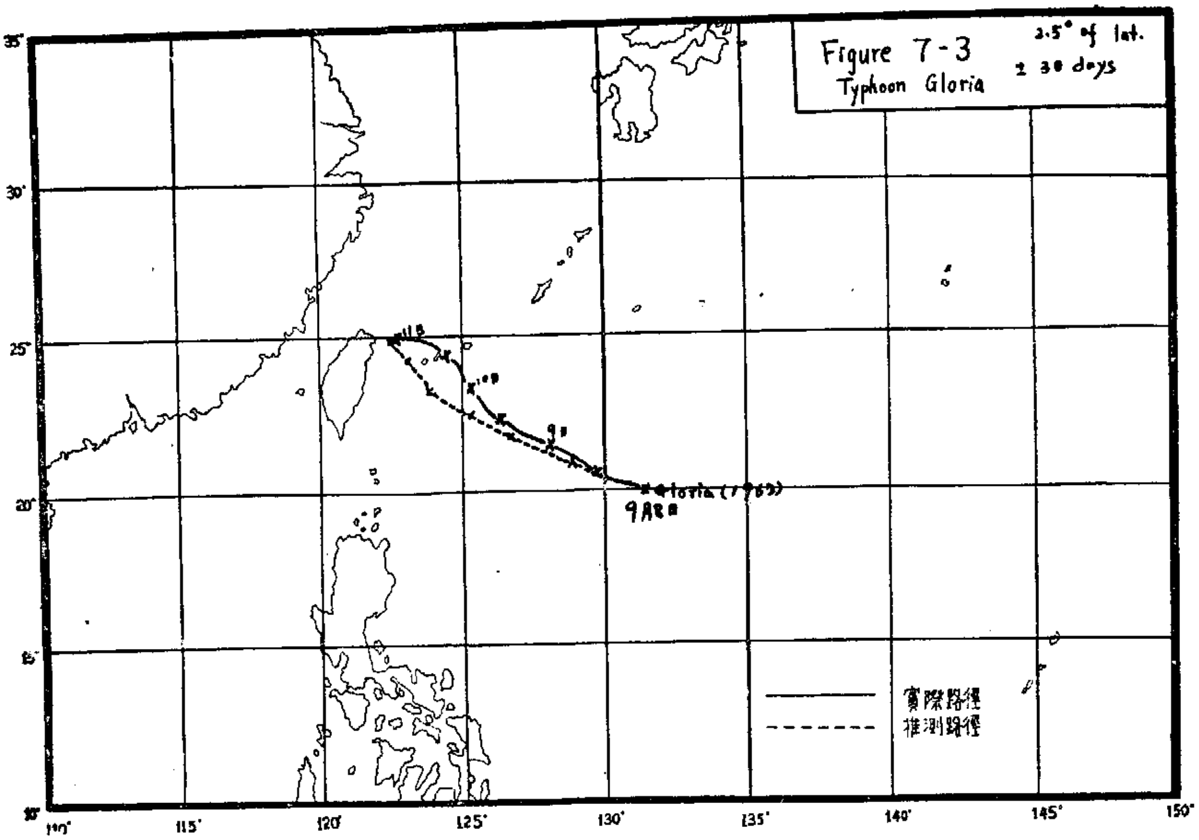

Figure 7-3
Typhoon Gloria

2.5° of lat.
± 30 days

11日
10日
9日
Gloria (1963)
9月8日
實際路徑
推測路徑
35°
30°
25°
20°
15°
10°
110°
115°
120°
125°
130°
135°
140°
145°
150°

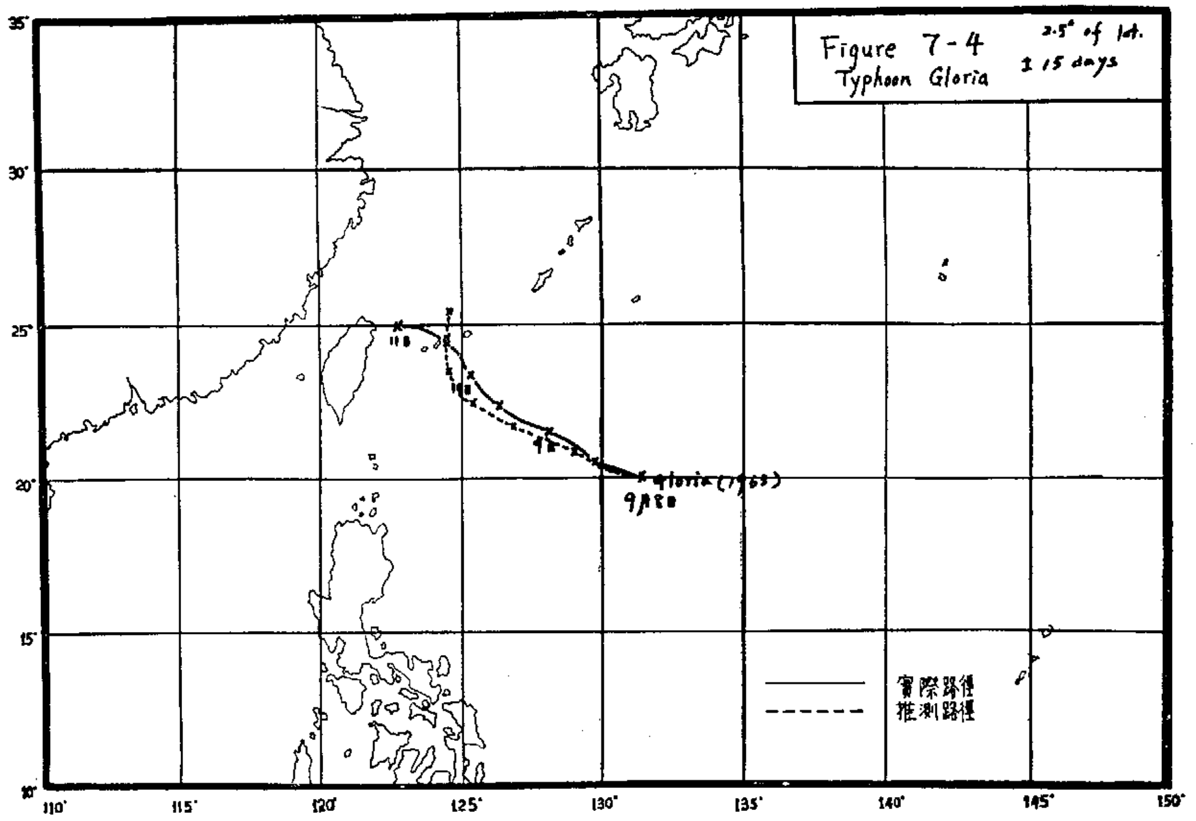

Figure 7-4
Typhoon Gloria

2.5° of lat.
± 15 days

11日
10日
9日
Gloria (1963)
9月8日
實際路徑
推測路徑
35°
30°
25°
20°
15°
10°
110°
115°
120°
125°
130°
135°
140°
145°
150°

Annual Report of the Institute of Physics, Academia Sinica, 1971

地轉風假設下區域性大氣運動之探討

王國雄　汪羣從 (Chun-Tsung Wang)

1. 導　論

亞熱帶海洋性氣候之演變歷年來經過甚多學者從不同角度加以探討。發現表面的摩擦（Surface friction）可感熱（Sensible heat）之傳遞以及潛熱（Latent heat）之釋放等皆有影響，尤以後者爲重要。

本文乃基於地轉風（Geotrophic wind）之假設爲出發點， 就上述三因素加以考慮，而得一較粗規模之大氣運動形態。表面摩擦，可感熱等之效應將藉經驗公式表示。潛熱的釋放由雲運動所促成，而雲運動由較大尺度的捲雲（Cirrus cloud）到尺度較小之積雲（Cumulus cloud）種類各異， 對於後者欲在大尺度模型中表示出其效應自是一件困難的事，況且此等運動的眞正力學機構（Mechanism）尙在研究中，及至目前還沒有一正確表示法被吾人應用，故在本文將利用一區域平均値（Local average value）以表示其效應 。 除上述而外本文將作如下之假設：

壓力分佈在垂直向爲靜平衡（Hydrostatic）

不考慮陸地影響

摩擦之考慮僅限於摩擦層頂（900 mb）

潛熱之釋放限於 500 mb 以下

各層的平均溼度爲常數。

2. 數理模型

2.1 基本方程式：

在直角壓力坐標系統（Pressure coordinate system）下控制大氣運動的基本方程式爲：

§ 等壓面動量方程式：

$$\frac{d\vec{V}}{dt}+\vec{k}\times f\,\vec{V}+g\,\nabla z=-g\frac{\partial\tau}{\partial p} \tag{1}$$

§ 垂直向動量方程式：

$$\frac{\partial z}{\partial p}=-\frac{1}{g\rho}=-\frac{RT}{gp} \tag{2}$$

§ 能量方程式：

$$\frac{dQ}{dt}=C_P\frac{dT}{dt}-\alpha\frac{dp}{dt} \tag{3}$$

上列各式中：$\vec{V}$＝等壓面上速度，$\vec{k}$＝垂直向之單位向量， f＝柯式係數（Coriolis parameter）， g＝重力加速度，z＝高度，τ＝剪力（Shear stress），p＝壓力，ρ＝空氣密度，R＝空氣之氣體常數，T＝溫度，$\frac{dQ}{dt}$＝空氣單位質量單位時間內所加之熱量，C_P＝等壓熱容，α＝空氣之單位質量體積（$=\frac{1}{\rho}$）， t＝時間。

$$\frac{d}{dt}=\frac{\partial}{\partial t}+\vec{V}\cdot\nabla+\omega\frac{\partial}{\partial p},\quad \nabla=\frac{\partial}{\partial x}\vec{i}+\frac{\partial}{\partial y}\vec{j}$$

ω 爲上昇速度，x, y 爲等壓面上向東，北之坐標軸，$\vec{i}$, $\vec{j}$ 爲該軸上之單位向量，

§ 地轉風方程式：

$$\vec{V} = \vec{k} \times \frac{g}{f_0} \nabla z \text{，或} \zeta = \frac{g}{f_0} \nabla^2 z \qquad (4)$$

$\nabla^2 = \frac{\partial^2}{\partial x^2} + \frac{\partial^2}{\partial y^2}$, f_0 爲 f 之平均値，ζ 爲旋轉度（$= \vec{k} \cdot \nabla \times \vec{V}$）。

2.2 預測方程式：

將位溫，θ (Potential teurpuature) 及靜穩定度 S (Static stability)

$$\theta = T\left(\frac{1000}{P}\right)^{R/C_P}, \quad S = -\frac{1}{\rho\theta} \frac{\partial\theta}{\partial P}$$

代入 Eqs. 1-4, 化簡可得 (Thompson, 1961),(Staff Members, 1965)

§. 旋轉度方程式：

$$\frac{\partial \nabla^2 z}{\partial t} + J(z, \zeta + f) - \frac{f_0{}^2}{g} \frac{\partial \omega}{\partial P} = -f_0 \vec{k} \cdot \nabla \times \left(\frac{\partial z}{\partial P}\right) \qquad (5)$$

$J =$ Jacobian 運算：$J(A, B) = \frac{\partial A}{\partial x} \frac{\partial B}{\partial y} - \frac{\partial A}{\partial y} \frac{\partial B}{\partial x}$

A, B 爲任何兩個無向量函數 (Scalar function),

邊界條件 (Boundary conditions) 爲在計算範圍 (Computation domain) 以外 z 値不隨時間而變。

初始條件 (Initial conditions) 爲 $t = 0$ 時，$z\ (x, y, p) = z_0(x, y, p)$ (Figs. 1-4).

§ 上昇速度方程式：

$$\frac{S}{g} \nabla^2 \omega + \frac{f^2{}_0}{g} \frac{\partial^2 \omega}{\partial p^2} = \frac{\partial}{\partial p} J(z, \zeta + f) - \frac{g}{f_0} \nabla^2 J\left(z, \frac{\partial z}{\partial p}\right) + f_0 \vec{k} \cdot \nabla \times \frac{\partial^2 \vec{\tau}}{\partial p^2}$$

$$- \frac{R}{C_P} \frac{1}{gp} \nabla^2 \frac{dQ}{dt} \qquad (6)$$

邊界條件爲 $P = 200$mb, 或 1000mb, $\omega = 0$;

同時在計算範圍邊界上 (大氣物理組同仁，1972) $\omega = -\frac{g^2}{Sf_0} J\left(z, \frac{\partial z}{\partial P}\right)$.

2.3 表面摩擦可感熱，潛熱等因素：

§. 表面摩擦：

大氣與海面交界處之摩阻力可設爲

$$\overline{\tau_{10}} = \overline{\rho_{10}}\ C_D\ |\overline{V_{10}}| \vec{V}_{10} \qquad (7)$$

式中 C_D 爲摩阻力係數 (Miller, 1969)

$$C_D = (1.0 + 0.07 |\overline{V_{10}}|) \times 10^{-3}$$

$\overline{\rho_{10}}$ = 海面空氣之平均密度，$|\overline{V_{10}}|$ = 海面空氣之平均速率，今設

$$\overline{\rho_{10}} = 1,18 \times 10^{-2} \text{mb sec}^2/\text{m}^2, \quad |\overline{V_{10}}| = 25\text{m/sec}.$$

對方程式 (5) (6) 而言 τ 之影響僅考慮最低層，在高空該項將不存在。

則 $$g\left(\frac{\partial \vec{\tau}}{\partial p}\right)_{P=900\text{mb}} = \frac{g\ \overline{\rho_0}\ C_D\ |\overline{V_{10}}|}{\varDelta p} \vec{V}_{10} = k \vec{V}_{10} \qquad (8)$$

$$k \cong 6.67 \times 10^{-6}\ \text{sec}^{-1}$$

§. 可感熱之傳遞：

當空氣以 $\vec{V}_{10}$ 之速度運行時，對流熱傳可按經驗公式計算

$$F_S = A'_1 |\vec{V}_{10}| \ (T_w - T_{10}) \tag{9}$$

F_S＝海面熱傳量 (Heat flux), A'_1 爲經驗係數 $(= C_P \ C_D \ \overline{\rho}_0 \ |\vec{V}_{10}|)$，海面空氣速度之絕對值，$T_S$＝海洋之溫度，$T_{10}$ 爲空氣在 1000mb 之溫度（吾人將假設 1000mb 爲海面壓力），可利用 850mb, 700mb 之各層溫度以求之

$$T_{10} = 2.42(T_{8.5} - \overline{T}_{8.5}) + 0.57(T_7 + \overline{T}_7) + 0.82\overline{T}_{10} \tag{10}$$

T_{10}, $T_{8.5}$ T_7 爲 1000mb, 850mb, 700mb 之溫度，$\overline{T}_{10}$, $\overline{T}_{8.5}$, $\overline{T}_7$ 爲各該層之平均溫度。
可或熱傳爲 (Miller, 1969)

$$\frac{dQ_s}{dt} = g\frac{\partial F_s}{\partial P} \doteq A_1 |\overline{V}_{10}| (T_s - T_{10}) \tag{11}$$

$$T_s - T_{10} > 0 \qquad A_1 \doteq 7.45 \times 10^{-4} \ m/\mathrm{sec}^2 \ \mathrm{deg}$$

$$T_s - T_{10} < 0 \qquad A_1 \doteq 7.45 \times 10^{-5} m/\mathrm{sec}^2 \ \mathrm{deg}$$

§. 潛熱之釋放：

潛熱釋放爲 (Gambo, 1963; Danard, 1966)

$$\frac{dQ_L}{dt} = -LF^* \, \omega \Delta S \cdot \beta \qquad \omega < 0$$

$$= 0 \qquad \omega \geq 0 \tag{12}$$

$$F^* = \frac{dq^*}{dt} = \frac{1}{1 + \frac{L}{C_P} Q_2} \left[Q_1 - \frac{gQ_1}{C_P} \ \frac{\partial z}{\partial p} \right] \tag{13}$$

式中 q^*＝飽和空氣之濕度

L＝水之凝結熱＝$2.22 \times 10^6 \ \mathrm{m}^2 \ \mathrm{sec}^{-2}$

$Q_1 = \left(\frac{\partial q^*}{\partial P} \right)_T = -1.48 \times 10^{-5} \ \mathrm{mb}^{-1}$

$Q_2 = \left(\frac{\partial q^*}{\partial T} \right)_P = 6.99 \times 10^{-4} \, {}^\circ K^{-1}$

$\Delta S = 1 - \frac{T - T_d}{7.5} \qquad T - T_d < 7.5$

$= 0 \qquad T - T_d \geq 7.5$

T_d＝空氣之露點溫度 (Dew point temperature)

$\beta = 1$ at 800 mb

$= 0.826$ at 600 mb

本文中

$$\frac{dQ}{dt} = \frac{dQ_L}{dt} + \frac{dQ_S}{dt} \tag{14}$$

在考慮潛熱的釋放時，爲簡單起見，初始大氣情況 $T - T_d < 7.5$ 的區域將設 $T - T_d = 2.5$ 計算。

3. 結　果

將 Eqs. 8, 11 及 12 代入 Eqs. 4,5 及 6 中，化成差分式 (Finite difference form)（王國雄 1972），卽可解 Eqs. 4,5 及 6 而探討大氣變化。在解 Eq. 6 時需保持 $\nabla^2 \omega$ 項係數大於 $0.2\frac{S}{g}$，以免該式喪失橢圓形態 (Elliptic type partial differential equation)。

Figures 1 至4分別爲 900mb, 700mb, 500mb 及 300mb 各層之高度分佈圖，
Figures 5 至7分別爲 800mb, 600mb 及 400mb 各層之上昇速度分佈圖，
各圖之上半部爲初始條件（ω 由上昇速度方程式求得），下半部爲 16 小時後之分佈圖， 各圖的差分坐標分別比照 Fig. 1. I 及 Fig. 5, I, 今就 Fig. 1 觀之，由 Fig. 1. I 可看出在坐標（12,6）有一低氣壓而在（16,8）附近有一比較高的氣壓，16小時後（12,6）移動到（11,6）點之略北處，同時（16,8）之高壓也漸漸廣大範圍，就整體觀之發現在本文所論之區域內大氣朝西向運動。在高空以 500mb 爲例（Fig. 3）也發現如上所述的運動趨勢。在 Fig. 5 可看出上昇速度之變化情形，在該圖之上半部（12,6）點有一很大的上昇速度（$-\omega > 20\times10^{-4}$ mb/sec), 16 小時後却在（11,7）有一很大的上昇速度，這也表示該低壓運動之趨勢由（12,6）點移至（11,6）點之偏北處。在上述上各圖中可看出（12,6）之低壓在漸漸減弱，此乃利用地轉風之假設的結果（Nitta, 1965）尤其是在靠計算範圍南端之地帶（該地之緯度在本文爲北緯10° 左右）地轉風之假設將會引起大於10%之誤差。然而利用地轉風的假設仍有很大的優點，其一就是減少了預測時所需的方程式，其二就差分所取的間隔及時間間隔而言，也可取得較大，如此在預測天氣變化可節省很多的計算機時間。

4. 誌謝

本文承彭立及簡來成二先生協助完成謹誌謝意。

參考文獻

Danard, M. B., "A quasi-giotrophic numerical methed incorporating effects of release of latent heat" Journal of Applied Meteorology, **5**, 85, 1966.

Gambo, K., "The role of sensible and latent heat in the baroclinic atmosphere" Journal of Meteorological Society of Japan, **41**, 233, 1963.

Miller, B. I. "Experiment in forcasting hurricane development with real data" Technical Memorandum ERLTM-NHRL **85**, 1969.

Nitta, T. "Some examples of numerical weather prediction with the special emphasis on the deuelopment and maintanence of relatively small scale cyclones" Journal of Meteorological Society of Japan, 43, 148, 1965.

Staff Memburs of Electronic Computation Center, "72-hr baroclinic forcast by the diabatic quasi-geotrophic model" Journal of Metesrological Society of Japan, 43, 246, 1965.

Thompson, P. D., Numerical Weather Analysis and Pridiction, 166 PP, 1961.

大氣物理組同仁，大氣及颱風運動模型 I. 邊界條件，中研院物理所集刊，1972。

王國雄，地轉風假設下區域性大氣運動之探討，臺灣大學機械研究所碩士論文，1972。

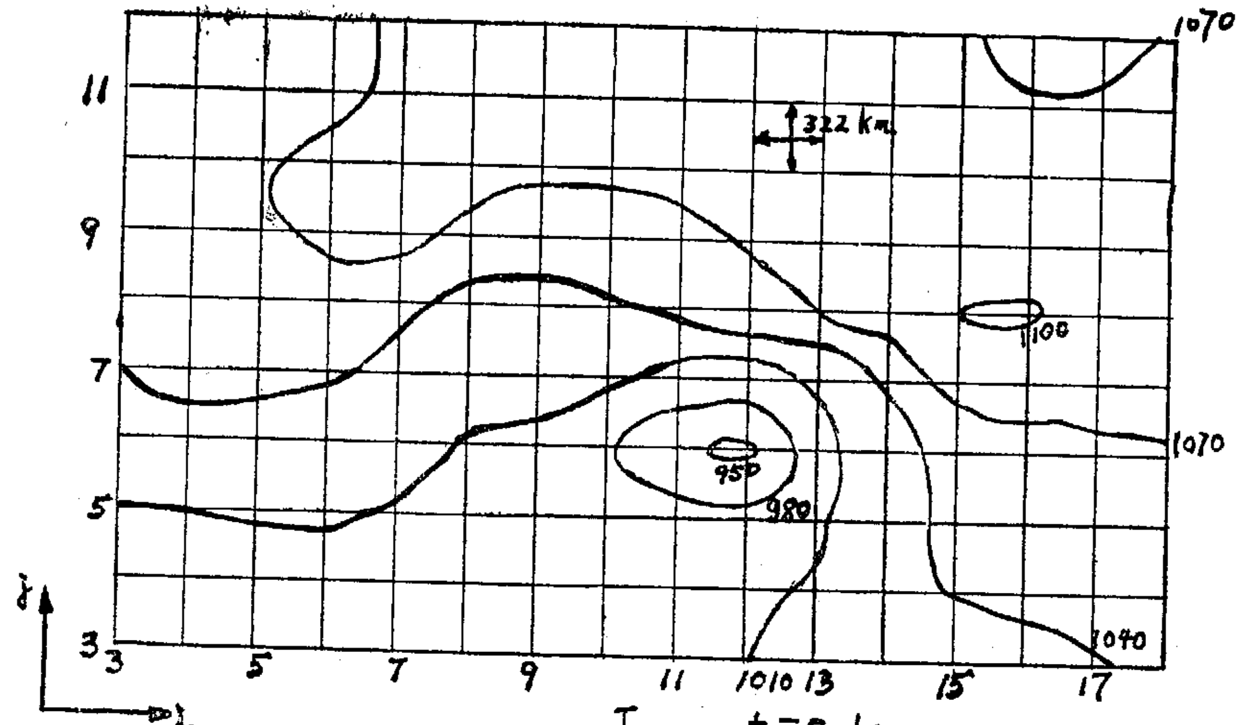
11
9
7
5
3
3
5
7
9
11
1010
13
15
17
γ
λ
322 km.
1070
1100
1070
950
980
1040

I. t=0 hr.

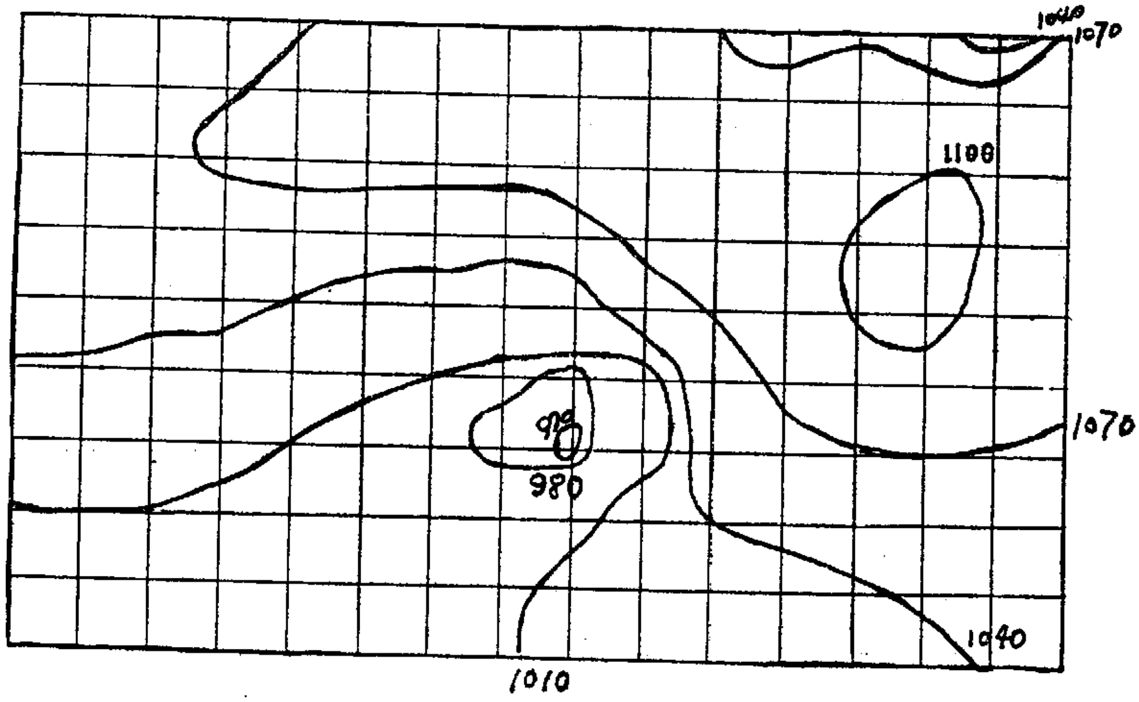
1040
1070
1100
1070
980
980
1040
1010

II. t=16. hrs.

Z in m.

Figure 1. Z - Field at 900 mb.

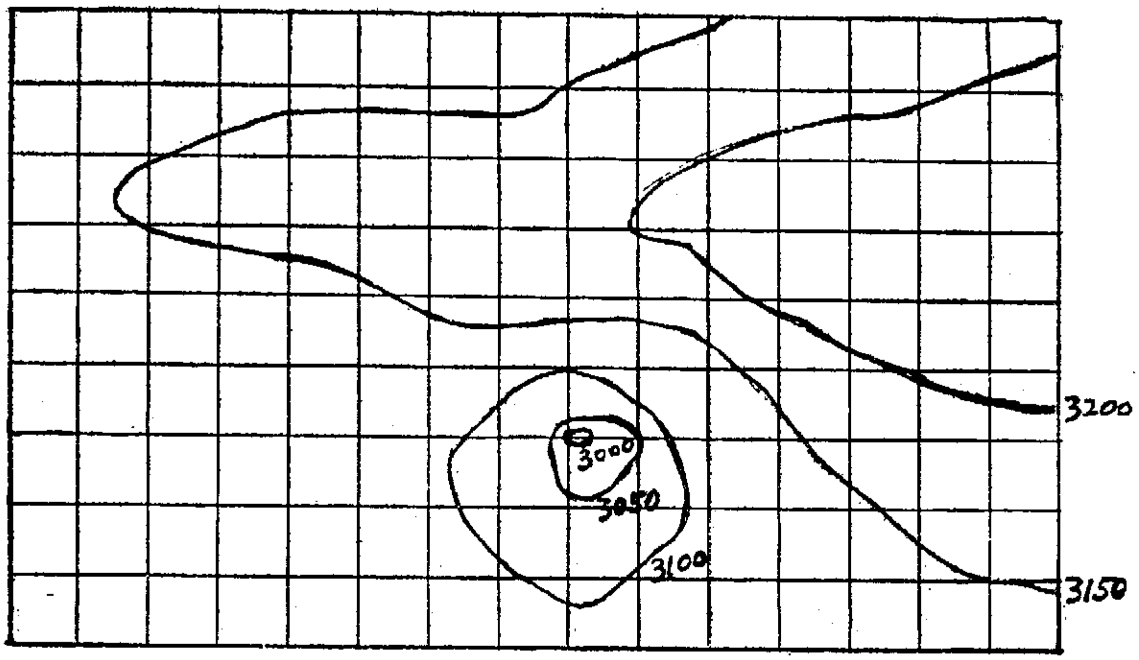
3000
3050
3100
3200
3150

I. t = 0. hr.

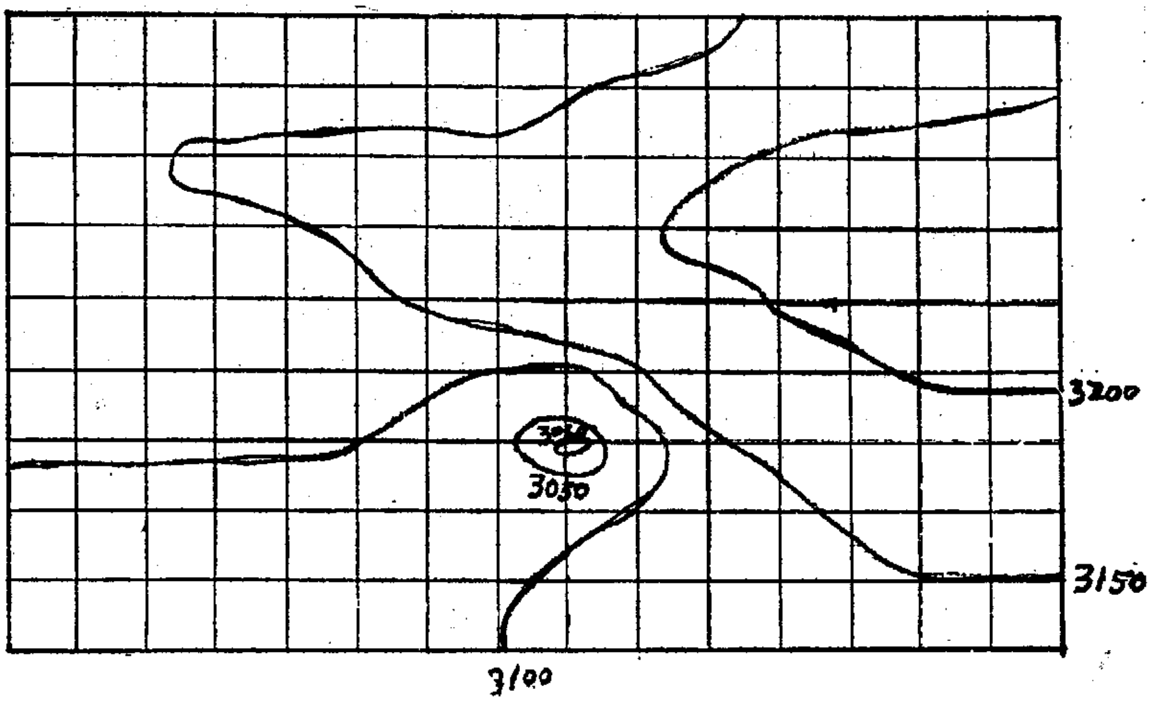
3050
3200
3150
3100

II. t = 16 hrs. Z in m.

Figure 2. Z - Field at 700 mb.

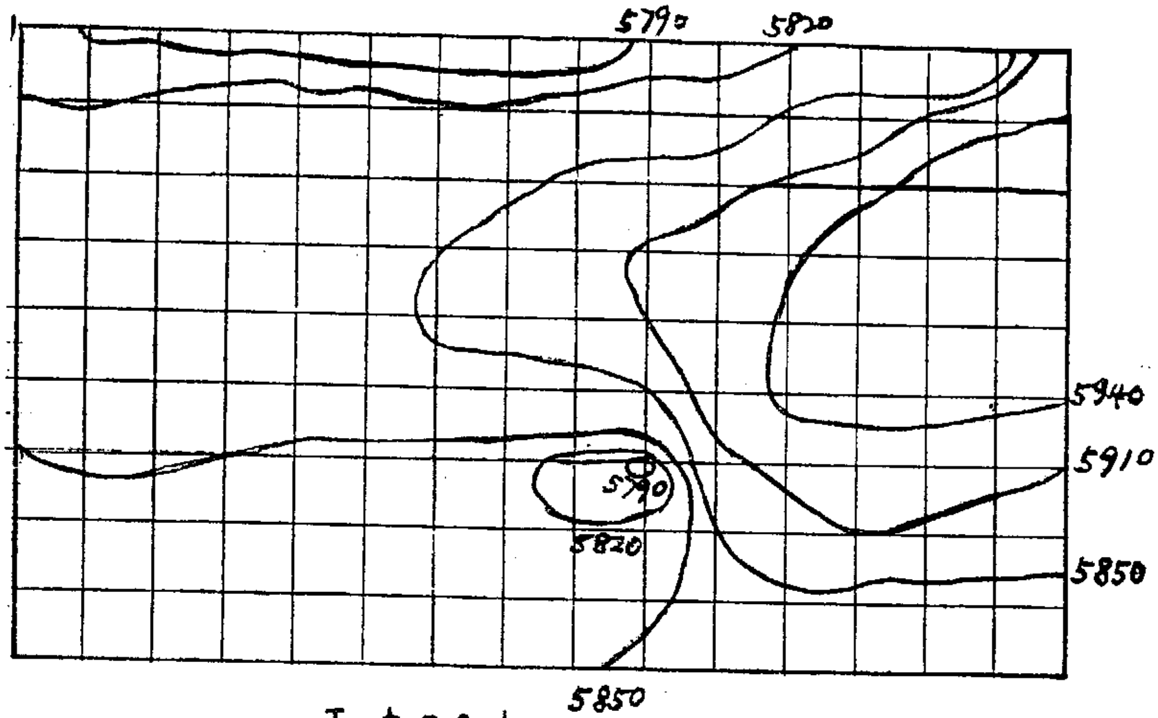
5790
5820
5940
5910
5850
5790
5820
5850

I. t = 0 hr.

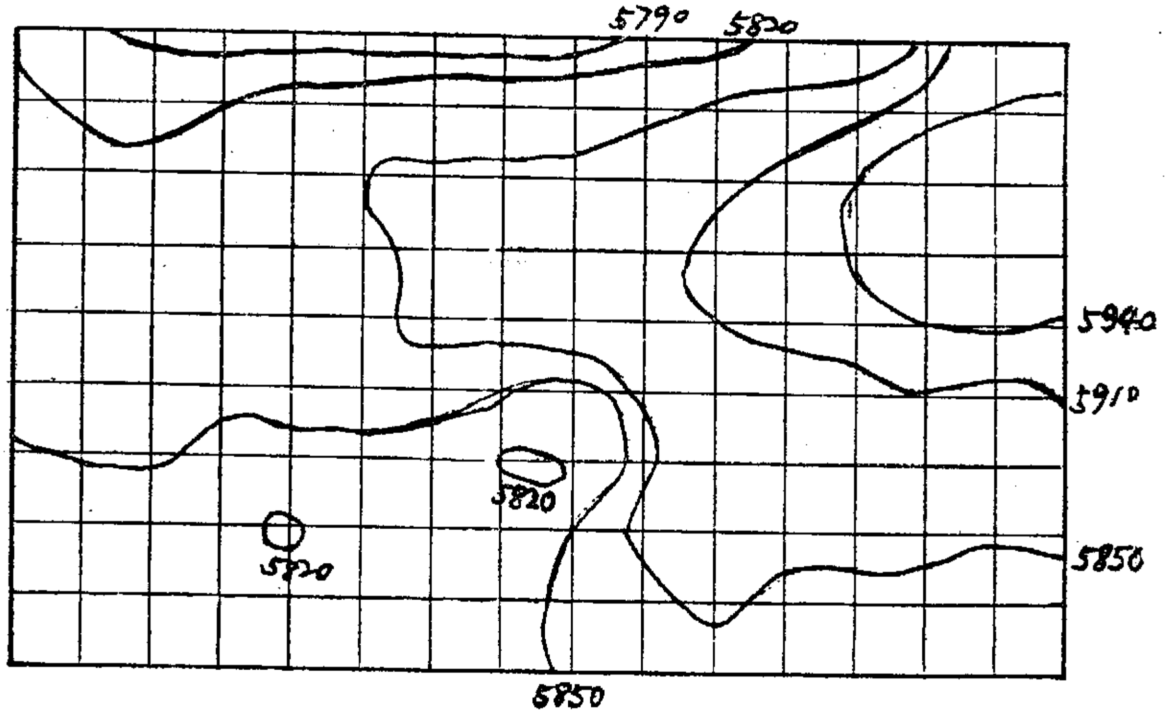
5790
5820
5940
5910
5820
5820
5850
5850

II. t = 16. hrs.

Z in m

Figure 3. Z-Field at 500 mb.

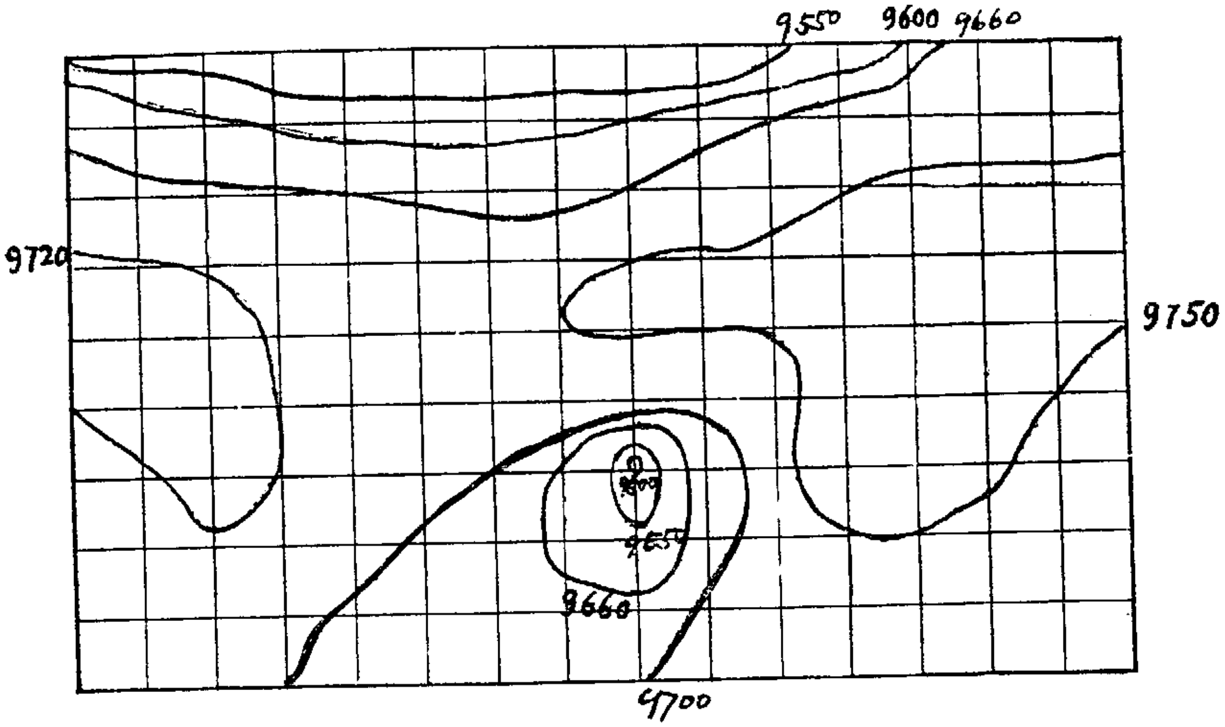
9550
9600
9660
9720
9750
9600
9650
9660
9700

I. t= 0 hr.

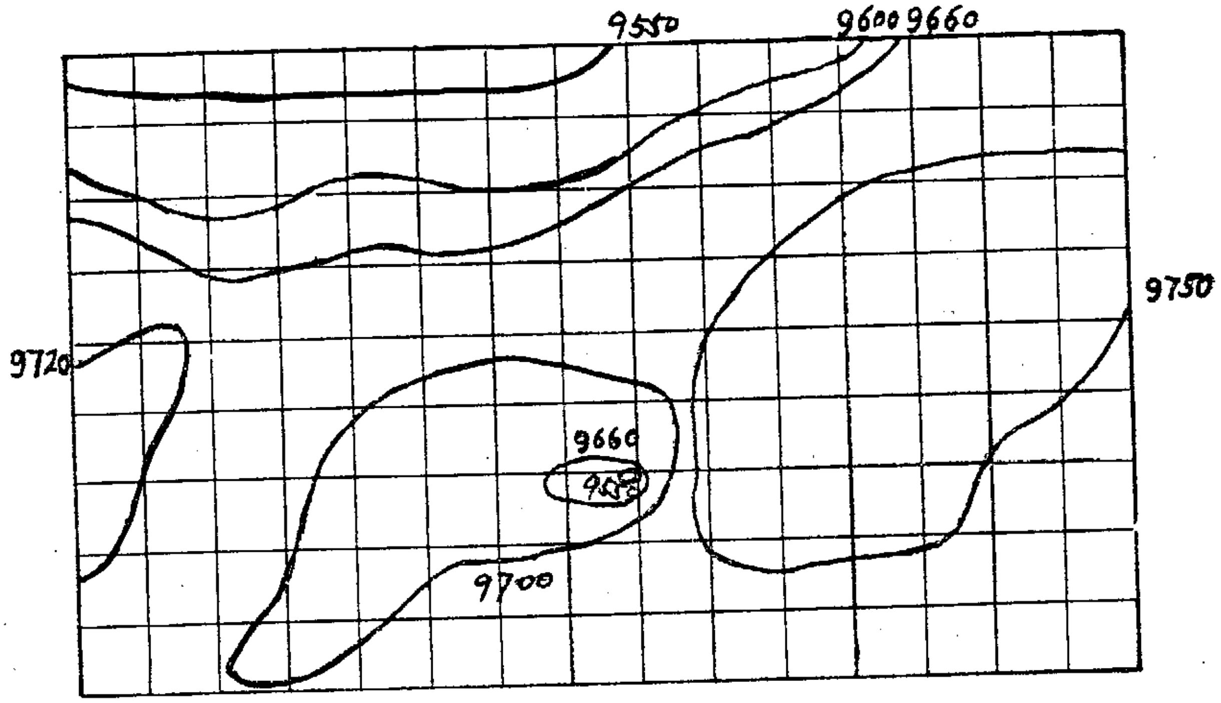
9550
9600
9660
9720
9750
9660
9650
9700

II. t=16 hrs.

Z in m.

Figure 4. Z-Field at 300 mb.

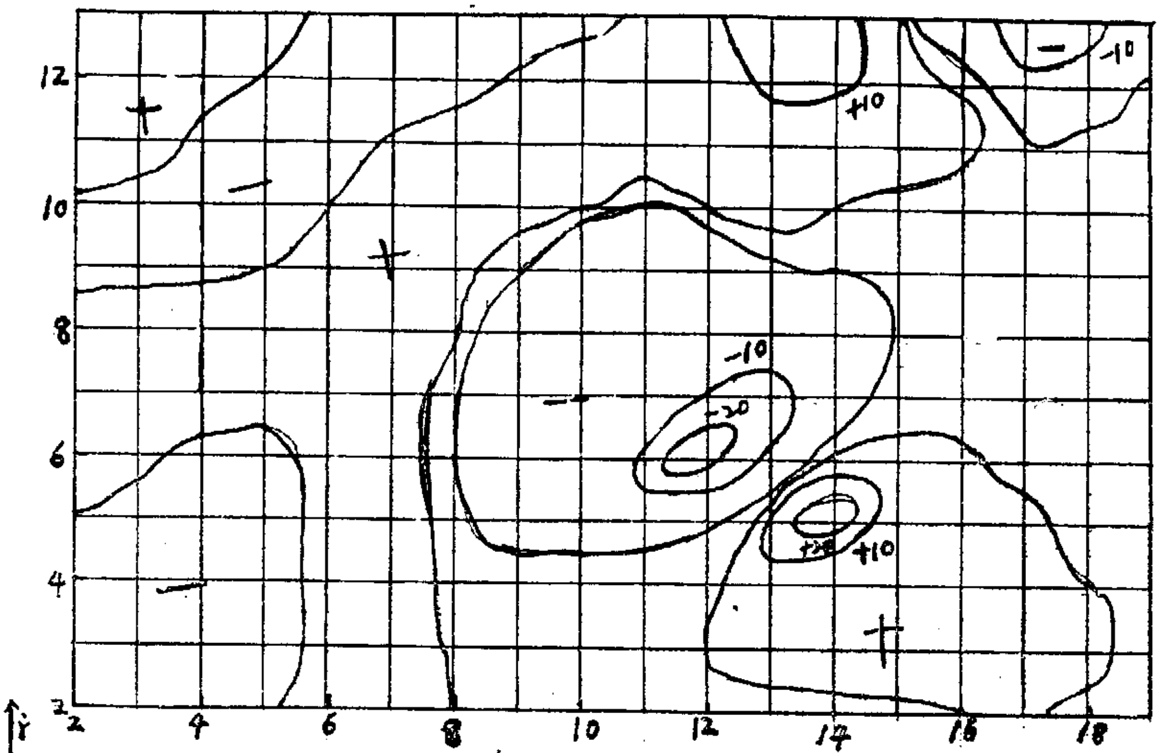

I. t = 0. hr. ω in $\times 10^{-4}$ mb/sec

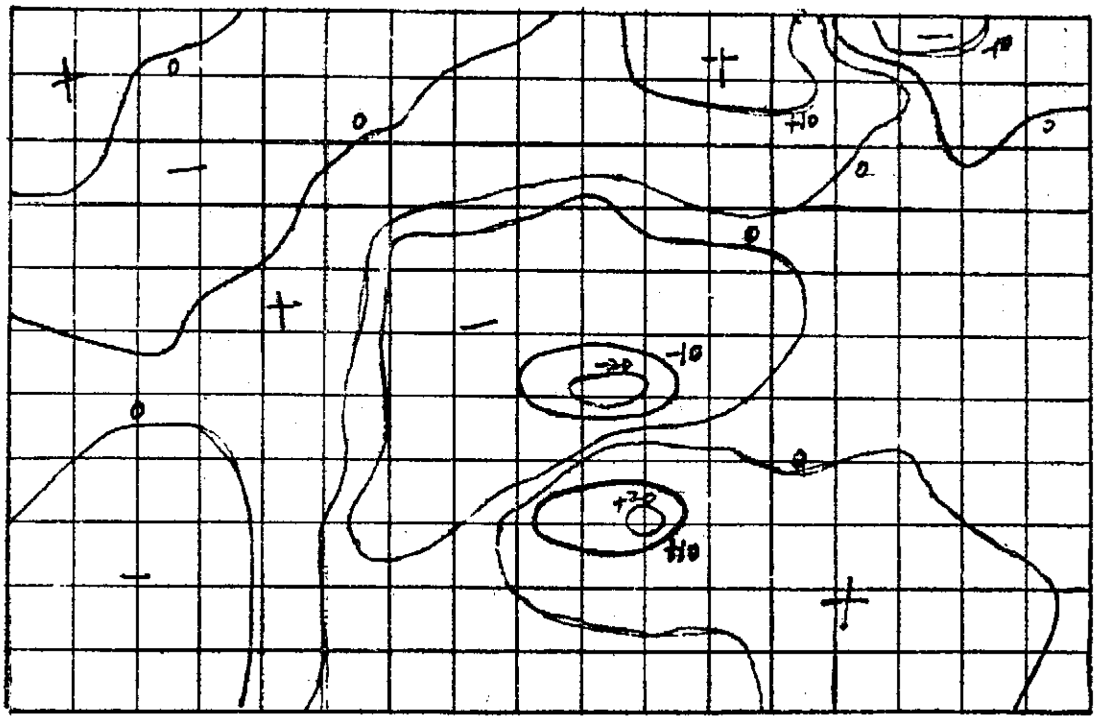

II. t = 16 hrs

Figure 5. ω - Field at 800 mb

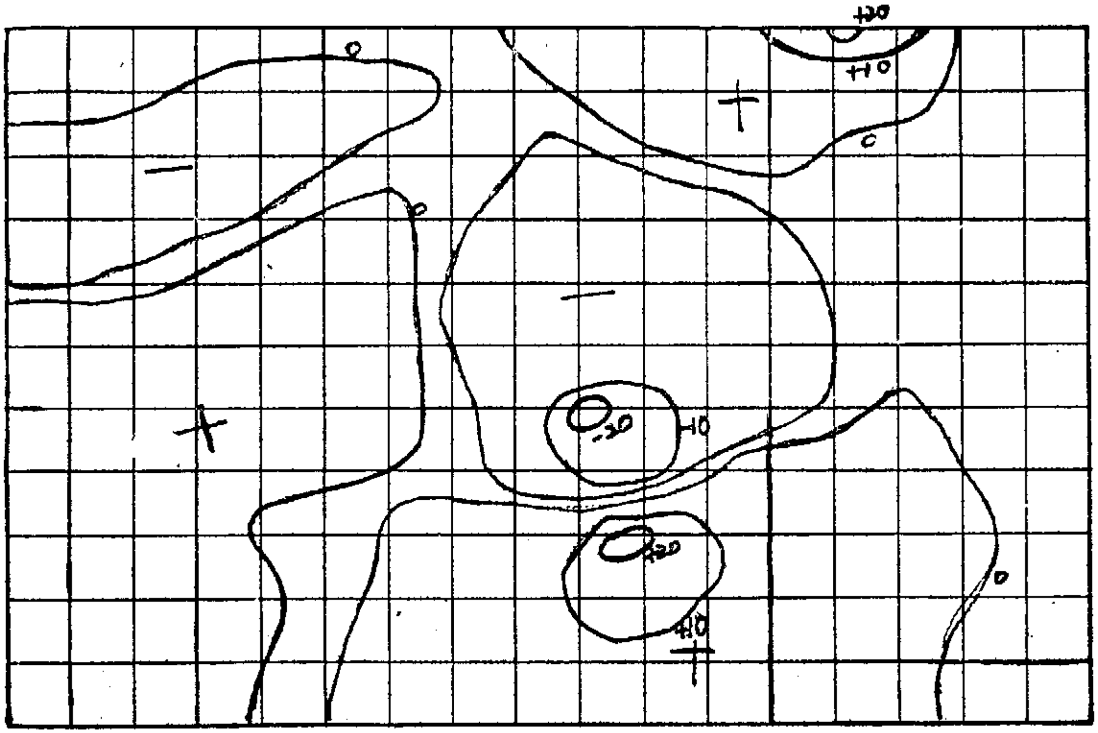
+20
+10
0
c
+
−
0
−
+
−20
+10
+20
+10
+
0

I t=0 hr.

ω in $\times 10^{-4}$ mb/sec

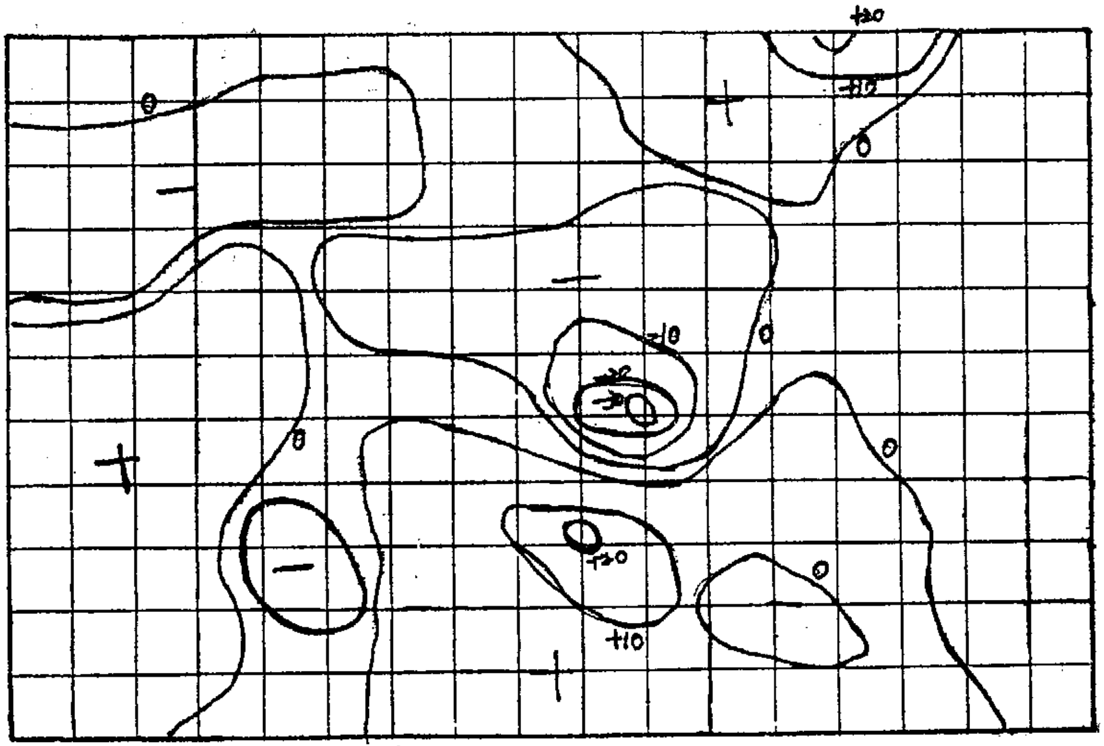
+20
+10
0
+
0
−
−
+10
+20
0
0
+
0
−
+20
0
+10
+

II t=16 hrs.

Figure 6. ω - Field at 600 mb.

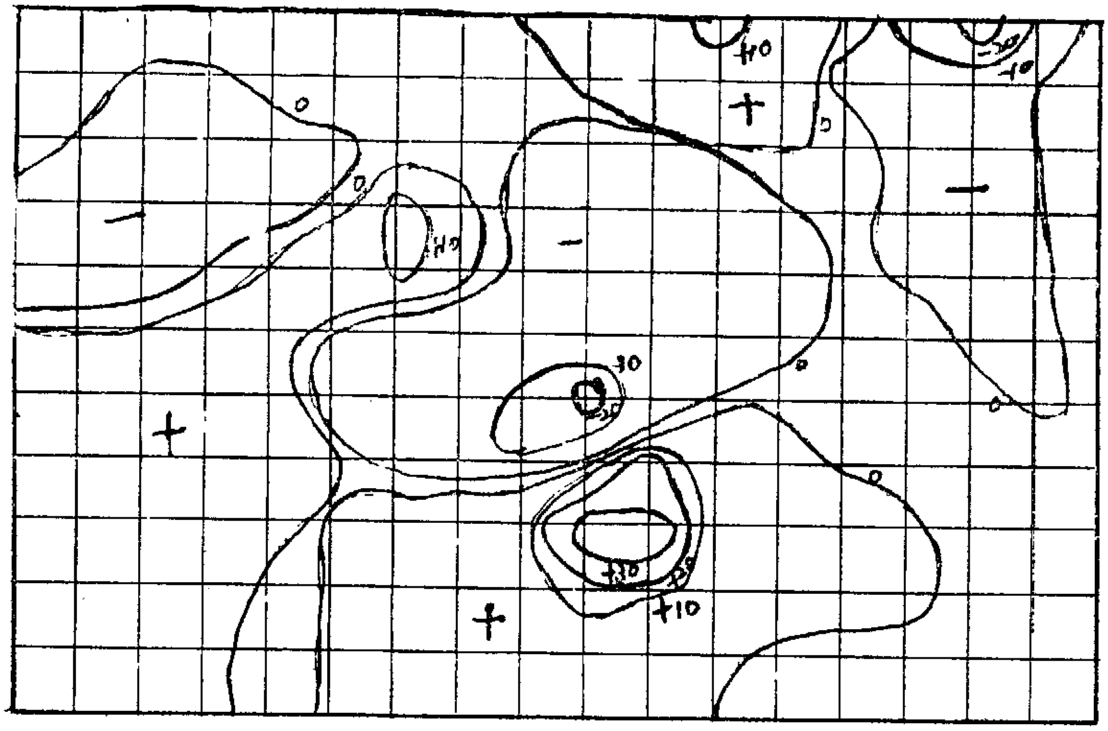
+10
-20
-10
0
+
0
0
-
+10
-
-
-30
-40
0
0
+
0
+
+20
+30
+10

I. t=0 hr.

ω in ×10^{-9} mb/sec

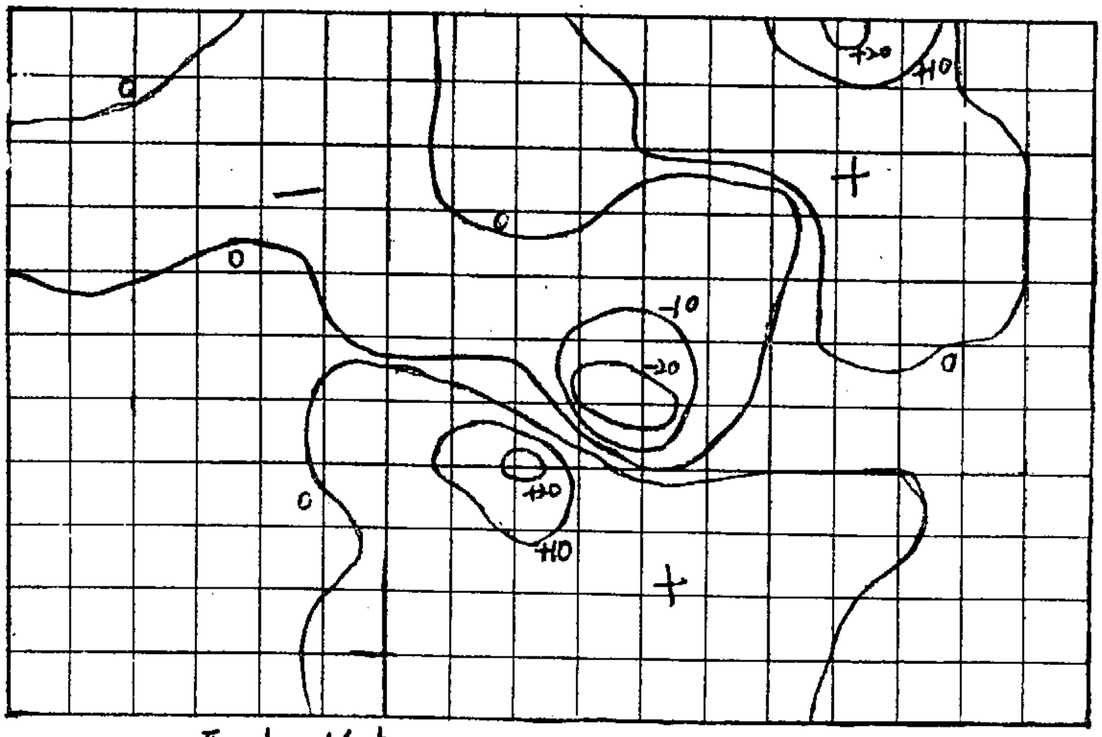
0
+20
+10
-
+
0
0
-10
-20
0
0
+20
+10
+

II. t = 16 hrs

Figure 7. ω- Field at 400 mb

Annual Report of the Institute of Physics, Academia Sinica, 1971

Energy Generation and Transformation in the Atmosphere Over the East China Sea During Winter*

L. C. Chien (簡來成)

Institute of physics, Academia Sinica

ABSTRACT

Energy generation and transformation is evaluated for seven layer model from 1000 mb. to 100 mb. by the use of IBM 1130 using daily aerological date from the notwork over the East China Sea during the period of continuous outburst of cold air predominated in January, 1966.

By the kinetic energy equation, we can researched into the generation and transformation of kinetic energy. The work done by the horizontal pressure force, horizontal transport, vertical transport, local change of kinetic energy, the divergence of eddy kinetic energy, and the energy transformed from the mean kinetic energy to eddy kinetic energy can be calculated by the use of daily aerological data. The dissipation is then obtained as the residual to balance the kinetic energy equation. It is clear, that during the continuous outburst of cold air, the East China Sea is a source region of kinetic energy. A large surplus of kinetic energy is exported across the boundary. Part of the kinetic energy is transported to the northeastern of Taiwan. The release of kinetic energy is directly associated with the process of sinking of cold air. It is the reason of rainfall over the northeastern part of Taiwan during winter.

Using the potential energy equation, we can discuss the generation and the transformation of potential energy. The horizontal transport, vertical transport, and local change of potential energy, the quantity transformed from the mean potential energy into eddy potential energy, the divergence of the eddy potential energy, and the potential energy transformed into kinetic energy can be evaluated by observed data. The residual to balance the potential energy equation is the energy supplied from the sea surface. As for the available potential energy, the East China Sea is a sink region. The import of available potential energy is mainly accomplished by the upper zonal flow and NE-monsoon.

1. INTRODUCTION

It is suggested by Margules (1903) that the significant process which produces kinetic energy in the atmosphere appears to be the simultaneous rising of warm air and sinking of cold air. One may suspect that the more vigorous energy trasformation process takes place in the lower and middle troposhere where baroclinity is more pronounced and kinetic energy is produced at the expanse of potential energy. In the upper troposphere and lower stratosphere there is some evidence of a reversal of this process, i. e. kinetic energy is transformed into potential energy.

---

* work supported by Natianal Science Council, 1970-1971,

The investigation of energy process has contributed substantially to the understanding of the atmosphere's general circulation. Growth and decay of synoptic-scale weather disturbances are strongly affected by the rate of energy generation and transformation. Thus to study the energy generation and transformation is important to the understanding of the synoptic scale atmosphere dynamices.

The study of energy generation and transformation has been done by may investigators. Jacobs (1951a, b) researched into the energy supported from the ocean to the atmosphere. Lorentz (1955) and White (1956) presented the mathematical form which could be used in the study of the general circulation by the concept of available potential energy. Recently, Wiin-Nielsen (1968) studied the energy generation and transformation in term of internal energy, potential energy, kinetic energy and dissipation. Smith and Horn (1969), Starr and Gaut(1969) developed symmetrical formujation of the zonal kinetic energy.

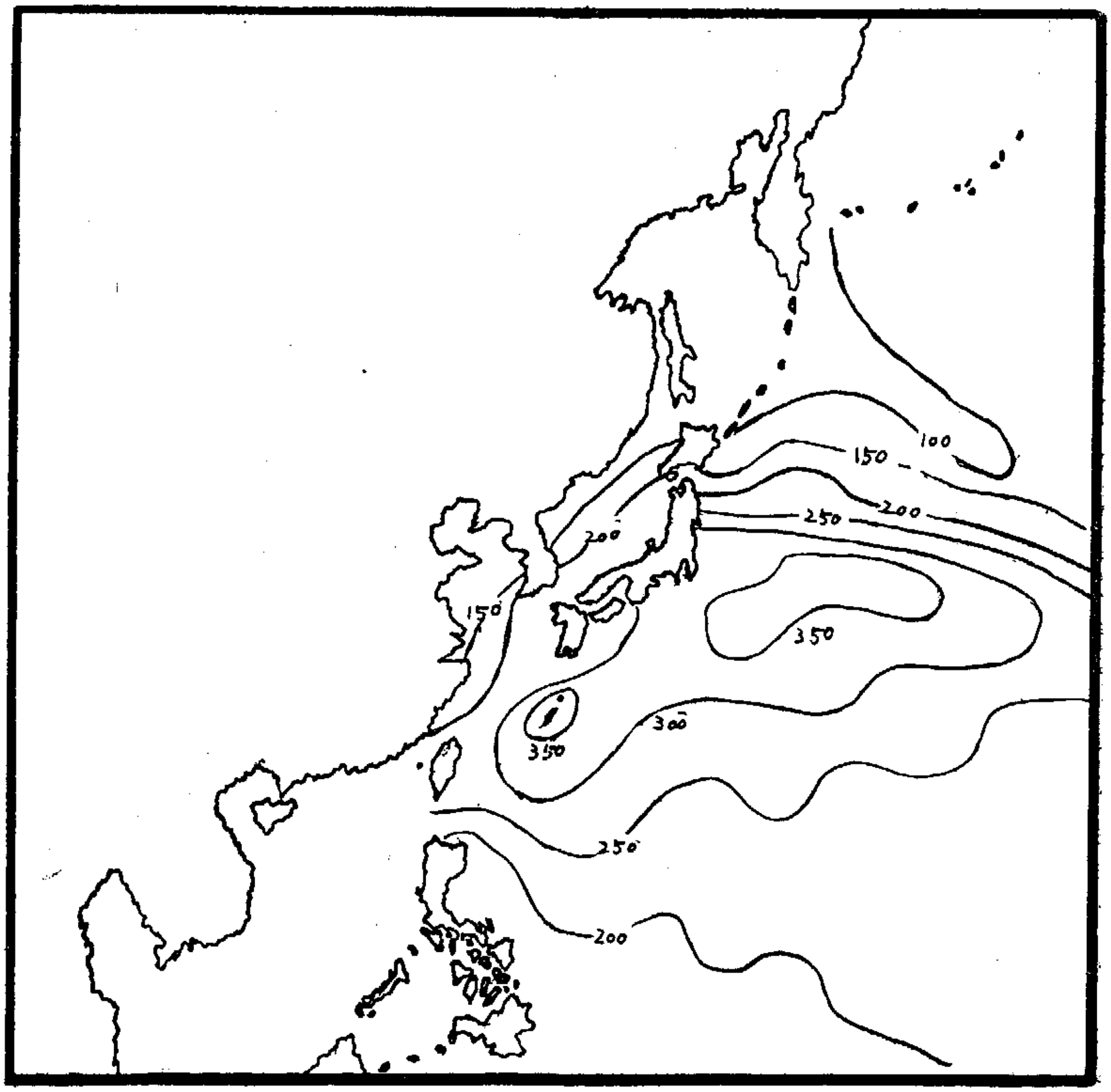

Fig. 1 *The annual values of the rate of total energy gained by the atmosphere, Unit: cal/cm*^{2}*. day*

Jacobs (1951a, b) found that the amount of energy transported from the ocean to the atmosphere is large on the East China Sea and on Japan Sea (Fig. 1). Japan Sea is surrounded by the land, And there are many observatories on its shore. The energy generation and transformation over the Japan Sea during winter has been studied by many Japanese authors, e. g. Manabe (1957, 1958) , Murakami (1959), Matsumoto et al (1963), Ninimiya (1964). Although the East China Sea is surrounded by Taiwan, Chinese Continent, Korea, Japan Islands, and Ryuku Islands, there has not been researched systematically. Recently, Liao (1968a, b) made a scheme and began to studied the air mass of the East China Sea. In Previous paper, Jean (1969), Liao and Jean (1971) the kinetic energy budget was studied in various partitions with daily wind and geopotential data during the period of a typical outburst of cold continental air.

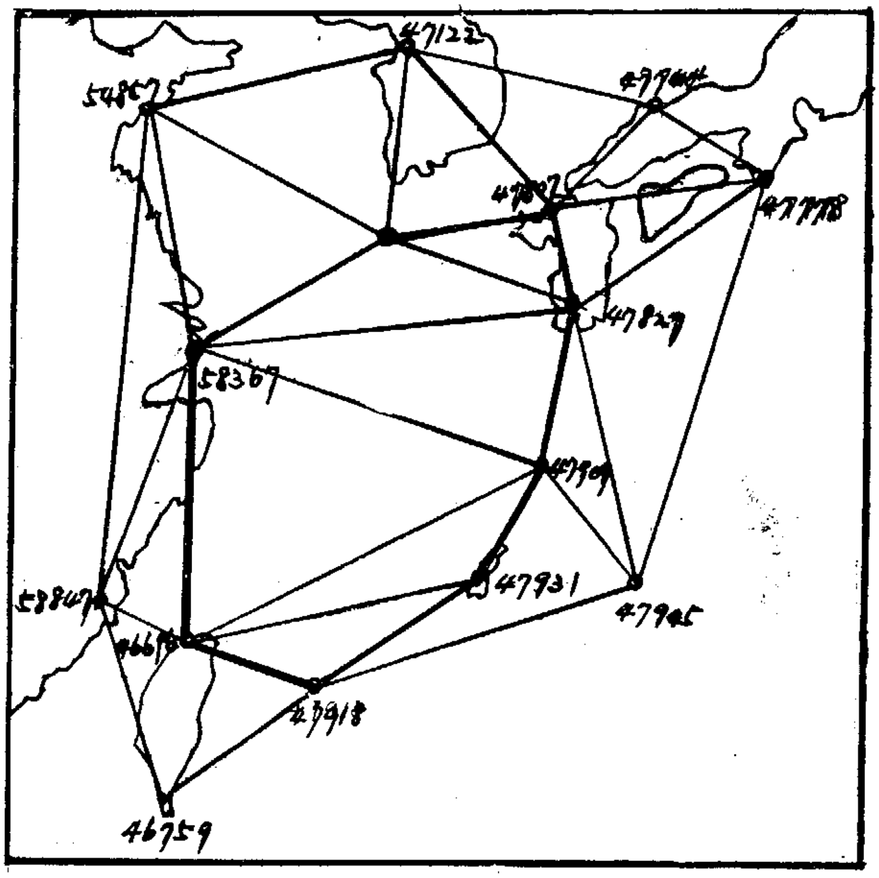

Fig. 2 *Stations and triangle grids used in computing energy generation and transformation, Heavy lines define the East China Sea.*

In this study, generation and transformation of energy is studied. Various kinetic energy paramenters and potential paramenters were evaluated for seven layer model from the sea surface to 100 mb., from January 25 to 31, 1963 over the East China Sea.

2. DATA AND COMPUTATION

In this study, I choose eight stations of data ocmparably completed as the vertex of the polygon and select another seven stations for computing the gradient of the quantities. The station distribution used in this study and triangle grids used in computing energy generation and transformation are shown in Fig. 2. The polygon area enclosed by the heavy line is defined, in this study, as "the East China Sea". The dimension of the East China Sea is

$$A = 685,240.4403\ km^2$$

The boundary of the East China Sea is subdivided into eight segments (Fig. 2).

All the data, the wind velocity, geopotential, temperature, are read from the Asia Synoptic Chart, Japan Meteorology Agency (January, 1966). And incorporate the observed reports of Mosulpo (47187) to complete the data of Jeju (47184).

The hydrostatic equation, $dp = -gdz$ will be used to substitute pressure for height as vertical coordinate. The vertical p velocity, ω, is represented by

$$\omega = \frac{dp}{dt} \tag{1}$$

and the principle of conservation of mass is expressed by

$$\nabla \cdot V = -\frac{\partial \omega}{\partial p} \tag{2}$$

The vertical p-velocity is obtained

$$\omega_{p_2} = -\int_{p_1}^{p_2} \nabla \cdot V dp + \omega_{p_1} \tag{3}$$

where ω_{p_1} and ω_{p_2} are ω at pressure level p_1 and p_2 respectively. for the area mean, we have

$$[\omega_{p_2}] = -\frac{1}{A}\int_{p_1}^{p_2} \oint V \cdot \boldsymbol{n} dS dp + [\omega_{p_1}] \tag{4}$$

where S is the boundary of the East China Sea, $\boldsymbol{n}$ the outward directed unit vector normal to the boundary. For shake of simplicity, we assume, in this paper, that the surface pressure is constant and equal to 1000 mb.. In consequence of such assumption the vertical p-velocity at the sea surface ω_{p_0} in equation (4) is approximated to be zero. Then $[\omega]$ at every level can be obtained by the use of equation (4).

The area mean values of energy variables over the East China Sea for seven prssure layers from the sea surface to 100 mb, were examined in detail in our previous reports (Jean 1969), Liao and Jean (1971).

3. BUDGET OF KINETIC ENERGY

Using pressure as the vertical coordinate, we may write the equation of motion for the horizontal wind in the form

$$\frac{\partial V}{\partial t} + V \cdot \nabla V + \omega \frac{\partial V}{\partial p} + fk \times V = -\nabla \varnothing - F, \tag{5}$$

where $\varnothing$ is the geopotential of any isobaric surface, $\varnothing = gz$, $\boldsymbol{F}$ the vector of horizontal frictional force per unit mass, f the horizontal component of Coriolis' paramenter, $\boldsymbol{k}$ the vertical unit vector. Now let each of the quantity in equation (5) be expressed by the mean (time mean) value and a departure from this mean, e. g. $q=\overline{q}+q'$, where $\overline{q}=\frac{1}{T}\int_0^T q\,dt$, $q'=\overline{q}-q$. With the use of this expression (5) may be rewtitten as

$$\frac{\partial V}{\partial t}+\overline{V}\cdot\nabla\overline{V}+\overline{\omega}\frac{\partial\overline{V}}{\partial p}+V'\cdot\nabla\overline{V}+\overline{V}\cdot\nabla V'+\overline{\omega}\frac{\partial V'}{\partial p}+\omega'\frac{\partial\overline{V}}{\partial p}$$
$$+V'\cdot\nabla V'+\omega'\frac{\partial V'}{\partial p}+fk\times V=-\nabla\overline{\varnothing}-\overline{F}-\nabla\varnothing'-F', \qquad (6)$$

Scalar-muitip[ing equation (6) by $\overline{V}$ and V' respectively, and making time averaging operation, we obtaine two kinds of energy equation for the horizontal wind in the form,

$$\overline{\overline{V}\frac{\partial V}{\partial t}}+\nabla\cdot\overline{K}\,\overline{V}+\frac{\partial}{\partial p}\overline{\overline{K}\omega}=-\overline{V}\cdot\nabla\cdot\overline{\varnothing}-I_e-\overline{V}\cdot\overline{F}, \qquad (7)$$

$$\overline{V'\frac{\partial V}{\partial t}}+\nabla\cdot k\overline{V}+\frac{\partial}{\partial p}\overline{k\omega}+E$$
$$=-\overline{V'\cdot\nabla\varnothing'}+I_e-\overline{V'\cdot F'}, \qquad (8)$$

in which

$\overline{K}=\frac{1}{2}(\overline{V})^2$, the mean kinetic energy,

$\overline{k}=\frac{1}{2}\overline{(V')^2}$, the eddy kinetic energy,

$$I_e=\overline{u}\left(\overline{\frac{\partial u'^2}{\partial x}+\frac{\partial u'v'}{\partial y}+\frac{\partial u'\omega'}{\partial p}}\right)+\overline{v}\left(\overline{\frac{\partial u'v'}{\partial x}+\frac{\partial v'^2}{\partial y}+\frac{\partial v'\omega'}{\partial p}}\right),$$

the conversion between the mean kinetic energy and the the eddy kinetic energy,

$$E=\frac{\partial}{\partial x}\overline{u'(u'\overline{u}+v'\overline{v})}+\frac{\partial}{\partial y}\overline{v'(u'\overline{u}+v'\overline{v})},$$

the net horizontal and vertical fiux of eddy kinetic energy

For *I*-th pressure layer, the integranted values of each term in equation (7) and (8) over the East China Sea, we obtained the following equations:

$$\frac{1}{g}\int_{p_{I-1}}^{p_I}\iint\overline{\overline{V}\cdot\frac{\partial V}{\partial t}}dAdp+\frac{1}{g}\int_{p_{I-1}}^{p_I}\oint\overline{V}\overline{K}\cdot ndSdp+\frac{1}{g}\int_{p_{I-1}}^{p_I}\iint\frac{\partial\overline{\overline{K}\omega}}{\partial p}dAdp$$
$$=-\frac{1}{g}\int_{p_{I-1}}^{p_I}\iint\overline{V}\cdot\nabla\varnothing dAdp-\frac{1}{g}\int_{p_{I-1}}^{p_I}\iint I_e\,dAdp-\frac{1}{g}\int_{p_{I-1}}^{p_I}\iint\overline{V}\cdot\overline{F}\,dAdp \quad (9)$$

$$\frac{1}{g}\int_{p_{I-1}}^{p_I}\iint\overline{V'\cdot\frac{\partial V}{\partial t}}dAdp+\frac{1}{g}\int_{p_{I-1}}^{p_I}\oint\overline{V}k\cdot ndSdp+\frac{1}{g}\int_{p_{I-1}}^{p_I}\iint\left[\frac{\partial\overline{k\omega}}{\partial p}+E\right]dAdp$$
$$=-\frac{1}{g}\int_{p_{I-1}}^{p_I}\iint[V'\cdot\nabla\varnothing'-I_e-V_\phi'\cdot F']dAdp \qquad (10)$$

For the sake of simplicity, the horlzontal mean over the East China Sea will be hereafter be denoted by

$$[q]=\frac{1}{A}\iint q\,dA$$

and for the vertical integration the following notation will be used:

$$\langle q\rangle = \frac{1}{g}\int_{p_1}^{p_2} q\,dp$$

Using the above notatings, equation (9) and (10) may be rewritten in the forms,

$$\left\langle\left[\overline{\overline{V}\frac{\partial V}{\partial t}}\right]\right\rangle + \left\langle\left[\nabla\cdot\overline{K}\,\overline{V} + \frac{\partial}{\partial p}\overline{K\,\omega}\right]\right\rangle = \langle[-\overline{V}\cdot\nabla\overline{\emptyset}]\rangle + \langle[-I_e]\rangle + \langle[-\overline{V}\cdot\overline{F}]\rangle, \qquad (11)$$

$$\left\langle\left[\overline{V'\frac{\partial V}{\partial t}}\right]\right\rangle + \left\langle\left[\nabla\cdot k\overline{V} + \frac{\partial}{\partial p}\overline{k\omega}\right]\right\rangle + \langle[\overline{E}]\rangle$$

$$= \langle[-\overline{V'\cdot\nabla\emptyset'}]\rangle + \langle[I_e]\rangle + \langle[-\overline{V'\cdot F'}]\rangle, \qquad (12)$$

The mean kinetic energy balance and eddy kinetic energy balance for seven pressure layers from the sea surface to 100 mb., is presented in Table 1 and Table 2 in term of the kinetic energy paramenters.

Table 1. Mean kinetic energy budget within each pressure layer

Layer (md.)	$\overline{K}$	$\langle[\overline{\overline{V}\frac{\partial V}{\partial t}}]\rangle$	$\langle[\nabla\cdot\overline{K}\overline{V}]\rangle$	$\langle[\frac{\partial}{\partial p}\overline{K\,\omega}]\rangle$	$\langle[I_e]\rangle$	$\langle[-\overline{V}\cdot\nabla\overline{\emptyset}]\rangle$	$\langle[-\overline{V}\cdot\overline{F}]\rangle$
1000-850	0.644	0.001	0.241	0.015	0.725	6.818	5.836
850-700	2.324	0.001	0.124	0.031	0.423	2.762	2.183
700-500	3.175	0.003	0.163	0.085	0.346	1.860	1.263
500-400	3.857	0.005	1.086	0.122	0.514	1.759	-0.032
400-300	4.121	0.006	2.398	0.183	0.614	3.453	-0.252
300-200	4.890	0.005	3.520	0.158	0.807	4.022	-0.468
200-100	3.438	0.006	2.665	0.187	0.537	6.580	3.185
Sum	22.449	0.027	10.197	0.781	3.963	25.254	12.219

K in unit 10^5 joules/m^2, other quantities in watts/m^2

Table 2. Eddy kinetic energy budget withn each pressure layer

Layer (mb.)	$\langle[\overline{V'\frac{\partial V}{\partial t}}]\rangle$	$\langle[\nabla\cdot\overline{k\,V}]\rangle$	$\langle[\frac{\partial}{\partial p}\overline{k\,\omega}]\rangle$	$\langle[\overline{E}]\rangle$	$\langle[-\overline{V'\cdot\nabla\emptyset'}]\rangle$	$\langle[I_e]\rangle$	$\langle[\overline{V'\cdot F'}]\rangle$
1000-850	0.000	0.018	0.002	0.016	0.725	-2.193	-1.054
850-700	0.001	0.015	0.008	0.022	0.423	-1.334	-0.957
700-500	0.001	0.034	0.023	0.186	0.346	-0.195	-0.093
500-400	0.002	0.022	0.011	0.240	0.714	-0.447	-0.008
400-300	0.003	0.057	0.002	0.127	0.714	1.264	1.639
300-200	0.003	0.316	0.017	0.388	0.807	2.315	2.393
200-100	0.004	0.196	0.053	0.215	0.537	1.664	1.733
Sum	0.014	0.658	0.116	1.194	4.156	1.074	3.708

Unit: watts/m^2

Viewing the tables, they show that strong generations take place in the upper and lower atmosphere, while the generation in the midtroposphere is very weak. Starting from the sea surface, we see a maximum of the generation in the boundary layer, which gradually decreases toward a minimum in the mid-troposphere, and then increases towad a second maximum in the upper part of the atmosphere. It is estimated that roughly 33 per cent of the generation occurs in the layer between 1000 mb. and 750mb., 19 per cent in the layer between 700 mb. and 400 mb., and 48 per cent in the layer between 400 mb. and 100 mb..

The work done by the pressure gradient can be rewritten as

$$-V\cdot\nabla\varnothing=-\nabla\cdot\varnothing V-\frac{\partial}{\partial p}\varnothing\omega-\omega\alpha \tag{13}$$

If we devide $\varnothing\omega$ into two parts, one being its space mean $[\varnothing]$ $[\omega]$ and other a departure from this mean, $\varnothing^*\omega^*$, Equation (13) can be transformed into the following form:

$$\langle[-\overline{V}\cdot\nabla\overline{\varnothing}]\rangle=\langle[-\overline{\omega}^*\overline{\alpha}^*]\rangle+\langle[-\nabla\cdot\overline{\varnothing^*\overline{V}}]\rangle+\langle[-\frac{\partial}{\partial p}\overline{\varnothing}^*\overline{\omega^*}\rangle, \tag{14}$$

$$\langle[-\overline{V'\cdot\nabla\varnothing'}]\rangle=\langle[-\overline{\omega'^*\alpha'^*}]\rangle+\langle[-\nabla\cdot\overline{\varnothing'^*V'}]\rangle+\langle[-\frac{\partial}{\partial p}\overline{\varnothing'^*\omega'^*}]\rangle. \tag{15}$$

The first term on the righ of equation (14) and (15) have positive values. Those represent the release of kinetic energy by overturning within atmospheric wave. Under this formulation, a decrease of available potential energy occurs when relatively warm air rises and cold air sinks.

Table 3. The transformation of mean gravitational potential energy

Layer (mb.)	$\langle[-\overline{V}\cdot\nabla\overline{\varnothing}]\rangle$	$\langle[-\overline{\omega}^*\overline{\alpha}^*]\rangle$	$\langle[-\nabla\cdot\overline{\varnothing}^*\overline{V}]\rangle$	$\langle[-\frac{\partial}{\partial p}\overline{\varnothing}^*\overline{\omega}^*]\rangle$
1000-850	6.818	5.454	3.688	-2.223
850-700	2.762	1.932	1.875	-1.045
700-500	1.860	1.655	1.528	-1.323
500-400	1.759	1.493	0.644	-0.378
400-300	3.543	2.833	0.769	-0.149
300-200	4.062	3.097	1.385	-0.460
200-100	6.580	4.672	2.706	-0.798
Sum	27.540	20.586	12.595	-6.376

Unit: watts/m²

Table 4. The transformation of eddy gravitational potential energy

Layer (mb.)	$\langle[-\overline{V'\cdot\nabla\varnothing'}]\rangle$	$\langle[-\overline{\omega'^*\alpha'^*}]\rangle$	$\langle[-\nabla\cdot\overline{\varnothing'^*V'}]\rangle$	$\langle[-\frac{\partial}{\partial p}\overline{\varnothing'^*\omega'^*}]\rangle$
1000-850	-2.193	1.572	-3.652	-0.113
850-700	-1.134	1.123	-0.812	-0.645
700-500	-1.195	0.774	-1.725	-0.244
500-400	-0.447	0.423	-0.688	-0.182
400-300	1.264	1.006	0.522	-0.234
300-200	2.315	1.272	1.670	-0.627
200-100	1.664	1.135	-0.048	-0.577
Sum	1.074	7.305	-4.045	-2.632

Unit: watts/m^2

The second term and the third term on the right of equation (14) and (15) express the horizontal and vertical flux of gravitational potential energy. The net inward horizontal flux of gravitational potential energy is 12.595 watts/m^2 and the amount of net outward horizontal flux due to the eddies is 3.587 watts/m^2. In consequence, adding equation (14) and (15), we have

$$\langle[-\overline{V\cdot\nabla\varnothing}]\rangle=\langle[-\overline{\omega^*\alpha^*}]\rangle+\langle[-\nabla\cdot\overline{\varnothing^*V}]\rangle+\langle[-\frac{\partial}{\partial p}\overline{\varnothing^*\omega^*}\rangle. \tag{16}$$

28.328 27.891 9.445 -9.008

In equation (16), we see that the net flux of gravitational potential energy, 0.423 watts/m^2, is insignificant and the magnitude of the gradient $\langle[-\overline{V\cdot\nabla\varnothing}]\rangle$ is almost the same with that of the conversion of available potential energy to kinetic energy $\langle[-\overline{\omega^*\alpha^*}]\rangle$. From this fact, it may be said that, so far as the work done by pressure gradient is concerned, the release of kinetic energy can be computed with good approximation as if the region were a closed system.

Mow consider the horizontal transport and vertiaal transport of kinetic energy. The horizontaloutflow, $-\frac{1}{g}\int\frac{1}{A}\oint VK\cdot\boldsymbol{n}dSdp$, which is small near the sea surface and has significant large in the upper half of the atmosphere. This indicates that there is a jet stream in the upper atmosphere over the East China Sea. The vertical transport term, $\frac{\partial}{\partial p}K\omega$, its numerical value is rather insignificant. The computations show that the net export of mean kinetic energy is 10.109 watts/m^2. Part of these exported energy is transported to the northeastern of Taiwan, and plays an important role for releasing the kinetic energy over the northeastern of Taiwan.

In equation (11) and (12), the appearance of I_e with opposite sign in both equations means that this term gives a conversion between the mean kinetic energy and the eddy kinetic energy, a loss in one representing a gain in the other. A positive sign of the conversion term indicates that the eddy kinetic energy is partly furnished from the mean kinetic energy. This amount is of value 4.166 watts/m^2.

In equation (12), the term E represent the net horizontal and vertica flux of deddy kinetic energy across the boundary since $u'u$ and $v'v$ in E expresses a kind of eddy kinetic energy.

Formerly, most of scholars recognized that the friction force is small and the work done by it may be neglected. The result of Kung (1966a, b), Smith (1969) and this study show that the work done by the friction force is the same order of magnitude as the work done by the pressure gradient. Therefore, the friction term is important and must not be neglected.

The kinetic energy dissipation in the boundary layer is estimated by Lettau (1962). The surface stress τ_{p0} and the boundary layer dissipation D_b are

$$\tau_{p0} = \rho_{p0} C^2 V \tag{17}$$

$$D_b = V \cdot \tau_{p0} \tag{18}$$

where ρ_{p0} iis the air density at the sea surface and may be estimated by the equation of state $\rho_{p0} = \frac{p_0}{RT_0}$. The energy dissipation in the atomosphere can be partitioned into contributions from the boundary layer D_b and free atmosphere D_f

$$D = D_b + D_f \tag{19}$$

To estimate frictional dissipation at the sea surface, E in equation (17) is put to be 0.03, the results are as follows:

D	=	D_b	+	D_f
15.927		4.523		11.404

The results show that the surface friction is about 28 per cent of the total dissipation. At the total rate of frictional dissipation 15.927 watts/m^2, might be expected to consume entirely the total kinetic energy within 57.46 hours provided that there is not any process of generation of kinetic energy.

4. BUDGET OF POTENTIAL ENERGY

Using the first law of thermodynamics

$$\frac{dQ}{dt} = c_p \frac{dT}{dt} + p \frac{d\alpha}{dt} \tag{20}$$

and the equation of state

$$p\alpha = RT \tag{21}$$

we obtain the equation

$$\frac{dQ}{dt} = c_p T\left(\frac{1}{Q} \frac{dQ}{dt}\right) \tag{22}$$

With the aid of equatino of continuity, we have

$$\frac{\partial \theta}{\partial t} + \nabla \cdot V\theta + \frac{\partial}{\partial p}\omega\theta = \frac{1}{c_p}\left(\frac{p_0}{p}\right)^{*} Q, \tag{23}$$

where dQ/dt is the rate of addition of heat, θ the potential temperature, c_p the specific heat at constant pressure, K the **ratio** R/c_p. If θ is represented by space mean plus a departure from this mean plus a departure from this mean θ^* equation (23) may be rewritten as

Table 5. Mean available potential budget within each pressure layer

Layer (mb.)	$[\partial A_M/\partial t]$	$[\frac{c_1}{2}\nabla\cdot\overline{V\theta^{*2}}]$	$[-\frac{c_2}{2}\frac{\partial}{\partial p}\overline{\omega Q^{*2}}]$	$[I_a]$	$[\overline{\omega}^*\ \overline{\alpha}^*]$	$-c_2[\overline{Q}^*\overline{Q}']$
1000-850	0.520	-3.062	-5.921	0.833	-5.454	-2.176
850-700	0.745	-3.768	-6.230	0.895	-1.932	-6.425
700-500	1.170	-2.732	-4.961	0.765	-1.655	-4.103
500-400	1.490	-1.171	-6.134	0.682	-1.493	-3.640
400-300	1.632	-0.635	3.871	1.436	-2.833	6.265
300-200	1.846	-0.870	5.862	1.537	-3.097	8.396
200-100	1.927	-0.842	9.353	1.465	-4.672	-5.061
Sum	9.930	-13.080	-4.160	7.609	-20.586	-6.745

Unit: watts/m^2

Table 6. Eddy available potential budget within each pressure layer

Layer (mb.)	$[\partial A_E/\partial t]$	$[-\frac{c_1}{2}\overline{\nabla\cdot V\theta'^{*2}}]$	$[-\frac{c_1}{2}\frac{\partial}{\partial p}\overline{\omega\theta'^{*2}}]$	$[A]$	$[-I_a]$	$[\overline{\omega'^*\alpha'^*}]$	$-c_2[\overline{Q'^*\theta'^*}]$
1000-850	0.417	-0.615	-1.475	0.421	-0.833	-1.672	-3.757
850-700	0.596	-0.723	-2.184	0.440	-0.895	-1.123	-3.889
700-500	0.752	-0.534	-1.492	1.141	-0.765	-0.974	-1.872
500-400	1.153	-0.262	-1.723	1.033	-0 682	-0.423	-0.904
400-300	1.168	-0.159	0.774	1.041	-1.436	-1.006	0.386
300-200	1.243	-0.187	1.180	1.931	-1.537	-1.792	0.838
200-100	1.487	-0.163	1.562	1.523	-1.465	-1.235	1.709
Sum	6.816	-2.643	-3.358	7.530	-7.069	-7.305	-7.489

Unit: watts/m^2

$$\frac{\partial\theta^*}{\partial t}+\nabla\cdot V\theta^*+\frac{\partial}{\partial p}\omega\theta^*+\frac{\omega}{S}\ \frac{\partial[\theta]}{\partial p}=\frac{1}{c_p}\left(\frac{p_0}{p}\right)^k\dot{Q}, \qquad (24)$$

Multiplying equation (24) by θ^* and θ'^*, and integrating with respect to time, horizontal space, we obtain the equations for the budget of mean available potential energy and eddy potential energy,

$$\langle[\frac{\partial A_M}{\partial t}]\rangle+\langle-\frac{c_1}{2}[\nabla\cdot\overline{V}\,(\overline{\theta}^*)^2+\frac{\partial}{\partial p}\overline{\omega}\,(\overline{\theta}^*)^2]\rangle$$

$$=\langle[I_a]\rangle+\langle[\overline{\omega^*\alpha^*}]\rangle+\langle-c_2[\overline{Q^*\theta^*}]\rangle, \tag{25}$$

$$\langle[\frac{\partial A_E}{\partial t}]\rangle+\langle-\frac{c_1}{2}[\nabla\cdot\overline{V(\theta'^*)^2}+\frac{\partial}{\partial p}\overline{\omega(\theta'^*)^2}]\rangle+\langle[A]\rangle$$

$$=\langle[-I_a]\rangle+\langle[\overline{\omega'^*\alpha'^*}]\rangle\rangle+\langle-c_2[Q'^*\theta'^*]\rangle, \tag{26}$$

where

$$\left[\frac{\partial A_M}{\partial t}\right]=-\frac{[\alpha]}{[\theta]}\frac{A}{\{\partial[\overline{\theta}]\}/\partial p}\left[\overline{\overline{\theta}^*\frac{\partial\theta^*}{\partial t}}\right],$$

$$\left[\frac{\partial A_E}{\partial t}\right]=-\frac{[\alpha]}{[\theta]}\frac{A}{\{\partial[\overline{\theta}]\}/\partial p}\left[\overline{\theta'^*\frac{\partial\theta^*}{\partial t}}\right],$$

$$c_1=\frac{AR}{\{\partial[\overline{\theta}]\}/\partial p}\left(\frac{p}{p_0}\right)^k\frac{1}{p},\quad c_2=\frac{AR}{c_p}\frac{1}{\{\partial[\overline{\theta}]\}/\partial p}\frac{1}{p}$$

$$[I_a]=c_1[\overline{\theta}^*(\nabla\cdot\overline{V'\theta'^*}+\frac{\partial}{\partial p}\omega'\theta'^*)^*], \tag{27}$$

$$[A]=-c_1[\nabla\cdot\overline{\theta^*V'\theta'^*}+\frac{\partial}{\partial p}\overline{\theta^*\omega'\theta'^*}]. \tag{28}$$

The appearance of $\langle[\overline{\omega^*\alpha^*}]\rangle$ with opposite sign in both equation (11) and (25) indicates that this term represents a conversion between mean available potential energy and mean kinetic energy. A minus sign of $\langle[\overline{\omega^*\alpha^*}]\rangle$ means that a conversion occurs from mean available potential energy to mean kinetic energy. As for equation (12) and (26), the term $\langle[\overline{\omega'^*\alpha'^*}]\rangle$ indicates that a conversion takes place from eddy available potential energy to eddy kinetic energy.

The first term on the righ of equation (25) and (26) is associated with the horizontal as well asvertical transport of sensible heat due to eddies, and represents a conversion between mean available potential energy to eddy available potential energy. The positive sign of in equation (25) indicates a conversion from eddy available potential energy to mean available potential energy.

In equation (28), $\langle[A]\rangle$ represents a net flux of $\overline{\theta^*\theta'^*}$ across the boundary and may be considered as indicating a part of divergence of eddy available potential energy. Table 5 and Table 6 reveal that the horizontal and vertical import of mean available potential energy and eddy available potential enrgy are of amount 17.240 watts/m^2 and 6.001 watts/m^2 respectively. The net import of available potential energy is of amount 25.241 wattss/m^2. The loss of available potential energy within the East China Sea due to the effect of $\langle[\overline{\omega^*\alpha^*}]\rangle$ and $\langle[\overline{\omega'^*\alpha'^*}]\rangle$ is mainly compensated by the net import of mean available potential energy and eddy available potential energy.

The residual to balance the potential energy equations are the energy supplied from the sea surface. The heat energy supplied from the ser surface during the outburst of the cold air is significant, of amount 14.232 watts/m^2, and plays an important role for the budget of potential energy over the East China Sea. Generally speaking, we find nonadiabatic heating over the East China Sea, since there is a temperature difference about 10°C between the atmosphere and sea surface.

It was shown by Jacobs (1951a) that in cold season vast amount of heat are supplied to the atmosphere from the sea surface. And the marked maximum in the supply of heat is encounted just east of the East China Sea.

Since the sensible heat supplied from the sea surface is concentrated near the earth's surface, turbulent vertical transport up to rather high levels of troposphere may accunt for much of the sizable values of heating found in Table 5 and Table 6. Heat supplied from the sea surface depends largly upon the transport of heat from warmer sea surface due to vertical eddies.

5. CONCLUSION

From 1000 mb. to 100 mb., the energy generation and transformation over the East China Sea during the period of the outburst of cold air is studied for seven layer model by the use of IBM 1130. The results obtained above are summarized as follows:

1. The East China Sea is the sink region of available potential energy. The imported mean potential energy is 17.240 watts/m^2, and the imported eddy available potential energy is 6.001 watts/m^2.
2. The mean available potential energy and eddy available potential energy are transformed into mean kinetic energy and eddy kinetic energy, of values 20.586 watts/m^2 and 7.305 watts/m^2 respectively.
3. The heat supplied from the sea surface to the atmosphere, 14.232 watts/m^2, plays an important role in the energy budget.
4. The energy generation is maximun in the boundary layer, which decreases toward a minimun inthe mid-troposphere, and increases toward a second maximum in the upper part of the atmosphere.
5. The East China Sea is the source region of kinetic energy. The net export of kinetic energy is 10.109 watts/m^2. part of these exported energy is transported to the northern of Taiwan, and plays an important role for the rainfall over the northern of Taiwan during this period.

It become possible to propose a crude picture concerning the generation and transformation of energy in the atmosphere during this period which is shown in Fig. 3. Here M. G. P. E., E.G. P.E., M.A.P.E., and E. A. P.E. are used to denote the mean gravitational potential energy, eddy gravitational potential energy, man available potential energy and eddy available potential energy respectively.

ACKNOWLEDGEMENT

The author would like to express his hearty thank to professor S. Y. Liao of National Central University and to Professor H. T. Yang of the University of Southern California for their guidance and encouragment throughout this study, and to thank Professor T. Murakami of Haiwaii University for discussion and for offering literature from him. The author is also grateful

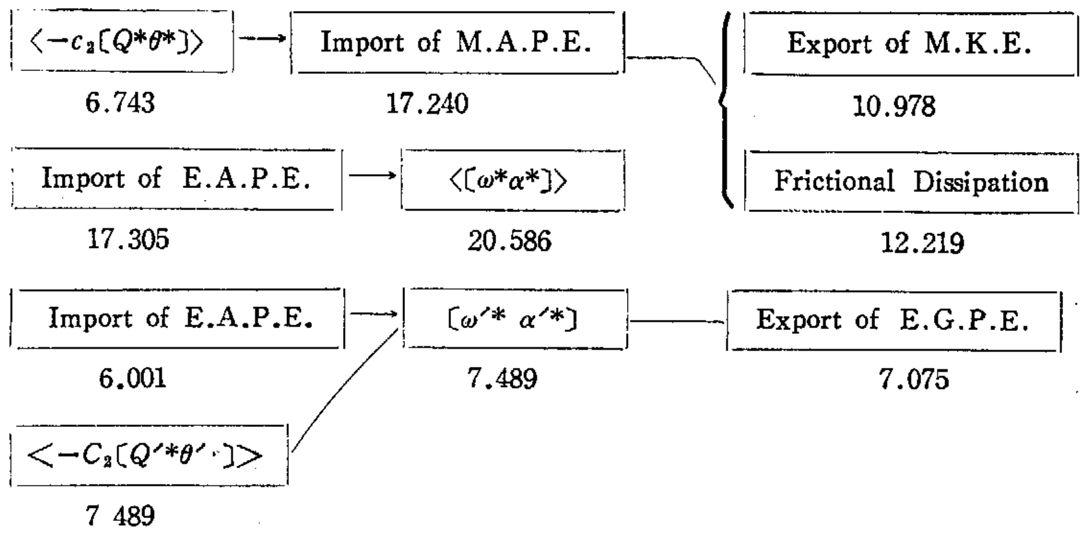
$\langle -c_2[Q^*\theta^*]\rangle$
6.743
Import of M.A.P.E.
17.240
Export of M.K.E.
10.978
Frictional Dissipation
12.219
Import of E.A.P.E.
17.305
$\langle[\omega^*\alpha^*]\rangle$
20.586
Import of E.A.P.E.
6.001
$[\omega'^*\ \alpha'^*]$
7.489
Export of E.G.P.E.
7.075
$\langle -C_2[Q'^*\theta'^*]\rangle$
7 489

Fig. 3. *The schematical indication of generation and transformation of energy during the period 26-31 January, 1966. Unit value is Watts/m*^{2}.

to Mr. C. H. Chen, Taiwan Provincial Institute of Family Plainning, for performing the electronic computer calculation for his work.

References

Jacobs, W. C. (1951a) Larhe-scale aspect of energy transformation over the ocean, Commpendium of Meterorlogy, 1057-1070.

Jacobs, W. C. (1951b) The energy exchange between sea and atmosphere and some of its consequences, Bull. Scrips. Inst. Ocean, Univ. Cal. 6, 27-122.

Jean, L. C. (1959) On the energy budget over the East China Sea during winter, Jour. of Sci. and Eng., Chung Hsing Univ. 6, 161-172.

Kung, E. C. (1966a) Kinetic energy generation and dissipation in large scale atmospheric circulation, Mon. Wea. Rev. 94, 67-82.

Kung, E. C. (1966b) Large-scale balance of kinetic energy in the atmosphere, Mon. Wea. Rev. 94, 627-640.

Liao, S. Y. (1963a) The air mass transformation over the East China Sea, Met. Bull. 14, No. 1, 39-48.

Liao, S. Y. and Jean, L. C. (1971) On the kinetic energy balance over the East China Sea during winter, Bull. of Inst. of Geoph., National Central Univ., No. 9, 30-39.

Lorentz, E. N. (1955) Available potential energy and the maintenance of general circulation, Tellus, 7, 157-167.

Manabe, S. (1957) On the modification of air-mass over Jaoan Sea When the outburst of cpld air predominated, Jour. Met. Soc. Japan, 35, 311-326.

Manabe, S. (1958) On the estimation of energy between the Japan Sea and the atmosphere during winter based onthe energy budget of both the atmosphere and the sea, Jour. Met. Soc. Japan, 36, 311-325.

Matsmoto, S., T. Asai and K. Ninomiya (1963) Heat and vapor budget in large and small scale over the middle Japan Islands, paper in Met. and Geophy., 15-81.

Murakami, T. (1959) The energy budget over fhe Far East during rainy season, Jour. Met. Soc. Japan, 37, 82-95.

Ninomiya, K. (1964) Water-substance budget over the Japan Sea aad Japan Islands during the period of heavy stsnow storm, Jour. Met. Soc. Japan, 42, 317-329.

Smith, P. J. and L. H. Horn (1969) On the contribution of a limited region of the atmosphere, Tellus 21, 202-206.

Starr, V. P. (1969) Symmetrical formulation of the zonal eddies in the atmosphere, Tellus 21, 185-191.

White, R. M. (1956) On conversion between potential and kinetic energy in the atmosphere, Tellus 8, 357-364.

Wiin-Nielsen, A. (1968) On the intensity of general circulation of the atmosphere, Rev. of Geophys. Vol. 6, No. 4.

冬季東海上大氣能量的產生與轉換

簡來成

摘要

東海爲臺灣，中國大陸，朝鮮半島日本的九州與琉球羣島所包圍，爲一做能量研究的理想區域。依據探空資料，用電子計算機計算冬季寒潮暴發期間，動能和位能的產生量與轉換量。

以動能方程式探討動能的產生與轉換。動能之水平傳遞量垂直傳遞量，當地時間變化量，水平壓力場所作的功，平均動能與渦流動能之轉換量，渦流動能之輻散量，位能與動能的轉換量，等均可由實際觀測數値算出。平衡動能方程式的剩餘量即爲摩擦力所作的功，動能產生量在海面對流層上半部份相當大，這顯示海面附近的能量來源是海面所供應的熱能，對流層上半部是爲高空盛行的西風所帶來的。當寒潮暴發期間，本區有大量的動能向外輸送，其中一部份輸送到臺灣的北部，這是臺灣北部下雨的原因之一。

以位能方程式探討位能的產生與轉換。位能之水平傳遞量，垂直傳遞量，當地時間變化，位能與動能的轉換量，平均位能與渦流位能的轉換量，位能之輻散量等均可由實際觀測値計算之。平衡位能方程式的剩餘量即海面所供應的熱能。由計算値可看出本區的位能是由外區所輸入：其一爲冬季盛行的東北季風，其二爲高空盛行之西風。

Annual Report of the Institute of physics, Academia Sinica, 1971

Diffraction of a Plane Pulse by a Rectangular Opening

Huai-chu Wang (王懷柱)

Aerospace Laboratory, N.Y.U., New York and Academia Sinica, Taipei

Abstract

The problem of diffraction and reflection of a plane pulse, such as the first shock of the sonic boom produced by SST airplane, by rectangular openings, such as windows, is solved by use of Bernoullis Seperation method in three variables $\zeta=(x^2+y^2+z^2)^{1/2}/Ct$, θ and φ. The three-dimensional effect is confined inside the unit sphere $\zeta=1$ or the sonic sphere $r=Ct$ with the corners of the opening as center. The solution exterior to the corner and inside the unit sphere is constructed by the seperation of variable ζ from θ and φ. The associated eigenvalue problem is subjected to the same differential equation in potential theory. A systematic procedure is presented such that the eigenvalue problem is reduced to that of a system of linear algebraic equations. Numerical results for the eigenvalues and functions are obtained and are applied to construct the conical solution for the diffraction of a plane pulse.

1. Introduction

The problem of diffraction and reflection of acoustic waves or electromagnetic wave by wedges, corners and other two-dimensional or axially symmetric obstacles has received extensive investigations. A survey of these investigations can be found in Reference 1.

The present investigation is motivated by the study of the effect of sonic boom on the openings of the structures, such as windows. The pressure wave created by a supersonic airplane is three-dimensional in nature. However, the radius of curvature of the wave front is usually much larger than the length scale of a structure. Therefore, the first shock of the incident wave can be approximated by progressing plane wave.

For two-dimensional structures in the shape of a rectangular block, the diffraction of a plane pulse by the first corner is given explicitly by the two-dimensional conical solution of Keller and Blank [2].

For the three-dimensional problem of the diffraction of sonic boom by the openning of the structures, the first step is the construction of the solution for the diffraction of a plane pulse by a corner of a opening. The formulation of the differential equation and the appropriate boundary conditions for the problem in three-dimensional conical variables is presented in the next section.

2. Formulation of the problem

For a weak shock, the flow can be assumed as irrotational in the first approximation, the disturbance pressure p′ obeys the simple wave equation

$$p'_{xx}+p'_{yy}+p'_{zz}-C^{-2}p'_{tt}=0 \tag{1}$$

Where C is the speed of propagation in the region outside the wall. The two edges of the wall OA and OA′ lie in the y-z plane (Fig.1).

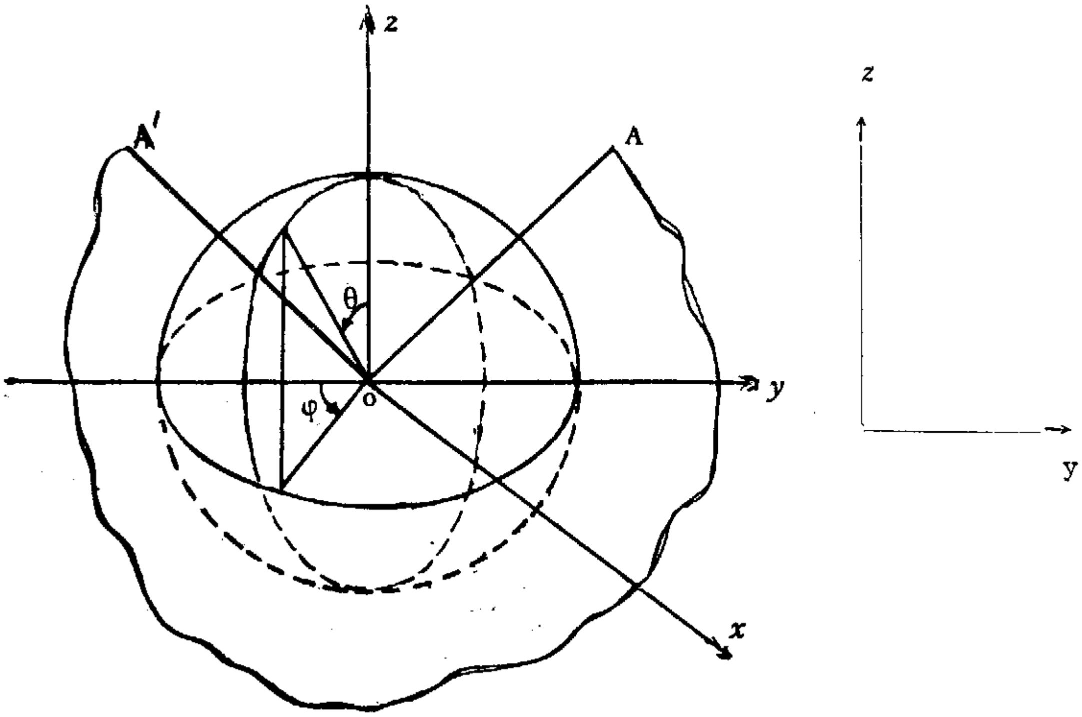

Fig. 1 *Coordinates System*

Let $t=0$ be the instant when the pulse front hits the wall. Since the normal disturbance velocity v_n must vanish on the rigid wall. This leads to the boundary condition $\partial p'/\partial n=0$. Due to the linearized equation of motion:

$$p_0' \frac{\partial p'}{\partial n} = -\zeta_0 \frac{\partial v_n}{\partial t}$$

where ζ_0 $(=\gamma p_0'/C_0^2)$ is the density of the air in front of the shock. The initial conditions are $p'=p_t'=0$, when $t \leq 0$. The three-dimensional disturbance due to the thin wall with edges perpendicular to each other is confined inside the sonic sphere of radius $r=Ct$, where $r=(x^2+y^2+z^2)^{1/2}$, with the origin at $x=y=z=0$. Outside the sonic sphere, the pressure distribution is given either by the regular reflection of the plane pulse from the surface of the thin wall according to the law of reflection or by the diffraction of the pulse by the edges according to the Huygen's principe. Solutions outside the sonic sphere are given in two conical variables in [2] by means of Busemann's conical flow method [3].

Following [4] the disturbance pressure p′ nondimensionalized by the strength of the incident pulse should be a function of the conical variables, $x/(Ct)$, $y/(Ct)$ and $z/(Ct)$ or in terms of the spherical coordinates by $\zeta=r/(Ct)$, θ and φ. The simple wave equation (1) then becomes:

$$\zeta^2(1-\zeta^2)\frac{\partial^2 p}{\partial \zeta^2}+2\zeta(1-\zeta^2)\frac{\partial p}{\partial \zeta}+\frac{1}{\sin\theta}\frac{\partial}{\partial\theta}(\sin\theta\frac{\partial p}{\partial\theta})+\frac{1}{\sin^2\theta}\frac{\partial^2 p}{\partial\varphi^2}=0 \quad (2)$$

inside the unit sphere (with $\zeta=1$) and exterior to the thin wall. The boundary conditions are

$$\frac{\partial p}{\partial\varphi}=0 \quad \text{for } \varphi=\pm 0, \pm\pi, \text{ and} -1\leq\mu\leq\frac{1}{\sqrt{2}} \qquad (3)$$

i.e. on the surfaces fo the wall. and

$$p=F(\theta,\varphi) \qquad (4)$$

on the unit sphere $\zeta=1$ and outside the wall. The solution which we consider have a jump discontinunities. The jump across the sphere is inversely proportional to the square root of the area of the ray tube, $(dS)^{1/2}$. Since all the rays reaching the sphere is come from the origin where $dS_0=0$, the jump across the sphere zero. Hence the pressure is continuous across the sphere $\zeta=1$. $F(\theta,\varphi)$ is the pressure distribution on the sphere and is defined by the solutions outside the sonic sphere in two conical variables given by [2] and [5].

By use of Bernoullis seperation method to construct the solution, the usual trial substitution $p(\zeta,\theta,\varphi)=z(\zeta)G(\mu,\varphi)$ is introduced where $\mu=\cos\theta$, then eqn (2) becomes:

$$\zeta^2(1-\zeta^2)z''(\zeta)+2(1-\zeta^2)\zeta z'(\zeta)-\lambda(\lambda+1)z(\zeta)=0 \qquad (5)$$

for $1>\zeta\geq 0$ and

$$\frac{\partial}{\partial\mu}\left[(1-\mu^2)\frac{\partial G}{\partial\mu}\right]+\lambda(\lambda+1)G+\frac{1}{1-\mu^2}\frac{\partial^2 G}{\partial\varphi^2}=0 \qquad (6)$$

for the domain in μ-φ plane with $|\varphi|<\pi$ and $-1\leq\mu\leq 1$. Since p and also G are single valued, G must be periodic in φ when $-1\leq\mu<1$, ie,:

$$G(\mu,\varphi+2\pi)=G(\mu,\varphi) \qquad (7)$$

The range of φ is therefore restricted from $-\pi$ to π and the two ends are connected by the periodicity condition(7).

The change of the variable θ to μ and the use of the seperation constant $\lambda(\lambda+1)$ are motivated by the intention of representing $G(\mu,\theta)$ by the spherical harmonics.

For eqn (6) the boundary conditions on the surfaces of the wall are

$$\frac{\partial G}{\partial\varphi}=0 \qquad \text{for } \varphi=\pm 0,\ \pm\pi,\ -1\leq\mu\leq\frac{1}{\sqrt{2}} \qquad (8)$$

p is bounded in particular at the two poles, $\theta=0$ and $\theta=\pi$ yields the following condition

$$|G|<\infty \qquad \text{at } \mu=\pm 1 \qquad (9)$$

The differential equation (6) and the boundary conditions (7) (8) (9) define an eigenvalue problem. In the next Sections the eigenvalues λ and the associated eigenfunctions, G_λ (μ,φ) are to be determined.

3. The eigenvalue problem

3.1. Construction of the solutions

The eigenvalue problem is now defined by the differential equation (6) and boundary conditions (7)(8)(9). In order to reduce the problem to that for a set of algebraic equations, two expressions of the eigenfunction G_λ (μ,φ) associated with the eigenvalue λ are to be sought; one for the region R^+, with $\mu>1/\sqrt{2}$ and the other for R^- with $\mu<1/\sqrt{2}$. These two solutions and their normal derivatives will be matched across the dividing surfaces $\mu=1/\sqrt{2}$ for $|\varphi|<\pi$.

Since the front of the plane wave is assumed prarllel to the wall, the pressure distribution on the sonic sphere centered at the corner is obviously antisymmetrical with respect to the plane $\varphi=0$. So the solutions in both the upper and lower regions are odd functions too. Thus the solution in the upper region which is periodic in φ on account of eqn (7) can be represented by the Fourier series in φ with a period of 2π:

$$G^{+}_{\lambda}(\mu,\varphi)=\sum_{m=1,2,\cdots} B_m p_{\lambda}^{-m}(\mu)\sin m\varphi \tag{10}$$

For each m, equation (6) yields the Legendre equation for $P_{\lambda}^{-m}(\mu)$:

$$\frac{d}{d\mu}\Big[(1-\mu^2)\frac{d}{d\mu}P_{\lambda}^{-m}(\mu)\Big]+\Big[\lambda(\lambda+1)-\frac{m^2}{1-\mu^2}\Big]P_{\lambda}^{-m}(\mu)=0 \tag{11}$$

Since eqn. (11) is defined for $1\geq\mu\geq-1$, $P_{\lambda}^{-m}(\mu)$ should be finite at $\mu=1$. $P_{\lambda}^{-m}(\mu)$ is identified as the generalized Legendre function defined by

$$P_{\lambda}^{-m}(\mu)=\Big(\frac{1-\mu}{1+\mu}\Big)^{m/2}F\Big\{-\lambda,\lambda+1,1+m,\frac{1-\mu}{2}\Big\} \tag{12}$$

Where F denotes the Gaussian hypergeometric function. The factor 1/r(1+m) is omitted on the right hand side of eqn. (12), since it is automatically absorbed into coefficients B_m.

For the lower region R^-, i.e., $-1\leq\mu\leq1/\sqrt{2}$ the eigenfunction G_{λ}^-, which fulfills the boundary conditions can be expressed by:

$$G_{\lambda}^-(\mu,\varphi)=\sum_{j=0,1,\cdots} D_jP_{\lambda}^{-j}(-\mu)\cos j\varphi \qquad \text{for } 0\leq\varphi\leq\pi \tag{13}$$

The argument is $-\mu$ so that the function is finite for $-1\leq\mu\leq1/\sqrt{2}<1$. To satisfy the asymmetry of the boundary data, $G_{\lambda}^-(\mu,\varphi)$ is extended to $\pi\leq\varphi\leq2\pi$ by the relation

$$G_{\lambda}^-(\mu,\varphi)=-G_{\lambda}^-(\mu,-\varphi) \tag{14}$$

Both expressions (10) and (13) fulfill the differential equation (6) and the boundary conditions (7),(8) and (9) appropriate for regions R^+ and R^- respectively.

Across the dividing surface of R^+ and R^-, where $\mu=1/\sqrt{2}$ and $0<|\varphi|<\pi$, the matching conditions are the continuity of the eigenfunction G_{λ} and its normal derivatives $\partial G_{\lambda}/\partial\mu$, The continuity of the second derivatives are then assured since both G_{λ}^+ and G_{λ}^- fulfill the differential equation (6). Thus:

$$G_{\lambda}^{+}\Big(\frac{1}{\sqrt{2}}^{+},\varphi\Big)=G_{\lambda}^{-}\Big(\frac{1}{\sqrt{2}}^{-},\varphi\Big) \qquad \text{for } 0\leq|\varphi|\leq\pi \tag{15a}$$

$$\frac{\partial G_{\lambda}^{+}\Big(\frac{1}{\sqrt{2}}^{+},\varphi\Big)}{\partial\mu}=\begin{cases}\dfrac{\partial G_{\lambda}^{-}\Big(\frac{1}{\sqrt{2}}^{-},\varphi\Big)}{\partial\mu} & \text{for } 0<|\varphi|<\pi\\ 0 & \text{for } |\varphi|=0,\pi\end{cases} \tag{15b}$$

The singularity along edges of the wall $\theta=45°$ (or $\mu=1/\sqrt{2}$) and $|\varphi|=0,\ \pi$ can be ascertained by investigating the behaviour of the local solution near the edge. By putting

$$\tilde{\mu}=\frac{1}{\sqrt{2}}-\mu$$

and $$\tilde{\varphi}=\varphi-\pi$$

and letting $|\tilde{\varphi}|\ll1$ and $|\tilde{\mu}|\ll1$, the equation (6) can be approximated by the Laplace equation

$$(1-\mu_0{}^2)\frac{\partial^2 G}{\partial\,\tilde{\mu}^2}+\frac{\partial^2 G}{\partial\tilde{\varphi}^2}=0$$

after neglecting the finite part. Since $p=0$ oustide the wall, and $p_n=0$ on the wall (Fig.2), the local solution thus behaves as that of a two-dimensional slit:

$$G\sim r^k \cos k\tau$$

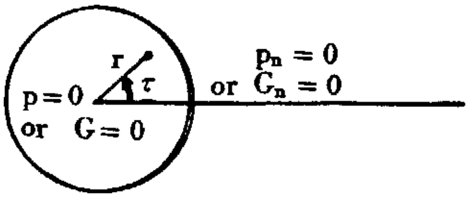

Fig.2 *Boundary conditions along the edge*

The boundary condition gives the value of k as 1/2 and the normal derivative on the edge behaves like

$$\frac{\partial G}{\partial r}\sim r^{-2/1} \qquad (16)$$

Although the eigenfunctions are continuous, its derivatives doesn't exist along the edge, but it is square integrable.

3.2. Derivation of systems of algebraic equations

For $G_\lambda{}^+(\mu,\varphi)$ and $G_\lambda{}^-(\mu,\varphi)$, the Legendre function are expressed by (12). Eqns. (15a) and (15b) can be reduced to a system of linear homogeneous algebraic equation for the unknown constants B_m and D_j by Fourier analysis. For this purpose it should be noted that for $m=$odd number$=1,3,5,\cdots$, $G_\lambda{}^+(\mu,\varphi)$ is an even function while for $m=$even number$=2,4,6,\cdots$ an odd functjon and for $j=$even number$=0,2,4,\cdots$, $G_\lambda{}^-(\mu,\varphi)$ is an odd function while for $j=1,3,5,\cdots$ an even function with respect to $\varphi=\pi/2$. Since the odd solutions and the even solutions are orthogonal to each other, the conditions of (15a) and (15b) for $G_\lambda{}^+$ and $G_\lambda{}^-$ should be fulfilled by their even terms and also by their odd term respectively. The eigenvalue and the associated even eigenfunction can be determined seperately from the eigenvalues and the associated odd function.

For $m=$odd number$=1,3,5,\cdots$ and $j=0,2,4,\cdots$, eqn. (15a) will be multiplied by $\cos l\varphi$ and integrated over the interval $0\leq\varphi\leq\pi$. An algebraic equation for the coefficients is obtained

$$\sum_{\substack{m=1,3,\cdots\\ j=0,2,\cdots}}\left[\frac{2mB_m}{m^2-j^2}P_\lambda{}^{-m}\left(\frac{1}{\sqrt{2}}\right)-\left(1+\delta_{j0}\right)D_jP_\lambda{}^{-j}\left(-\frac{1}{\sqrt{2}}\right)\frac{\pi}{2}\right]=0 \qquad (17)$$

For the same numbers of m and j, condition (15b) is multiplied by $\sin k\varphi$ and integrated over 0 and π, another algebraic equation for the coefficients is obtained:

$$\sum_{\substack{m=1,3,\cdots\\ j=2,4,\cdots}}\left[B_m\dot{P}_\lambda{}^{-m}\left(\frac{1}{\sqrt{2}}\right)\left(\frac{\pi}{2}+D_j\dot{P}_\lambda{}^{-j}\left(-\frac{1}{\sqrt{2}}\right)\frac{2m}{(m^2-j^2)}\right]=0 \qquad (18)$$

For $m=$even number$=2,4,9\cdots$and $j=$odd number$=1,3,5\cdots$,eqn.(15a) will then be multiplied by $\cos l\varphi$ and (15b) by $\sin k\varphi$ and integrated over 0 and π likewisely, two another algebraic equations are brought about:

$$\sum_{\substack{m=2,4,\cdots\\ j=1,3,\cdots}}\left[\frac{2mB_m}{m^2-j^2}P_\lambda^{-m}\left(\frac{1}{\sqrt{2}}\right)-D_jP_\lambda^{-j}\left(-\frac{1}{\sqrt{2}}\right)\frac{\pi}{2}\right]=0 \tag{19}$$

$$\sum_{\substack{m=2,4,\cdots\\ j=1,3,\cdots}}\left[B_m\dot{P}_\lambda^{-m}\left(\frac{1}{\sqrt{2}}\right)\frac{\pi}{2}-D_j\dot{P}_\lambda^{-j}\left(-\frac{1}{\sqrt{2}}\right)\frac{2m}{m^2-j^2}\right]=0 \tag{20}$$

3.3 Numerical determination of eigenvalhes

To obtain the numerical solutions the infinite series in eqns. (17),(18),(19) and (20) will be truncated with M and J. This has been proved [4] that the convergence of the eigenvalues and eigenfunctions of the truncated problem has been assumed and the eigenvalue between the matching conditions of eqns. (15a) and (15b) and the matching of the Fourier coefficients is also assumed. It is also proved there that the relation between M and J should be so chosen that the ratio M/J equals one. Here in this paper M=J=6 is thus adopted. So that eqns. (17) and (18) as well as (19) and (20) yield 2(M+J)=24 linear homogeneous equations for the 24 constants $B_1, B_2, \cdots\cdots B_{12}$ and $D_0, D_1, \cdots\cdots D_{11}$. These solutions are nontrivial only if λ is a root of the characteristic equation

$$\Delta_c(\lambda)=|a_{hi}|=0 \tag{21}$$

For the system (17) and (18)

$$a_{hi}=\frac{(2i-1)}{(2i-1)^2-[2(h-1)]^2}P_\lambda^{-(2i-1)}\left(\frac{1}{\sqrt{2}}\right) \qquad \begin{array}{r} h=1,2,\cdots,J=6\\ i=1,2,\cdots,M=6\end{array}$$

$$a_{hi}=-\frac{\pi}{4}(1+\delta_{0,(h-1)})\ \delta_{h,(j-m)}P_\lambda^{-2(h-1)}\left(\frac{1}{\sqrt{2}}\right) \qquad \begin{array}{r} h=1,2,\cdots,J=6\\ i=M+1,\cdots,M+J=12\end{array}$$

$$a_{hi}=\frac{\pi}{4}\delta_{(h-m),i}\dot{P}_\lambda^{-2(i-1)}\left(\frac{1}{\sqrt{2}}\right) \qquad \begin{array}{r} i=1,2,\cdots,\mathrm{J}=6\\ h=J+1,\cdots,(M+M=12\end{array}$$

$$a_{hi}=\frac{2(h-M)-1}{[2(h-M)-1]^2-[2(i-M-1)]^2}\dot{P}_\lambda^{-2(i-m-1)}\left(\frac{1}{\sqrt{2}}\right) \qquad \begin{array}{r} h=J+1,\cdots,J+M=12\\ i=M+1,\cdots,M+J=12\end{array}$$

While for the system of (19) and (20)

$$a_{hi}=\frac{2i}{(2i)^2-(2h-1)^2}\mathrm{P}_\lambda^{-2i}\left(\frac{1}{\sqrt{2}}\right) \qquad \begin{array}{r} h=1,2,\cdots,J=6\\ i=1,2,\cdots,M=6\end{array}$$

$$a_{hi}=-\frac{\pi}{4}\delta_{h,(i-M)}P_\lambda^{[-2(i-m)-1]}\left(-\frac{1}{\sqrt{2}}\right) \qquad \begin{array}{r} h=1,2,\cdots,J=6\\ i=M+1,\cdots,M+J=12\end{array}$$

$$a_{hi}=\frac{\pi}{4}\delta_{(h-J)i}\dot{P}_\lambda^{-2(h-J)}\left(\frac{1}{\sqrt{2}}\right) \qquad \begin{array}{r} h=J+1,\cdots,J+M=12\\ i=1,2,\cdots,M=3\end{array}$$

$$a_{hi}=\frac{2(h-J)}{[2(h-J)]^2-[2(i-M)-1]^2}\dot{P}_\lambda^{-[2(i-m)-1]}\left(-\frac{1}{\sqrt{2}}\right) \qquad \begin{array}{r} h=J+1,\cdots,J+M=12\\ i=M+1,\cdots,M+J=12\end{array}$$

Where dots over $P_\lambda^{-m}(\mu)$ refer to differentiation with respect to μ. F or the given pair of $M=6$ and $J=6$, the determinant $\Delta_c(\lambda)$ can be evaluated as a function of λ. Because of the relation

$$P_\lambda^{-\nu}(\mu)=P_{-\lambda-1}^{-\nu}(\mu) \tag{22}$$

the function is symmetrical about $\lambda=-1/2$. For the given range of λ, say $-1/2\leq\lambda\leq3.5$, the eigenvalues for this part of the problem are located by the roots of $\Delta_c(\lambda^*)=0$. When the derivative of $\Delta_c(\lambda)$ at a root $\lambda=\lambda^*$ is not zero, the coefficients B_m, D_j are proportional to the cofactors of the determinant, i.e.,

$$B_m=N_B^{-1}A_{1,k+1} \qquad k=0,1,2,\cdots,M;\ m=1,2,\cdots$$

$$D_j = N_S^{-1} A_{1,M+1+L} \qquad L=0,1,2,\cdots,J;\ j=0,1,2,\cdots\cdots$$

Where $S=1$ or 2; with N_1 denotes the constant defined by the normalization condition for the first set of equations (17 and 18; $m=1,3,\cdots$; $j=0,2,4,\cdots$), while N_2 for the second set (eqns. 19 and 20; $m=2,4,\cdots$; $j=1,3,5,\ \cdots$), i.e.,

$$\int_{\frac{1}{\sqrt{2}}}^{1} d\mu \int_0^{\mu} [G^{+}_{\lambda*}(\mu,\varphi)]^2 d\varphi + \int_{-1}^{\frac{1}{\sqrt{2}}} d\mu \int_0^{\pi} [G^{-}_{\lambda*}(-\mu,\varphi)]^2 d\varphi = 1 \tag{23}$$

The equations for N_1 and N_2 are:

$$N_1^{\,2} = \frac{\pi}{2}\left\{\int_{\frac{1}{\sqrt{2}}}^{1} \sum_{m=1,3,\cdots}^{2M-1} \left[P^{-m}_{\lambda*}(\mu) A_{1,\frac{m+1}{2}}\right]^2 d\mu \right.$$
$$\left. + \int_{-1}^{\frac{1}{\sqrt{2}}} \sum_{j=0,2,\cdots}^{2(J-1)} \left[P^{-j}_{\lambda*}(-\mu) A_{1,\frac{j+2}{2}}\right]^2 (1+\delta_{0j}) d\mu \right\} \tag{24}$$

$$N_2^{\,2} = \frac{\pi}{2}\left\{\int_{\frac{1}{\sqrt{2}}}^{1} \sum_{m=2,4,\cdots}^{2M} \left[P^{-m}_{\lambda*}(\mu) A_{1,m/2}\right]^2 d\mu \right.$$
$$\left. + \int_{-1}^{\frac{1}{\sqrt{2}}} \sum_{j=1,3,\cdots}^{(2J-1)} \left[P^{-j}_{\lambda*}(-\mu) A_{1,(j+1)/2}\right]^2 d\mu \right\} \tag{25}$$

By a numerical program the eigenvalues of the lst and 2nd set of the determinants are determined and the coefficients belonging to each λ are obtained and tabulated below:

	$\lambda=0.2954$	$\lambda=1.4248$	$\lambda=2.0391$	$\lambda=2.4795$	$\lambda=3.1440$	$\lambda=3.4953$
B_1	-7.16288×10^{-1}	2.01873	8.25470×10^{-1}	-3.82423	1.34669	$-4.923.44$
B_3	-6.86121×10^{-1}	1.04923	-3.67672	-9.83673×10^{-1}	-9.07537	-1.95304
B_5	-1.89302	3.08676	-5.37737	-2.45695	-1.11275×10	-1.15350
B_7	-7.16099	1.19176×10	-1.67208×10	-9.92521	-3.38143×10	-5.03899
B_9	-3.33079×10	5.62043×10	-6.99883×10	-4.84279×10	-1.40566×10^{2}	-2.59818×10
B_{11}	-2.25658×10^{2}	3.86899×10^{2}	-4.37529×10^{2}	-3.45948×10^{2}	-8.82509×10^{2}	-1.97036×10^{2}
D_0	-5.45418×10^{-1}	-8.09500×10^{-1}	-2.44411×10^{-1}	-8.98648×10^{-1}	-4.73302×10^{-1}	7.82393×10^{-1}
D_2	1.43911×10^{-2}	-1.66298×10^{-1}	-3.22036	-1.80261	-7.83749	4.65323
D_4	8.45154×10^{-4}	-3.20195×10^{-2}	-4.57067×10^{-3}	-1.33905×10^{-2}	7.60879×10^{-2}	1.27953×10^{-1}
D_6	7.99126×10^{-5}	-2.26414×10^{-4}	2.80292×10^{-4}	5.07442×10^{-4}	1.71854×10^{-3}	1.15571×10^{-3}
D_8	9.30607×10^{-6}	-2.28582×10^{-5}	2.72872×10^{-5}	-3.90014×10^{-5}	1.17734×10^{-4}	5.70147×10^{-5}
D_{10}	1.26006×10^{-6}	-2.83174×10^{-6}	3.37377×10^{-6}	4.09645×10^{-6}	1.19833×10^{-5}	4.65793×10^{-6}

	$\lambda=1.1299$	$\lambda=2.2848$	$\lambda=3.0092$	$\lambda=3.4051$
B_2	-1.68744	4.50867	2.80098	1.01421×10
B_4	-2.26381	4.20257	-7.52432	5.61075
B_6	-6.79367	1.2354×10	-1.04935×10	1.47895×10
B_8	-2.66980×10	4.81284×10	-3.13769×10	5.74324×10
B_{10}	-1.26718×10^{2}	2.27893×10^{2}	-1.27040×10^{2}	2.73351×10^{2}
B_{12}	-8.66149×10^{2}	1.56374×10^{3}	-7.63452×10^{2}	1.90252×10^{3}
D_1	-1.69925	-3.89283	-1.06215	6.12147
D_3	9.33711×10^{-3}	-1.32916×10^{-1}	-6.69116	3.24872
D_5	-5.80530×10^{-4}	-2.81713×10^{-3}	-1.91604	-1.87143×10^{-2}
D_7	-5.61049×10^{-5}	-1.95200×10^{-4}	1.10846	-6.79087×10^{-4}
D_9	6.62528×10^{-6}	-1.93937×10^{-5}	1.04728×10^{-5}	-5.02826×10^{-5}
D_{11}	9.07635×10^{-7}	-2.38166×10^{-6}	1.28081×10^{-6}	-5.16359×10^{-6}

Table 1.

4. Construction of the conical solution

4. 1. The numerical determination of associated function $Z_\lambda(\zeta)$

The eigenvalues λ's and the eigenfunctions G_λ of eqn. (6) are determined in the preceeding sections. For the determination of the conical solution inside the unit sphere, it is necessary to construct the solution $z_\lambda(\zeta)$ of the differential equation (5) for the given λ subject to the boundary conditions at $\zeta=0$ and $\zeta=1$, they are:

$$z(0)<\infty \quad \text{and } z(1)=1 \tag{26}$$

Since $\zeta=0$ and $\zeta=1$ are the regular singular points the solution to be finite at $\zeta=0$ can be represented by the power series:

$$z_\lambda(\zeta)=a_0\zeta^\lambda\left[1+\frac{\lambda(+1)}{4\lambda+6}\zeta^2+\cdots\right] \tag{27}$$

By setting $a_0=1$, the differential equation can be integrated numerically from a small value of ζ_0 (say 0.001) with the initial data:

$$\tilde{z}_\lambda(\zeta_0)=\frac{z_\lambda(\zeta_0)}{a_0}=\zeta_0{}^\lambda\left[1+\frac{\lambda(\lambda+1)}{4\lambda+6}\zeta_0{}^2\right] \tag{28}$$

and

$$\tilde{z}'_\lambda(\zeta_0)=\lambda\ \zeta_0{}^{\lambda-1}\left[1+\frac{(\lambda+1)(\lambda+2)}{4\lambda+6}\zeta_0{}^2\right] \tag{29}$$

The numerical integration for $\tilde{z}_\lambda(\zeta)$ is continued until ζ is clase to 1 (say 0.99).

For the determination of $\tilde{z}_\lambda$ (1), the values of $\tilde{z}_\lambda$ (ζ) and $\tilde{z}'_\lambda$ (ζ) at the last station are matched with those given by the series solution of $\zeta-1$, which is valid only in the neighbourhood of $\zeta=1$

i. e.,

$$\widetilde{z_\lambda}(\zeta)=\widetilde{z_\lambda}(1)\left\{1+\frac{\lambda(\lambda+1)}{2}(1-\zeta)\log(1-\zeta)\,[1+O(1-\zeta)]\right\}$$
$$+a_1\,(1-\zeta)\,\{1+O\,(1-\zeta)\} \tag{30}$$

Since the problem is linear, the correct solution is $z_\lambda(\zeta)=\widetilde{z_\lambda}(\zeta)/\widetilde{z_\lambda}(1)$ and the correct value for a_1 in eqn. (30), which is needed to start the numerical integration is

$$a_1=\frac{-\widetilde{z_\lambda}'(\zeta)}{\widetilde{z_\lambda}(1)}-\frac{\lambda(\lambda+1)}{2}[1+\log(1-\zeta)] \tag{31}$$

Thus for a given boundary data on the sonic sphere $F(\mu, \varphi)$ (s. eqn. (4)) which is defined by the solutions outside the sonic sphere in two conical variables ρ and τ (ref. next section)

4. 2. 2-dimensional conical solution

Outside the unit sphere, the solutions are given by the two-dimensional conical solutions of Keller and Blank [2].

Following Ting [5], the thin wall can be represented by segment OA on the y-axis with EAB as x'-axis (Fig. 3). If ϵ is the shock strength of weak shock defined as $(p_1-p_0)/p_0$, where p_0 and p_1 are the pressure in front and behind the shock respectively.

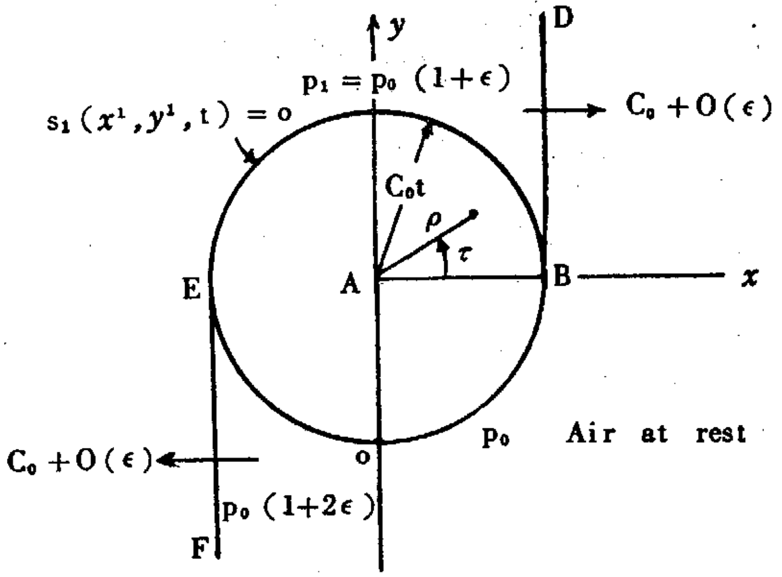

Fig. 3. *Plane pulse hits a 2-d. thin wall.*

After hitting the wall, $t\geq 0$. part of the shock BD advances into still air undisturbed, the disturbed pressure behind BD is $p_0\,\epsilon$, while the other part EF is reflected. The disturbed pressure behind the shock EF is $2\epsilon p_0$, *i. e.* with double intensity. The disturbance due to the edge A is confined inside the Mach cone

$$S_1(x', y', t)=\rho-C_0t=\sqrt{x'^2+y'^2}-C_0t=0 \tag{32}$$

Since p is defined as the nondimensionalized perturbed pressure by

$$p=\frac{p'}{p_0\epsilon} \tag{33}$$

The diffraction by either one of the edges of the openning is given by a two-dimensional conical solution and the Busemann conical transformation is introduced

$$\rho^*=\overline{\rho}/[1+(1-\overline{\rho}^2)^{1/2}] \tag{34}$$

with

$$\overline{\rho}=r/Ct$$

$$\tau^*=\tau$$

In these new variables ρ^* and τ^*, the simple wave equation for p reduces to a Laplace equation

$$p_{\rho_*\rho_*}+(1/\rho^*)p_{\rho_*}+(1/\rho^{*2})p_{\tau_*\tau_*}=0 \tag{35}$$

After taking out 1 from the dimensionalized pressure the boundary conditions become an odd function of τ^* (as shown in Fig. 4)

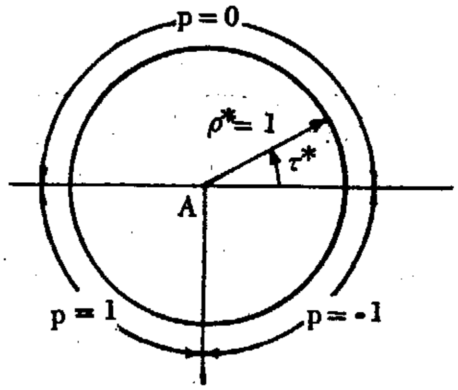

Fig. 4, z-plane

In order to Solve for $p(\rho^*, \tau^*)$, the exterior of the thin wall in the z-plane is mapped into the upper half of the w-plane (Fig. 5) by the transformation

$$w=\Omega e^{\lambda\omega}=(iz)^{1/2} \tag{36}$$

Using the reflection principle p is extented into the whole circle and a boundary value problem in the unit circle is obtained and the solution is [5]

$$p_c(\omega)=\frac{1}{\pi}\arctan\frac{1-\Omega^2}{1+\Omega^2+2\sqrt{2}\cos\omega}-\frac{1}{\pi}\arctan\frac{1-\Omega^2}{1+\Omega^2-2\sqrt{2}\cos\omega} \tag{37}$$

The arctangent is taken in the interval o and π. It is clear that from the result above, the pressure in front of and behind the wall are different.

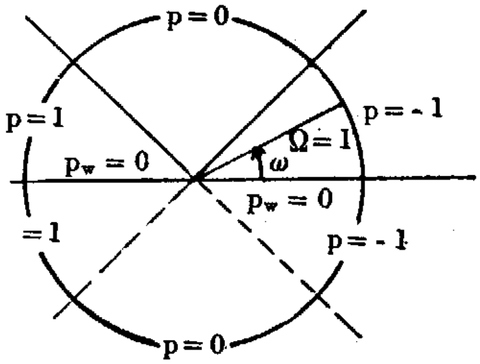

Fig. 5, *ω-plane*

The surface of the unit sphere is to be divided into four regions (Fig. 6)

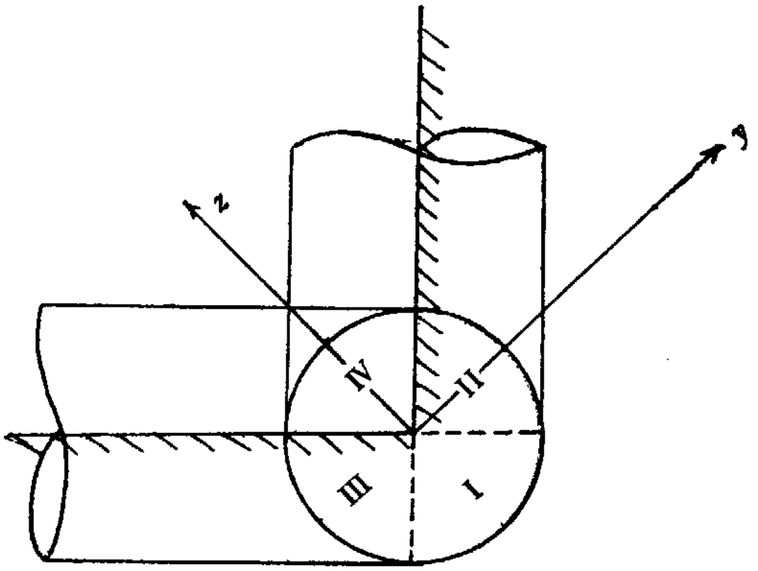

Fig. 6, *Four regions on the unit sphere*

(1) not covered by either of these circular cylinders
(2) covered only by the cylinder with axis OA
(3) covered only by the cylinder with axis OB
(4) covered by both cylinders.

With the plane $\varphi=0$ defined as the plane of the thin wall and for the relationship between μ, φ and x, y, z expressed by

$$\begin{aligned} x&=\sqrt{1-\mu^2}\ \sin\varphi \\ y&=-\sqrt{1-\mu^2}\ \cos\varphi \\ z&=\mu \end{aligned} \tag{38}$$

the four regions and the boundary data are defined as:

(1) Region I

$$0\le x\le 1,\ -\frac{\sqrt{2(1-x^2)}}{2}\le y\le\frac{\sqrt{2(1-x^2)}}{2},\qquad z=-\sqrt{1-x^2-y^2}\ \text{(in front of the wall)}$$

$$F(\mu,\ \varphi)=1 \tag{39}$$

$$-1\le x\le 0,\ -\frac{\sqrt{2(1-x^2)}}{2}\le y\le\frac{\sqrt{2(1-x^2)}}{2},\qquad z=-\sqrt{1-x^2-y^2}\ \text{(behind the wall)}$$

$$F(\mu,\ \varphi)=-1 \tag{40}$$

(2) Region II:

$$-1\le x\le 1-\frac{\sqrt{2(1-x^2)}}{2}\le z\le\frac{\sqrt{2(-x^2)}}{2},\qquad y=\sqrt{1-x^2-z^2}$$

$$F(\mu,\ \varphi)=p_c(\bar{\rho}_1,\ \tau_1) \tag{41}$$

(3) Region III:

$$-1\le x\le 1,\ -\frac{\sqrt{2(1-x^2)}}{2}\le z\le\frac{\sqrt{2(1-x^2)}}{2},\qquad y=-\sqrt{1-x^2-z^2}$$

$$F(\mu,\ \varphi)=p_c(\bar{\rho}_2,\ \tau_2) \tag{42}$$

(4) Region IV:

$$-1\le x\le 1,\quad -\frac{\sqrt{2(1-x^2)}}{2}\le y\le \frac{\sqrt{2(1-x^2)}}{2},\qquad z=\sqrt{1-x^2-y^2}$$

$$F(\mu,\ \varphi)=p_c(\overline{\rho}_1,\ \tau_1)+p_c(\overline{\rho}_2,\ \tau_2) \tag{43}$$

Where p_c is defined by eqn. (37) and $\overline{\rho}_i$, τ_i are defined by:

$$\overline{\rho}_i=(a_i+b)^{1/2}\qquad (i=1 \text{ or } 2)$$

with $$b=\sqrt{1-\mu^2}\ \sin\varphi$$

$$a_1=\begin{cases} R\ \cos\left(\frac{\pi}{4}-\alpha\right)\\ R\ \sin\left(\frac{\pi}{4}-\alpha\right)\\ -R\ \sin\left(\frac{\pi}{4}-\alpha\right)\\ -R\ \cos\left(\frac{\pi}{4}-\alpha\right)\end{cases}\qquad a_2=\begin{cases} R\ \sin\left(\frac{\pi}{4}-\alpha\right) & \text{for } z\ge 0,\ y\le 0\\ R\ \cos\left(\frac{\pi}{4}-\alpha\right) & \text{for } z\ge 0,\ y\ge 0\\ -R\ \cos\frac{\pi}{4}-\alpha) & \text{for } z\le 0,\ y\le 0\\ -R\ \sin\frac{\pi}{4}-\alpha) & \text{for } z\le 0,\ y\ge 0\end{cases}$$

with $$R=[1-(1-\mu^2)\ \sin^2\varphi]^{1/2}$$

$$\alpha=\cos^{-1}\left|\frac{\varphi}{R}\right|$$

$$\tau_i=\begin{cases}\pi-\sin^{-1}(a_i/\overline{\rho}_i) & \text{for } x\ge 0\\ \sin^{-1}(a_i/\overline{\rho}_i) & \text{for } x\le 0\end{cases}$$

4.3. The 3-dimensional conical solution

The disturbance pressure $p(\zeta,\ \theta,\ \varphi)$ inside the unit sphere can be represented by the eigenfunction expansion:

$$p(\zeta,\ \mu,\varphi)=\sum_{\lambda} K_\lambda\ Z_\lambda(\zeta)G_\lambda(\mu,\ \varphi) \tag{44}$$

with the eigenvalues λ and eigenfunctions $G_\lambda\ (\mu,\ \varphi)Z_\lambda(\zeta)$ and the boundary conditions on the unit sphere ($\zeta=1$), $F(\mu,\ \varphi)$, which are described in the previous section and are add functions with respect to the plane $\varphi=0$, the coefficients K_λ can be determined from the boundary data by the following expression:

$$K_\lambda=\frac{\iint G_\lambda(\mu,\ \varphi)F(\mu,\ \varphi)\ d\mu\ d\varphi}{\iint G_\lambda^2(\mu,\ \varphi)\ d\mu\ d\varphi}$$

$$=\frac{1}{2}\left\{\int_{\frac{1}{\sqrt{2}}}^{1} d\mu\ \int_{-\pi}^{\pi} G_\lambda^{+}(\mu,\ \varphi)F(\mu,\ \varphi)d\varphi+\int_{-1}^{\frac{1}{\sqrt{2}}} d\mu\int_{-\pi}^{\pi} G_\lambda^{-}(\mu,\ \varphi)\ F(\mu,\ \varphi)d\varphi\right\}$$

The factor 1/2 is due to the normalization condition for G_λ in which the integration with respect to φ is carried over only half the interval. In the numerical determination of K_λ the double integral can be reduced to a line integral, since the boundary data and the eigenfunctions are odd functions in φ. The result are:

$$K_\lambda=\int_{\frac{1}{\sqrt{2}}}^{1} \sum_{m=1,2,\ldots} B_m\ P_\lambda^{-m}(\mu)f_m(\mu)d\mu$$

$$+\int_{-1}^{\frac{1}{\sqrt{2}}} \sum_{j=0,1,\cdots} D_j P_\lambda^{-j}(-\mu)f_j(\mu)d\mu \tag{45}$$

where

$$f_m = \int_0^{\pi} F(\mu, \varphi) \sin m\varphi \, d\varphi$$

$$f_j = \int_0^{\pi} F(\mu, \varphi) \cos j\varphi \, d\varphi$$

Obviously,

$$f_m = 0 \qquad \text{for } m = 2, 4, 6, \cdots$$

$$f_j = 0 \qquad \text{for } j = 1, 3, 5, \cdots$$

hence eqn. (45) can further be simplified as:

$$K_\lambda = \int_{\frac{1}{\sqrt{2}}}^{1} \sum_{m=1,3,\ldots} B_m P_\lambda^{-m}(\mu) f_m(\mu) d\mu + \int_{-1}^{\frac{1}{\sqrt{2}}} \sum_{j=0,2,\ldots} D_j P_\lambda^{-j}(-\mu) f_j(\mu) d\mu \tag{46}$$

By the numerical program K_λ are Calculated:

λ	K_λ
0.2954	−1.76159
1.4248	−0.20696
2.0391	−0.02628
2.4796	0.11333
3.1440	−0.00714
3.4953	−0.05403

Table 2

5. Results and conclusion

In this paper, a conical solution for the diffraction of a plane acoustic pulse by the corner of a rectangular opening in the wall of a structure is obtained by seperation of variables.

With the knowledge of K_λ, the pressure distribution due to the diffraction of the plane pulse inside the sphere is given by eqn. (44) and the pressure distribution along the edge of the opening outside the sonic sphere is given by eqn. (37). Fig. 7 shows the pressure distribution along rays θ=const. on the wall. Fig. 8 shows the pressure variation with time at points $x=0$, -0.5 and -1.0 along the line normal to the wall through the center of the opening. The discontinuities in the slopes of the pressure occur at the crossing of the sonic cones around an edge and that of the sonic sphere. It is shown that the pressure decays faster as time goes on at points with larger value of θ.

With the pressure distribution as function of time and space obtained, the vibration phenomenons of the structure can further be studied.

Acknowledgement

The author gratefully acknowledges Professor Lu Ting(丁汝博士), Department of Mathematics, New York University for his valuable comments and many helpful discussions, and also wishes to thank Mrs. Fanny Kung (弓鄒鈺勳女士) for her many assistances in the programming.

References

1. Fried lander, F. G., "Sound Pulse", Cambridge University Press, New York, 1958.
2. Keller, J. B. and Blank, A., "Diffraction and Reflection of Pulses by Wedges and Corners," Communication on Pure and Applied Mechanics, Vol. 4, No. 1, pp. 75-94, June 1951.
3. Busemann, A., "Infinitesimale Kegelige Ueberschallstroemung," Deut. Akam. der Luft., (1942-43)
4. Ting, L. and Kung, F., "Diffraction of a pulse by a three-dimensional corner," NASA Contractor Report CR-1728, Washington, D. C. March, 1971
5. Ting, L., "Diffraction and reflection of weak shocks by structures," Journal of Math. & Physics, Vol. XXXII, July-October 1953.

矩形開口對平面脈衝波的繞射

王懷柱

摘要

超音速航機飛行時所產生之音爆波達於地面時，對建築物而言，可視爲平面波。本文乃分析建築物之窗戸對此等平面脈衝波所引起之繞射與反射等情形。利用變數分離法將波動方程式的解寫出。三維現象僅出現於以各窗角爲中心之音球內。在此音球中之解則係連帶特徵値問題。此問題經過一系列過程後可化成線性代數的聯立方程式。再藉數値法求得特徵値及其所屬之特徵函數，從而得到平面波繞射之錐形解。

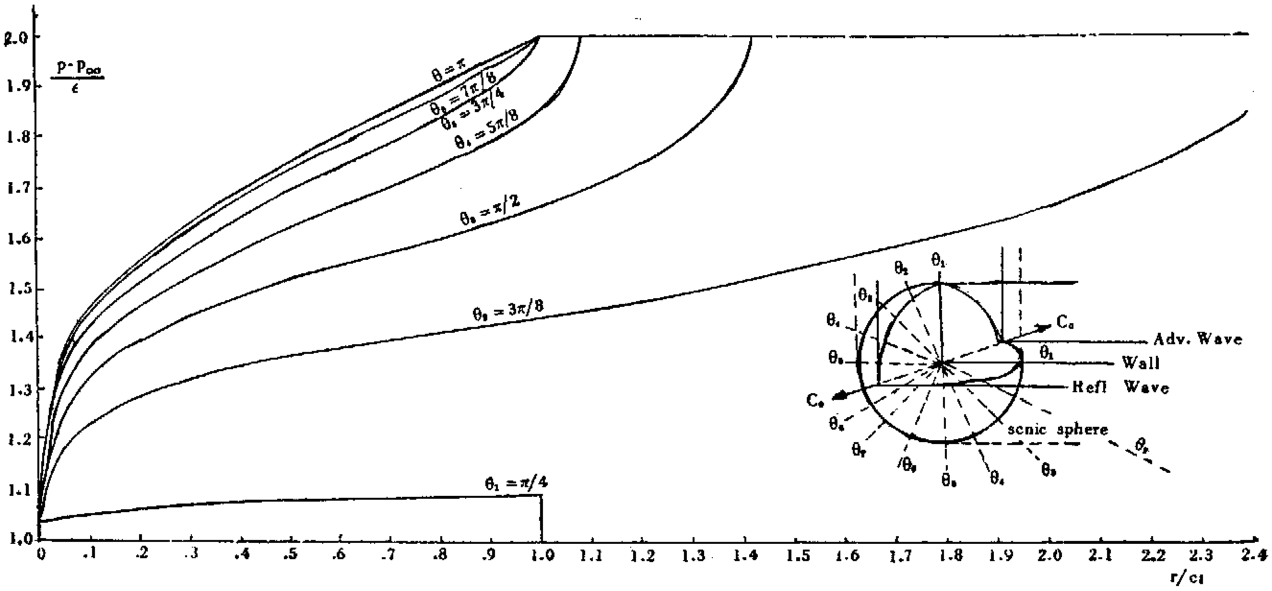

Fig.7. Pressure distribution on the wall $(\varphi = 0, \pi)$ along θ=const. inside the sonic sphere

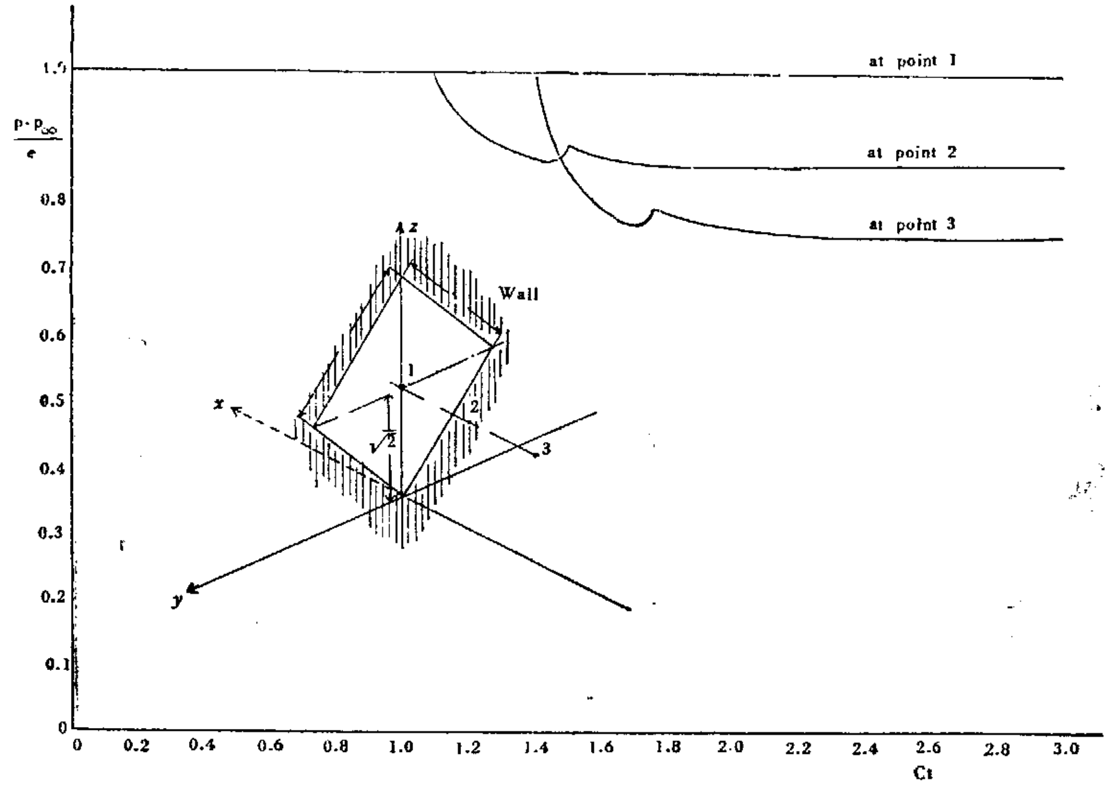

Fig.8. Pressure Variation at points along the Line normal to the Wall through the center of the opening.

Annual Report of the Institute of Physics, Academia Sinica, 1971

船舶縱向下水之探討

李雅榮、戴堯天(Yau-Tien Dai)、劉衿友、陳義男、汪群從(Chun-Tsung Wang)

一、緒　　言

在有限度港灣之海面上，超大型船舶下水時，船之運動性能及其停止位置之預測，對於船舶是否能安全下水是一個重要問題。

近年來，更由於船舶建造趨於大型化，相對的，船臺前面之下水海面就變得狹窄了。因此對於預測船下水之運動性能，在準確度上，其要求亦就更加嚴格，基於此點，我們很迫切需要尋找出一種精確度較高之分析方法，來適應此種造大型船舶的趨勢。

對於預測船舶下水之運動性能，宮下（1961）曾由力量平衡關係，導出船舶下水方程式並解出其速度變化情形，但這只是理論上之解析而已，事實上在分析中，浮力及水阻力係數很難用函數關係表示出來。因此速度分佈就不可能用宮下氏之方法求出其眞正解。本文利用幾何關係求出下水過程任一位置之浮力，並取用水阻力係數的統計値（ Andrews, 1946），求出下水速度變化之近似解。

本文同時依據梶田（1966）所導出實船與船模間之相似法則，將臺船下水資料較完整之 28,000 載重噸散裝貨輪做成船模，並仿照臺船之下水臺做成模型，而後加以實驗，測出下水速度之分佈情況。

最後從臺船公司取得上述 28,000 載重噸散裝貨輪下水時所觀測的資料，與理論分析及船模實驗所得之結果，相互比較，以求印證。

二、理論分析

當下水角度甚小時，船舶下水之運動方程式爲（宮下，1961）

$$(\theta-C_f)(W-B)-C_dW'=\frac{W+W'}{2g}\frac{dV^2}{dx}+C_W\ B^{2/3}V^2 \tag{1}$$

其中 θ：船體龍骨之斜角；C_f：擦摩阻力係數；W：船體之重量；B：船之浮力；C_d：制動鎖阻力係數；W'：制動鎖之重量；V：船隻下水速度；

解 V 可得

$$V=\sqrt{\exp\left[-\int_0^x P(x)\,dx\right]\left\{\int_0^x Q(x)\exp\left[\int_0^x P(x)dx\right]dx\right\}} \tag{2}$$

式中

$$P(x)=\frac{2g}{W+W'}C_W\ B^{2/3}$$

$$Q(x)=\frac{2g}{W+W'}\left[(\theta-C_f)(W-B)-C_d\ W'\right]$$

在下水過程中， C_f 與 C_d 之變化很小，可視爲常數。C_W 隨浮力而變化，即$C_W=\left(\frac{B}{W}\right)$（Andrews, 1946），$B(x)$ 可由船舶外形，下水臺形狀及下水過程求得。

以臺船公司 28,000 載重噸散裝貨輪爲分析對象，其浮力，速度之計算結果如圖一及二所示(李雅榮1972).

三、船模下水實驗

1. 理論根據

模型下水試驗的相似條件爲（梶田，1966）：

1.模型與原型中之船體、船臺、海面情況必須幾何相似，而其縮小比例爲$\alpha_L=\frac{L_M}{L_S}$

2.模型與原型在時間上之比爲$\alpha_T=\frac{T_M}{T_S}$則$\alpha_T=\sqrt{\alpha_L}$

3.模型與原型之速度比爲$\alpha_V=\frac{V_M}{V_S}$，則$\alpha_V=\sqrt{\alpha_L}$

4.模型與原型之加速度比爲$\alpha_A=\frac{A_M}{A_S}$，則$\alpha_A=1$

5.模型與原型之質量比爲$\alpha_M=\frac{M_M}{M_S}$，則$\alpha_M=\alpha_\rho\alpha_L^3$

其中$\alpha_\rho=\frac{\rho_M}{\rho_S}$（流體密度比）

6.模型與原型所受外力(如摩擦阻力，制動鎖阻力等)之比爲$\alpha_F=\frac{F_M}{F_S}$，則$\alpha_F=\alpha_\rho\alpha_L^3$

2. 實驗裝備：

將臺灣造船公司已下水之28,000載重噸散裝貨輪及其下水臺按以上之相似法則作成不安定模型

取$\alpha_L=\frac{1}{100}$　　$\alpha_\rho=\frac{\rho_{\text{淡水}}}{\rho_{\text{海水}}}\doteq 1$

則：$\alpha_V=\frac{1}{10}$

$\alpha_T=\frac{1}{10}$

$\alpha_A=1$

$\alpha_M=\frac{\alpha_\rho}{(100)^3}=10^{-6}$

$\alpha_F=10^{-6}$

其實驗設備如圖三所示。

3. 實驗結果：

將製成之船模循一定實驗步驟(李雅榮，1972)進行下水試驗，試驗結果換算成實船試驗結果如圖二所示。

四、結　　論

使用宮下（1961）之船舶下水理論，假設等值之摩擦力係數及制動鎖阻力係數，並取用統計數值之水阻力係數，所計算之結果與船模實驗及實船下水之結果比較，除艉浮起後一段因係一不穩定過程而略有差異外，其餘結果尙甚接近。

圖二同時顯示該散裝貨輪下水時之速度變化情形，該船實長 168m，因之從下水開始到船停止之距離不超過二個船長。

參考資料實

宮下季郎，福井隆雄，篠崎省吾　進水速力に關する研究　造船協會論文集110號，12, 1961

梶田悅司　模型進水試驗法について　造船協會論文集 119號　1966

B. Andrews　Some practical aspets of ship launching　SNAME 1946, P. 424～437

福井隆雄　進水速力に關する研究　造船協會論文集 111號　6, 1962

李雅榮　船舶縱向下水之探討，　臺灣大學碩士論文，　民國六十一年六月

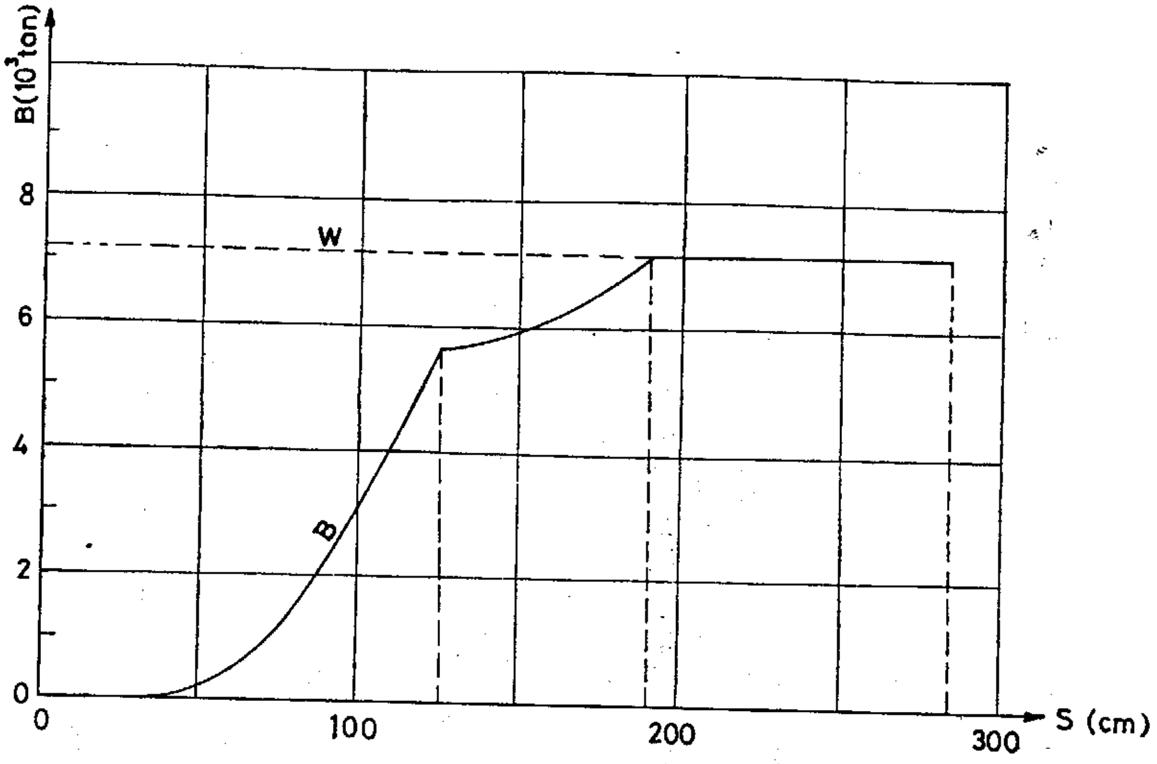

圖一　浮力與距離關係圖

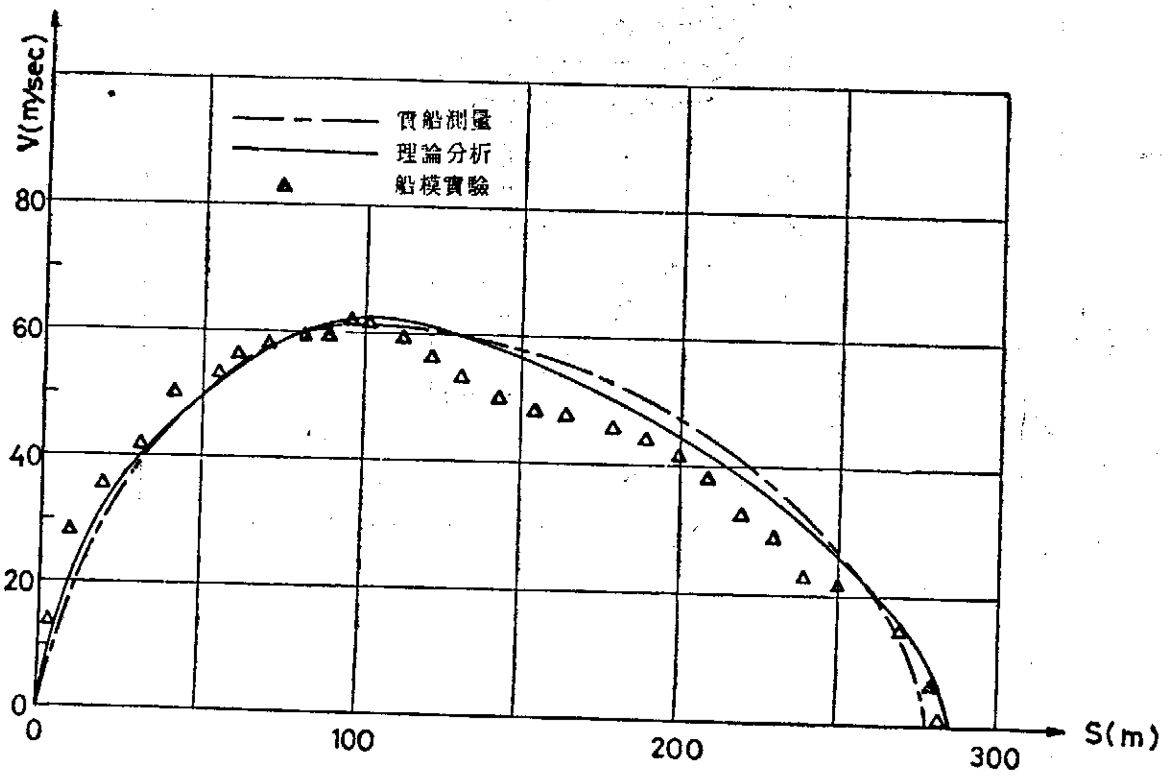

圖二　速度距離關係圖

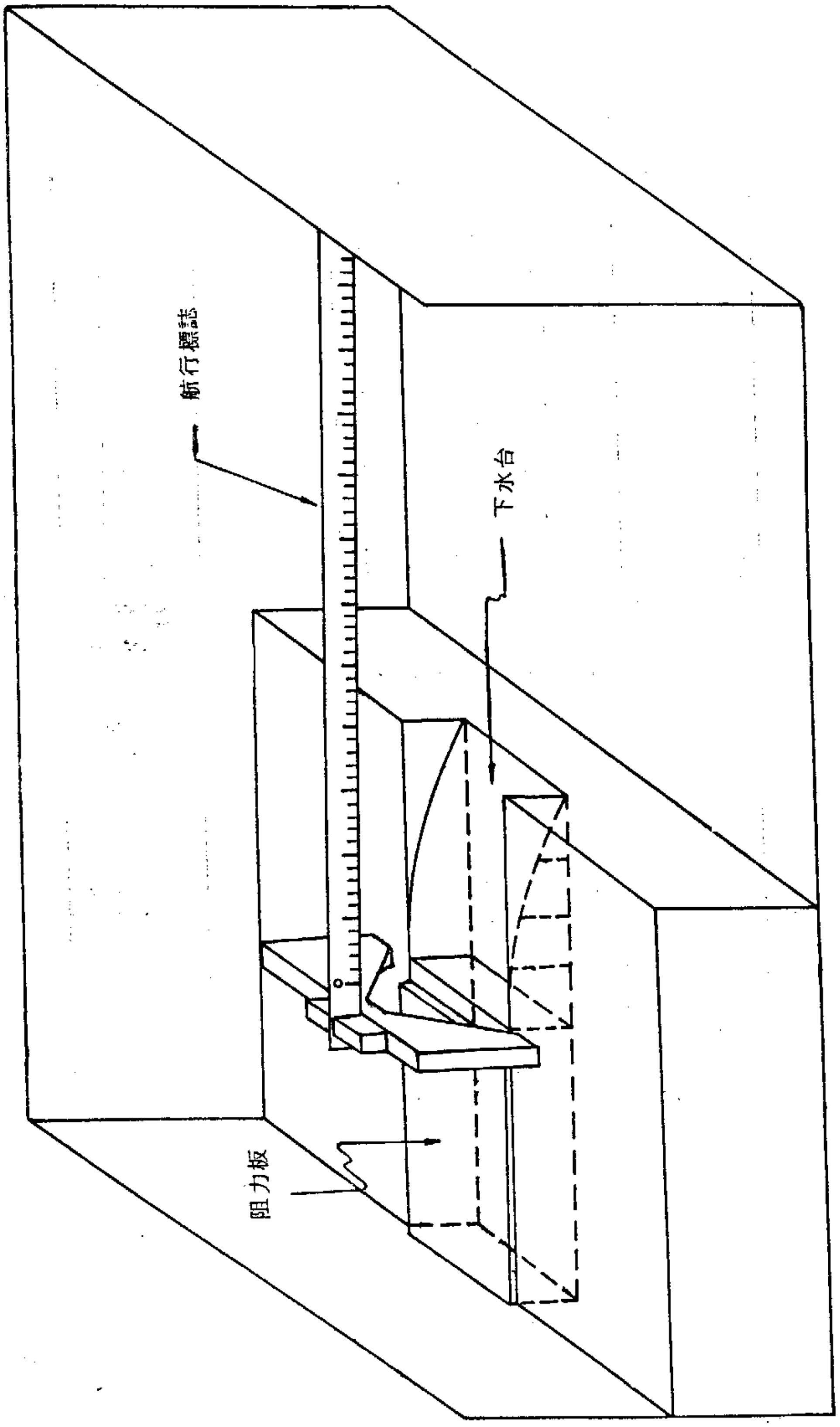
航行標誌
下水台
阻力板

圖三 船模下水實驗裝置